THE FLOW STRUCTURE OF INTERACTING BARCHAN DUNES

BY

JESSICA ANN PALMER

THESIS

Submitted in partial fulfillment of the requirements
for the degree of Master of Science in Geology
in the Graduate College of the
University of Illinois at Urbana-Champaign, 2010

Urbana, Illinois

Adviser:

Professor James L. Best

ABSTRACT

High-resolution particle-image velocimetry (PIV) experiments have been conducted over a fixed-bed to examine the effects of interacting barchan dunes on the flow structure. The barchan dune models were based upon an idealized contour map, the shape and dimensions of which were based upon previous empirical studies of dune morphology. The experimental setup comprised two, co-axially aligned barchan dune models that were spaced at different distances apart. Three volumetric ratios (V_r, upstream barchan dune: downstream barchan dune) of 0.025, 0.056, 0.175, replicated the different behaviors of interacting barchan dunes as observed in the field and laboratory by Endo *et al.* (2004), and were accompanied by an investigation of identically-sized dunes. Models were placed in an Eiffel-type, open-circuit wind tunnel with a working test-section 6090 mm long by 914 mm wide by 457 mm high and a free-stream turbulence intensity of 0.16%. Flow quantification was achieved using particle imaging velocimetry (PIV) at 0.5Hz. PIV measurements of the mean and turbulent flow field were made in the streamwise–wall-normal plane, along the centerline of the barchans(s), at an average Reynolds number of 59,000.

The presence of an upstream barchan dune of equal volume to the downstream barchan dune (V_r=1) induces a 'sheltering effect' on the flow, manifested by a significantly shorter separation bubble and both reduced streamwise velocity and turbulence intensity in the downstream barchan dune leeside, as compared to an isolated barchan. The volumetric ratio associated with the 'splitting' behavior (V_r=0.175) of Endo *et al.* (2004) shows enhanced turbulence production over the downstream barchan dune leeside, that is proposed to be caused by interacting shear layers from the up- and down- stream dunes. The upstream dune also creates a shear layer in its leeside that extends onto the stoss-side of the downstream barchan, and is proposed to be responsible for dune 'splitting'. For volumetric ratios associated with 'ejection' and 'absorption' behaviors (Vr=0.056 and 0.025, respectively), the upstream barchan dune does not significantly impact the flow in the leeside of the downstream barchan dune. In these cases, the small coherent turbulent structures generated from the upstream dune lose their coherence before reaching the downstream barchan crest, or may reach the downstream dune shear layer but are too insignificant in intensity and size to interact with the larger flow structures generated in

the leeside of downstream barchan dune. The upstream dune leeside for the ‘ejection’ and ‘absorption’ behaviors is characterized by smaller separation zone lengths, and smaller turbulence intensities, than the ‘splitting’ behavior. In this case, it is speculated the potential for downstream erosion is reduced and the downstream barchan maintains its morphology.

Dedicated to Marie, Ngaio & Mom:
Thank you for your endless support

ACKNOWLEDGMENTS

I would like to extend my sincere gratitude to Professor Kenneth T. Christensen for the use of his facilities and equipment and especially the wonderful opportunity to work and interact with his research group. I acknowledge Professor Kenneth T. Christensen, Ricardo Mejia-Alvarez, Dr. Gianluca Blois, Hannah Min and Professor Bruce L. Rhoads for their insight, assistance, and invaluable contribution to this work. Ricardo Mejia-Alvarez was instrumental in the preparation and execution of the experiments, the data processing and post-processing, as well as providing insight towards the interpretation of the results. Gianluca Blois was indispensable as a guide throughout the experimental and writing phases, and played an important role as an editor. Hannah Min infused energy and enthusiasm into the last weeks of experimenting at a time when my own energy was lacking, and I am truly grateful to her. I would also like to thank Yanhua (Felix) Wu for my introduction to PIV. There is not enough space to adequately express the contributions of Professor Jim L. Best, but I will summarize in a few words: guidance, patience, encouragement, and time. Without Jim, none of this would have been possible and I am truly grateful. His patience never tired, and for that I am truly indebted! Finally, I would like to acknowledge the support and encouragement extended to me by my family and also my dear friends, especially the Hussey family, Emma Swift, Mara Morgenstern, Holli Burgon and Alex Petroff. The completion of my thesis was made possible by the Jackson Award, established and supported by Dr. Roscoe Jackson, an alumnus of the Department of Geology.

TABLE OF CONTENTS

CHAPTER 1

INTRODUCTION

1.1 Rationale and approach

The Earth's surface is sculpted by geologic processes. Geologists refer to the geologic process of weathering, erosion, sediment transport and deposition as *gradation*, which pertains to any planet exhibiting an atmosphere and rocky surface, criteria that Earth, Mars, Venus and, tentatively, Saturn's sixth moon, Titan, fall under (Greeley and Iverson, 1985). While all of the above mentioned planets display aeolian features, only planet Earth has liquid water at the surface, the implication being that only Earth displays aeolian *and* subaqueous features. The Earth's surface is divided into landmass and water, yet bedforms (such as ripples and dunes) are ubiquitous. The unifying link is that water and air are both fluids capable of initiating sediment transport through the shear stress they exert on a surface. There is a density disparity between water (998.2 kgm^{-3} at 20°*C*) and air (1.205 kgm^{-3} at 20°*C*). However, two different fluid mediums with the same Reynolds number are considered 'dynamically similar' as they are presumed to produce similar turbulent flow phenomena (Greeley and Iverson, 1985).

A bedform is a sedimentary structure composed of grains found upon a more or less flat, grain-dominated or hard floor, or found superimposed upon another bedform. Wilson (1972) defined a bedform as 'a regularly repeated pattern which forms on a solid surface because of the shearing action of a fluid'. The term 'bedform' includes both ripples and dunes. The primary distinction between subaerial ripples and dunes lies in their respective mechanisms of formation (Wilson, 1972; Greeley and Iverson, 1985). A subaerial ripple forms due to impacting saltating grains; a subaerial dune forms due to flow effects. Moreover, a dune is characterized by either a greater sediment size and/or flow velocity (Allen, 1997). The dimensions of a ripple are orders of magnitude below that of a dune; moreover, ripples migrate and change morphology at a significantly faster time scale than dunes (Wilson, 1972; Greeley and Iverson, 1985). The origin of the ripple-dune transition ultimately lies within the flow structure (Bennett and Best, 1996; Lopez *et al*., 2000; Robert and Uhlman, 2001; Schindler and Robert, 2005).

The aeolian dune morphology, size and velocity are functions of the flow direction and speed, vegetation, topography, sediment supply, and groundwater salinity (Langford *et al*., 2009). The

origin, evolution, and stability of a dune are a function of the dynamic interactions and feedback between the flow structure, bedform morphology and sediment transport over a bed (e.g. Leeder, 1983; Nelson *et al.*, 1993; Best, 2005; Livingstone *et al*., 2007; Ojha and Mazumder, 2008; Figure 1.1). The shear stress exerted upon the bed by the flow initiates sediment transport, thus creating perturbations which evolve into bedforms; the resulting topography, in turn, acts upon the flow by generating flow resistance. This feedback generates turbulence, thereby altering the mean and turbulent characteristics of the flow (Nelson *et al.*, 1993). Form drag (which generates flow resistance) is the resulting force on the bedform caused by a pressure differential created by the low pressure zone in the bedform leeside and the high pressure zone beyond flow reattachment (Maddux *et al*., 2003a).

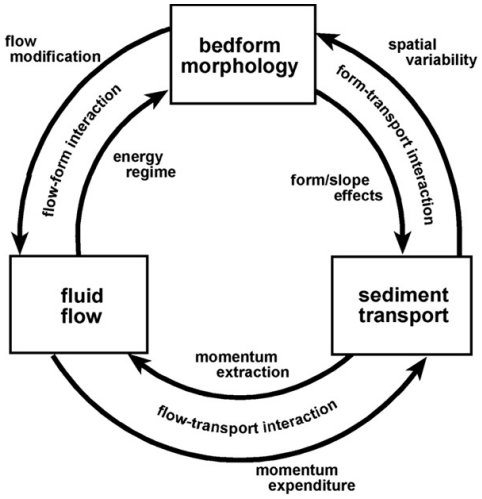

Figure 1.1: A flow-chart illustrating the input and feedback system which comprises the bedform morphology, fluid flow and sediment transport (after Livingstone *et al*., 2007; based upon Leeder, 1983).

'Flow-bed coupling', where the bedform geometry is intrinsically tied to the flow structure and vice versa, poses a challenge to researchers on multiple fronts (Nelson *et al.*, 1993): firstly, many sedimentary structures are characterized by complex geometries which demand independent investigation and analysis; secondly, when found in nature, ripple and dune bedforms are very often modified from the idealized morphology generated within a laboratory setting. The deviation from an idealized bedform can occur for multiple reasons, such as when the bedform is subject to changing wind directions resulting in axial asymmetry or the generation of second-order roughness due to the presence of superimposed bedforms.

1.2 Defining a barchan dune

McKee's (1979) classification of aeolian dunes, one of many available classification schemes, divides dunes into six broad categories: transverse, dome, parabolic, longitudinal, star and reversing. Transverse dunes are further divided into barchan dunes, barchanoid ridges and transverse ridges.

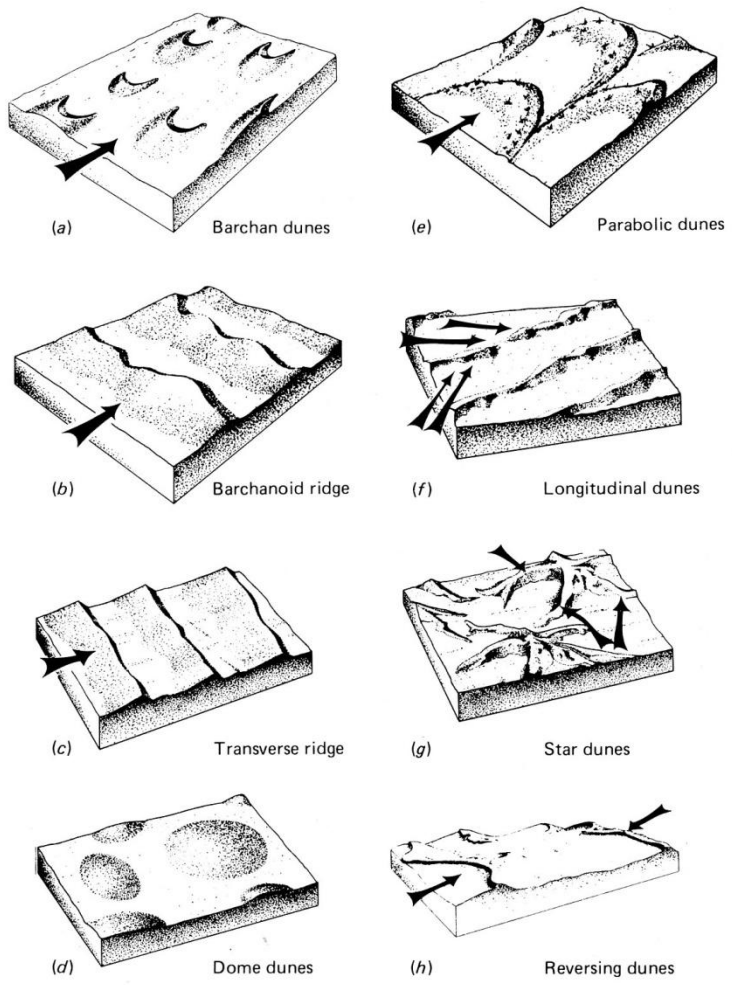

Figure 1.2: Illustrations of various dune types according to flow direction and sediment supply (After McKee, 1979; Greeley and Iverson, 1985).

Longitudinal dunes are parallel either to the dominant flow direction, or, to a resultant 'vector' in the case of multiple flow directions (Greeley and Iverson, 1985). The centerline axis of a parabolic dune is parallel to the flow, whilst the crest of a transverse dune is perpendicular to the flow. Multiple wind directions produce a star dune, while a dome dune is not influenced by any single wind direction. One specific type of transverse dune is the barchan dune. A barchan dune

is distinguishable from other dunes by its characteristic planform crescentic shape and forms under the presence of a unidirectional flow and a starved sediment supply (Figure 1.2; Bagnold, 1941). When a barchan dune is subjected to oblique flows, its horns become asymmetrical, and with sufficient flow direction variability longitudinal dunes may develop or even more complex barchan dune morphologies (Figures 1.3 and 1.4).

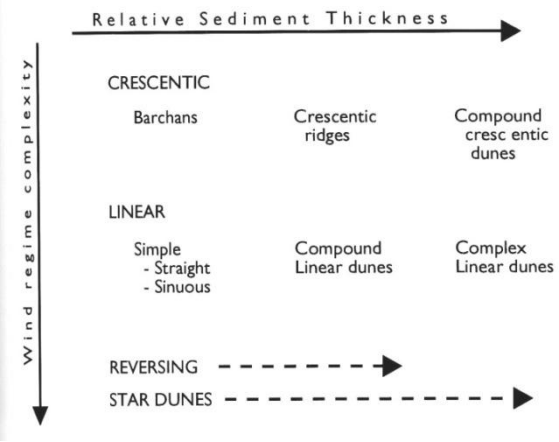

Figure 1.3: A morphological classification of aeolian dunes based upon the flow direction variability and sediment supply (after Lancaster, 1995; based in part on McKee, 1979 and Pye and Tsoar, 1990).

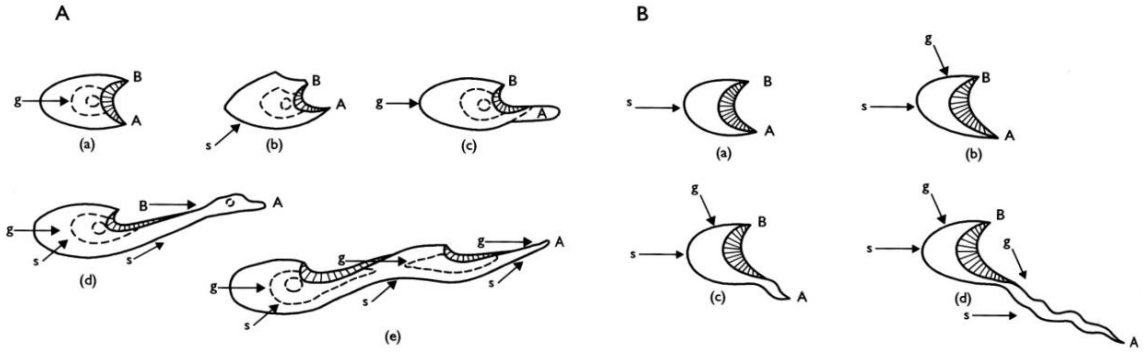

Figure 1.4: A schematic diagram of barchan dune modification by the wind regime; the symbol '*s*' represents strong winds, '*g*' represents gentle winds. Symbols A and B represent the barchan dune horn termination point (after Lancaster, 1995; figure A is based on Bagnold, 1941 and figure B is based on Tsoar, 1984).

Traditionally, barchan dunes were considered only within the aeolian realm; this approach has been reassessed as new discoveries reveal these features develop in a multitude of environments and flows, ranging from continental shelves to Mars and from wind regimes to water regimes (Ernstsen *et al*., 2005; Bishop, 2007; Daniell and Hughes, 2007; Bourke *et a*l., 2008). The method of visualizing and measuring barchan dune morphology and migration has significantly

changed by the introduction of satellites and remote sensing, enabling a consistent survey of barchan dune evolution over time.

1.3 The importance of studying barchan dunes

The quantification of barchan dune morphology, flow and sediment transport rates allows for a variety of applications; ranging from interpreting the geological record to understanding the human impact on dunes and vice versa. Bagnold (1941) pioneered the quantification of aeolian bedforms by delving into the relationships between particle size and the flow regime. He recognized their direct application to the fields of geology and geomorphology. Barchan dunes are important with respect to the geological record as they can help elucidate sediment supply and climatic changes that enable paleoenvironmental reconstructions (Wassun, 1984; Hesse, 2009; Tsoar *et al*., 2009). Knowledge gained by observing and studying bedforms on Earth can be translated to bedforms discovered on other planets or celestial bodies (Claudin and Andreotti, 2006). The presence of bedforms on Earth and other planets, in turn, offers insight into their respective environments and processes. Presently, the mass movement of sand in the form of a dune poses a problem to cultivated areas as the abrasive quality of sand is capable of eroding manmade structures (Greeley and Iverson, 1985). Even more striking is the human impact on dune fields situated close to villages, manifested by an increasing rate of dune erosion (Kiss *et al*., 2009).

The research conducted from Bagnold's era until the 1990s focused primarily on understanding and quantifying the formation and morphology of barchan dunes (Finkel, 1959; Norris, 1966; Hastenrath, 1967, 1987; Hesp and Hastings, 1998). From the 1990s onward, researchers have broadened their focus from dune morphology to also examining the flow over and between dunes, and flow interactions with sediment. Researchers often make use of flumes and wind tunnels to understand the dynamics that shape dunes and ripples. Many fixed-bed studies have examined flow over asymmetrical and symmetrical bedforms characterized by either high or low leeside angles (Vanoni and Nomicos, 1960; Raudkivi, 1963, 1966; Vanoni and Hwang, 1967; Rifai and Smith, 1971; McCorquodale and Giratalla, 1973; Vittal *et al.*, 1977; Itakura and Kishi, 1980; Tsoar, 1985; Fehlman, 1985; Van Mierlo and de Ruiter, 1988; Nelson and Smith, 1989; Lyn, 1993; Nelson *et al.*, 1993; Castro and Wiggs, 1994; McLean *et al.*, 1994; Nelson *et al.*, 1995; Bennett and Best, 1995; Wiggs *et al.*, 1996; Kadota and Nezu, 1999; Venditti and Bennett,

2000; Walker, 2000; Best and Kostaschuk, 2002; Maddux *et al.*, 2003a,b; Walker and Nickling, 2003; Yue *et al.*, 2005; Coleman *et al.*, 2006; Fernandez *et al.*, 2006; Venditti, 2007; Dong *et al.*, 2007; Ojha and Mazumder, 2008; Stoesser *et al.*, 2008; McLean *et al.*, 2008; Balachandar and Patel, 2008). The benefits of conducting a fixed-bed experiment include obtaining finely resolved data on the flow and the stability of the dune; however, fixed-bed experiments do not incorporate the potential effects imposed by suspended sediment and bedload, for instance, turbulence dampening (Yalin, 1977; Best and Leeder, 1993; Lucik and Teiderman, 1988; Schindler and Robert, 2005). The data obtained experimentally potentially can be incorporated into numerical models and used to test field observations. An extensive range of bedforms have also been observed in the field, with the specific intent to acquire data on the mean and turbulent flow fields above aeolian and subaqueous dunes (McLean and Smith, 1979; Sweet and Kocurek, 1990; Soulsby *et al.*, 1991; Lapointe, 1992; Kostaschuk and Church, 1993; Wiggs *et al.*, 1996; Kostaschuk and Villard, 1996; Kostaschuk and Villard, 1998; Kostaschuk, 2000; Best and Kostaschuk, 2002; Venditti and Bauer, 2005; Parsons *et al.*, 2005; Sukhodolov *et al.*, 2006; Holmes and Garcia, 2008; Lynch *et al.*, 2008; Walker *et al.*, 2009). Complementing the experimental and field literature of flow over bedforms are theoretical and computational analyses which attempt to model the physical mechanisms controlling bedform morphology and sediment transport (McLean and Smith, 1986; Van Dijk *et al.*, 1999; Parsons *et al.*, 2004; Keylock *et al.*, 2005; Schatz and Herrmann, 2006; Paarlberg *et al.*, 2007; Yang and Tan, 2008; Paarlberg *et al.*, 2009). Even nearly 70 years after some of the first in-depth studies regarding barchan dune morphology and migration by R.A. Bagnold, current research is still exploring the relationship between the flow and bedform, as well as understanding the broader significance of barchan dunes in dune fields. Single and multiple bedforms have been the subject of numerous papers and have provided a foundation for investigating more complicated topics. The interaction between bedforms is documented but, by and large, overlooked. Barchan dune interactions with neighboring barchan dunes have been documented in the field (Gay, 1962; Howard *et al.*, 1978; Breed and Breed, 1979; Mulligan, 1995; Parker Gay Jr., 1999; Besler, 2002; Ewing *et al.*, 2006; Bourke *et al.*, 2009), but little is known about the flow field and controlling mechanisms.

1.4 The present research

The present study examines the mean and turbulent flow structure over interacting barchan dunes to address the potential mechanisms responsible for the distinctive kinematic behavior observed by Endo *et al.* (2004). Two parameters will be investigated: interdune spacing and the relative volumetric ratio. Four volumetric ratios, three of which replicate the volumetric ratios used by Endo *et al.* (2004), will be investigated at each interdune spacing. Specifically, this study will seek to investigate the nature of flow over interacting barchan dunes, quantify any variation in reattachment length of the separated flow in the downstream barchan dune leeside and any change in turbulence intensity with respect to interdune spacing and volumetric ratio. High-resolution particle-image velocimetry(PIV) experiments will be conducted over a fixed-bed, allowing measurement of mean flow, turbulence intensity, turbulent kinetic energy, Reynolds stresses and vorticity.

The next three chapters (Chapters 2-4) review literature on barchan dune morphology, mean and turbulent flow over bedforms and bedform interactions. Chapter 5 presents the methodology of the experimental setup and procedure. The experimental results are presented in Chapter 6 and analyzed in Chapter 7. The final conclusions are summarized in Chapter 8.

CHAPTER 2

THE ORIGIN, MORPHOLOGY AND MIGRATION OF BARCHAN DUNES

The morphology of a barchan dune is controlled by fundamental physical attributes (i.e. turbulent boundary layer, mass conservation, sediment flux and shear stress) which provide the foundation for numerical models. Numerical models attempting to recreate barchan dune shape, specifically the shape formation and evolution, have been proposed by Wippermann and Gross (1986), Howard *et al.* (1978), Nishimori *et al.* (1998), Herrmann and Sauermann (2000), Sauermann *et al.* (2000), Andreotti et al. (2002b), Kroy *et al.* (2002), Lima *et al.* (2002), Herrmann (2002), Momiji and Bishop (2002), Hersen et al. (2004), Schwämmle and Herrmann (2005), Herrmann *et al.* (2005), Giri and Shimizu (2006), Herrmann (2006a), Ortiz and Smolarkiewicz (2006) and Ortiz and Smolarkiewicz (2009). The initial 'zeroth-order' model was modified as it failed to reach a steady state, and was succeeded by the 'continuum saltation model' proposed by Sauermann *et al*. (2001) and the 'minimal model' proposed by Kroy *et al.* (2002). Following papers have built upon these two models to better approximate barchan dune morphodynamics. The numerical models are validated by observations and measurements of naturally-occurring barchan dunes, although the physical laws dictating the elementary morphology of a barchan dune accommodate a degree of variability that is difficult to incorporate within a model. Ideally, barchan dunes are symmetrical about a centerline axis which is parallel to the flow direction. Found in nature, barchan dunes are typically asymmetrical, due to oblique flow directions, uneven surfaces, vegetation, collisions with other barchan dunes (Clos-Arceduc, 1969; Hersen and Douady, 2005) or other factors capable of disrupting their shape (Sauermann *et al*., 2000). Field measurements offer empirically-derived relationships of dune morphology and migration (Lancaster, 1996).

2.1 Origin of barchan dunes

Barchan dunes occur within wind regimes that have a directional variability of 15° and lower, constituting a relatively unidirectional flow (Lancaster, 1989). The aeolian and subaqueous environments where barchan dunes form are characterized by a lack of vegetation as well as a starved sand supply upon a typically hard substrate.

2.1.1 Occurrence

The majority of documented barchan dunes are found in coastal deserts or along their margins such as the coast of southern Peru (Finkel, 1959; Hastenrath, 1967, 1987; Lettau and Lettau, 1969; Parker Gay Jr., 1999), the Namib Desert in Namibia (Slattery, 1990), the southern Moroccan coast (Sauermann *et al*., 2000), and the Lençóis Maranhenses coastal desert located in northeastern Brazil (Jimenez *et al*., 1999) (Figure 2.1). Barchan dunes are isolated bedforms that often develop in dune fields located in sand transport corridors, which are areas linking a sediment source to a depositional area (Lancaster, 1989), such as Imperial Valley, California (Norris, 1966), northern Kuwait (Al-Awadhi *et al*., 2000), the Taklimakan Desert (Dong *et al*., 2000) and the Minqin Oasis in China (Wang *et al*., 2007).

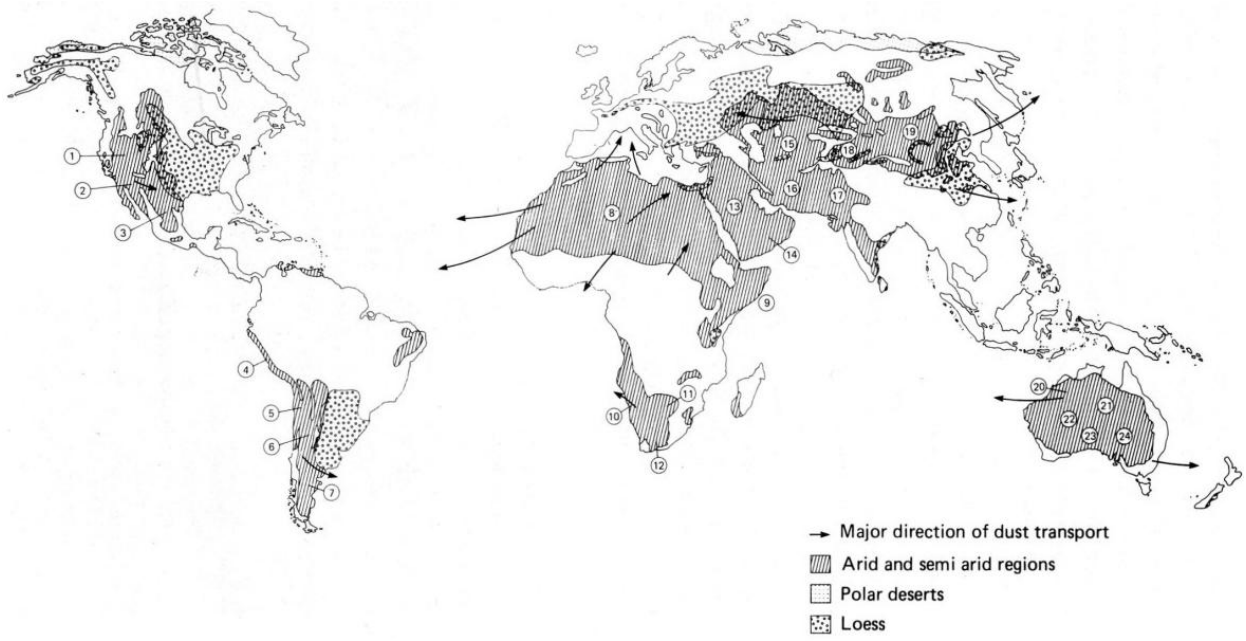

Figure 2.1: A map showing the world-wide distribution of deserts, arid and semiarid regions, polar deserts and loess deposits as well as the primary transport routes of dust (indicated with arrows). The indicated deserts are: (1) Great Basin, (2) Sonoran, (3) Chichuahuan, (4) Peruvian, (5) Atacama, (6) Monte, (7) Patagonian, (8) Sahara, (9) Somali-Chabli, (10) Namib, (11) Kalahair, (12) Karroo, (13) Arabian, (14) Rab'al Khali, (15) Turkestan (16) Iranian, (17) Thar, (18) Taklimakan, (19) Gobi, (20) Great Sandy, (21) Simpson, (22) Gibson, (23) Great Victoria, and (24) Sturt (after Greeley and Iverson, 1985).

A barchan dune field serves not only as a breeding ground for barchan dunes, but also enables the collision and subsequent interaction of barchan dunes, and in some cases, produces barchanoid ridges comprised of laterally linked barchan dunes as seen in the White Sands Desert,

New Mexico (Ewing *et al.*, 2006). Barchan dunes are also found in less visible environments: the subaqueous and Martian realms. Barchan dunes have been documented on the continental shelf (Newell and Rigby, 1957; Kenyon and Stride, 1967; Lonsdale and Malfait, 1974; Lonsdale and Spiess, 1977), submarine channels (Wynn *et al*., 2002; Todd, 2005), in rivers (McCulloch and Janda, 1964; Carling *et al.*, 2000), tidal areas (Illing, 1954; Allen, 1968) and shallow water straits (Daniell and Hughes, 2007). Barchan dunes have also been discovered in Proctor Crater on Mars (Fenton and Bandfield, 2003).

2.1.2 Formation

Many researchers have simulated the formation of bedforms from a plane bed (Miao *et al*., 2001; Venditti *et al*., 2005). Aeolian bedforms develop due to the '(1) presence of [a] nucleus, (2) grain-by-grain action of the wind, (3) interaction between form and flow, (4) bedform migration, [and] (5) bedform equilibrium' (Wilson, 1972; Greeley and Iverson, 1985). However, aeolian barchan dunes have a minimum size, which creates a dilemma with regards to the formation of barchan dunes: what is the precursor to the barchan dune and how is it initiated?

The formation of a barchan dune results from the accumulation of grains due to changes in bed roughness and fluctuations of the flow (Pye and Tsoar, 1990). In Figure 2.2, a patch of sand begins to resemble a barchan dune. In order for sediment to accumulate into a substantial sand body, the flow must deposit sediment out of suspension or bedload (saltation). The deposition mechanism lies in reducing the flow momentum by a sediment 'saltation cloud' (Bagnold, 1941; Greeley and Iverson, 1985). The sand body must reach a minimum length of several meters (i.e. 4-6 m) to eventually evolve into a dune; otherwise the 'saltation cloud' does not have the distance necessary to deposit sediment. The slipface forms once the height of the barchan dune is sufficient enough to induce flow separation; this critical height is approximately 0.3 m (Bagnold, 1941; Greeley and Iverson, 1985).

The characteristic crescent shape is apparent before the barchan dune fully matures with a developed slip face, because the grains are more easily moved along the edges rather than along the centerline axis (Pye and Tsoar, 1990). The particular formation of the barchan dune morphology is believed to be dependent upon the rate of advance, which has an inverse relationship to the height (Bagnold, 1941; Greeley and Iverson, 1985); as the local slip face

height decreases from the center towards the edges, the edges move at a faster rate forming the barchan dune horns.

A mature barchan dune maintains its equilibrium based upon the sediment flux and flow regime. The barchan dune behaves as a stable and dynamic open-system when the sediment flux is zero. When the flow regime changes (i.e. its direction or magnitude), the barchan dune also results in a different shape and volume, V_d. Likewise, if the sediment flux changes from zero, either by an increase or decrease in sediment supply or by more or less sediment exiting the barchan, this will also result in morphological changes to the barchan dune. Many barchan dunes observed in the field are stable, potentially migrating for decades (Norris, 1966).

Figure 2.2: An image of the forerunner to a barchan dune; the sand pile is located in southern Morocco and is ~10 m in length and width (after Andreotti et al., 2002a).

2.1.3. Sediment transport

Primary sediment transport modes are grains moving as bedload or in suspension. Bedload transport is comprised of saltation and traction, but also includes surface creep and reptation (Greeley and Iverson, 1985; Pye and Tsoar, 1990). Saltation describes the grain jumping along the bed-floor. Surface traction describes grains rolling or sliding along the bed-floor. Surface

creep and reptation describe the grain crawling along the bed-floor. Saltating grains, upon impact with the floor, propel other grains into the flow (Figure 2.3b). Saltating grains also have an asymmetrical trajectory over the saltating length, l_{sal} (Figure 2.3a). Suspension describes the lifting and transport of particles in the flow without surface contact. Suspension occurs when the wall-normal velocity fluctuations exceed the settling velocity of the grain (Pye and Tsoar, 1990). The sediment transport modes are illustrated in Figure 2.4.

Sediment deposition modes (Figure 2.5) can be summarized as tractional deposition, grainfall deposition and grainflow deposition (Bagnold, 1941; Hunter, 1977; Kocurek and Dott, 1981; Greeley and Iverson, 1985). Tractional deposition is the process by which saltating (or impact creeping) grains find repose over time through shelter by other grains or objects. Grainfall deposition entails the grain falling out of suspension and ceasing forward movement, primarily due to flow separation zone found in the lee side of the dune. Grainflow deposition, otherwise referred to as avalanching, is the process where grains found at the dune brink avalanche along the slipface.

The particle flux (i.e. sediment flux) is instrumental in creating aeolian and subaqueous bedforms (Herrmann, 2006b). We proceed by considering the forces acting on a particle in a turbulent flow, namely, the drag force, F_d, lift force, F_l, and gravitational force, F_g (Figure 2.6). The drag on a particle of size d is:

$$F_d = C_d \rho u_*^2 \frac{\pi d^2}{4} \tag{1}$$

where C_d is the drag coefficient (which is dependent upon the Reynolds number; $C_d \approx 0.44$ for $Re > 1000$), ρ is the fluid density, u_* is the shear velocity, and d is the grain diameter (Herrmann, 2006b). The lift on a particle is:

$$F_l = \Delta p \frac{\pi d^2}{4} = C_L \rho u^2 \frac{\pi d^2}{2} \tag{2}$$

where $C_L = 0.0624$, u is the velocity at height $0.35d$ (Chepil, 1958; Herrmann, 2006b). The force of gravity acting on a particle is:

$$F_g = \rho_d \frac{\pi d^3}{6} \tag{3}$$

where ρ_d is the particle density. The drag force and lift force are responsible for the particle flux. The lift force results from the differential static pressure, Δp, above and below the grain (Herrmann, 2006b). The drag force results from the shear stress, τ, upon the grain surface exerted by the flow. The shear stress, τ, is defined as:

$$\tau = \rho u_*^2 \quad (4)$$

The drag force acts parallel to the direction of flow while the lift force acts upwards in opposition to the gravitational force; in other words, the aerodynamic forces (i.e. the lift, F_l, and drag forces, F_d) act against the force of gravity acting upon the mass of the grain (Figure 2.6; Pye and Tsoar, 1990). When the lift and drag exceed the gravitational forces, the grain dislodges from the bed and becomes mobile.

In Figure 2.7, the threshold velocity, u_{*t} (cms^{-1}) increases as the square-root of particle size. Sediment transport via saltation begins when u_{*t} exceeds a critical value, defined by the particle size. The threshold friction speed represents the lowest wind velocity necessary to initiate sediment motion for the range of grain sizes shown (Greeley and Iverson, 1985). The sand grain size spectrum ranges from very fine silt, diameter ≈ 5 μm, to fine sand, $d \approx 200$ μm. Grain sizes falling below 100 μm are less susceptible to movement due to cohesive forces and minimal surface exposure to the flow; the primary mode of transport for grain sizes $d<100$ μm, once sediment motion is initiated, is suspension due to their small mass. Grains that have $d>100$ μm are heavier and subsequently less inclined to move. While these larger grains are capable of providing shelter and protection to smaller grains from the flow, they also are more vulnerable to the flow by protruding into the flow and exposing more surface area to the flow. The lowest *y*-point on the threshold velocity curve indicates the grain size most susceptible to move occurs at ~ 100 μm, in the realm of fine sand, under the transport mechanism of saltation, suggesting that saltation is most likely the 'critical mode of [sediment] transport' (Figure 2.7; Greeley and Iverson, 1985).

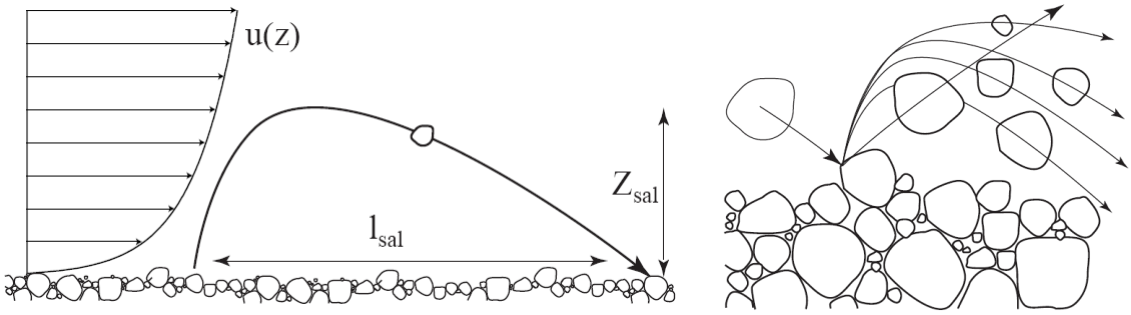

Figure 2.3: (a) A grain's saltation length, l_{sal}, and height, Z_{sal}; (b) a saltating grain impacting a grain dominated bed and projecting other grains into the flow (after Andreotti *et al*. 2002a).

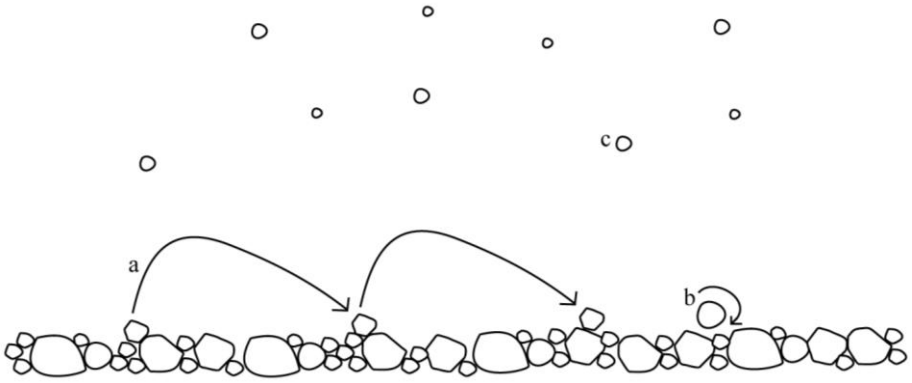

Figure 2.4: Sediment transport modes: (a) saltation; (b) surface traction; (c) suspension.

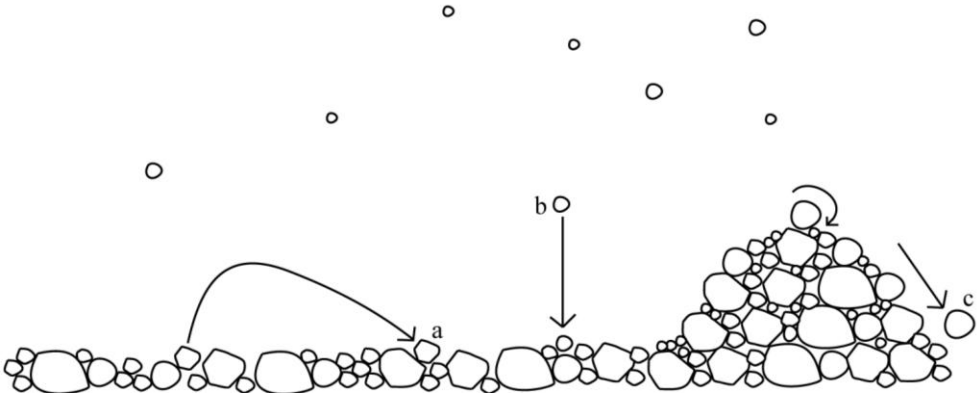

Figure 2.5: Sediment deposition modes: (a) tractional deposition; (b) grainfall deposition; (c) grainflow deposition (avalanching).

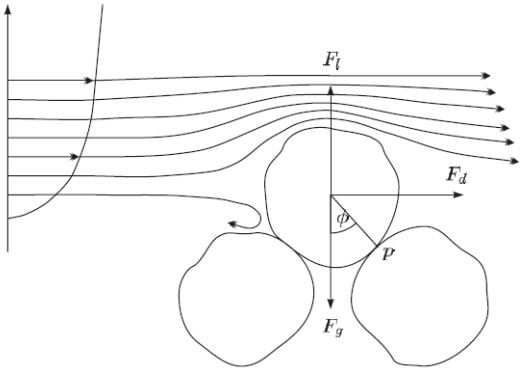

Figure 2.6: The forces upon a grain with the surface exposed to the flow (after Herrmann, 2006b).

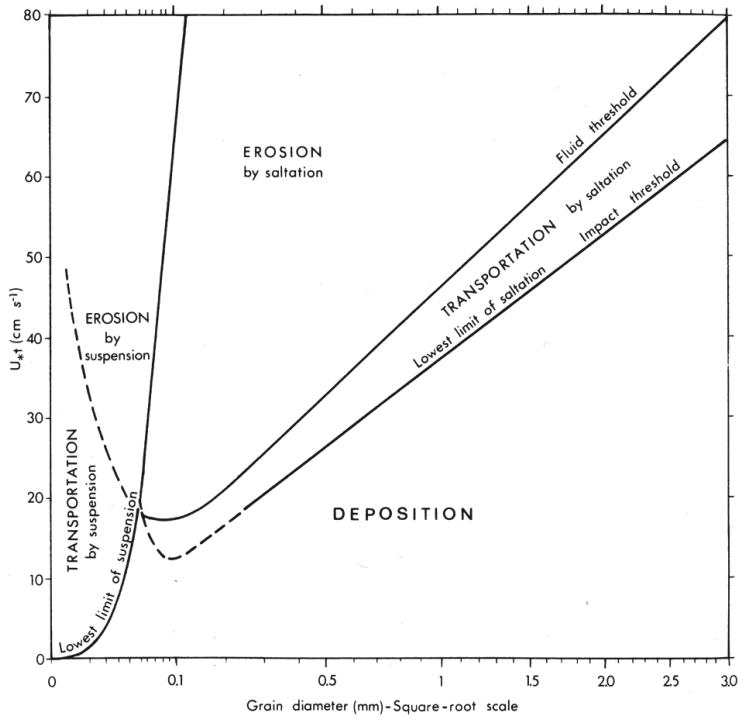

Figure 2.7: The particle diameter (mm) as a function of the fluid threshold friction velocity, u_{*_t} (cms^{-1}) (after Pye and Tsoar, 1990). Boundaries are drawn between modes of sediment transport (suspension and saltation) and deposition.

2.2 Barchan dune morphology

Barchan dunes exhibit a gentle convex windward slope (i.e. stoss-slope) and a downwind slope (i.e. lee-slope). The leeside contains a slip face measured at approximately 33-34°, accompanied by two peripheral horns (or arms) which extend downwind (Pye and Tsoar, 1999; Figure 2.8). Slope angles may range from $8<\beta<22°$ for the stoss-slope and $30<\theta<34°$ for the lee-slope (Hastenrath, 1987; Embabi and Ashour, 1993). Barchan dunes are characterized by a concavo-convex stoss-slope. The lee-slope (i.e. slipface) curvature may range from straight to convexo-concave, convexo-straight, or multi-step (Embabi and Ashour, 1993). The intersection of the centerline axis with the sharp edge marking the beginning of the slip face is referred to as the brink point, B_P.

A general trend observed in the field is that small dunes typically have a distinct crest and a distinct B_P; the B_P extends beyond the crest along a convex segment (Figure 2.9). Large dunes typically display a coincident crest and B_P (Hastenrath, 1967; Embabi and Ashour, 1993; Sauermann *et al.*, 2000; Andreotti *et al.*, 2002a). The threshold distinguishing small dunes from

large dunes is not specified, despite a wide range of aeolian dune heights between 1 m and 140 m (Herrmann, 2005). Moreover, researchers have reported volumetrically-equivalent barchan dunes exhibiting both coincident and non-coincident crests and B_P (Cooke *et al.*, 1993; Andreotti *et al.*, 2002a). However, it has been demonstrated through computational simulations that transverse dunes downstream of another dune has a brink that is closer to the crest (Schwämmle and Herrmann, 2004; Parteli *et al*., 2006).

Single barchan dunes are the simplest type of barchanoid bedforms. Multiple barchan dunes joined together at the horns form barchanoid ridges (Figure 2.10). Megabarchans are very large, isolated barchan dunes with superimposed dunes or ripples on their stoss side (Figure 2.10). Linked megabarchans form a continuous transverse dune ridge, called megabarchanoid ridges. As the volume of a dune increases (and consequently its height), so does the spacing between neighboring dunes (Blumberg, 2006). The average spacing of a megabarchan dune is 2.08 km but ranges from 1.5 km to 3.8 km; its average height, *H*, is 68 m, but ranges from 25 m to 140 m (Blumberg, 2006). For this present study, only the simple barchan dune will be investigated. The barchan dune adopted and used in the present study is presented in section 5.2.3.

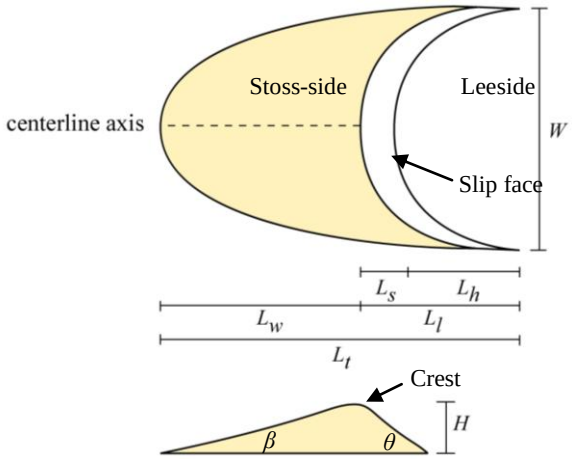

Figure 2.8: A planform and profile view of a barchan dune with defined dimensions: *W* is the width; *L* is the total length; L_s is the length of the stoss-side; L_l is the length of the leeside; *H* is the height of the dune crest.

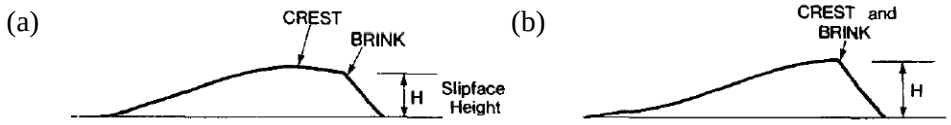

Figure 2.9: Schematic diagram of a barchan dune centerline axis profile defining: (a) a non-coincident crest and brink and (b) a coincident crest and brink (after Hesp and Hastings, 1998).

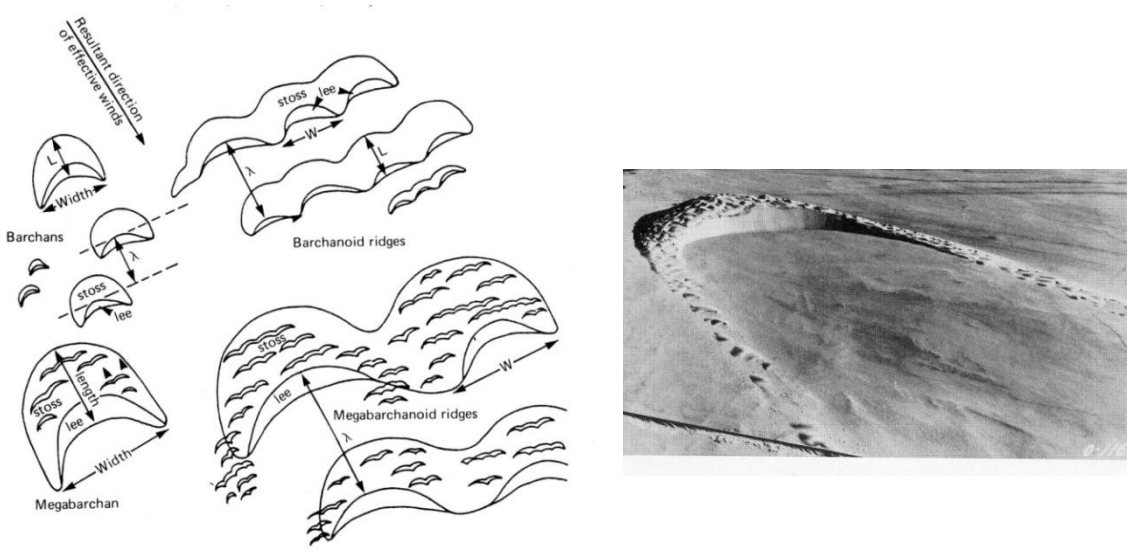

Figure 2.10: The range of complex and compound barchan dunes and barchanoid ridge. Compound (i.e. megabarchan) barchan dunes are characterized by superimposed bedforms (after Greeley and Iverson, 1985). No scale is available for the photograph.

2.2.1 Morphological cycle

Embabi and Ashour (1993) suggest from their field observations that slope form evolves with dune size, as part of a larger 'geomorphologic cycle'; slope form constitutes the slope angle and curvature. In Figure 2.11, the morphological cycle of an aeolian barchan is presented in four stages: initial, youth, mature and old (Embabi and Ashour, 1993). The authors indicate that the evolution in size and shape is, in part, the result of increasing sediment supply. The initial stage is comprised of a 'domal or oval shaped' dune with convex slopes, characterized by a length of 20-30 m and a height of 50-70 cm. The youth stage represents development of the characteristic crescent shape where the stoss side is concavo-convex and the lee side is convexo-straight. The dimensions range between 40-80 m in length and width with height between 1-3 m. The mature stage has a concavo-convex stoss slope and a straight lee slope, and is characterized by a length and width falling between 100-500 m, accompanied by a height of ~20 m. Finally, the old stage constitutes barchans with a length and width of up to 1,000 m and a height of up to 40 m. At this point, multiple slipfaces and crests are visible. Embabi and Ashour (1993) suggest that at this stage, new barchans are formed, exiting the horns as small domal shaped dunes. This process assumes that the isolated barchan dunes have no interactions with neighboring dunes. In the absence of sediment flux, the size of a dune is constant while the shape may be altered by variations in the flow; however, the barchan dune must reach the minimum size threshold

(described in section 2.3.3) in order to maintain its crescentic shape. To date, the primary attention on the evolution of dune shape and size has focused on dune to dune interactions.

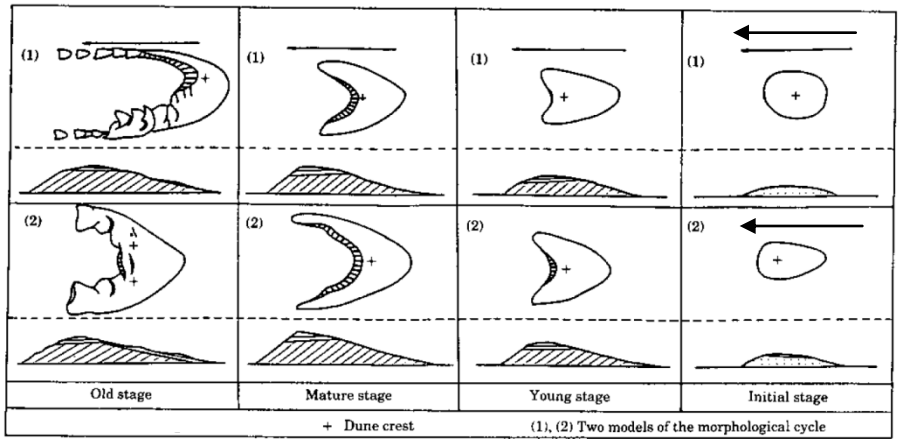

Figure 2.11: The four phases of the morphological cycle for two models (after Embabi and Ashour, 1993).

2.2.2 Morphologic relationships

Morphologic relationships have been quantified by affine, logarithmic and power law equations. The most discussed morphologic relationship is that of barchan dune height (m) to width (m). Linear regressions generated from field and experimental measurements of barchan dunes have been reported by Finkel (1959), Long and Sharp (1964), Norris (1966), Hastenrath (1967, 1978), Mabutt (1977), Khalaf and Al-Ajmi (1993), Hesp and Hastings (1998), Sauermann et al. (2000), Hersen (2004) and Wang et al. (2007) in the following form:

$$W = \alpha H + W_0 \tag{5}$$

The respective terms, α and W_o, for each set of data are defined in Table 2.1. Hesp and Hastings (1998) found the field measurements had a better fit when represented by a logarithmic curve:

$$logW = 0.1257H + 1.1266 \quad R^2 = 0.848 \tag{6}$$

Wang et al. (2007) argue against the inclusion of a y-intercept in a linear regression or logarithmic regression, as when H=0, then W=*0*.

Author	*Data source*	α	W_0 *(m)*	R^2
Finkel (1959)	Finkel (1959)	10.00	4.0	N/a
Hesp and Hastings (1998)	Finkel (1959)	9.58	5.75	0.72
Hastenrath (1987)	Hastenrath (1967, 1987)	8.19	9.52	N/a
Hesp and Hastings (1998)	Finkel (1959), Hastenrath (1967, 1987), Khalaf and Al-Ajmi (1993), Hesp and Hastings (1998)	8.82	7.65	0.81
Hesp and Hastings (1998)	Finkel (1959), Long and Sharp (1964), Norris (1966), Hastenrath (1967, 1987), Khalaf and Al-Ajmi (1993), Hesp and Hastings (1998)	8.37	15.77	0.78
Sauermann *et al.* (2000)	Sauermann *et al.* (2000)	11.1	5.6	0.97
Andreotti *et al.* (2002)	Finkel (1959), Long and Sharp (1964), Hastenrath (1967, 1987), Sauermann *et al.* (2000)	8.6	8.8	N/a
Wang *et al.* (2007)	Finkel (1959), Long and Sharp (1964), Hastenrath (1967, 1987), Khalaf and Al-Ajmi (1993), Hesp and Hastings (1998), Sauermann *et al.* (2000), Wang et al. (2007)	14.3	N/a	N/a
This study: Figure 2.12	Finkel (1959), Hastenrath (1967, 1987), Khalaf and Al-Ajmi (1993), Sauermann *et al.* (2000), Wang et al. (2007)	13.79	0.05	0.66
This study: Figure 2.13	Finkel (1959), Long and Sharp (1964), Norris (1966), Hastenrath (1967, 1987), Khalaf and Al-Ajmi (1993), Sauermann *et al.* (2000), Wang et al. (2007)	7.74	0.03	0.61

Table 2.1: The linear regression relating dune height and width reported for a range of data sets (the sources are provided in 'data source'). R^2 indicates how well the linear regression fits the data; when R^2 approaches 1, a strong correlation exists. As an aside, the barchan dunes measured by Finkel (1959) in the Pampa de la Joya, Peru, were composed of volcanic ash and not quartz grains, a fact reflected in their outlying dune dimensions on data graphs (Hesp and Hastings, 1998).

The length, width and height dimensions are individually proportional to one another but not collectively, suggesting the mechanisms contributing to dune propagation rely upon a relationship between the initial L_t and W (Andreotti *et al*., 2002). The physical relationship between H and W of a barchan dune is established, yet it remains unclear what controlling parameters limit H from increasing beyond a threshold at a given W. Hesp and Hastings (1998) suggest the stoss-side side slopes (i.e. normal to the wind direction and centerline axis) may be responsible for imitating dune height, H. A relationship between the dune slipface height H to the dune width W, and dune side slope angle ϕ, is expressed by the following equation:

$$H = \frac{W}{2tan\phi} \tag{7}$$

where an average value of 11° is considered reasonable for the side angle ϕ (dune side is normal to the flow direction). Using the above approximation, Hesp and Hastings (1998) predict a linear

regression relating *H* and *W* closely resembling the Finkel (1959) dataset linear regression (Figure 2.14).

The relationship between barchan dune height and length was investigated by Sauermann *et al.* (2000). Only the slipface length, L_s, is directly proportional to *H*:

$$L_s = \frac{H}{tan\theta} \tag{8}$$

where θ ranges between 31° to 35°. There is a linear relationship between each length, L_h, L_w, and L_t to *H* (Figure 2.15a):

$$L_t = 14.2H + 17.5 \quad R^2 = 0.94 \tag{9}$$

$$L_w = 4.6H + 18.5 \quad R^2 = 0.85 \tag{10}$$

$$L_h = 7.7H - 1.6 \quad R^2 = 0.88 \tag{11}$$

The relationship between barchan dune height and volume was investigated by Sauermann *et al.* (2000). The volume, V_d, and height, *H*, are related by the following equation:

$$V_d = bH^{\sigma} \tag{12}$$

Sauermann *et al.* (2000) conclude that the barchan dune is not scale invariant due to the fact that the data generates σ=2.4 which is below the cubic linear regression that would indicate scale invariance (Figure 2.15b). Elbelrhiti et al. (2008) related the dune volume, V_d, to the dune width, W (Figure 2.16):

$$V_d \sim \frac{1}{40} W^3 \tag{13}$$

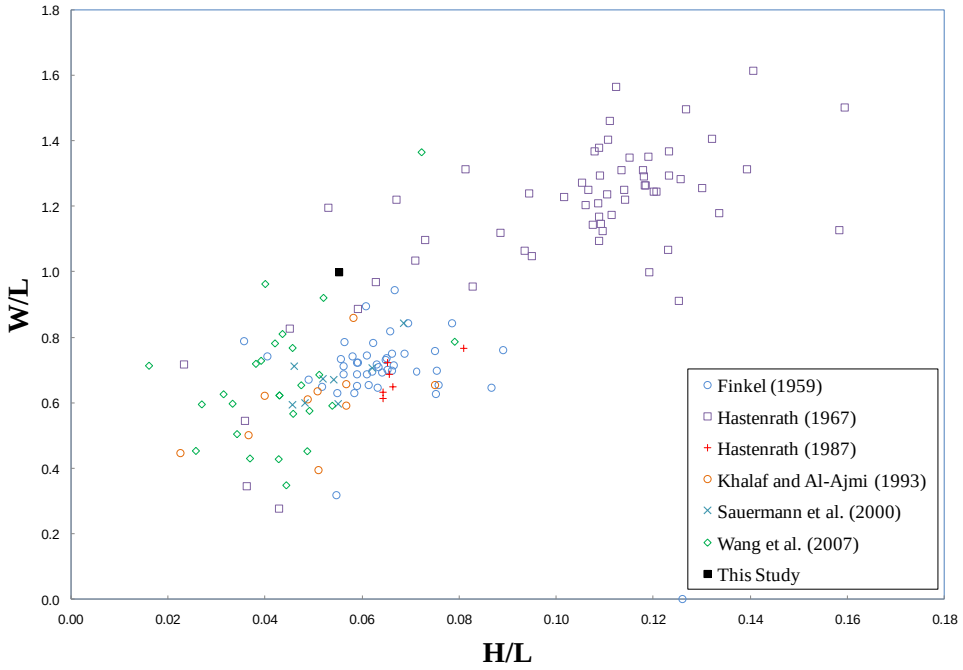

Figure 2.12: The relationship between slipface height, *H* and dune width, *W* (distance between the horns), normalized by the total length, L_t (defined as the stoss-side length combined with the leeside length). The data presented includes field data and experimental data from a range of sources. Note that the Long and Sharp (1964) data omits dune numbers 5, 9, 17, 40, and 41, following Hesp and Hastings (1998). See APPENDIX A for a compilation of the data measurements.

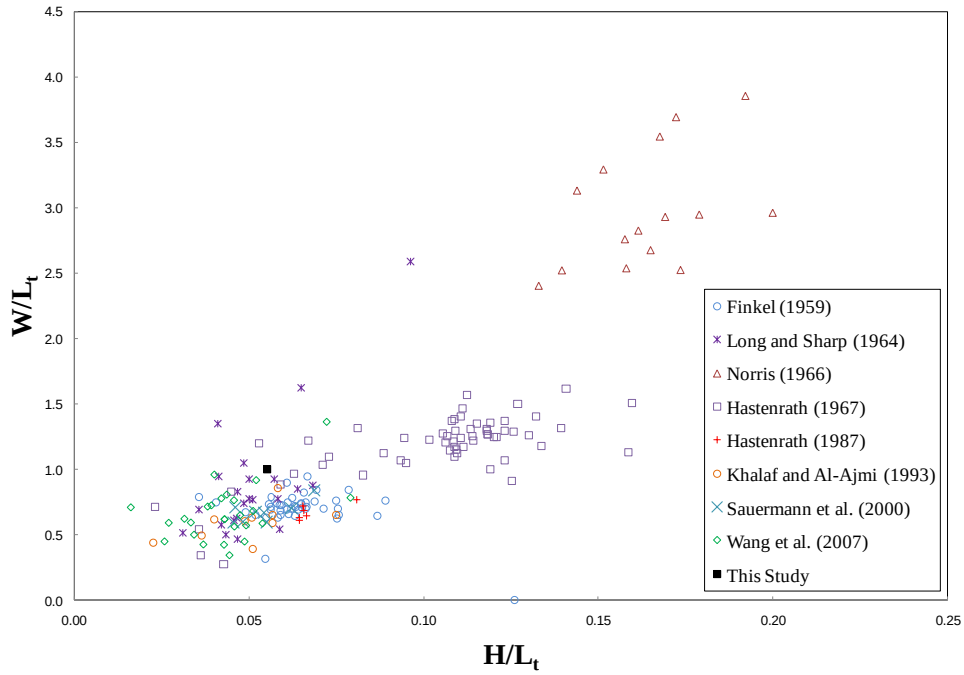

Figure 2.13: The relationship between slipface height, *H* and dune width, *W* (defined as the distance between the horns), normalized by the total barchan dune length, L_t (defined as the stoss-side length combined with the leeside length). The data presented includes field data and experimental data from a range of sources. Note that the Norris (1966) and Long and Sharp (1964) datasets have been omitted following Hesp and Hastings (1998).

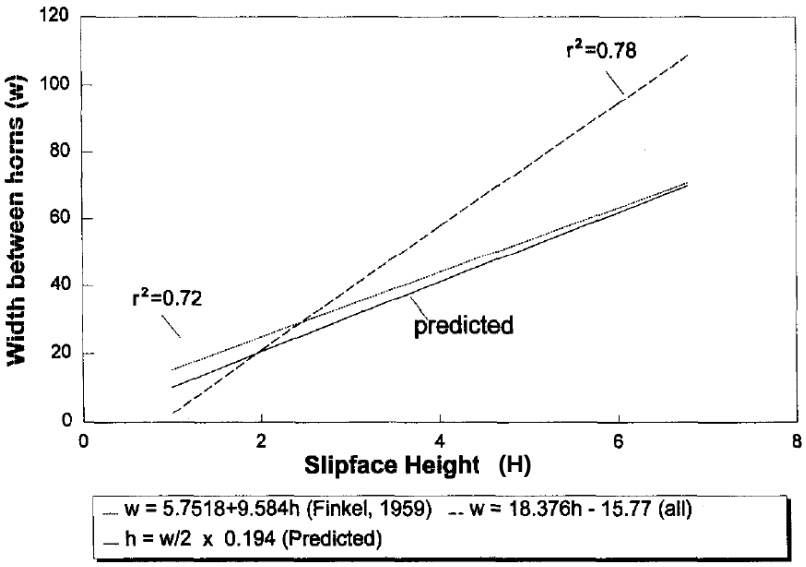

Figure 2.14: A comparison between linear regressions derived from the field measurements of Finkel (1959), the dataset of 'all' field measurements including datasets from Finkel (1959), Norris (1966), Hastenrath (1967, 1987), Long and Sharp (1964), Khalaf and Al-Ajmi (1993), and Hesp and Hastings (1998), and the predicted relationship between slipface height and width between horns (after Hesp and Hastings, 1998).

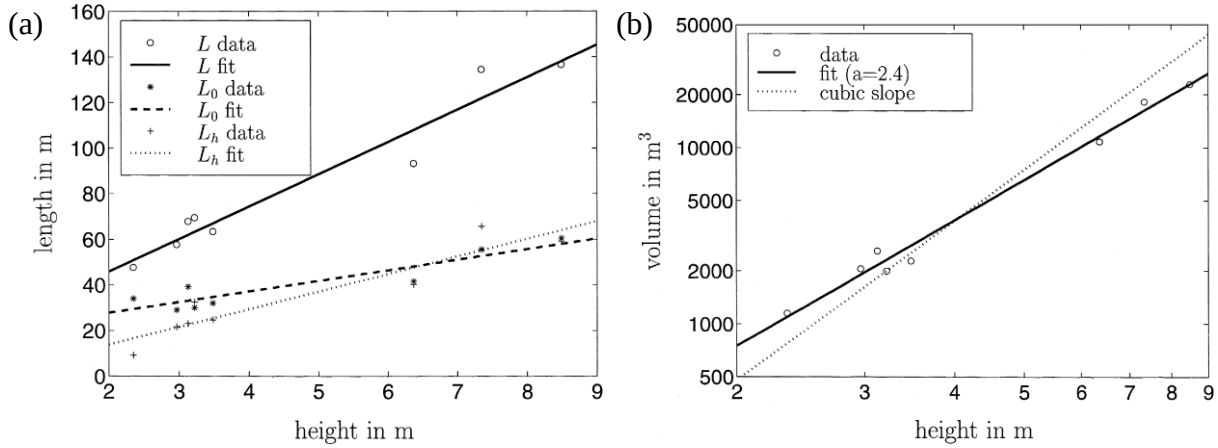

Figure 2.15: (a) The relationship between barchan dune height, *H*, and length, L_t. (b) The relationship between barchan dune height, *H*, and dune volume, V_d (Sauermann *et al.*, 2000).

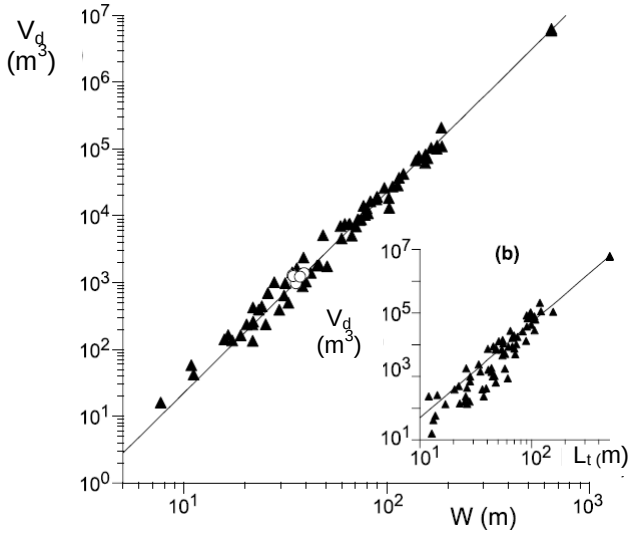

Figure 2.16: The dune volume, V_d, plotted against the dune width, W; the inset plot shows the dune volume, V_d, plotted against the dune length, L_t (Elbelrhiti *et al*., 2008).

2.2.3 Minimum size

Consensus in the current literature indicates that barchan dunes have a minimum size (Andreotti *et al*., 2002a). The smallest dimensions reportedly possible under aeolian conditions are 1-1.5 m in height, H, by 10 m in length, L_t (Hersen *et al*., 2002; Herrmann, 2006b). So far, reproducing barchan dunes in a wind tunnel has only resulted in erodible barchan-shaped piles that do not propagate downstream, as seen in Figure 2.17 (Bagnold, 1941; Cooke et al., 1993; Dauchot *et al*., 2002; Andreotti *et al*., 2002; Hersen *et al*., 2002). Due to a significantly different fluid to grain density ratio, the minimum size of subaqueous barchan dunes is far smaller than the aeolian barchan dune minimum, thus allowing the reproduction of barchan dunes in water flumes.

The inertia exerted upon a single grain results in a characteristic distance referred to as the inertia length, l_{drag}, defined as the maximum distance the grain can travel:

$$l_{drag} = \frac{\rho_s}{\rho_f} d \tag{14}$$

The density of the sediment and fluid are denoted by ρ_s and ρ_f and the average sediment diameter is d. The inertia length, l_{drag}, of a single grain is proportional to the flux saturation length, l_s (Sauermann *et al.*, 2001; Hersen *et al.*, 2002), defined within the model of Sauermann *et al*. (2001) as:

$$l_s = \frac{2\alpha}{\gamma}\frac{u_s^2}{g}\frac{\tau_t}{\tau - \tau_t} \quad (15)$$

Where u_s is the saturated velocity, α and γ are model parameters of the saltation length, g is the acceleration of gravity, τ is the shear stress of air, $\tau_t = \rho u_{*t}^2$, where u_{*t} is a shear velocity threshold. Sand flux is the rate of incoming to outgoing sand. With time, the sand flux becomes completely saturated, so the flow is no longer capable of adding new grains without depositing grains, thus reaching a saturated state. The saturation length l_s varies locally according to the fluctuations experienced through the sediment flux (Hersen *et al.*, 2002; Parteli *et al.*, 2007). The lower limit of barchan dune size is therefore dependent upon the saturation length, l_s. Barchan dunes with a width to inertia length ratio (W/l_{drag}) below or equal to 20 are nonexistent in the field or experimentally (Figure 2.18; Hersen *et al.*, 2002; Endo *et al.*, 2005). Barchan dunes below the inertia length, l_{drag}, experience an ever-increasing flux so the dune experiences erosion while large barchan dunes experience an oversaturated grain flux, resulting in deposition in the leeside (Hersen *et al.*, 2002).

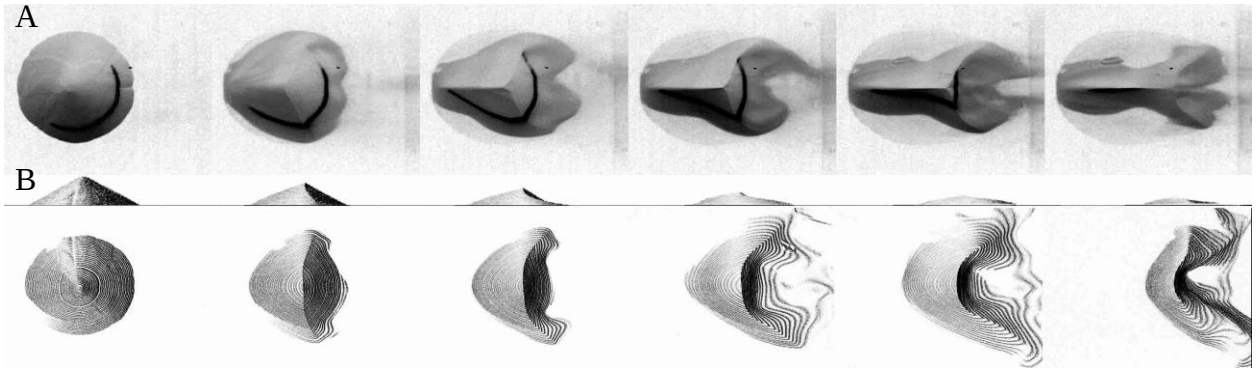

Figure 2.17: Time-series evolution of a conical pile of sediment in a wind tunnel evolving into the barchan dune morphology and then eroding away. Series A had no incoming sediment while series B did have incoming sediment (Andreotti *et al.*, 2002).

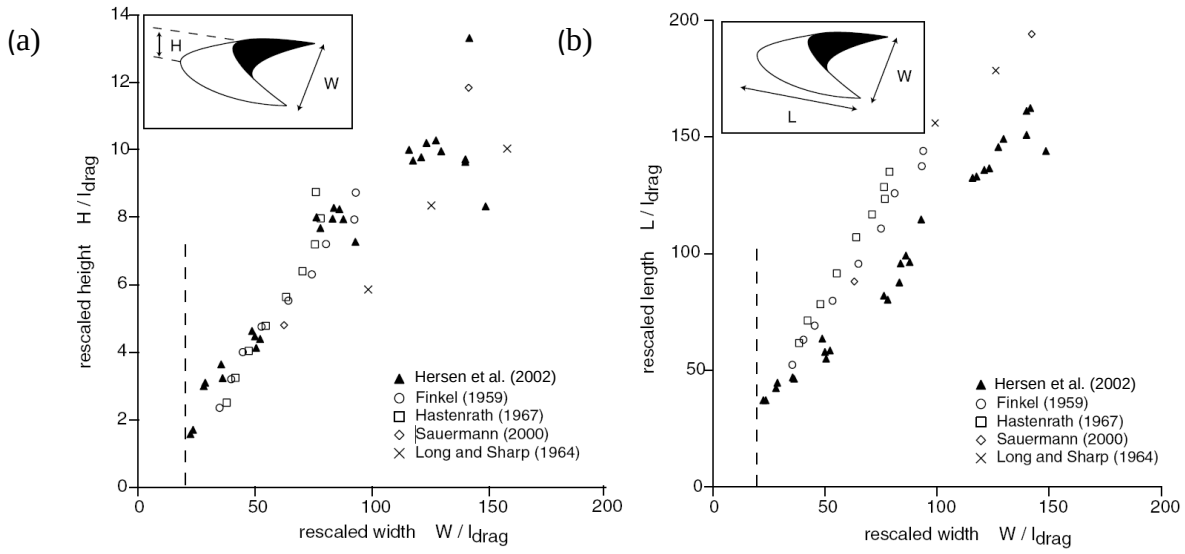

Figure 2.18: (a) Normalized dune width, *W*, plotted against the normalized dune height, *H* and (b) normalized dune width, *W*, plotted against the normalized length, L_t; the normalization parameter is the inertia length, l_{drag} defined in the text. No barchan dunes are observed below $W/l_{drag}<20$ in (a) and (b) (after Hersen *et al*., 2002).

2.2.4 Scale invariance and shape variability across different environments

Researchers agree that barchan dunes are not scale-invariant (Embabi and Ashour, 1983; Embabi and Ashour, 1993; Sauermann *et al*., 2000; Sauermann, 2001; Andreotti *et al*., 2002a). Notably, the barchan dune dimensions *L*, *H* and *W*, are not equally proportional. As *H* increases, W increases at a faster rate than L, resulting in a wider dune shape (Andreotti *et al*., 2002a). The primary difference between large and small dunes lies in the position of the brink point (Figure 2.19) (Sauermann *et al*., 2000). The relative location of the slip face changes due to the dependence of the slip face length L_s upon *H*; the ratio of L_s to *L* increases with *H* (Herrmann *et al*., 2005; Herrmann, 2006):

$$L_s = \frac{H}{tan\theta} \tag{16}$$

The slipface angle is at repose, generally between $31°<\theta<35°$. The evolution of the slope is a function of dune size. As dune size increases, the stoss-slope and lee-slope curvature changes, with an increase in straight sections, shorter convex sections, which are replaced by straighter sections, and finally, curvature increases on the stoss side (Embabi and Ashour, 1993). However, according to Sauermann *et al*. (2000), there are morphological elements that are scale-invariant such as the stoss-side, due to the fact that it can be approximated by a paraboloid. The

morphological variation between barchan dunes that occur in the field compared to barchan dunes produced experimentally in a flume or wind tunnel should be examined, as scale invariance has direct implications with regard to investigating barchan dunes experimentally. Dimensions of naturally-occurring aeolian barchan dunes may reach an order of 1,000 times the magnitude of a barchan dune formed in a flume or wind tunnel (Figure 2.20).

The shape variability of barchan dunes across different environments, from aeolian to subaqueous environments, should be investigated. To quantify the comparison between barchan dunes, the dune length and roundness should be determined. In Figure 2.20, Endo et al. (2005) compared the width, W_t, and total length, L_t, of subaqueous and subaerial barchan dunes observed in the field with the subaqueous barchan dunes produced experimentally in their study. Addressing the relationship between naturally-occurring subaqueous and subaerial barchan dunes, subaqueous barchan dunes exhibit a slightly wider shape compared to their aeolian counterpart, based upon the dataset of Lonsdale and Malfait (1974). The dataset of Allen (1968) comprised subaqueous field barchan dunes, and was two order-of-magnitudes smaller than the other field datasets, grouping with the experimental barchan dunes. W_t and L_t are not normalized in Figure 2.21. The barchan dune total length L_t can be further divided into the horn length L_h and the body length L_b (Figure 2.21). L_b is defined as the length of the toe to the bayhead (a point along the leeside baseline that intersects the centerline), and L_h is defined as the length from the bayhead until the termination point. In Figure 2.22, the same datasets included in Figure 2.21 are presented comparing L_b/W_h to L_h/W_h. Two flow conditions (unidirectional and oscillatory) are outlined as well. The results indicate that, overall, aeolian barchan dunes have relatively longer horns ($L_h/W_h > 0.35$) relative to subaqueous barchan dunes, for those found in the field and the laboratory. Endo *et al.* (2005) grouped the field subaqueous barchan dunes within the 'oscillatory flow' category with barchan dunes produced experimentally under oscillatory flow. The limited data of subaqueous barchan dune morphology (Allen, 1968; Lonsdale and Malfait, 1974) falls within the 'water waves' category, indicating that the barchan dunes were subjected to oscillatory flows. The experiments conducted under a unidirectional flow in a flume were characterized by longer L_b/W_h than the aeolian barchan dunes found in the field, and longer L_h/W_h relative to the subaqueous barchan dunes produced by oscillatory flows. Assuming the boundaries between airflow, unidirectional water flow, and oscillatory water flow do exist,

implying there are indeed different morphologies for various flows and flow conditions, it remains unclear what the controlling factors are.

In addition to horn to body length, the barchan dune baseline roundness also changes with flow conditions. In Figure 2.23, a schematic of two barchan dunes is shown, where the leeside baseline is referred to as the 'inner arc' while the stoss-side baseline is referred to as the 'outer arc'; the arcs are denoted by a bold line. Quantification of the roundness is explained in the caption of Figure 2.23. Subaerial barchan dunes have a morphology that is a cross between the morphology represented by inset images B and D (Figure 2.23). The subaqueous barchan dunes produced experimentally in an oscillatory flow range between the morphology in inset box B and D. The morphology of aeolian barchan dunes is most closely represented by inset box A and B, but also contains data points that move towards inset box D.

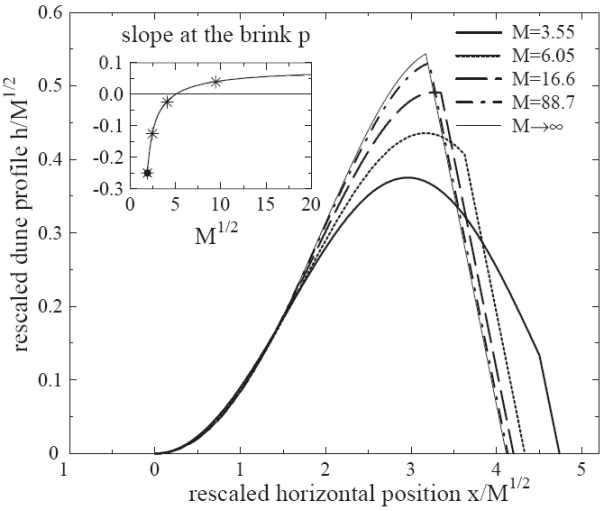

Figure 2.19: Comparison of longitudinal profiles of barchan dunes, specifically at the slope at the brink point (after Andreotti *et al*., 2002a).

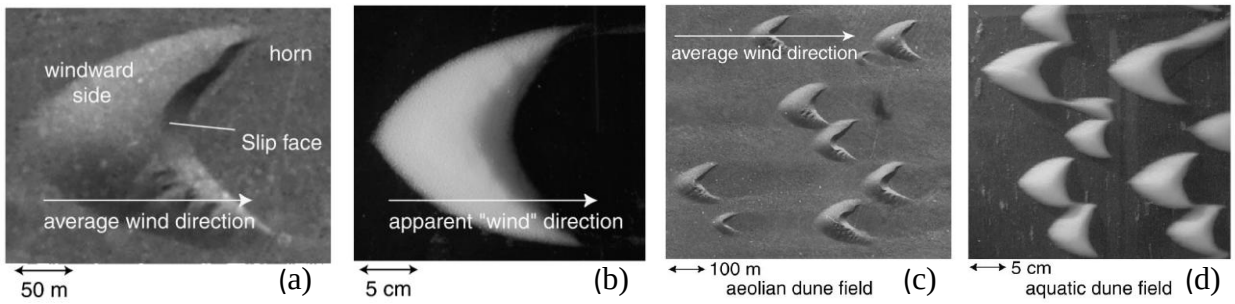

Figure 2.20: Images (a) and (c) are aerial photos of an aeolian barchan dune and dune field in southern Morocco. Images (b) and (d) are pictures of subaqueous barchan dunes generated in a flume. In image (a) the barchan dune horns are not symmetrical and show some inconsistencies believed to be the result of an apparent change in wind direction (after Hersen, 2002).

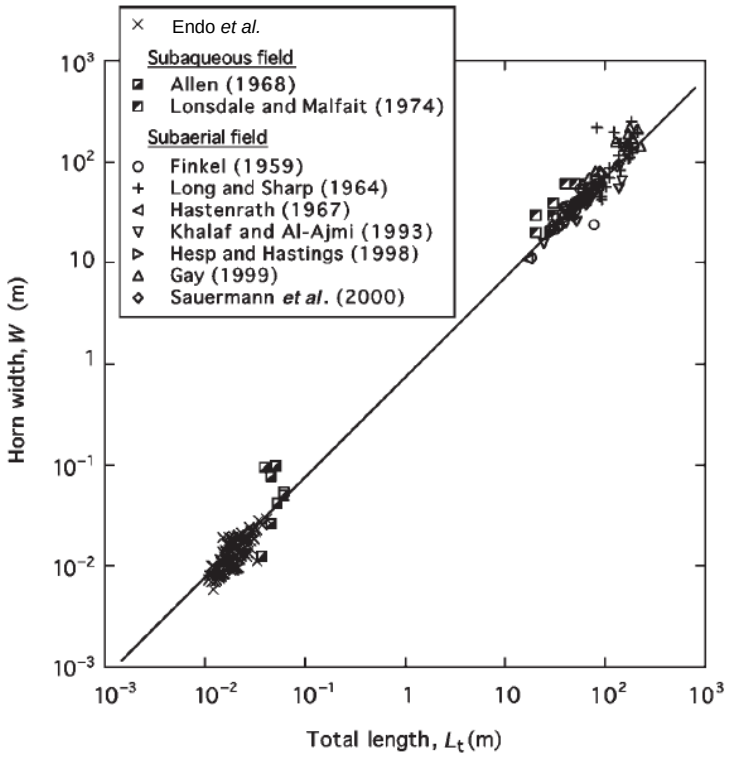

Figure 2.21: Comparison between field and experimental measurements of barchan dune total length, L_t, and width, W (after Endo *et al*., 2004).

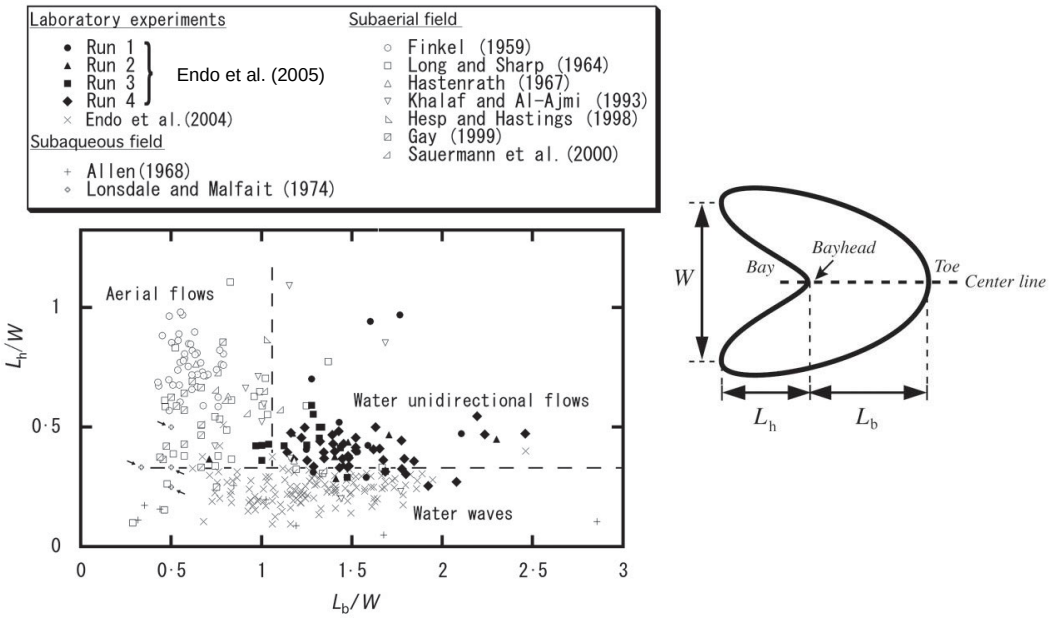

Figure 2.22: Comparison between barchan dune measurements of body length L_b and horn length L_h normalized by horn to horn width W_h, compiled from the subaerial and subaqueous realms and oscillatory flows (water waves). The dashed lines represent the superimposed boundaries between aerial flows, unidirectional water flows and water waves. Definition sketch shows a plan-view of the barchan dune baseline, where the variables horn length L_h, body length L_b, and width W, are defined (after Endo *et al*., 2005).

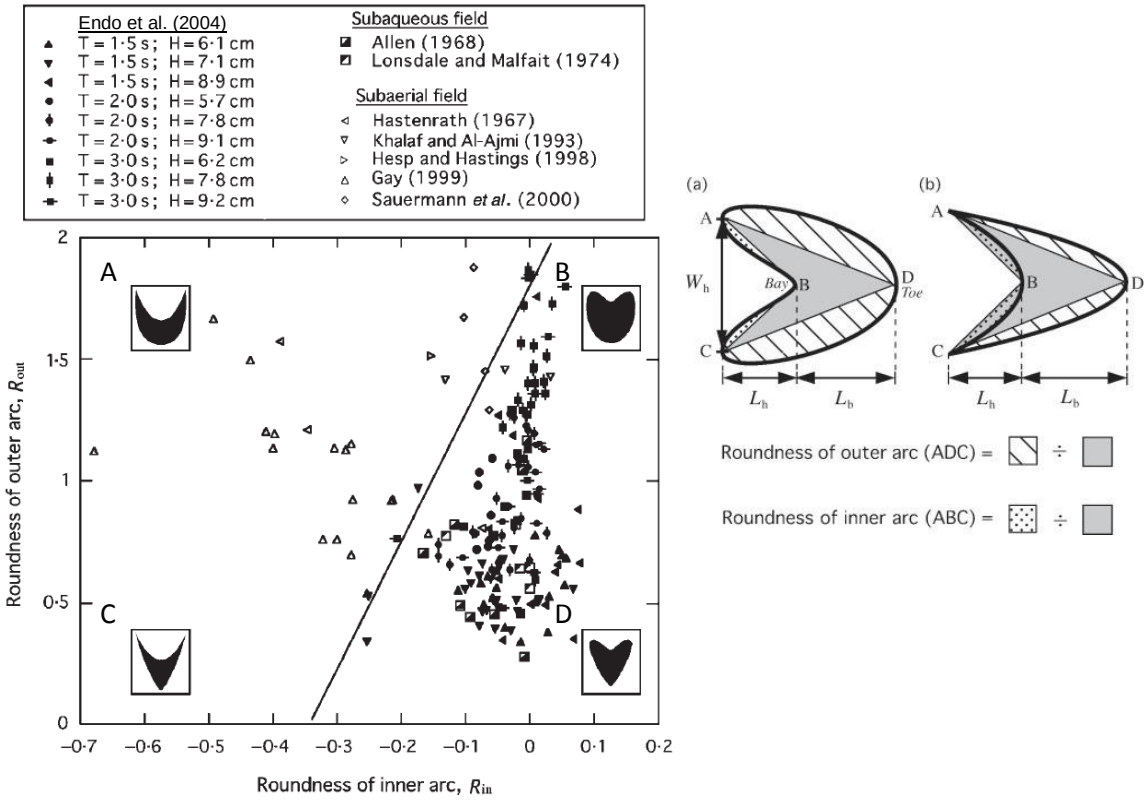

Figure 2.23: A plan view schematic of a barchan dune: (a) and (b) represent roundness end members. The outer arc (the line connecting points ADC; otherwise known as the stoss-side baseline) is calculated by dividing the striped area by the solid area, while the inner arc (the line connecting points ABC; otherwise known as the leeside baseline) is calculated by dividing the dotted area by the solid area (after Endo *et al*., 2004).

2.2.5 Quantifying curvature

The barchan dune is composed of many curves - the baseline, the brink, the stoss slope, the slipface, and side slopes - which are typically approximated using ellipses and parabolas. When viewed in planform, a barchan dune baseline can be deconstructed into two parts: the windward baseline (outer arc) and the downwind baseline (inner arc; Figure 2.24). The windward baseline can be approximated by a partial ellipse and the downwind baseline can be expressed as a parabola (Lettau and Lettau, 1969; Sauermann *et al.*, 2000; Wang *et al.*, 2007). Field measurements gathered by Wang *et al.* (2007) of the windward and downwind baseline shapes were plotted against their respective geometrical approximations (ellipse and parabola) with a general fit (Figure 2.25).

The brink is the curve that separates the slip face from the stoss-slope and resembles a parabola (Sauermann *et al.*, 2000; Herrmann, 2005). To consider the brink curve in greater detail, Wang *et al.* (2007) resorted to differential geometry.

The longitudinal centerline profile of a barchan dune (parallel to flow direction) is characterized by convex, concave and straight sections (Figure 2.26). The central-axis section of the slope from the toe of the dune until mid-way is typically concave and then abruptly transitions into a convex slope from the mid-way point until after the crest. The stoss-side profile can be approximated by a parabolic surface with a defined upper limit at the brink marking the slipface, but the resulting shape is totally convex contrary to the standard barchan dune profile (Sauermann *et al.*, 2000). Momiji and Bishop (2002) successfully modeled the stoss-side slope from the height, *H*, sediment diameter, *d*, and approaching shear velocity, u_*.

A lateral cross-section of naturally-occurring barchan dunes (normal to the flow direction) displays symmetrical and asymmetrical slopes resembling Gaussian curves (Hesp and Hastings, 1998; Figure 2.26). Both slopes are characterized by a declining grade; the slope angle is 9 – 18° at the base and 11-15° halfway; the slope angle decreases to 4-9° as it approaches the top of the dune until finally reaching 1° at the crest (Hesp and Hastings, 1998). The average lateral slope grade is 11° (Howard *et al.*, 1978; Hesp and Hastings, 1998). The slope asymmetry observed in the cross-section is most likely a result of an oblique wind direction. Sauermann et al. (2000) plotted the field measurements of barchan dunes against a parabola (Figure 2.27), showing an overall good fit.

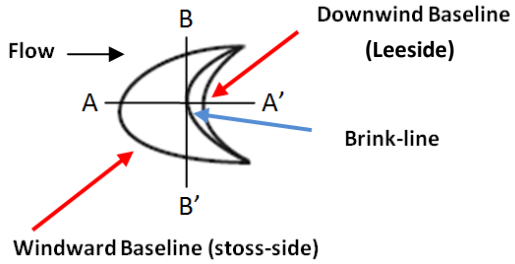

Figure 2.24: A planform-view schematic diagram of a barchan dune defining the centerline-axis profile (A-A') and the lateral cross-section (B-B'). The windward and downwind baselines are indicated by the red arrows. The blue arrow indicates the brink-line.

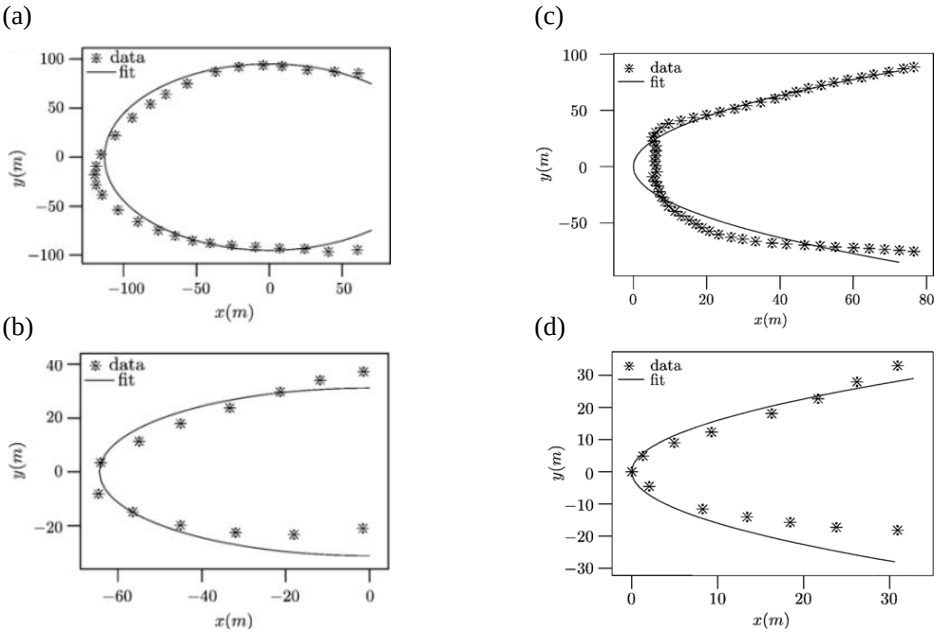

Figure 2.25: Field data of two barchans, (a) and (b), windward baseline compared to a fitted ellipse, where *a=113.182 m* and *b=95.197 m* for the barchan in image (a) and *a=64.464 m* and *b=31.132 m* for the barchan in image (b). Field data of two barchans, (c) and (d), downwind baseline compared to a fitted parabola, where $c=0.010\ m^{-1}$ in image (c) and $c=0.040\ m^{-1}$ in image (d) (after Wang *et al*., 2007).

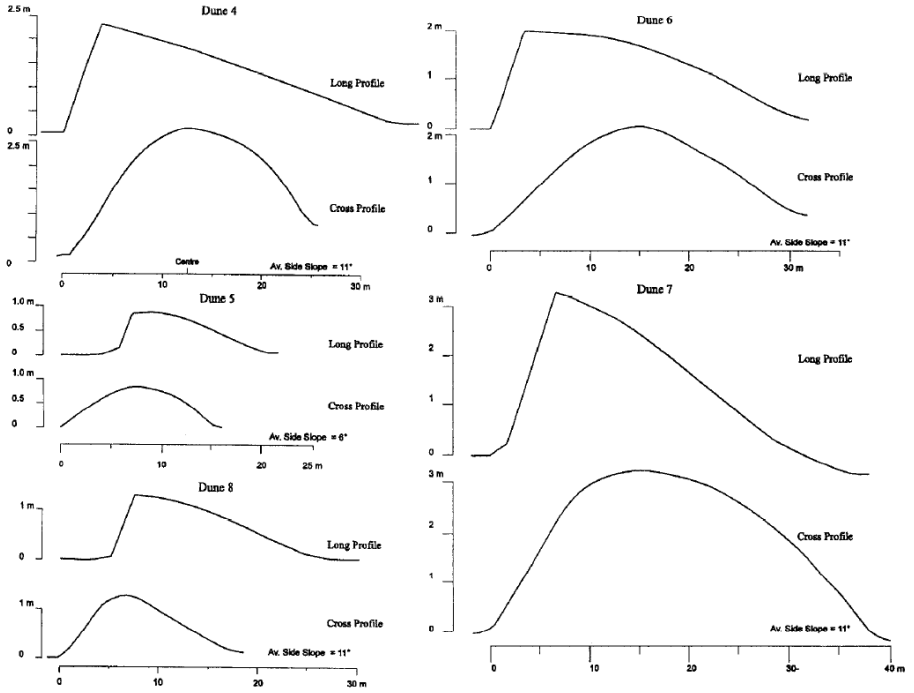

Fig. 5. Long profiles (dune centreline axis) and cross-profiles of a selection of barchans near the Huab River, Namibia. The cross-profiles were surveyed normal to the dune and cross the brinkline immediately just upwind of the top of the slipface.

Figure 2.26: Longitudinal and lateral profiles along the line of symmetry of multiple barchan dunes (after Hesp and Hastings, 1998).

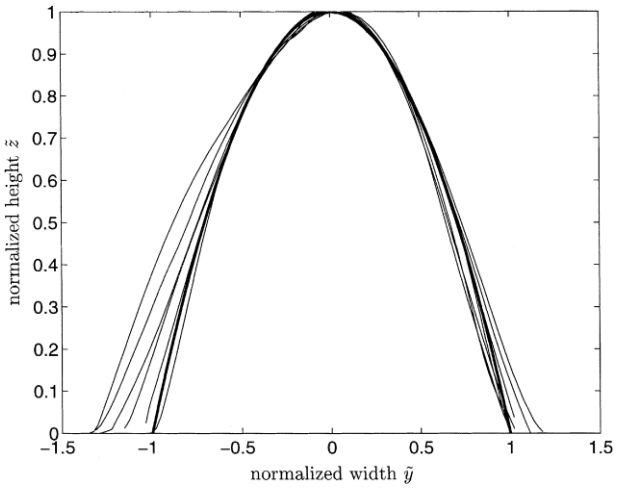

Figure 2.27: Lateral profiles of multiple barchan dunes compared to a parabola (thick line) (after Sauermann *et al*., 2000).

2.3 Barchan dune migration

The migration of a barchan dune corresponds directly to the flow velocity and particle Reynolds number (Niño and Barahona, 1997; Sauermann *et al*., 2000; Endo *et al*., 2005). The mechanism by which barchan dunes propagate is sediment erosion on the dune stoss-side, where the flow dislodges the grains and transports them via saltation, and sediment deposition at the crest or brink, due to a velocity reduction. The grains are redistributed on the dune leeside via avalanches (Andreotti *et al.*, 2002a).

2.3.1 Migration rate

The standard migration rate for a relatively small barchan dune, where H=3 m, is approximately 50 m/year, but can range from 15 m/year to 60 m/year; for a larger barchan dune, where H=15 m, the migration rate ranges from 4 m/year to 15 m/year (Hersen *et al*., 2002; Andreotti *et al*., 2002a). Barchan dunes in cold climates, such as Antarctica, migrate at an average rate of 1.5 m/year, due to hindering factors such as 'entrained ice, soil moisture and a reversing wind regime' (Bourke *et al*., 2009).

The migration rate of a barchan dune is directly proportional to the flow velocity and inversely related to dune height (Herrmann *et al.* 2005). Essentially, a smaller barchan dune migrates at a faster rate than a larger barchan dune (Figure 2.28). The barchan dune migration rate, c (i.e. the celerity of the barchan dune) can be approximated based upon the principle of mass

conservation, by relating the sediment flux at the crest, Q_s, and the crest height, H, by the following relationship (Hersen *et al*., 2002; Andreotti *et al*., 2002a):

$$c \cong \frac{Q_s}{H} \tag{17}$$

The sediment flux, Q_s, at the crest is no longer dependent upon H, for barchan dunes exceeding the saturation length, l_s (Bagnold, 1941; Hersen *et al*., 2002). This is expressed through the inverse relationship between the migration rate, c, and the dune height, H (Figure 2.29a; Cooke *et al*., 1993; Parker Gay Jr., 1999; Hersen *et al*., 2002). A standard sediment flux, Q_s, is 100 m^2s^{-1} (Andreotti *et al*., 2002a).

The timescale for a barchan dune in the field to cover a distance equivalent to its length, i.e. the turnover time, is on the order of months; a barchan dune where H=3 m, has a turnover time ranging from 5 months to 2 years while a larger barchan dune where H=15 m has a turnover time ranging from 6 years to 25 years (Andreotti *et al*., 2002a). For a barchan dune produced experimentally in a flume, the turnover time is on the order of minutes; for a barchan dune where H=3 mm, the turnover time is 30 minutes (Hersen *et al*., 2002; Andreotti *et al*., 2002a).

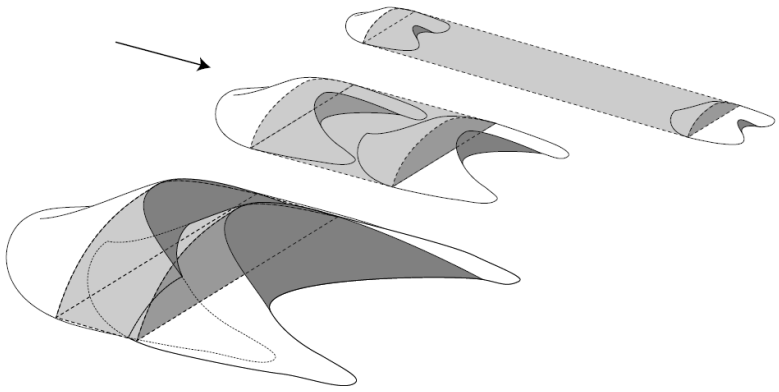

Figure 2.28: An illustration of the displacement of a barchan dune over the same interval of time (shaded region), showing the largest displacement for the smallest barchan dune and the smallest displacement for the largest barchan dune (after Andreotti *et al*., 2002a).

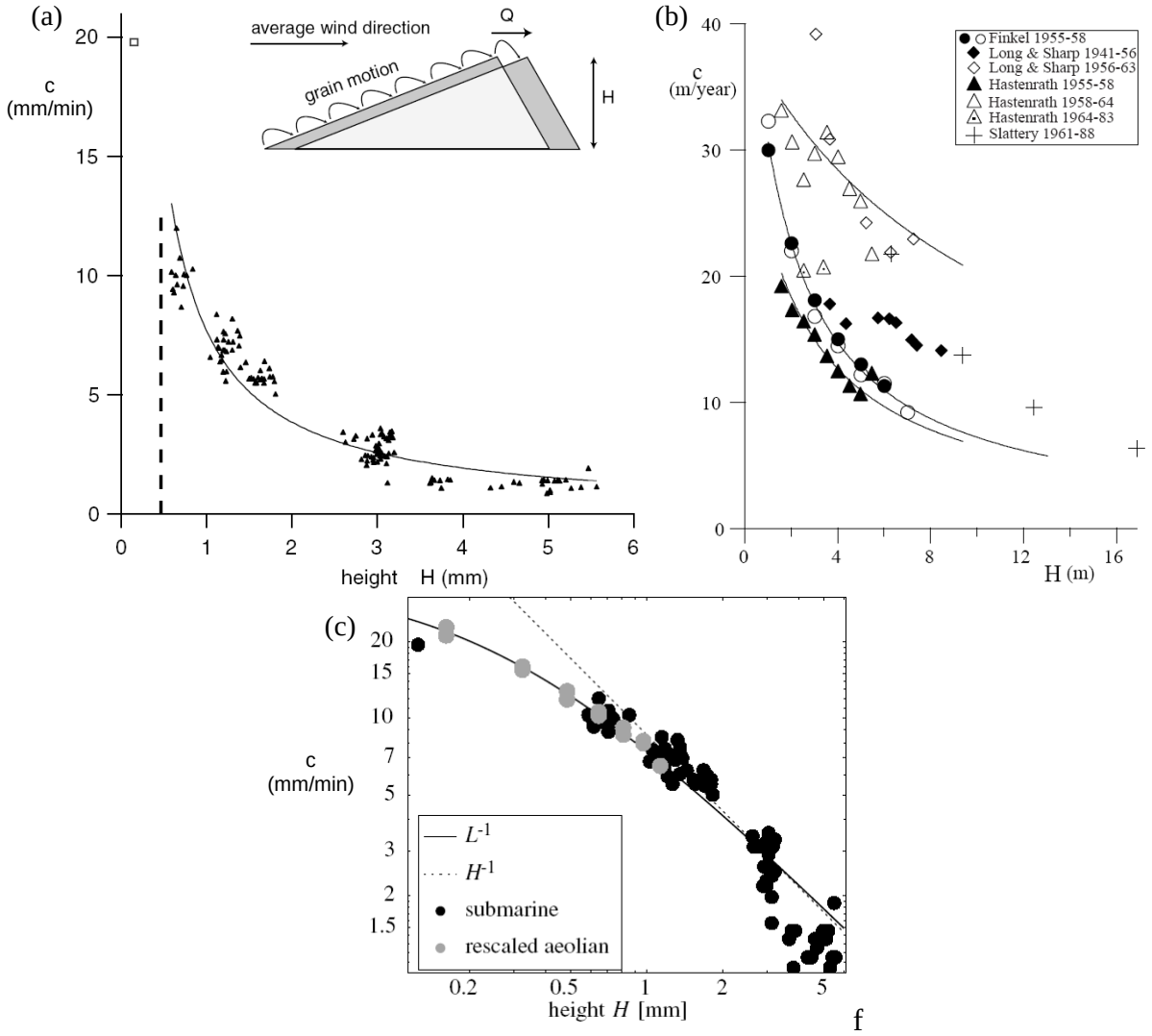

Figure 2.29: The relationship between barchan dune height, *H*, and migration rate, *c*: (a) after Hersen *et al*., 2002; (b) after Andreotti *et al*., 2002a; (c) after Kroy and Guo, 2004. The aeolian data included in (c) was rescaled by 6.2×10^3.

2.4 Summary

This chapter has reviewed the origin of barchan dunes, focusing on their occurrence in aeolian and subaqueous environments and their processes of formation. In addition, a thorough discussion of barchan dune morphology and morphologic relationships has provided the basis for determining whether barchan dunes are scale invariant, as well as determining their minimum size. A variety of methods to describe barchan dune curvature have been outlined. Finally, the rate at which barchan dunes migrate, typically 15-60 m/year for a 3 m high barchan dune, and the relationship between barchan dune volume and celerity has been presented.

CHAPTER 3

FLOW OVER NEGATIVE STEPS, HUMPS, 2-D AND 3-D DUNES

3.1 Introduction

2-D and 3-D dunes form in both open-channel flows and aeolian flows through boundary layer processes involving sediment erosion and deposition. In this chapter, the flow around dunes, and other solid objects analogous to dunes, will be outlined. In order to simplify the discussion, only solid non-erodible objects immersed in a boundary layer at high Reynolds numbers will be considered to examine the flow characteristics. In Figure 3.1, an example of a solid object placed upon a flat bed in a boundary layer flow is shown. Two types of vortices are generated: (1) the boundary layer vortex V_{bl}, which is caused by the production of shear stress from the interaction of the solid surface and the fluid; and (2) the separation bubble vortex V_{sb}, which is caused by the separation of the flow from the solid body surface resulting in the formation of the separation bubble located downstream of the solid object between the shear layer and the floor. In the case of a blunt object, such as a cylinder, a vortex V_u upstream of the object will develop at the leading edge.

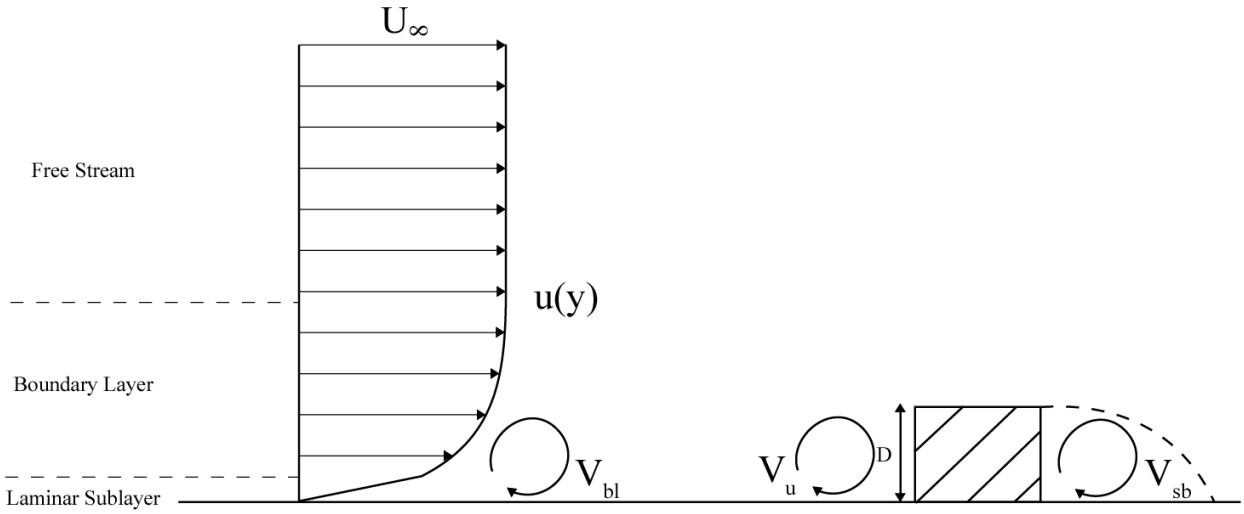

Figure 3.1: A schematic of the velocity profile of a turbulent boundary layer and a wall-mounted solid body (represented as a box with diameter D). The two vortex types, V_{bl} and V_{sp}, are positioned to illustrate where they occur. U_∞ represents the free stream velocity and u(y) represents the streamwise velocity with respect to height.

Solid objects traditionally used to investigate the flow around bedforms include the 2-D negative step and the wall-mounted hump. Topographically-induced flow effects may be modeled by

incorporating negative steps and wall-mounted humps to serve as experimental proxies for more complex geometries such as a barchan dune. The following subsections discuss the flow around a negative step, hump, 2-D dune and 3-D dune, in order of increasing geometrical complexity in order to highlight flow similarities between them and establish knowledge about recurring turbulent phenomena.

3.2 Flow over negative steps

The simplest case of topographically-induced separation is the 2-D negative step (i.e. backward-facing step). It is possible to relate turbulent flow phenomena generated by a negative step to that of a 2-D and 3-D dune (Figure 3.2). This analogy is based upon the negative step brink-point *BP* as a representation of the dune brink-point *BP*. The *BP* is the location where the flow separates from the solid body surface, for a negative step and a dune. The flow reattaches to the floor surface downstream of the *BP*, forming a recirculation bubble which is characterized by an adverse pressure gradient coupled with a jump in turbulence intensity (Kadota and Nezu, 1999). The flow reattachment length x_r is schematically represented in Figure 3.2.

A wide range of literature spanning four decades has investigated flow over a negative step and it continues to be the subject of ongoing research (e.g. Raudkivi, 1963; Etheridge and Kemp, 1978; Kuehn, 1980; Durst and Tropea, 1981; Sinha *et al*., 1981; Armaly *et al*., 1983; Adams *et al*., 1984; Nakagawa and Nezu, 1987; Nezu and Nakagawa, 1989; Isomoto and Honami, 1989; Ra *et al*., 1990; Ötügen, 1991; Beaudoin *et al*. 2004). In Figure 3.3, a schematic representation of negative step geometry is presented. The instantaneous flow reattachment point fluctuates up to $\pm 2H$ around the mean x_r in the leeside of a negative step (Nezu and Nakagawa, 1989; Kadota and Nezu, 1999). The reattachment length x_r can be considered the most important feature in a separated-reattached flow. The literature review highlights that x_r is a function of the Reynolds number *Re* ($Re=VD/\nu$), the step height H_s, the expansion ratio *ER* ($Er=H_d/H_u$), the momentum thickness of the approaching flow, the upstream boundary layer profile and the inlet turbulence intensity (Armaly *et al*., 1983; Le *et al*., 1997). V is 66% of the maximum inlet velocity, D is the diameter of the upstream channel ($D=2H_u$), and ν represents the kinematic viscosity of the fluid (Armaly *et al*., 1983).

The following trends were reported by Armaly *et al.* (1983): (1) with increasing Reynolds number, x_r increases in the laminar regime ($Re<1{,}200$), decreases in the transitional regime

(1,200<*Re*<6,600), and stabilizes in the turbulent regime (*Re*>6,600). (2) Within the turbulent regime, the flow retains its two-dimensionality and exhibits a single recirculation region where $x_r/H_s \approx 8$; within the transitional regime, the flow becomes three-dimensional and exhibits additional recirculating regions along the wall (Armaly *et al*., 1983). (3) With a decreasing *ER*, the normalized reattachment length x_r/H_s decreases (Durst and Tropea, 1981; Armaly *et al*., 1983). (4) The effects of the negative step on the flow are negligible after $6H_s$ (Bradshaw and Wong, 1972; Kim *et al*., 1978; Westphal *et al*., 1984; Adams *et al*., 1984; Le *et al*., 1997).

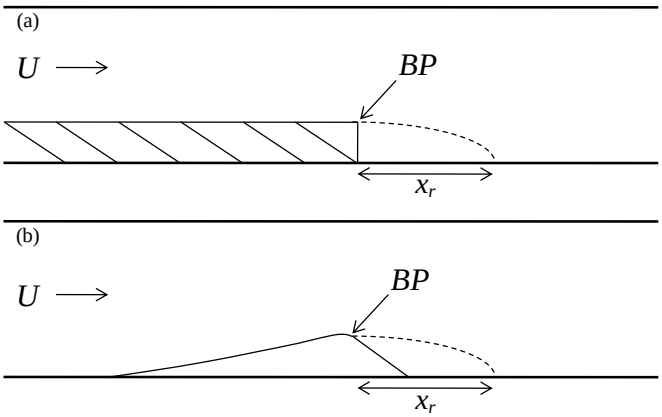

Figure 3.2: Comparison between the geometry of (a) a negative step and (b) a dune. BP represents the brink-point. The separation bubble is denoted by the dashed line.

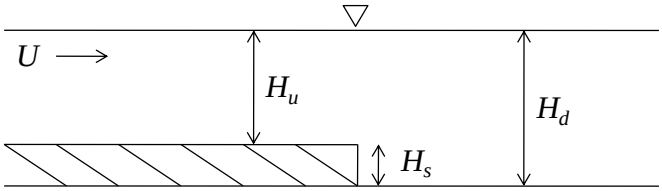

Figure 3.3: The 2-D negative step length scales defined. The height of the negative step is H_s. The expansion ratio, H_d/H_u, is the ratio of the height of the downstream-step section H_d with respect to the height of the upstream-step section H_u.

3.3 Flow over hills

The next degree in geometric complexity is the case of turbulent flow over hills, investigated experimentally with wall-mounted humps. A hump differs from the negative step by introducing streamline curvature and acceleration generated from stoss-slope curvature (Figure 3.4). The shape and curvature of a hump centerline profile is similar to a 2-D and 3-D dune centerline profile. A number of experimental studies have investigated the flow over wall-mounted humps with the intention of improving the aerodynamics of airfoils by reducing flow separation (e.g.

Seifert and Pack, 2002; You *et al*., 2006; Morgan *et al*., 2006). However, studies investigating the flow over hills through wall-mounted humps are more applicable to the present work (Jackson and Hunt, 1975; Mason and Sykes, 1979; Bradley, 1980; Walmsley *et al*., 1982; Mason and King, 1984; Walmsley and Salmon, 1985; Jensen and Zemen, 1985; Mason, 1986; Taylor *et al*., 1987; Hunt *et al*., 1988; Almeida *et al*., 1993; Breuer *et al*., 2009).

Breuer *et al.* (2009) investigated experimentally and numerically flow over a series of coaxial hills (inter-hill spacing was 9*h*) at a range of Reynolds numbers, $100 \leq Re \leq 10{,}595$ ($Re=hU/\nu$). Three coherent structures were identified from the numerical simulation, presented in Figure 3.5: 'A' - inclined 'elongated streamwise structures' (akin to 'streaks'); 'B' - extremely 'elongated streamwise structures' extending off the upstream hill crest and adjacent to the stoss-side of the downstream hill; and 'C' - shear layer spanwise structures, generated by Kelvin-Helmholtz instabilities (Figure 3.5e) that deform into streamwise structures (Figure 3.5a). With increasing *Re:* (1) the reattachment length progressively decreased until *Re*=5,600, and then increased at *Re*=10,595; and (2) the reattachment length fluctuations progressively decreased. Breuer *et al.* (2009) observed a small recirculating vortex at the leading edge of the windward side of the hill and at the crest at *Re*=10,595.

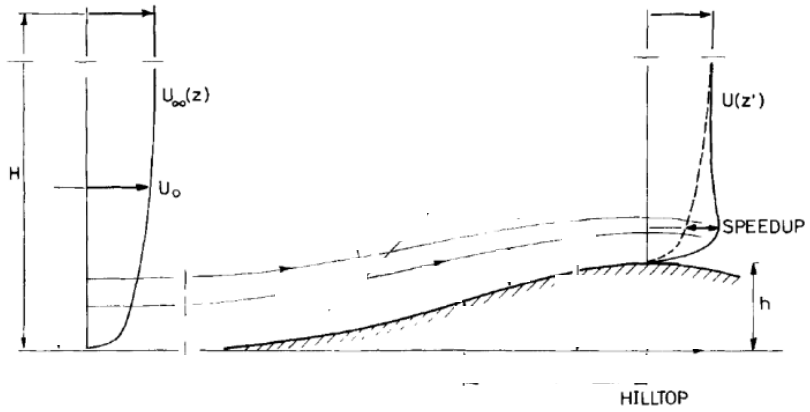

Figure 3.4: A sketch of a hump showing the velocity profile upstream of the hill and at the hill crest (after Zemen and Jensen, 1987). *H* is the height of the boundary layer; U_o is the 'unperturbed' velocity; $U_\infty(z)$ is the free stream velocity; *U(z')* is the velocity at height *z*'; *h* is the height of the hill;

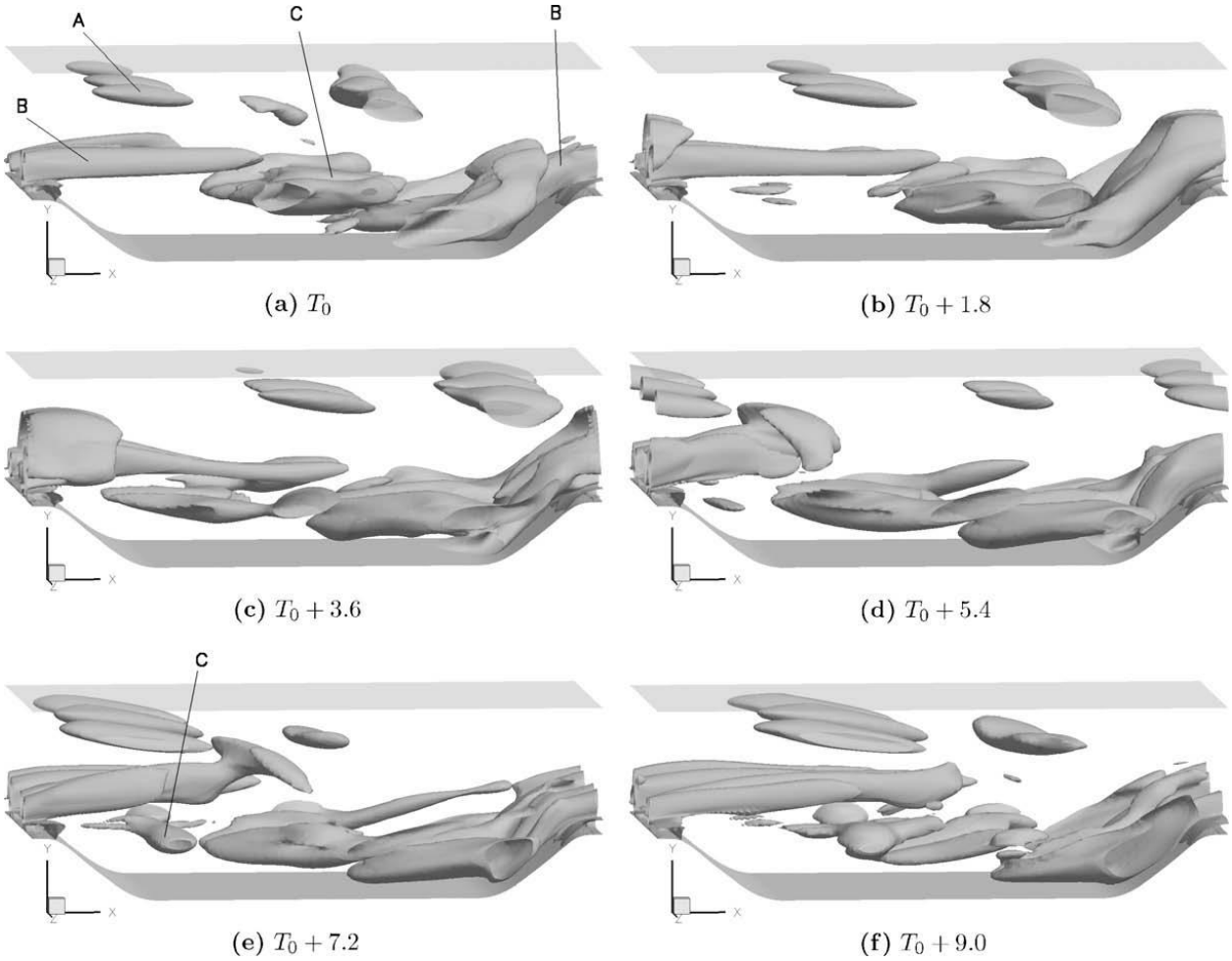

Figure 3.5: Three coherent structures identified by a numerical model: A -'elongated streamwise structures' (i.e. streaks); B – extremely 'elongated streamwise structures'; C - shear layer spanwise structures (after Breuer *et al*., 2009).

3.4 The mean flow structure of 2-D and 3-D dunes

3.4.1 Time-averaged flow characteristics

The nature of the time-averaged flow over a 2-D bedform has been widely established (e.g. Nelson *et al.*, 1993; Bennett and Best, 1995; Wiggs *et al.*, 1996; Walker and Nickling, 2003; Best, 2005). In Figure 3.6a, flow over an asymmetrical 2-D dune, where the slipface is at angle-of-repose, is delineated into five zones based upon the streamwise and wall-normal velocity components: (1) 'Separation zone'; (2) 'Shear layer'; (3) 'Expanding flow'; (4) 'Internal boundary layer'; and (5) 'Maximum velocity' (McLean and Smith, 1979. 1986; Nelson and Smith, 1989; McLean, 1990; Nelson *et al.*1993; McLean *et al.*, 1994, 1999; Bennett and Best, 1995; Maddux *et al.*, 2003a; Kleinhans, 2004; Best, 2005). The characteristics of these five

zones are: (1) the ‘separation zone’: the flow detaches at the crest, forming a flow reversal zone within the dune leeside (Figure 3.7a; Bennett and Best, 1995). (2) The ‘shear layer’: a shear layer develops bounding the separation zone and the overlying flow; a wake is generated and propagates upwards towards the free surface (i.e the water-air contact). (3) The ‘expanding flow’: beyond the recirculation bubble, the overlying flow descends as illustrated in Figure 3.7b (represented by the blue circular region). (4) The ‘Internal Boundary Layer’ (IBL): the reappearance of the *IBL* on the stoss-side of the downstream dune is a direct result of the reattachment of the flow to the bed (Nelson *et al.*, 1993). In Figure 3.6b, the growth of the *IBL* with distance is shown. The *IBL* maximum thickness is 0.25*H* at the crest (Venditti and Bauer, 2005). (5) The ‘maximum velocity’: flow accelerates over the dune stoss-side, reaching a maximum streamwise velocity at the crest.

The primary effects upon the local flow field downstream of the dune crest are directly a result of flow separation (Bennett and Best, 1995). Nelson *et al.* (1993) refer to the flow separation cell and subsequent downstream propagating wake as the ‘momentum defect region’. The wake spreads out into the downstream flow generating discrete ‘spatial accelerations’ joined by topographically-controlled accelerations, culminating in a clear distortion of the mean flow momentum equilibrium. The wake reaches a maximum thickness of ~1-2*H* before the following downstream dune’s crest. By the downstream dune’s crest, the mixing of the diffusing wake is complete and the flow is recovered (Venditti and Bauer, 2005). In the case of multiple dunes, the lingering influences of multiple upstream wakes are visible within the expanding flow region, particularly in shallow open-channel flows such as rivers (Maddux, 2002). For larger flow depths (i.e. aeolian boundary layer flows), the interior region is fairly uniform and can be represented by the ‘law of the wall’ (Maddux, 2002).

Although the primary components identified in the mean flow structure of 2-D dunes still pertain to 3-D dunes (i.e. separation cell, spreading wake and shear layer, *IBL*, etc.) significant differences exist (Maddux *et al*., 2003a; Best, 2005; Venditti, 2007). As a dune assumes a three-dimensional form, the dynamics of the flow become increasingly more complex due to the presence of secondary circulation expressed as spanwise vorticity deforming into quasi-streamwise voriticity (Best, 2005). Allen (1968) was the first to investigate the near-bed flow over a broad range of 3-D bedform geometries, including the barchan dune (Figure 3.8). This plan view perspective clearly shows flow steering, which diverts flow around the flanks of the

barchan dune on the dune stoss-side, as well as flow separation zone and the line of flow reattachment, located within the dune leeside. Downstream of flow reattachment, the recovered flow converges with the flow flanking the barchan dune.

Maddux et al. (2003a,b) introduced a sinuous crestline along the spanwise-wall-normal plane (Figure 3.9) to an otherwise 2-D dune, and reported the following differences: 2-D dunes produce more turbulence and less friction than 3-D dunes. The flow over a 3-D dune near the bed steers around the bedform, along the flanks of the bedform. This 'flow steering' produces areas of increased velocity, which in turn, increase the skin friction and the form drag. Maddux et al. (2003a) conclude from comparisons between their experiments and numerical model, that 'flow steering' is reserved for near-bed flow rather than being vertically distributed in the flow interior. The average streamwise velocity component is greatest over the 3-D dune crestline node, which is located midway between the dune crest (highest point) and the lowest point along the crestline; the maximum velocity occurs at the crest of a 2-D dune. The greatest spanwise velocity for the 3-D dune occurred in the dune leeside, beyond the crestline node. Unlike the 3-D dune morphology, the boundary shear stress of the 2-D dune morphology may be set by the fluctuations in Reynolds shear stress rather than the mean flow. It is suggested in the case of 3-D dunes that the local variation in near bed velocities could generate a greater boundary shear stress.

Venditti (2007) investigated flow over 2-D and 3-D dunes of varying geometries and concluded, that three-dimensionality introduces compound complexity for predicting and modeling flow resistance. The full width saddle (FWS) is the closest geometry to a barchan dune among the geometries investigated by Venditti (2007), but had a barely detectable separation bubble and shear layer in the leeside (Figure 3.10). The comparison between the 2-D dune and the 3-D FWS revealed that the total boundary shear stress and velocity for the FWS increased relative to the 2-D dune while the presence of secondary flow due to the FWS shape resulted in reduced turbulence. Venditti (2007) argues that within the FWS leeside, the flow diverges due to secondary flow patterns moving fluid away from the axis centerline, suggesting the existence of two secondary circulation cells bounding the axis centerline. The FWS bedform shape also reduced flow resistance compared to the full width lobe (FWL) and 2-D dune straight geometries.

(a)

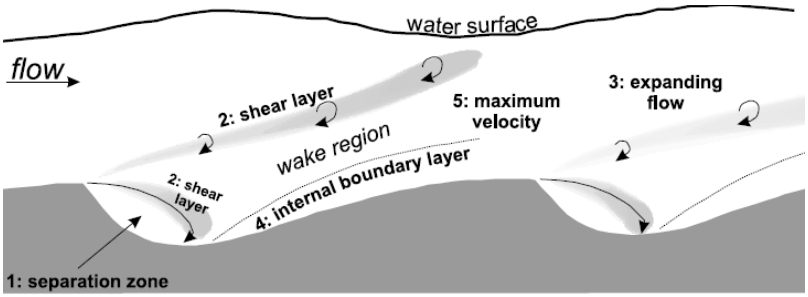

(b)

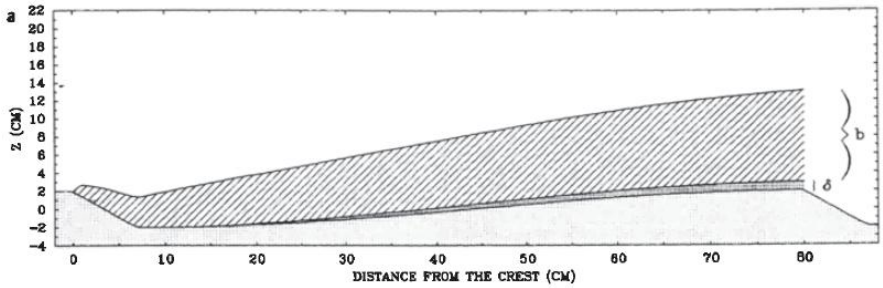

Figure 3.6: (a) An illustration of the five regions of the flow structure above a two-dimensional dune (after Best, 2005). (b) The height of the internal boundary layer, δ, and wake region, *b* over a 2-D bedform. The flow above the wake region is comprised of interfering wakes of upstream bedforms as well as weak acceleration resulting from the topographic changes (after Nelson et al., 1993).

(a)

(b)

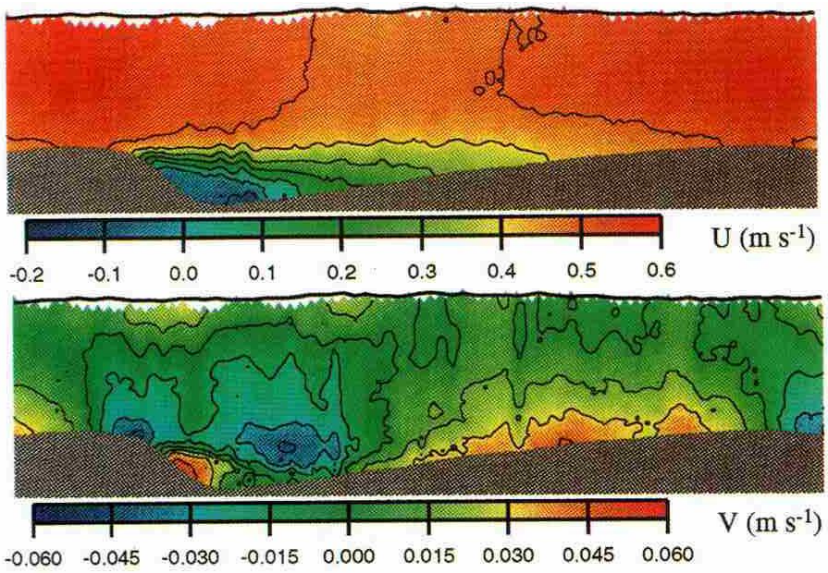

Figure 3.7: The time-averaged flow over a series of 2-D dunes: (a) the streamwise velocity component (b) the wall-normal velocity component (after Bennett and Best, 1995).

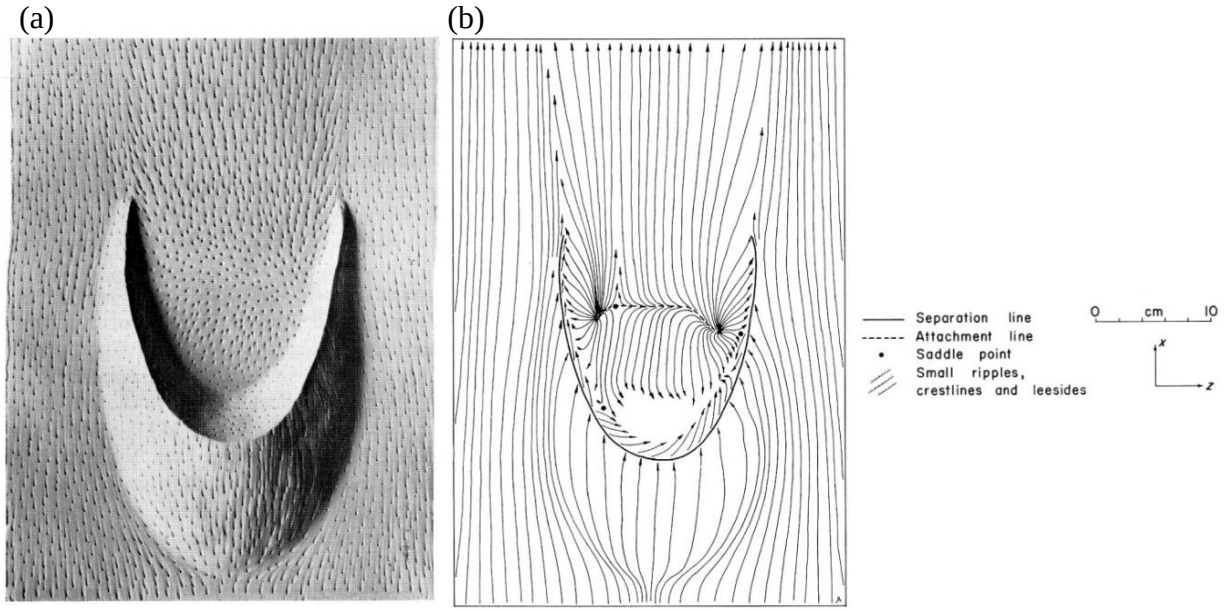

Figure 3.8: (a) Flow over a barchan dune. Flow is from bottom to top; (b) bed streamlines derived from the barchan dune model presented in (a) (after Allen, 1968).

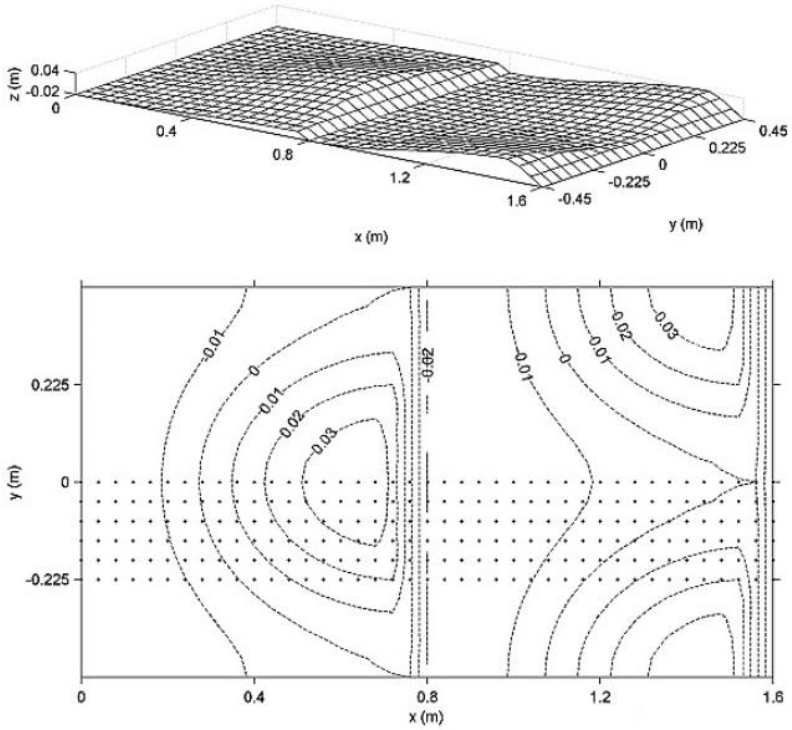

Figure 3.9: The three-dimensional dune geometry: (a) a three-dimensional grid of the geometry; (b) a plan view contour map of the geometry (after Maddux *et al*., 2003a).

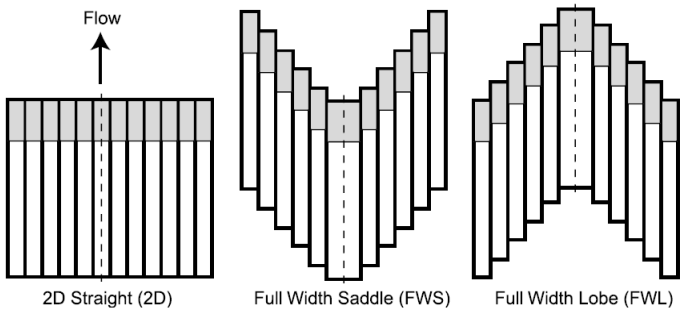

Figure 3.10: The shapes used to investigate three-dimensionality effects upon turbulence; white area denotes the stoss-side while gray area denotes the leeside (Venditti, 2007).

3.4.2 Flow Separation Zone

In the leeside of a dune, the flow detaches from the dune surface resulting in the development of a reverse-flow recirculation eddy (Figure 3.11). Flow separation is responsible for the majority of flow resistance induced by the dune (Vanoni and Hwang, 1967; Wijbenga, 1900; Ogink, 1989; Julien *et al.*, 2002; Paarlberg *et al.*, 2007). Flow within the recirculation bubble is vertically confined as there is no net discharge from the bed to the top of the separation zone (Paarlberg *et al.*, 2007). While flow separation is a well-established phenomena, few papers have examined flow separation in the leeside of a barchan dune; the primary subject of flow over dunes belongs to 2-D transverse dunes (Smith and McLean, 1977; Engel, 1981; Buckles *et al.*, 1984; Nelson and Smith, 1989; Sweet and Kocurek, 1990; Bennett and Best, 1995; Kostaschuk and Villard, 1996; Rasmussen *et al.*, 1996; Parsons *et al.*, 2004a; Best, 2005; Paarlberg *et al.*, 2007).

The flow reattachment length x_r is defined as the length between the crest or brink point, where the flow detaches, to the point of reattachment, R (Figure 3.12). The point of reattachment is the location where the streamwise velocity component changes sign, from negative to positive (Schatz and Herrmann, 2006). Table 3.1 presents a summary of reported separation lengths x_r/H (normalized by the crest or brink height, H) over dunes.

The reattachment length x_r is primarily dependent on the flow velocity, flow direction, angle of incidence (Figure 3.13), bedform geometry (slope curvature, stoss and brink angle, etc.), flow depth, and 'atmospheric thermal stability' (Sweet and Kocurek, 1990; Schatz and Herrmann, 2006; Dong *et al.*, 2007; Balachandar *et al*., 2007). Some researchers (Engel, 1981; Paarlberg *et al.*, 2007) argue that the separation bubble shape in the dune leeside and x_r/H are largely independent of the flow conditions (i.e. Reynolds number, average velocity and the normalized

flow depth (H_u/H)). Kadota and Nezu (1999) and Breuer *et al.* (2009), on the other hand, assert the dependence of x_r/H upon the flow conditions; with increasing Reynolds number, x_r/H initially decreases and then stabilizes. The presence of a downstream dune results in a shorter x_r relative to the single dune or negative step (Kadota and Nezu, 1999). For multiple coaxial dunes, x_r/H experiences a lower decay rate with increasing Re and Fr compared to a single dune. Balachandar *et al.* (2007) demonstrated that at shallow depths x_r/H increased in comparison to deeper flows . In addition, they suggest that the dune length may influence x_r/H; for instance, a shorter barchan dune length, L_t, would generate a shorter separation bubble.

The relationship between the bedform morphology and the normalized reattachment length, x_r/H, has been investigated by many researchers. Schatz and Herrmann (2006) found that dunes characterized by sharp brink points (where the crest and brink coincide) had the longest x_r/H, while dunes characterized by rounded brink points (non-coincident crest and brink) had shorter x_r/H. Furthermore, a coincident crest and brink point (i.e. sharp profile) results in a longer x_r/H than a non-coincident crest and brink point (i.e. gentle profile) (Paarlberg *et al.*, 2005; Schatz and Herrmann, 2006; Paarlberg *et al.* 2007). As expected, a higher brink point results in a longer separation zone length (Paarlberg *et al.*, 2007). Parsons *et al.* (2004a) also reported longer x_r/H for greater dune heights with equivalent stoss angles. Dong *et al.* (2007) investigated x_r/H with respect to increasing the stoss-slope angle β and discovered that for $\beta<15°$, x_r/H increases and for $\beta>15°$, x_r/H is relatively steady.

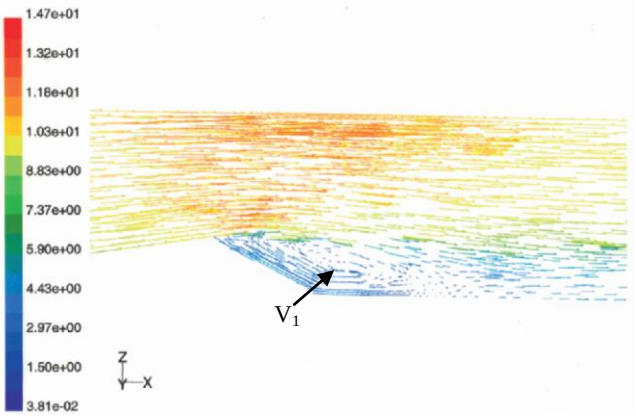

Figure 3.11: The simulated velocity field surrounding a barchan dune, featuring a large vortex in the dune leeside, V_1 (Herrmann, 2007).

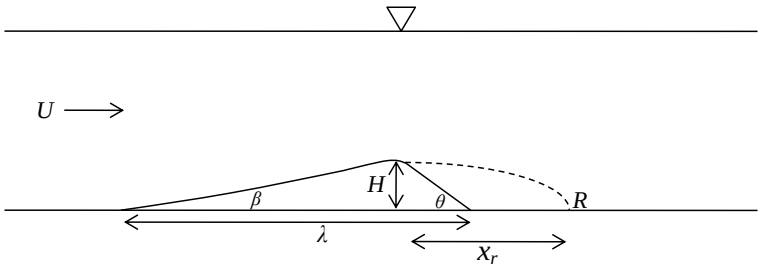

Figure 3.12: A streamwise profile of a dune flow field depicting the flow separation region.

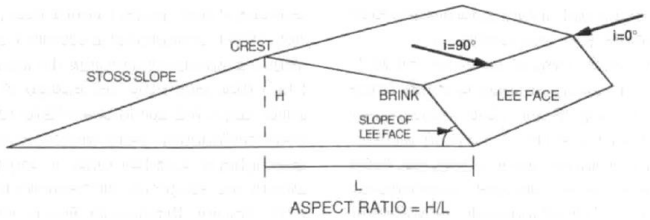

Figure 3.13: The definition of the angle of incidence, *i* (after Sweet and Kocurek, 1990).

Source	Reattachment Length		Dune Morphology	Flow Conditions			
	x_r/H range	x_r/H average	H (mm)	Y (mm)	U ms^{-1}	Re x 10^{-4}	Fr
Nelson *et al.* (1993)[1]*	N/a	4	20 & 40	195-220	0.43	7.7	0.31
Bennett and Best (1995)**[1]	N/a	4.25	40	100	0.57	5.1	0.58
Frank and Kocurek (1996)[2]	1.6-5.4	4	1000-10,000	N/a	N/a	N/a	N/a
Kadota and Nezu (1999)[1]	N/a	4.05	20	80	0.25	1.75	0.29
Schatz and Herrmann (2006)[3]	3-9	N/a	1500-3000	N/a	N/a	N/a	N/a
Dong *et al.* (2007)[4]	4.8-10.8	N/a	25	120	8	6.6	7.4
Stoesser *et al.* (2008)[3]	N/a	5	20	80	0.3	2.5	0.34

Table 3.1: Summary of past research on flow over dunes and reattachment length. [1] Flume experiments; [2] Field Study; [3] Computational simulation; [4] Wind tunnel experiments. * Velocity is averaged over multiple runs; Reynolds number and Froude number based upon averaged velocity. **Reported measurements at dune crest. N/a indicates data unavailability.

3.4.3 Distinction between negative steps and dunes

The primary distinctions between negative steps and dunes are geometric dissimilarity and three-dimensionality (in the case of 3-D dunes). The flow over a dune is characterized by accelerating flow ascending the stoss-slope, which results in a shorter recirculation bubble length relative to the negative step recirculation bubble length (Engel, 1981; Kadota and Nezu, 1999; Maddux *et al*., 2003a). In open-channel flows, the stoss-side acceleration also contributes to contrasting free surface profiles between negative steps and dunes: the free surface elevation increases directly

past the dune crest, and is more pronounced than the surface variation over a negative step (Kadota and Nezu, 1999). Downstream of the dune crest, the free surface elevation decreases directly past the reattachment point, while downstream of the negative step reattachment point the free surface elevation increases (Kadota and Nezu, 1999). Additionally, the turbulence intensity dissipation is amplified downstream of a dune relative to a negative step (Nelson *et al*., 1993; Maddux *et al*., 2003a).

3.5 The turbulent flow structure of 2-D and 3-D dunes

By understanding the turbulence distribution over a dune the bed shear stress and sediment transport can be calculated; furthermore, the relationship between large-scale turbulence, bedform morphology and free surface topography can be established (Best, 2005). The majority of experimental research has been conducted in open-channel flow over single 2-D dunes or a train of coaxially aligned 2-D dunes, and ranges from investigation of the time-averaged flow properties, to study of the effect of flow depth and dune roughness (Müller and Gyr, 1986; Mierlo and de Ruiter, 1988; Lyn, 1993; McLean *et al*., 1993; Coleman and Melville, 1996; Kadota and Nezu, 1999; Hyun *et al*., 2003; Balachandar *et al*., 2007; Balachandar and Patel, 2008).

3.5.1 Coherent turbulent flow structures

The velocity in the dune leeside is reduced dramatically, resulting in the transfer of mean-flow energy to turbulence production. In an open-channel flow, the macroturbulent coherent structures produced behind a dune crest are vortices located in the separation bubble, characterized by spanwise vorticity and large-scale 'kolk-boil' vortices, akin to hairpin vortices, characterized by streamwise vorticity (Figure 3.14a-b; Kadota and Nezu, 1999). The vortices within the separation bubble develop along the shear layer due to Kelvin-Helmholtz instabilities, while the 'kolk-boil' vortices form at flow reattachment. The separation bubble vortex spanwise vorticity deforms into streamwise vorticity, forming the 'kolk-boil' vortex. The separation bubble vortices have a different structure compared to the elongated and inclined 'kolk-boil' structures (Kadota and Nezu, 1999). The 'kolk-boil' vortex (i.e. 'roller', 'hairpin') is categorized as a Quadrant 2 event ($-u'$ and v') and is characterized by strong convection towards the free surface; upon reaching the free surface, the vortex structure 'erupts' forming a 'boil' (Jackson, 1976; Yalin, 1992; Babakaiff and Hickin, 1996; Best, 2005).

A ‘boil’ is the physical manifestation of a large-scale vortex structure reaching the water surface and generally brings with it higher amounts of sediment (Kostaschuk and Church, 1993; Lapointe, 1992; Babakaiff and Hickin, 1996; Bennett and Venditti, 1997; Venditti and Bennett, 2000; Best, 2005). Field measurements by Kostaschuk (2000) support the existence of wake flapping and vortex shedding, especially with regards to their role as a mechanism of sediment transport. The ‘kolk-boil’ vortices comprise one possible flow mechanism responsible for sediment transport and dune formation (Bennett and Best, 1995; Best, 2005). Numerous computational studies have simulated the flow structure for single 2-D dunes and trains of 2-D dunes in open-channel flow (Perić *et al*., 1988; Mendoza and Shen, 1990; Johns *et al*., 1993; Yoon and Patel, 1996; Patel and Lin, 2004; Yue *et al*., 2005a, b; Yue *et al*., 2006; Stoesser *et al*., 2008). Stoesser *et al.* (2008) successfully modeled ‘rollers’, synonymous with the separated spanwise vortices generated in the dune leeside shear layer (Figure 3.15). These spanwise vortices deform into streamwise vortices (i.e. hairpin vortices) due to a secondary instability, which is generated by the lack of cross-stream vortex continuity. The rollers advect towards the free surface, erupting into a ‘boil’.

In an open-channel flow, the shear layer is instrumental in determining the flow across the entire depth (Balachandar *et al*., 2007). The shear layer is a region of increased turbulence intensity for both components, streamwise and wall-normal, as well as high Reynolds stress (Balachandar *et al*., 2007). Stoesser *et al.* (2008) discovered the highest turbulence levels occur at the dune crest and flow reattachment point. In the case of a train of 2-D dunes, Balachandar et al. (2007) demonstrate that elevated turbulence is carried to the next downstream dune while the outer flow region maintains similarity.

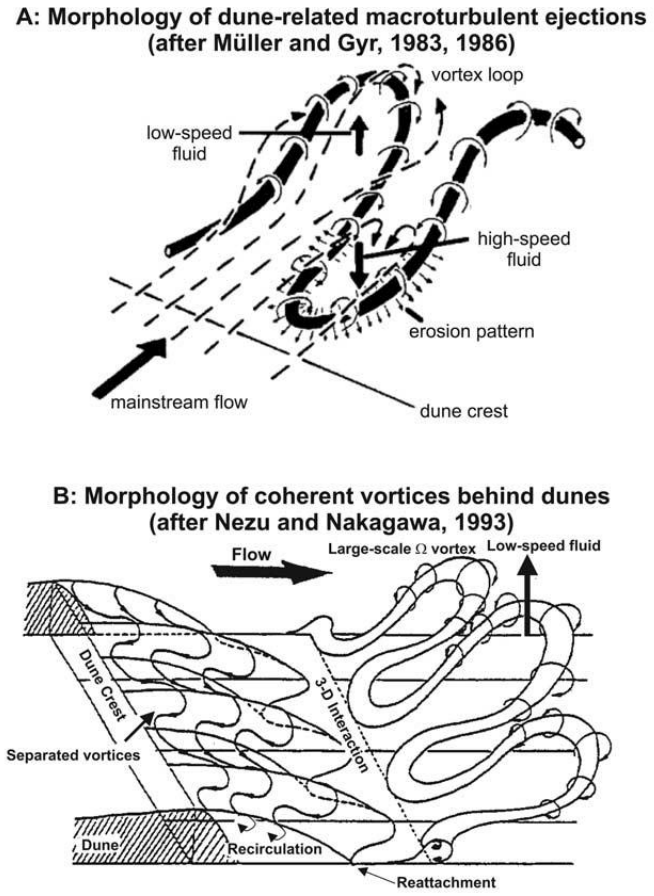

Figure 3.14: A. Hairpin vortex structure (after Müller and Gyr, 1983; 1986; Best, 2005); B. Separated and hairpin vortex structures (Nezu and Nakagawa, 1993; Best, 2005).

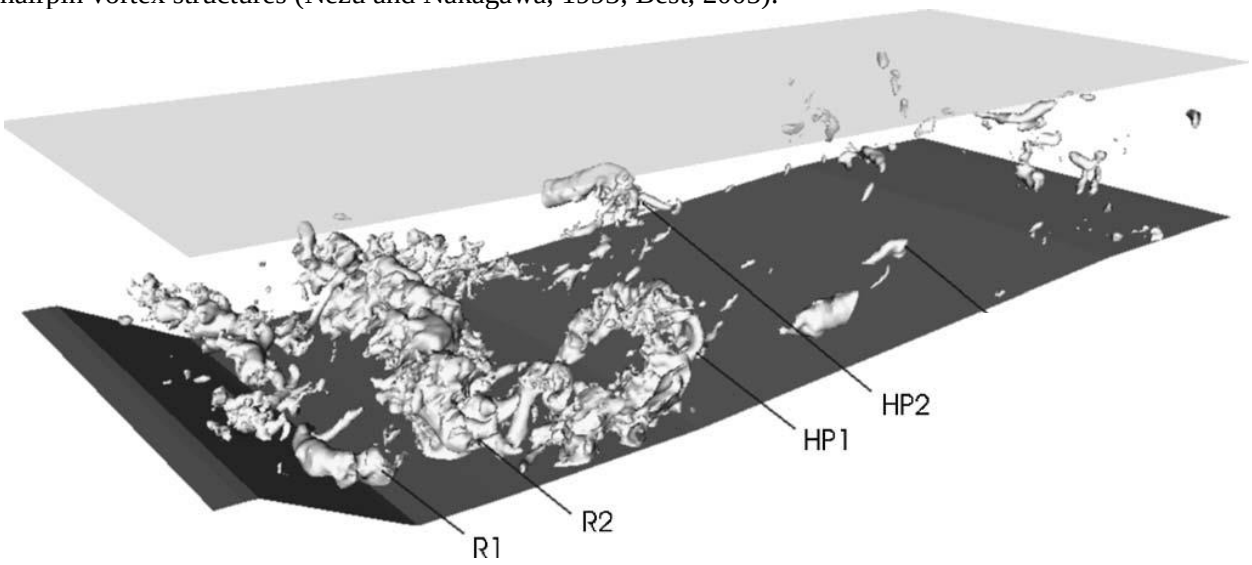

Figure 3.15: Instantaneous simulated vortex structures at a random moment in time: R1 and R2 are spanwise 'rollers' characterized by a height of the boundary layer thickness and dune height, respectively. HP1 and HP2 are inclined coherent structures akin to hairpin structures (after Stoesser *et al*., 2008).

3.5.2 Surface Shear Stress

The issue of predicting sediment transport through the friction velocity $u_*$and surface shear stress τ_0 values, which are approximated from the velocity profiles and boundary layer theory, was addressed by Walker and Nickling (2003) by directly measuring the surface shear over an isolated and series of fixed 2-D dunes using Irwin-type differential pressure sensors. Surface shear stress, τ_0, and shear velocity, u_*, are expressed as:

$$\tau_0 = -\rho u_*^2 \tag{18}$$

$$u_* = \frac{k}{ln(z-z_0)}(u_z - u_t), \tag{19}$$

where ρ is the fluid density, k is the von Kármán's constant equaling 0.41, u_z is the horizontal velocity at height z, z_0 is the aerodynamic roughness height (e.g. dune height) and u_t is the impact threshold velocity (Bagnold, 1941; Wiggs *et al.*, 1996; Walker and Nickling, 2003). The distribution of τ_0 over a single 2-D dune, normalized by the crest τ_0, is presented in Figure 3.16a. The quasi-steady τ_0 abruptly decreases at the toe of the 2-D dune before steadily increasing until the crest (2.5 times the normalized τ_0 found at the toe). Within the dune leeside and separation bubble, the τ_0 value remains relatively low, but experiences an overall increase between $8<x/H<25$. The τ_0 over a barchan dune is mapped in Figure 3.17; there is a considerable drop in τ_0 in the dune leeside. Figure 3.16 also shows a dip in τ_0 at the reattachment point *R*, which is attributed in part to an instrumental error. The downward trend and notable drop in shear stress at the dune toe is indicative of a stagnation point accompanied by an increase in turbulence (supported by the shear stress signal CV_{ss} in Figure 3.16b). This behavior is accredited to the destabilizing effect of concave streamline curvature (Walker and Nickling, 2003). The accelerating flow up the stoss-side results in increasing τ_0 and an increasingly stable flow (as seen in Figure 3.16b, showing a decreasing CV_{ss}). Notably, the fastest velocity run (18 ms^{-1}) consistently shows the smallest variability in the shear stress τ_0 signal (CV_{ss}), which implies a more stable and steady flow. The leeside and downstream τ_0 reflect the flow separation bubble and the redevelopment of the boundary layer by 6*H* downstream of the point of reattachment, reaching equilibrium by 25-30*H* (Walker and Nickling, 2003).

The change in τ_0 on the stoss-side of a dune directly contributes to the morphology of the dune as well as sediment transport (Figure 3.17). Although a smaller τ_0 at the dune toe would indicate a

place of lower or little sediment transport, field and flume evidence indicates otherwise (Walker, 1999; McKenna Neuman *et al.*, 2000; Walker and Nickling, 2003). The explanation lies in the near-surface, accelerating, stable and steady flow, as it is the primary transporter of sediment up the stoss slope rather than turbulence-generated stress (McKenna Neuman *et al.*, 2000; Walker and Nickling, 2003).

The geometry of the barchan dune slope is responsible for streamline curvature, which in turn, acts upon the flow structure through shear stress causing sediment transport (Figure 3.18; Wiggs *et al.*, 1996). Walker and Nickling (2003) suggest a steady flow at high velocities will erode the crest culminating in 'dune lowering'. McKenna Neuman *et al.* (2000) on the other hand, suggest high velocities will result in sediment deposition at the crest culminating in dune building, while lower velocities hovering above the sediment threshold value will erode sediment at the crest, leading to 'dune lowering'. According to McKenna Neuman *et al.* (2000), the dune axial profile is the controlling parameter: a coincident crest and brink is relatively 'sharp-crested', and therefore lacks any stabilizing effects from streamline convexity; a separate crest and brink results in a more gentle profile, and therefore, is conducive to streamline convexity (Figure 3.18; Walker and Nickling, 2003). Streamline convexity allows the flow to expand and deposit sediment. The flow separation bubble is unstable at low velocities, thereby allowing streamline convexity and sediment deposition at the crest which further suggests the dune morphology may evolve from 'sharp-crested' to 'round-crested'. Another interesting distinction has been made between sharp-crested and sinusoidal shapes (Jackson and Hunt, 1975; Hunt *et al.*, 1988), the latter of which experience a maximum shear stress before the crest (Walker and Nickling, 2003). Walker and Nickling (2003) attribute the spatial disparity between the shear stress maxima of the sharp-crested form to the low pressure zone created by the separation bubble, but this point remains debatable.

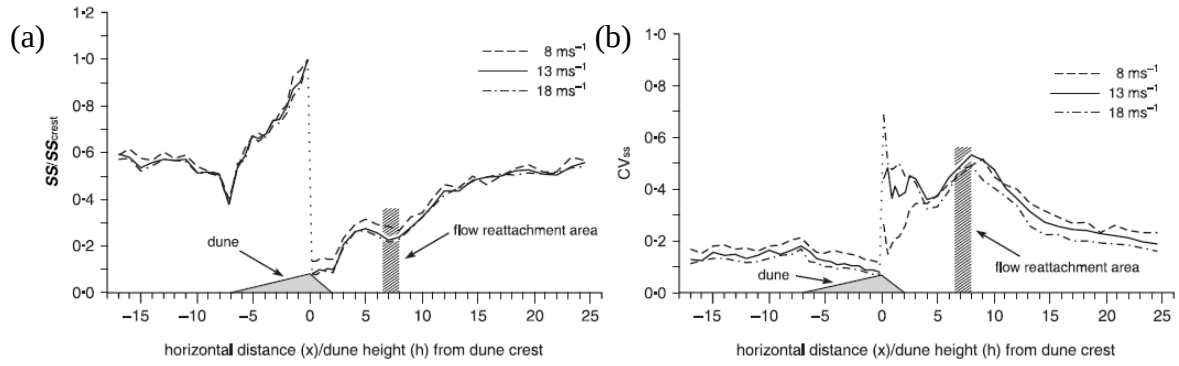

Figure 3.16: (a) The shear stress (SS/SS_{crest}) normalized by the shear stress at the crest and (b) the variation in the shear stress signal (CV_{ss}) at three velocities (8, 13 and 18 ms^{-1}) for an isolated transverse dune model (after Walker and Nickling, 2003).

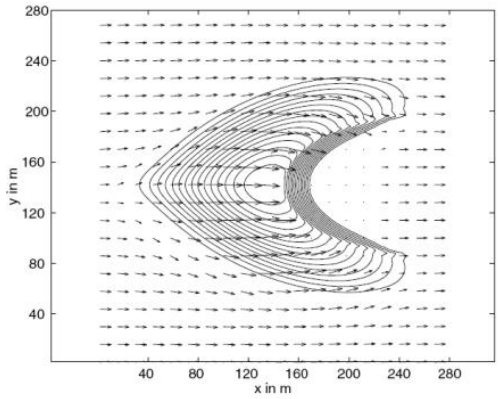

Figure 3.17: A vector map depicting the shear stress as the flow moves from left to right over a barchan dune. The strength of the lateral shear stress is emphasized. No contour interval was provided, but the authors estimate from the width, ~170 m, that the dune height is ~22 m, with a contour interval of 1.5 m. The length of the dune is ~200 m (after Schwämmle and Herrmann, 2005).

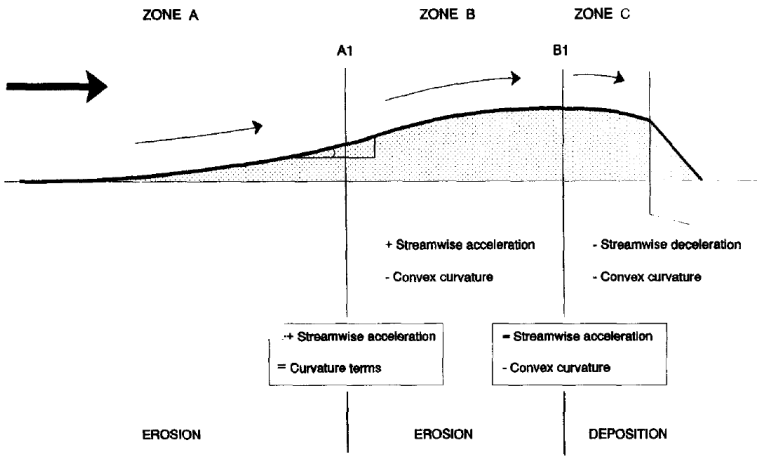

Figure 3.18: Streamline curvature over a dune is divided into three zones: Zone A, Zone B, and Zone C. The effects upon sediment transport and deposition are indicated for each zone (after Wiggs *et al*. 1996).

3.6 Summary

Important analogies have been drawn between 2-D and 3-D dunes and negative steps and wall-mounted humps. For a negative step in open-channel flow, the reattachment length x_r is a function of the Reynolds number, the step height and angle, the expansion ratio, the approaching flow's momentum thickness, the upstream boundary layer profile and the inlet turbulence intensity. Within the turbulent regime (Re>6,600), x_r stabilizes with increasing Re (x_r/H_s≈8) and the flow retains its two-dimensionality. With a decreasing expansion ratio, the normalized reattachment length x_r/H_s also decreases. Turning to the wall-mounted hump condition, x_r increases at Re=10,595, while the x_r fluctuations progressively decrease. The flow structures over a wall-mounted hump include: (1) inclined 'elongated streamwise structures' (akin to 'streaks'), (2) extremely 'elongated streamwise structures' and (3) shear layer spanwise structures that deform into streamwise structures. The primary coherent turbulent structures associated with dunes are the: (1) separation bubble vortex in the dune leeside and (2) the 'kolk-boil' vortex. The time-averaged flow characteristics of flow over a 2-D dune comprise five zones: the 'separation zone', the 'shear layer', the 'expanding flow', an 'internal boundary layer', and the zone of 'maximum velocity'.

CHAPTER 4

INTERACTIONS BETWEEN BEDFORMS AND THE THESIS RESEARCH STATEMENT

4.1 Introduction

The tendency of bedforms, such as ripples and dunes, to migrate and interact with surrounding bedforms has been described and documented from field and laboratory observations (Endo *et al.*, 2004; Kocurek and Ewing, 2005; Hersen and Douady, 2005; Jerolmack and Mohrig, 2005) and computational simulations (Hersen *et al.*, 2004; Katsuki *et al.*, 2005; Durán *et al.*, 2005). A bedform interaction is the exchange of sediment between neighboring bedforms, manifested by changes in morphology (form and size) and distinctive kinematic behaviors. Bedform interactions are the result of the interplay between bedform morphology, flow structure, sediment exchange and momentum exchange. Jerolmack and Mohrig (2005) propose that current understanding of bedform instability (specifically, barchan dune instability) is limited, particularly with regards to ripple bed or dune field maintenance. Static images displaying the morphological evolution of a bedform interaction shed little light as to their physical nature, prompting an inquiry into the dominating mechanisms surrounding bedform interactions and more broadly speaking, riverbed or dune field evolution.

4.2 Barchan dune morphodynamic interactions

A barchan dune interaction is a complex system comprised of multifarious interactions between flow regimes, sediment transport, bedform morphology and dune alignment. There is agreement within the literature (Endo *et al.*, 2004; Kocurek and Ewing, 2005; Durán *et al.*, 2005) that the relative volumetric ratio, V_r, of the initial size between the approaching upstream barchan dune, V_{up}, to the downstream barchan dune, V_{down}, determines the kinematic behavior and final morphology:

$$V_r = \left(\frac{V_{up}}{V_{down}}\right) \tag{24}$$

It remains unclear whether, in addition to the relative volumetric ratio, V_r, an absolute bedform size threshold exists to determine the type of interaction (Endo *et al.*, 2004). The following section will review the current literature regarding barchan dune interactions.

4.2.1 Observations in the laboratory

The first laboratory study simulating a barchan dune collision was conducted by Endo *et al.* (2004), followed by Hersen and Douady (2005) and Groh *et al.* (2009). The barchan dune interaction classification, presented by Endo *et al.* (2004), documents three behaviors (Figure 4.1): (a) absorption; (b) ejection; and (c) split. The relative volumetric ratio (V_r) increased for behaviors (a)-(c), while a coaxial dune alignment was maintained. The absorption behavior is produced by the smallest volumetric ratio (V_r= 0.025), and refers to the absorption of the smaller approaching barchan dune by the larger downstream barchan dune. Ejection behavior is produced by a higher volumetric ratio (V_r= 0.055), and refers to the process by which a barchan dune (smaller than the initial upstream barchan dune) exits the leeside of a larger barchan dune (initially the downstream barchan dune). Split behavior is produced by the largest volumetric ratio (V_r= 0.17), and refers to the disjunction of the downstream barchan dune by the approaching smaller upstream barchan dune prior to contact, resulting in the generation of two barchan dunes. Endo *et al.* (2004) qualitatively describe the behavior process and provide insight into the morphodynamics of barchan dune interactions; however, their experiments fail to address primary control mechanisms as well as the sediment exchange between the two bedforms. Their experiments also maintained a coaxial barchan dune alignment, which is unrealistic in nature; by offsetting the barchan dunes, the subsequent interaction should differ from the coaxial barchan dune interaction. A complimentary paper by Katsuki *et al.* (2005) to the experimental work by Endo *et al.* (2004) is discussed in section 4.4.3.

Hersen and Douady (2005) examined the collision mechanism of offset barchan dunes with an initial volumetric ratio of $V_r \approx 0.01$. (The volume V_0 was estimated using an approximation of the dune width w_0 (Hersen *et al.*, 2004; Hersen and Douady, 2005):

$$V_0 = bw_0^3 \tag{25}$$

with the value given for coefficient *b* being 0.011. Colored glass beads (red and green) allowed the visualization of the sediment exchange between the upstream barchan dune and the downstream barchan dune (Figure 4.2). The results show the left horn of the upstream barchan dune merging with the stoss-side of the downstream barchan dune. The right-horn of the downstream barchan dune progressively migrated downstream ahead of the remaining dune body, forming a new symmetrical dune at 152 s; the exiting dune comprised only red beads, representing the initial downstream barchan dune sediment. The mass of the ejected barchan

dune equals that of the initial upstream barchan dune, indicating a balanced mass-exchange. The final upstream barchan dune recovered a symmetrical and steady shape at 312 s. As the offset-alignment between the two barchan dunes was decreased to 0 (i.e. coaxial alignment), the number of barchan dunes produced increased (Figure 4.3). While Hersen and Douady (2005) go further than Endo *et al.* (2004) by addressing the mass- exchange between barchan dunes, the structure of the flow remains uninvestigated.

Groh *et al.* (2009) conducted water tank experiments examining the streamwise-wall-normal-plane of a barchan dune's axis of symmetry (i.e. the dune centerline) throughout a barchan dune interaction. The camera was placed directly in front of the test section; this posed a problem due to the presence of the barchan dune's horns, obscuring the leeside. To resolve this problem, the authors isolated the axis by placing an insert in the test section to reduce the width; this effectively produced a two-dimensional dune. Groh *et al.* (2009) performed experiments for two tandem configurations (Figure 4.4a-b). The first configuration consisted of a smaller barchan dune positioned ~0.05 m upstream of a larger barchan, with a relative volumetric ratio of V_r=0.25. The second configuration consisted of a larger barchan dune positioned ~0.075 m upstream of a smaller barchan dune, with a relative volumetric ratio of V_r=4. For both configurations, the end morphology resulted in 1 barchan dune, indicative of absorption behavior (Figure 4.4). The results of the first experiment by Groh *et al.* (2009) are inconsistent with the results of Endo *et al.* (2004). According to Endo *et al.* (2004), the volumetric ratio 0.25 should have produced a behavior resembling split behavior. This disparity may be the result of a number of factors, namely, a different e**x**perimental setup, initial dune spacing and flow conditions. Moreover, the absence of three-dimensionality in Groh *et al.* (2009) may have altered the flow patterns and in turn, the sediment transport. Endo *et al.* (2004) do not have an experiment comparable to the second configuration of Groh *et al.* (2009).

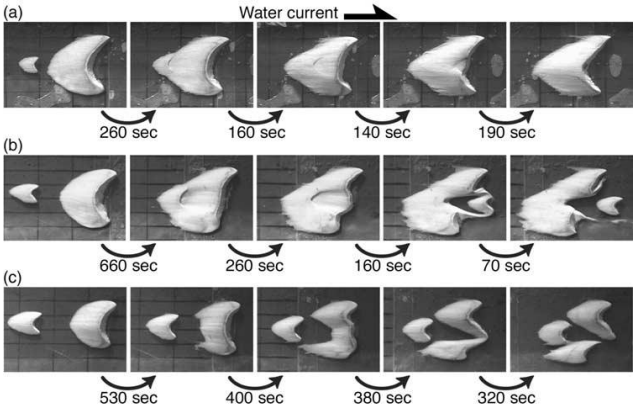

Figure 4.1: A time series of three barchan dune interactions: (a) absorption; (b) ejection; (c) split (after Endo *et al.*, 2004).

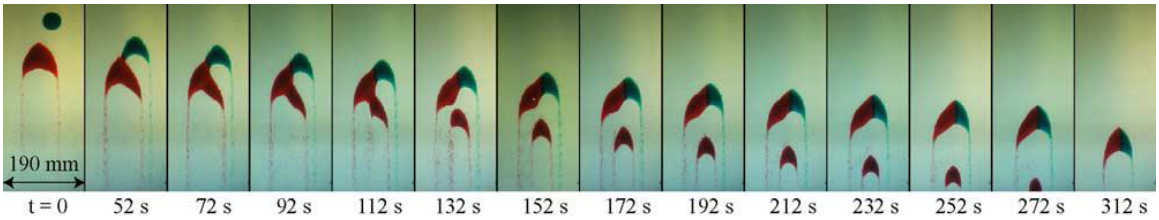

Figure 4.2: A time series depicting the interaction of two offset barchan dunes (after Hersen and Douady, 2005).

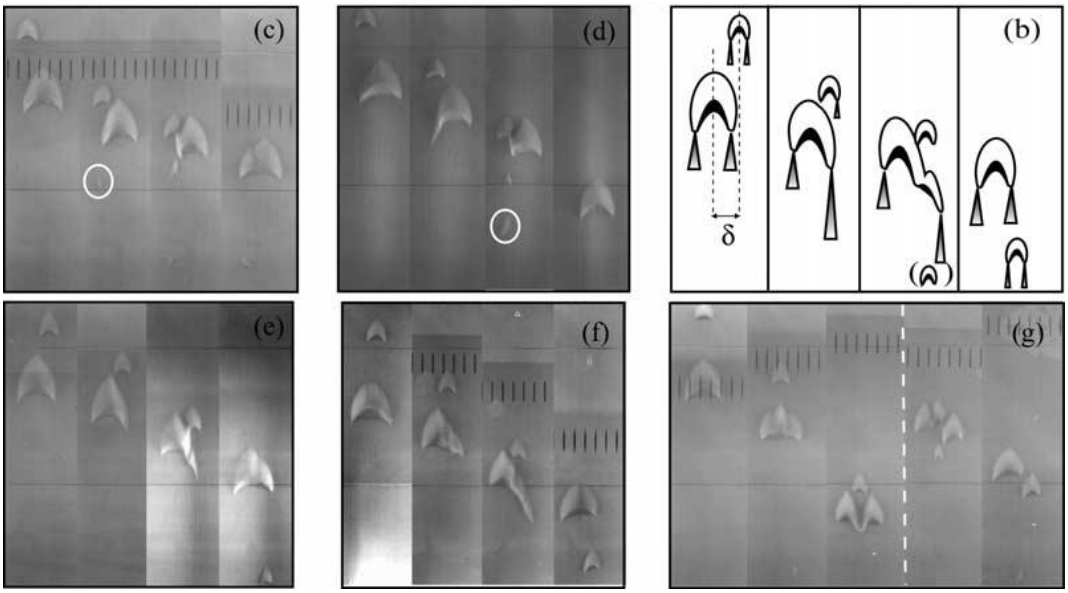

Figure 4.3: The interaction of offset and coaxial barchan dunes, which result in the generation of new barchan dunes (after Hersen and Douady, 2005). (b) a schematic of the barchan dune collision. The elongated triangles extending from the horns represent sediment exiting the horns; (c) an upstream barchan dune position to the left of the downstream barchan dune axis center. The distance from the center progressively decreases from images d-g.

(a) (b)

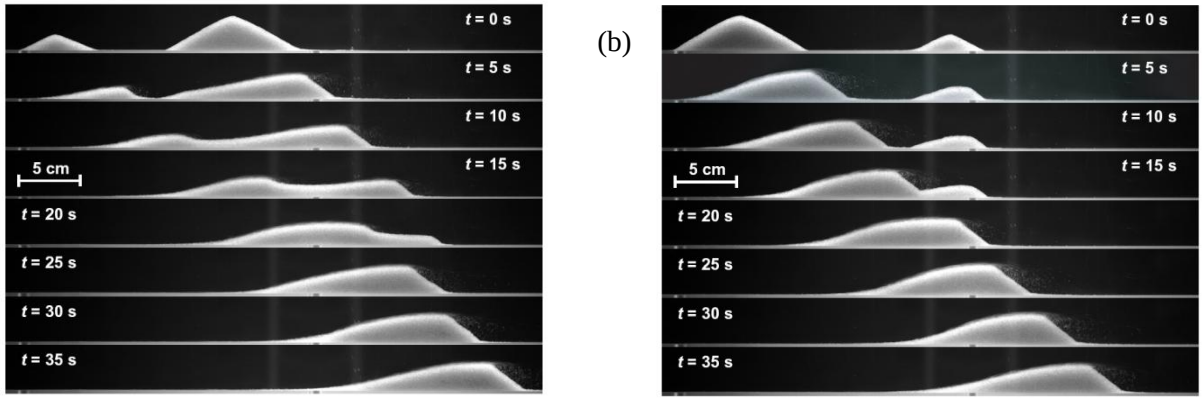

Figure 4.4: Temporal and spatial evolution of barchan dune interactions depicting the absorption behavior: (a) a small upstream dune and larger downstream dune initial configuration; (b) a larger upstream dune and smaller downstream dune initial configuration (after Groh *et al.*, 2009).

4.2.2 Observations in the field

Barchan dune interactions have been documented in deserts (Figure 4.5) and on Mars (Figure 4.6; Gay, 1962; Howard *et al.*, 1978; Breed and Breed, 1979; Mulligan, 1995; Parker Gay Jr., 1999; Besler, 2002; Ewing *et al.*, 2006; Bourke *et al*., 2009). To date, there are no studies that track or describe barchan dune interactions in subaqueous environments. Satellite images, aerial photos, and Lidar imagery capture stages of dune interactions, providing invaluable data with which to compare laboratory experiments and computer models. Features that deviate from the standard isolated barchan dune, such as compound barchan dunes and barchanoid ridges, are commonly identified in deserts (Parker Gay Jr., 1999).

Elbelrhiti *et al.* (2008) estimated the volumes of two interacting barchan dunes at various stages (Figure 4.7). Initially, the two offset barchans are joined (i.e. 'fused') by the extension of the upwind barchan dune horn (Figure 4.7a (i)); the upwind barchan dune has an estimated volume of 600 m^3 while the downstream barchan dune has an estimated volume of 800 m^3. The upwind barchan dune continually grows from (ii) to (iv), at which point the downwind barchan dune separates and migrates further downwind. Additional barchan dunes are ejected out of the leeside of the larger upwind barchan dune in (iv) and (v), with an estimated volume of 150 m^3. In Figure 4.7(vi) the estimated volume of the large barchan dune is 1400 m^3. Elbelrhiti *et al.* (2008) conclude that the system was receiving a net influx of sediment.

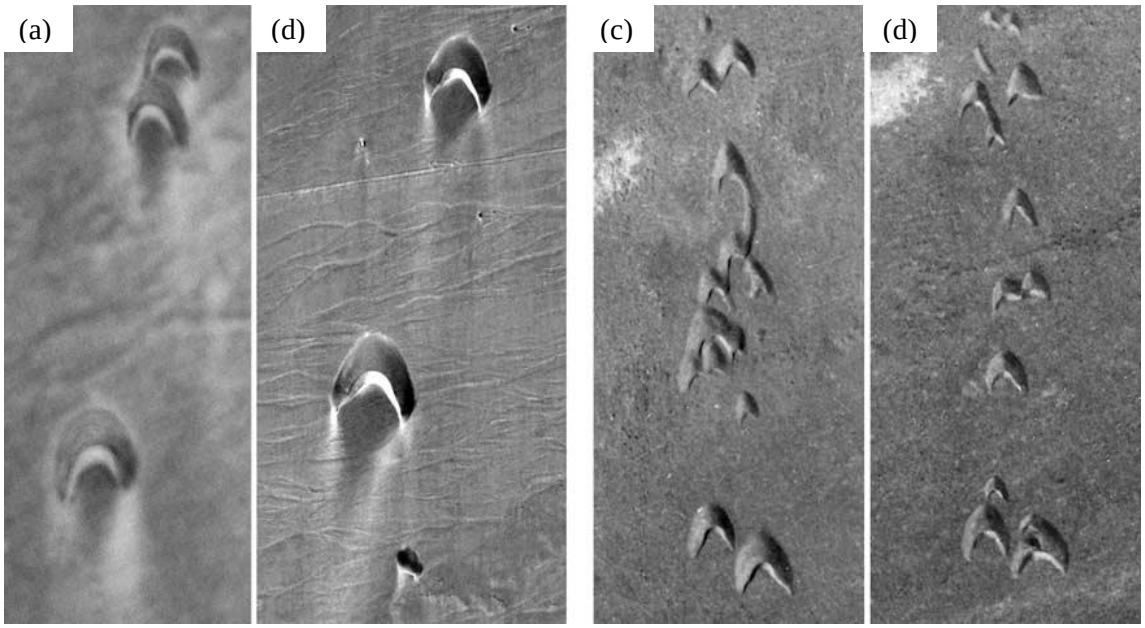

Figure 4.5: Interacting barchan dunes observed in La Joya, Peru – images (a) and (b) - and the Atlantic Sahara in Morocco – images (c) and (d) (after Elbelrhiti *et al*., 2008).

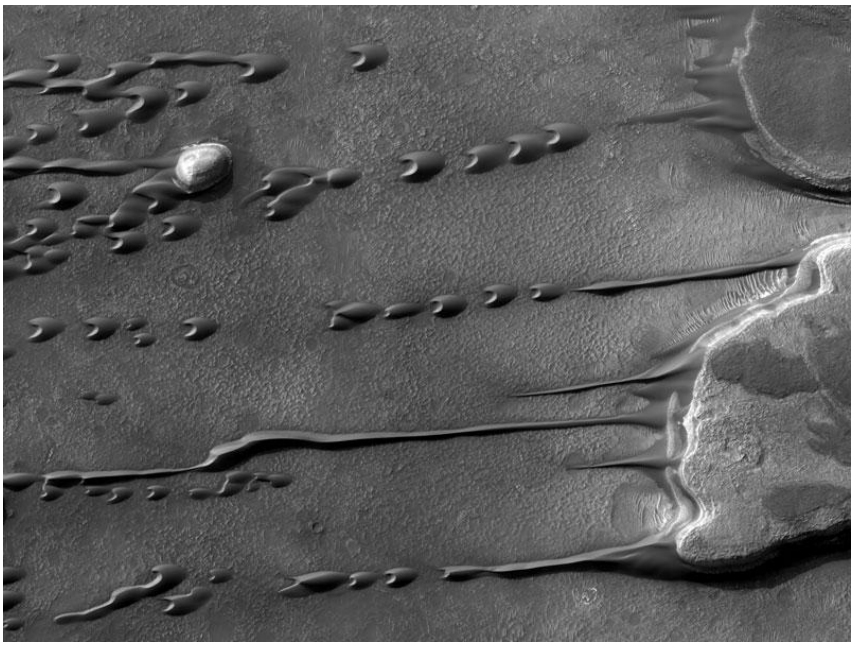

Figure 4.6: Trains of barchan dunes extending from mesas located in southern Mars. No scale available (HiRISE, MRO, LPL (U. Arizona), NASA).

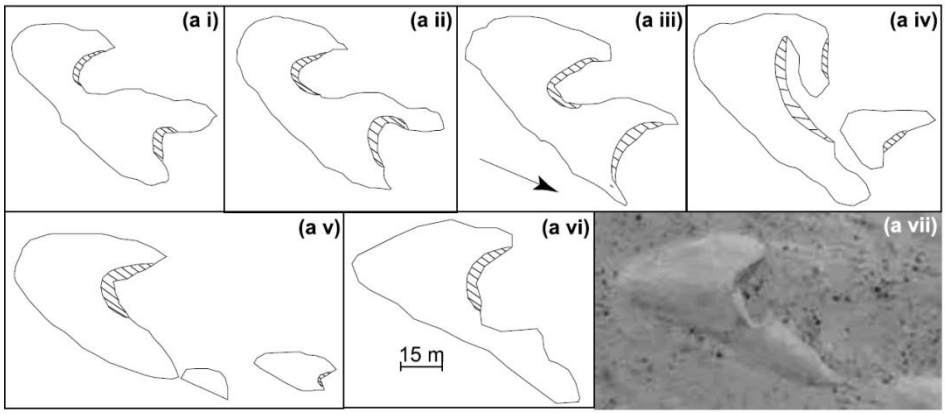

Figure 4.7: A time series depicting a barchan dune interaction observed in Morocco (after Elbelrhiti *et al.*, 2008).

4.2.3 Numerical models

The first numerical model to directly simulate a barchan dune collision was conducted by Schwämmle and Herrmann (2003), followed by Katsuki *et al.* (2005), Durán *et al.* (2005), and Herrmann (2007). Other numerical models simulating 2-D dune collisions have been conducted by Momiji *et al.* (2000).

By considering only sediment transport in their model, Katsuki *et al.* (2005) simulated three barchan dune interactions described by Endo *et al.* (2004): absorption (i.e. coalescence), ejection, and split (i.e. reorganization). A numerical simulation by Durán *et al.*, (2005) documented four interactions resulting from the collision of a smaller upstream barchan dune with a larger downstream barchan dune (Figure 4.8): (a) coalescence, (b) and (c) breeding, (d) budding, and (e) and solitary wave behavior. Durán *et al.* (2005), Endo *et al.* (2004) and Katsuki *et al.* (2005) set the control parameter of barchan dune interactions as the relative volumetric ratio of the initial upstream barchan dune and the downstream barchan dune. Despite the different nomenclature, the documented processes of Endo *et al.* (2004) and Durán *et al*. (2005) are similar or possibly the same.

Coalescence behavior is the equivalent to absorption behavior described by Endo *et al.* (2004) and has a volumetric ratio of 0.06. Breeding behavior is the equivalent to ejection behavior and has a volumetric ratio between $0.08<V_r<0.12$. Budding behavior is the equivalent to split behavior and has a volumetric ratio of 0.17 (the same V_r as Endo *et al.*, 2004). A morphological phase diagram depicts the initial volumetric ratio boundary that determines the interaction

behavior (Figure 4.9). A non-linear relationship exists between the initial volumetric ratio between the upstream dune and the downstream dune and the final volumetric ratio. A relatively small volumetric ratio V_r <0.07, produces coalescence behavior. The authors attribute coalescence behavior to a short slip face which is obscured during the collision. At larger volumetric ratios, 0.25>V_r > 0.14, the slip face is instrumental in favoring mass exchange, and two behaviors can occur: breeding or budding. Volumetric ratios greater than V_r > 0.25 produce solitary wave behavior.

While it appears as if the upstream dune crosses through the downstream dune, there is a definite mass exchange between sand grains. The intermediate stages of the morphologic evolution, called 'the hybrid state', is explained by Durán *et al.* (2005) as being controlled by the initial overlap of the upstream barchan dune upon the stoss-slope of the downstream barchan dune and the resultant 'mass exchange' between the upstream barchan dune and the downstream barchan dune. The 'mass exchange' is a function of the flow shear stress, which is in turn modified by the morphodynamic barchan dune shape. For the behaviors that produce more than one dune, the following occurs: as the smaller dune (upstream dune) is ascending the stoss-slope of the larger dune (downstream dune), the shear stress decreases on the stoss-side of the downstream barchan dune due to the separation zone of the upstream dune. The initial upstream barchan dune accumulates sediment, becoming larger and this is accompanied by a reduced migration rate. Meanwhile, the initial downstream barchan dune has a smaller volume and a higher migration rate. The two final barchan dunes move apart and stabilize. The final volumes and number of dunes produced after an interaction have many implications in terms of dune spacing and size distribution within dune fields.

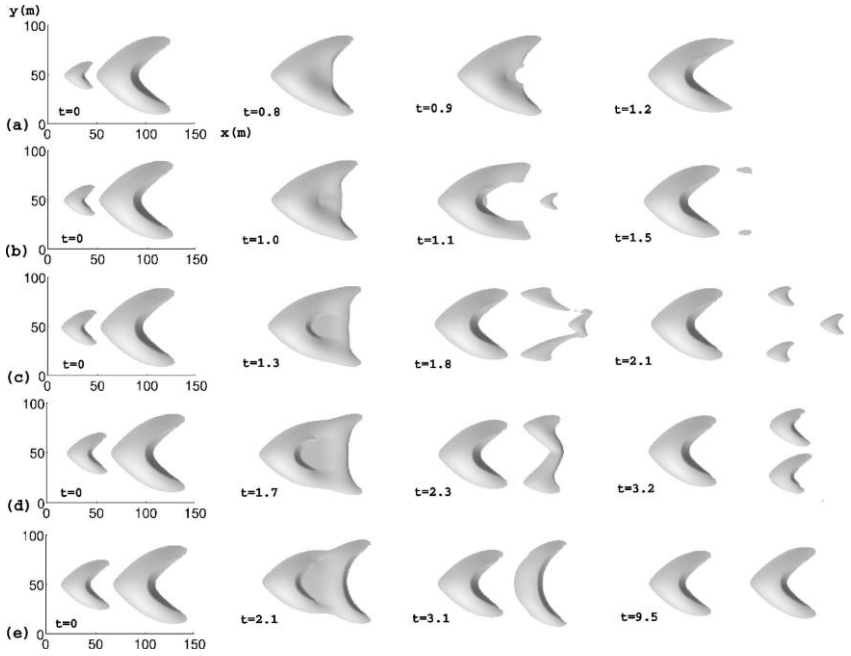

Figure 4.8: Simulated barchan dune interactions with varying volumetric ratios under boundary layer flow conditions: (a) V_r=0.06; (b) V_r=0.08; (c) V_r=0.12; (d) V_r= 0.17; (e) V_r=0.3. The initial downstream barchan dune has a volume of $6x10^3$ m^3. The time, t, is in months while the y-axis is in m (Durán *et al*., 2005).

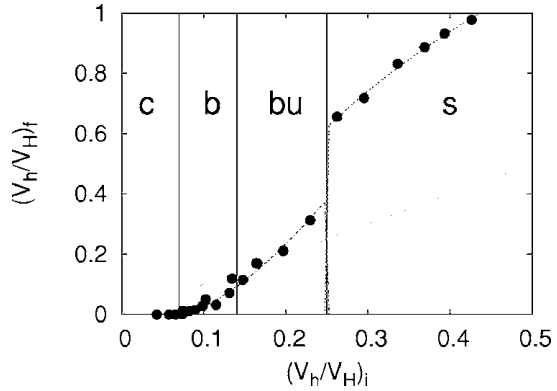

Figure 4.9: A morphologic phase diagram of the final volumetric ratio post-collision as a function of the initial volumetric ratio of the upstream barchan dune to the downstream barchan dune. The plot is divided into regions depicting various behaviors: "c" represents coalescence behavior, "b" represents breeding behavior, "bu" represents budding behavior, and "s" represents solitary wave behavior (After Durán *et al.*, 2005).

4.3 The influence of bedform interactions on the flow

There is a lack of work that addresses flow structure of bedform interactions; however, a few papers touch upon this subject. Schatz and Herrmann (2006) found that closely-spaced dunes resulted in the shortening of the separation zone length by ~25%. Fernandez *et al.* (2006)

examined changes in the mean and turbulent flow structure comparing subaqueous bedforms with and without bedform superimposition. The addition of an upstream ripple to the stoss-side of a downstream ripple significantly increased the turbulence intensity, TKE and Reynolds stress. Fernandez *et al.* (2006) suggested that absolute bedform height alone does not determine the turbulence intensity; rather, a superimposed bedform potentially generates greater turbulence. Moreover, the phenomena of interacting shear layers was introduced with superimposed bedforms, and at some point, the shear layers may behave as one large separation zone in the downstream bedform leeside. These changes in flow structure have critical implications with regards to shear stress and sediment transport, where the presence of the upstream bedform may potentially erode the downstream bedform, effectively reducing its height.

Schindler and Robert (2005) examined the flow over mobile 2-D and 3-D bedforms across the ripple-dune transition. The results of a stable 3-D dune show diminished turbulence intensities and Reynolds stresses relative to the irregular 2-D dune with superimposed ripples; this suggests shear layer dampening which arises due to a strong upstream topographic acceleration negatively affecting the shedding of vortices from the shear layer, in the case of subaqueous bedforms. The vertical location of the shear layer increases to between $0.25<y/H<0.4$. Schindler and Robert (2005) identified Q1 ('inward interaction') and low frequency Q3 ('outward interaction') events at, and adjacent to, the shear layer, respectively, accompanied by increasing Q2 ('ejections') and Q4 ('sweeps') events below and above the shear layer, respectively (Bennett and Best, 1995). These events sustained high turbulence which resulted in sediment erosion. Schindler and Robert (2005) speculated that suspended sediment dampens turbulence intensity and Reynolds stress.

4.4 Dune fields as complex systems

4.4.1 Stability and size selection

Hersen *et al.* (2004) concluded that a single barchan dune is fundamentally unstable due to sand flux. The barchan dune sand output is localized at the two horns, and is, to a degree, independent of barchan dune size. Given that the dune width grows at a faster rate than the dune height, an increase in width, for a barchan dune at equilibrium, produces a sand influx that exceeds the sand out-flux, causing the barchan dune to become larger (Hersen and Douady, 2005). Moreover, as a barchan dune grows, the surface area of the width also grows on the windward side; thus, the barchan dune is more likely to receive and accumulate more sediment (Hersen *et al.*, 2004).

Meanwhile, the horn area, where the barchan dune loses sediment, does not change significantly. If a barchan dune shrinks, the opposite effect occurs; the barchan dune will potentially lose more sediment than it accumulates. The sand flux instability implies that solitary dunes should either grow due to an ever-increasing sand input, or become smaller, eventually disappearing. Once a dune grows, it slows down, increasing the likelihood of a collision with another dune. On a larger scale, barchan dune fields are likewise, unstable. The barchan dune collisions produce a 'coarsening' of the dune field as larger barchan dunes 'absorb' smaller barchan dunes; any fluctuation in the sediment flux of one barchan dune may result in drastic changes in the downstream dune field.

The roles that dune-to-dune interactions serve with respect to moderating the spatial-and-size-distribution of barchan dunes within a dune corridor and river bed has been addressed by Hersen *et al.* (2004), Hersen and Douady (2005), Jerolmack and Mohrig (2005), Elbelrhiti *et al.* (2005), Kocurek and Ewing (2005), Elbelrhiti *et al.* (2008) and Durán *et al.* (2009). Observations of barchan dunes in deserts indicate that groups of evenly-distributed barchan dunes are characterized by uniform size (Durán *et al*., 2009). Elbelrhiti *et al.* (2008) investigated the possible controls of homogeneous high-density barchan dune corridors in Morocco and compared them to low-density barchan dune corridors in Peru. A dune corridor is composed of organized barchan dunes which are characterized by similar volumes and spacings. External controls, such as the total sand flux, the barchan dune grain size distribution, and wind strength, were ruled out as potential regulators of barchan dune size. Rather, Elbelrhiti *et al.* (2008) concluded the 'dynamical mechanisms' moderating barchan dune size, were: (1) the barchan dune volume, which is controlled by sand accumulating on its stoss-side and sand exiting through the horns, and, (2) the collision between individual barchan dunes and subsequent mass exchange. However, barchan dune collisions are not solely responsible for regulating size distribution in a dune corridor; nor are the initial barchan dune sizes responsible for regulating size as solitary barchan dunes are inherently unstable (Hersen *et al*., 2004; Hersen and Douady, 2005). Elbelrhiti *et al*. (2008) conclude that the '[dynamical] mechanisms are not scale invariant'; essentially, different relative barchan dune volumetric ratios do not produce the same collision behavior and final volumetric ratio. The variability of the wind regime, however, may play a significant role in regulating barchan dune size, especially in storm events which produce a greater 'dune output [sand] flux' (Elbelrhiti *et al*., 2008).

4.4.2 Interdune spacing

The influence of bedform interactions on interdune spacing is the subject of recent work (Werner and Kocurek, 1999; Andreotti *et al*., 2002a; Lima *et al*., 2002; Ewing *et al*., 2006; Bishop, 2007; Derickson *et al*., 2008, Durán *et al*., 2009). Bedform distribution and population is considered to be related to 'smaller-scale interactions'. It has been observed that a bedform interaction, such as coalescence, 'triggered' additional bedform interactions, creating a 'cascade' of interactions (Coleman and Melville, 1994; Jerolmack and Mohrig, 2005). Durán *et al*. (2009) measured the barchan dune distribution in Morocco, and concurred with the previous assertion, stating the distribution 'emerges from the interplay of dune collisions and sand flux balance'. The dune leeside experiences little to no sediment transport, implying that the downstream dune must begin 'at or downwind of the flow reattachment point' (Schatz and Herrmann, 2006). The flow separation zone length is the minimum distance possible between 'closely spaced dunes' (Schatz and Herrmann, 2006). Dunes are considered to be 'isolated' based upon whether the distance to a neighboring dune exceeds ~three times their length (Schatz and Herrmann, 2006).

Various relationships have been proposed relating dune spacing to another parameter. Parteli *et al*. (2006) related 2-D transverse dune spacing to the brink point height, discovering that interdune spacing did not exceed four times the brink point height. Elbelrhiti *et al.* (2008) related the dune spacing to the width of the dune:

$$\eta \propto \frac{1}{W^2} \tag{26}$$

where η is the dune packing density. The implication is that smaller barchan dunes have a greater dune packing density than larger dunes. Durán *et al*. (2009) proposed a scale invariant model relating the relative dune width to dune spacing.

The influence of dune spacing upon 2-D bedform interactions, specifically, the change in kinematic behavior as a function of the initial spacing of bedforms in tandem was investigated by Jerolmack and Mohrig (2005), who found that bedform spacing had profound implications upon the bedform morphodynamics. The local topography is composed of bedforms and is responsible for the variability in bedform morphodynamic evolution, as it causes changes in the local flow structure (Gabel, 1993; Jerolmack and Mohrig, 2005). The initial distance between bedforms ranged from 0.40 m to 0.67 m to 1.40 m. Their results show that with decreasing *initial* distance

between the bedforms, the topography of the bed becomes increasingly complex, generating multiple bedforms of various morphologies (Figure 4.10). For the 0.40 m and 0.67 m initial spacing runs, splitting produced a significant increase in the number of bedforms with time, accompanied by a decrease in the mean bedform length. For the 1.40 m initial spacing run, the bedform split once.

Durán *et al.* (2009) applied a probability density function to barchan dune measurements, conducted in Morocco. They concluded that the barchan dune size distribution is scale invariant by comparing multiple barchan dune fields. In the absence of dune collisions, barchan dune distribution would relate directly to the dune size. However, in a populated dune field where collisions frequently occur and will, in some instances, produce small single and multiple barchan dunes, it was suggested that there is no 'simple correlation between dune size and inter-dune spacing'. Durán *et al.* (2009) show that interdune spacing, I_s, scales with the 'average dune size of the [dune] field' directly:

$$I_s = \frac{S^2}{(\bar{W})^2} \tag{27}$$

Where S is the size distribution standard deviation and $\bar{W}$ is the average dune width in a dune field. They conclude that within a dune field barchan dunes are 'uniformly distributed' and this can be predicted considering only the sediment flux and 'ideal binary collisions'. However, their statistical analysis does not incorporate more complex barchan dune interactions, or their flow mechanisms.

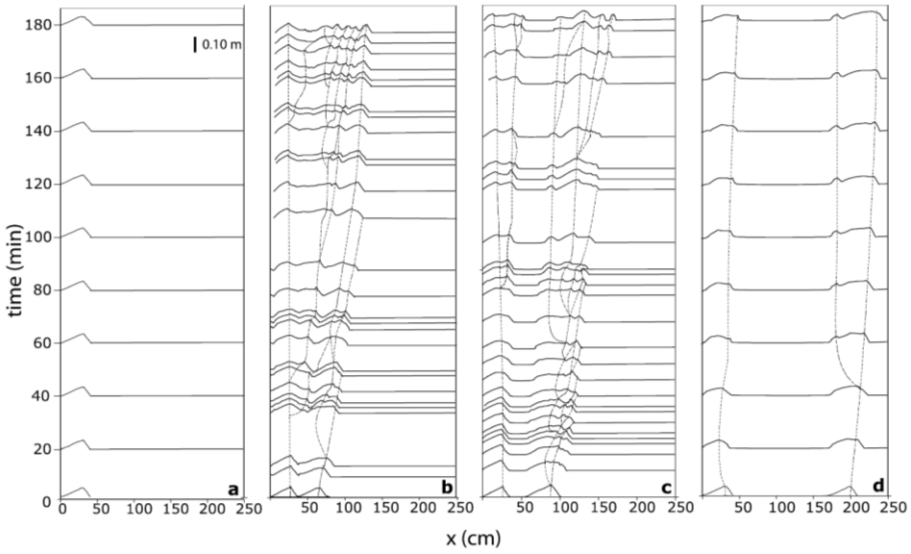

Figure 4.10: The temporal and spatial evolution of the bedform profile: (a) is an isolated bedform; (b) is two bedforms with an initial distance of 0.40 m; (c) is two bedforms with an initial distance of 0.67 m; (d) is two bedforms with an initial distance of 1.40 m (after Jerolmack and Mohrig, 2005).

4.5 Research Statement

4.5.1 Research purpose and approach

The simple case of investigating flow over a single barchan dune provides key information concerning the mean and turbulent flow structure and shear stress exerted by the flow on the dune. However, it is clear that barchan dune interactions have a stabilizing role and a profound implication upon barchan dune spacing and size; yet the nature of flow over interacting barchan dunes has yet to be investigated. It is well known that the morphology of a bedform modifies the flow structure and vice versa. During a barchan dune interaction, the morphology undergoes distinct changes due to sediment exchange, controlled by coherent turbulent structures and the bed shear stress. The different stages of barchan dune morphology throughout the interaction, in turn, influence the flow structure. The morphodynamics of interacting barchan dunes have been investigated and modeled; the fluid dynamics of interacting barchan dunes have not and demand attention. Progress is limited by the experimental constraints of working with mobile sediment. In this study, fixed-bed experiments were designed to examine the effects on the mean and turbulent flow as two barchan dunes incrementally approached each other. The present study replicates the volumetric ratios reported in Endo *et al.* (2004) in order to link the documented morphodynamics to the mean and turbulent flow structure.

4.5.2 Research objectives

The aim of the present research is to document the mean and turbulent flow structure over an isolated barchan dune and barchan dunes in tandem. The isolated barchan dune serves as a benchmark with which to compare more complex experimental configurations. The effect of an approaching barchan dune on the mean and turbulent flow field of a stationary downstream barchan dune will shed light on the flow mechanisms responsible for the variety of observed barchan dune interactions. The key variables examined in this study are the spacing and relative volumetric ratio of the upstream barchan dune relative to the downstream barchan dune. The study will investigate:

(1) What is the nature of flow over interacting barchan dunes?
(2) How does size of the averaged separation bubble change with respect to interdune spacing and volumetric ratio?
(3) How does the turbulence intensity change with respect to interdune spacing and volumetric ratio?

In order to address these questions and to place the results within the context of previous studies, both mean flow velocity components are examined, in addition to mapping the turbulence intensity, turbulent kinetic energy, Reynolds stresses and vorticity. The characterization of secondary flow within the barchan dune leeside aims to able further understanding of its role with respect to barchan dune interactions.

CHAPTER 5

RESEARCH METHODOLOGY

Two-dimensional particle image velocimetry (PIV) is utilized in the present research to study the flow field over three-dimensional barchan dunes. In light of the vast number of conceivable permutations made possible by altering the alignment and spatial proximity of two barchan dunes, one flow condition was rendered realistic for each experiment. The flow Reynolds number, *Re*, and the particle Reynolds number, Re_H, for each experimental run are presented in Table 5.1 and are defined as:

$$Re = \frac{U_\infty \delta}{\nu} \tag{23}$$

$$Re_H = \frac{U_\infty H}{\nu} \tag{24}$$

where U_∞ is the free stream velocity, the characteristic length is the boundary layer depth, δ, or the dune crest height, H, and ν = the kinematic viscosity. The boundary layer thickness, δ, represents the height at which the velocity reaches 99% of the free stream velocity, U_∞. The ratio between the boundary layer thickness, δ, and the crest height, H, for each experimental run is presented in Table 5.1. *Re* for the present set of experiments is approximately 59,000 (Table 5.1) indicating a fully developed turbulent boundary layer flow.

This chapter details the experimental setup and procedures used to conduct this study. The experimental setup section includes a description of the experimental facility, the geometric scaling of a barchan dune establishing geometric similitude, an outline explaining the production of physical barchan dune models and the PIV setup specifying the data capture. The experimental procedure is presented, followed by the PIV data post-processing detailing the data interrogation and validation. The optimization techniques applied to the experiments to improve the data are shown. Finally, the potential sources of error are discussed.

Experiment	U_∞ (ms^{-1})	δ (m)	H (m)	ν (m^2s^{-1} x 10^{-5})	Re_H	*Re*	δ/H
Isolated	9.48	0.10076	0.0135	1.5967	8013	59806	7.46
AA-0	9.52	0.09999	0.0135	1.5875	8091	59928	7.41
AA-0.5	9.46	0.09853	0.0135	1.5967	7999	58378	7.30
AA-1	9.47	0.09842	0.0135	1.5921	8030	58540	7.29
AA-2	9.47	0.09935	0.0135	1.5921	8026	59064	7.36
AB-0	9.48	0.10076	0.0135	1.5967	8015	59824	7.46
AB-0.5	9.43	0.09768	0.0135	1.5967	7973	57691	7.24
AB-1	9.44	0.09945	0.0135	1.5875	8028	59139	7.37
AB-2	9.43	0.09892	0.0135	1.5875	8019	58758	7.33
AC-0	9.46	0.09820	0.0135	1.5921	8022	58347	7.27
AC-0.5	9.45	0.09696	0.0135	1.5967	7990	57389	7.18
AC-1	9.45	0.09616	0.0135	1.5921	8013	57075	7.12
AC-2	9.45	0.09756	0.0135	1.5921	8013	57907	7.23
AD-0	9.46	0.10259	0.0135	1.5921	8017	60924	7.60
AD-0.5	9.45	0.09762	0.0135	1.5921	8013	57942	7.23
AD-1	9.42	0.09877	0.0135	1.5921	7983	58408	7.32

Table 5.1: The flow Reynolds number *Re* and the particle Reynolds number Re_H for each experimental run. A summary of the flow conditions and dune morphology; the free stream velocity, U_∞, boundary layer thickness, δ, the barchan dune height, *H*, and the viscosity, *v*. The ratio between the boundary layer thickness with respect to the barchan dune crest height, δ/H averages 7.32.

5.1 Experimental setup

5.1.1 Wind tunnel

Experiments were conducted in the *Laboratory for Turbulence and Complex Flow* located in Talbot Laboratory at the University of Illinois, Urbana-Champaign. The measurements were collected along the streamwise-wall-normal plane in an Eiffel-type, open circuit, boundary-layer wind tunnel (Figure 5.1) with a documented turbulence intensity of 0.16% in the free stream (Wu and Christensen, 2007). The working test-section of the tunnel is 6090 mm long by 914 mm wide by 457 mm high. A Mylar plastic sheet (2743.2 mm long by 1016 mm wide and 0.127 mm thick) was secured to the floor by two methods: (1) multiple rows of double-sided tape running parallel to the flow spanning the Mylar sheet width and (2) packing tape binding the Mylar along the edges to the aluminum floor.

Figure 5.1: The wind tunnel facility used in this study.

5.2 Manufacturing barchan dune models

5.2.1 Scaling

The barchan dune unit model used herein was generated from a contour map of an idealized barchan dune presented by Hersen (2004) (Figure 5.2). The aspect ratio of the barchan dune model falls within the range of reported measurements found in nature and the laboratory (Finkel, 1959; Long and Sharp, 1964; Norris, 1966; Hastenrath, 1967; Hastenrath 1987; Khalaf and Al-Ajmi, 1993; Sauermann *et al.*, 2000; Wang *et al.*, 2007), thus fulfilling the geometric similarity criteria and justifying the use of the fixed barchan dune model (Figure 5.3).

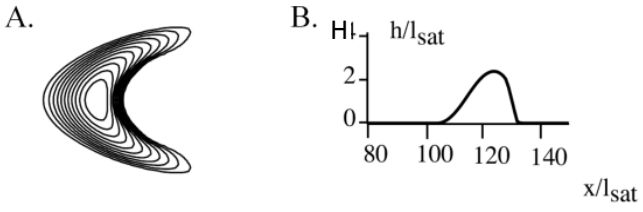

Figure 5.2: A. The contoured image was selected as the basis for the physical barchan dune unit model, as it represented an idealized morphology. The contour interval is 0.2 h/l_{sat}. B. The centerline axis profile dimensions are presented; the axes *x* and *H* are normalized by the saturation length, l_{sat} (after Hersen, 2004).

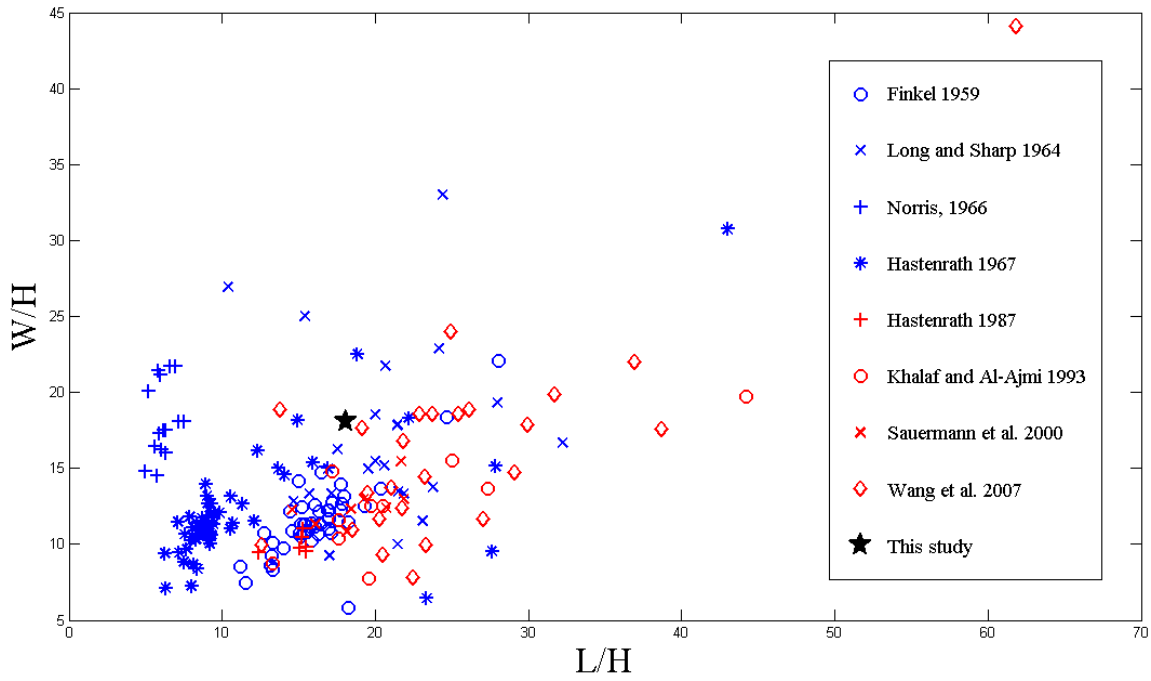

Figure 5.3: Plot illustrating the aspect ratio of field measurements of numerous barchan dunes relative to the aspect ratio of the barchan dune unit model employed for this study.

5.2.2 Conversion of 2-D contours to a 3-D surface

The ArcGIS software package was used to interpolate the contoured 2-D image into a 3-D surface. ArcGIS is a Geographic Information Systems software package composed of a suite of application components. **Appendix A** describes in detail how to use ArcGIS to generate a 3-D interpolated surface.

To convert the 2-D contour map to a 3-D topography, the contour map lines in Figure 5.2 were digitized into polyline features (*x*,*y*) within ArcGIS during an ArcEditor session. Each polyline was assigned a 'z-value' representing the vertical relief, enabling a "*topo to raster*" interpolation to be performed using ArcToolbox. The tool "*raster to point*" conversion feature, also located in ArcToolbox, converted the raster into an evenly-distributed point grid, thereby populating the 3-D surface with points containing *x*, *y*, and *z* values at a high point density. The final *x*, *y*, *z* point file was formatted as a matrix in order to be imported into *z-print*, the 3-D printer program.

5.2.3 Producing Physical Models

The production of physical barchan dune models required the 3-D interpolated topographic surface to be imported into a 3-D powder-deposition printer. The 3-D printer prints the models

layer-by-layer with plaster in powder form, maintaining a vertical resolution of 80 μm (Wu and Christensen, 2007). Multiple solid plaster models can be manufactured at a time by stacking them on top of one another. After the barchan dune models were extracted from the 3-D powder-deposition printer, they were placed on Polypropylene boards in preparation to be glued. The models were first lightly adhered at both ends (the horn tips and toe of the barchan) with glue to the Polypropylene mounts to prevent warping. To cement the plaster models, a solution containing Xylene and Elmer's Super Glue was applied to the entire surface, which infiltrated and dried in the model over a 6-hour period. The 3-D powder-deposition printer technique was significantly more cost-and time-efficient than the alternative approach of producing plastic models in a machine shop. The final dimensions of the barchan dune unit model were 0.244 m long by 0.244 m wide by 0.0135 m high (Figure 5.4). The unit model is the largest model and is referred to as "Model A". The other three barchan dune models are smaller replicas of the unit model and are referred to in descending volume as "Model B, Model C and Model D" (Model D is the smallest model) (Table 5.2).

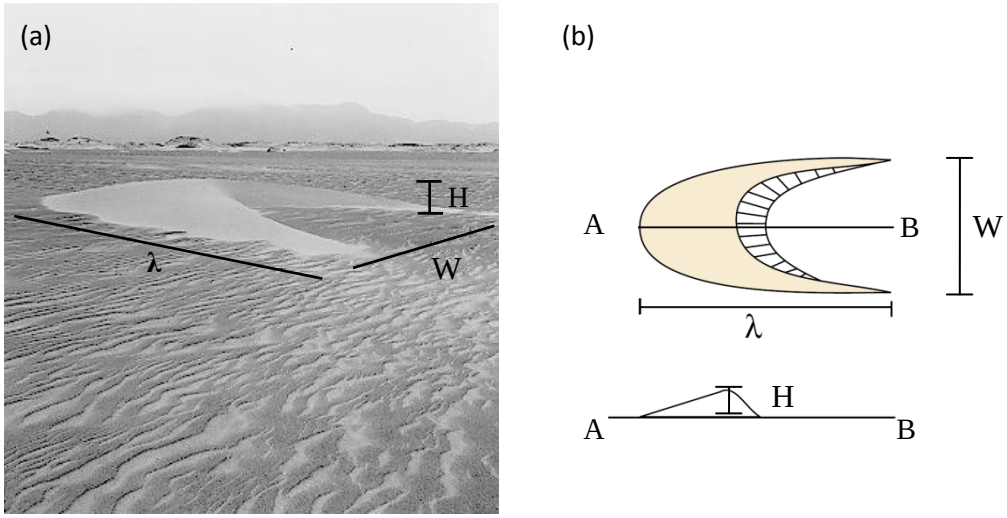

Figure 5.4: The dimensions of the barchan dune unit model are length, L_t=λ=24.4 cm, width, W =24.44 cm, and height, H=1.35 cm. (a) A barchan dune in the field; (b) a schematic of a barchan dune (Modified after www.ux1.eiu.edu/~cfjps/1300/barchan2.gif).

Model	Width W (m)	Length λ (m)	Height H (m)	Volume (m^3 $1x10^{-4}$)	Volumetric Ratio (Endo et al., 2004)	Volumetric Ratio (this study)
A	0.244	0.244	0.014	1.2724	---	1.00
B	0.135	0.136	0.007	0.2222	0.170	0.175
C	0.093	0.093	0.005	0.0710	0.055	0.056
D	0.073	0.073	0.004	0.0316	0.025	0.025

Table 5.2: The dimensions and volume of each barchan dune model. The volumetric ratio reported by Endo et al. (2004) is compared with the volumetric ratio used in this study.

5.3 Particle imaging velocimetry (PIV)

5.3.1 Fundamentals of PIV

Resolving the instantaneous fluctuations in a turbulent flow regime requires an experimental setup which accommodates the size, frequency and development of coherent structures. The introduction of quantitative techniques has improved the ability to investigate the flow structure. Basic qualitative visualization methods based upon the introduction of tracers, such as ink, bubble and smoke, have given way to more advanced quantitative techniques such as Particle Imaging Velocimetry (PIV) and Doppler-based methods such as Acoustic Doppler Velocimetry (ADV) and Laser Doppler Velocimetry (LDV). PIV, ADV and LDV are currently the most established techniques.

PIV is an optical flow visualization technique developed to obtain mean whole flow field properties and turbulent flow statistics. The PIV system is comprised of a digital camera (in the case of stereo-PIV, two cameras), a synchronizer, a frame grabber (to transfer the images from the camera to a computer), and a light source (typically a double-pulsed laser). Combinations of optical lenses are used to direct the laser light to the desired plane location. The camera is synchronized with the laser light sheet pulses while it is capturing images.

PIV is founded upon the principle where, given an object's displacement over a known period of time, it is possible to derive the object's velocity. In order to obtain the velocity of the flow across a large area, the flow must be seeded with particles that follow the flow, acting as flow proxies. Traditionally, olive oil (d=1μm) has been used to seed the airflow. It can be assumed that the velocity of the individual seeding particles accurately reflects the velocity of the flow. To seed the flow in a wind tunnel, compressed air entering an enclosed compartment, shown in

Figure 5.5, filled with olive oil forces it to become volatile. The seeder compartment is placed at the mouth of the wind tunnel.

Before obtaining data, the camera must be aligned with the floor of the wind tunnel or flume, and the laser light sheet must be normal to the floor. The camera's focus must be adjusted to expose the plane illuminated by the laser light sheet. Once the flow is properly seeded with a satisfactory concentration, it is possible to collect data. The synchronizer, which is controlled by the user, triggers the camera and laser simultaneously, capturing two paired images with a known time delay, Δt. The olive oil particles appear as white dots in the images, as shown in Figure 5.6, which can be statistically correlated or traced between the two paired images. By knowing the Δt between paired images and the distance between particles, the velocity can be derived. Paired images are captured continuously at a defined frequency (e.g. 0.5 Hz).

5.3.2 PIV experimental setup

For the set of experiments conducted for this study, 2,500 paired-images containing two-dimensional velocity fields (U,V) along the streamwise-wall-normal plane (x,y) were collected for each experimental run using an 11 Mpx CCD camera (Figure 5.7a). The velocity field is composed of the streamwise velocity component, U, and the wall-normal velocity component, V. The stoss-side data Δt=75 μs (Δt=100 μs for AB-0, AC-0, and AD-0) and the leeside data Δt=140 μs. The leeside required a longer Δt than the stoss-side in order to resolve the slower velocity in the flow separation bubble. A 500 μm-thick laser light sheet was produced by two Nd:YAG lasers (200 mJ/pulse, 5 ns pulse duration) (Figure 5.7b), conditioned through an arrangement of spherical and cylindrical lenses, and projected to the working section by a high-energy mirror (Figure 5.8).

The barchan dune models were painted matte black and then painted with multiple applications of rhodamine 6G dye (and rhodamine B dye for some experiments) dissolved in ethanol and added to transparent acrylic paint (see **Appendix C** for instructions). All leeside experiments were painted with only rhodamine 6G. The experiments conducted on the stoss-side of the downstream barchan dune model at the following spacings (AA-0, AB-0, AA-touching, AB-touching, AC-touching, AD-touching) were painted first with multiple applications of rhodamine 6G and then with rhodamine B. Experiments AC-0 and AD-0 were painted only with rhodamine B. No additional roughness (i.e. glass spheres, etc.) was added to the surface.

Rhodamine 6G is a fluorescent solute which effectively changes the wavelength of the laser light (Figure 5.9). A bandwidth filter (532 ±2 nm) was mounted in front of the camera lens, allowing only unaltered light produced by the laser to penetrate through the filter, thus protecting the CCD from any permanent, fixed reflections produced from the barchan surface. Moreover, the reduction in reflections produced by the laser light sheet drastically improves the PIV data.

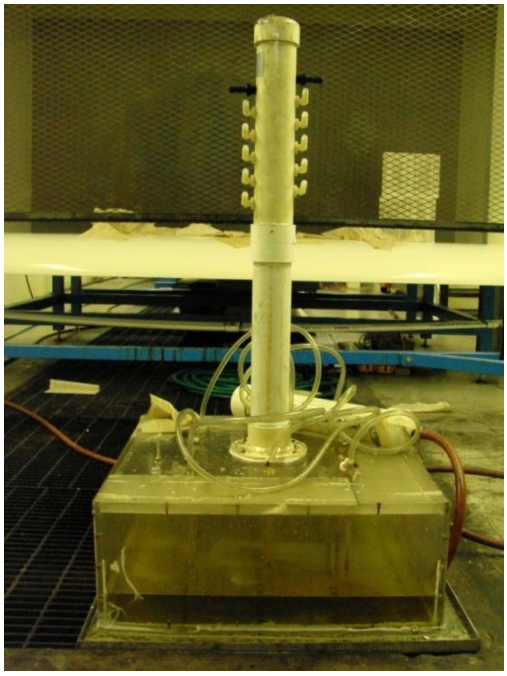

Figure 5.5: The pressurized compartment containing virgin olive oil to produce seeding is situated in front of the honeycomb screens of the wind tunnel entrance.

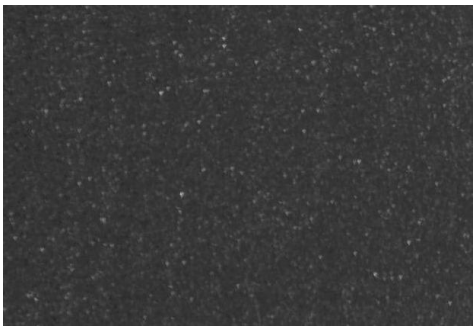

Figure 5.6: An example of olive oil seeding as it appears in a captured image, as white circles or dots of varying intensity.

(a) (b)

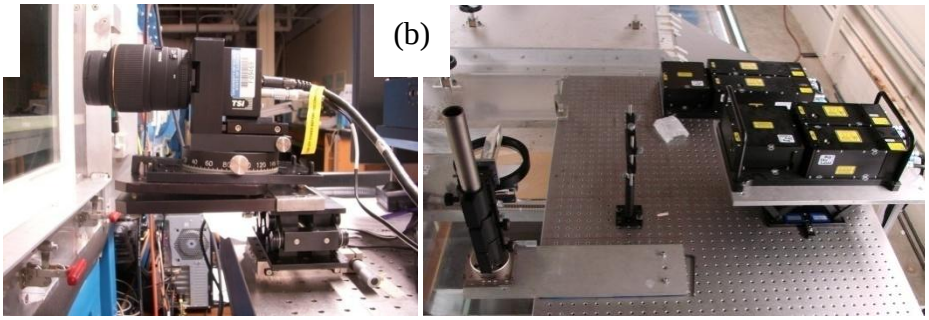

Figure 5.7: (a) The 11 Mpx CCD camera used to obtain paired images; (b) The Nd:YAG lasers positioned above the wind tunnel and the combination of optics and mirrors directing the laser light into the test working section.

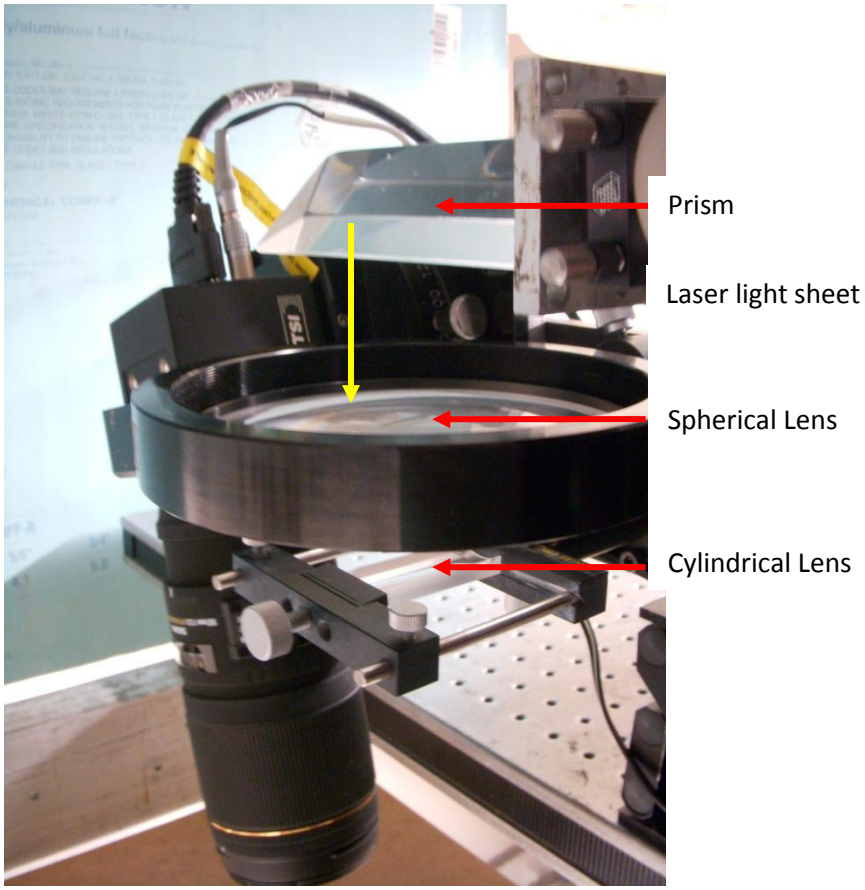

Figure 5.8: The optical system of spherical and cylindrical lenses, directing the laser light sheet into the wind tunnel.

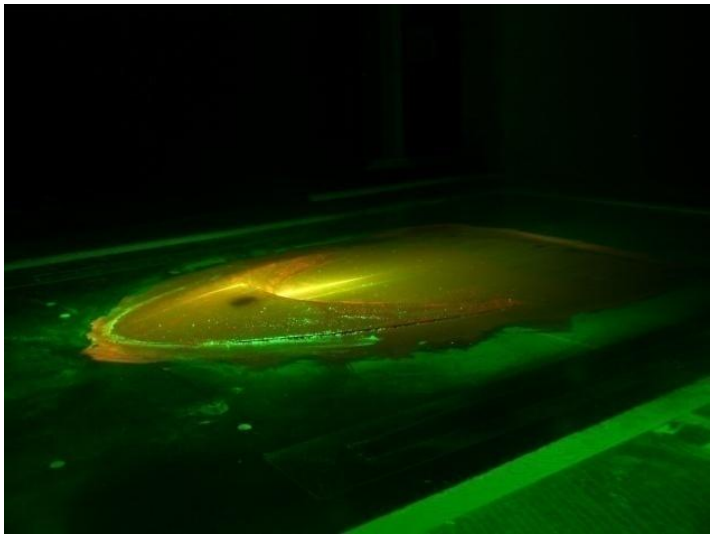

Figure 5.9: The downstream barchan dune model is illuminated by the laser light sheet, illustrating the effectiveness of the rhodamine-paint mixture in changing the wavelength (photo courtesy of Ricardo Mejia-Alvarez).

5.4 Experimental procedure

Five sets of experiments were conducted, four of which are based upon the experiments conducted by Endo et al. (2004): *Isolated, 1:1 Ratio (AA), Split (AB), Ejection (AC),* and *Absorption (AD).* The experiments replicate reported behaviors dependent on the volumetric ratio between coaxially-aligned barchan dunes in tandem (Table 5.2). For the experiments conducted in this study, two coaxially aligned barchan dune models in tandem were placed in the working section of the wind tunnel, with the exception of the *Isolated* barchan dune experiment, which investigates the flow over one barchan dune unit model (Model A). The upstream barchan dune model is moved progressively upstream (Model A, B, C, or D), while the downstream barchan dune model is fixed (Figure 5.10). In every experiment the downstream (and isolated) barchan dune was the largest model, Model A. The barchan dune models were adhered to the bed with PoliGrip denture adhesive.

The centerline-axis of downstream barchan dune model was measured using PIV along the streamwise-normal plane (Figures 5.11 and 5.12). The region of interest was too large to capture in one field of view and thus, two fields-of-view were captured separately to maximize the resolution of the velocity field (Figure 5.13). The experiments conducted along the centerline-axis included one field of view visualizing the downstream barchan dune's crest and leeside, while the second field-of-view captured the stoss-side of the barchan dune model as well as the

interdune-area located upstream of the downstream barchan dune model. For the *1:1 Ratio, Split, Ejection* and *Absorption* experiments, 6-7 spacings (touching, 0λ, 0.5λ, 1λ, 2λ, 4λ, and 6λ) were acquired for the leeside. For the *1:1 Ratio, Split, Ejection* and *Absorption* Experiments, four spacings (touching, 0, 0.5, and 1) were acquired for the stoss-side and interdune-area. The leeside and stoss-side were captured for the *Isolated* experiment along transects A and B.

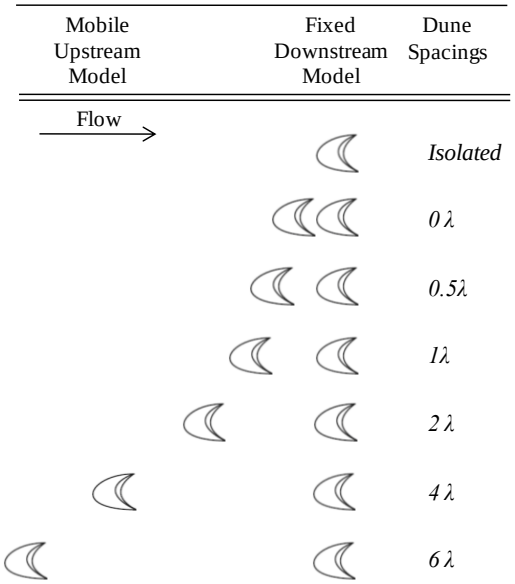

Figure 5.10: A diagram depicting the spacing between the barchan dune models investigated in this study.

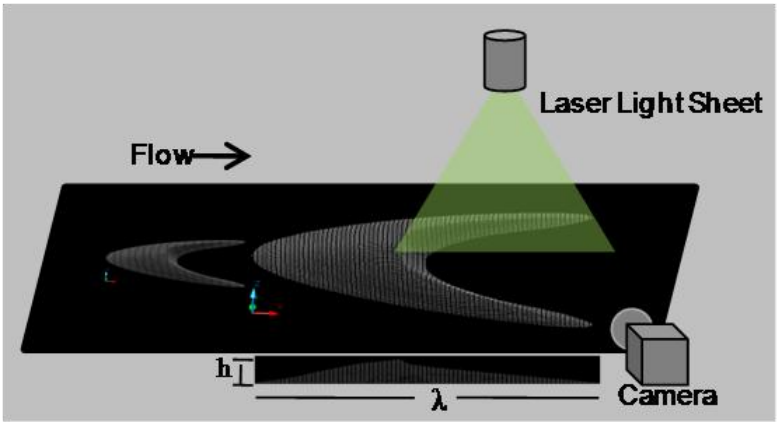

Figure 5.11: A schematic diagram depicting the experimental PIV setup in the wind tunnel.

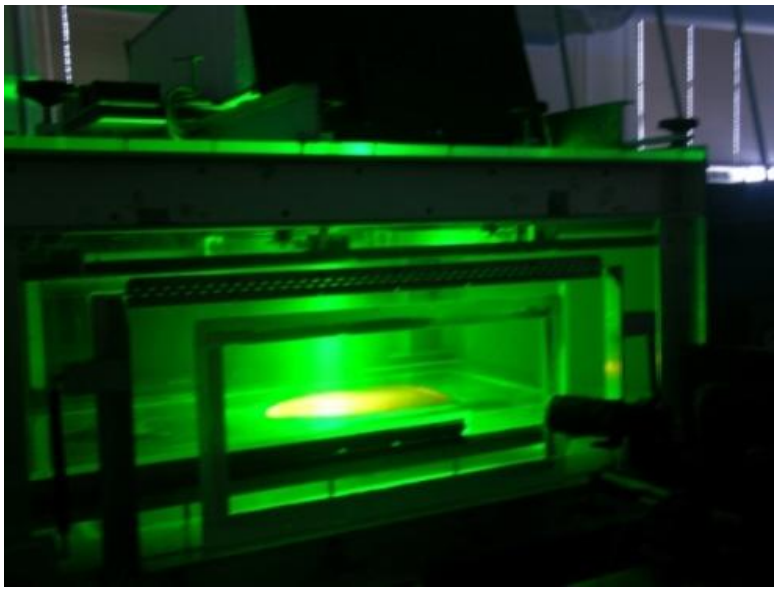

Figure 5.12: An example of a typical experimental run, featuring the PIV experimental setup in the wind tunnel particularly the laser light illumination (photo courtesy of Ricardo Mejia-Alvarez).

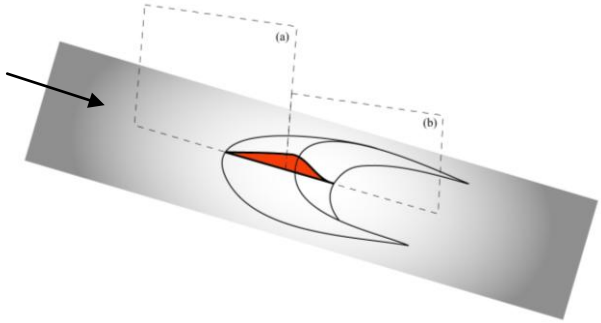

Figure 5.13: Two fields of view were captured independently: (a) stoss-side; (b) leeside. The leeside field of view is smaller because the camera was moved towards the barchan to increase the resolution.

5.5 Data post-processing

After acquiring the PIV data, each paired-image must be processed. Each image within the pair is divided into a square grid forming multiple rectangles (referred to as spots) (Adrian, 1991); each spot should have ≥5 particles because the average displacement is based on group of particles rather than individual particles (Keane and Adrian, 1992). Each subsequent spot overlaps the next spot by 50% (Figure 5.14). As no offset is imposed between paired images, each rectangular spot in the first image is also found in the second image. The similarity of the location of the 'local groups of particles' as they move from the first image to the second image is determined by statistical analysis, employing cross-correlation methods opposed to auto-

correlation methods (Keane and Adrian, 1992). The process of determining displacement using cross-correlation is herein referred to as the *interrogation process*.

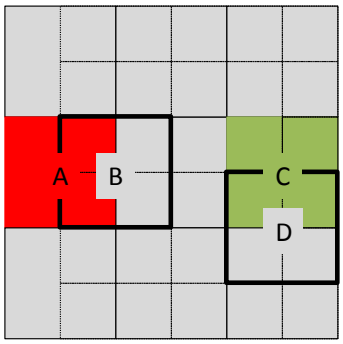

Figure 5.14: An example of the rectangular 50% overlapping grid: A-B show a horizontal overlap; C-D show a vertical overlap.

The PIV image conditioning, interrogation and validation was performed in *Insight 3G*. The image conditioning 'dewarpingImageProcessor' function was applied only to the experiments conducted on the leeside of the downstream barchan dune to correct for the distortion (or warping) introduced by the angle of the camera lens. The camera lens was positioned at an angle relative to the laser light sheet in order to visualize the leeside. In effect, the camera was looking upstream into the barchan dune leeside. The CCD array was rotated with respect to the lens in order to meet the Scheimpflug condition, which essentially is the position at which perfect focus is acquired across the CCD (Prasad and Jensen, 1995).

In order to dewarp the images, the following described process is applied: A calibration target is aligned with the laser light sheet. The calibration target is composed of a square grid of white circles with a grid spacing of 10mm x 10mm, and two planes in the z-direction, offset by 1mm (Figure 5.15). A captured image of the calibration target is referred to as the 'perspective calibration image'. To obtain a useable perspective calibration image, ideally a strong contrast between grid circles and background is needed. An algorithm within *Insight 3G* generates a map applying a third-order polynomial fit between the machine world (grid based in pixels generated by image) and physical world (grid in physical units).

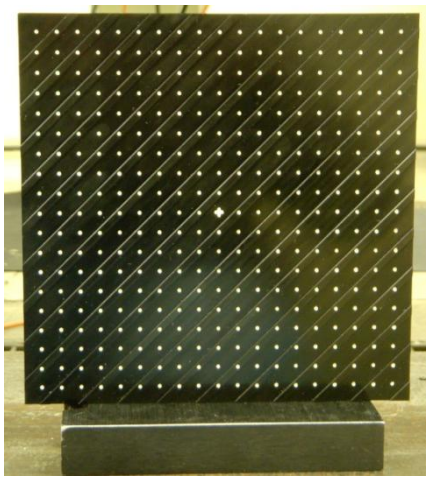

Figure 5.15: The calibration target with two planes offset by 1mm in the z-direction, and a grid spacing of 10mm x 10 mm.

The leeside (post image-dewarping) and unconditioned stoss-side image-pairs were interrogated using a two-frame cross-correlation technique to derive the velocity vectors. A mask was defined over the area where the barchan dune was visible in the stoss-side and leeside image-pairs, preventing the area from being interrogated. The image-pair interrogation algorithm is summarized in Table 5.3.

Insight 3G PIV Processor Setup	
Grid Engine	RecursiveNyquistGrid
Spot Mask Engine	NoMask
Correlation Engine	FFTCorrelator
Peak Engine	GaussianPeak

Table 5.3: The interrogation specifications for *Insight 3G*.

The “Grid Engine” divides the first image into a square grid (referred to as “spots”) within the input image, specified by the user, to process the vector field. The “RecursiveNyquistGrid” was selected because it allows multiple interrogation passes. After the first interrogation pass (the “Start Spot Size”) and first validation pass (described later), the images are re-interrogated (the “Final Spot Size”), improving the vector replacement rate. Moreover, the spot size can be specified for each pass, enabling a broad first interrogation pass and a refined second interrogation pass.

The “NoMask” was selected for the “Spot Mask Engine” parameter; a “Spot Mask Engine” enables “spot” shapes other than rectangles (which is the default “Grid Engine” shape); for our

purposes, a rectangular "spot" was acceptable. The "Correlation Engine" determines which peaks are real signals and which peaks are noise (i.e. generated by incorrect particle correlations across paired-images).

The "FFTCorrelator" (FFT=fast fourier-transform) was selected as the "Correlation Engine" because it is computationally more efficient method than a direct computation of the cross-correlation.

The "Peak Engine" compares particles from the first image to the second image by matching their pixel intensity (represented as a peak) and then stores the velocity data. The particles span across more than one pixel; this requires an estimation of the peak of correlation through signal analysis of the pixel intensity by approximating a Gaussian curve. The "GaussianPeak" was selected as the "Peak Engine" because it has a high subgrid precision, and is recommended when the FFTCorrelator is selected as the "Correlation Engine" (*Insight 3G manual*).

For this set of experiments the interrogation specifications are summarized in Table 5.4. The first image within the image-pair is referred to as Frame A and the second image is referred to as Frame B. Pass 1 and Pass 2 define the RecursiveNyquistGrid start spot size and final spot size; window 1 refers to Frame A and window 2 refers to Frame B. The window offset defines an offset between Frame A and Frame B. The time separation defines the time delay between capturing Frame A and Frame B. The grid spacing refers to the number of pixels between adjacent spots; essentially, the grid spacing is 50% of the window (i.e. spot) size. The field of view represents the dimensions of the image and is normalized by the boundary layer thickness δ. The number of realizations is the total number of paired images captured for each experimental run. A maximum displacement between frame A and B was optimized at 45 pixels for the leeside, and 40 pixels for the stoss-side.

After the image-pair are interrogated, the vector field is validated using a macro with criteria defined by the user. Validation can be employed after the first and second interrogation passes. The purpose of validation is to remove wrong vectors and to replace those vectors with interpolation. The number of vectors replaced may decrease with the second interrogation pass. The vector replacement rate for the stoss-side ranged from 0.2-0.4% indicating high subpixel accuracy. The macro criteria applied to the first pass and second pass are presented in Tables 5.5 and 5.6, respectively:

Insight 3G Interrogation Specifications		
Parameters	Stoss-side	Leeside
Pass 1: x by z (pix) Window 1	32 x 32	64 x 64
Window 2	36 x 36	70 x 70
Pass 2: x by z (pix) Window 1	32 x 32	64 x 64
Window 2	32 x 32	64 x 64
Window offset in x (pix)	0	0
Time Separation Δt (μs)	75 and 100	140
Grid Spacing $\Delta x^+=\Delta y^+=\Delta^+$	16	12
Field of view (δ=0.0989 m) (x/δ x y/δ)	1.8 x 1.2	1.1 x 0.6
Number of Realizations	2500	2500

Table 5.4: The PIV interrogation parameters as defined in *Insight 3G* during data processing.

Criteria	Stoss-side	Leeside
Absolute Range U: min, max (px)	-8, -22	---
Absolute Range V: min, max (px)	-4, -8	---
Median: Tolerance (px), Neighborhood size (px)	3, 5x5	6, 5x5
Mean: Tolerance (px), Neighborhood size (px)	3, 3x3	5, 5x5
Rohaly-Hart Analysis (RHP): Kernel, Tolerance, Neighborhood size	Median, 1, 5x5 and 3x3	---
Mean: Tolerance, Neighborhood size, (check Interpolate fill holes)	5x5, 30	---
Smooth: Neighborhood size, Gaussian Radius	3x3, 1.1	3x3, 1.1

Table 5.5: The first pass validation macro criteria.

Criteria	Stoss-side	Leeside
Absolute Range U: min, max (px)	-8, -30	---
Absolute Range V: min, max (px)	-8, -8	---
Median: Tolerance (px), Neighborhood size (px)	3, 3x3	3, 3x3
Mean: Tolerance (px), Neighborhood size (px)	3, 3x3	---
Rohaly-Hart Analysis (RHP): Kernel, Tolerance, Neighborhood size	Median, 1, 5x5 and 3x3	Median, 1, 5x5 and 3x3
Mean: Tolerance, Neighborhood size, (check Interpolate fill holes)	5x5, 30	3x3, 30
Smooth: Neighborhood size, Gaussian Radius	3x3, 0.85	3x3, 0.85

Table 5.6: The final pass validation macro criteria.

5.6 Optimization of PIV experiments

The major issue encountered during experiments was the intense reflection from the barchan horn, which in addition to harming the camera, significantly skewed the results (Figure 5.16a). The following modifications and optimizations to the experimental procedure were discovered by trial and error. The seeding in the flow saturates the entire laboratory and, although the laser and its optics are covered and protected by a Styrofoam box, this does not prevent all seeding and dust from entering and being deposited on the laser optics every 3 runs. Thus the laser optics, Plexiglas roof and wall (in front of the camera) were cleaned to counter the seeding saturation. The results improved dramatically after each cleaning. In addition to cleaning the laser optics, 1-2 coats of the Rhodamine-6G-Acrylic-Paint-mixture was applied every 7-8 runs to the portion of the downstream barchan and the floor where the laser hit. This helped to reduce reflections from the horn and dune leeside. These two methods resulted in very effective images, with a significant reduction in reflection and pixel saturation as seen in Figures 5.16b and c. The remaining reflections were negligible and create little interference in obtaining results close to the floor. Image subtraction was attempted but produced skewed results created holes in the data through over-subtraction (Figures 5.17 and 5.18). The preferable method was thus the combination of cleaning the laser optics and Plexiglas with painting the barchan and floor.

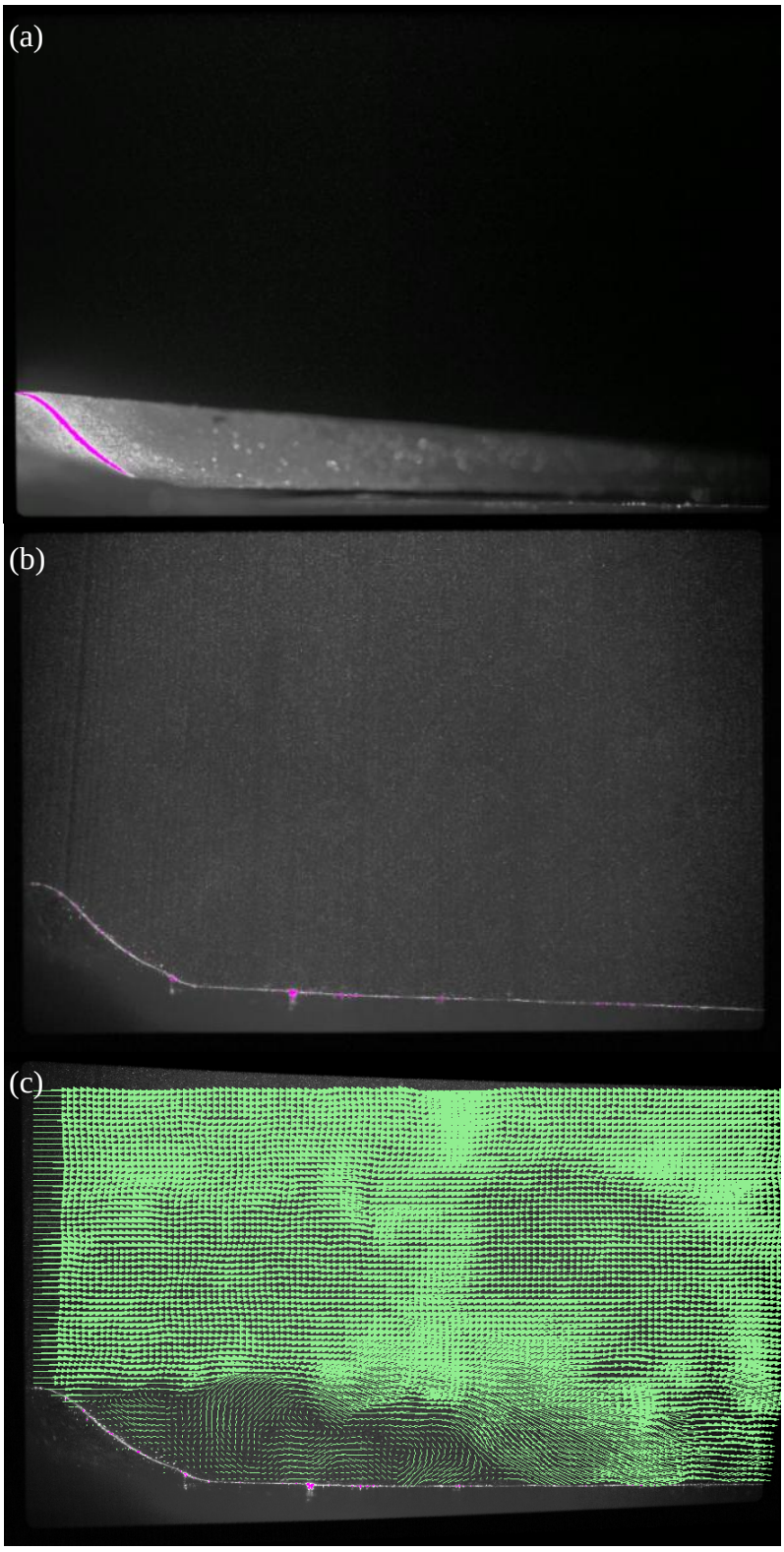

Figure 5.16: (a) A PIV image of the barchan without Rhodamine-6G-Acrylic-paint-mixture or optic cleaning. (b) A PIV image of the barchan with the Rhodamine-6G-Acrylic-Paint-Mixture. (c) A PIV image showing the validated vector field of image (b).

Figure 5.17: A sample PIV image showing some reflections on the horn and produced by excessive seeding deposition.

Figure 5.18: The same image presented in Figure 5.17 with subtraction applied. Note the black areas where the seeding has been eliminated from the image. These black zones significantly skew the results, creating holes in the data.

5.7 Length of sample measurement

The undisturbed flow approaching the barchan dune has fully developed turbulence characteristics and the measured mean flow field is statistically representative after 1000 images (Figure 5.19).

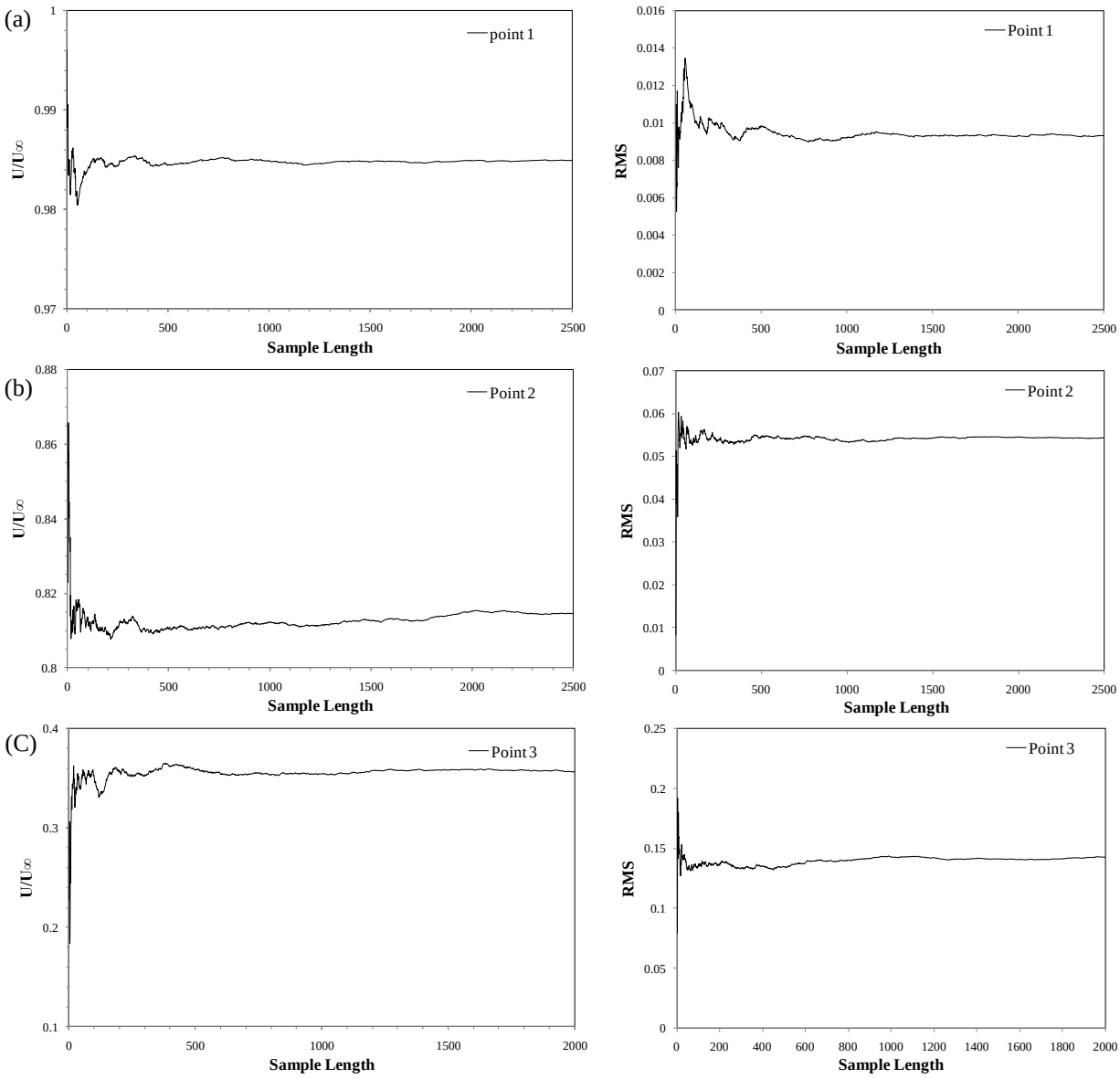

Figure 5.19: Time series of Ū and RMS: (a) Point 1 is located at -10.7, 8.1; (b) Point 2 is located at -1.4, 2.7; (c) Point 3 is located at 2.6, 1.7.

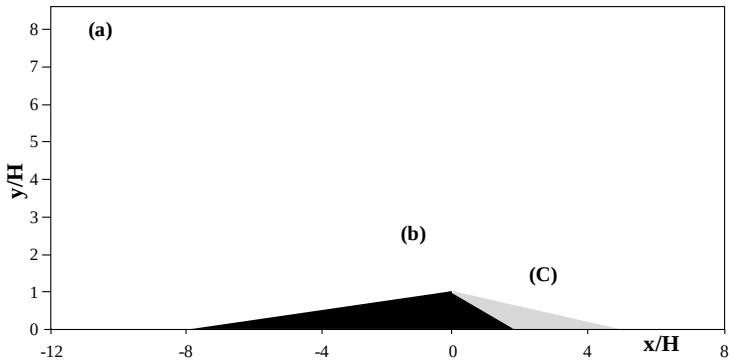

Figure 5.19 cont. The location of the points presented at (a)-(c).

5.8 Measurement error

For this study, the sources of error are the PIV system, the coaxial alignment between the two barchan dunes, and the image sampling length. The PIV system essentially comprises a laser light sheet and an 11 Mpx CCD camera. The laser optics (specifically the prism and the cylindrical and two spherical lenses) were cleaned approximately every 3-4 experiments to counter reflections. This introduced an offset up to 2 mm between the original and new laser light sheet position (the offset was calculated by measuring the distance between laser light lines, which bleach the rhodamine-paint mixture). The precise re-alignment of the laser light sheet with the original normal-to-crest line (axis line) is difficult as it is manually operated. The prism controls the cross-stream swath. To realign the light-sheet so that it is perpendicular to the floor, a mirror is placed on the floor, and while the laser is manually run at the lowest intensity at a low frequency (e.g. 2 Hz), the prism is rotated until the reflected lines, off of the mirror, collapse. When the laser light sheet is not perpendicular to the floor, two refracted lines are produced. However, the accuracy of this process is subject to human error due to the fact that a person is manually controlling the prism as well as judging the correct laser light sheet location while a bright laser reflection is pulsing. The upstream barchan was repetitively moved, which may have introduced measurement error, as the barchan dune centerline axis is not marked on the barchan dune, but is approximated using a ruler. Also, by painting the downstream barchan dune every 8-7 runs, the height and roughness inevitably experienced slight changes as well.

Regarding the results section, the size of the contour increments for both velocity component contour plots is larger than the sub-pixel accuracy produced by PIV data interrogation thereby reducing noise in the visualization of results. The independent acquisition of the stoss-side and

leeside resulted in different magnification factors to convert the data from pixels to physical units. Consequently, the stoss-side and lee side velocities and axis are normalized independently from one another to accommodate the different data acquisitions. For the composite plot x- and y-axes to be consistent, the leeside magnification factor was based upon the height of the dune, *H*, and the ratio between the stoss-side *H* and leeside *H*. Applying the stoss-side to leeside height ratio to the magnification factor enabled the calculation of the leeside magnification factor. In some contour plots, there is a jump (i.e. an imperfect overlap) that is the result of either the leeside data is being not perfectly dewarped and/or, stitching data that was obtained at different times introduces experimental error.

CHAPTER 6

RESULTS

6.1 Introduction

In this chapter, the results of two-dimensional PIV experiments conducted in the streamwise-wall-normal plane are presented. In the interest of maximizing the PIV image resolution, data from the stoss-side and leeside of the downwind barchan dune were obtained independently. When both the stoss-side and leeside data are available, they are presented together on one plot, to clearly illustrate the whole flow field over the isolated or downwind barchan dune. When the leeside data (for experimental spacings AA-0.5, AA-1, AA-2) are absent, the horizontal axes of the dunes are still aligned with the composite plots (i.e. showing both the stoss-side and leeside), easing the task of the comparison between figures by maintaining consistency for the reader. For every plot presented in this chapter, the ordinate x-axis and abrasive y-axis are normalized by the height of the barchan dune crest, H=0.0135 m.

The 2,500 instantaneous vector fields for each experimental spacing condition were averaged to obtain the velocity ensemble-average maps of the streamwise U, and wall-normal V, components of velocity. The velocity components are presented separately to examine different characteristics of the flow and are normalized by the free stream velocity, U_∞, defined as the velocity outside of the boundary layer, δ (refer to Chapter 5 for details).

As discussed in the literature review, the structure of the flow field around a barchan dune has yet to be deeply investigated. The flow over a barchan dune has strong similarities with the widely-studied cases of subaerial and subaqueous 2-D transverse dunes; this analogy will be developed in light of its direct application to define flow regions identified in the barchan dune results and, moreover, to draw comparisons. Many studies have studied the flow over a series of 2-D dunes, where the spacing between two sequential dunes has ranged from 0 to 0.5H to 2.8H (Nelson and Wolfe, 1993; Bennett and Best, 1995; Walker, 2000; Walker and Nickling, 2003; Stoesser et al., 2008). For a series of aqueous 2-D dunes, it has been widely established that the flow may be delineated into five regions (see chapter 3; Best, 2005):

(1) The flow separates at the crest and produces a recirculation region referred to as the separation bubble, within the dune leeside. The flow reattaches at between four to six dune

heights downwind of the dune crest (Engel, 1981; Best, 2005). The flow separation bubble is a secondary flow pattern. In the case of barchan dunes, the pattern of flow reversal is represented in three-dimensions as a helical vortex, where the vortex follows the topography of the dune, moving fluid along the barchan dune horns.

(2) The presence of the separation bubble is responsible for the development of a shear layer, which acts as a momentum exchange border, separating the separation bubble from the overlying faster flow.

(3) There is a region of flow expansion located slightly downwind of the separation bubble, spanning the vertical section between the floor and the free surface. The x-z plane of the bulk flow expands after flow reattachment due to a local increase in hydrostatic pressure. For open-channel flows, there is an increase in the flow depth caused by an undulating free surface; this does not apply to aeolian boundary layers.

(4) An internal boundary layer (IBL) begins to develop at the point of flow reattachment along the downstream dune stoss-slope (Nelson and Wolfe, 1993; Walker, 2000). In air, the form of the dune forces the flow and the IBL develops downstream of reattachment. The IBL terminates at the crest of the dune where it is disrupted by flow separation and the generation of a shear layer.

(5) The streamwise velocity, U, reaches its maximum intensity at the crest where the streamline curvature is at a maximum due to topographic forcing.

Despite the disparities between open channel flow and subaerial flow, some of the flow patterns described above are present in the mean flow structure of both flows over bedforms. Particularly, the flow separation zone and the shear layer can be considered common features; these are important as they contribute to the generation of turbulence and dominate the shear stress distribution, physical quantities of the flow responsible for sediment transport and bedform evolution (Best, 2005).

6.2 The structure of flow over an isolated barchan dune

The flow over an isolated barchan dune provides a benchmark with which to compare more complex multiple-barchan dune configurations. For the following two sections (6.2.1 and 6.2.2), the flow structure over a single subaerial barchan dune will be examined, focusing attention on streamwise (U/U_∞) and wall-normal (V/U_∞) velocity components as well as turbulence intensity

(T_u and T_v), turbulent kinetic energy (*TKE*), dimensionless Reynolds stress (τ_d) and vorticity (ω_d). The observations will first address the stoss-side followed by the leeside. The stoss-side is defined as the area between x/H=-13 to x/H=0 (the crest), while the leeside is defined as the area between x/H=0 to x/H=8.

6.2.1 Mean flow

The results of the isolated barchan dune mean flow field are presented as a contour plot of the streamwise (U/U_∞) and wall-normal (V/U_∞) components of velocity in Figures 6.1 and 6.2 respectively. The results of the isolated barchan dune clearly define regions of the flow identified in past research - the existence of the flow separation bubble, a bounding shear layer, the expanding flow downwind of the dune, an internal boundary layer, and a region of maximum velocity.

6.2.1.1 U/U_∞ stoss-side

The following features of flow can be identified from the streamwise velocity ensemble-average map (Figure 6.1): a flow deceleration region within the vertical range of $0<y/H<1$, located at $-11.7<x/H<-5.9$ and a flow acceleration region above y/H=2. In accordance with past observations (Walmsley and Howard, 1985; Wiggs *et al*., 1996; Mckenna Neuman *et al*., 1997; Walker, 2000; Walker and Nickling, 2003), it is noted here that there is a reduction in velocity at the leading edge of the dune (i.e. the dune toe), which is presumed to be accompanied by a reduction in shear stress (Walker and Nickling, 2003); the velocity deceleration is attributed to an adverse pressure gradient due to rising topography (Bullard *et al*., 2000). Concave streamline curvature at the dune toe has been argued to increase turbulence, thereby enhancing the shear stress and countering the shear stress reduction due to flow deceleration in this region (Walker and Nickling, 2003).

In Figure 6.3, the horizontal profiles of the streamwise velocity component demonstrate that close to the floor (y/H=0.29) the flow begins to decelerate at $x/H \approx -11.7$ and continues to decelerate until the horizontal profile is terminated at $x/H \approx -5.9$. The profile at y/H=0.78 shows a small deceleration after which the flow stabilizes by x/H=5. By y/H=2, the streamwise velocity is constant until it is topographically-forced and accelerated up the stoss slope of the barchan dune. Due to the absence of an upstream barchan dune and its wake effects, the flow approaching the

isolated barchan dune is a fully-developed boundary layer, and thus there is no IBL developing on the stoss slope.

6.2.1.2 V/U_∞ stoss-side

The only feature identified from the ensemble-average map of wall-normal velocity (Figure 6.2) within the stoss side is a region of ascending flow. As the flow accelerates due to topographic forcing, it is also projected upward, in order to remain parallel to the stoss slope. Despite the three-dimensionality of the barchan dune form, which allows part of the flow to go around the dune along its sides (Allen, 1968), the flow is still strongly deflected by the surface of the dune, as would be expected in the case of a 2-D transverse dune. The upward flow on the stoss slope will be referred to within this thesis as the *topographic forcing region*, the maximum intensity of which (depicted by the 0.08 V/U_∞ contour line, labeled 'e'), is located mid-stoss slope (x/H= -5 to x/H= -2) and decreases radially in magnitude.

6.2.1.3 U/U_∞ leeside

The following features can be identified from the ensemble-average map of streamwise velocity (Figure 6.1): the flow separation bubble, the wake region, and the maximum streamwise velocity region. The flow clearly separates at the crest, detaching from the wall to form a longitudinally-elongated recirculation bubble, characterized by a clockwise rotating vortex. The region of reverse flow is well-defined, with the streamwise component of the velocity reaching a maximum intensity of -0.21 U/U_∞ between x/H=2.69 and x/H=2.81 (indicated by the gray arrow in Figure 6.1; visible in the vertical profile in Figure 6.4). The flow reattachment length x_r of 4.6H falls within the 4H-6H range of 2-D dune flow reattachment points reported by Engel (1981) and Best (2005). The maximum streamwise velocity region (labeled '*a*' in Figure 6.1), is located above the separation region where the 0.8 U/U_∞ contour line reaches its minimum height above the bed.

6.2.1.4 V/U_∞ leeside

From the ensemble-average map of wall-normal velocity (Figure 6.2), it is possible to detect the upwelling and downwelling flow in the separation bubble, the flow expansion zone, and the small jet of upward flow extending off of the crest. The separation bubble is characterized by descending flow (arbitrarily defined as below the -0.02 V/U_∞ contour line) on its downwind flank

and upwelling flow directly in the dune leeside. The upwelling flow is confined within the separation zone, labeled ‘e’. Part of the downwelling flow region (downwind of the upwelling region) belongs to the separation bubble and part belongs to the flow expansion region. The area constituting the region of flow expansion is labeled ‘g’ and spans ~6*H* longitudinally and ~3*H* horizontally (in the streamwise direction), giving an aspect ratio of 2. A small jet of fluid extending from the dune crest, referred herein to as the *crestal jet* (labeled ‘d’) is identified in Figure 6.2; this feature appears not only in the isolated condition, but for the majority of the spacing conditions for each volumetric ratio, and changes in length and width accordingly. The flow over a single 2-D dune, according to Frank and Kocurek (1996), begins to recover at 8*H* by forming an IBL (Walker, 2000).

6.2.2 Turbulence statistics, Reynolds Stress, and vorticity

The turbulence intensity T_u and T_v, and dimensionless turbulent kinetic energy *TKE*, Reynolds stress τ_d and vorticity ω_d, were derived from the following equations, where *u’* and *v’* represent the fluctuations from the mean velocity $\bar{u}$ and $\bar{v}$ of the streamwise and wall-normal velocity components, respectively (modified from Dong *et al*., 2009):

$$v = \bar{u} + u^{'}, \qquad v = \bar{v} + v' \tag{28}$$

$$T_u = \frac{\sqrt{\overline{u'^2}}}{U_\infty},\ T_v = \frac{\sqrt{\overline{v'^2}}}{U_\infty} \tag{29}$$

$$TKE = \frac{\overline{u'^2} + \overline{v'^2}}{{U_\infty}^2} \tag{30}$$

$$\tau_d = -\frac{\overline{u'v'}}{{U_\infty}^2} \tag{31}$$

$$\omega_d = \frac{1}{U_\infty}\left(\frac{\delta v}{\delta x} - \frac{\delta u}{\delta z}\right) \tag{32}$$

6.2.2.1 Turbulence Intensity T_u

As seen in Figure 6.5, an elongated, near-horizontal region (labeled ‘*l*’), characterized by high values ranging from $0.12 < T_u < 0.16$, extends downwind from the crest along the shear layer, similar to the results of Walker and Nickling (2002) and Dong et al. (2009). The turbulence intensity near the dune slipface is notably diminished relative to the adjacent wake region (labeled ‘*m*’). The fluctuation of the streamwise velocity reaches a maximum of 16%. The

significant increase in the turbulence intensity in the leeside is due to the convection of vortices generated along the shear layer that borders the separation zone. On the stoss-side of the dune, turbulence is relatively low, except for an elevated level at, and slightly beyond, the toe (or leading edge) of the dune (labeled '*n*'); this behavior was explained by Walker and Nickling (2003) as the result of concave streamline curvature over a dune that destabilizes the flow and generates turbulence.

6.2.2.2 Turbulence Intensity T_v

On the stoss side of the dune, the wall-normal component of the turbulence intensity (Figure 6.6) shows a vertical gradient increasing towards the floor above the upper stoss slope (*x/H*=-4 to *x/H*=0). The highest turbulence production is located in the wake of the dune extending beyond the field of view and reaching 10% T_v (labeled '*o*'); this implies that the greatest wall-normal velocity fluctuations occur within the shear layer. The longitudinal axis of the zone of high T_v is asymmetrical with respect to the shear layer.

6.2.2.3 Turbulent kinetic energy TKE

The *TKE* is slightly enhanced at the toe of the dune (labeled '*p*' in Figure 6.7). Downstream of the dune crest, the turbulence increases along the shear layer, where the maximum *TKE*, 0.04, occurs between 2.8< *x/H*<5.4 (labeled '*q*'). The high *TKE* region is elongated and its axis slightly dips towards the floor. Directly adjacent to the slipface, the *TKE* is significantly lower (labeled '*r*'). At *x/H*=5, there is a hole in the data that causes an inflection in the contours.

6.2.2.4 Reynolds stress τ_d

In Figure 6.8, the Reynolds stress reveals two regions in the leeside: a region of higher τ_d values (labeled '*s*') corresponding to the shear layer and a region of low τ_d values (labeled '*aa*') bordering the dune slipface; these results are similar to the results of Walker and Nickling (2003) and Dong *et al*. (2009). The maximum τ_d region, where τ_d =0.01, lies between 3<*x/H*<5.5.

6.2.2.5 Vorticity ω_d

The vorticity is predominately negative indicating a clockwise rotation of fluid (Figure 6.9). The strongest ω_d is constrained to the leeside, where a near-horizontal zone of maximum ω_d (defined by the -5 contour) extends from the dune crest (labeled '*cc*'). The occurrence of the maximum vorticity intensity coincides with the presence of the shear layer, in conjunction with the

maximum turbulence intensity. Directly along the slipface and the floor, the vorticity is positive, in keeping with the results of Dong et al. (2009).

The presence of these common flow features highlights the similarity between the 3-D aeolian barchan dune employed herein and 2-D dunes; in particular, the flow over an isolated barchan dune is dominated by the flow separation bubble, flow reattachment, a shear layer, a vertically-expanding flow region, an IBL, and a region of maximum velocity.

6.3 Mean flow and turbulent structure of barchan dunes in tandem according to volumetric ratio

The normalized ensemble-average maps for each experiment (AA, AB, AC, and AD) are grouped together to illustrate the evolution of flow as the distance between the barchan dunes, when aligned in tandem, decreases. Each experiment reproduces the volumetric ratios reported by Endo et al. (2004), as discussed in Chapter 4 and presented in Table 6.1. To facilitate a quick reference to each set of experiments, each barchan dune model was assigned a letter according to its size (in descending order): A, B, C, and D. Each experimental name is the combination of the downstream barchan dune model and upstream barchan dune model letters: AA, AB, AC and AD. The fixed downstream barchan dune is size model A, which was used in the isolated barchan dune experiment. To simplify the observations for the reader, the upwind barchan dune will herein be referred to as *UBD* while the downwind barchan dune will be referred to as *DBD*.

Each experiment was conducted at multiple interdune spacings, where the position of the UBD relative to the DBD was defined by the total length L_t, which is also referred to as the wavelength, λ, of the DBD. The conditions for every experiment conducted are summarized in Table 6.2. For some spacing conditions, both the leeside and the stoss-side of the downwind dune were investigated. However, due to time constraints, a few spacing conditions show data only on the stoss-side, and in some instances, the condition may be completely omitted.

The stoss-side refers to the section encompassing the upwind and stoss-slope of the visualized barchan dune model, while the leeside refers to the lee-slope and downwind section. The stoss-side and leeside data for the DBD were obtained independently from one another and under different camera configurations, as discussed in Chapter 5. The resolution of the leeside data is greater, and thus the field of view is smaller than the stoss-side.

Each experiment will be discussed within an independent section. Contour lines in the mean flow field figures will be specifically referred to in order to clearly define and discuss the evolution of the mean flow structure. The isolated condition ensemble-average maps of both velocity components are included as the first plots to provide a readily-accessible benchmark. The results show the presence of the primary features already identified and discussed for the isolated condition, indicating a standard flow pattern over barchan dunes.

For the purpose of identifying trends, the velocity data from each experiment (AA, AB, AC, and AD) is compared to the isolated barchan dune model experiment, which serves as a benchmark, using the following velocity profiles:

(1) The vertical profiles of the streamwise U/U_∞ velocity component are presented at eight sampling locations (x/H=-10.5, -7.8, -3.9, 0, 2.5, 3.75, 5, and 6) for each experimental condition (0λ, 0.5λ, 1λ, and 2λ) where there is available data.

(2) The vertical gradient of the streamwise U/U_∞ velocity component is presented at eight sampling locations (x/H=-10.5, -7.8, -3.9, 0, 2.5, 3.75, 5, and 6) for each experimental condition (0λ, 0.5λ, 1λ, and 2λ) where there is available data.

(3) The horizontal profiles of the streamwise U/U_∞ velocity component are presented at four sampling locations (y/H=0.29, 0.78, 1 and 2) for each experimental condition (0λ, 0.5λ, 1λ, and 2λ) where there is available data.

(4) The horizontal profiles of the wall-normal V/U_∞ velocity component are presented at four sampling locations (y/H=0.29, 0.78, 1 and 2) for each experimental condition (0λ, 0.5λ, 1λ, and 2λ) where there is available data.

A comparative analysis of the streamwise U/U_∞ and wall-normal V/U_∞ velocity components is used to synthesize the results and to emphasize the influence of decreasing the distance between dunes upon the flow.

The results of the tandem barchan dune configurations feature regions of the flow already identified for the isolated barchan dune. The common features identified from the streamwise velocity component U/U_∞ on the stoss-side for the 0.5λ-2λ spacings, include the zones of deceleration and acceleration. The common features identified from the streamwise velocity component U/U_∞ on the leeside for the 0λ-2λ spacings, include the zones of maximum velocity,

the flow separation bubble and the wake region. The flow feature found on the stoss-side identified from the wall-normal velocity component V/U_∞, is the region of topographic-forcing, which is characterized by upwelling fluid. The flow features found on the leeside from the wall-normal velocity component V/U_∞ include the crestal jet, the upwelling zone and the DBD expansion zone.

Experiment	Volumetric Ratio (upstream dune model/ downstream dune model)	Volumetric ratio (Endo et al., 2004)
Isolated (A)	---	---
AA	1	---
AB	0.175	0.17
AC	0.056	0.055
AD	0.025	0.025

Table 6.1: The volumetric ratio of the experiments conducted herein compared to the volumetric ratios reported in Endo et al. (2004). The volumetric ratio is the ratio of the volume of the upstream barchan dune relative to the volume of the downstream barchan dune.

Experimental Condition (Spacing - λ)	Experiment AA	Experiment AB	Experiment AC	Experiment AD
0	Stoss & Lee	Stoss & Lee	Stoss & Lee	Stoss & Lee
0.5	Stoss only	Stoss & Lee	Stoss & Lee	Stoss & Lee
1	Stoss only	Stoss & Lee	Stoss & Lee	Stoss & Lee
2	Stoss only	Stoss & Lee	Stoss & Lee	Lee only
4	none	Lee only	Lee only	Lee only
6	none	Lee only	Lee only	Lee only

Table 6.2: A summary of the acquired data for each experimental configuration.

6.3.1 Volumetric ratio AA: mean flow structure

6.3.1.1 The effect of λ on the U/U_∞ stoss-side

The greatest contrast between the 0λ-2λ spacings (Figure 6.10) and the isolated dune is the presence of the leeside flow features (i.e. the wake) belonging to the UBD at 0λ. The maximum streamwise velocity region for the 0λ spacing lies over the crest between $0<x/H<0.74$, which is an upstream and vertical upward shift from the isolated dune maximum velocity location, $2.28<x/H<2.37$. It is not possible to determine the position of the maximum velocity region for 0.5λ- 2λ spacings due to the unavailability of the leeside data.

Vertical profiles of U/U_∞ at four stoss-side locations show the 2λ velocity is similar to the isolated dune velocity (Figure 6.12). The near-bed velocity (in the vertical range of $0<y/H<2.5$) progressively decreases with decreasing λ. Where $y/H>2.5$, the velocity for the 0λ-2λ spacings, is similar to the isolated dune velocity. The vertical profile at $x/H=-10.5$ (Figure 6.12a) shows the greatest velocity reduction for the 0λ-2λ spacings, which indicates that the effect of the UBD on the velocity diminishes with horizontal distance.

The shape of the U/U_∞ vertical profiles can be analyzed from their vertical gradient (Figure 6.13). The effect of the UBD is visible at the closest spacings, 0λ-1λ. At each horizontal location ($x/H=-10.5$, -7.8, -3.9, and 0), the vertical gradient shows a peak progressively increasing with decreasing λ, with the 0λ spacing showing the strongest peak. The vertical position of the peak shifts upwards with increasing λ. The vertical gradient of the isolated dune does not exhibit a peak; instead, the gradient profile increases toward the bed linearly at a rate of 0.12 between $8<y/H<1$ at horizontal locations $x/H=-10.5$ and $x/H=-7.8$ (Figures 6.13a and b) and between $8<y/H<1.3$ at horizontal location x/H=-3.9 (Figure 6.13c), and between $8<y/H<1.5$ at horizontal location $x/H=0$ (Figure 6.13d). The isolated dune vertical gradient increases monotonically at a higher rate of 0.84 at $y/H<1$ at horizontal locations $x/H=-10.5$ and $x/H=-7.8$ (Figures 6.13a and b), $y/H<1.3$ at horizontal location x/H=-3.9 (Figure 6.13c) and $y/H<1.5$ at horizontal location $x/H=0$ (Figure 6.13d).

Figure 6.16 presents horizontal profiles of the streamwise velocity component at four vertical locations ($y/H=0.29$, 0.78, 1.00 and 2.01). The 0.5λ-2λ horizontal profiles at $y/H=0.29$ (Figure 6.16d) show the *deceleration zone* is located at the foot of the dune between $-11<x/H<-5.9$. The close proximity of the UBD wake results in a dramatically reduced, but accelerating velocity between $-11.9<x/H<-5.9$ for the 0λ; this explains the absence of the deceleration zone at 0λ. The 0λ-2λ horizontal profiles at $y/H=1$ (Figure 6.16b) show the *acceleration zone* within the range of $-5<x/H<-1$. The horizontal profiles at $y/H=2$ (Figure 6.16a) show the acceleration zone is visible within the range of $-6<x/H<0$. The acceleration of flow is produced by topographic acceleration and streamline convergence over the barchan dune.

The 0λ-2λ horizontal profiles at $y/H=2$ (Figure 6.16a) show that the velocity is similar to the isolated dune velocity. At $y/H=2$, the velocity is steady, remaining between 0.75 and 0.8 U/U_∞. At $y/H=1$, 0.78 and 0.29 (Figure 6.16b-d), the 0λ- 2λ horizontal profiles progressively diverge

from the isolated dune profile with decreasing λ. For 0λ-2λ, the effect of λ on the streamwise component of the velocity is greatest at y/H=0.29, indicating that the effect of λ increases moving vertically downwards towards the floor.

Figure 6.18 compares the position of the 0.6 U/U_∞ contour line termination point (labeled 'T_p' in Figure 6.10) along the stoss-slope of the DBD with respect to λ. With decreasing λ, T_p shifts downstream and vertically upwards, following the dune topography. The final position at 0λ is further downstream than the isolated dune, indicating that the streamwise velocity component at 0λ is strongly retarded compared to the isolated dune velocity, due to the presence of the UBD wake.

6.3.1.2 The effect of λ on the U/U_∞ leeside

Only the 0λ spacing has complete leeside data; the other spacings have leeside data that extend from the crest to x/H=1. The comparison between the isolated dune and the 0λ spacing can be considered the most significant. The separation bubble is visible in the U/U_∞ contour map of the 0λ spacing (Figure 6.10b), and also in the U/U_∞ vertical and horizontal profiles (Figures 6.14 and 6.16). The separation bubble is characterized by a negative streamwise velocity. The reverse flow within the separation bubble reaches a maximum intensity of -0.19 U/U_∞ at 0λ, compared to -0.21 U/U_∞ for the isolated dune case (indicated by a gray arrow in Figure 6.10). The shape of the separation bubble is both longitudinally and vertically compressed at 0λ in relation to the isolated condition. At 0λ, the flow reattaches 4.26H±0.08H downwind from the crest (indicated by a black arrow), which is 0.32H shorter than the reattachment point for the isolated dune.

The vertical and horizontal location of the maximum velocity zone is presented for the 0λ-2λ spacings in Figure 6.19. The maximum velocity zone is represented by the minimum of the 0.8 contour line (labeled '*a*' in Figure 6.10). At 0λ, the maximum velocity zone moves upstream towards the crest (x/H=0) from the isolated dune location (x/H=2.3) and shifts vertically upwards; this is a result of decreased velocity in the leeside of the 0λ spacing due to the sheltering effect of the UBD. The 0.5λ-2λ have leeside data that only extends to x/H=0.97, which limits the determination of the maximum velocity zone.

Figure 6.14 shows the U/U_∞ vertical profiles at four locations (x/H=2.5, 3.75, 5, 6). The 0λ velocity is reduced relative to the isolated dune velocity when y/H>1.1 (y/H>0.7 - Figure 6.14d). The 0λ velocity at y/H<1.1 (y/H<0.7 -Figure 6.14d) exceeds the isolated dune velocity. Outside

the shear layer, the isolated dune velocity is greater than the 0λ velocity; inside the shear layer, the 0λ velocity is less negative than the isolated dune velocity.

Figure 6.15 shows the vertical gradient for the leeside U/U_∞ vertical profiles. At each of the four locations (x/H=2.5, 3.75, 5, 6), the vertical gradient shows a peak for the isolated dune and 0λ spacing. The strength of the peak decreases moving downstream, and the vertical location of the peak, which represents the location of the shear layer, moves downwards (Figure 6.20).

The U/U_∞ horizontal profiles of the 0λ spacing and the isolated dune on the leeside are similar at the vertical locations y/H=0.29, 0.78, and 1.0 (Figure 6.16b-d). However, at y/H=2 between $0<x/H<7.58$ (Figure 6.16a), the 0λ spacing velocity progressively decreases with horizontal distance, constituting 93% of the isolated dune velocity at x/H=0 and 84% at x/H=7.58.

6.3.1.3 The effect of λ on the V/U_∞ stoss-side

The wall-normal contour maps (Figure 6.11) feature the UBD expansion zone, which is partly visible only at 0λ (labeled '*h*' in Figure 6.11b) and is characterized by downwelling fluid, and the topographic-forcing region, which is characterized by upwelling fluid. At 0λ, due to its close proximity, the UBD expansion zone protrudes into the topographic-forcing region, resulting in inflected 0.02 and 0.03 V/U_∞ contour lines on the windward size of the topographic-forcing region (labeled '*b'*). By 0.5λ, the windward side of the topographic-forcing region shows less inflection (labeled '*b'* in Figure 6.11c). The topographic forcing zone decreases in area (mostly due to a thinner 0.02-0.03 V/U_∞ contour band; Figure 6.21) and magnitude with decreasing λ. At 0λ (Figure 6.11b), the maximum velocity reached within the topographic forcing zone is 0.07 V/U_∞, while at 0.5λ-2λ, the maximum velocity reached is 0.08 V/U_∞.

The isolated dune V/U_∞ horizontal profiles (Figure 6.17) show that at y/H=0.29, 0.78, 1.00 and 2.01, the 0.5λ-2λ velocities are similar to the isolated dune velocity. The velocity initially is ~0 V/U_∞ and then increases with horizontal distance due to topographic forcing. The primary effect is seen at 0λ, where the velocity is negative at x/H=-11.9, indicating downwelling fluid due to the expansion region of the UBD; the velocity becomes less negative and then positive with horizontal distance. At x/H=-11.9, the 0λ velocity at y/H=0.29 is -0.014 V/U_∞ (Figure 6.17d), at y/H=0.78 is -0.050 V/U_∞ (Figure 6.17c), at y/H=1 is -0.059 V/U_∞ (Figure 6.17b), and at y/H=2 is -0.048 V/U_∞ (Figure 6.17a). Essentially, the velocity at 0λ is progressively more negative with height above the floor until y/H=1.

6.3.1.4 The effect of λ on the V/U_∞ leeside

On the leeside of the DBD, the crestal jet, the upwelling zone and the DBD expansion zone are visible from the V/U_∞ contour maps (Figure 6.11). The crestal jet is located directly beyond the dune crest; it is absent at the 0λ spacing (Figure 6.11b) but is present at the 0.5λ -2λ spacings (labeled '*d*' in Figure 6.11c-e). With decreasing λ, the crestal jet size decreases, disappearing by 0λ. The upwelling zone is labeled '*e*' and the expansion zone is labeled '*g*' in Figure 6.11a,b. The -0.02 to -0.04 V/U_∞ contour lines of the expansion zone (labeled '*f*') are less inflected at the 0λ spacing relative to the isolated dune. The V/U_∞ horizontal profiles (Figure 6.17) clearly show the upwelling and expansion zones for the isolated dune and the 0λ spacing. Comparing the isolated dune flow features to the 0λ spacing, the following trends were observed: (1) the upwelling zone area decreased from $1.3H^2$ (the area within the 0.04-0.08 contour) for the isolated dune to $1.1H^2$ for the 0λ spacing; (2) the DBD expansion zone area increased from $16.9H^2$ (isolated dune) to 23.4 H^2 (0λ spacing); (3) the magnitude of V/U_∞ within the upwelling zone and expansion zone increased at 0λ relative to the isolated dune.

6.3.1.5 Summary

On the stoss-side, the influence of the UBD on the streamwise velocity component decreases moving vertically upwards, away from the floor. The UBD wake reduces the velocity, as seen by the downstream shift in the 0.6 U/U_∞ termination point relative to the isolated dune position. The deceleration at the toe of the dune, visible in the 0.5λ-2λ horizontal profiles at y/H=0.29 (Figure 6.16d), has been documented by Walker (2000) and represents the spanwise movement of the flow around the barchan dune. The area of the topographic forcing region at 0λ relative to the isolated dune is smaller. On the leeside, at 0λ there is an upstream and vertical upward shift of the maximum velocity region relative to the isolated dune position, as well as a shorter reattachment length x_r. At 0λ the area of the upwelling decreases and expansion zones increases relative to the isolated dune. Moreover, the magnitude of V/U_∞ within the upwelling and expansion zones is greater at 0λ than the isolated dune.

6.3.2 Volumetric ratio AA: turbulence statistics, Reynolds Stress, and vorticity

6.3.2.1 Streamwise turbulence intensity component, T_u: Figure 6.22

On the stoss-side, an elongated region of elevated T_u generated from the UBD appears at 1λ (denoted by the 0.08 contour; labeled 'w_u' in Figure 6.22d) and increases in magnitude with

decreasing λ. At 0λ, the T_u reaches a maximum intensity of 16% (Figure 6.22b). The vertical upper limit of the elongated region ranges from 1.8*H*-2.8*H*. On the leeside, the turbulence intensity T_u in the DBD flow separation region and further downstream is characterized by an elongated region of elevated turbulence, extending off the crest and beyond the field of view (labeled '*l*'). At 0λ, T_u reaches a maximum magnitude of 18%, which is greater than the isolated dune maximum T_u level of 16%. However, the horizontal extent of the 0.16 contour at 0λ is shorter than the isolated dune by 1.2*H*; additionally, the area encompassed by the 0.16 contour at 0λ is 1.7H^2 and 2.0H^2 for the isolated dune. Adjacent to the DBD slipface the T_u levels are notably diminished relative to the downstream wake region (labeled '*m*').

6.3.2.2 Wall-normal turbulence intensity component, T_v: Figure 6.23

On the stoss-side, the highest T_v occurs within the UBD leeside and wake. There is increased T_v with decreasing λ (denoted by the 0.05-0.10 contour); the influence of the UBD is first observed at 1λ, by the appearance of the 0.05 contour. At 0λ, a maximum of 10% T_v is detected between -12<x/H<-10. The horizontal extent of the elongated region of elevated T_v extends beyond the crest of the DBD (labeled 'w_v' in Figure 6.23b). The maximum T_v in the DBD leeside (labeled '*o*') is 10% for both the 0λ spacing and the isolated dune. The area encompassed by the 0.1 contour at 0λ is 1.6H^2 and 1.3H^2 for the isolated dune, indicating that T_v is greater at 0λ. The turbulence levels above the crest, between 1<*y/H*<4, are 60% greater than the isolated condition at 0λ.

6.3.2.3 Turbulent Kinetic Energy, TKE: Figure 6.24

On the stoss-side, an elongated region of elevated *TKE* generated from the UBD appears at 1λ (denoted by the 0.008 contour; labeled '*p*' in Figure 6.24d) and increases in intensity with decreasing λ. At 0λ, the *TKE* maximum reaches 0.04 (Figure 6.24b). The vertical upper limit of the elongated region ranges from 1.9*H*-2.5*H*. The *TKE* within the DBD flow separation region and further downstream is characterized by an elongated region of elevated *TKE* extending off the crest and beyond the field of view (labeled '*q*'). The 0λ leeside elongated region reaches a maximum *TKE* level of 0.04, comparable to the isolated dune. The full downstream extent of the 0.04 contour is larger at 0λ than the isolated dune by 0.37*H*; the area encompassed by the 0.04 contour is larger at 0λ compared to the isolated dune, with a difference of 0.1H^2. The flow above the shear layer, ~*y/H*>1, is characterized by higher *TKE* levels relative to the isolated dune at 0λ.

6.3.2.4 Reynolds Stress, τ_d: Figure 6.25

The UBD effect on the stoss-side is first observed at 1λ by the presence of the 0.002 contour line (Figure 6.25d). Similar to the turbulence intensity and *TKE*, the Reynolds stress is characterized by elongated regions of progressively elevated τ_d levels with decreasing λ (labeled '*bb*'). By 0λ, the maximum Reynolds stress extending from the UBD is in view, and exceeds $0.01U_\infty^2$ (Figure 6.25b). The UBD effect on the leeside at 0λ is expressed through greater τ_d levels above the shear layer, and a larger area of maximum intensity (represented by the 0.01 contour; labeled '*s*') relative to the isolated dune by $0.5H^2$.

6.3.2.5 Vorticity, ω_d: Figure 6.26

The UBD effect is visible only at 0λ on the stoss-side (denoted by the -0.5 contour; labeled '*dd*' in Figure 6.26b). This is due to the fact that the crest is out of the field of view and still relatively far upstream; the maximum vorticity occurs just beyond the crest. It is also a result of how the contours are defined and the subsequent resolution of the flow field to detect subtle changes. The leeside is characterized by a region of high ω_d directly beyond the dune crest (labeled '*cc*'). The UBD effect at 0λ produces a shorter region of maximum ω_d by $0.7H$, relative to the isolated dune; as expected, the area of the maximum ω_d at 0λ is smaller than the isolated dune area, by $0.2H^2$.

6.3.2.6 Summary

On the stoss-side, elevated T_u, T_v, *TKE,* and τ_d is first observable at 1λ; elevated ω_d is only observable at 0λ. The elevated T_u, and τ_d reach beyond the DBD crest at 0.5λ and 0λ, while the elevated T_v and *TKE* reach beyond the DBD crest at 0λ-1λ. The downstream extent of elevated ω_d reaches approximately $-9.4H$. On the leeside, at 0λ the magnitude of T_u reaches 18%, which is 2% greater than the maximum T_u reached by the isolated dune. The area encompassed by the 16% contour is smaller at 0λ than the isolated dune. The area of maximum T_v is greater at 0λ in comparison to the isolated dune area. The area of maximum *TKE* and τ_d is larger at 0λ compared to the isolated dune area. The area of maximum ω_d is smaller at 0λ relative to the isolated dune area. The presence of the UBD amplifies turbulence in the leeside for the AA 0λ spacing.

6.3.3 Volumetric ratio AB

6.3.3.1 The effect of λ on the U/U_∞ stoss-side

The contour maps of U/U_∞ (Figure 6.27) show the increasing presence of the UBD wake with decreasing λ. At 0λ, the UBD separation bubble is visible. Figure 6.29 shows vertical profiles taken at four stoss-side locations (x/H=-10.5, -7.8, -3.9 and 0); at each location the 2λ vertical profile collapses with the isolate dune vertical profile. The velocity progressively decreases with decreasing λ, in the vertical range of $0<y/H<3$.

Figure 6.30 shows the U/U_∞ vertical gradient for the vertical profiles in Figure 6.29. The gradient peak is seen to progressively increase in strength with decreasing λ, indicating that the effect of the UBD on the flow is strongest at the closest spacings, 0λ-1λ.

The U/U_∞ horizontal profiles (Figure 6.33a) show that at y/H=2, the velocity of the 0λ-2λ spacings is similar to the isolated dune velocity. The velocity progressively decreases with decreasing λ at y/H=0.78 and 0.29 (Figure 6.33c,d). The greatest velocity disparity is seen at y/H=0.29 (Figure 6.33d). The common features of the flow at 0.5λ-2λ include the zones of deceleration and acceleration. The horizontal profile at y/H=0.29 (Figure 6.33d), shows the deceleration zone is located at the foot of the dune between $-11<x/H<-5.9$ for spacings 0.5λ- 2λ and the isolated case. The acceleration zone is visible within the 0λ-2λ horizontal profiles at y/H=1 within the range of $-4.93<x/H<0.68$ and at y/H=2 within the range of $-6.5<x/H<0$ (Figure 6.33a,b). The 0λ spacing lacks a zone of deceleration due to the UBD recirculation bubble, which reattaches at x/H=-9.7, and the UBD wake, both evident in the U/U_∞ contour map (Figure 6.27b). At y/H=1 and 2 (Figures 6.33a,b) the 0λ velocity is initially greater than the isolated dune velocity at x/H=-11.9 due to the acceleration over the UBD dune.

The location of the 0.6 U/U_∞ contour line termination point (labeled 'T_p' in Figure 6.27) on the DBD stoss-slope progressively moves downstream and upwards, following the dune topography, with decreasing λ (Figure 6.35).

6.3.3.2 The effect of λ on the U/U_∞ leeside

The influence of the UBD wake upon the velocity can be examined in the overall trend of the reattachment length x_r with decreasing λ and the location of the maximum velocity zone (labeled '*a*' in Figure 6.27). In Figure 6.27, the reattachment distance x_r for the spacings 0λ, 0.5λ, 1λ, and

2λ are 5.18*H*, 5.23*H*, 5.28*H*, and 5.22*H*, respectively, which exceed the isolated dune reattachment length x_r of 4.58*H*. With decreasing λ, the DBD x_r displays no linear trend, but remains longer than the isolated dune x_r (Figure 6.36). The horizontal position of the maximum velocity zone (Figure 6.37a) is relatively stable with decreasing λ, but maintains a position further upstream with respect to the isolated dune horizontal position. The vertical position of the maximum velocity (Figure 6.37b), on the other hand, increases with decreasing λ, maintaining a vertical position above that of the isolated dune. The location of the maximum velocity zone indicates that the velocity at 0λ-2λ is reduced and that the DBD wake is amplified.

The separation bubble is apparent from the 0λ-2λ vertical profiles (Figure 6.31a-c). At *x/H*=5 (Figure 6.31c), it is clear that the isolated dune recovers before the 0λ-2λ spacings. By *x/H*=6 (Figure 6.31d), the 0.5λ-2λ vertical profiles collapse but trail the isolated dune velocity by ~0.08 U/U_∞.

In Figure 6.32, the U/U_∞ vertical gradient of the vertical profiles reported in Figure 6.31 show the gradient peak for the 0λ-2λ spacings does not exceed the isolated dune peak at horizontal locations *x/H*=2.5, 3.75 and 5 (Figure 6.32a-c). At *x/H*=6 (Figure 6.32d), the peak of the 0.5λ-2λ spacings is similar to the isolated dune, reaching 0.59 $\delta U^*/\delta y^*$ at *y/H*=0.85; the 0λ peak reaches 0.51 $\delta U^*/\delta y^*$ at *y/H*=0.74. The strength of the gradient peak decreases with increasing horizontal distance, demonstrating a decreasing effect of flow separation on the flow. The vertical location of the peak decreases with decreasing λ and with horizontal distance for the 0λ-2λ spacings.

The U/U_∞ horizontal profiles (Figure 6.33) show the 0λ-2λ velocities increasingly diverge from the isolated dune velocity with horizontal distance at all vertical locations (*y/H*=0.29, 0.78, 1.00, and 2.01). The 0λ- 2λ profiles are similar at *y/H*=0.29, 0.78, 1.00, and 2.01. However, at *y/H*=0.78, the velocity of the 0λ-2λ spacings does not collapse until 4.3*H* due to the differing upwelling zone areas.

6.3.3.3 The effect of λ on the V/U_∞ stoss-side

The common feature in the wall-normal velocity contour map (Figure 6.28) at the 0λ-2λ spacings is the topographic forcing region, which is characterized by upwelling fluid. The maximum velocity of the topographic forcing region, reached at 0λ is 0.07 V/U_∞ (Figure 6.28b) while the maximum velocity reached at 0.5λ-2λ is 0.08 V/U_∞ (Figure 6.28c-e). With decreasing λ, the area of the region of topographic forcing progressively decreases relative to the isolated dune case

(Figure 6.38). At 0λ, the UBD upwelling zone (labeled '*i*') and UBD expansion zone (labeled '*h*') are visible. The protrusion effect of the UBD expansion zone upon the topographic forcing region (labeled '*b*') produces inflected 0.02 (only at 0λ), 0.03 and 0.04 V/U_∞ contours. The protrusion effect (expressed as inflected 0.02, 0.03 and 0.04 V/U_∞ contour lines) increases with decreasing λ.

Referring to the V/U_∞ horizontal profiles (Figure 6.34), the 0.5λ-2λ velocities are very similar to the isolated dune velocity. The 0.5λ-2λ spacings and isolated dune velocities are initially ~0 V/U_∞ and then increase with distance until x/H=-3.2, at the vertical locations y/H=1.00 and 2.01, at which point, they decrease. The most notable velocity difference occurs at 0λ, due to the presence of the UBD features. The horizontal profile at y/H=0.29 (Figure 6.34d) shows the 0λ velocity at x/H=-11.9 is enhanced relative to the isolated dune and 0.5λ-2λ spacings, reaching 0.053 V/U_∞; this represents the UBD upwelling zone. The horizontal profile at 0λ lies over the base of the expansion zone, which accounts for the fluctuating velocity between -10.7 <x/H<-8.2. Between -8.2<x/H<-5.92, the 0λ velocity increases; interestingly, the 0λ horizontal profile has a similar trend to the isolated dune and 0.5λ-2λ spacing profiles.

6.3.3.4 The effect of λ on the V/U_∞ leeside

The expansion zone occupies the area downstream of the upwelling zone and is characterized by downwelling flow. The topographic forcing region protrudes into the DBD expansion zone, producing inflected -0.02 (only at 0λ), -0.03 and -0.04 V/U_∞ contour lines (labeled '*f*') at the 0λ-2λ spacings. The V/U_∞ horizontal profiles (Figure 6.34) at all four vertical locations show that the 0λ-2λ horizontal profiles follow a similar trend to the isolated dune horizontal profile, due to the presence of the expansion zone. At y/H=0.29, 0.78 and 1.00 (Figure 6.34b-d), the 0λ and 0.5λ velocities are closer to the isolated dune velocity than the 1λ and 2λ velocities. At y/H=2.01 between 4.46<x/H<7.85, the 0λ-2λ profiles collapse and increasingly diverge from the isolated dune profile with distance. The following trends were observed with decreasing λ: the crestal jet area decreased; the upwelling zone area decreased from 2λ to 0.5λ, and increased at 0λ (Figure 6.39a); and the DBD expansion zone area increased (Figure 6.39b). The upwelling zone velocity increases with decreasing λ, reaching a maximum velocity of 0.07 V/U_∞ at 0λ. In addition, the area of the upwelling zone is greater than the isolated barchan, except at 0.5λ. The velocity of the expansion zone is reduced at the 0λ-2λ spacings relative to the isolated dune; moreover, the area

encompassed by the -0.07 V/U_∞ contour line within the expansion zone increases with decreasing λ (Figure 6.28).

6.3.3.5 Summary

On the stoss-side, the streamwise velocity component featured the wake of the UBD, in addition to the separation bubble at 0λ. The wall-normal velocity component featured a decreasing area and magnitude of upwelling flow, constituting the topographic forcing region (Figure 6.38). On the leeside, the streamwise velocity component shows the DBD wake amplified by the presence of the UBD as manifested by the upstream position of the zone of maximum velocity at 0λ-2λ relative to the isolated dune, as well as an increasingly vertical position with decreasing λ. The reattachment length at 0λ-2λ is longer than the isolated dune. The wall-normal velocity component shows a smaller crestal jet and upwelling zone area (except at 0λ) but a larger expansion zone area with decreasing λ (Figure 6.39).

6.3.4 Volumetric ratio AB: turbulence statistics, Reynolds Stress, and vorticity

6.3.4.1 Streamwise turbulence intensity component, T_u: Figure 6.40

The AB volumetric ratio shares the same phenomena observed as the AA volumetric ratio, i.e. the presence of two elongated regions, one of which extends off of the crest of the UBD and the other of which extends off the crest of the DBD. On the stoss-side, the UBD elongated region appears at 1λ (denoted by the 0.08 contour; labeled 'w_u' in Figure 6.40d) and extends further downstream at 0.5λ reaching the crest (Figure 6.40c). At 0λ, the UBD elongated region appears to be fully in view, reaching a maximum intensity of 16%. The vertical upper limit of the elongated region ranges from 0.9*H*-2*H*. On the leeside, the most notable trend regarding the DBD region of high T_u is that the maximum T_u reaches 18% at the 0λ-2λ spacings, a 2% increase from the isolated dune maximum T_u. The horizontal extent of the 0.18 contour line decreases with decreasing λ; at 0λ-2λ the 0.16 contour reaches 5.01*H*, 6.53*H*, 7.16*H*, and 7.32*H*, respectively (labeled '*l*'). For the isolated dune, the 0.16 contour line reaches 6.69*H*. The area encompassed by the 0.16 contour is greater for the 0λ-2λ spacings compared to the isolated dune (Figure 6.44a).

6.3.4.2 Wall-normal turbulence intensity component, T_v: Figure 6.41

On the stoss-side, the UBD influence is first observed at 0.5λ, by the appearance of the 0.05 contour. At 0λ, a maximum of 10% T_v is noted. The elongated region of elevated T_v extends beyond the DBD crest (labeled 'w_v' in Figure 6.41b). Most notably when examining the leeside, is that while the maximum intensity is the same for all tandem spacings 0λ-2λ relative to the isolated dune, the area of maximum T_v (denoted by the 0.10 contour line; labeled '*o*' in Figure 6.41) is greater than the isolated dune at spacings 0λ-2λ (Figure 6.44b). The greatest area of maximum T_v is at 0λ; the area progressively decreases with increasing λ. Moreover, remnant T_v extending from the UBD is visible at 0λ.

6.3.4.3 Turbulent Kinetic Energy, TKE: Figure 6.42

On the stoss-side of the DBD, an elongated region of elevated *TKE* appears at 1λ (denoted by the 0.008 contour; labeld '*p*' in Figure 6.42d) and increases in magnitude with decreasing λ. At 0λ, the *TKE* reaches a maximum of 0.036. The vertical upper limit of the region of high *TKE* ranges from 1*H* to 2.25*H* at 0λ. Within the leeside, the region of high *TKE* for the 0λ-2λ spacings reaches a maximum of 0.04, which is also the maximum *TKE* reached by the isolated dune. The area encompassed by the 0.04 contour is greater at 0λ-2λ than the isolated dune; the area decreases from 0λ through to 1λ, but increases at 2λ (Figure 6.44c). The horizontal extent of the 0.04 contour decreases with decreasing λ. The horizontal extent of the 0.04 contour is greater at 0λ -2λ relative to the isolated dune. The flow above the shear layer, ~y/H>1, is characterized by higher TKE levels relative to the isolated dune at 0λ.

6.3.4.4 Reynolds Stress, τ_d: Figure 6.43

On the stoss-side, the τ_d is characterized by elongated regions of progressively elevated levels with decreasing λ. The UBD effect is first observed at 0.5λ by the presence of the 0.002 contour (labeled '*bb*' in Figure 6.43c). By 0λ, the maximum τ_d is in view, and reaches a maximum of 0.01 (Figure 6.43b). The influence of the UBD on the leeside at 0λ-2λ is expressed through elevated τ_d above the shear layer (~*y/H*>1), and a significantly larger area of maximum intensity (represented by the 0.01 contour; labeled '*s*') relative to the isolated dune. The area encompassed by the 0.01 contour decreases from 0λ to 1λ and then increases at 2λ (Figure 6.44d).

6.3.4.5 Vorticity, ω_d: Figure 6.44

The influence of the UBD is visible only at 0λ on the stoss-side (denoted by the -0.5 contour; labeled '*dd*' in Figure 6.44b), where the maximum intensity reaches -5. The horizontal extent of the high ω_d terminates at -4*H*. Within the leeside, the area of high ω_d (denoted by the -5 to -10 contour; labeled '*cc*' in Figure 6.44) is smaller for the 0λ-2λ compared to the isolated dune. The area encompassed by the -5 contour is the smallest at 0λ.

6.3.4.6 Summary: Figure 6.45

On the stoss-side, elevated T_u and *TKE* is first observable at 1λ. Elevated T_v and τ_d is first observable at 0.5λ; higher ω_d is observable only at 0λ. The downstream extent of higher T_u, T_v, *TKE*, and τ_d reaches beyond the DBD crest at 0λ. The downstream extent of higher ω_d reaches approximately -4*H*. On the leeside, the maximum T_u reached by the 0λ-2λ spacings is 2% greater than the isolated dune. The area of 16% T_u, 10% T_v, 0.04 *TKE* and 0.01 τ_d for the 0λ-2λ spacings is greater than the isolated dune. The greatest area of T_v, *TKE* and τ_d occurs at 0λ while the greatest area of T_u occurs at 1λ and 2λ. The area encompassed by -5 ω_d for the 0λ-2λ spacings is smaller than the isolated dune. The presence of the UBD amplifies turbulence in the leeside for the AB volumetric ratio.

6.3.5 Volumetric ratio AC

6.3.5.1 The effect of λ on the U/U_∞ stoss-side

The U/U_∞ contour map in Figure 6.46b clearly shows recirculation region of the UBD at 0λ which reattaches *x/H*=-9.2 with a reattachment length x_r of 1.2*H*. By 0.5λ (Figure 6.46c), the UBD recirculating region is no longer visible in the field of view and the velocity field more closely resembles that of the isolated barchan dune.

The common features of the flow for the tandem spacings 0.5λ-2λ, on the stoss-side of the DBD, include the zones of deceleration and acceleration. The horizontal profiles at *y/H*=0.29 (Figure 6.52d) show the deceleration zone is located at the foot of the dune between -11.3<*x/H*<-5.9 for spacings 0.5λ- 2λ and the isolated barchan dune. At *y/H*=0.78 (Figure 6.52c) the 0.5λ- 2λ horizontal profiles reveal that the deceleration zone is visible between -11.3<*x/H*<-5. At *y/H*=1.00 (Figure 6.52b), the acceleration zone is visible between -6.16<*x/H*<-1.78 from the 0.5λ- 2λ horizontal profiles; at *y/H*=2.01 (Figure 6.52a), the acceleration zone is visible between

-6.7<x/H<1.65. The U/U_∞ horizontal profiles at y/H=0.29 and 0.78 (Figure 6.52c-d), show the velocity progressively decreases with decreasing λ (excluding 0λ). At y/H=2.01 (Figure 6.52a), the 0.5λ-2λ horizontal profiles collapse with the isolated dune profile; the 0λ profile is very similar. The 0λ horizontal profile lacks a zone of deceleration at y/H=0.29 (Figure 6.52d), due to the presence of the UBD and the UBD recirculation bubble and wake. The 0λ velocity shows an overall increase between -10.92<x/H<-6.47, interrupted by a short velocity decrease due to the UBD recirculation bubble between -9.84<x/H<-9.4. At y/H=0.78 and y/H=1 (Figure 6.52b-c), the 0λ horizontal velocity is enhanced relative to 0.5λ-2λ velocities between -11.9<x/H<-9.4, most likely the result of topographically-induced acceleration over the UBD; the velocity of 0λ between -9.4<x/H<-3.2 is reduced relative to 0.5λ-2λ due to the UBD wake effect.

Figure 6.48 presents the U/U_∞ vertical profiles taken at four stoss-side locations. The vertical profiles of U/U_∞ clearly indicate that the strongest influence of the UBD is at 0λ. Further downstream the influence of the UBD is less evident. Figure 6.49 shows the U/U_∞ velocity gradient of the vertical profiles (Figure 6.48).

With decreasing λ, the 0.6 U/U_∞ termination point (labeled 'T_p' in Figure 6.46) moves downstream and upwards, following the topography of the DBD (Figure 6.54). At 0.5λ-2λ the 0.6 U/U_∞ termination point is upstream of the isolated dune location. At 0λ the 0.6 U/U_∞ termination point is downstream of the isolated dune location.

6.3.5.2 The effect of λ on the U/U_∞ leeside

The common flow features include the recirculation region, the DBD wake and the zone of maximum velocity, visible in the contour maps and vertical profiles (Figures 6.46 and 6.50). The maximum reverse velocity reached within the recirculation region at 0λ, 0.5λ, 1λ and 2λ is -0.18, -0.20, -0.19 and -0.19 U/U_∞, respectively, and these are all weaker than the isolated dune velocity -0.21 U/U_∞. The reattachment distance x_r for the spacings 0λ, 0.5λ, 1λ, and 2λ are 4.49H, 4.52H, 4.70H, and 4.77H, respectively, fluctuating around the isolated dune reattachment length, x_r of 4.58. The DBD wake is represented by the 0.2-0.6 U/U_∞ contours. The influence of the UBD wake on the velocity can be examined in the overall trend of the reattachment length of the DBD recirculation region with decreasing λ, the location of the maximum velocity zone, and the similarity of the vertical gradient. With decreasing λ, the DBD reattachment length x_r is generally shortened but fluctuates above and below the isolated dune reattachment length x_r

(Figure 6.55). The zone of maximum velocity is represented by the 0.08 U/U_∞ contour line minima (labeled '*a*'). The horizontal position of the maximum velocity zone is further downstream for all spacings relative to the isolated dune location but has no overall trend (Figure 6.56a). The vertical position, on the other hand, increases with decreasing λ (Figure 6.56b). In Figure 5.51, the vertical gradient of the velocity profiles in Figure 5.50 shows that there is little effect of the UBD on the velocity in the leeside; the intensity of the peak (indicating the shear layer) at x/H=2.5 and 3.75 is slightly smaller for λ=0 than the other conditions.

6.3.5.3 The effect of λ on the V/U_∞ stoss-side

At 0λ (Figure 6.47b), the UBD upwelling zone (labeled '*i*') and UBD expansion zone (labeled '*h*') are visible; the UBD topographic forcing region is partly in the field of view. By 0.5λ (Figure 6.47c), the UBD flow features are no longer within the field of view. The V/U_∞ horizontal profiles (Figure 6.53) indicate that the UBD effect is the strongest at 0λ, where the close proximity of the UBD and its flow features produces significantly different velocities up to 0.055 V/U_∞ relative to the isolated dune benchmark. The UBD upwelling zone locally increases the velocity by up to 0.03 V/U_∞ between $-11.0<x/H<-10.3$ relative to the isolated dune, while the UBD expansion zone locally decreases the velocity by 0.055 V/U_∞ between $-10.0<x/H<-7.8$. The common feature of flow for the 0λ-2λ spacings is the topographic forcing region, which is characterized by upwelling fluid (Figure 6.47). With decreasing λ, the topographic forcing region area decreased (Figure 6.57); furthermore, there is a progressive velocity reduction with decreasing λ, demonstrated by the 0λ-2λ V/U_∞ horizontal profiles.

6.3.5.4 The effect of λ on the V/U_∞ leeside

The common flow features in the wall-normal velocity contour map (Figure 6.47) include the crestal jet (labeled '*d*'), the zones of upwelling (labeled '*e*') and expansion (labeled '*g*'). For the 0λ-1λ spacings (Figure 6.47b-d), the expansion zone is located further upstream than the isolated dune expansion zone. The upstream side of the expansion zone is characterized by concave -0.02 to -0.04 V/U_∞ concave contour lines (labeled '*f*'), which are the result of upstream flow zones influencing the downwelling fluid within the expansion zone. The horizontal profiles indicate that the 0-2 velocity is similar to the isolated dune velocity (Figure 6.53). The most notable trends observed with decreasing λ are the decreasing crestal jet area, the increasing upwelling zone area, except at 0λ, (Figure 6.58a) and the overall increase in the DBD expansion zone area

(Figure 6.58b). With decreasing λ, the expansion zone occupies an area closer to the floor, and the -0.02 to -0.04 V/U_∞ contours becoming increasingly inflected and concave on the windward side of the expansion zone.

6.3.5.5 Summary

On the stoss-side, the streamwise velocity component featured the separation bubble at 0λ, which has a reattachment length of 1.2*H*. The wall-normal velocity component featured UBD flow features at 0λ; subsequently, these features have the greatest effect on the velocity. There is a reduction in velocity with decreasing λ as indicated by the decreasing topographic forcing area. On the leeside, the streamwise velocity component shows at 0λ-2λ, the maximum velocity zone is downstream and vertically higher than the isolated dune, indicating that the fastest velocity is positioned over the separation bubble. The reattachment length at 0λ-2λ fluctuates about the isolated dune reattachment length. The wall-normal velocity component shows a smaller crestal jet area and a larger upwelling zone (except at 0λ) and expansion zone area with decreasing λ.

6.3.6 Volumetric ratio AC: turbulence statistics, Reynolds Stress, and vorticity

6.3.6.1 Streamwise turbulence intensity component, T_u: Figure 6.59

On the stoss-side, the region of high T_u downstream of the UBD appears at 0.5λ (denoted by the 0.08 contour; labeled 'w_u' in Figure 6.59c). At 0λ, the UBD is within the field of view, as well as the region of high T_u downstream of the UBD which reaches 12%. The vertical upper limit of the elongated region ranges from 0.5*H*-1.6*H*. The downstream extent of the elongated region goes beyond the crest, *x/H*=0. On the leeside, the DBD region of high T_u reaches a maximum T_u of 16% at the 0λ-2λ spacings (labeled '*l*' in Figure 6.59), which is comparable to the isolated dune maximum T_u. The area of maximum T_u increases with decreasing λ, except at 0λ, where the area decreases (Figure 6.64a). The area of the 0λ-2λ spacings is smaller than the isolated dune area by 0.5-1.0H^2. For the 0λ-2λ spacings, the 0.16 contour horizontal extent is shorter than that of the isolated dune, which is 5.4*H*; the isolated dune 0.16 contour begins at 1.26*H* and ends at 6.70*H*.

6.3.6.2 Wall-normal turbulence intensity component, T_v: Figure 6.60

The UBD influence is clearly observed at 0λ, where a maximum T_v of 8% is reported. The horizontal extent of the elongated region of elevated T_v reaches approximately -1.9*H* (labeled 'w_v' in Figure 6.60b). On the leeside, the maximum T_v (labeled '*o*') reaches 10% at 0λ-1λ but

reaches 9% at 2λ. The area of maximum T_v (defined by the 0.10 contour) for the 0λ-2λ spacings is smaller than the isolated dune area (Figure 6.64b). The area is greatest at 0.5λ.

6.3.6.3 Turbulent Kinetic Energy, TKE: Figure 6.61

On the stoss-side of the DBD, an elongated region of elevated *TKE* appears at 0.5λ (denoted by the 0.008 contour; labeled '*p*' in Figure 6.61c) and increases in intensity with decreasing λ. At 0λ, the *TKE* maximum reaches 0.024 (Figure 6.61b). The vertical upper limit of the elongated region ranges from 1*H*-1.8*H* at 0λ. For spacings 0λ-2λ, the elongated region in the leeside reaches a maximum *TKE* level of 0.036 (labeled '*q*'), which is below the maximum level reached by the isolated dune. The 0.5λ spacing has the greatest *TKE* out of the 0λ-2λ spacings; the 0.036 contour extends from 2.7*H* to 5.8*H*.

6.3.6.4 Reynolds Stress, τ_d: Figure 6.62

The UBD effect on the stoss-side is observed only at 0λ (denoted by the 0.002-0.006 contours; labeled '*bb*' in Figure 6.62b). The region of high τ_d extending from the UBD crest reaches approximately -1.8*H*. On the leeside the influence of the UBD results in smaller areas of maximum τ_d (denoted by the 0.01 contour; labeled '*s*' in Figure 6.62) at spacings at 0λ-2λ relative to the isolated dune (Figure 6.64d). The position of maximum τ_d moves upstream with decreasing λ.

6.3.6.5 Vorticity, ω_d: Figure 6.63

The effect of the UBD on the stoss-side is visible only at 0λ (denoted by the -0.5 to -10 contours; labeled '*dd*' in Figure 6.63b). The region of high ω_d terminates at -4*H*. In the leeside, the area of maximum ω_d (denoted by the -0.5 to -10 contours) is comparable to the isolated dune (Figure 6.64e). The -5 contour reaches 2.14*H* for the isolated dune, while for the 0λ-2λ spacings, the -5 contour reaches 1.92 *H*, 2.08*H*, 2.18*H*, and 2.08*H*, respectively. In other words, only the maximum ω_d at 1λ exceeds the isolated dune maximum ω_d.

6.3.6.6 Summary: Figure 6.64

The increase in T_u and *TKE* on the stoss-side of the DBD is first observable at 0.5λ. The increase in T_v, τ_d and ω_d, is only observable at 0λ. The downstream extent of elevated T_u and *TKE* reaches beyond the DBD crest at 0λ. The downstream extent of elevated T_v, τ_d and ω_d, reaches mid-stoss-slope of the DBD, between -4.0*H* and -1.8*H*. Within the leeside, the greatest T_u, T_u, and *TKE*

occur at 0.5λ. The isolated dune has greater T_u, T_u, *TKE* and τ_d than the 0λ-2λ spacings. The isolated dune has comparable ω_d to the 0λ-2λ spacings. The presence of the UBD dampens turbulence in the leeside for the AC volumetric ratio.

6.3.7 Volumetric ratio AD

6.3.7.1 The effect of λ on the U/U_∞ stoss-side

The UBD recirculation bubble, which reattaches at -8.15*H*, and the UBD wake are visible at 0λ, within the U/U_∞ contour map (Figure 6.65b) and the U/U_∞ horizontal profile at y/H=0.29 (Figure 6.71d). The common flow features for the tandem spacings 0.5λ and 1λ on the stoss-side of the DBD include the zones of deceleration and acceleration (Figure 6.65). The deceleration and acceleration zones are best identified in the U/U_∞ horizontal profiles (Figure 6.71). The deceleration zone is observed close to the floor from the 0.5λ and 1λ horizontal profiles at y/H=0.29 between -11.7<x/H<-6 (Figure 6.71d). At y/H=0.78, 1.00, and 2.01 (Figure 6.71a-c), the 0.5λ and 1λ velocities collapse with the isolated dune velocity. At y/H=0.29, the 0λ velocity initially follows the trend of the 0.5λ and 1λ velocities at x/H=-11.9, but the presence of the UBD at x/H=-11.5 disrupts the flow field.

Figure 6.67 shows U/U_∞ vertical profiles taken at four stoss-side locations. Upstream of the DBD, at x/H=-10.5 (Figure 6.67a), the velocity of the 0.5λ and 1λ spacings is reduced from the isolated dune velocity between 0<y/H<1.18, and enhanced between 1.18<y/H<6.9; at y/H>6.9, the 0.5λ and 1λ profiles collapse with the isolated dune profile. The 0λ profile at x/H=-10.5 (Figure 6.67a), does not extend to the floor due to the UBD; consequently, the 0λ velocity is enhanced beyond the isolated dune velocity between 0.47<y/H<4.1 due to topographically-induced acceleration; at y/H>4.1, the 0λ velocity is reduced by relative to the isolated dune velocity. At x/H =-7.8, -3.9, and 0 (Figure 6.67b-c), the 0.5λ and 1λ profiles collapse with the isolated dune profile; the 0λ velocity, however, is reduced compared to the isolated dune velocity at y/H <1.4 for the vertical profile at x/H=-7.8 and y/H<2.1 for the vertical profile at x/H=-3.9 and 0. Figure 6.68 shows the vertical gradient of the U/U_∞ vertical profiles presented in Figure 6.67.

Figure 6.73 compares the position of the 0.6 U/U_∞ contour line termination point (labeled 'T_p' in Figure 6.65) along the stoss-slope of the DBD with respect to λ. The termination point shifts upstream at 1λ and 0.5λ relative to the isolated dune and then downstream at 0λ towards the crest

(x/H=0) (Figure 6.73a). The vertical location of the termination point follows the dune topography, and consequently, shifts vertically downwards at 1λ and 0.5λ, and then vertically upwards at 0λ (Figure 6.73b).

6.3.7.2 The effect of λ on the U/U_∞ leeside

The common flow features include the recirculation region and the DBD wake and zone of maximum velocity in Figure 6.65. The maximum velocity reached at 0λ, 0.5λ, and 1λ within the recirculation region is -0.19, -0.20, and -0.19 U/U_∞, respectively, slightly less compared to the isolated dune velocity -0.21 U/U_∞. The flow reattachment lengths x_r for the tandem spacings 0λ, 0.5λ, and 1λ are 4.65H, 4.567H, and 4.74H, respectively, fluctuating around the isolated dune reattachment length x_r of 4.58. The DBD wake is represented by the 0.2-0.6 U/U_∞ contours which are visible at 0λ.

The trends observed with decreasing λ primarily concern the reattachment length of the DBD recirculation region and the location of the maximum velocity zone. With decreasing λ, the DBD reattachment length x_r fluctuates, but overall, becomes shorter (Figure 6.74). The reattachment length for all tandem spacings remains longer than the isolated dune reattachment length. The horizontal and vertical position of the maximum velocity zone decreases and then increases with decreasing λ; the final position at 0λ is the furthest downstream and the highest, vertically (Figure 6.75). The vertical position remains above the isolated dune position at 0λ-1λ, indicating that the UBD wake reduces the velocity (Figure 6.75b).

Figure 6.69 shows the U/U_∞ vertical profiles at four horizontal locations; the 0λ-1λ velocities are similar to the isolated dune velocity at each location. For the locations x/H=2.5, 3.75, 5 and x/H=6 where y/H>1.3, the 0λ-1λ velocities are reduced relative to the isolated dune velocity. At x/H=2.5, 3.75, 5 and x/H=6 where y/H<1.3 (Figure 6.69a, d), the 0λ-1λ U/U_∞ is enhanced relative to the isolated dune velocity.

Figure 6.70 shows the vertical gradient for the U/U_∞ vertical profiles presented in Figure 6.69. At each of the four horizontal locations, the vertical gradient has a peak which represents the shear layer. Downstream, the strength of the peak decreases, and the location of the peak, moves vertically downwards until x/H=5. At x/H=2.5 (Figure 6.70a), the 0λ-1λ peak occurs at y/H=0.94. At x/H=3.75 (Figure 6.70b), the 0λ-1λ peak occurs at y/H=0.89. At x/H=5 (Figure 6.70c), the 0λ-1λ peak occurs at y/H=0.82. At x/H=6 (Figure 6.70d), the 0λ-1λ peak occurs at y/H=0.88. The 0λ

has the smallest peaks while the isolated dune has the strongest peaks; the 0.5λ and 1λ peaks are positioned between the 0λ and isolated dune peaks.

The streamwise component of the velocity is larger than the isolated dune velocity between $0.4<x/H<5.6$ at $y/H=0.29$, 0.78 and 1 (Figure 6.71); downstream of 5.6*H*, the velocities collapse.

6.3.7.3 The effect of λ on the V/U_∞ stoss-side

The common flow feature for 0λ-1λ is the region of topographic forcing, characterized by upwelling fluid (Figure 6.66). The topographic forcing region has a maximum velocity zone that borders the DBD stoss-slope, and is denoted by the 0.08 V/U_∞ contour line (located between $-5.5<x/H<-2$). At 0λ (Figure 6.66b), the UBD topographic forcing zone (labeled 'j') and expansion zone (labeled 'h') are visible. The UBD upwelling zone is too small to resolve in the V/U_∞ contour map. By 0.5λ (Figure 6.66c), the UBD flow features are no longer within the field of view. The UBD expansion zone protrudes into the topographic-forcing region, resulting in inflected 0.02 - 0.04 V/U_∞ contour lines on the windward size of the topographic-forcing region, most notably at 0λ (labeled '*b'*). By 0.5λ, the windward side of the topographic-forcing region shows less inflection of the 0.02 and 0.03 V/U_∞ contour lines (label '*b'*).

Figure 6.72 shows V/U_∞ horizontal profiles at four vertical locations. The 0.5λ-1λ profiles are similar to the isolated dune profile; however, their velocity progressively decreases relative to the isolated dune with decreasing λ. The 0λ horizontal profile at all vertical locations in Figure 6.72 reflects the presence of the UBD, which causes the flow to accelerate due to the presence of the dune between $-11.9<x/H<-11.4$. The recirculation bubble is visible at $y/H=0.29$ (Figure 6.72d) between $-10.12<x/H<-7.56$. After $x/H=-7.56$, the flow recovers and approaches the isolated dune velocity.

With decreasing λ, the topographic forcing region area progressively decreases in area relative to the isolated dune case (Figure 6.76). The maximum velocity reached within the topographic forcing region is smaller at 0λ, 0.07 V/U_∞ (Figure 6.66b), compared to the 0.5λ and 1λ (Figure 6.66c,d).

6.3.7.4 The effect of λ on the V/U_∞ leeside

The wall-normal contour map (Figure 6.66) shows the crestal jet (labeled '*d*') becomes smaller with decreasing λ. The upwelling zone (labeled '*e*') did not vary greatly between spacings, but

increased in area from 1λ to 0.5λ and then decreased at 0λ, following the trend at ratio AC (Figure 6.77a); the upwelling zone area is smaller to the isolated barchan area. The expansion zone area is relatively stable with decreasing λ, showing a minor increase at 0λ (Figure 6.77b). Figure 6.72 shows V/U_∞ horizontal profiles at four vertical locations. The 0λ-1λ velocities show the same trend as the isolated dune velocity; however, in the horizontal range of $0<x/H<3.7$, the 0λ-1λ velocity is reduced by 0.01 V/U_∞ relative to the isolated dune velocity, which is within the estimated error.

6.3.7.5 Summary

On the stoss-side, the streamwise component of the velocity does not show any significant effect of the UBD until 0λ, primarily due to the proximity of the UBD and the UBD separation bubble and wake. For the wall-normal component of the velocity, there is a progressive reduction in velocity from 1λ to 0.5λ. The 0λ velocity reflects the presence of UBD features, such as the topographic forcing zone, the upwelling zone and expansion zone. On the leeside, the 0λ streamwise and wall-normal components of the velocity are similar to the 0.5λ-1λ and isolated dune velocities.

6.3.8 Volumetric ratio AD: turbulence statistics, Reynolds Stress, and vorticity

6.3.8.1 Streamwise turbulence intensity component, T_u: Figure 6.78

On the stoss-side, downstream of the UBD, the region of elevated T_u appears at 0.5λ (denoted by the 0.08 contour; labeled 'w_u' in Figure 6.78c); at 0λ, the region of high T_u is fully visible, extending from the UBD crest, and reaches a maximum of 12%. The vertical upper limit of the elongated region ranges from 0.5H-1.5H. On the leeside, the DBD elongated region reaches a maximum T_u of 16% at the 0λ-1λ spacings, comparable to the isolated dune maximum T_u (labeled 'l'). The 0.16 contour line extends to ~6H for the 0λ-1λ spacings, 0.7H shorter than the isolated dune. The area encompassed by 16% T_u is greater for the isolated dune by 0.3H^2 compared to the 0λ-1λ spacings (Figure 6.83a).

6.3.8.2 Wall-normal turbulence intensity component, T_v: Figure 6.79

The UBD influence is clearly observed at 0λ, where a maximum of 7% T_v is reported. The horizontal extent of the elongated region of elevated T_v reaches approximately -3.8H (labeled 'w_v' in Figure 6.79b). There is no observable increase in T_v at 0.5λ and 1λ. On the leeside, the

maximum T_v is 10% at all tandem spacings 0λ-1λ, which is comparable to the isolated dune (labeled '*o*'). Downstream of the DBD, the area of maximum T_v decreases with decreasing λ (Figure 6.83b). The area at 0.5λ is the same as the isolated dune area. At 1λ, the area is greater than the isolated dune by ~0.1H^2. The 0.1 contour horizontal extent decreases with decreasing λ, from 6.36*H* at 0.5λ and 1λ to 6*H* at 0λ.

6.3.8.3 Turbulent Kinetic Energy, TKE: Figure 6.80

On the stoss-side of the DBD, an elongated region of elevated *TKE* appears at 0.5λ (denoted by the 0.008 contour; labeled '*p*' in Figure 6.80c) and increases in intensity at 0λ. At 0λ, the *TKE* maximum reaches 0.02 (Figure 6.80b). The vertical upper limit of the elongated region ranges from 1*H*-1.8*H* at 0λ. On the leeside, the region of high *TKE* for tandem spacings 0λ-2λ reaches a maximum of 0.4 (labeled '*q*'), which is comparable to the maximum *TKE* reached by the isolated dune. The full downstream extent of the 0.04 contour decreases with decreasing λ; the full horizontal extent of 0.4 *TKE* at 1λ, 0.5λ and 0λ is 2.5*H*, 1.9*H*, and 1.0*H* respectively. The isolated dune downstream extent of 0.4 *TKE* is 1.4*H*, indicating that the 0.4 contour is shorter at 0λ and 0.5λ. The area encompassed by the 0.4 contour is greater for the isolated dune than the 0λ-1λ (Figure 6.83c).

6.3.8.4 Reynolds Stress, τ_d: Figure 6.81

On the stoss-side, the UBD effect on τ_d is observed at 0λ (denoted by the 0.002-0.006 contours; labeled '*bb*' in Figure 6.81) but not at 0.5λ and 1λ. The τ_d reaches a maximum of 0.006. Within the DBD leeside, the UBD has little effect on τ_d in the area outside the shear layer. The maximum τ_d reached in the leeside is 0.01 (labeled '*s*'). The area encompassed by the 0.01 contour is greater at 0.5λ and 1λ relative to the isolated dune, but smaller at 0λ (Figure 6.83d).

6.3.8.5 Vorticity, ω_d: Figure 6.82

On the stoss-side, the UBD effect is visible only at 0λ, by the appearance of the -0.5 to -5 contours (labeled '*dd*' in Figure 6.82b); the maximum ω_d reached is -5 within the UBD elongated region of high ω_d. In the leeside, the UBD effect on 0λ and 1λ produces a shorter and smaller zone of maximum ω_d (denoted by the -5 contour; labeled '*cc*') relative to the isolated dune (Figure 6.83e). At 0.5λ, the -5 contour area and downstream extent is the same as the isolated dune.

6.3.8.6 Summary: Figure 6.83

The greatest increase in T_u, T_v, *TKE*, τ_d and ω_d, on the stoss-side of the DBD, is seen at 0λ. The downstream extent of elevated levels of T_u, T_v, τ_d and ω_d reaches mid-stoss-slope of the DBD, at approximately -3.8*H*. The downstream extent of elevated *TKE* reaches beyond the DBD crest into the leeside. Focusing on the leeside, the isolated dune has greater T_u compared to the 0λ-1λ T_u. The 1λ spacing has greater T_v than the isolated dune; the 0.5λ spacing had similar T_v to the isolated dune, while the 0λ had less T_v. The maximum *TKE* begins further upstream at 0.5λ and 1λ relative to the isolated dune; the isolated dune, however, has a greater area of maximum *TKE* than the 0λ-1λ spacings. The τ_d is greater at 0.5λ and 1λ, but smaller at 0λ in comparison to the isolated dune. At 0λ and 1λ, the area of maximum ω_d is smaller than the isolated dune area, while the area at 0.5λ is equivalent. Generally speaking, the presence of the UBD dampens turbulence in the leeside for the AD volumetric ratio; the greatest turbulence dampening is at 0λ.

6.4 Figures

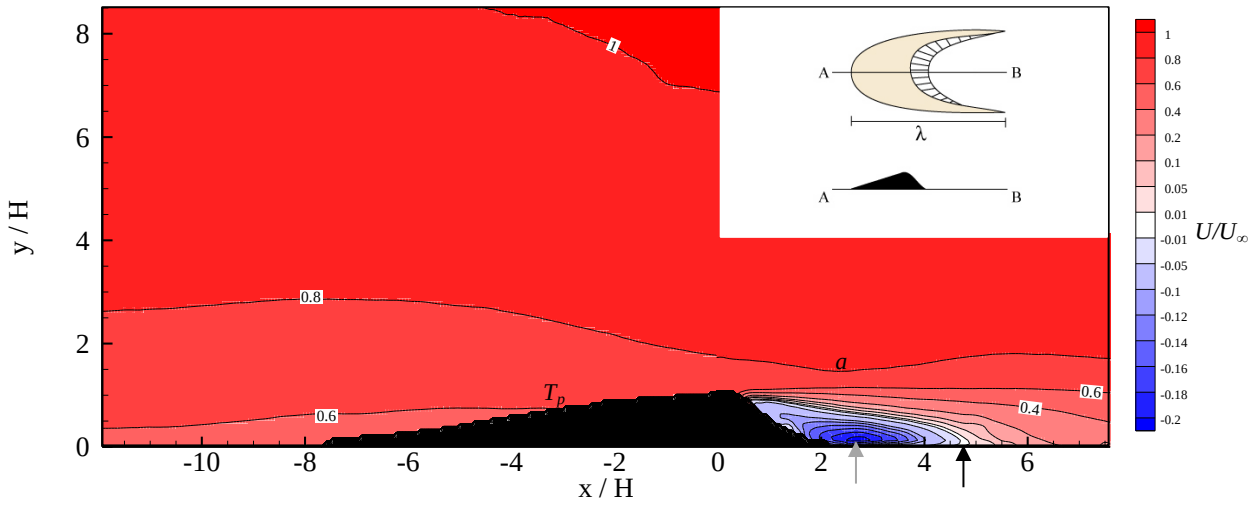

Figure 6.1: A contour plot of the ensemble-average of the streamwise velocity, U/U_∞, component for the isolated barchan dune condition (*Re*=59,806). The black triangular object represents the dune profile. The upper right schematic featured in the plot depicts the experimental condition from a plan view and profile view. Red indicates downstream flow direction, blue upstream flow, and white indicates zero velocity. The contour values span from -0.2 to 1. The gray arrow points to the highest negative velocity in the flow separation zone. The flow reattachment point (black arrow) forms a stagnation point at the floor located within the ±0.01 contour band. The maximum velocity region is labeled '*a'*. The 0.6 contour line termination point is labeled 'T_p'.

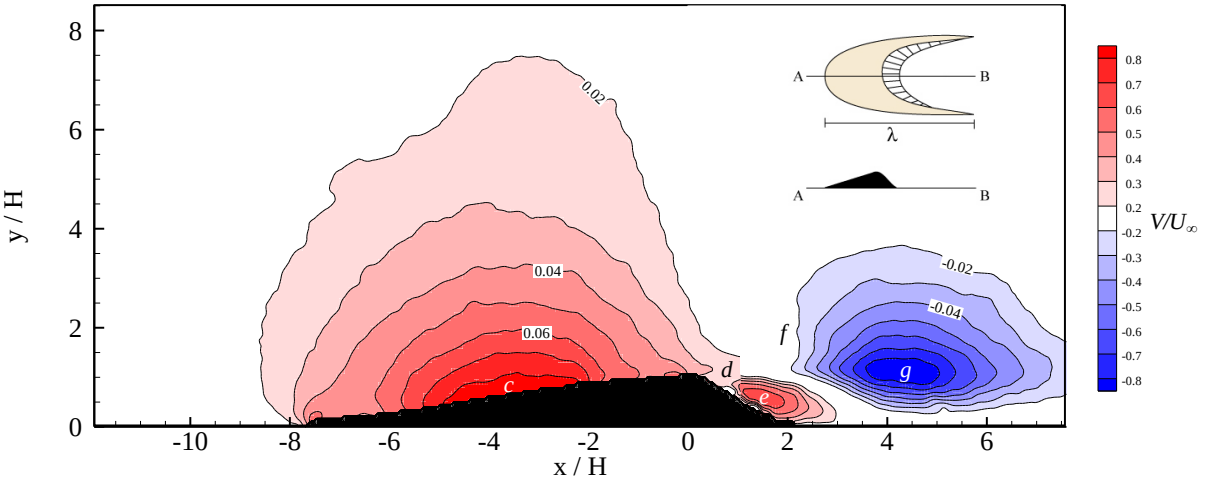

Figure 6.2: A contour plot of the ensemble-average of the wall-normal velocity, V/U_∞, component for the isolated barchan dune condition (*Re*=59,806). The black triangular object represents the dune profile. The upper right schematic featured in the plot depicts the experimental condition from a plan view and profile view. Red indicates upward flow, blue indicates downward flow and white indicates zero velocity. The contour values span from -0.08 to 0.1.

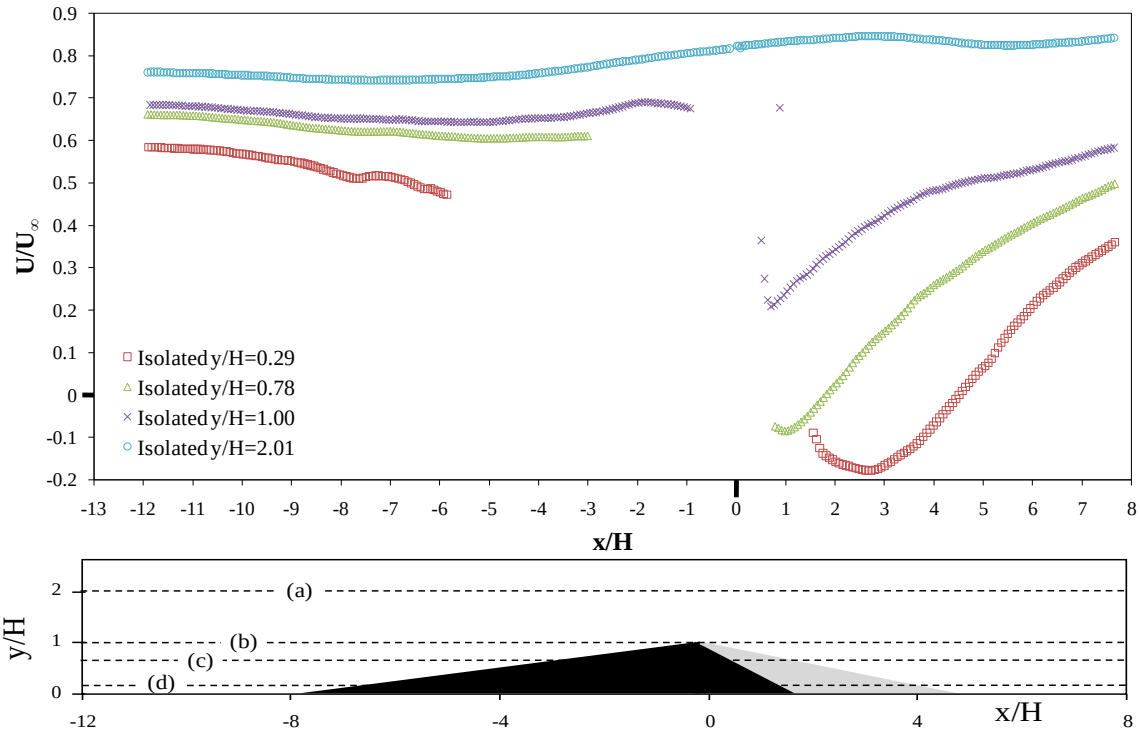

Figure 6.3: A horizontal profile of the streamwise, U/U_∞, velocity component at four vertical locations: (a) y/H=2.01; (b) y/H=1.00; (c) y/H=0.78; (d) y/H=0.29. The breaks in the profiles are due to the presence of the barchan.

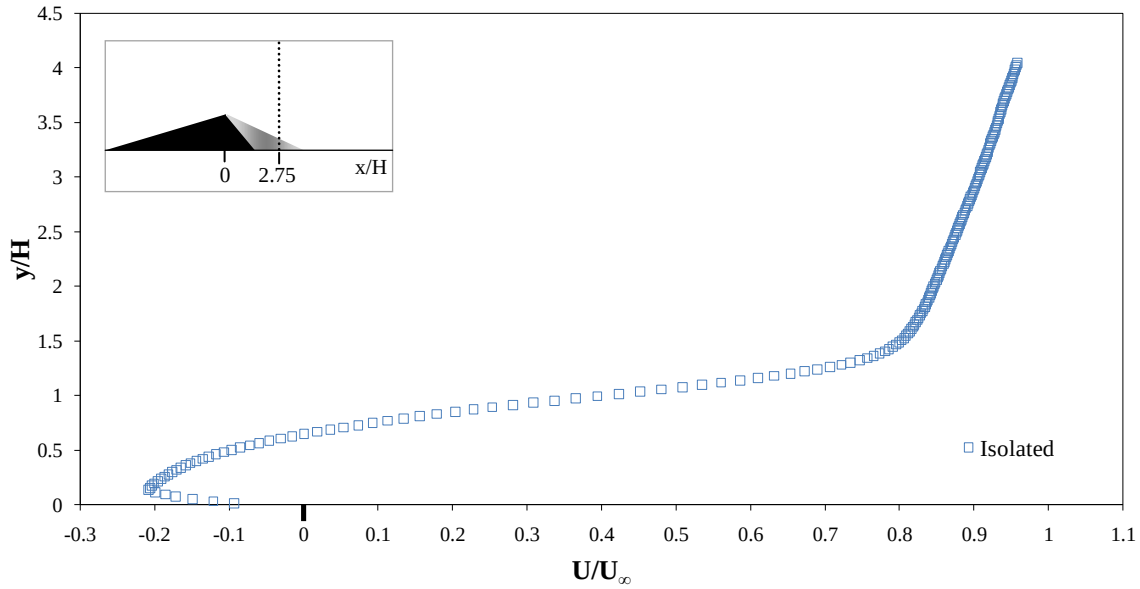

Figure 6.4: A vertical profile of the streamwise velocity component at x/H=2.75, where the maximum intensity of the reverse flow in the separation bubble is documented at -0.22 U/U_∞.

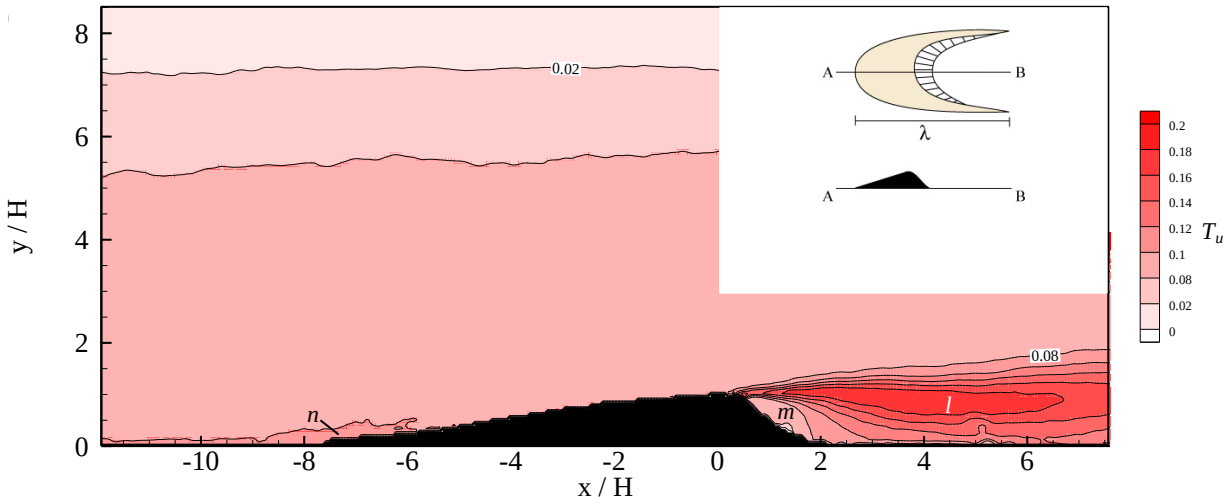

Figure 6.5: Contour map of the streamwise component of the turbulence intensity T_u, for the isolated dune. In the leeside, the area of high T_u is labeled '*l*' and the area of low T_u is labeled '*m*'. On the stoss-side, the area of elevated T_u at the DBD toe is labeled '*n*'.

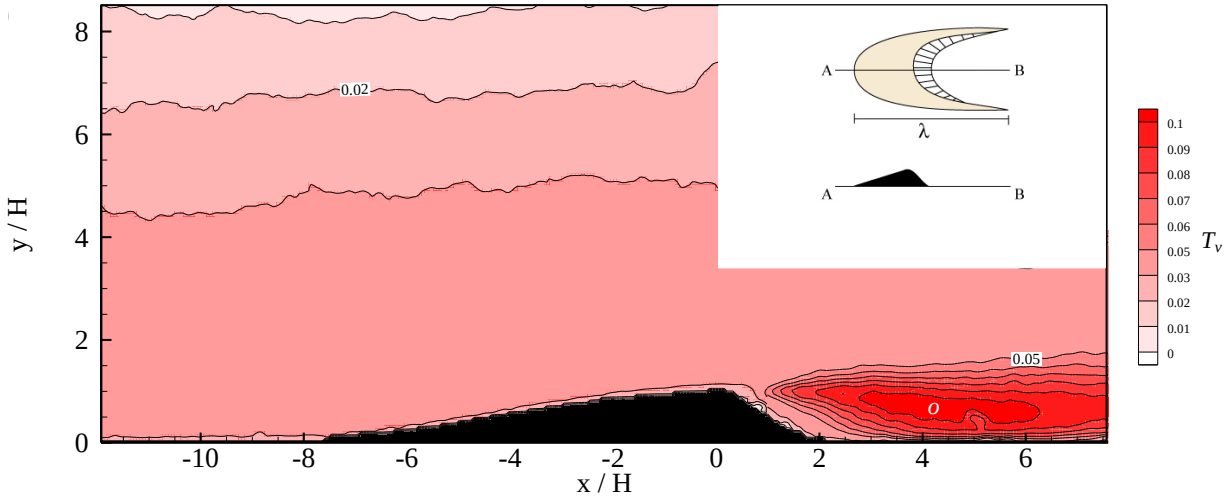

Figure 6.6: Contour map of the wall-normal component of the turbulence intensity T_v, for the isolated dune. Within the leeside, the area of high T_u is labeled '*o*'.

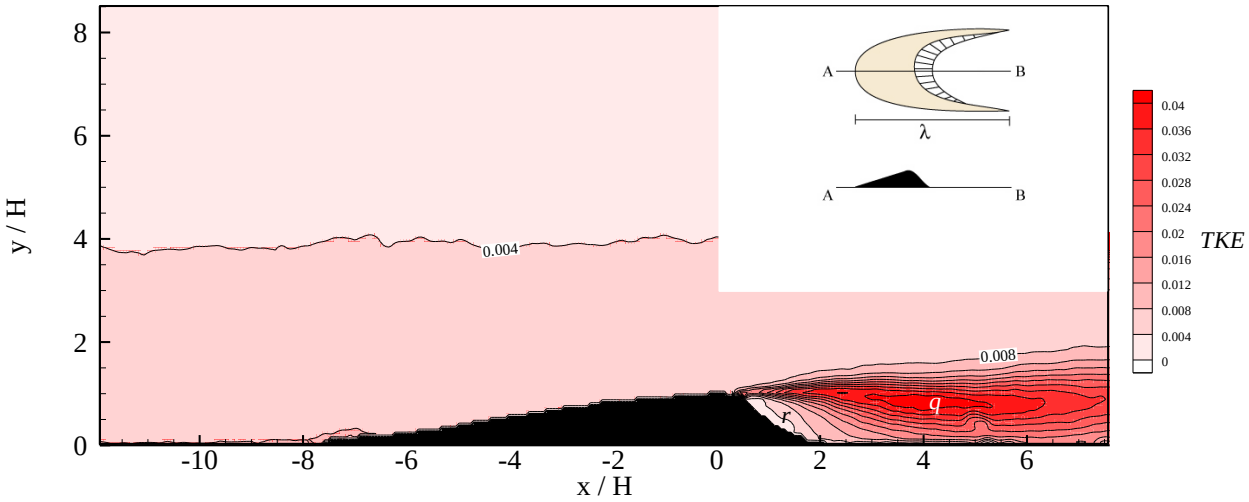

Figure 6.7: Contour map of the turbulent kinetic energy *TKE*, for the isolated dune. Within the leeside, the area of high T_u is labeled '*q'* and the area of low T_u is labeled '*r'*.

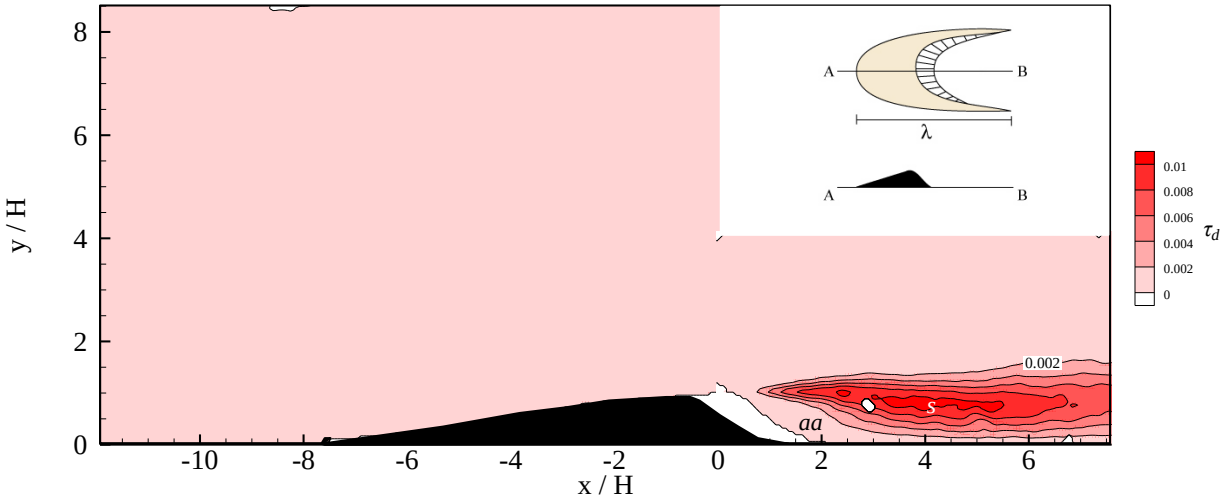

Figure 6.8: Contour map of the Reynolds Stress τ_d, for the isolated dune. Within the leeside, the area of high T_u is labeled '*s'* and the area of low T_u is labeled '*aa'*.

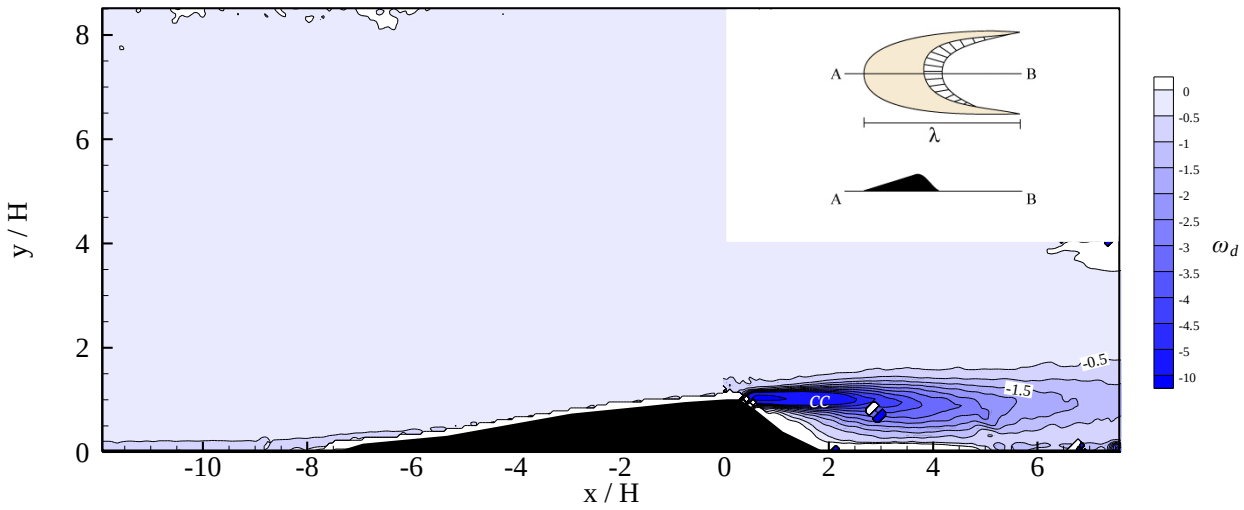

Figure 6.9: Contour map of the vorticity ω_d, for the isolated dune. Within the leeside, the area of high T_u is labeled '*cc*'.

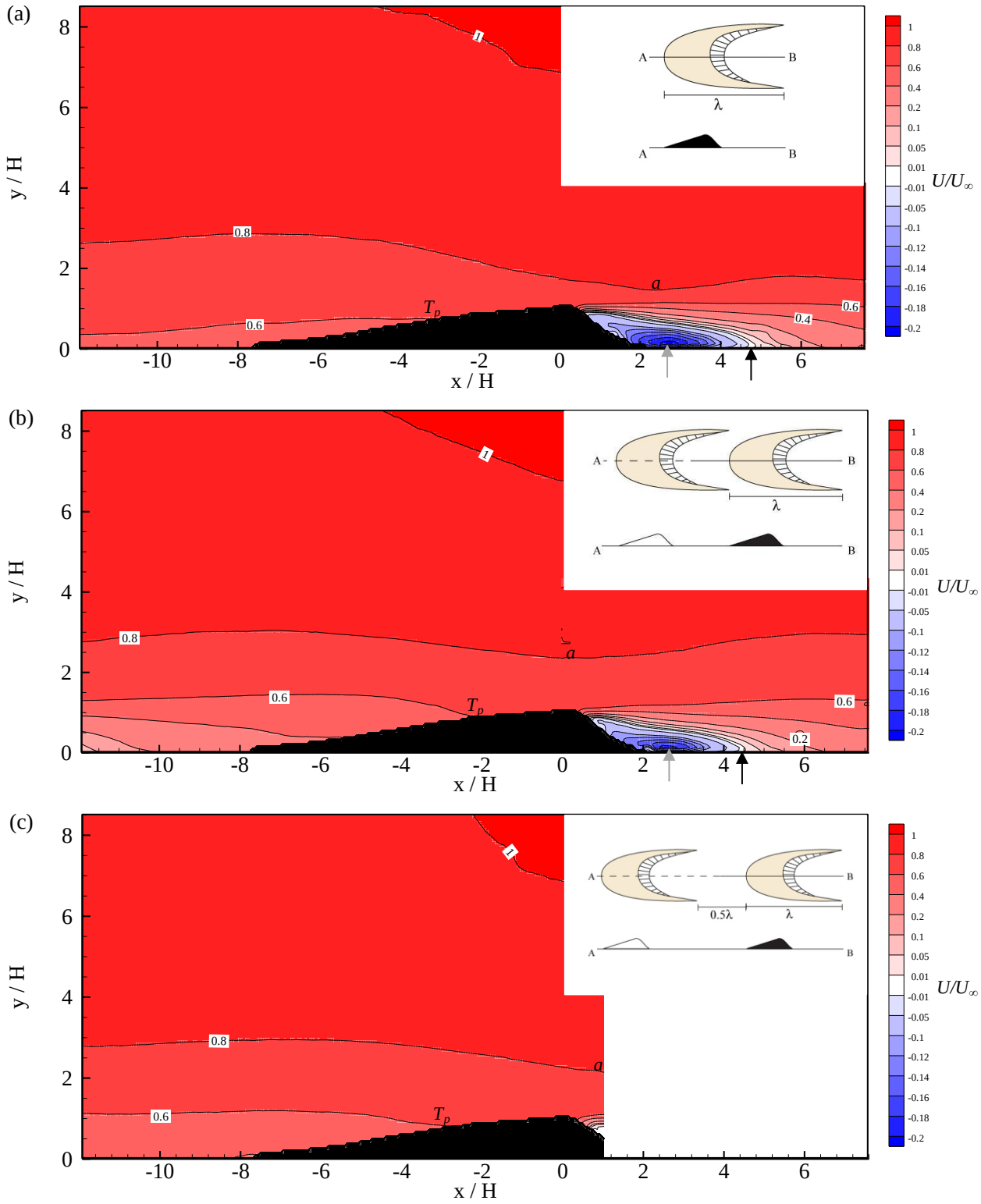

Figure 6.10 (continued on next page)

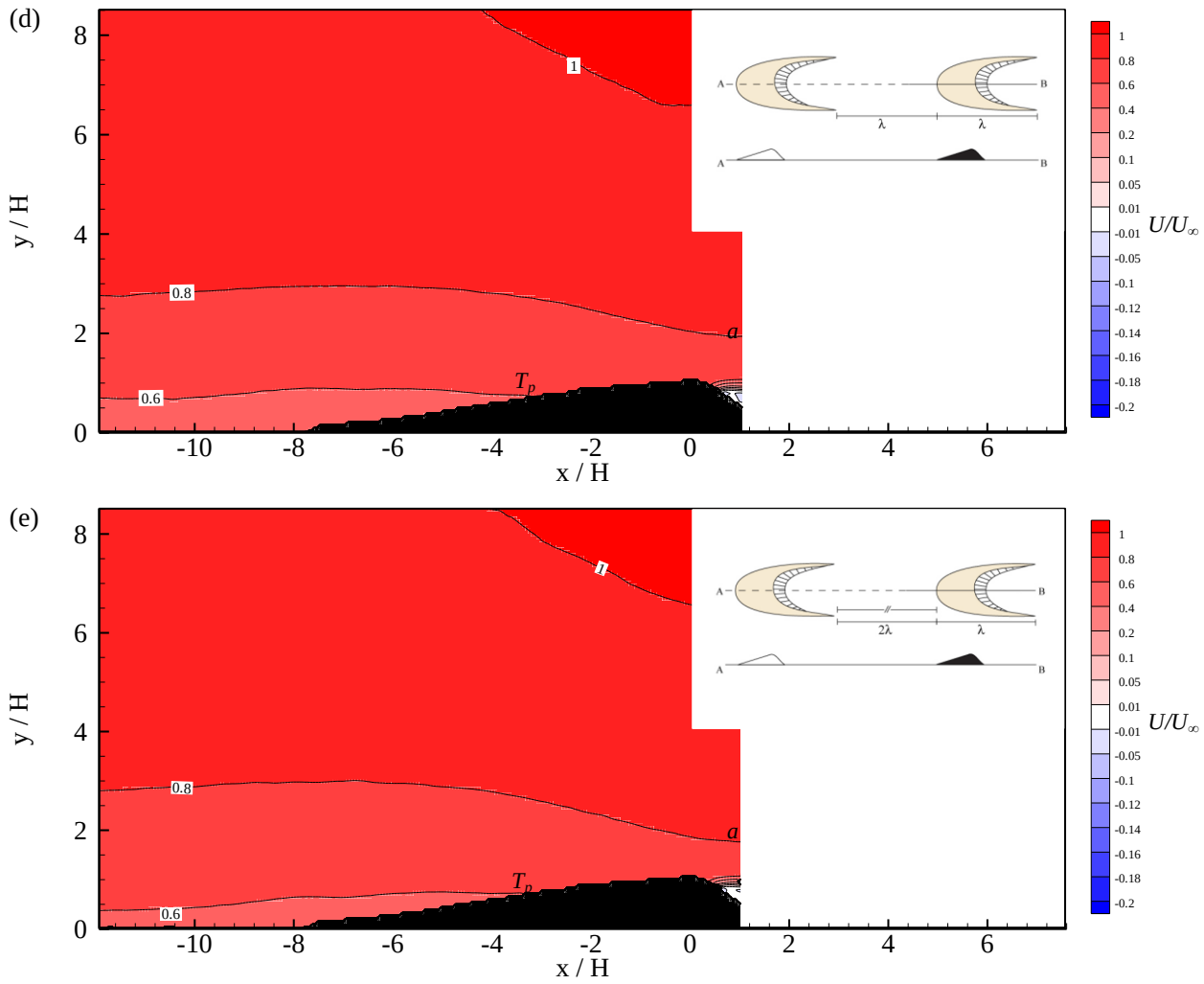

Figure 6.10: The U/U_∞ velocity field of the AA volumetric ratio: (a) Isolated condition (*Re*=59,806); (b) 0λ condition (*Re*=59,928); (c) 0.5λ condition (*Re*=58,378); (d) 1λ condition (*Re*=58,540); (e) 2λ condition (*Re*=59,064). The black triangular object represents the dune profile. The upper right schematic featured in the plot depicts the experimental condition from a plan view and profile view. The contour plot refers to the ensemble-average of the streamwise velocity component: red indicates downstream flow direction, blue upstream downward flow motion, and white indicates zero velocity. The contour values span from -0.2 to 1. The gray arrow indicates the maximum upstream velocity in the separation bubble. The black arrow indicates the flow reattachment point. The maximum velocity region is labeled '*a'*. The 0.6 contour line termination point is labeled 'T_p'.

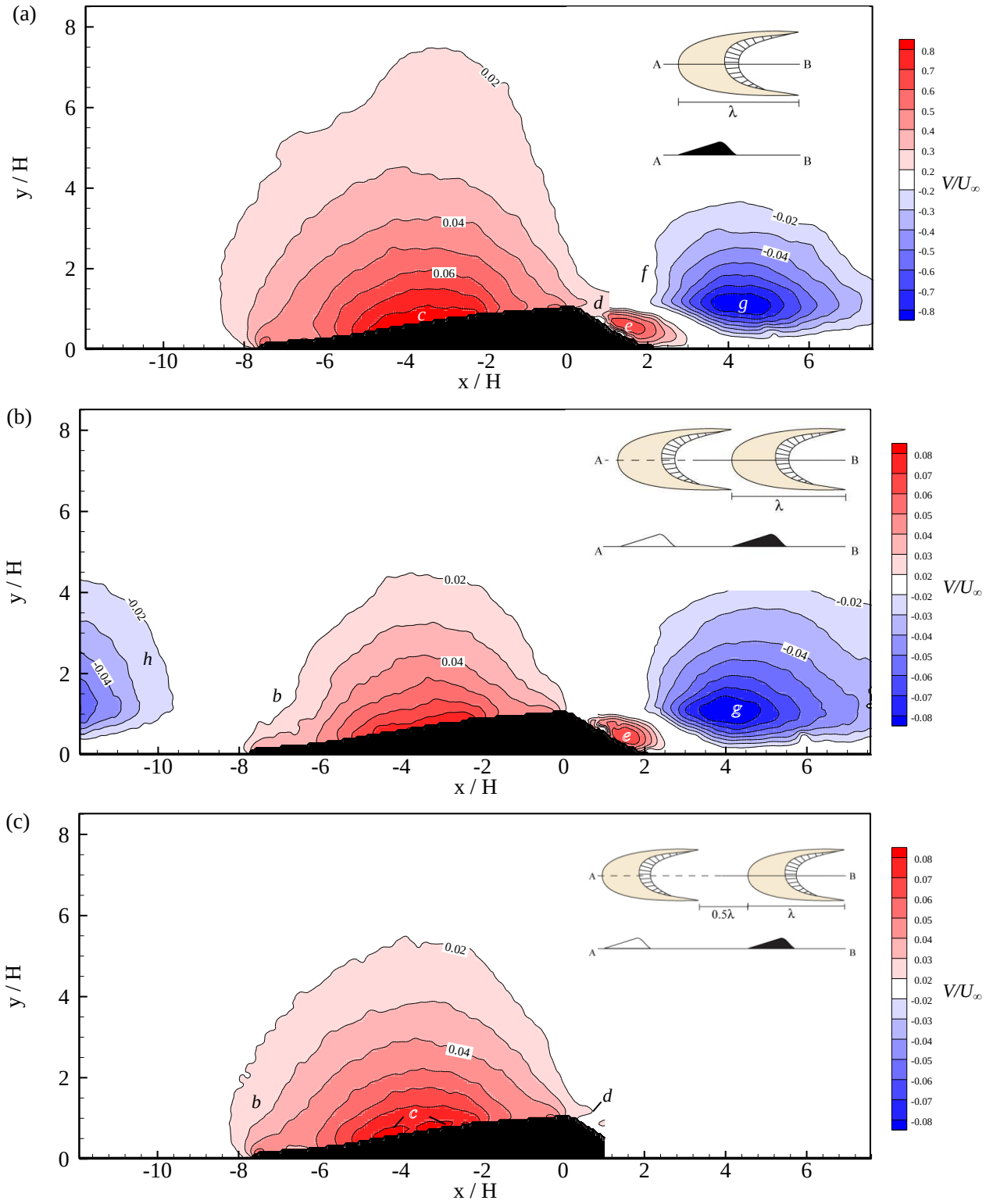

Figure 6.11 (continued on next page)

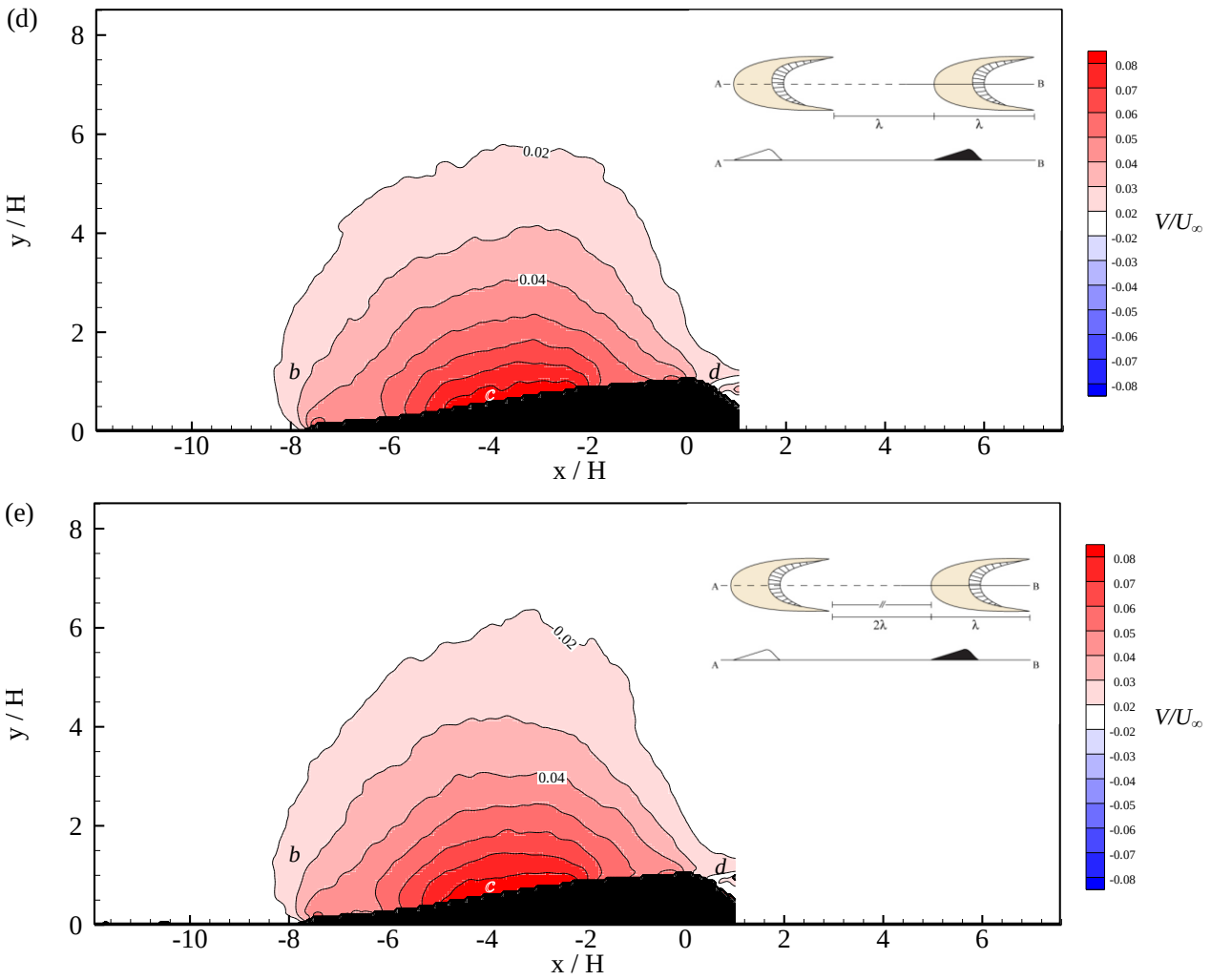

Figure 6.11: The V/U_∞ velocity field of the AA volumetric ratio: (a) Isolated condition (*Re*=59,806); (b) 0λ condition (*Re*=59,928); (c) 0.5λ condition (*Re*=58,378); (d) 1λ condition (*Re*=58,540); (e) 2λ condition (*Re*=59,064). The black triangular object represents the dune profile. The upper right schematic featured in the plot depicts the experimental condition from a plan view and profile view. The contour plot refers to the ensemble-average of the wall-normal velocity component: red indicates upward flow direction, blue indicates downward flow direction and white indicates zero velocity. The contour values span from -0.2 to 1. The flow features referred to in the text are identified with labels *b-j*: *b* – contour inflection; *c* – maximum velocity zone; *d* – crestal jet; *e* – upwelling zone; *f* – contour inflection; *g* – expansion zone; *h* – UBD expansion zone; *i* – UBD upwelling zone; *j* – UBD topographic forcing zone.

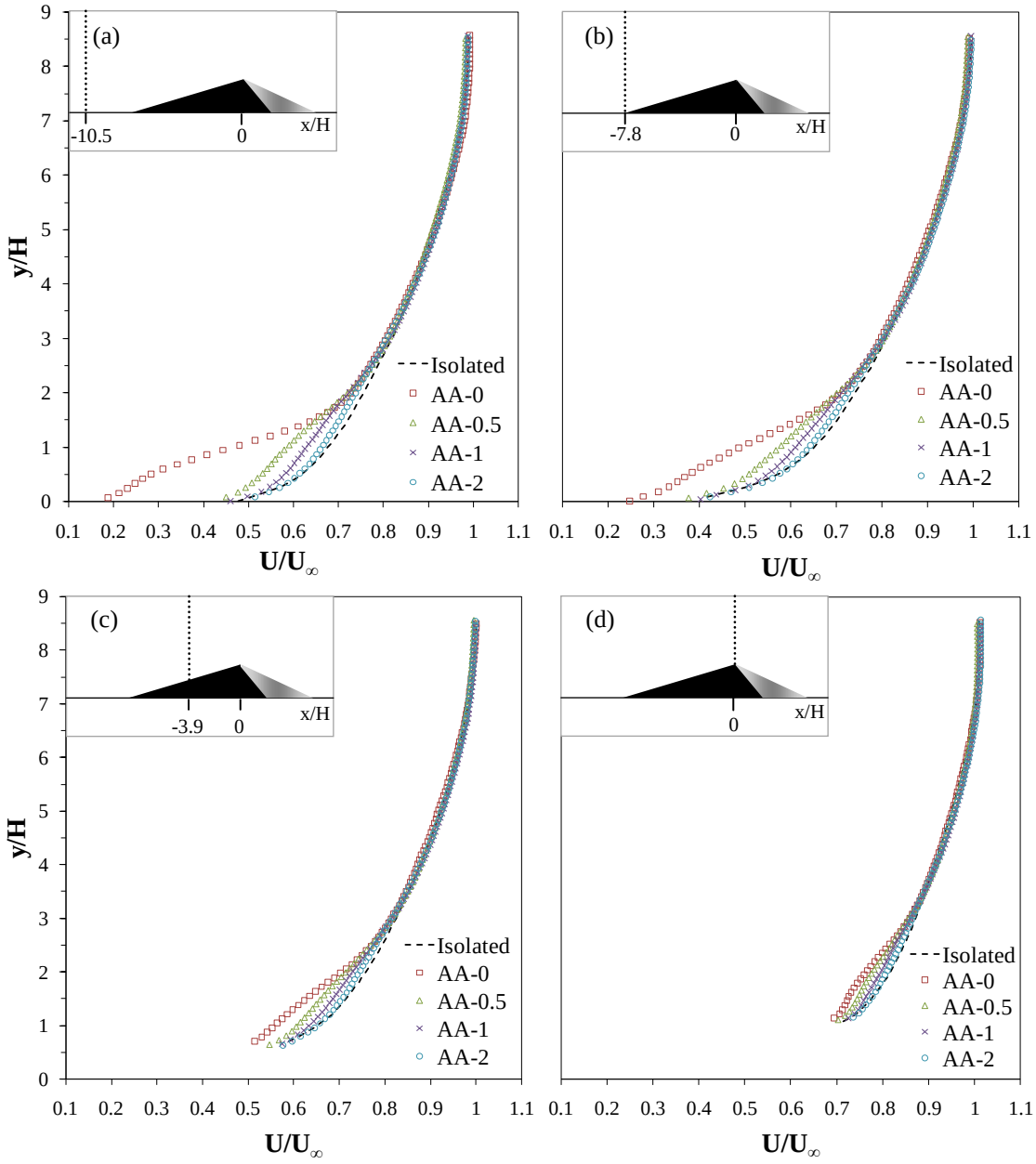

Figure 6.12: Vertical profiles of the streamwise velocity component, U/U_∞, on the stoss-side of the DBD: (a) x/H=-10.5; (b) x/H=-7.8; (c) x/H=-3.9; (d) x/H=0.

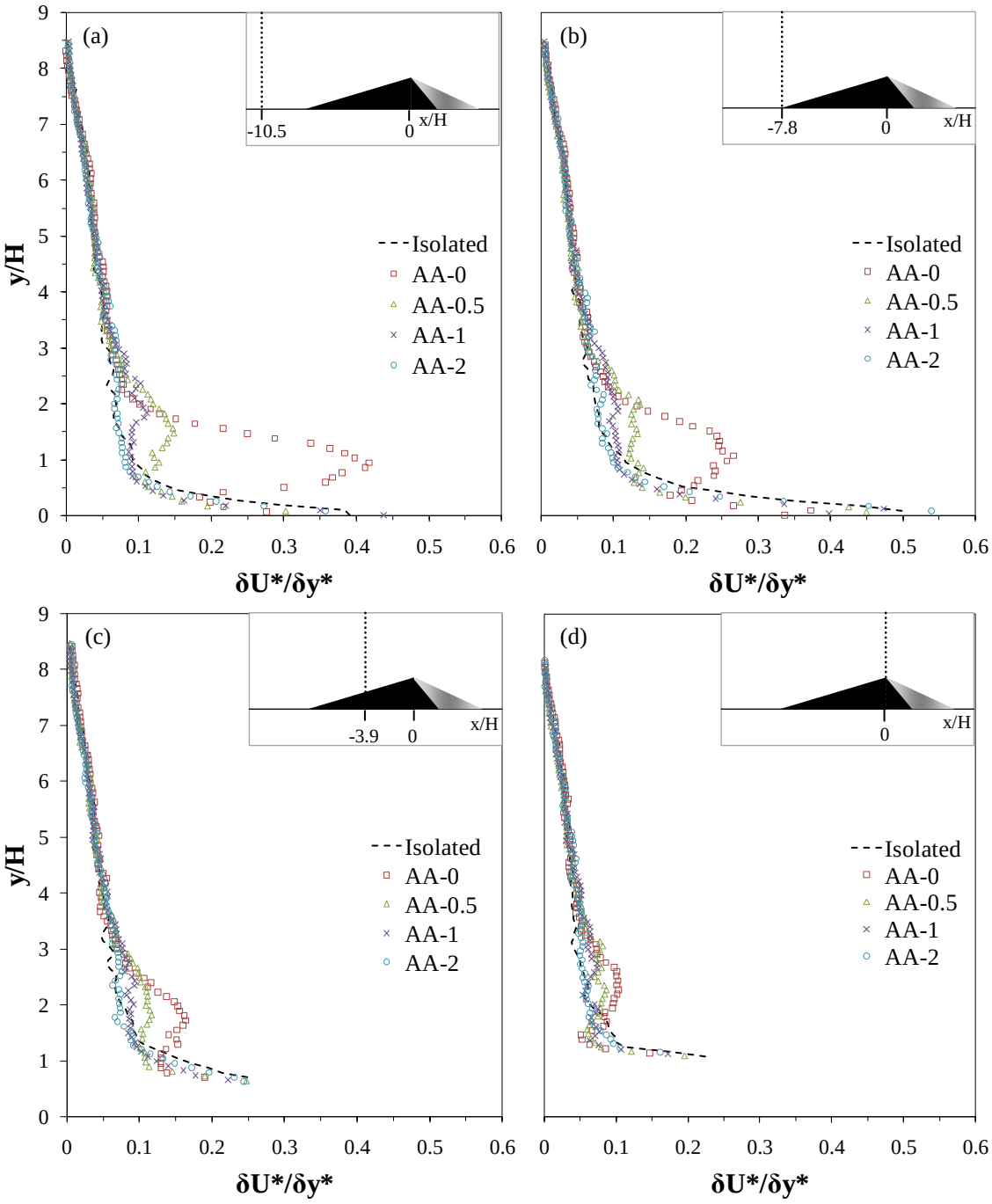

Figure 6.13: Vertical profiles of the streamwise velocity gradient, $\delta U^*/\delta y^*$, on the stoss-side of the DBD: (a) x/H=-10.5; (b) x/H=-7.8; (c) x/H=-3.9; (d) x/H=0.

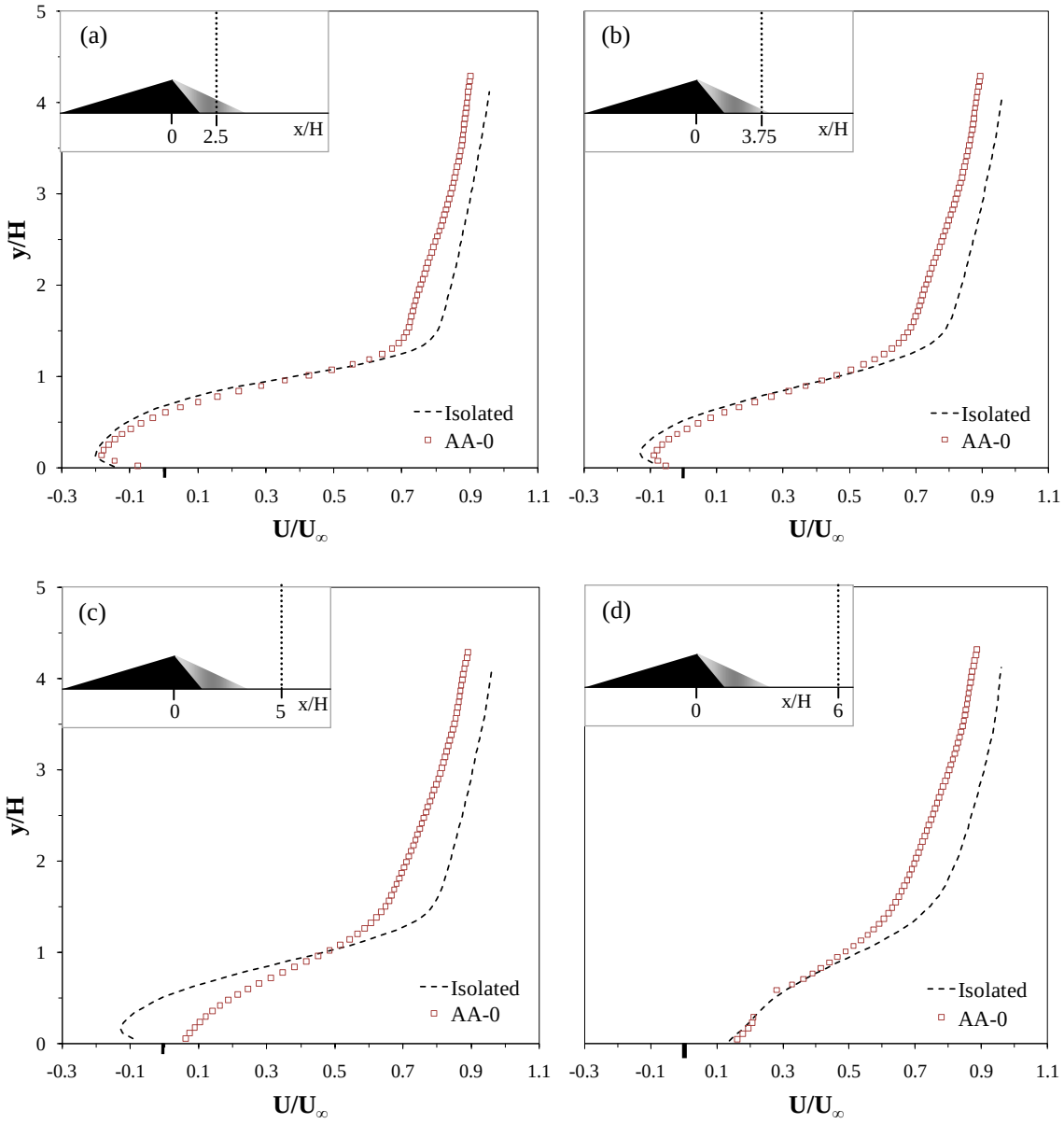

Figure 6.14: Vertical profiles of the streamwise velocity component, U/U_∞, on the lee-side of the DBD: (a) x/H=2.5; (b) x/H=3.75; (c) x/H=5; (d) x/H=6.

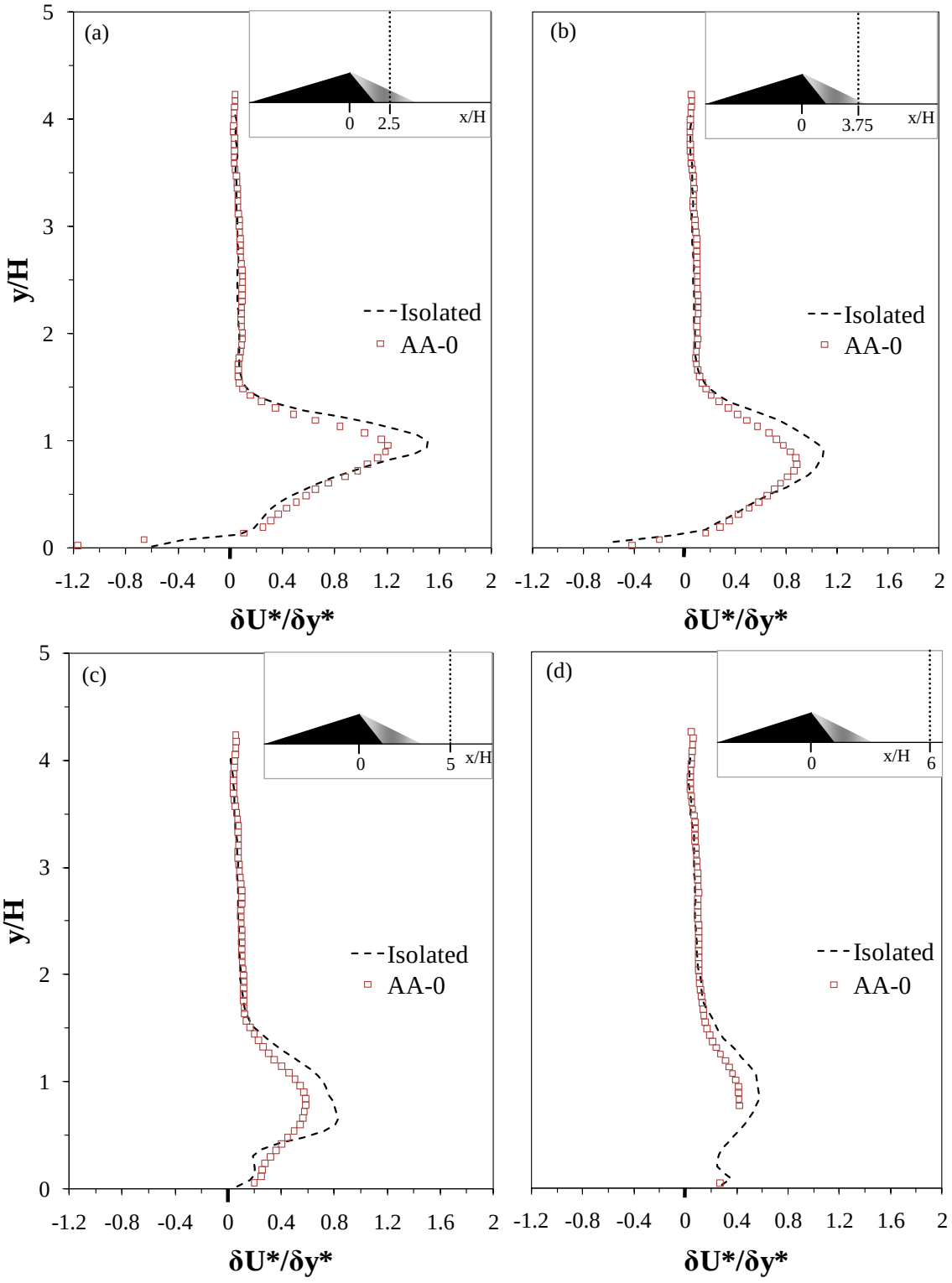

Figure 6.15: Vertical profiles of the streamwise velocity gradient, $\delta U^*/\delta y^*$, on the lee-side of the DBD: (a) (a) x/H=2.5; (b) x/H=3.75; (c) x/H=5; (d) x/H=6.

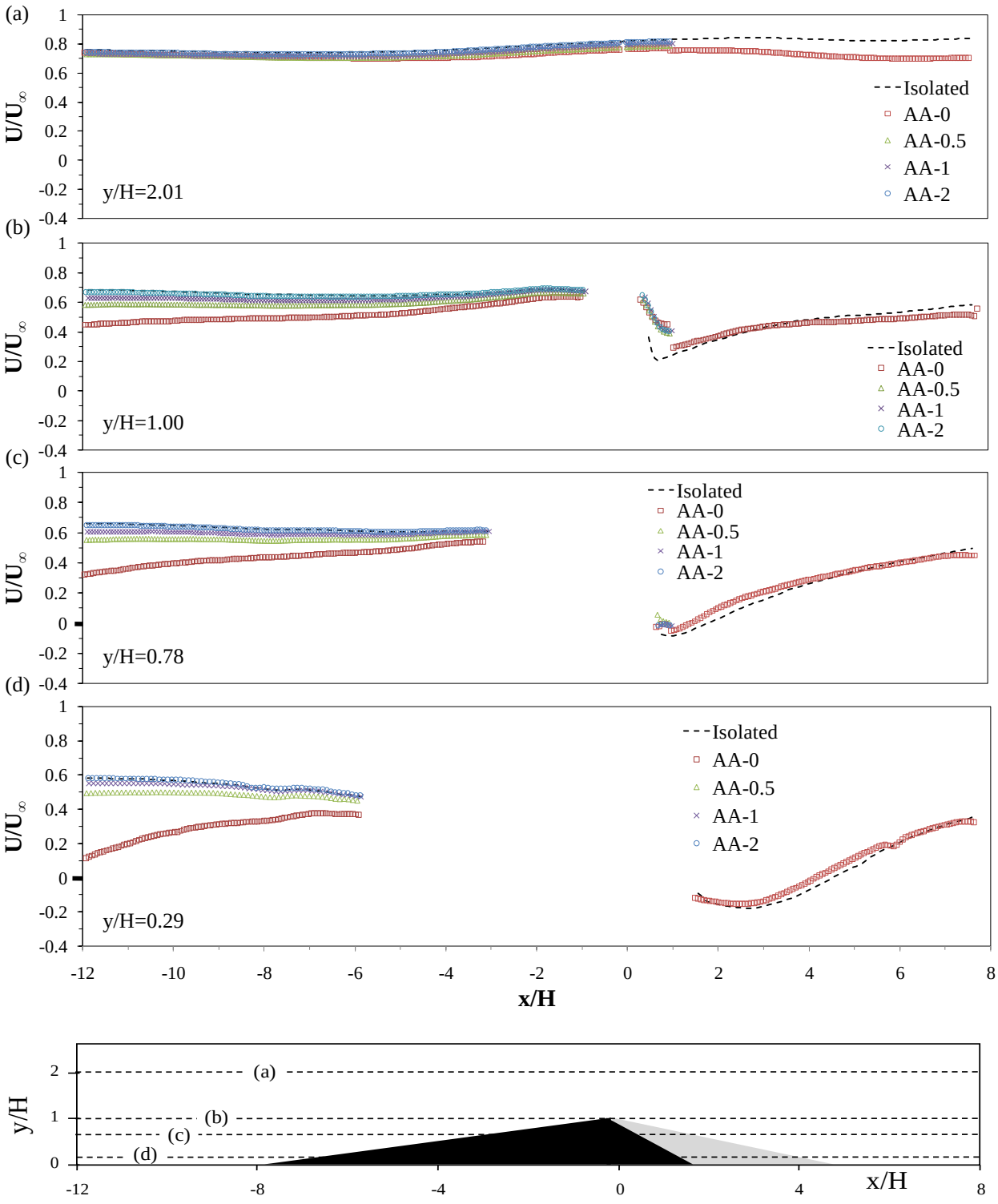

Figure 6.16: Horizontal profile of the streamwise velocity component, U/U_∞: (a) y/H=2.01.; (b) y/H=1.00; (c) y/H=0.78; (d) y/H=0.29.

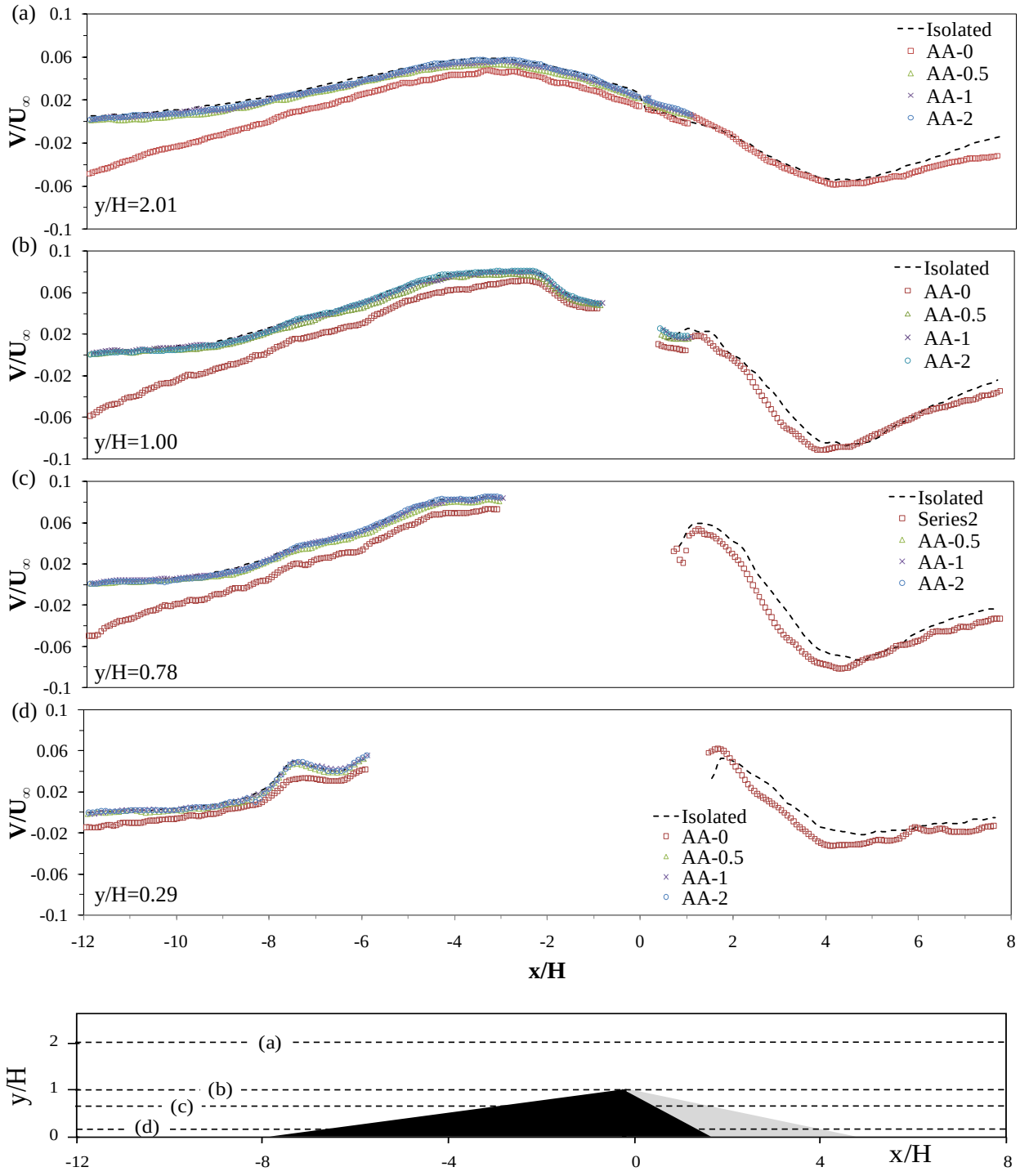

Figure 6.17: Horizontal profile of the wall-normal velocity component, V/U_∞: (a) y/H=2.01.; (b) y/H=1.00; (c) y/H=0.78; (d) y/H=0.29.

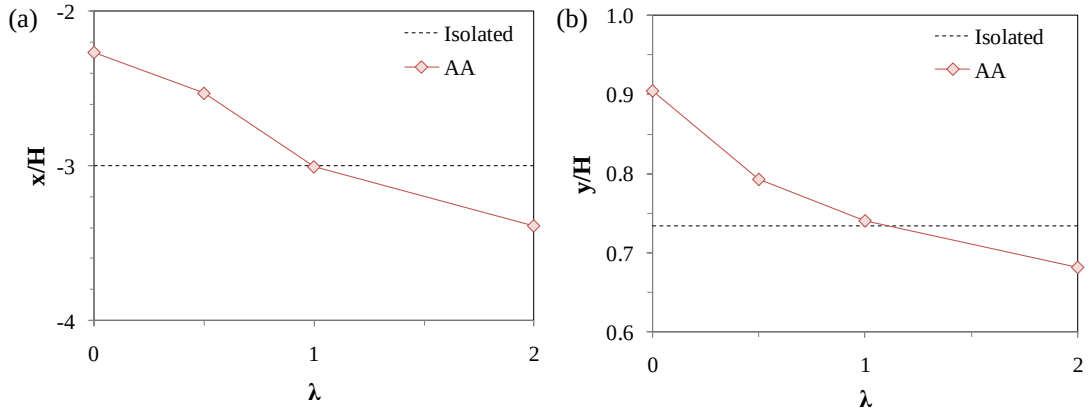

Figure 6.18: The location of the 0.6 U/U_∞ contour line termination point T_p, along the stoss-slope of the DBD with increasing λ: (a) the horizontal position (x/H); (b) the vertical position (y/H).

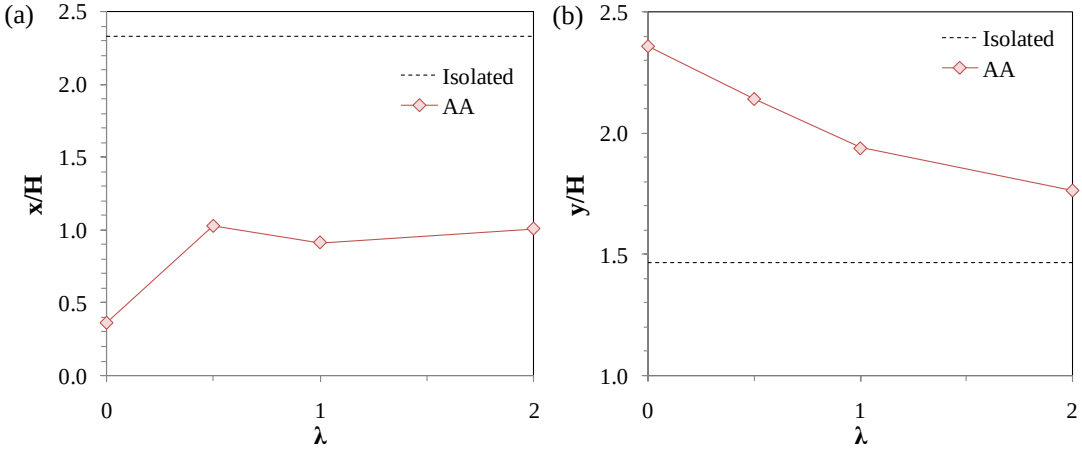

Figure 6.19: The location of the 0.8 contour line minima in the streamwise velocity U/U_∞ component contour map: (a) the horizontal position x/H; (b) the vertical position y/H.

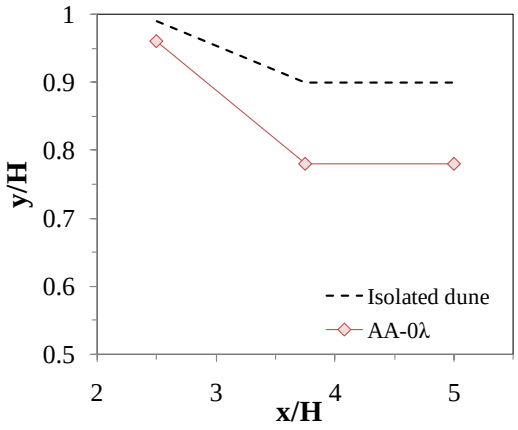

Figure 6.20: The vertical position of the peak of the vertical gradient of the streamwise velocity component (vertical profiles collected at x/H=2.5, 3.75, 5 and 6) for the isolated dune and 0λ spacing on the lee-side of the DBD.

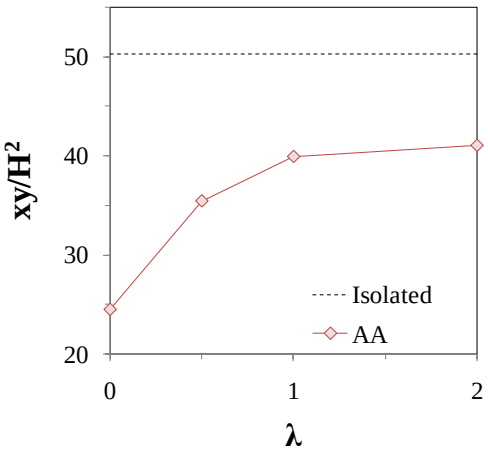

Figure 6.21: The area of the topographic forcing zone with increasing λ. The area is defined as xy/H^2.

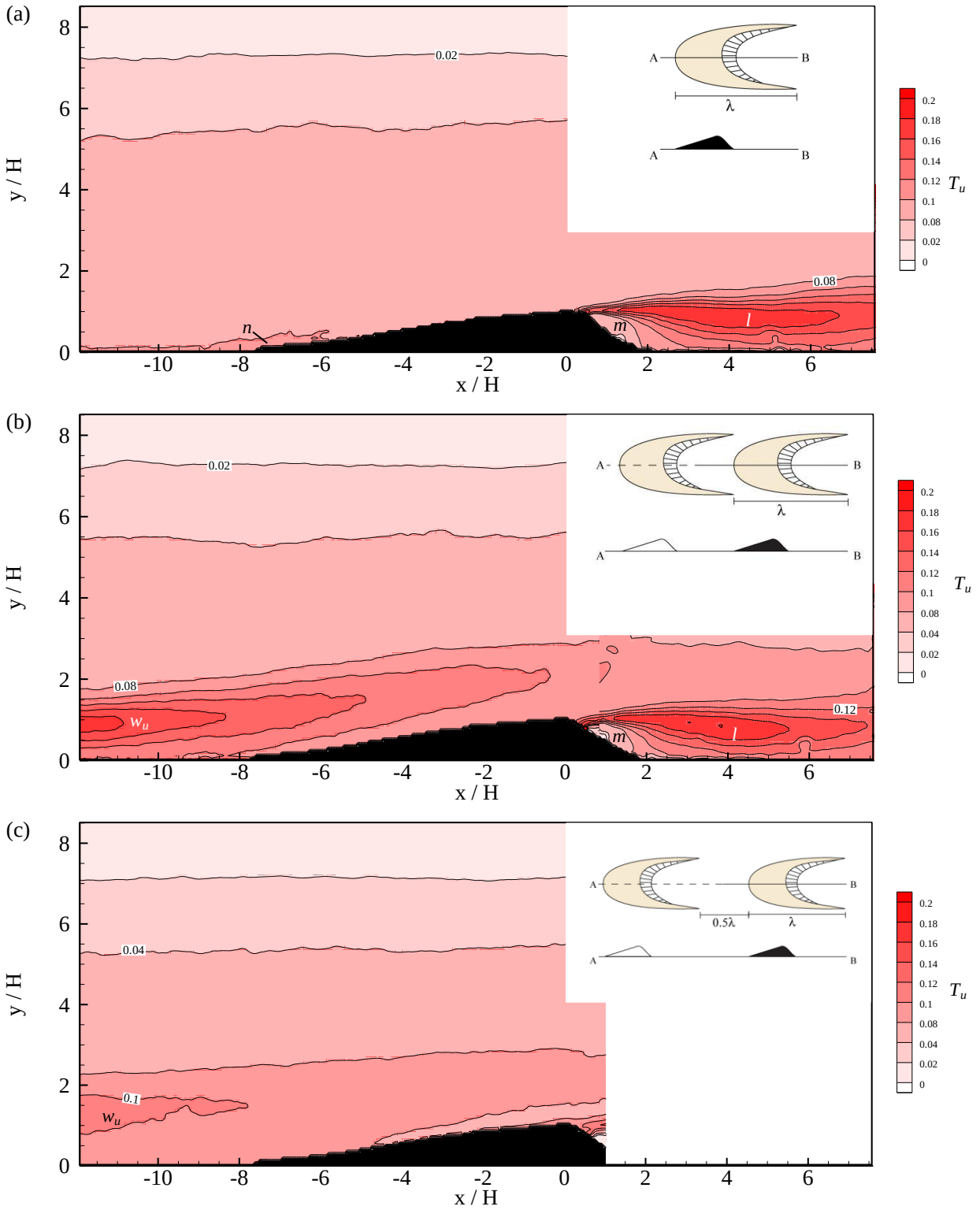

Figure 6.22 (continued on next page)

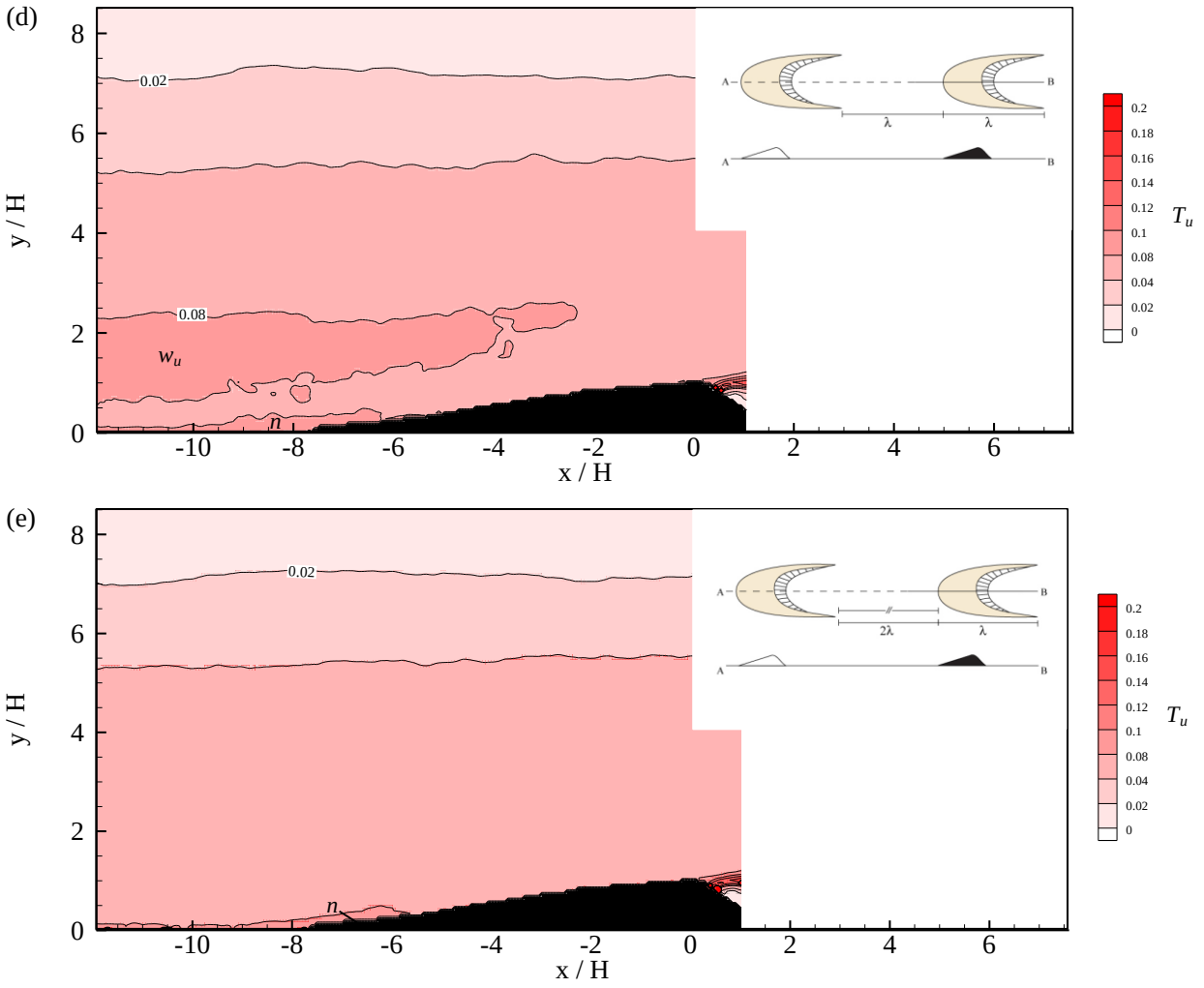

Figure 6.22: Contour maps of the streamwise component of the turbulence intensity T_u ($\sqrt{u'^2}/U_\infty$) for the volumetric ratio AA: (a) isolated dune condition; (b) 0λ spacing; (c) 0.5λ spacing; (d) 1λ spacing; (e) 2λ spacing. On the stoss-side, the area of high T_u extending from the UBD is labeled 'w_u' while the high T_u at the DBD toe is labeled 'n'. On the leeside, the area of high T_u is labeled 'l' while the area of low T_u is labeled 'm'.

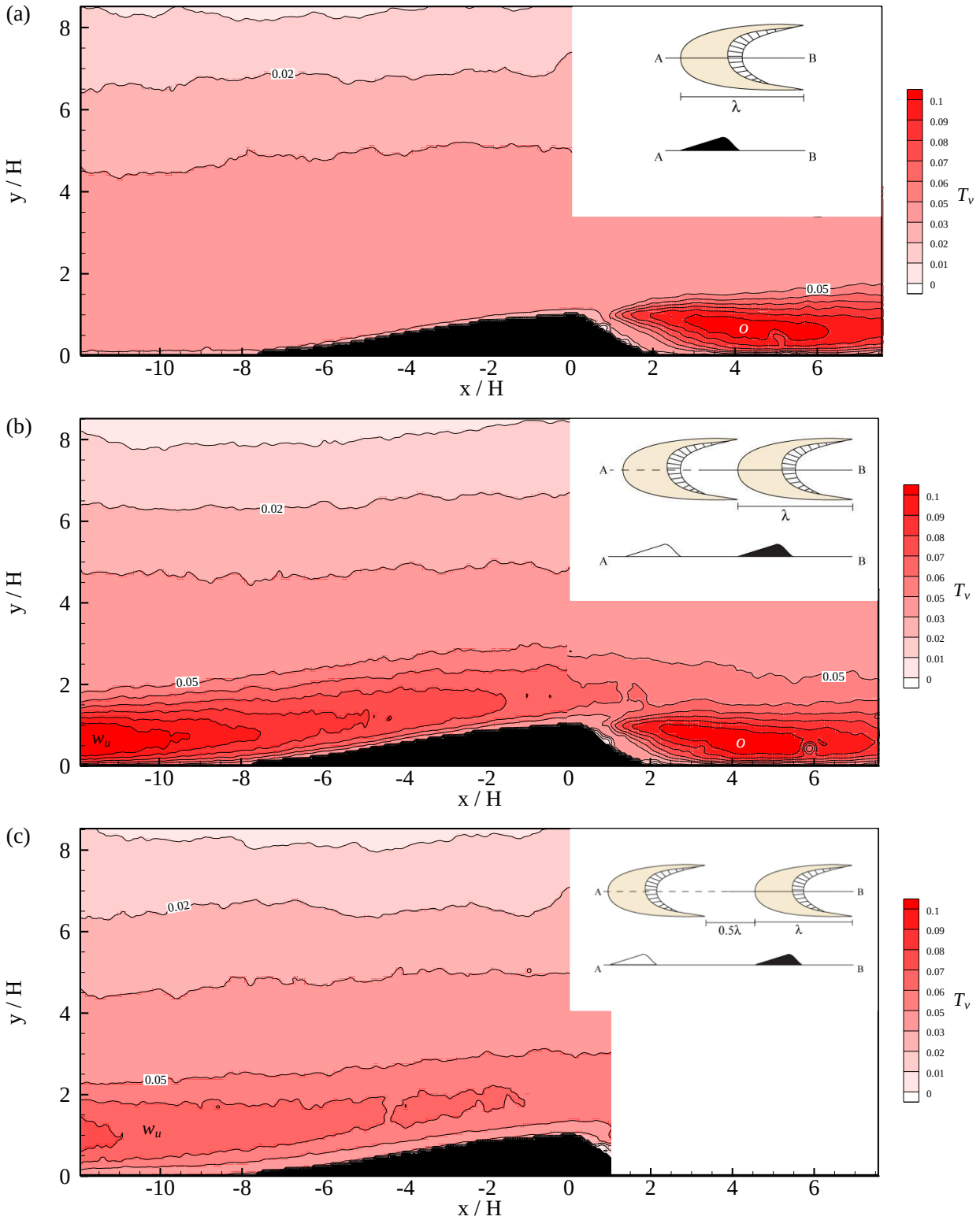

Figure 6.23 (continued on next page)

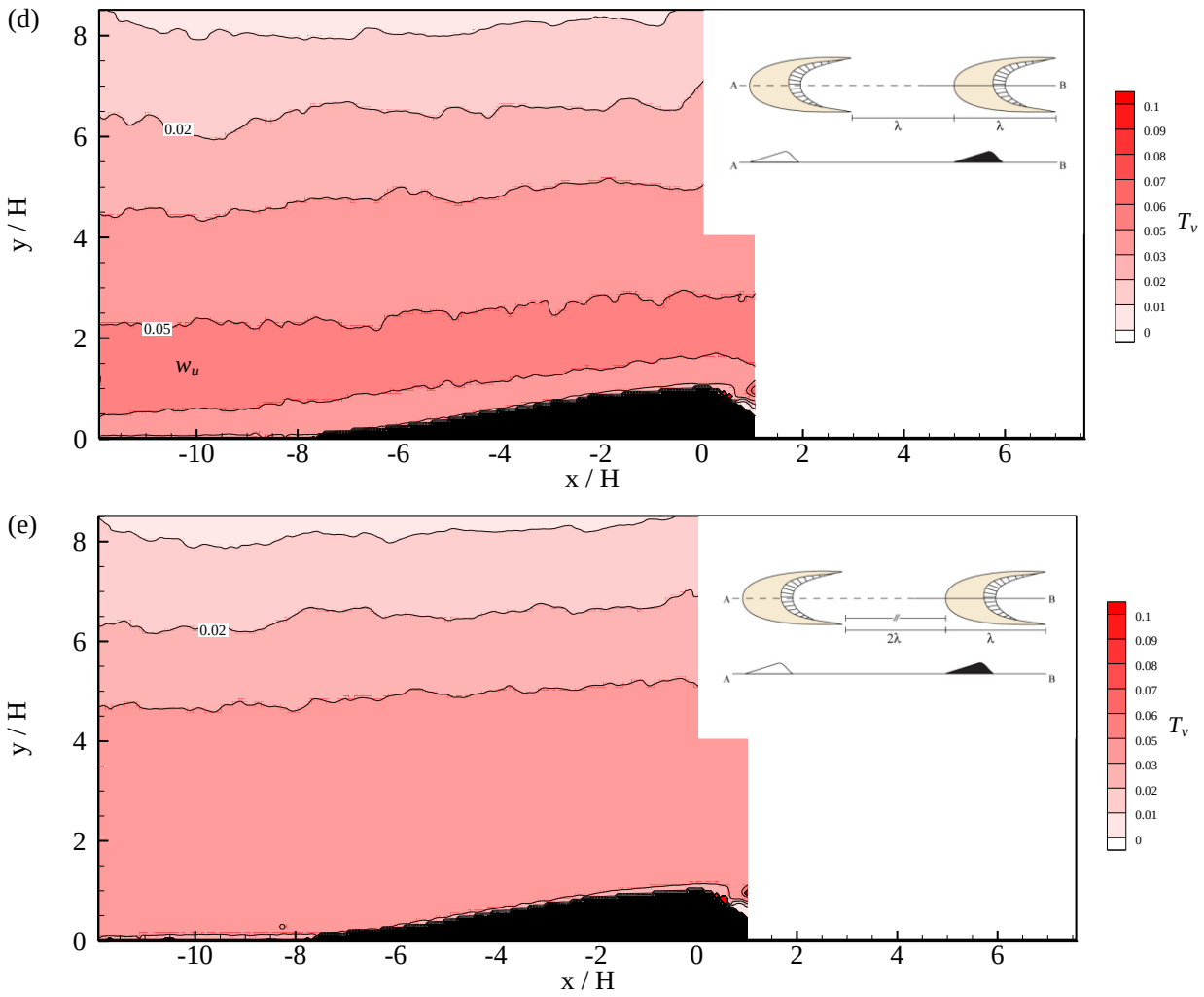

Figure 6.23: Contour maps of the wall-normal component of the turbulence intensity ($\sqrt{v'^2}/U_\infty$) for the volumetric ratio AA: (a) isolated dune condition; (b) 0λ spacing; (c) 0.5λ spacing; (d) 1λ spacing; (e) 2λ spacing. On the stoss-side, the area of high T_v extending from the UBD is labeled 'w_v'. On the leeside, the area of high T_v is labeled 'o'.

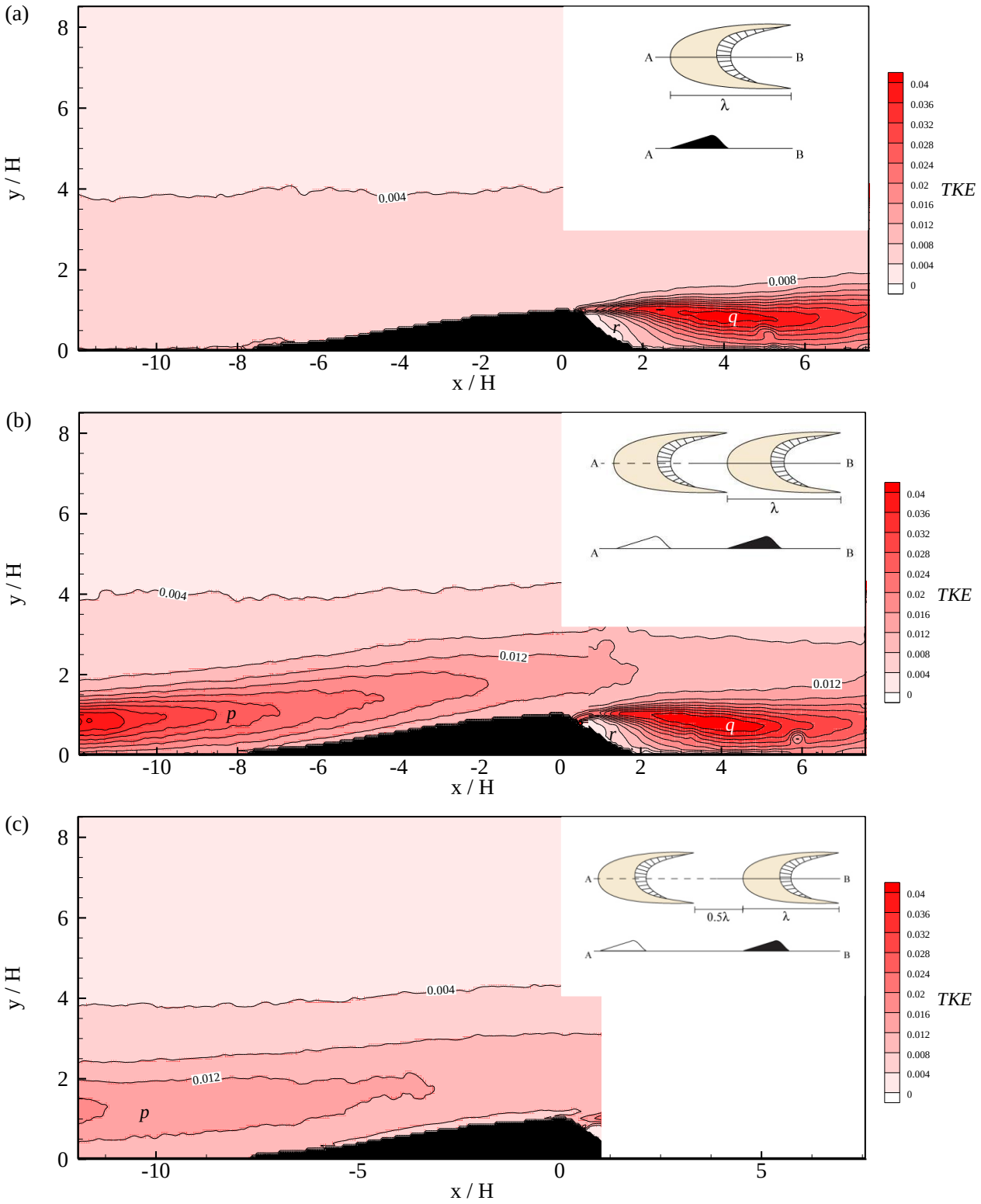

Figure 6.24 (continued on next page)

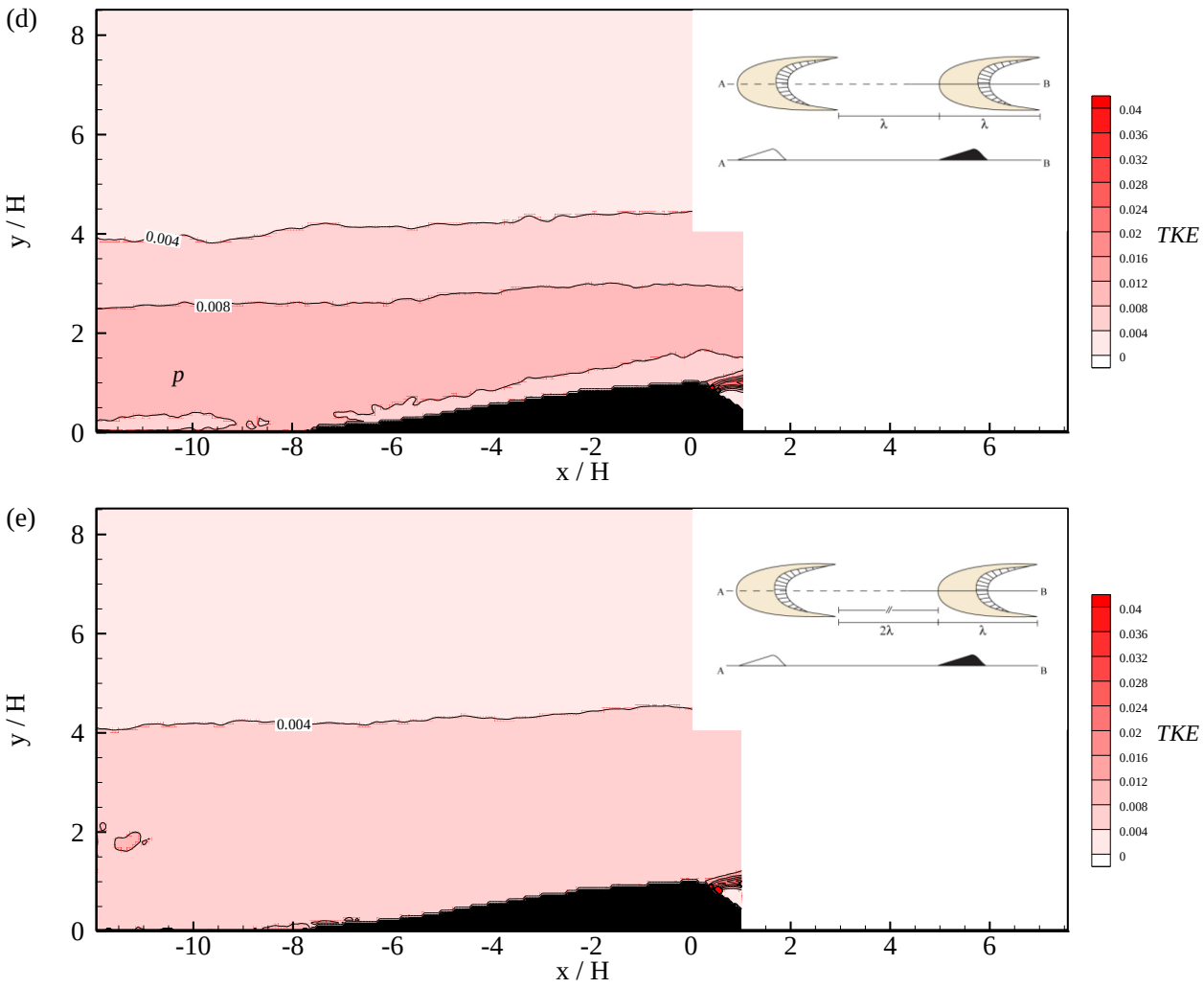

Figure 6.24: Contour maps of the mean turbulent kinetic energy *TKE* ($u'^2 + v'^2/U_\infty^2$) for the volumetric ratio AA: (a) isolated dune condition; (b) 0λ spacing; (c) 0.5λ spacing; (d) 1λ spacing; (e) 2λ spacing. On the stoss-side, the area of high *TKE* extending from the UBD is labeled '*p*'. On the leeside, the area of high *TKE* is labeled '*q*' and the area of low T_u is labeled '*r*'.

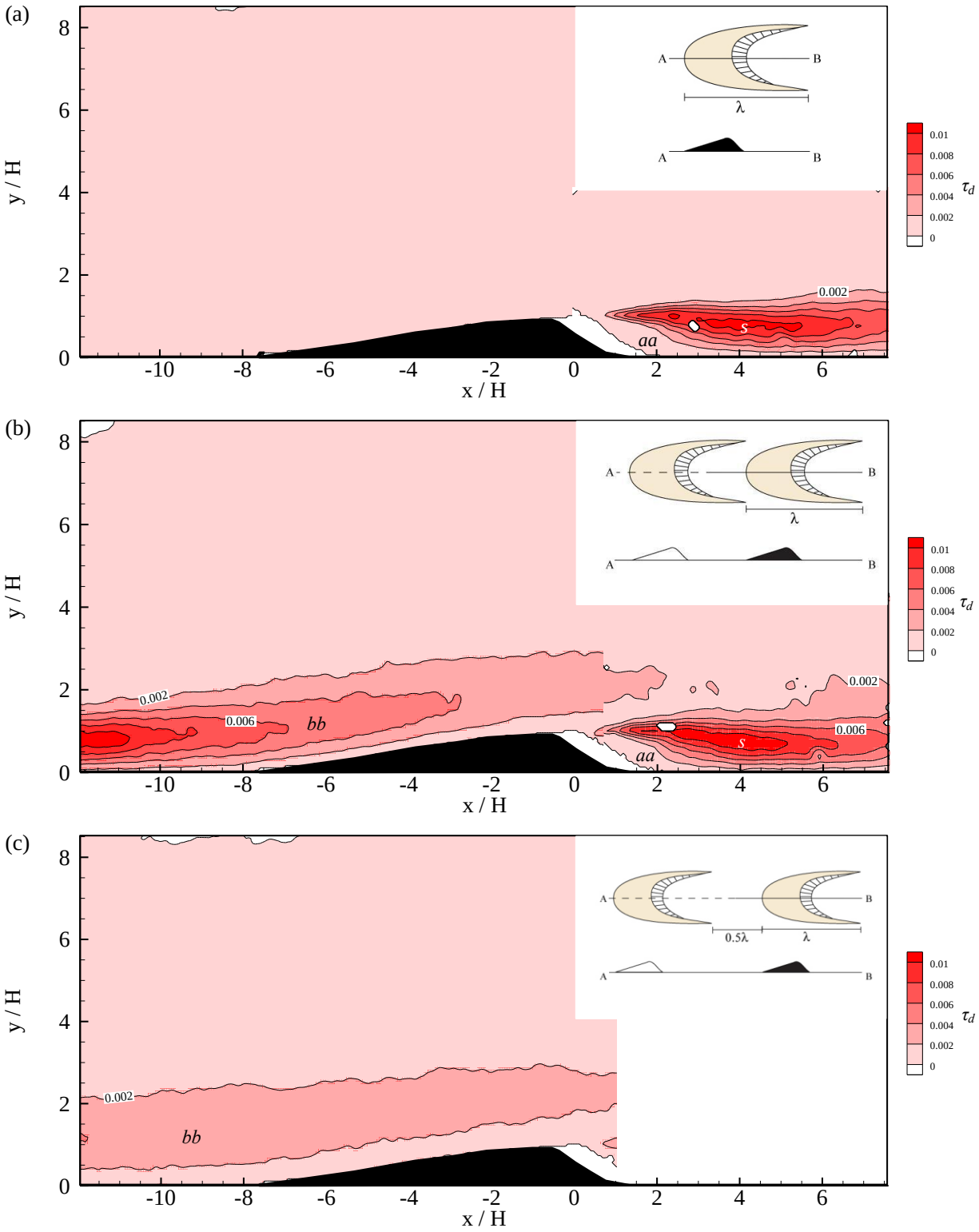

Figure 6.25 (continued on next page)

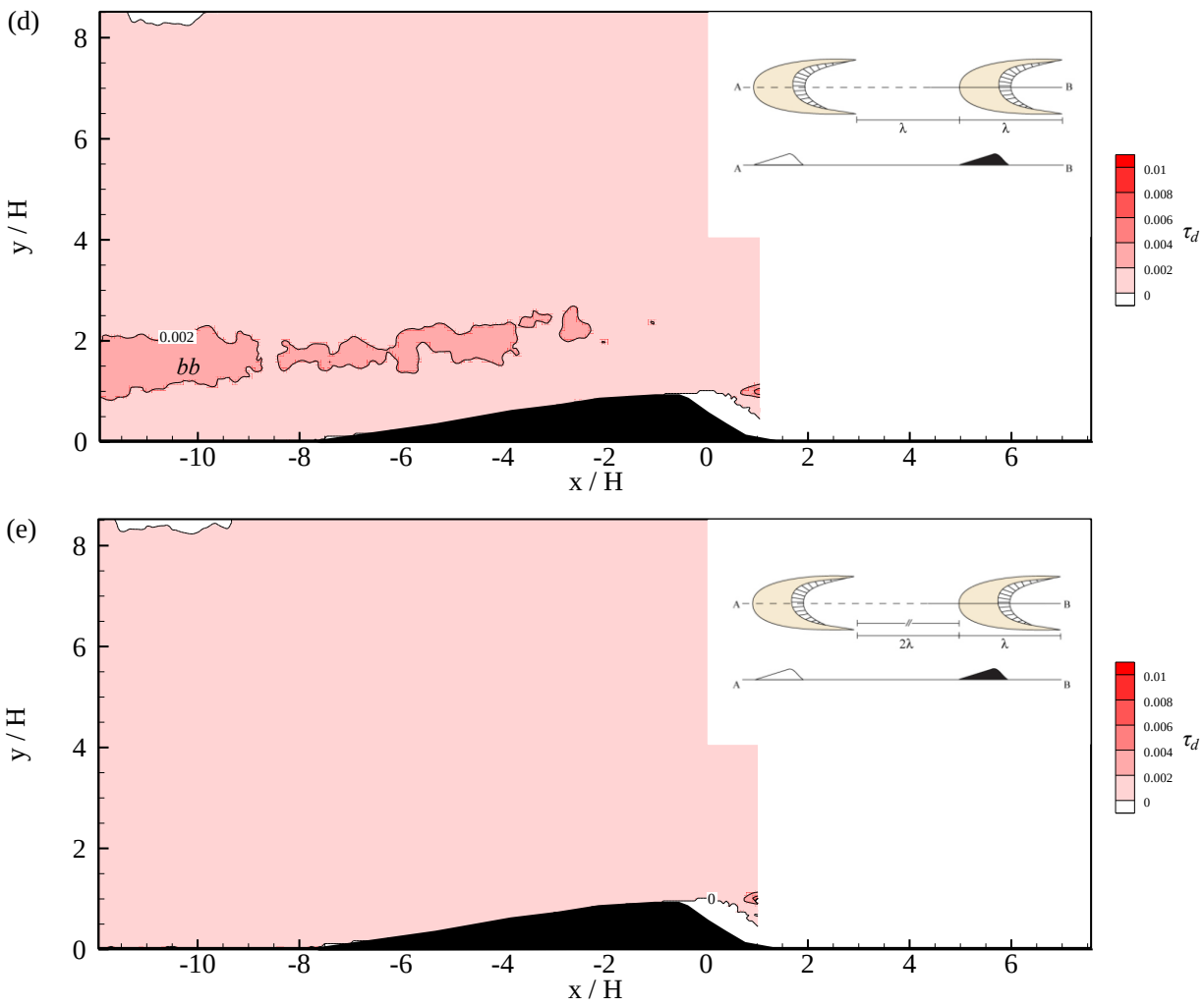

Figure 6.25: Contour maps of the Reynolds stress τ_d ($-u'v'/U_\infty^2$) for the volumetric ratio AA: (a) isolated dune condition; (b) 0λ spacing; (c) 0.5λ spacing; (d) 1λ spacing; (e) 2λ spacing. On the stoss-side, the area of high τ_d extending from the UBD is labeled '*bb'*. On the leeside, the area of high τ_d is labeled '*s'* and the area of low τ_d is labeled '*aa'*.

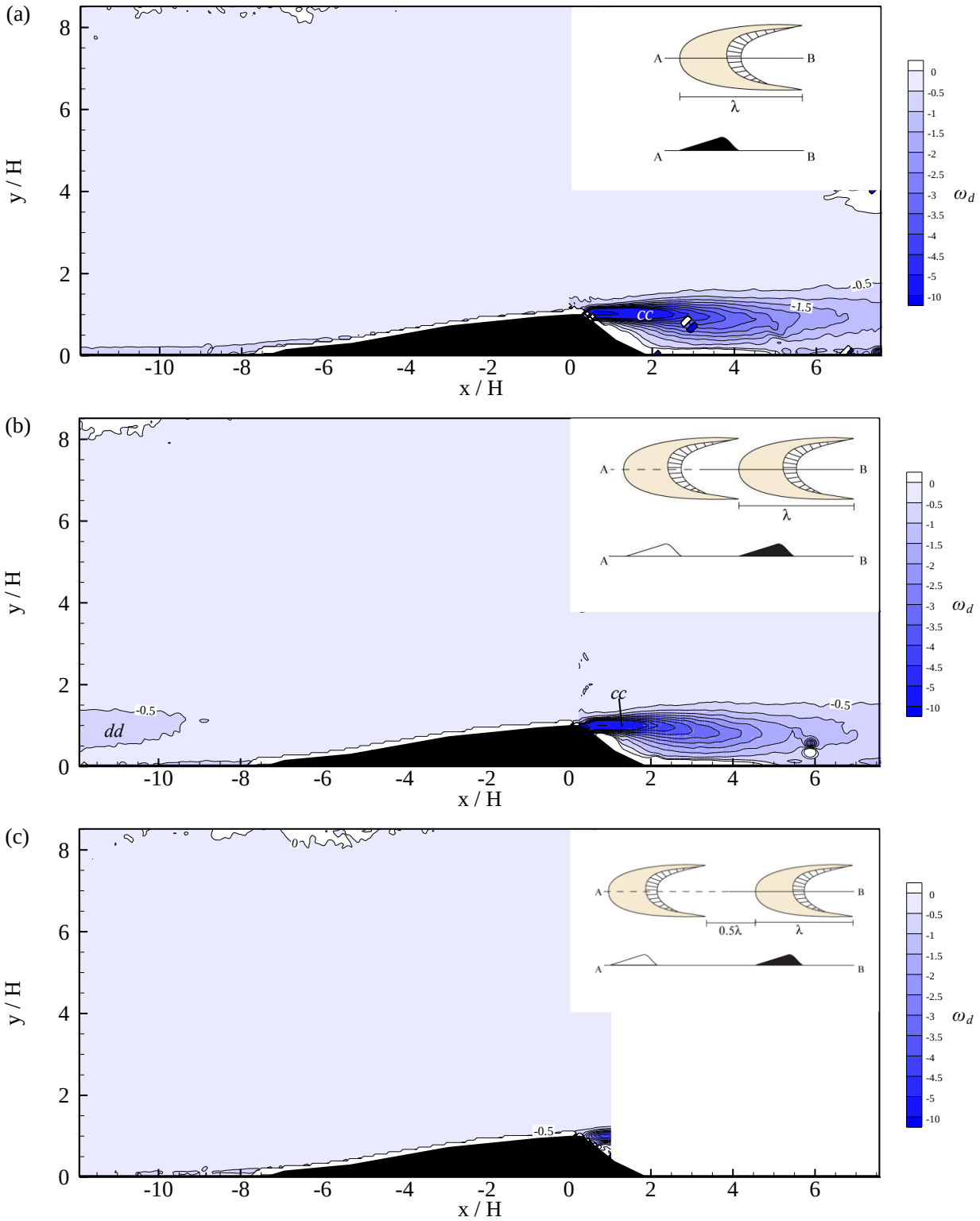

Figure 6.26 (continued on next page)

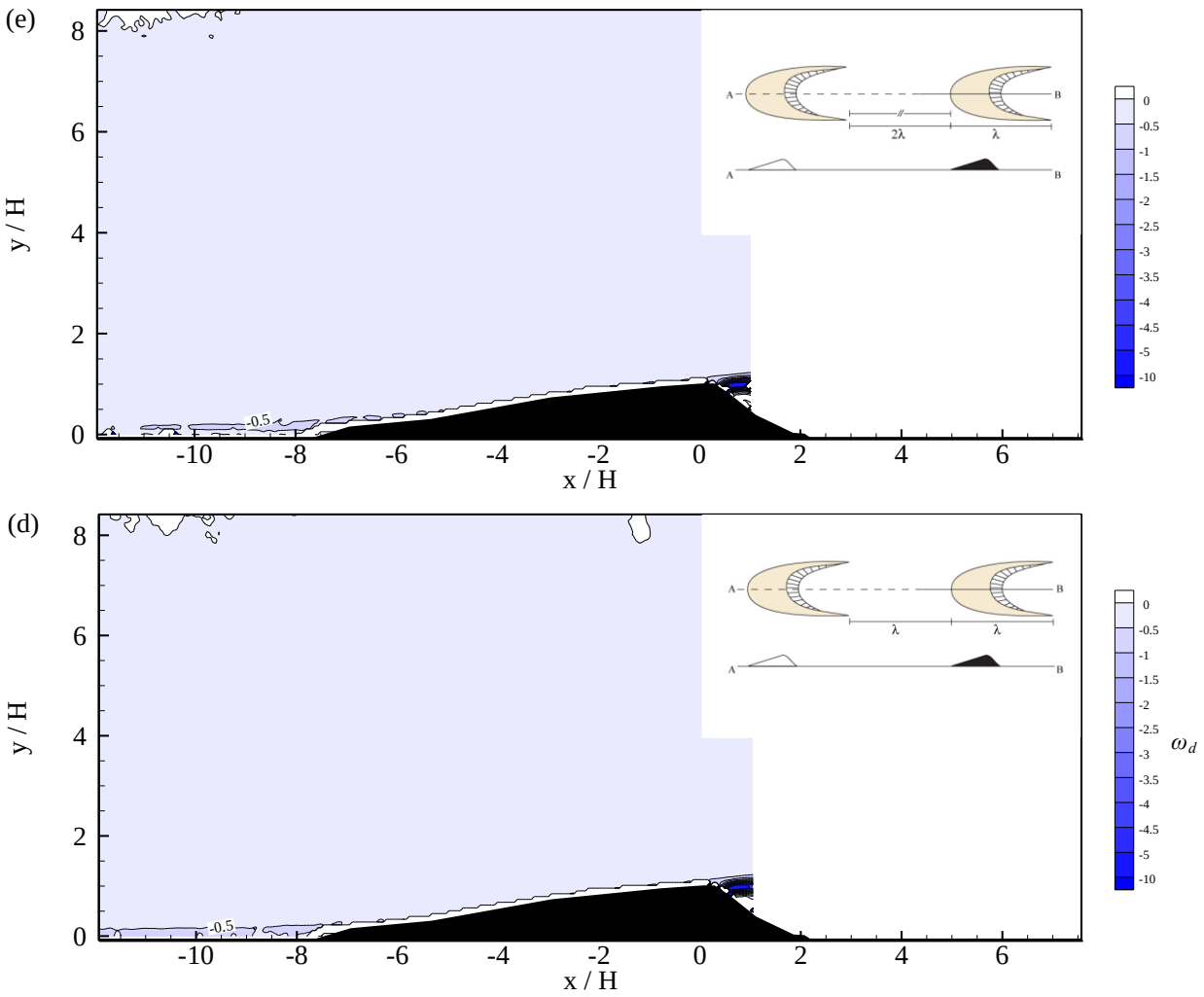

Figure 6.26: Contour maps of the vorticity ω_d for the volumetric ratio AA: (a) isolated dune condition; (b) 0λ spacing; (c) 0.5λ spacing; (d) 1λ spacing; (e) 2λ spacing. On the stoss-side, the area of high ω_d extending from the UBD is labeled '*dd'*. On the leeside, the area of high ω_d is labeled '*cc'*.

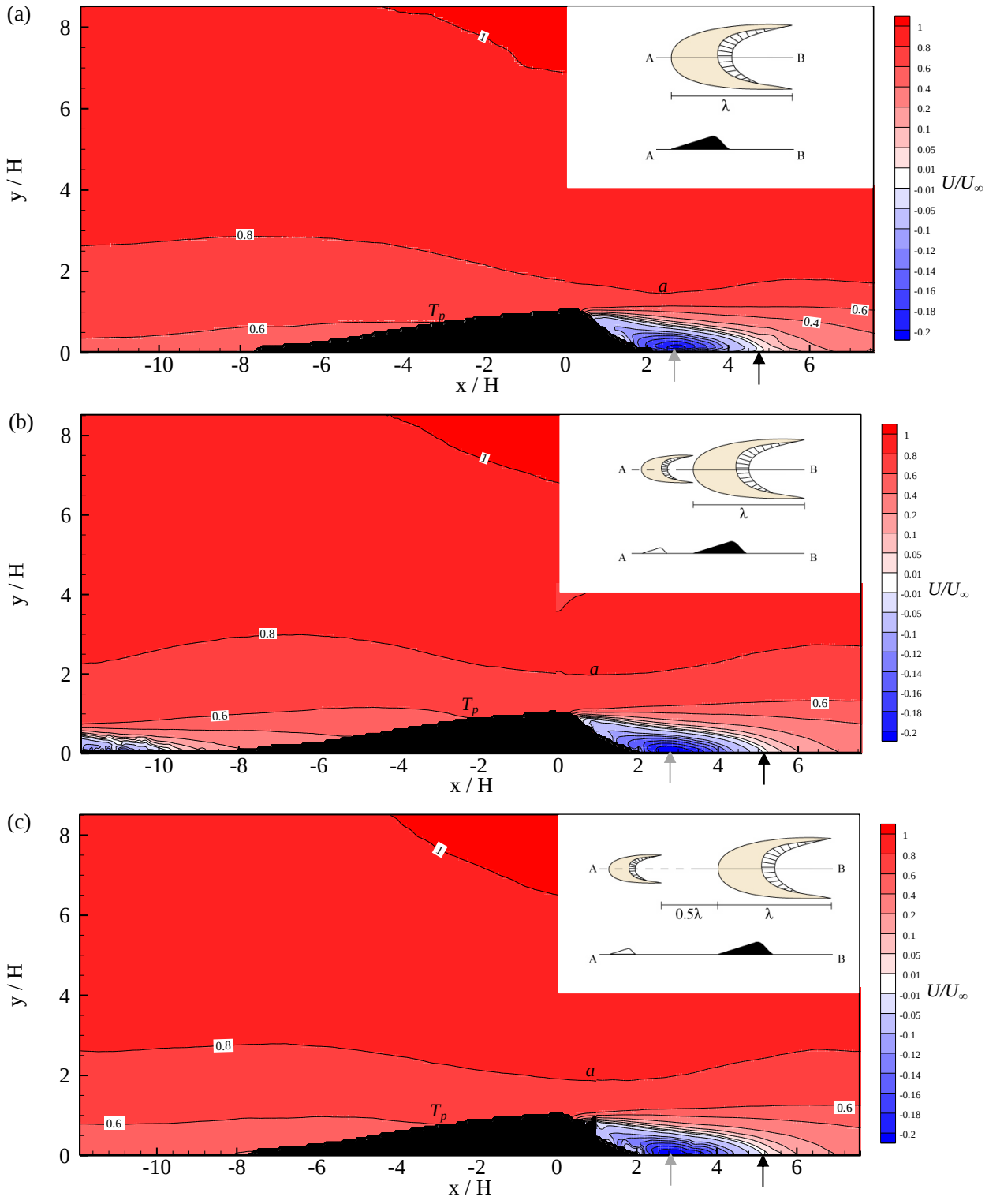

Figure 6.27 (continued on next page)

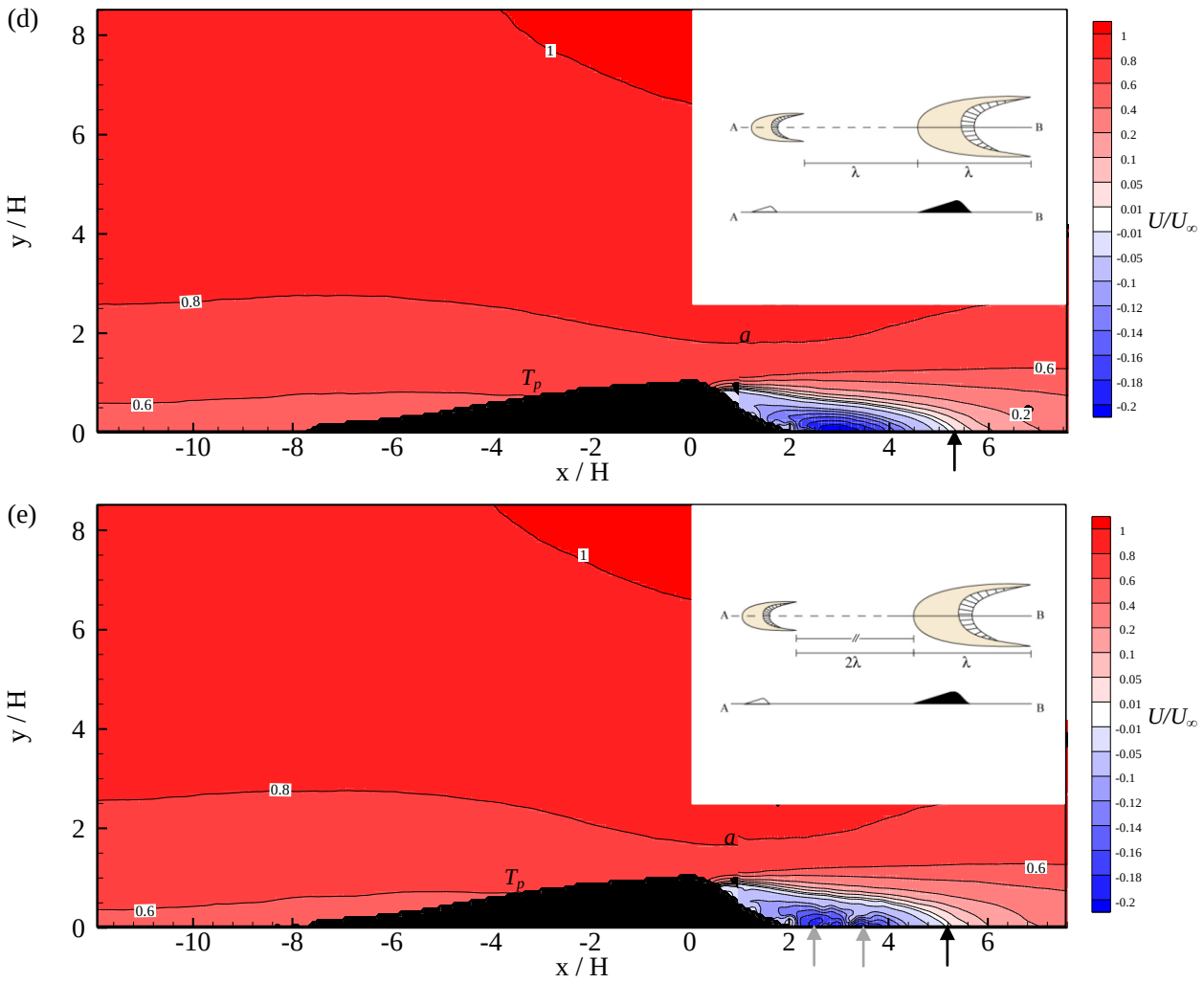

Figure 6.27: The U/U_∞ velocity field for the AB volumetric ratio: (a) Isolated condition (*Re*=59,806); (b) 0λ condition (*Re*=59,824); (c) 0.5λ condition (*Re*=57,691); (d) 1λ condition; (*Re*=59,139); (e) 2λ condition (*Re*=58,758). The black triangular object represents the dune profile. The upper right schematic featured in the plot depicts the experimental condition from a plan view and profile view. The contour plot refers to the ensemble average of the streamwise velocity component: red indicates downstream flow direction, blue upstream downward flow motion, and white indicates zero velocity. The gray arrow indicates the maximum upstream velocity in the separation bubble. The black arrow indicates the flow reattachment point. The maximum velocity region is labeled '*a'*. The 0.6 contour line termination point is labeled 'T_p'.

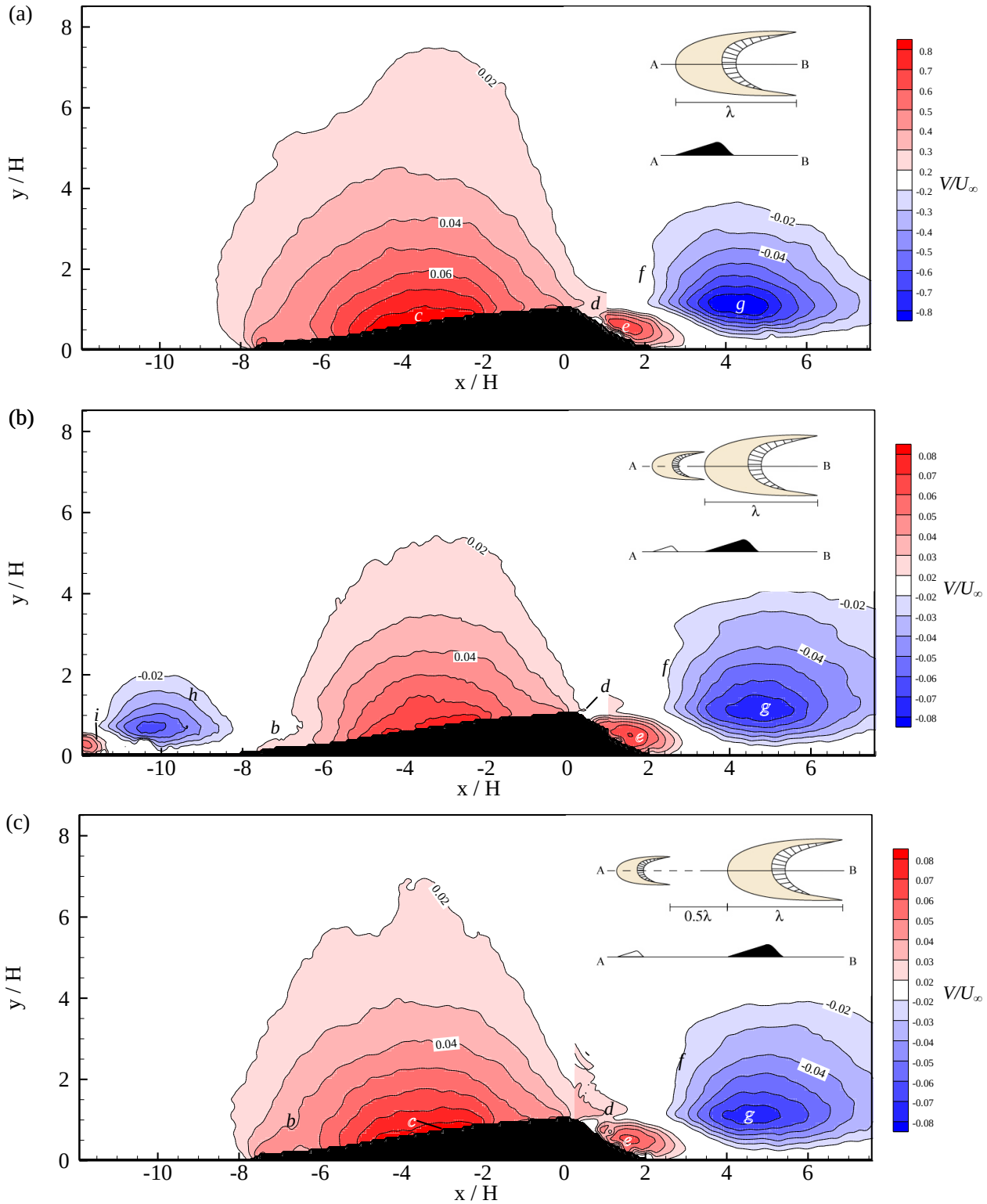

Figure 6.28 (continued on next page)

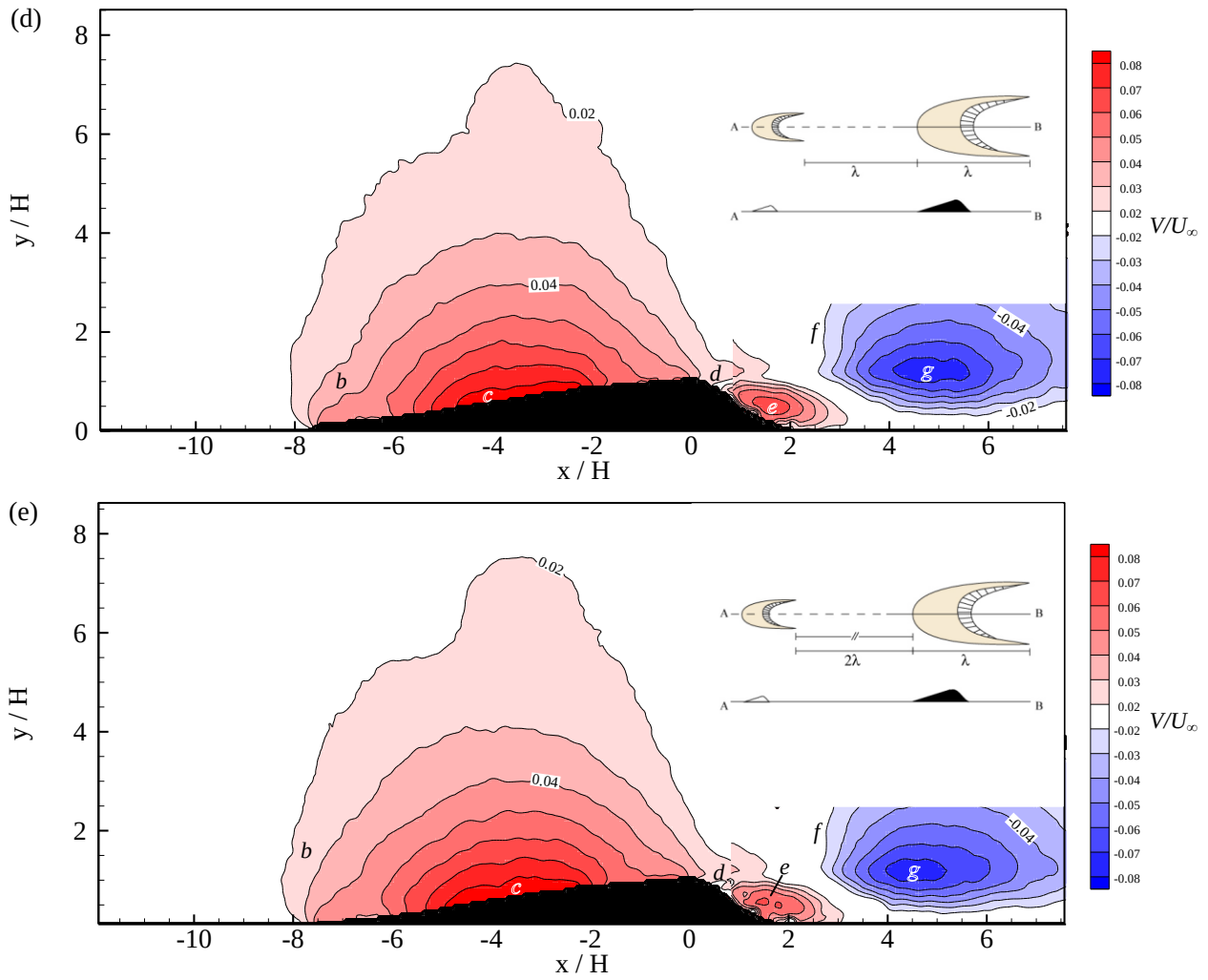

Figure 6.28: The V/U_∞ velocity field for the AB volumetric ratio: (a) Isolated condition (*Re*=59,806); (b) 0λ condition (*Re*=59,824); (c) 0.5λ condition (*Re*=57,691); (d) 1λ condition; (*Re*=59,139); (e) 2λ condition (*Re*=58,758). The black triangular object represents the dune profile. The upper right schematic featured in the plot depicts the experimental condition from a plan view and profile view. The contour plot refers to the ensemble average of the wall-normal velocity component: red indicates upward flow direction, blue indicates downward flow direction and white indicates zero velocity. The flow features referred to in the text are identified with labels *b-j*: *b* – contour inflection; *c* – maximum velocity zone; *d* – crestal jet; *e* – upwelling zone; *f* – contour inflection; *g* – expansion zone; *h* – UBD expansion zone; *i* – UBD upwelling zone; *j* – UBD topographic forcing zone.

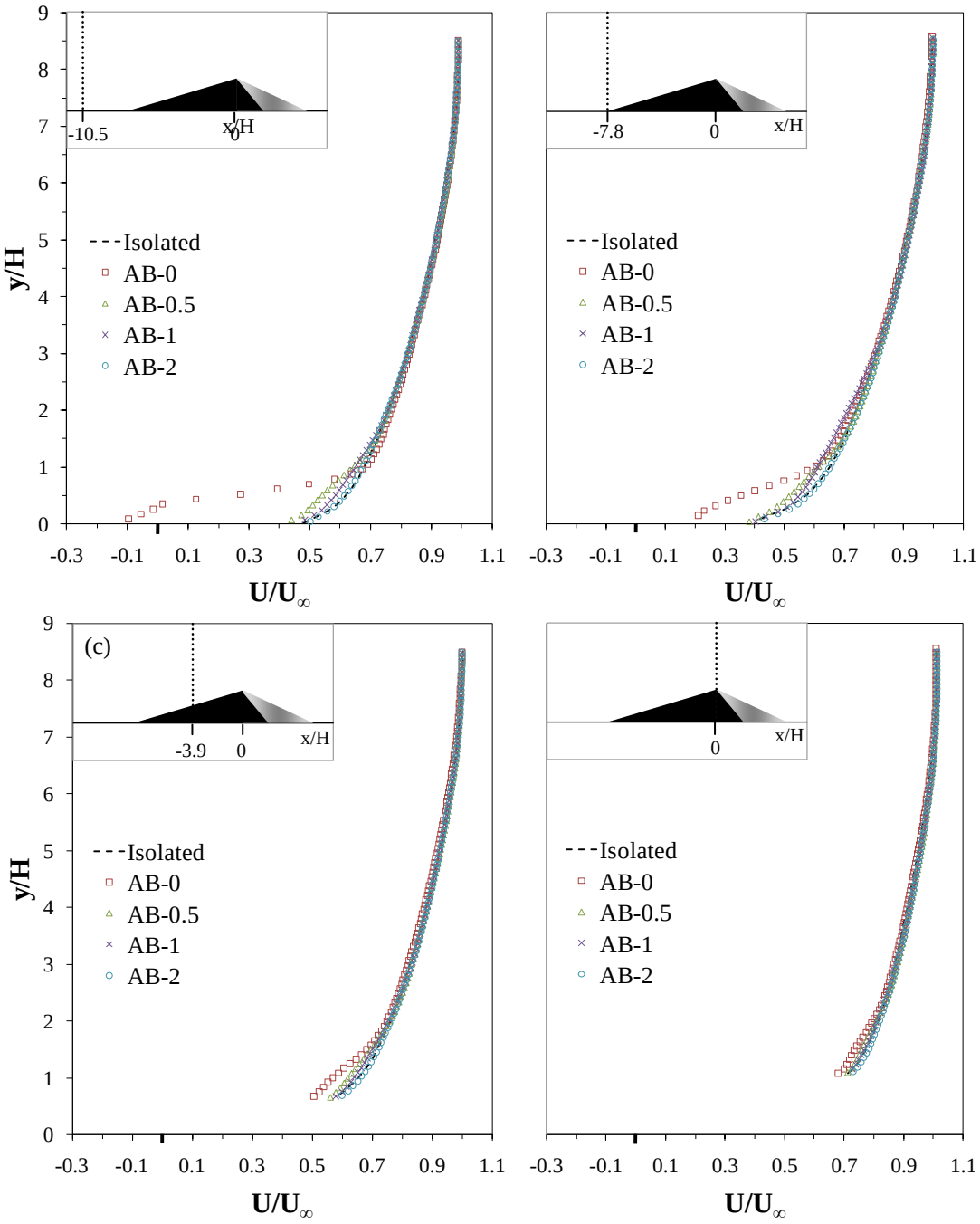

Figure 6.29: Vertical profiles of the streamwise velocity component (U/U_∞) on the stoss-side of the DBD: (a) *x/H*=-10.5; (b) *x/H*=-7.8; (c) *x/H*=-3.9; (d) *x/H*=0.

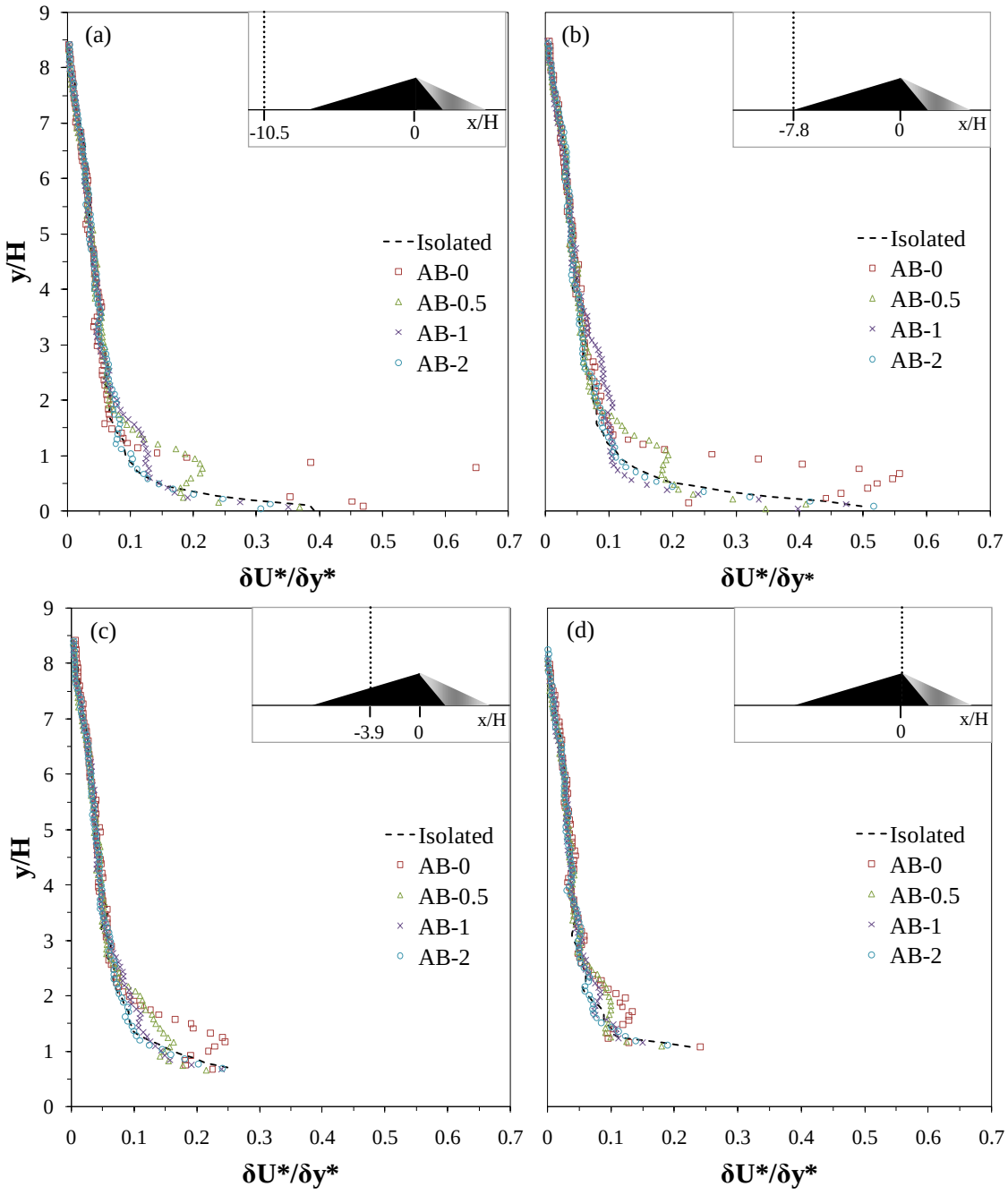

Figure 6.30: Vertical profiles of the streamwise velocity gradient (δU*/δy*) on the stoss-side of the DBD: (a) *x/H*=-10.5; (b) *x/H*=-7.8; (c) *x/H*=-3.9; (d) *x/H*=0.

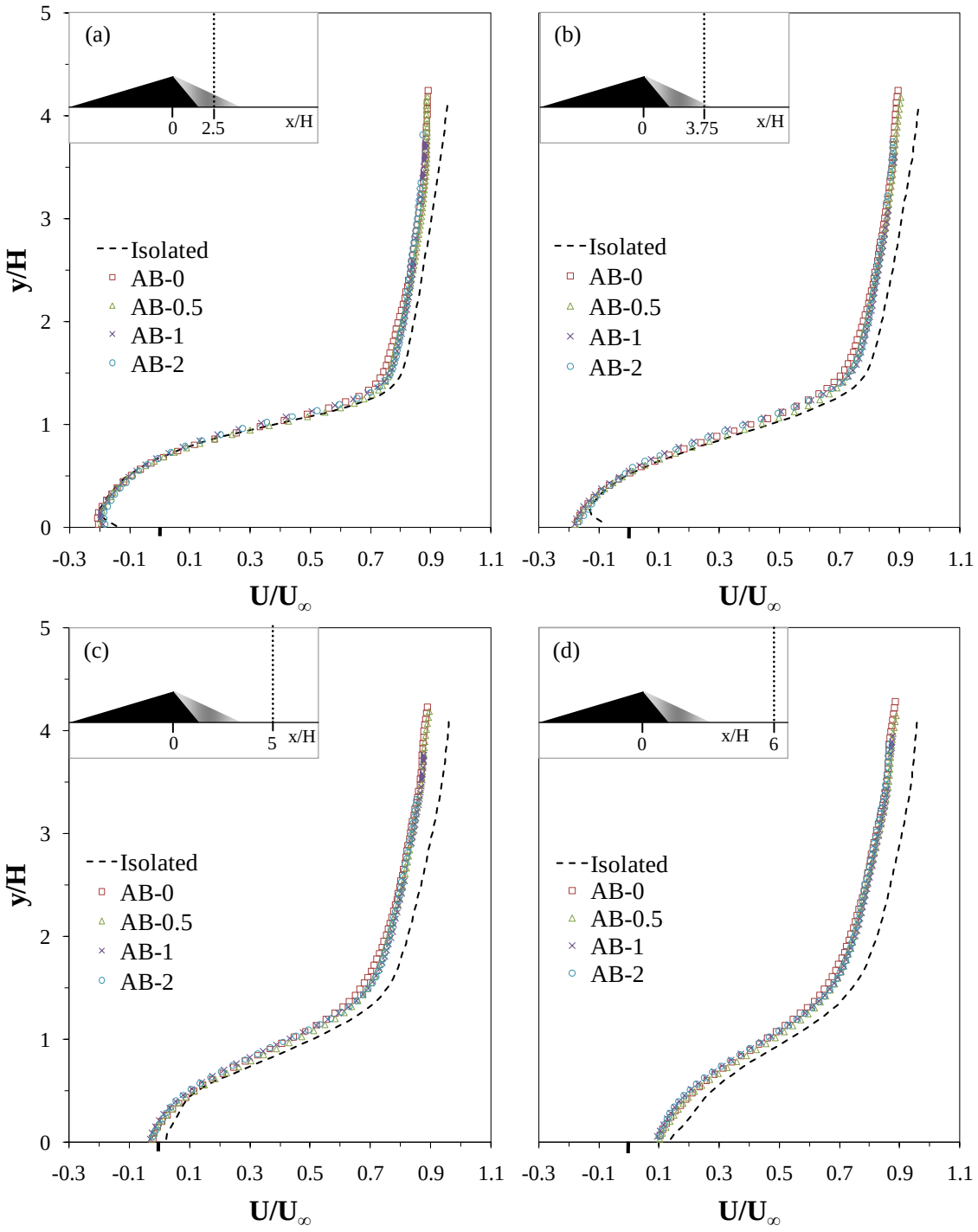

Figure 6.31: Vertical profiles of the streamwise velocity component (U/U_∞) on the lee-side of the DBD: (a) x/H=2.5; (b) x/H=3.75; (c) x/H=5; (d) x/H=6.

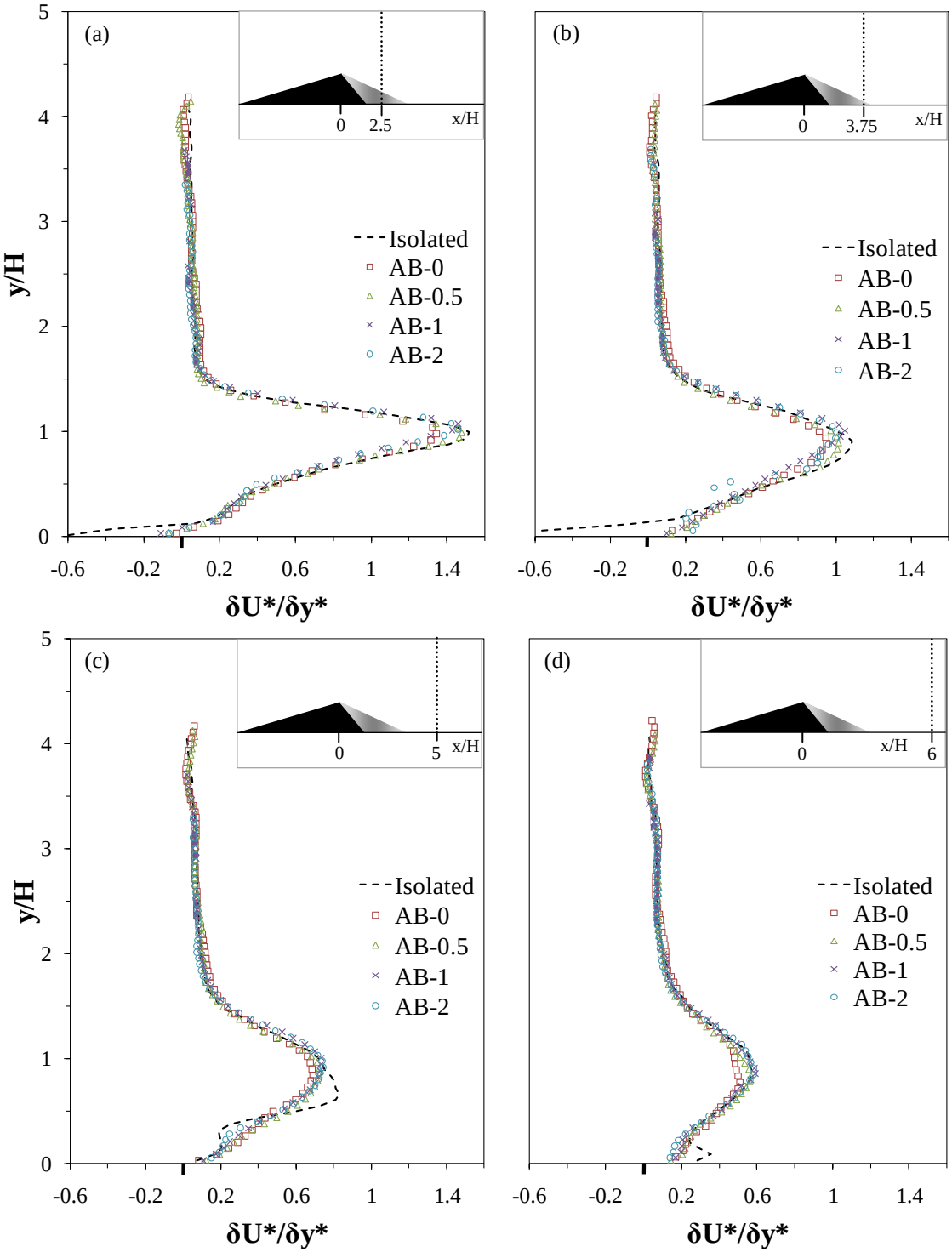

Figure 6.32: Vertical profiles of the streamwise velocity gradient (δU*/δy*) on the lee-side of the DBD: (a) *x/H*=2.5; (b) *x/H*=3.75; (c) *x/H*=5; (d) *x/H*=6.

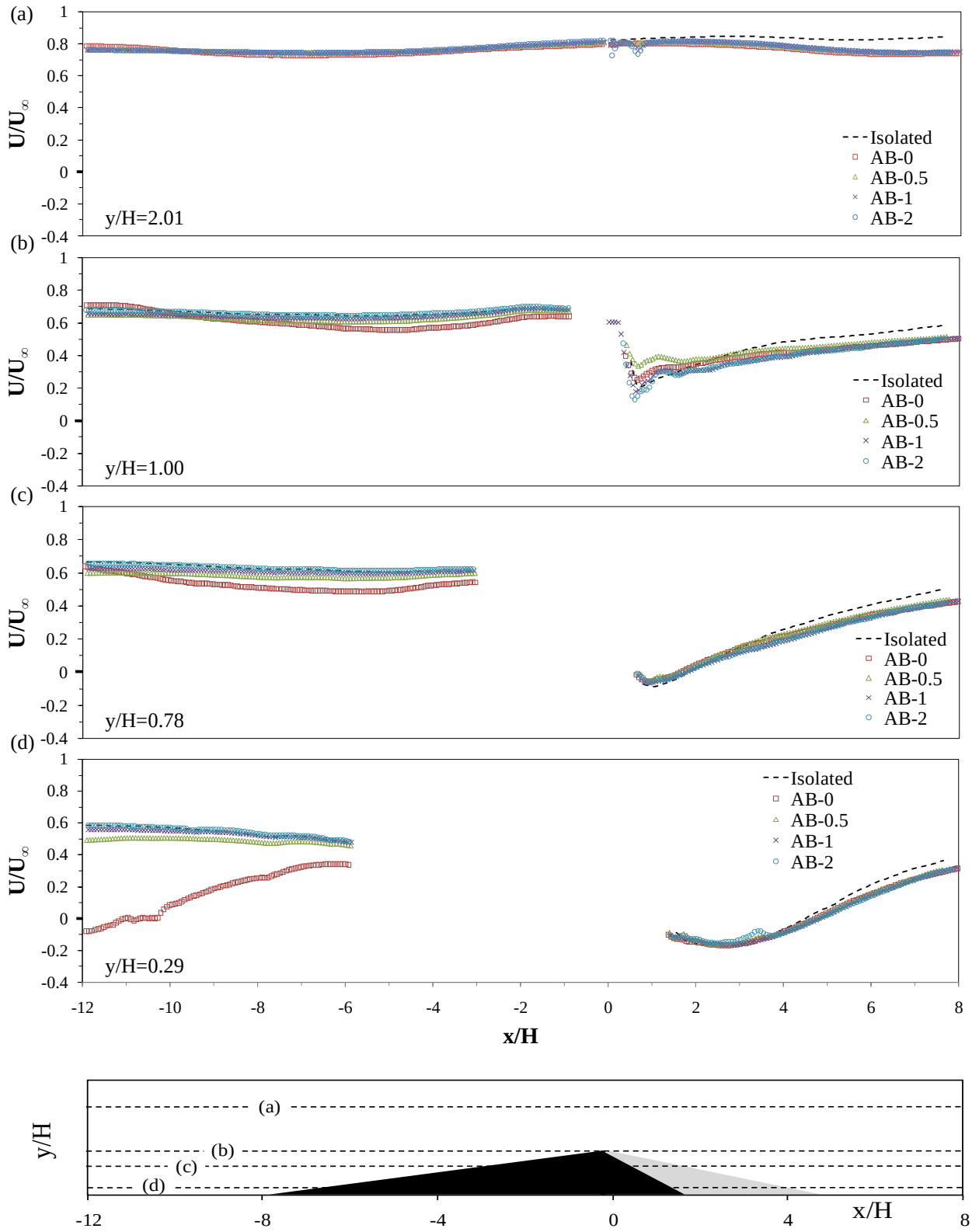

Figure 6.33: Horizontal profile of the streamwise velocity component (U/U_∞): (a) *y/H*=2.01.; (b) *y/H*=1.00; (c) *y/H*=0.78; (d) *y/H*=0.29.

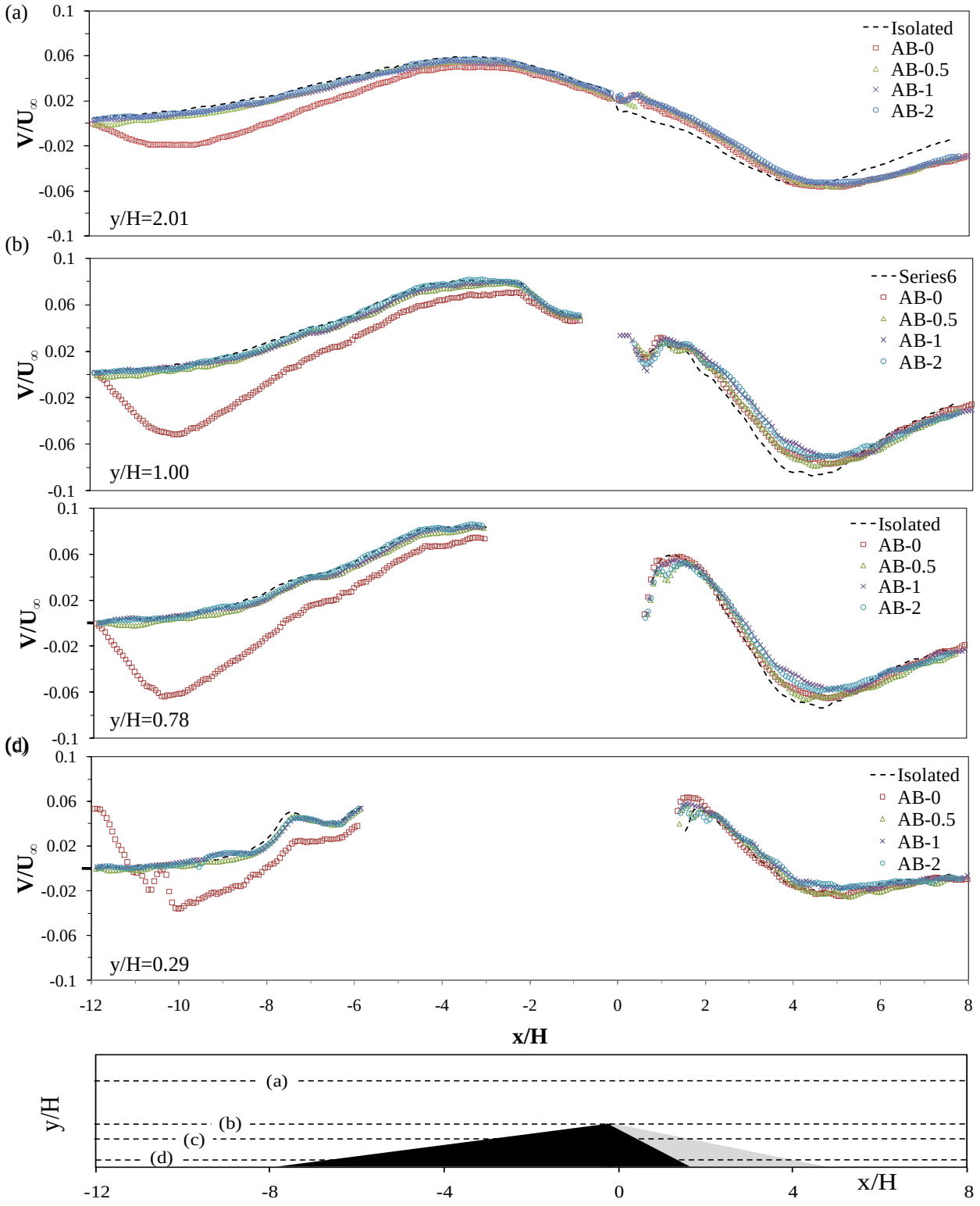

Figure 6.34: Horizontal profile of the wall-normal velocity component, V/U_∞: (a) y/H=2.01.; (b) y/H=1.00; (c) y/H=0.78; (d) y/H=0.29.

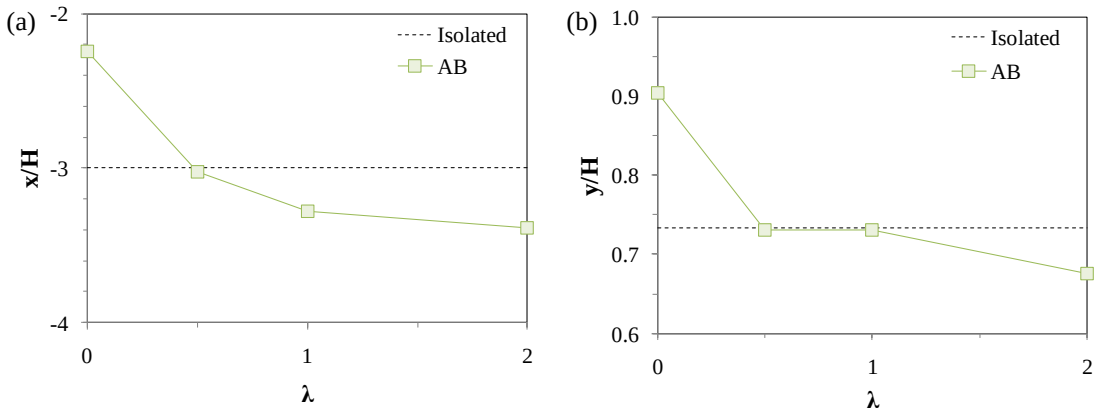

Figure 6.35: The location of the 0.6 U/U_∞ contour line termination point along the stoss-slope of the DBD with increasing λ: (a) the horizontal position, *x/H*; (b) the vertical position, *y/H*. Labeled 'T_p' in Figure 6.28.

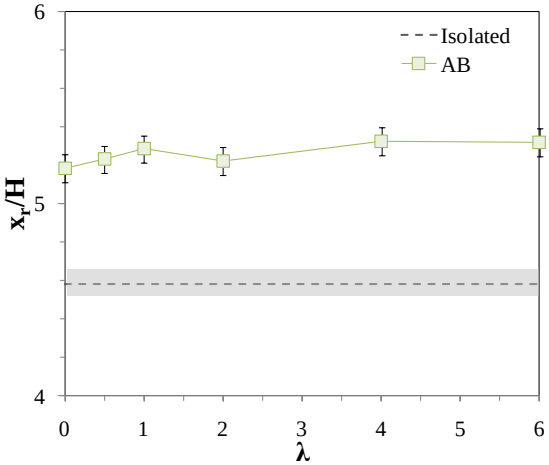

Figure 6.36: The reattachment length x_r of volumetric ratio AB and the isolated dune case, plotted with error bars.

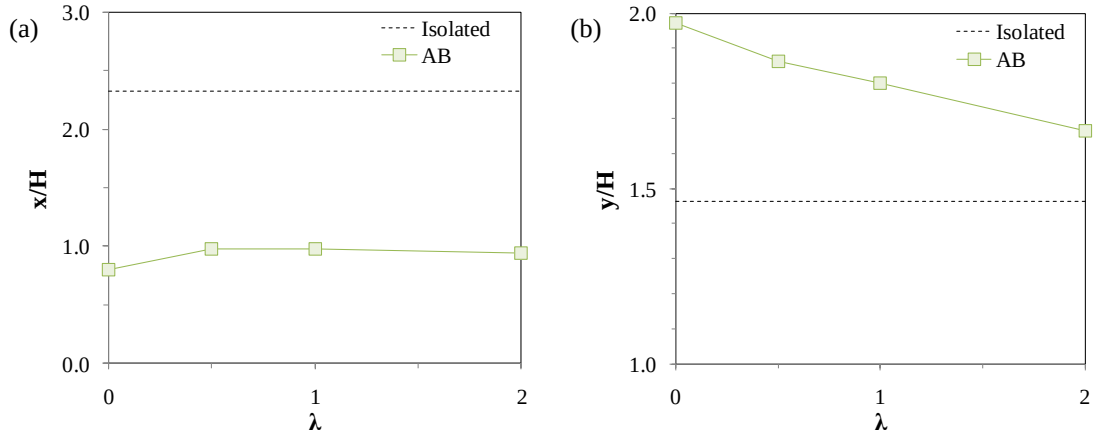

Figure 6.37: The maximum velocity zone position, determined by the location of the 0.8 contour line minima in the streamwise velocity U/U_∞ component contour map in Figure 6.28: (a) the horizontal position *x/H*; (b) the vertical position *y/H*. Labeled '*a*' in Figure 6.28.

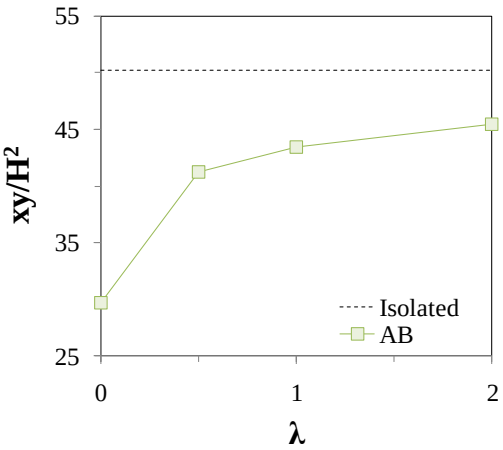

Figure 6.38: The topographic forcing zone area on the stoss-side of the DBD.

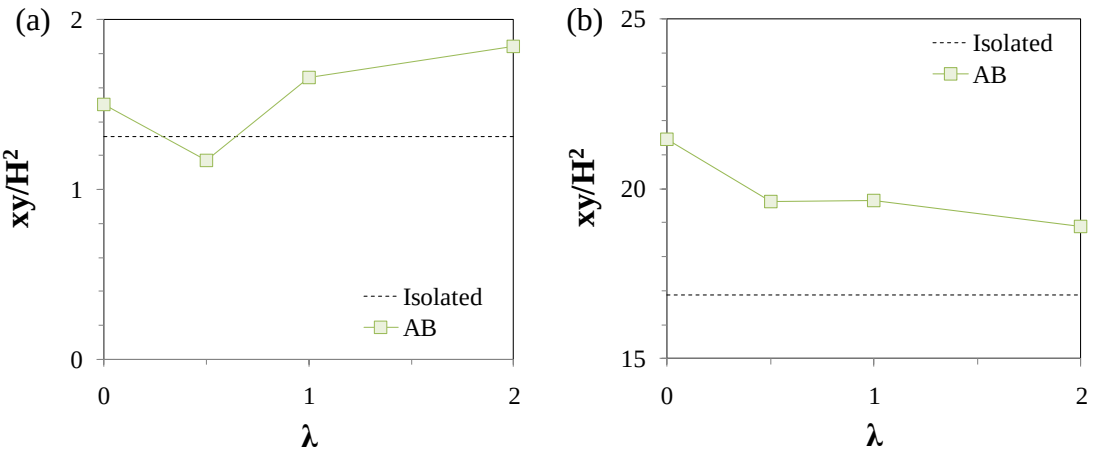

Figure 6.39: The area with increasing λ of (a) the upwelling zone and (b) the expansion zone. The expansion zone extends beyond the field of view, so the complete area is unknown. The area that is provided is the area of the expansion zone that is visible.

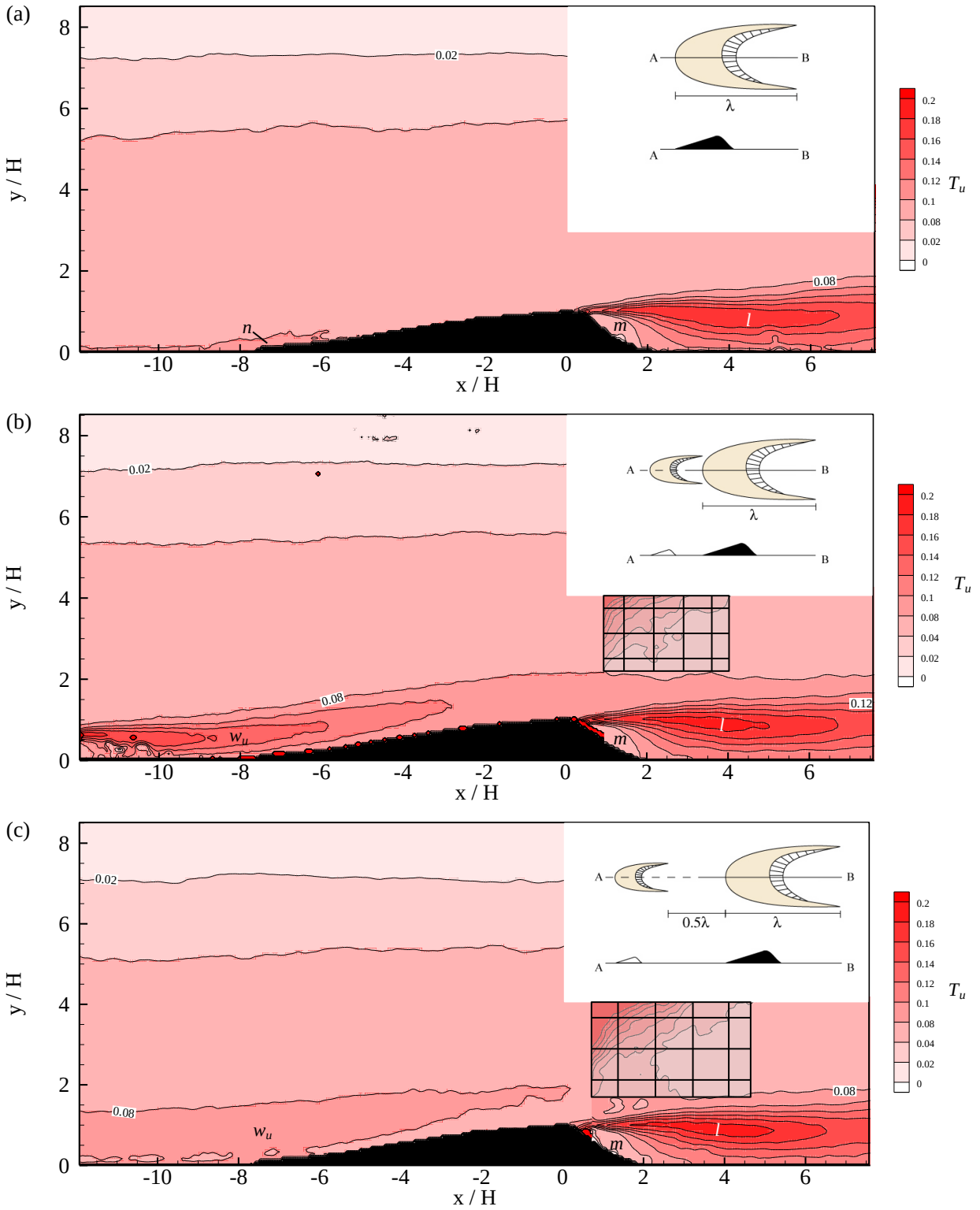

Figure 6.40 (continued on next page)

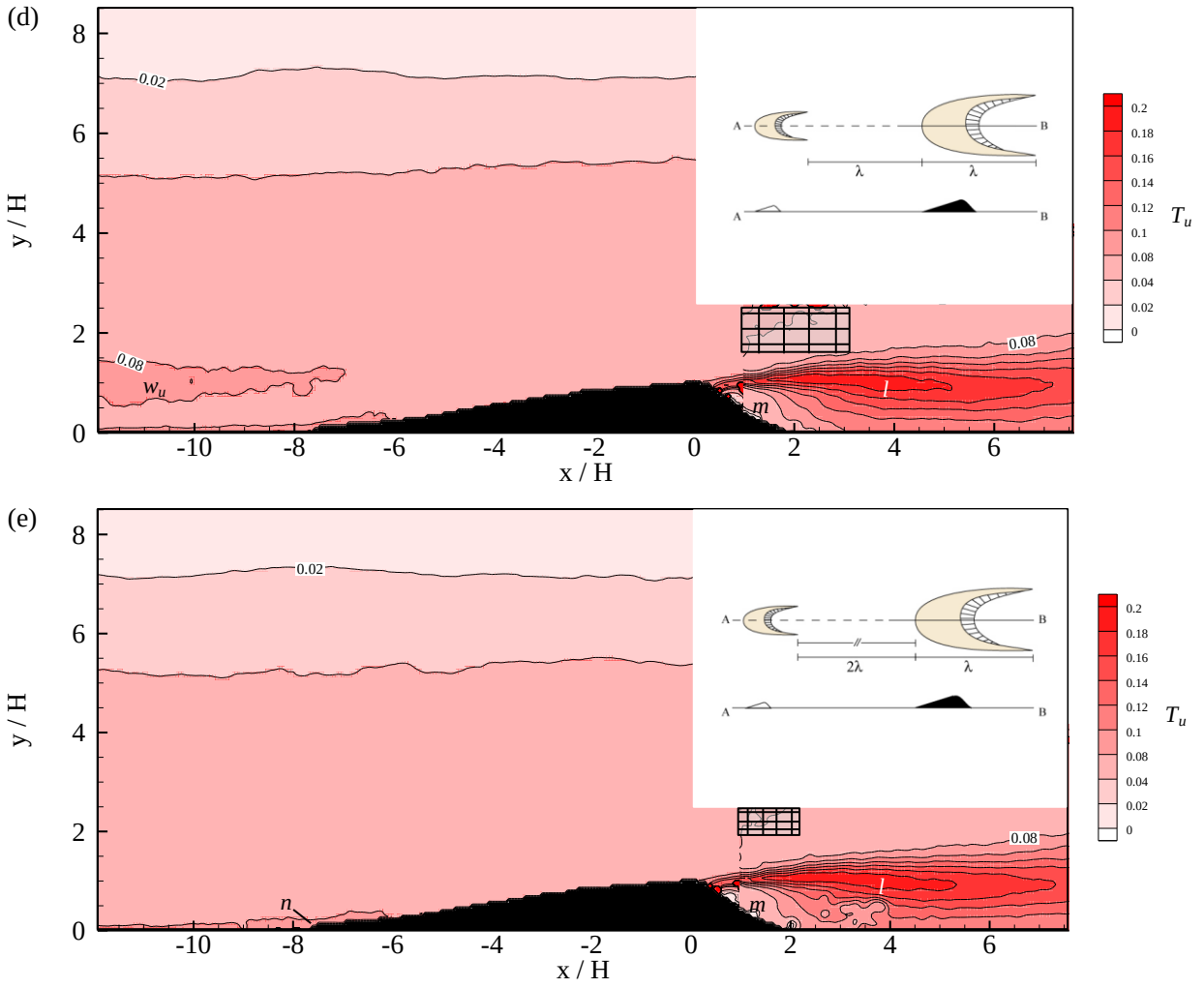

Figure 6.40: Contour maps of the streamwise component of the turbulence intensity T_u ($\sqrt{u'^2}/U_\infty$) for the volumetric ratio AB: (a) isolated dune condition; (b) 0λ spacing; (c) 0.5λ spacing; (d) 1λ spacing; (e) 2λ spacing. On the stoss-side, the area of high T_u extending from the UBD is labeled 'w_u' while the high T_u at the DBD toe is labeled 'n'. On the leeside, the area of high T_u is labeled 'l' while the area of low T_u is labeled 'm'.

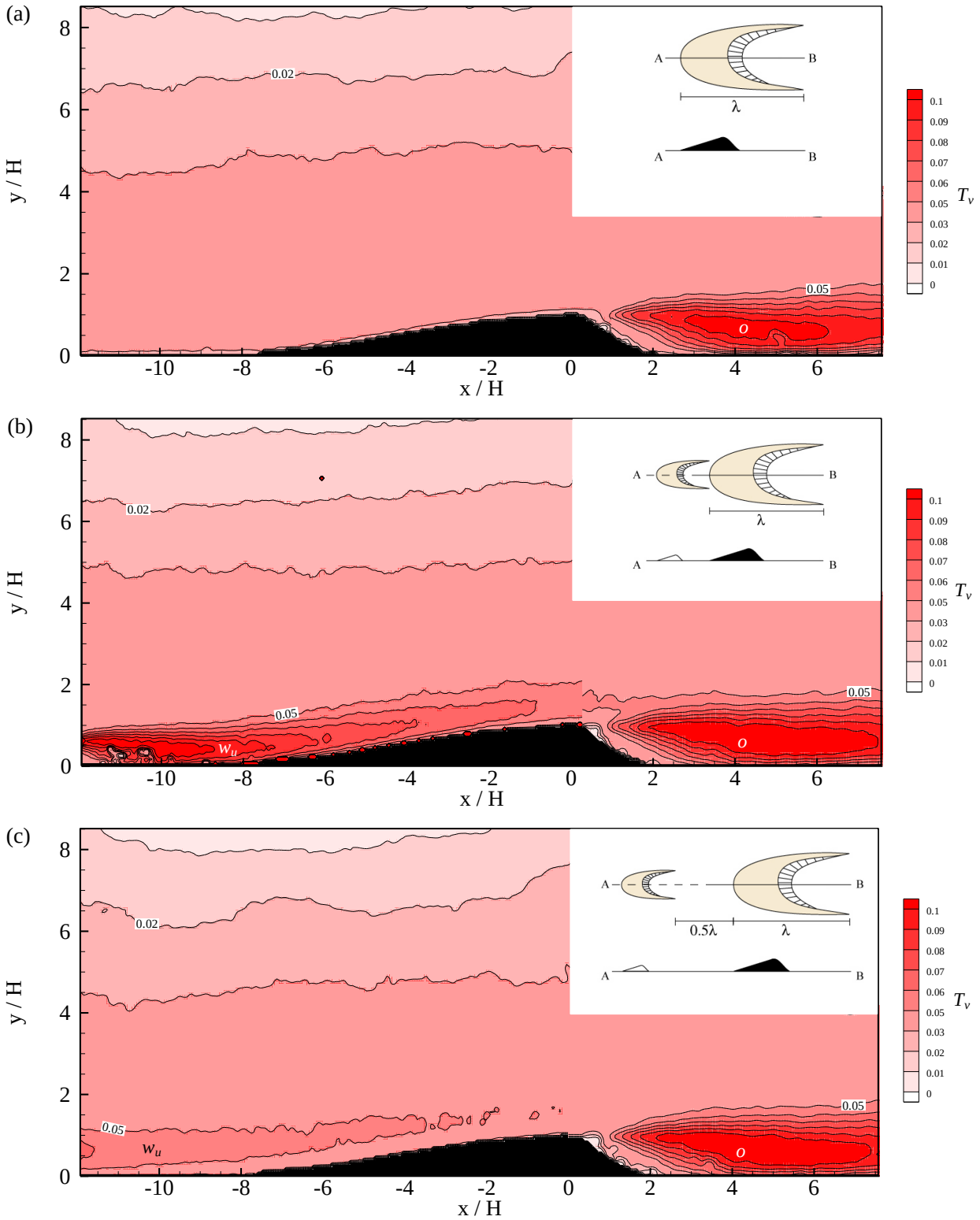

Figure 6.41 (continued on next page)

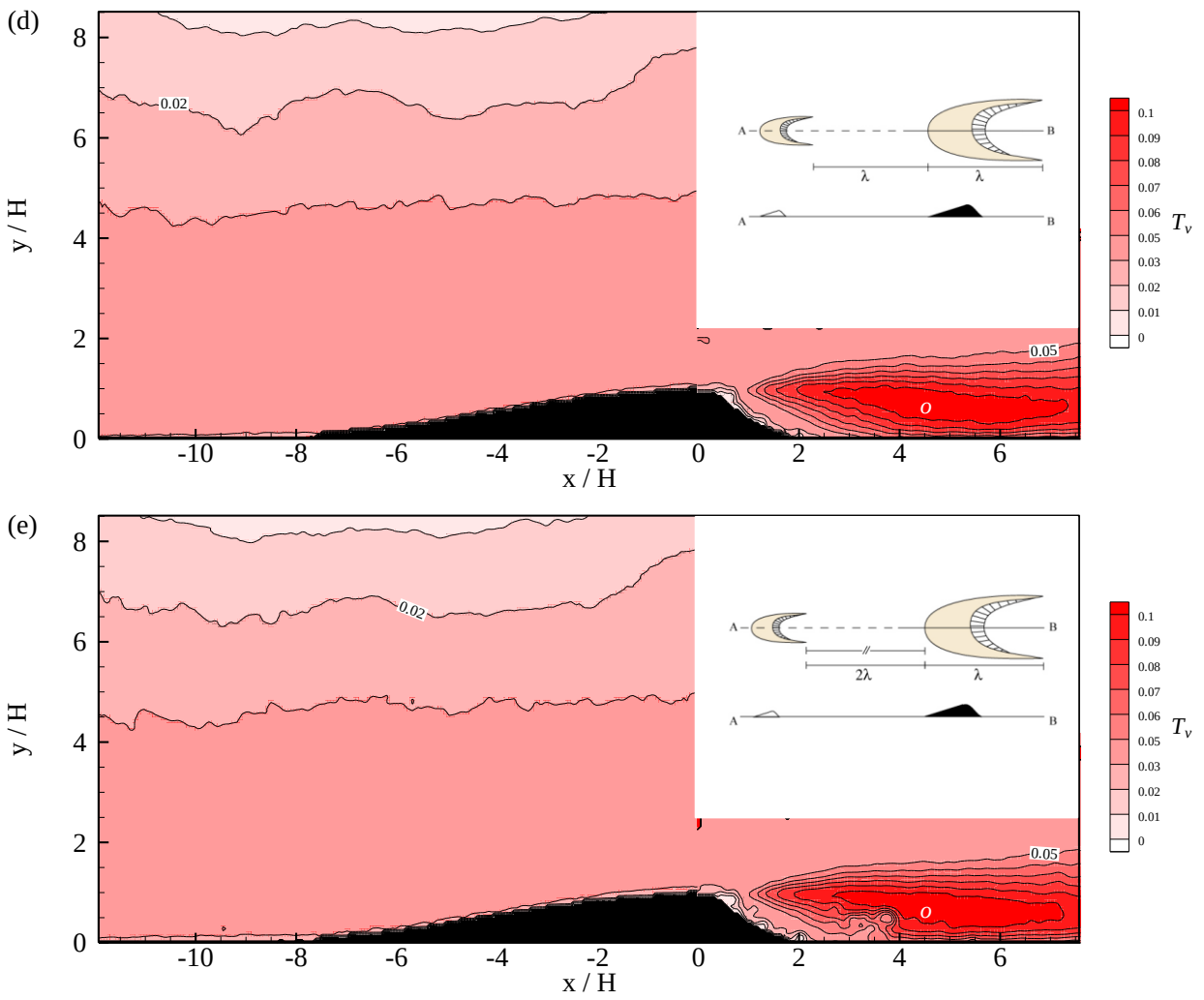

Figure 6.41: Contour maps of the wall-normal component of the turbulence intensity ($\sqrt{v'^2}/U_\infty$) for the volumetric ratio AB: (a) isolated dune condition; (b) 0λ spacing; (c) 0.5λ spacing; (d) 1λ spacing; (e) 2λ spacing. On the stoss-side, the area of high T_v extending from the UBD is labeled 'w_v'. On the leeside, the area of high T_v is labeled 'o'.

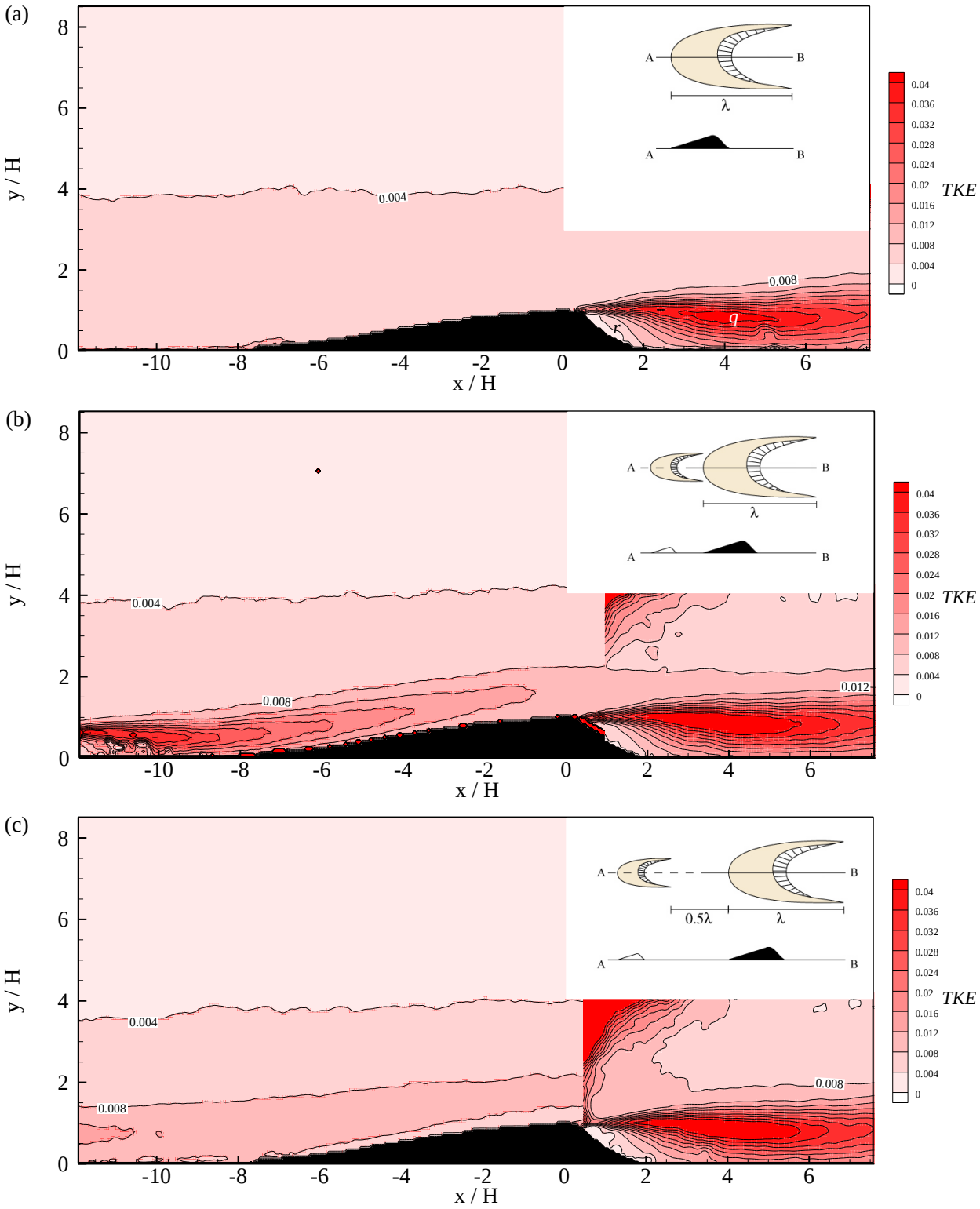

Figure 6.42 (continued on next page)

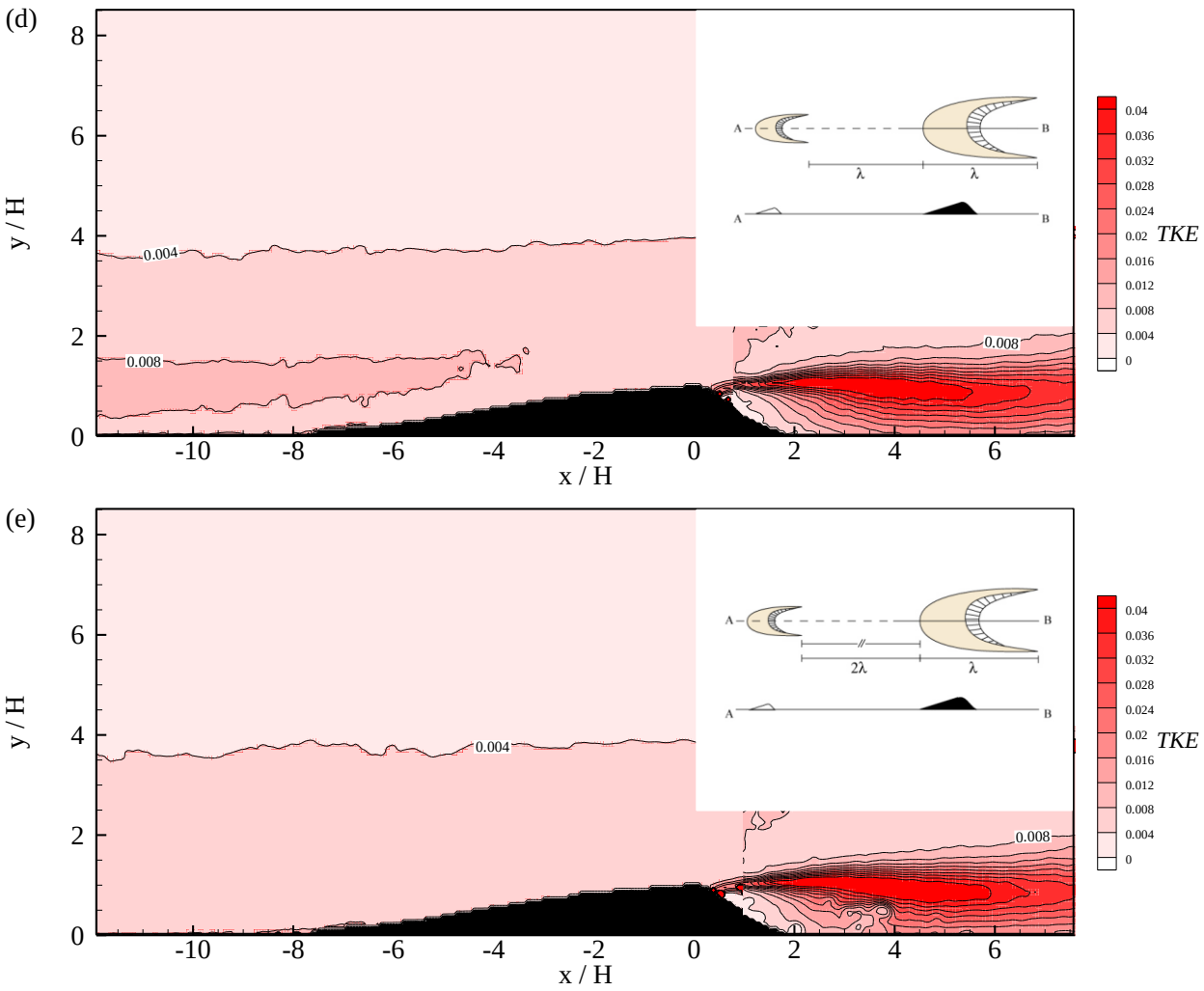

Figure 6.42: Contour maps of the mean turbulent kinetic energy *TKE* ($u'^2 + v'^2/U_\infty^2$) for the volumetric ratio AB: (a) isolated dune condition; (b) 0λ spacing; (c) 0.5λ spacing; (d) 1λ spacing; (e) 2λ spacing. On the stoss-side, the area of high *TKE* extending from the UBD is labeled '*p*'. On the leeside, the area of high *TKE* is labeled '*q*' and the area of low T_u is labeled '*r*'.

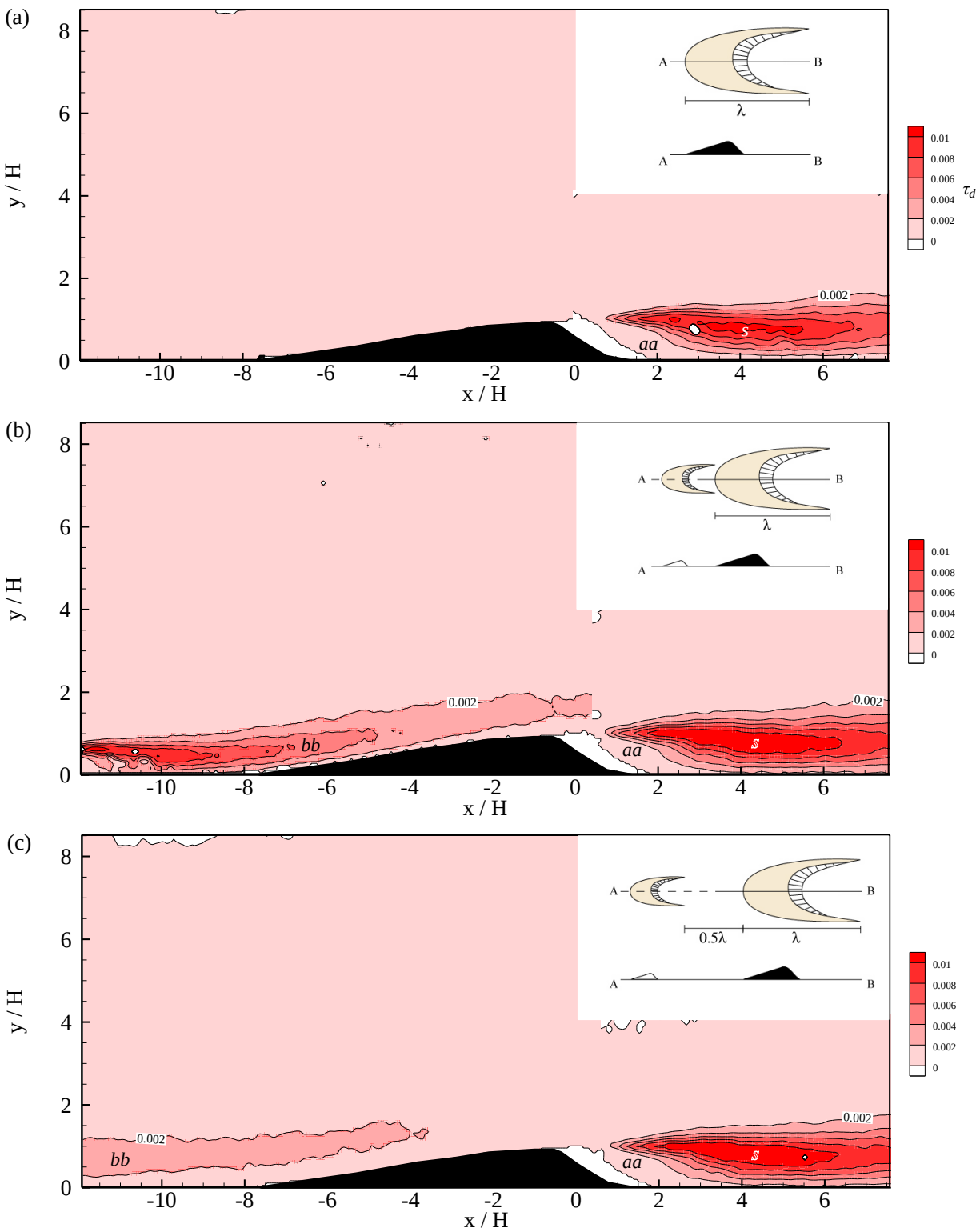

Figure 6.43 (continued on next page)

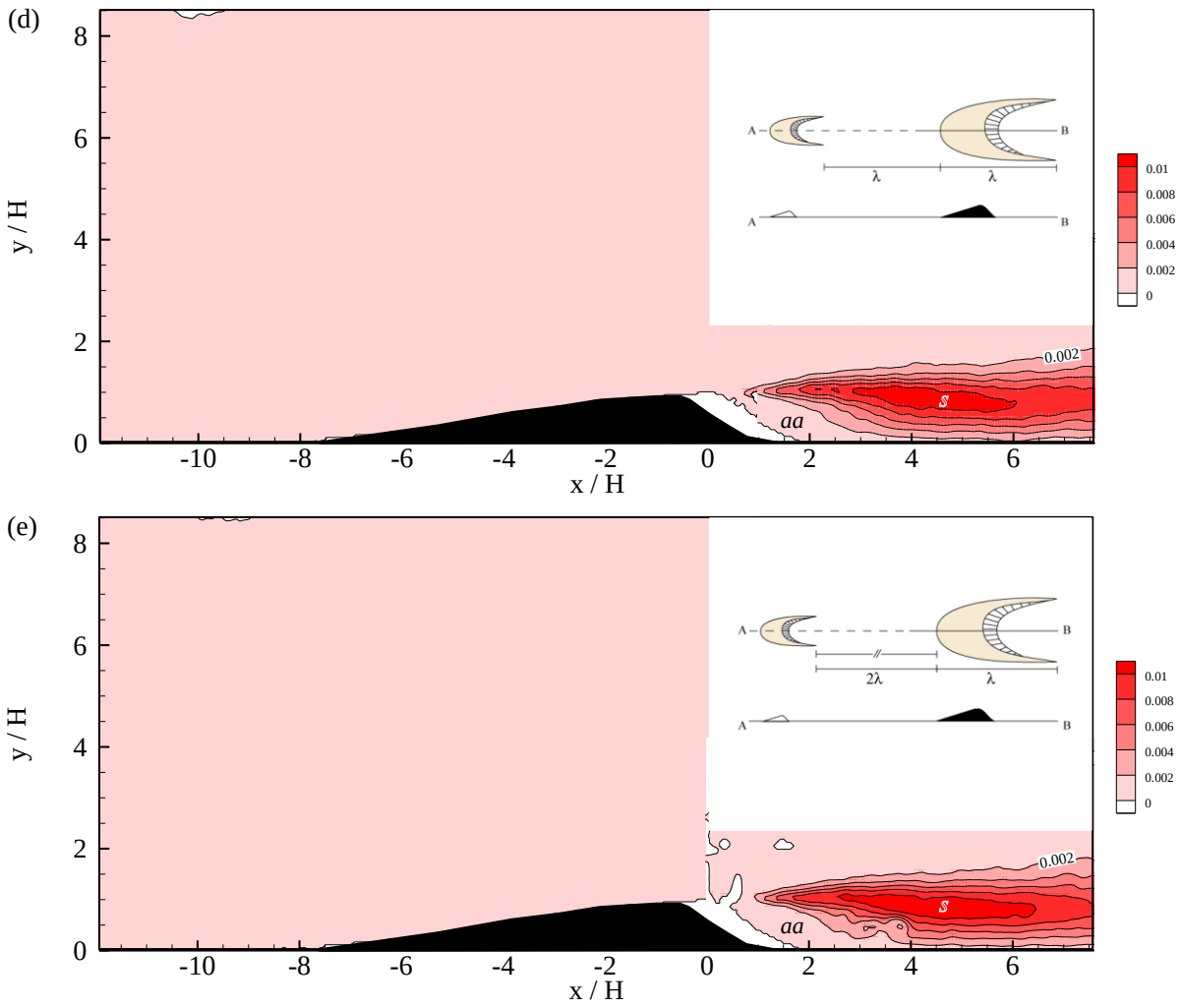

Figure 6.43: Contour maps of the Reynolds stress τ_d ($-u'v'/U_\infty^2$) for the volumetric ratio AB: (a) isolated dune condition; (b) 0λ spacing; (c) 0.5λ spacing; (d) 1λ spacing; (e) 2λ spacing. On the stoss-side, the area of high τ_d extending from the UBD is labeled '*bb'*. On the leeside, the area of high τ_d is labeled '*s'* and the area of low τ_d is labeled '*aa'*.

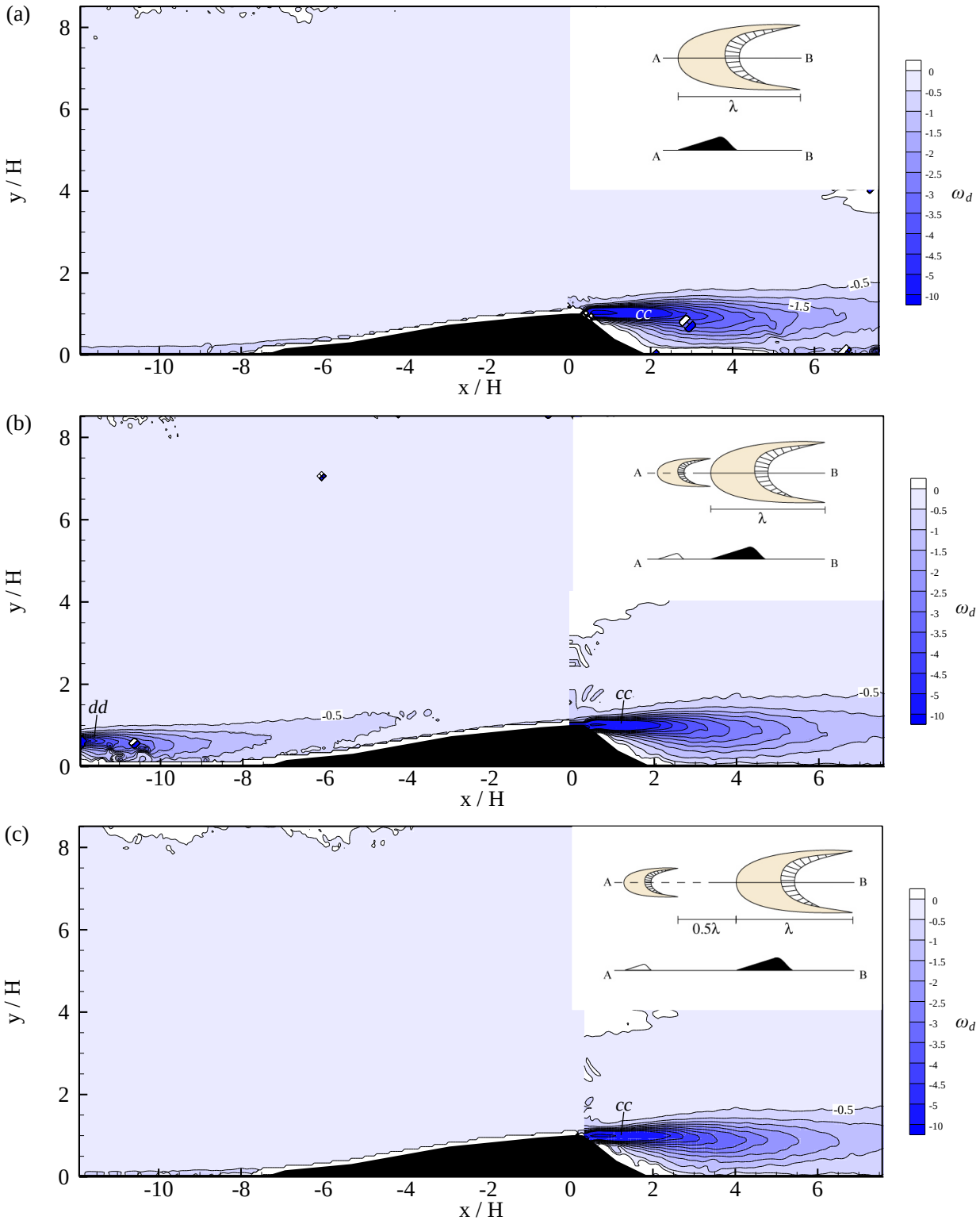

Figure 6.44 (continued on next page)

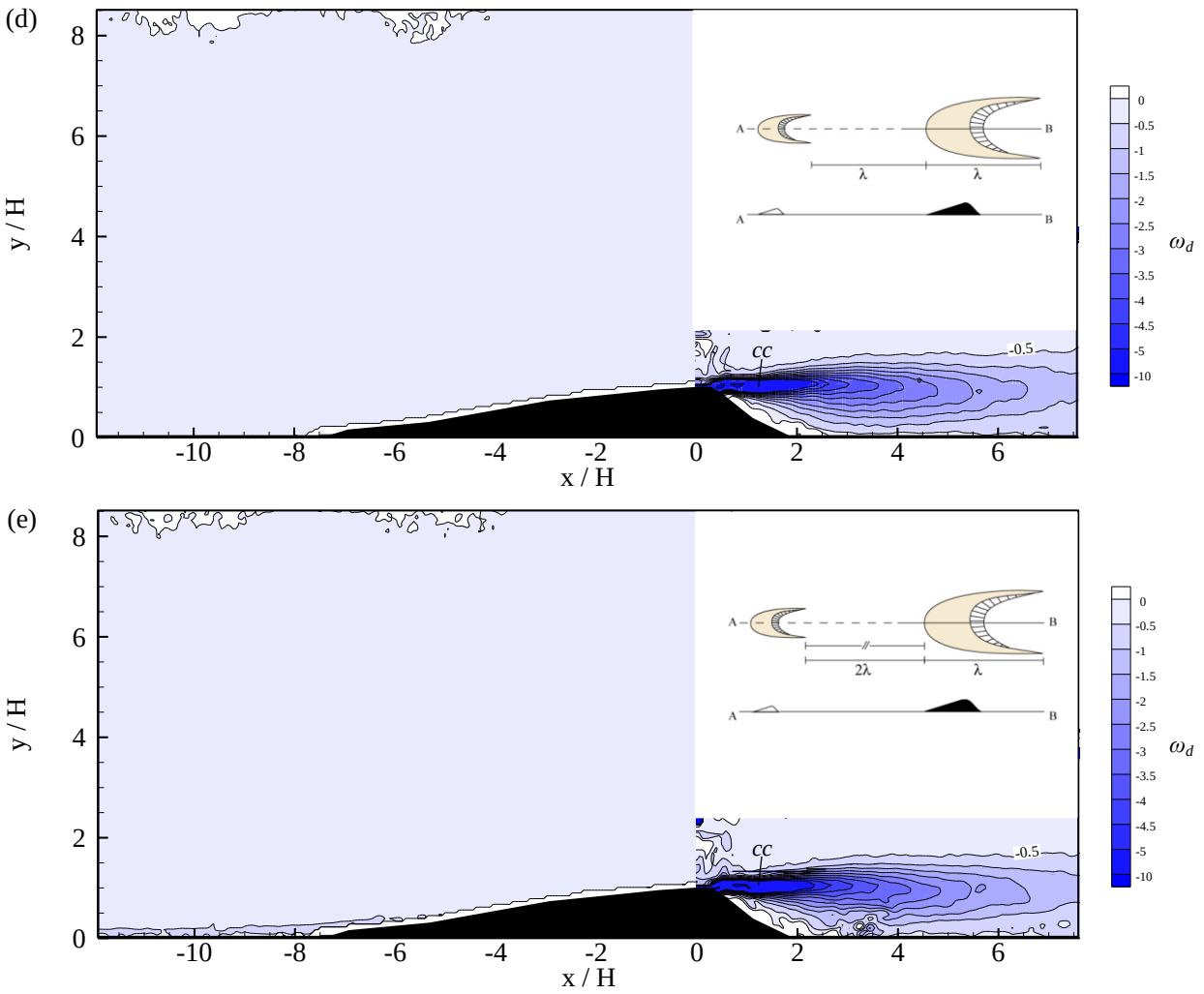

Figure 6.44: Contour maps of the vorticity ω_d for the volumetric ratio AB: (a) isolated dune condition; (b) 0λ spacing; (c) 0.5λ spacing; (d) 1λ spacing; (e) 2λ spacing. On the stoss-side, the area of high ω_d extending from the UBD is labeled '*dd'*. On the leeside, the area of high ω_d is labeled '*cc'*.

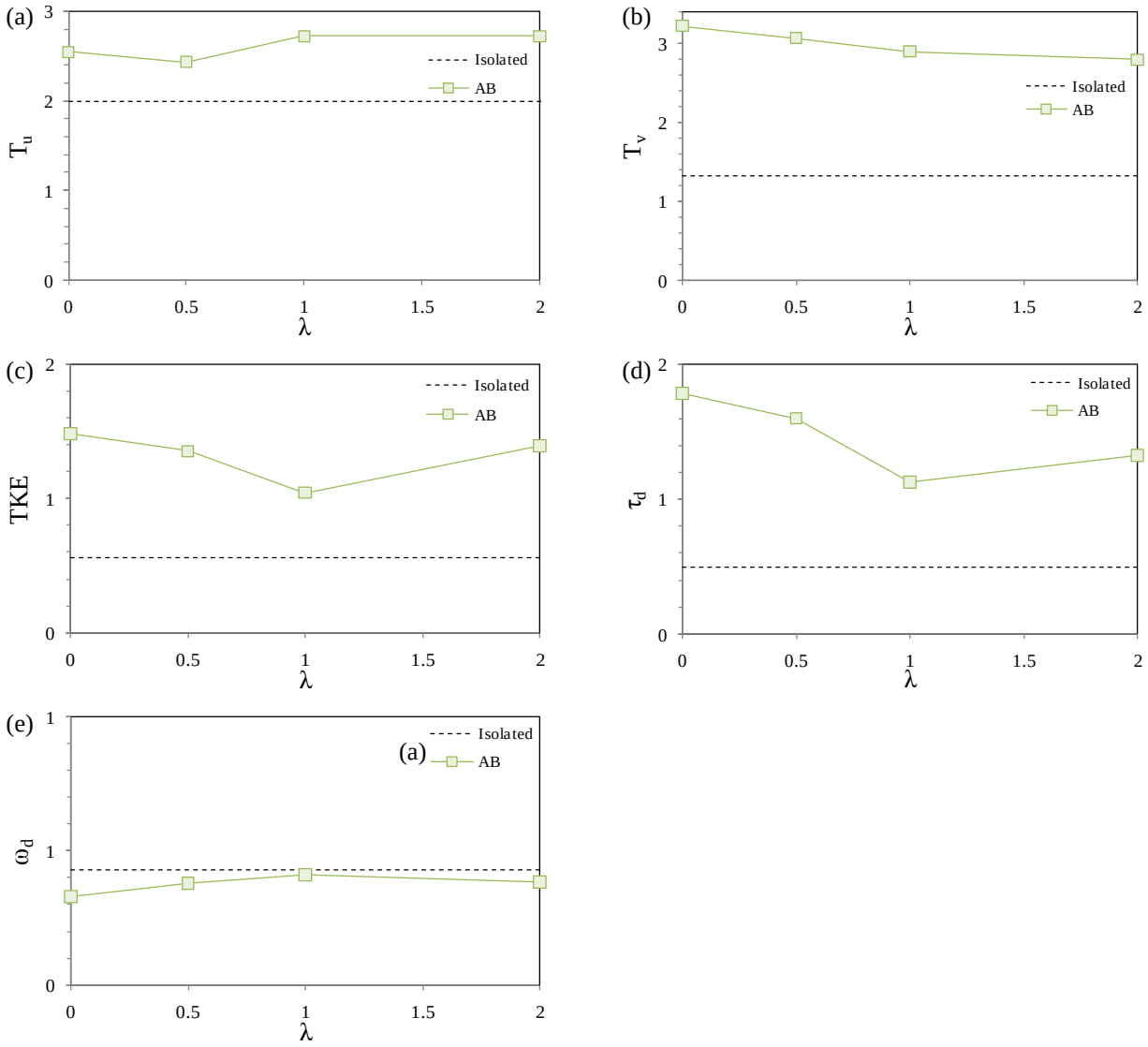

Figure 6.45: Comparison between the area of maximum T_u, T_v, *TKE*, τ_d, and ω_d between the isolated dune and volumetric ratio AB: (a) T_u – area of 0.16-0.2 contour; (b) T_v – area of 0.1 contour (c) *TKE* – area of 0.04 contour; (d) τ_d – area of 0.01 contour; (e) ω_d – area of -5 to -10 contour. The contour area is approximated using the area of an ellipse.

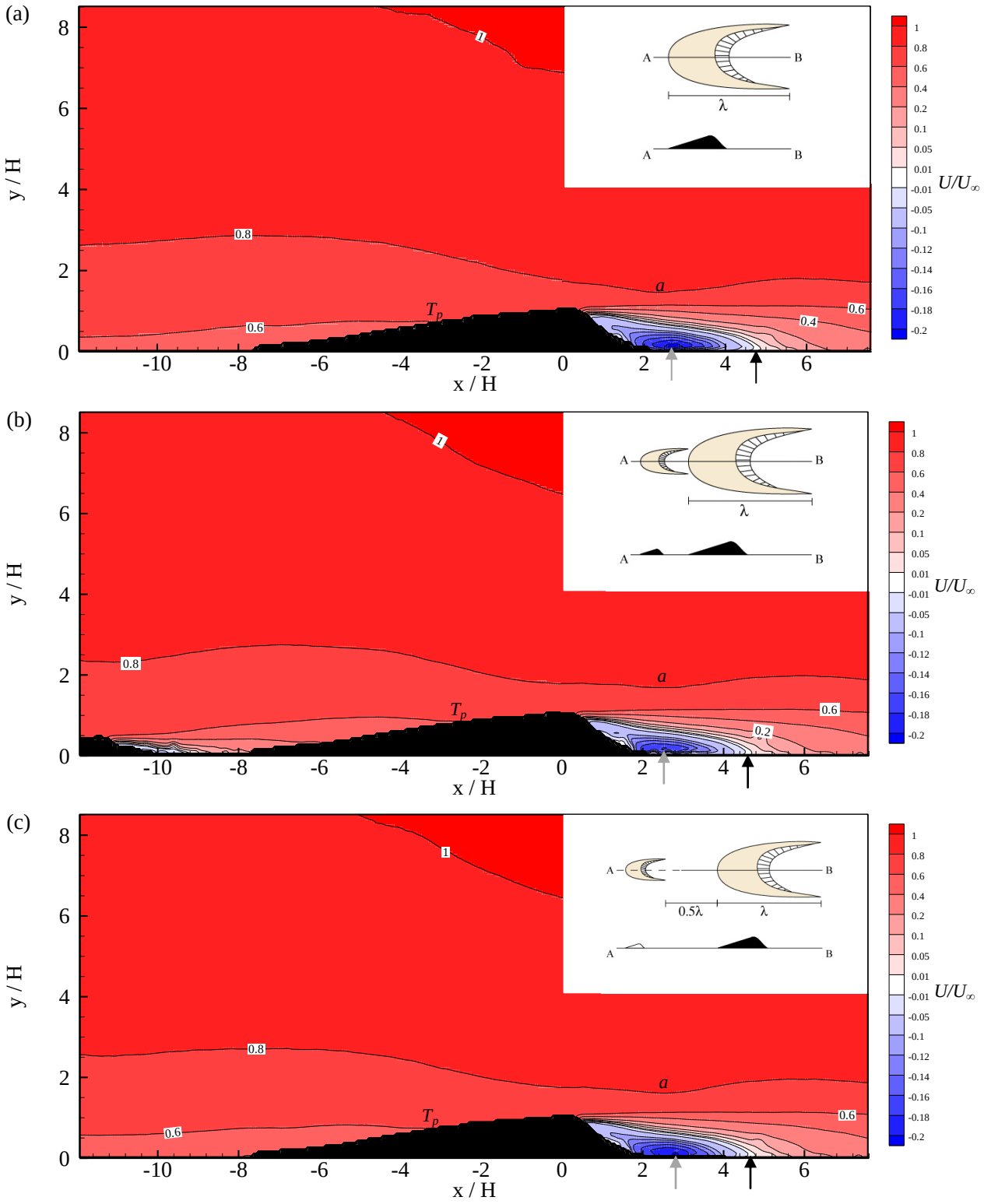

Figure 6.46 (continued on next page)

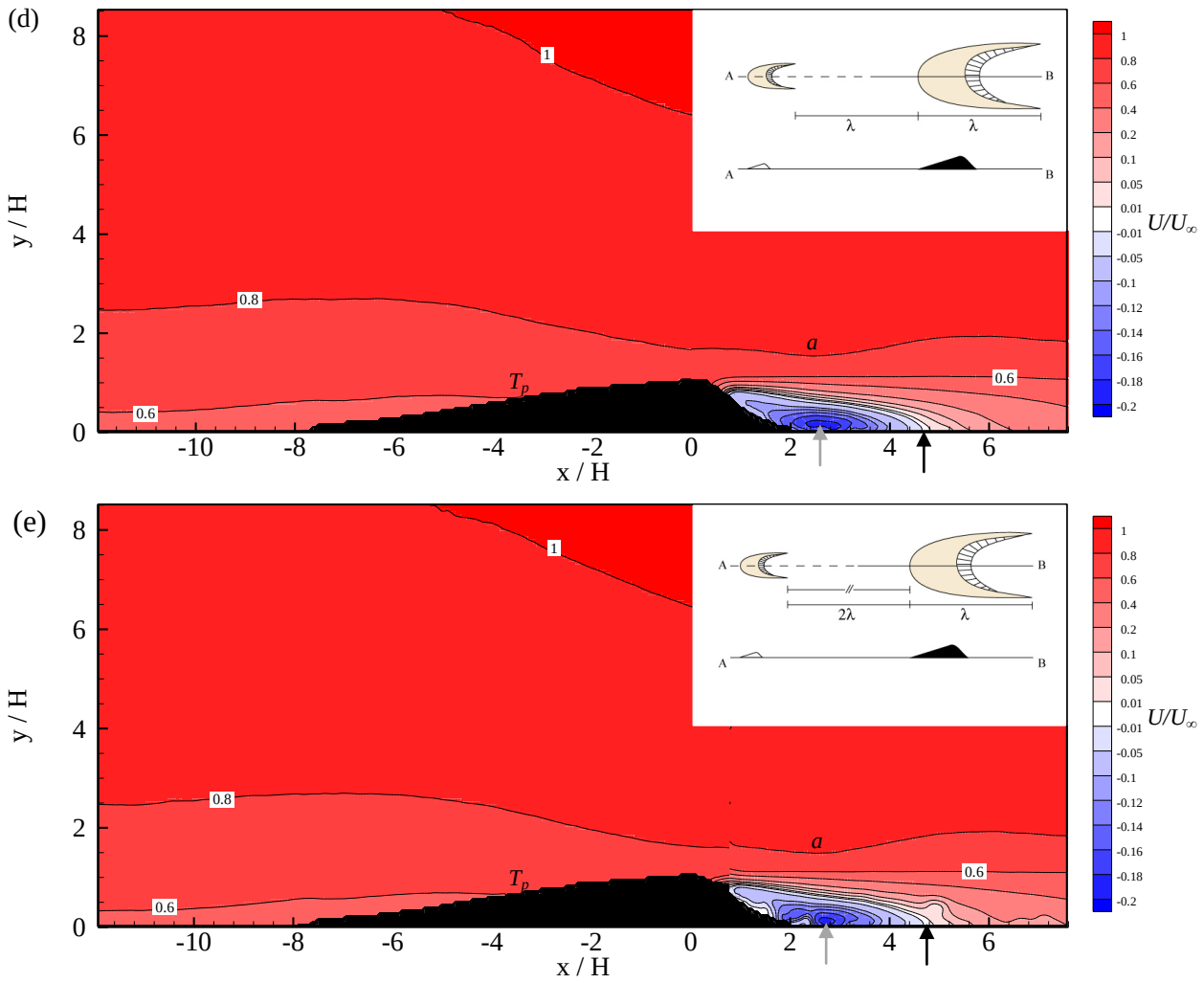

Figure 6.46: The U/U_∞ velocity field for the AC volumetric ratio: (a) Isolated condition (*Re*=59,806); (b) 0λ condition (*Re*=58,347); (c) 0.5λ condition (*Re*=57,389); (d) 1λ condition; (*Re*=57,075); (e) 2λ condition (*Re*=57,907). The black triangular object represents the dune profile. The upper right schematic featured in the plot depicts the experimental condition from a plan view and profile view. The contour plot refers to the ensemble average of the streamwise velocity component: red indicates downstream flow direction, blue upstream downward flow motion, and white indicates zero velocity. The gray arrow indicates the maximum upstream velocity in the separation bubble. The black arrow indicates the flow reattachment point. The maximum velocity region is labeled '*a'*. The 0.6 contour line termination point is labeled 'T_p'.

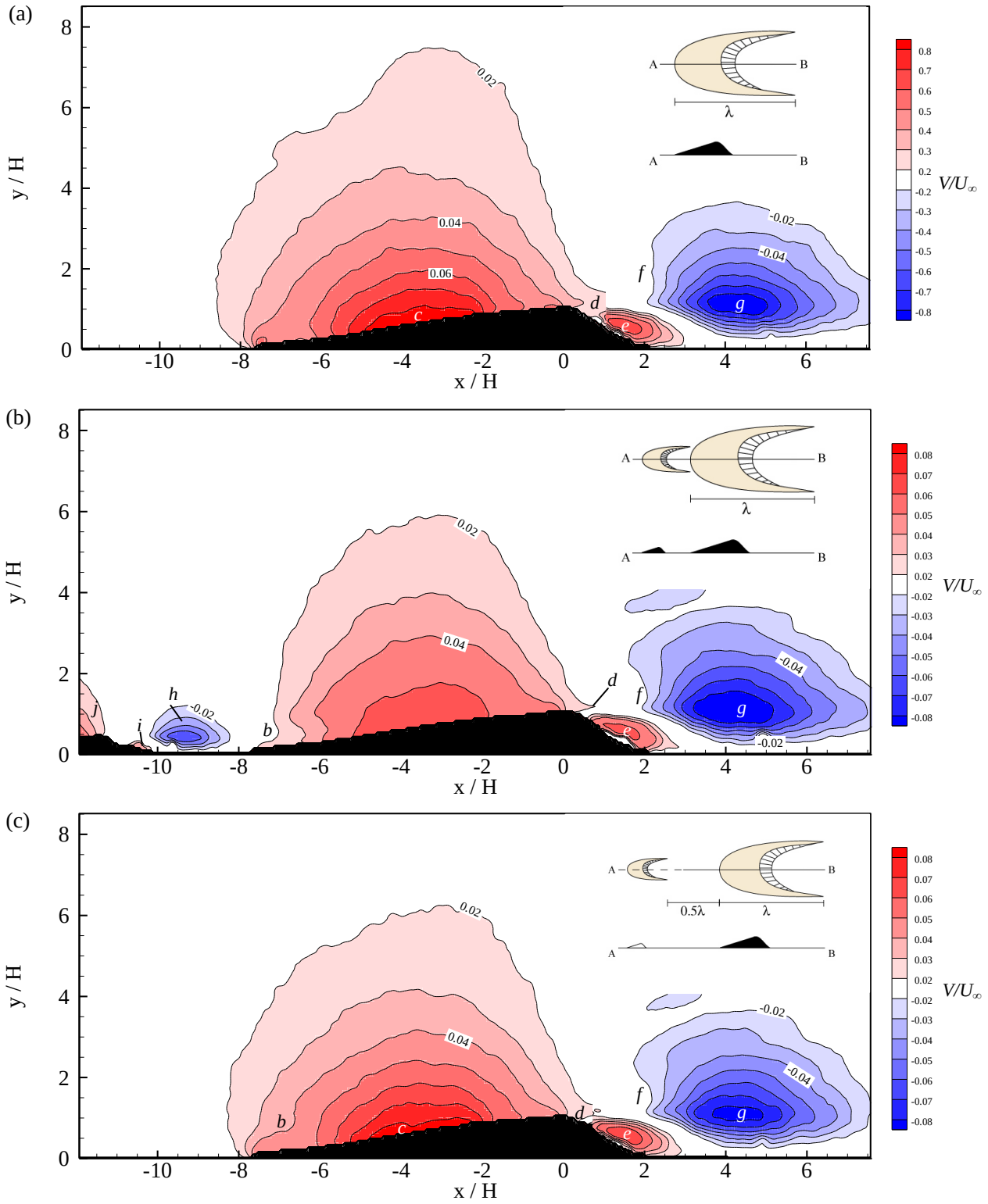

Figure 6.47 (continued on next page)

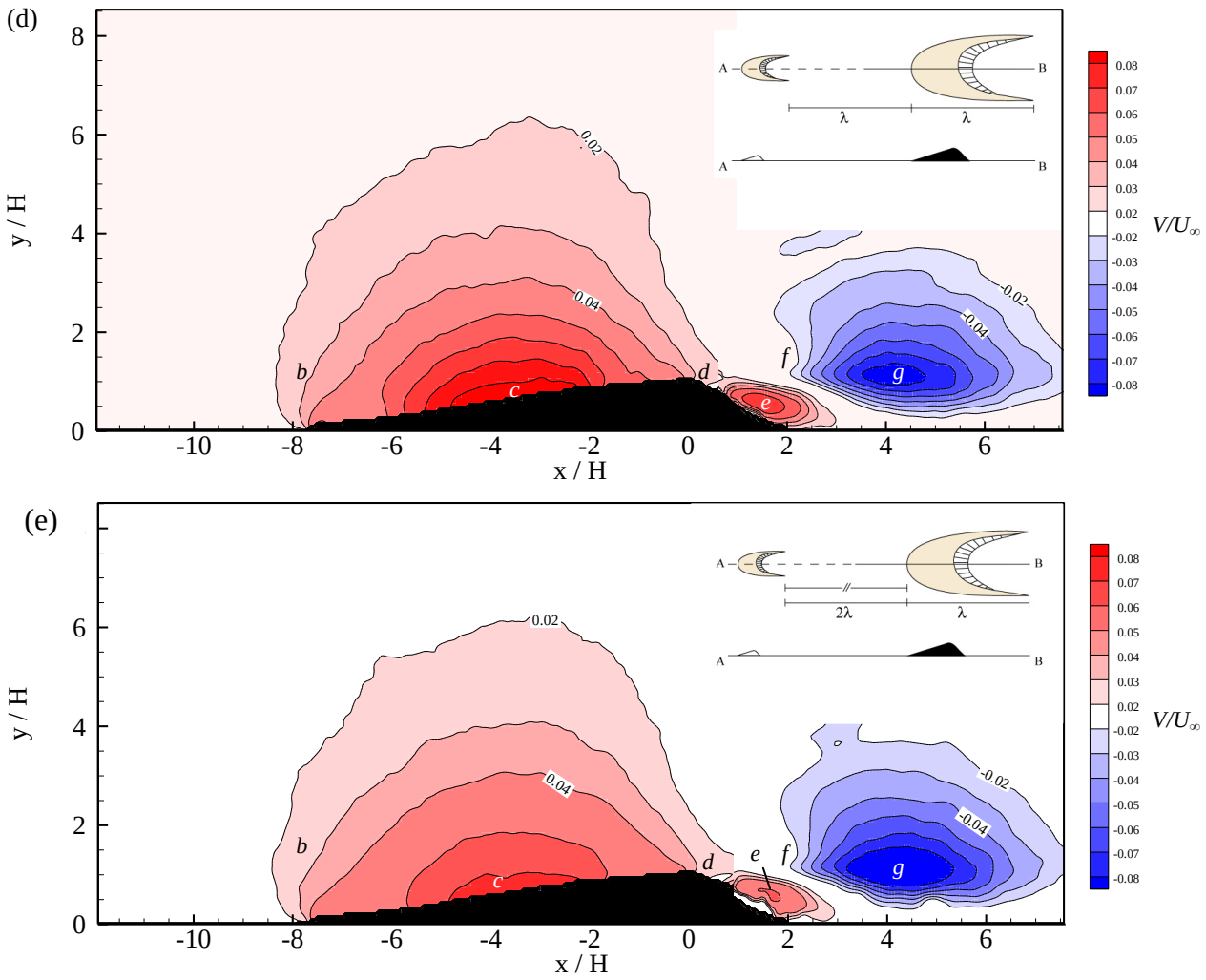

Figure 6.47: The V/U_∞ velocity field for the AC volumetric ratio: (a) Isolated condition (*Re*=59,806); (b) 0λ condition (*Re*=58,347); (c) 0.5λ condition (*Re*=57,389); (d) 1λ condition; (*Re*=57,075); (e) 2λ condition (*Re*=57,907). The black triangular object represents the dune profile. The upper right schematic featured in the plot depicts the experimental condition from a plan view and profile view. The contour plot refers to the ensemble average of the wall-normal velocity component: red indicates upward flow direction, blue indicates downward flow direction and white indicates zero velocity. The flow features referred to in the text are identified with labels *b-j*: *b* – contour inflection; *c* – maximum velocity zone; *d* – crestal jet; *e* – upwelling zone; *f* – contour inflection; *g* – expansion zone; *h* – UBD expansion zone; *i* – UBD upwelling zone; *j* – UBD topographic forcing zone.

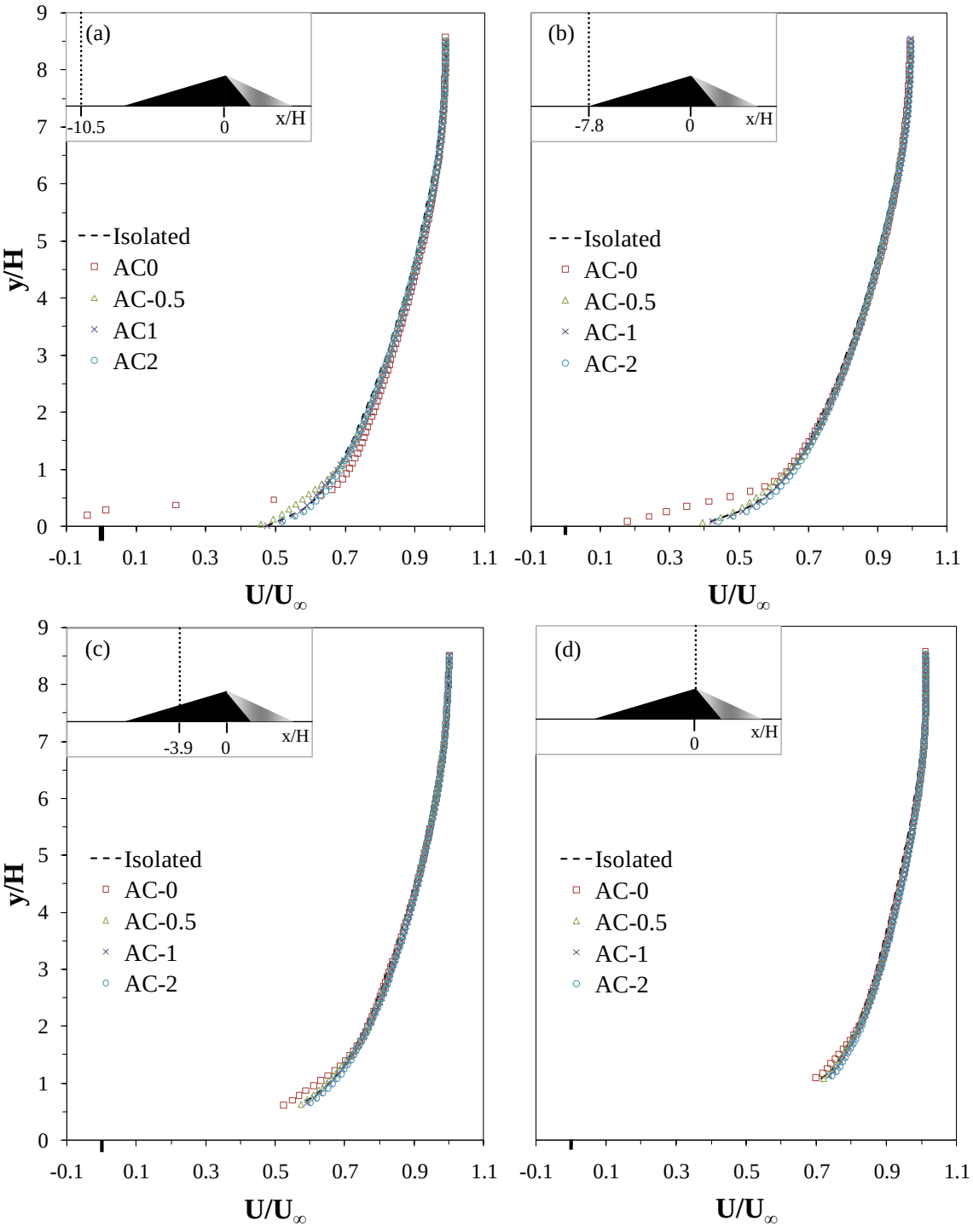

Figure 6.48: Vertical profiles of the streamwise velocity component, U/U_∞, on the stoss-side of the DBD: (a) x/H=-10.5; (b) x/H=-7.8; (c) x/H=-3.9; (d) x/H=0.

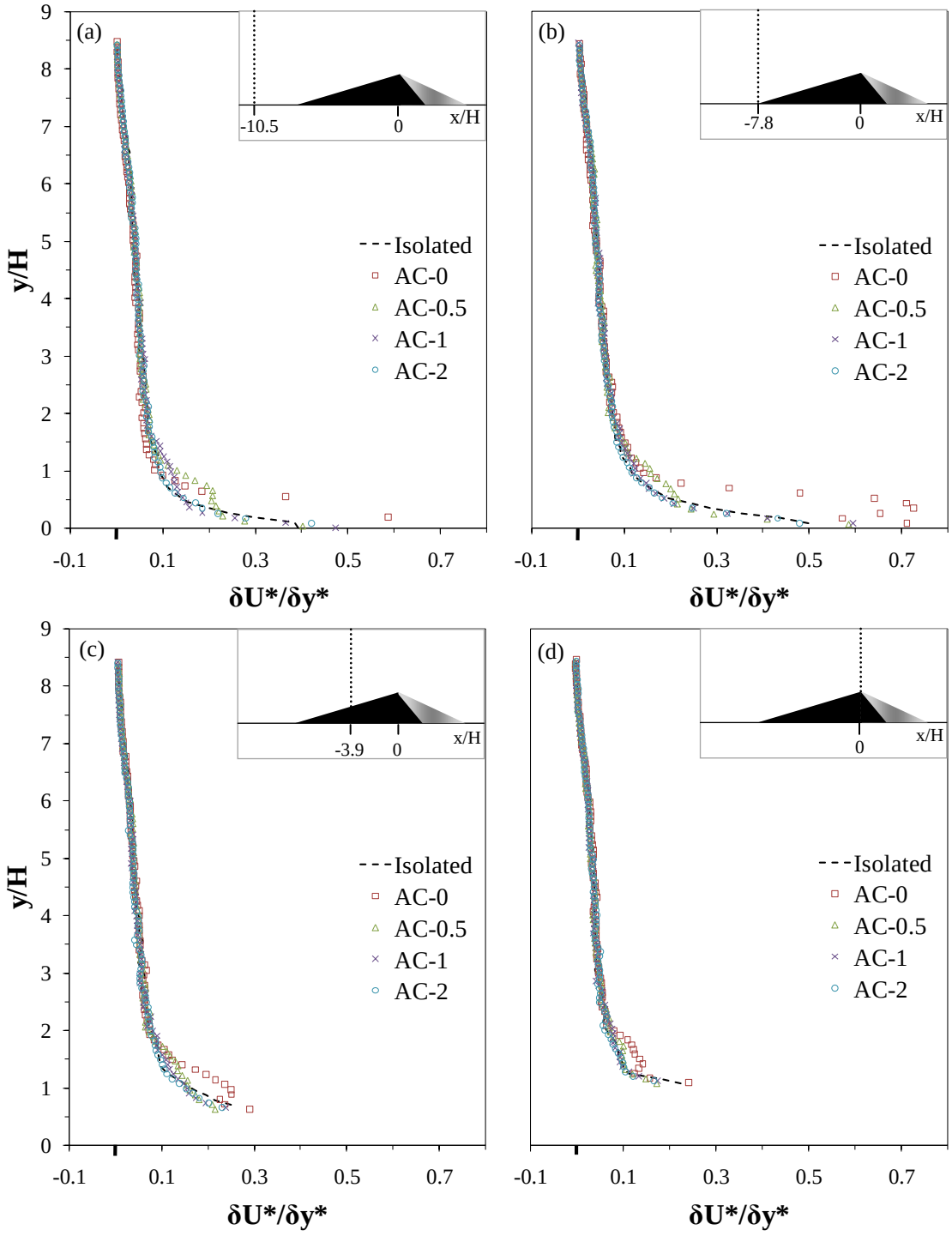

Figure 6.49: Vertical profiles of the streamwise velocity gradient, $\delta U^*/\delta y^*$, on the stoss-side of the DBD: (a) x/H=-10.5; (b) x/H=-7.8; (c) x/H=-3.9; (d) x/H=0.

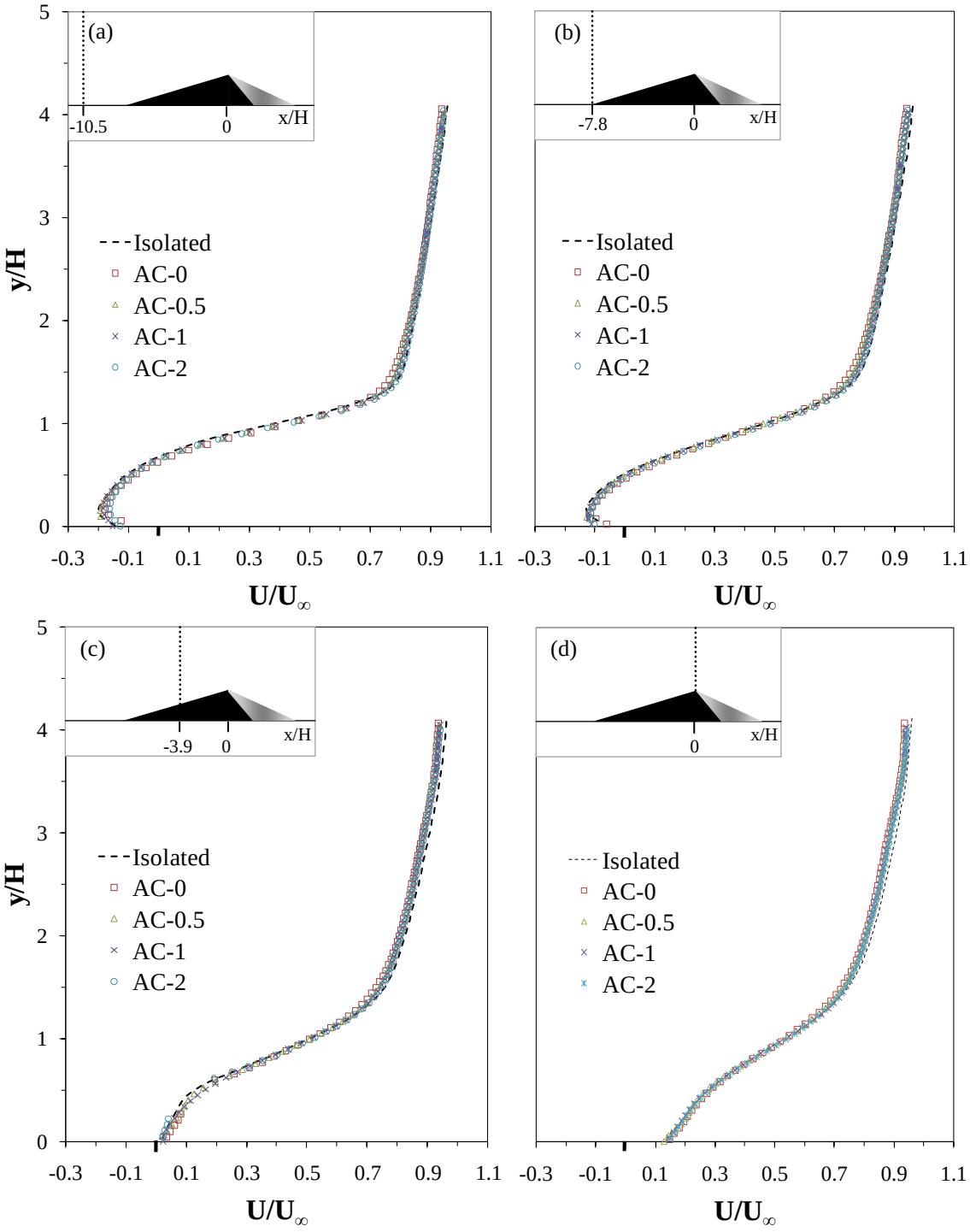

Figure 6.50: Vertical profiles of the streamwise velocity component, U/U_∞, on the lee-side of the DBD: (a) x/H=2.5; (b) x/H=3.75; (c) x/H=5; (d) x/H=6.

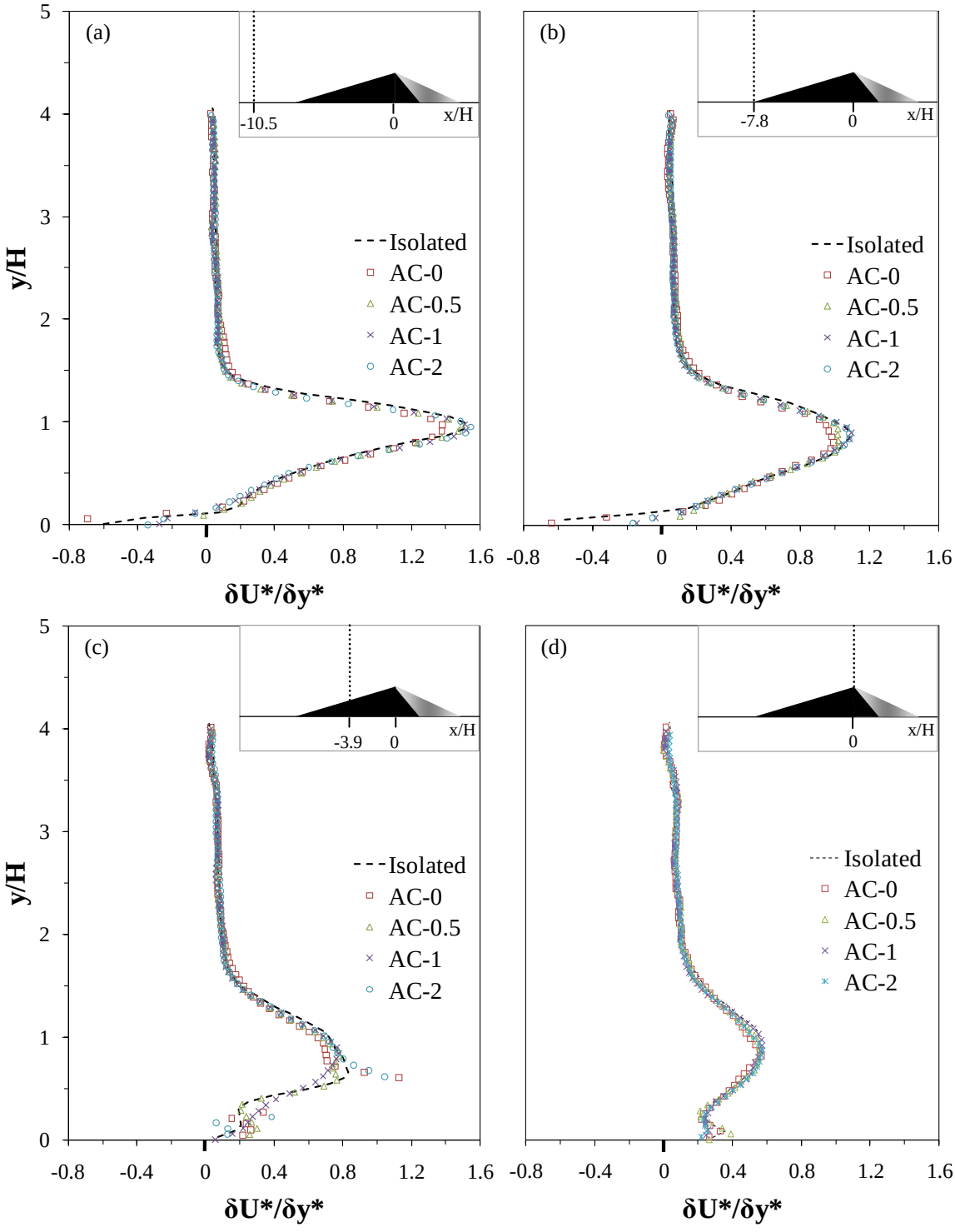

Figure 6.51: Vertical profiles of the streamwise velocity gradient, $\delta U^*/\delta y^*$, on the lee-side of the DBD: (a) x/H=2.5; (b) x/H=3.75; (c) x/H=5; (d) x/H=6.

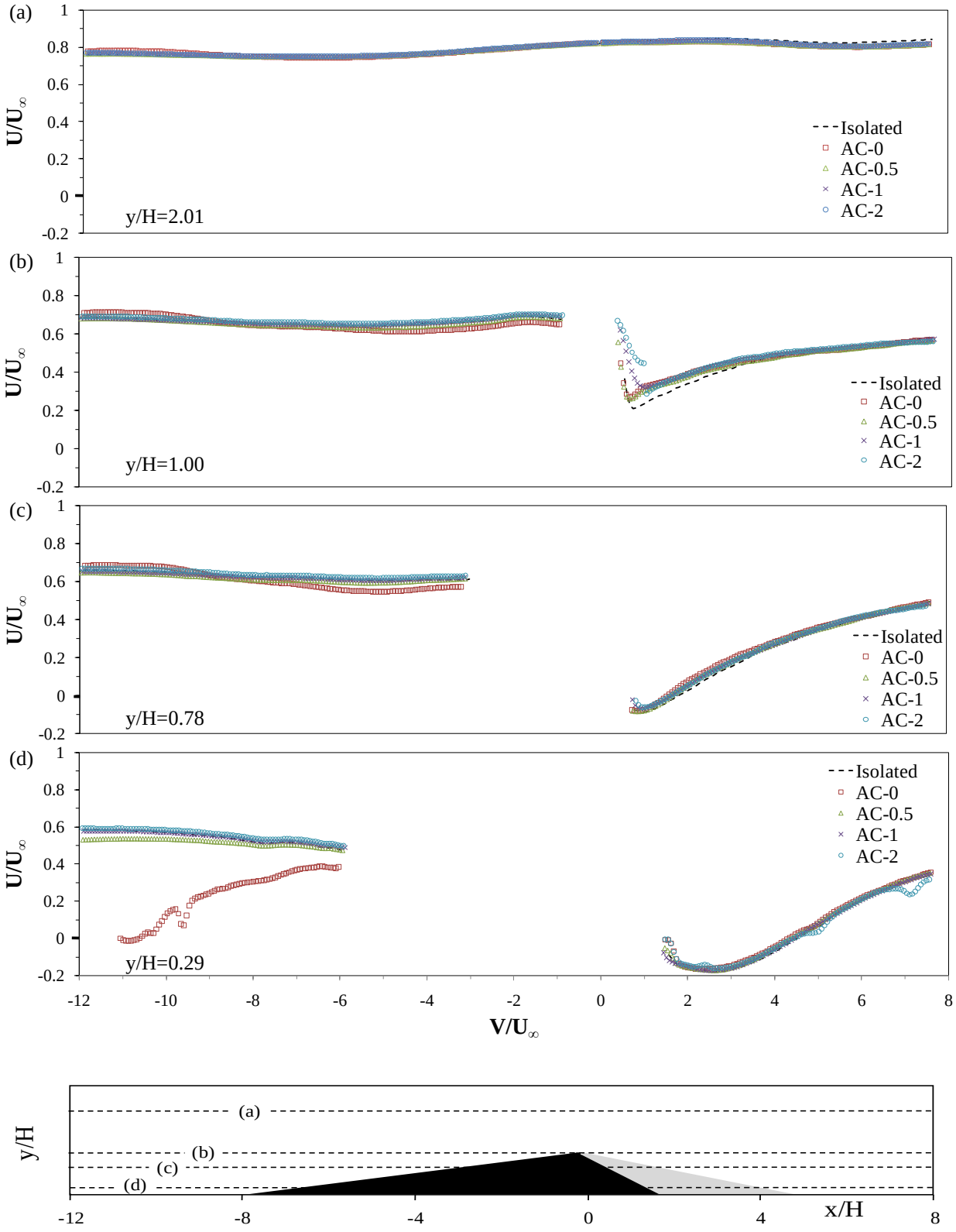

Figure 6.52: Horizontal profile of the streamwise velocity component, U/U_∞: (a) y/H=2.01.; (b) y/H=1.00; (c) y/H=0.78; (d) y/H=0.29.

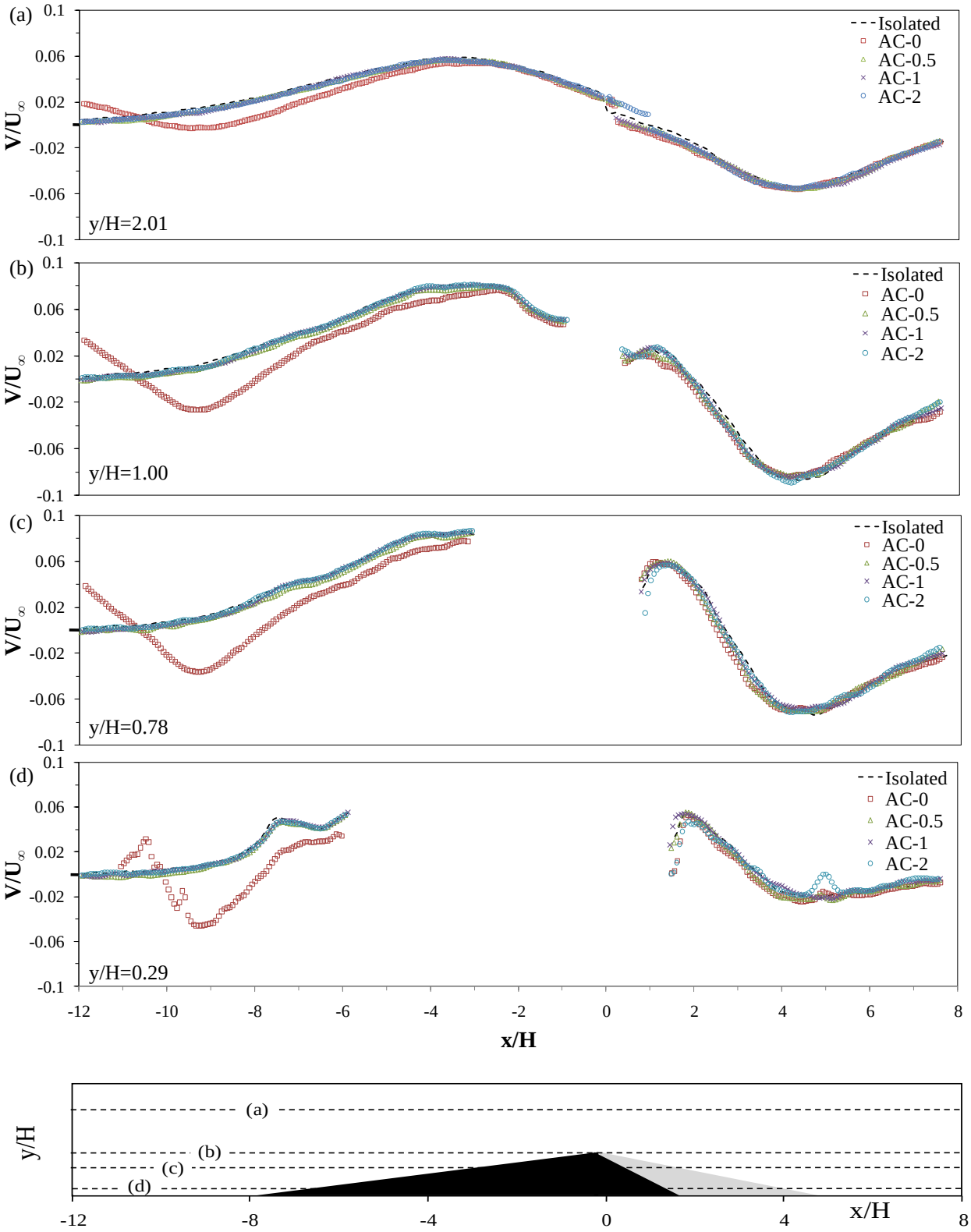

Figure 6.53: Horizontal profile of the wall-normal velocity component, V/U_∞: (a) y/H=2.01.; (b) y/H=1.00; (c) y/H=0.78; (d) y/H=0.29.

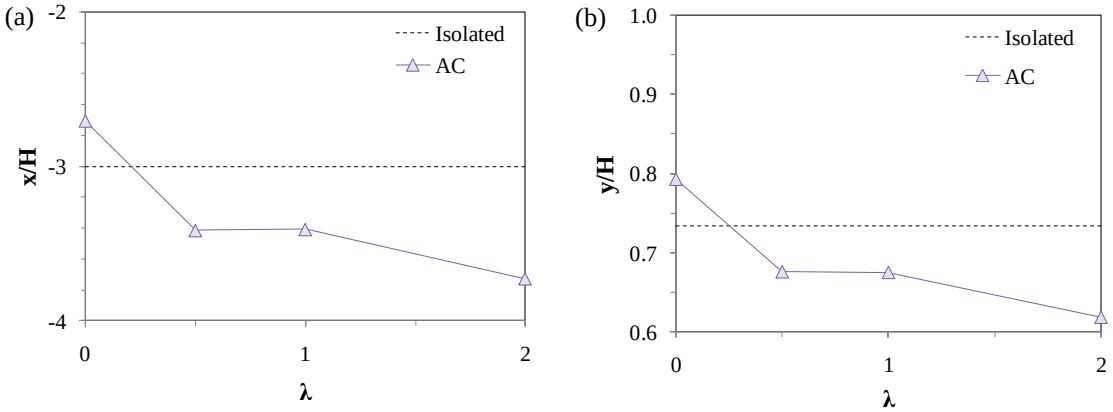

Figure 6.54: The location of the 0.6 U/U contour line termination point along the stoss-slope of the DBD with increasing λ: (a) the horizontal position (x/H); (b) the vertical position (y/H). Labeled 'T_p' in Figure 6.41.

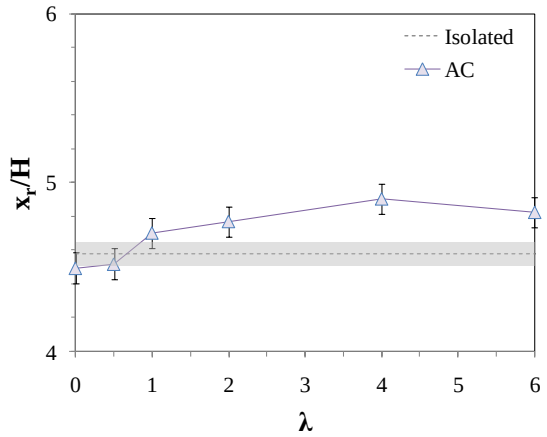

Figure 6.55: The reattachment length x_r of volumetric ratio AC and the isolated dune, with error bars.

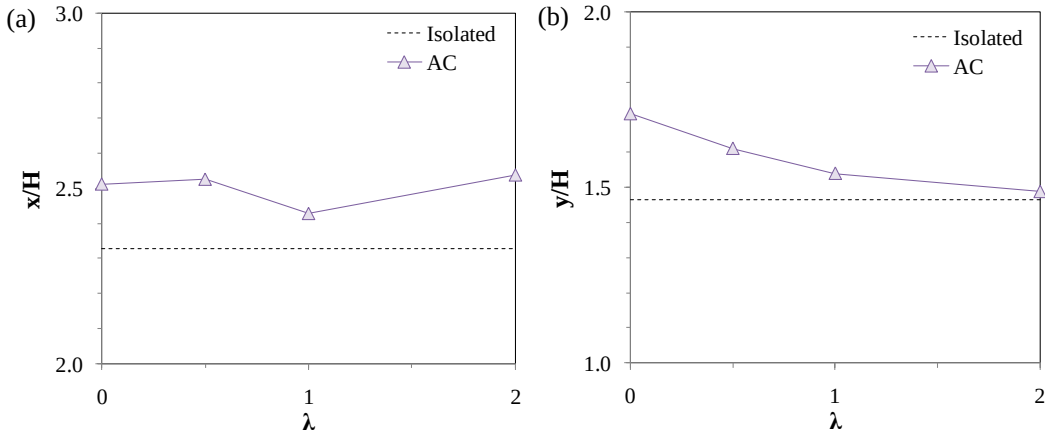

Figure 6.56: The maximum velocity zone position, determined by the location of the 0.8 contour line minima in the streamwise velocity U/U_∞ component contour map in Figure 6.46: (a) the horizontal position *x/H*; (b) the vertical position *y/H*.

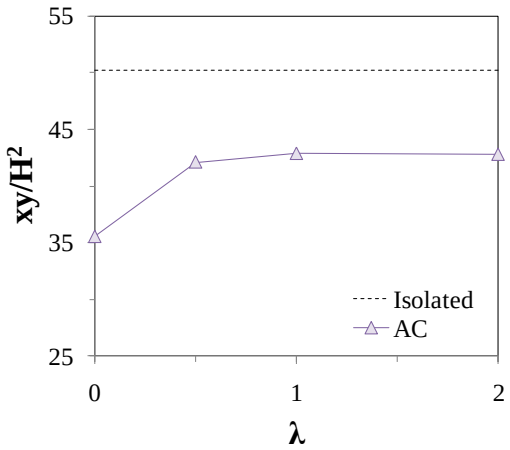

Figure 6.57: The topographic forcing zone area on the stoss-side of the DBD.

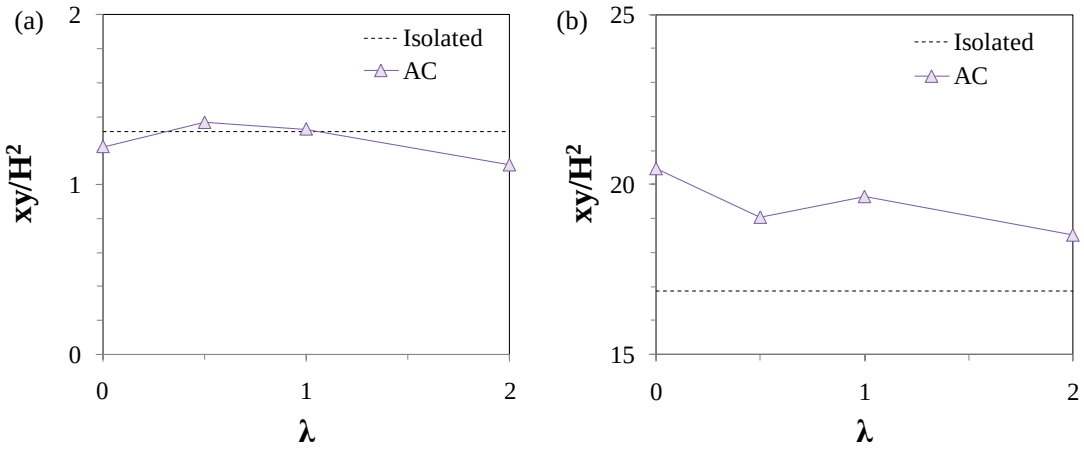

Figure 6.58:The area with increasing λ of (a) the upwelling zone and (b) the expansion zone. The expansion zone extends beyond the field of view, so the complete area is unknown. The area that is provided is the area of the expansion zone that is visible.

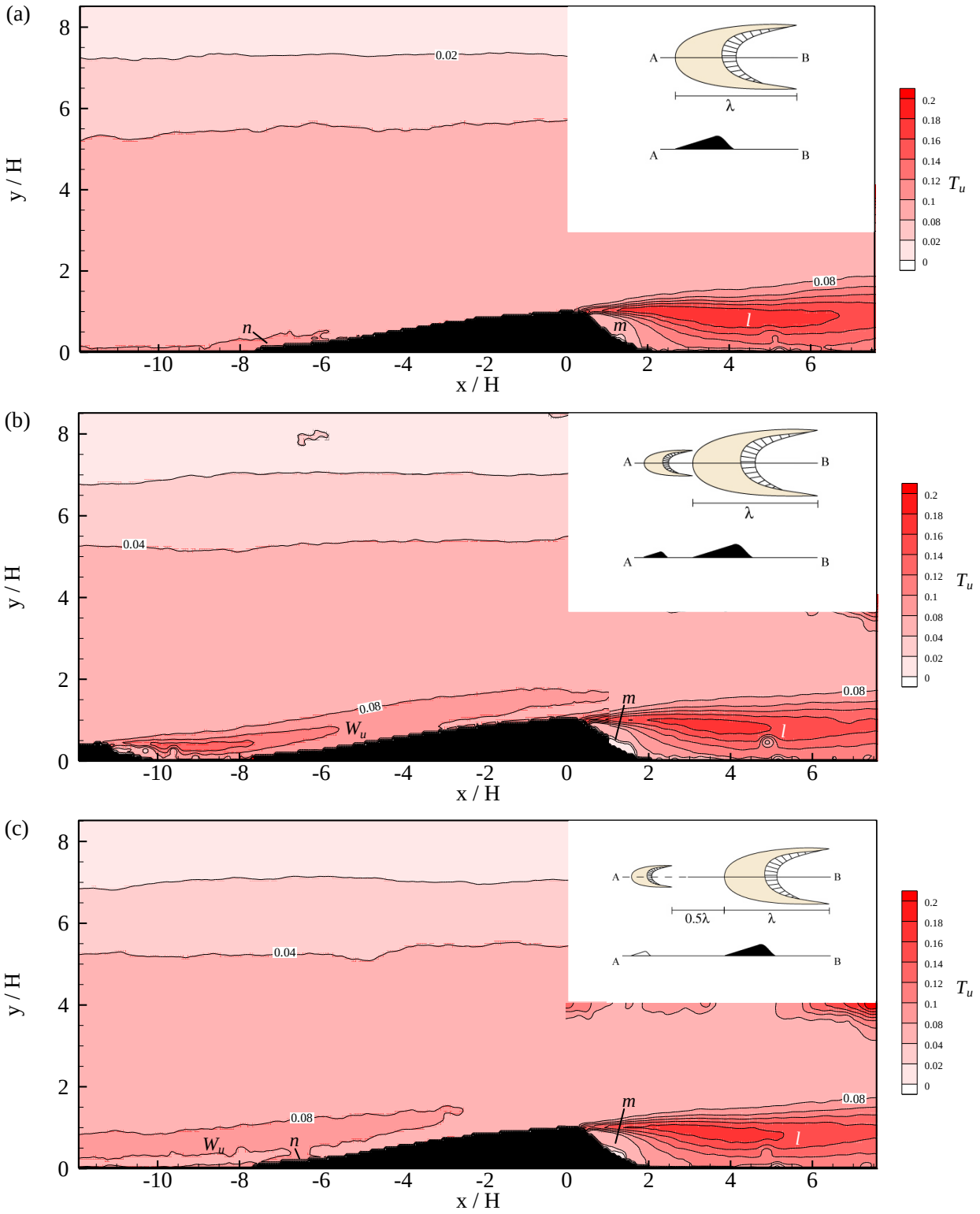

Figure 6.59 (continued on next page)

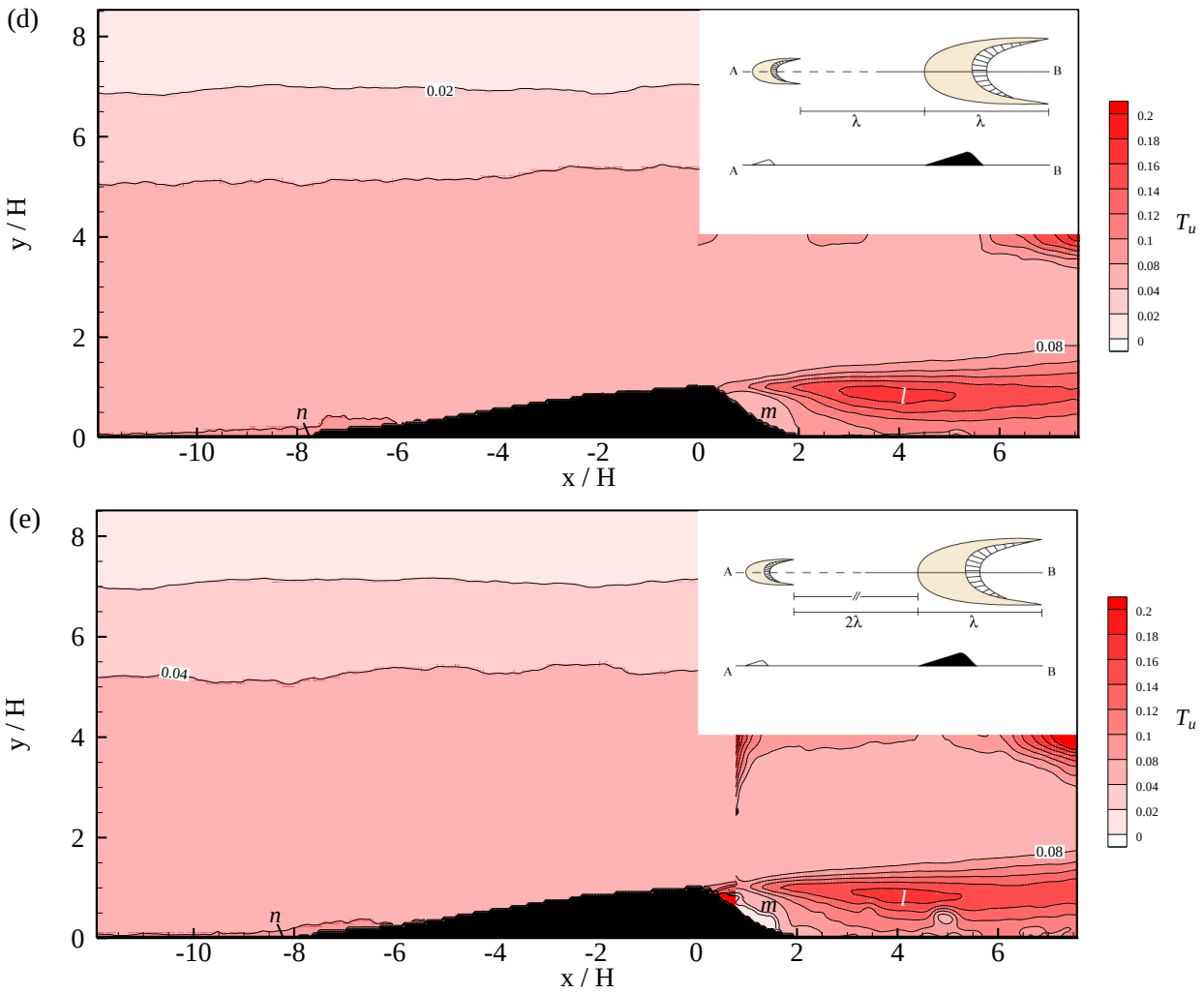

Figure 6.59: Contour maps of the streamwise component of the turbulence intensity ($\sqrt{u'^2}/U_\infty$) for the volumetric ratio AC: (a) isolated dune condition; (b) 0λ spacing; (c) 0.5λ spacing; (d) 1λ spacing; (e) 2λ spacing. On the stoss-side, the area of high T_u extending from the UBD is labeled 'w_u' while the high T_u at the DBD toe is labeled 'n'. On the leeside, the area of high T_u is labeled 'l' while the area of low T_u is labeled 'm'.

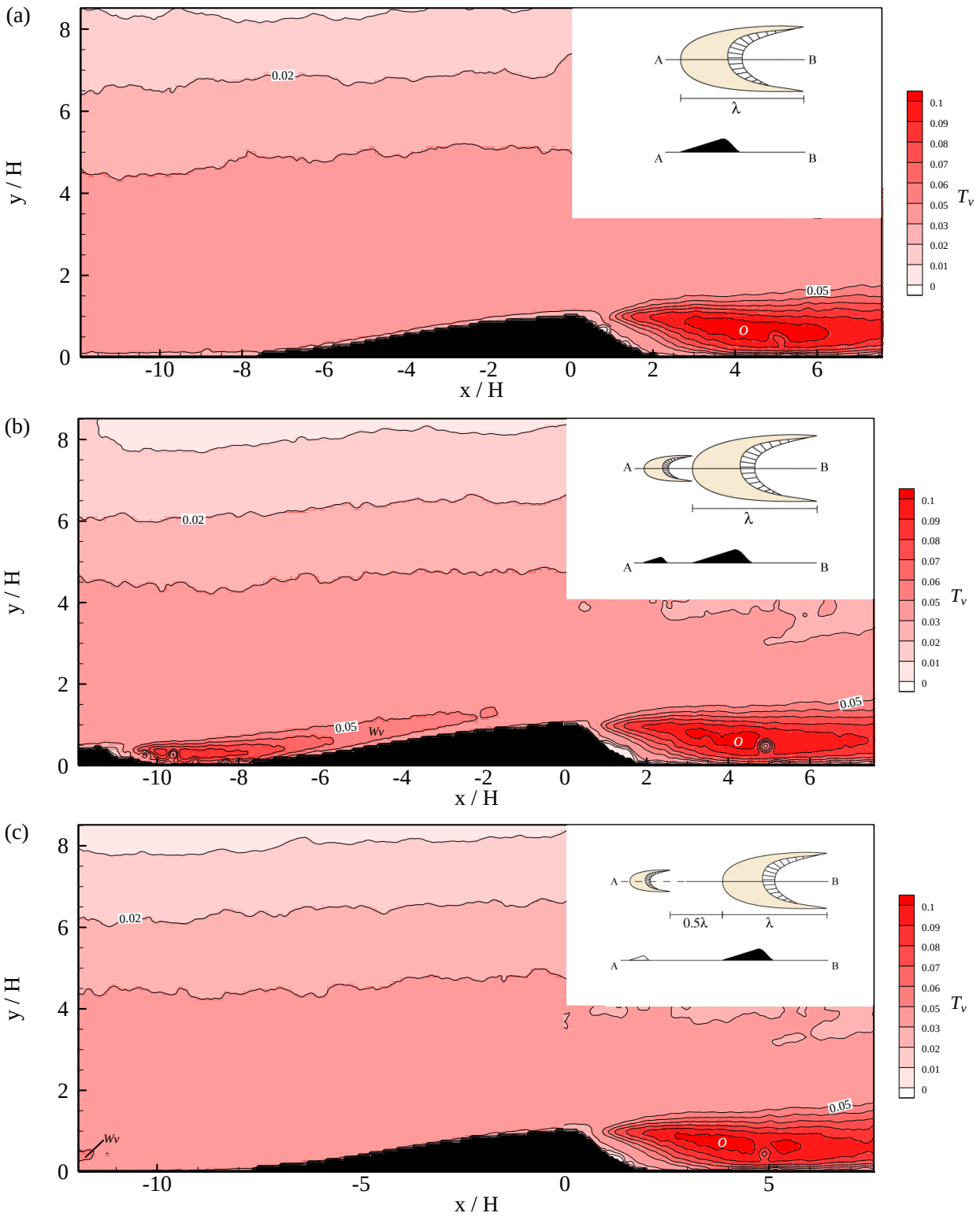

Figure 6.60 (continued on next page)

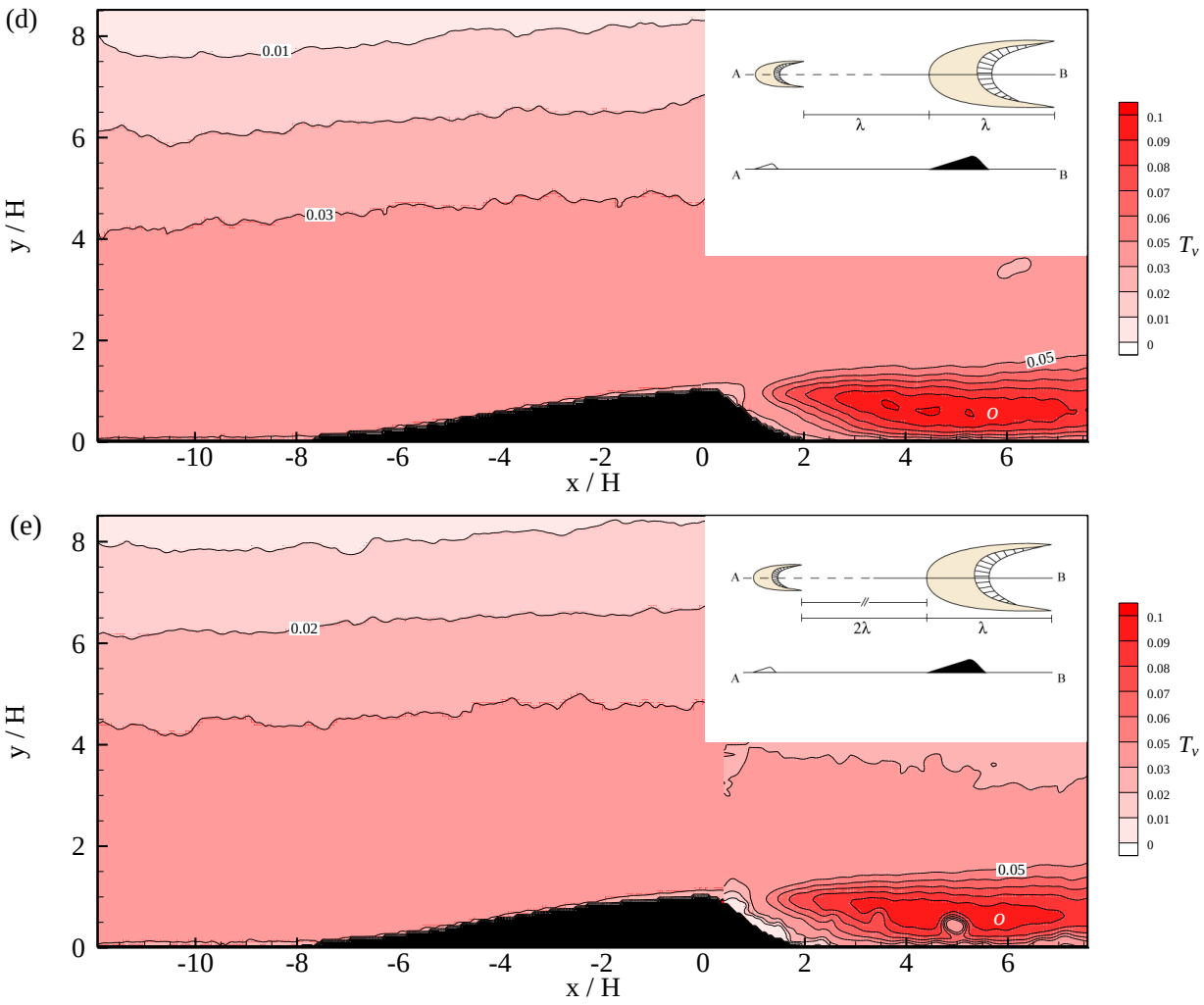

Figure 6.60: Contour maps of the wall-normal component of the turbulence intensity ($\sqrt{v'^2}/U_\infty$) for the volumetric ratio AC: (a) isolated dune condition; (b) 0λ spacing; (c) 0.5λ spacing; (d) 1λ spacing; (e) 2λ spacing. On the stoss-side, the area of high T_v extending from the UBD is labeled 'w_v'. On the leeside, the area of high T_v is labeled 'o'.

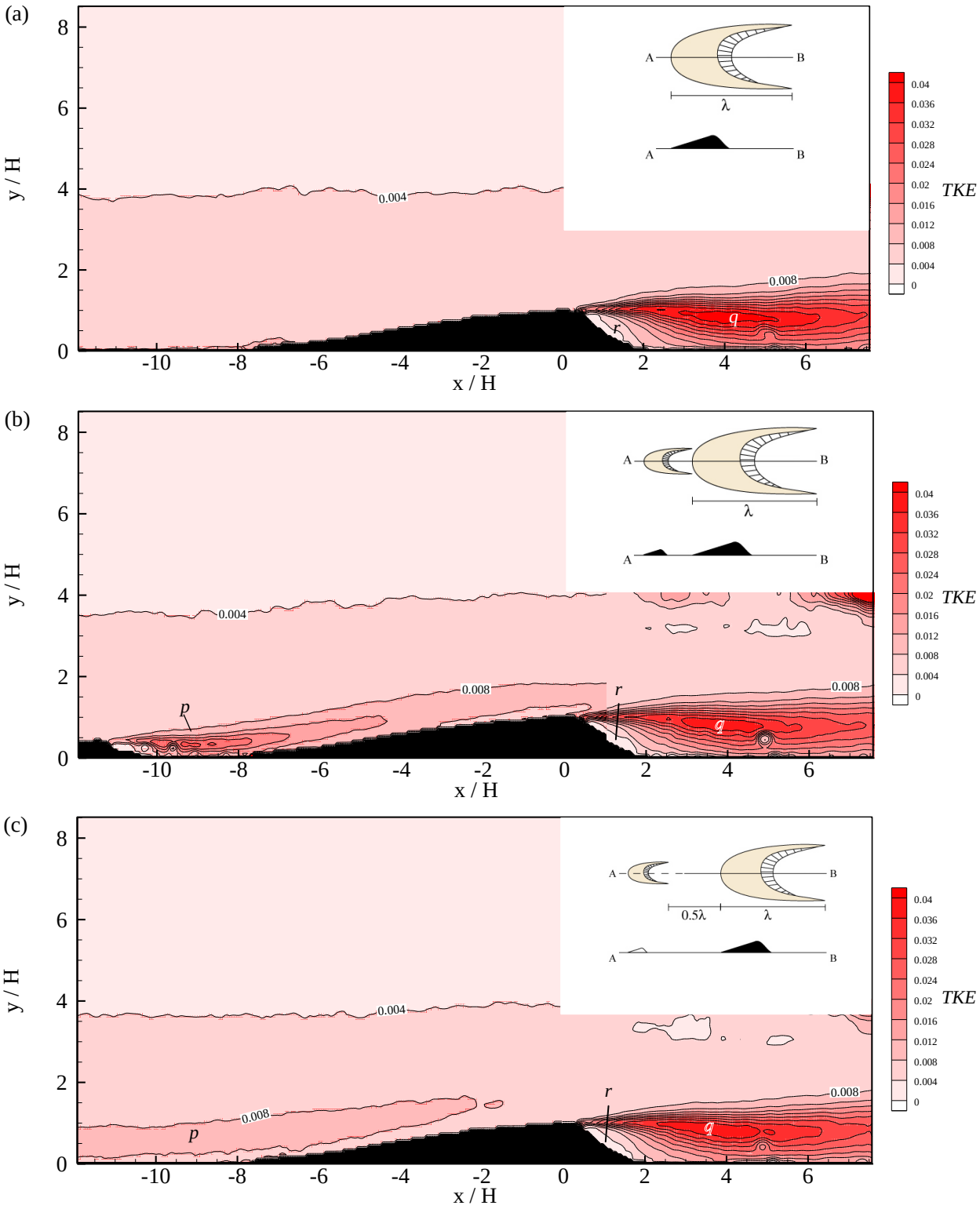

Figure 6.61 (continued on next page)

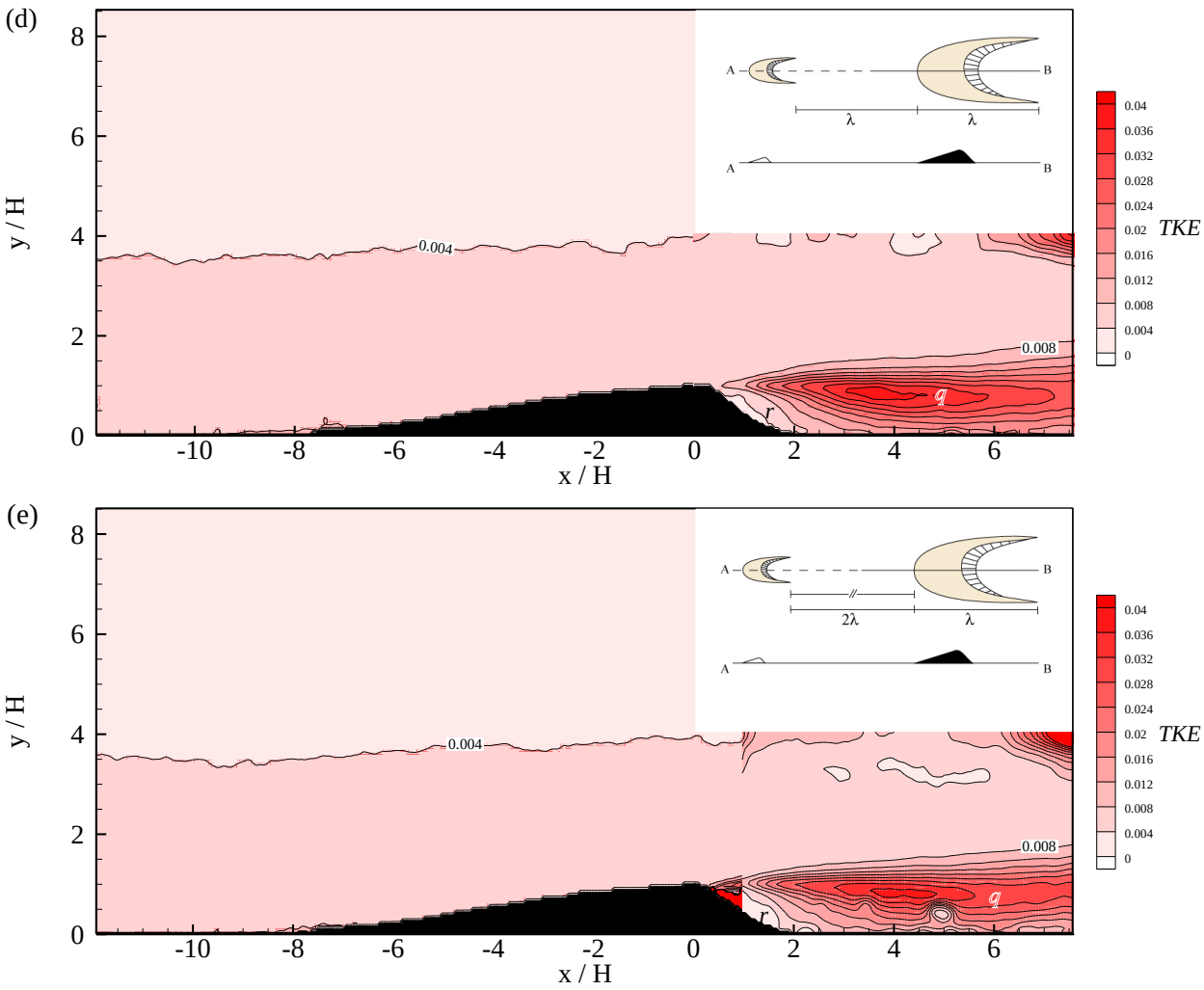

Figure 6.61: Contour maps of the mean turbulent kinetic energy *TKE* ($u'^2 + v'^2/U_\infty^2$) for the volumetric ratio AC: (a) isolated dune condition; (b) 0λ spacing; (c) 0.5λ spacing; (d) 1λ spacing; (e) 2λ spacing. On the stoss-side, the area of high *TKE* extending from the UBD is labeled 'p'. On the leeside, the area of high *TKE* is labeled 'q' and the area of low T_u is labeled 'r'.

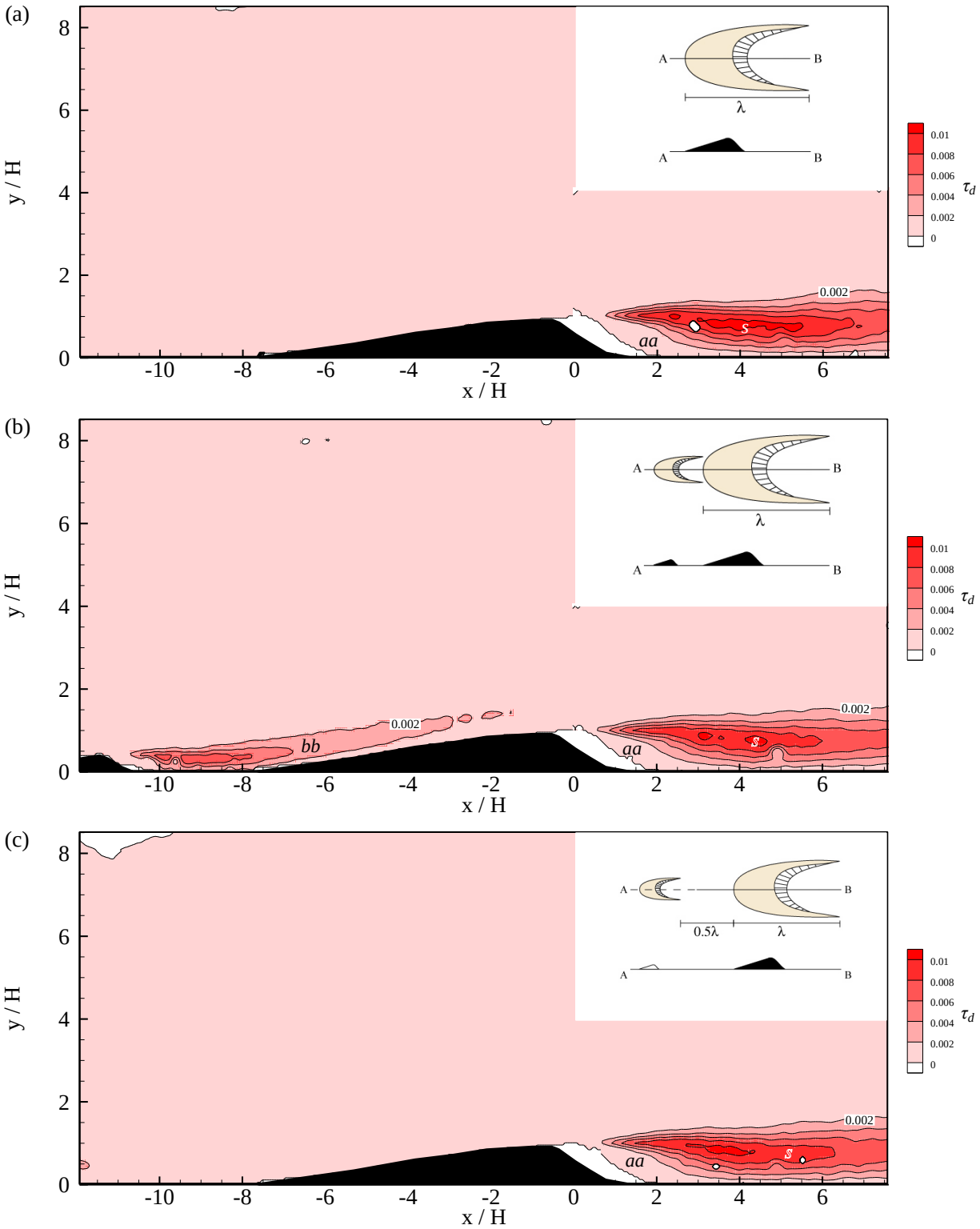

Figure 6.62 (continued on next page)

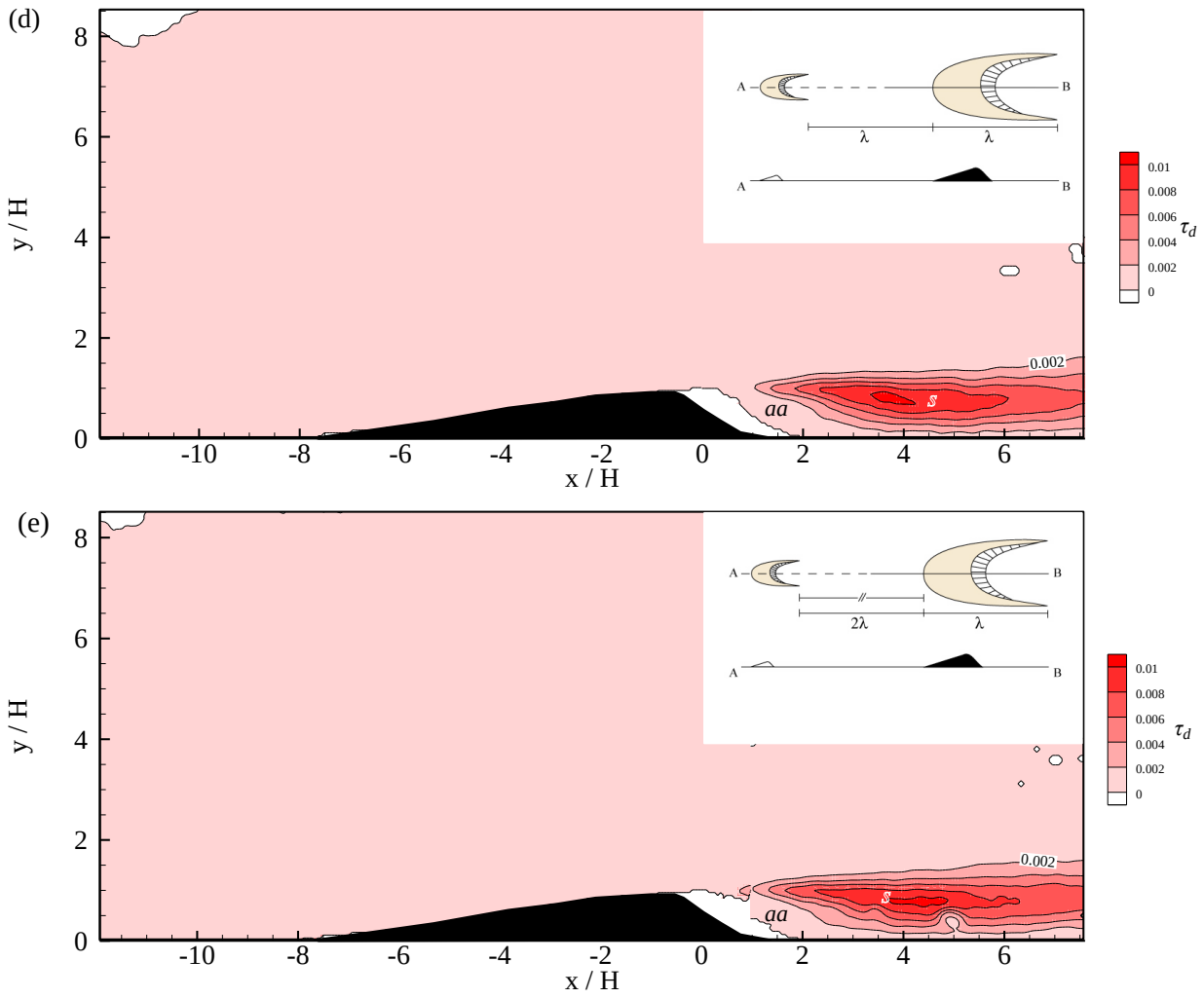

Figure 6.62: Contour maps of the Reynolds stress τ_d ($-\overline{u'v'}/U_\infty^2$) for the volumetric ratio AC: (a) isolated dune condition; (b) 0λ spacing; (c) 0.5λ spacing; (d) 1λ spacing; (e) 2λ spacing. On the stoss-side, the area of high τ_d extending from the UBD is labeled '*bb'*. On the leeside, the area of high τ_d is labeled '*s'* and the area of low τ_d is labeled '*aa'*.

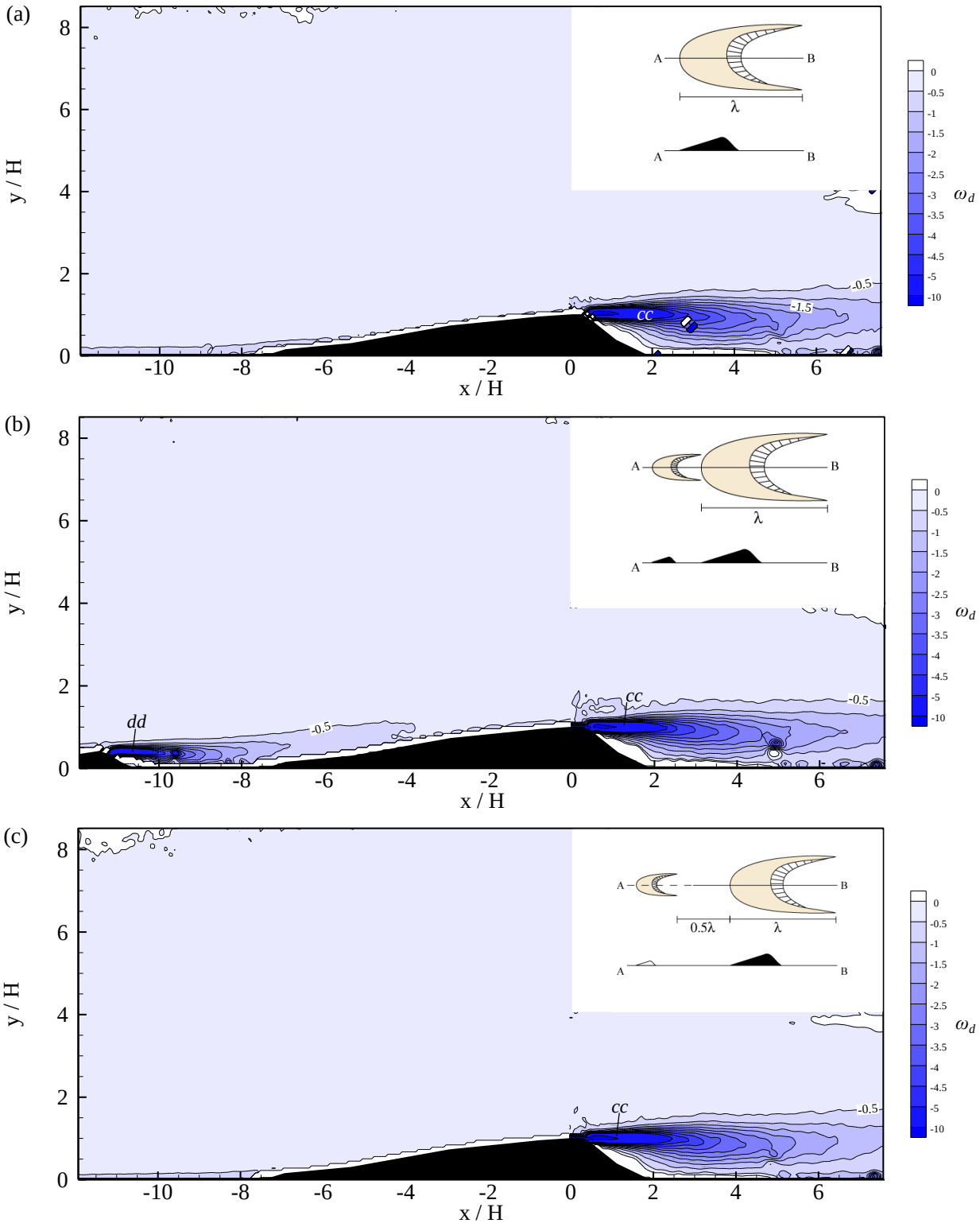

Figure 6.63 (continued on next page)

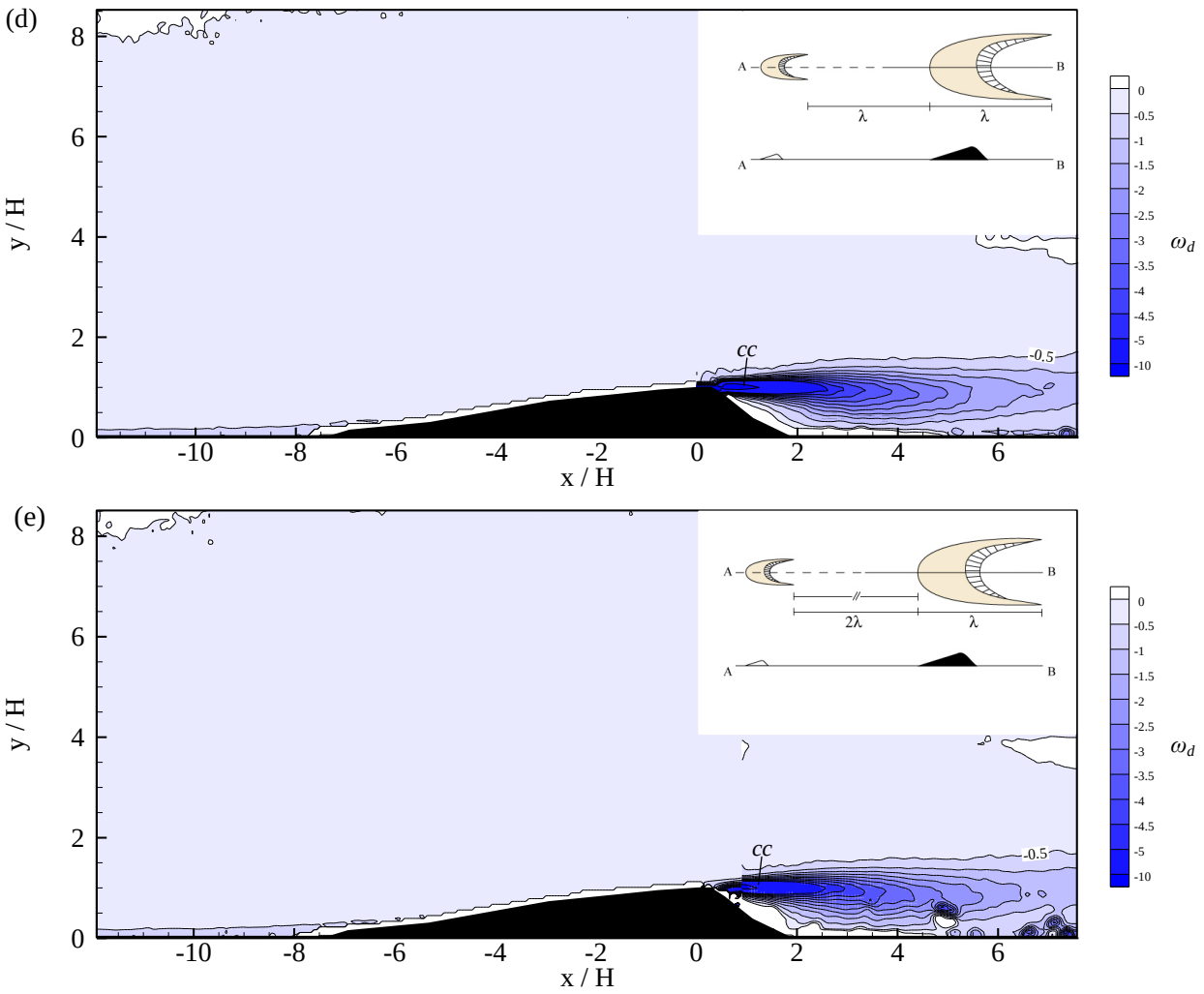

Figure 6.63: Contour maps of the vorticity ω_d for the volumetric ratio AC: (a) isolated dune condition; (b) 0λ spacing; (c) 0.5λ spacing; (d) 1λ spacing; (e) 2λ spacing. On the stoss-side, the area of high ω_d extending from the UBD is labeled '*dd'*. On the leeside, the area of high ω_d is labeled '*cc'*.

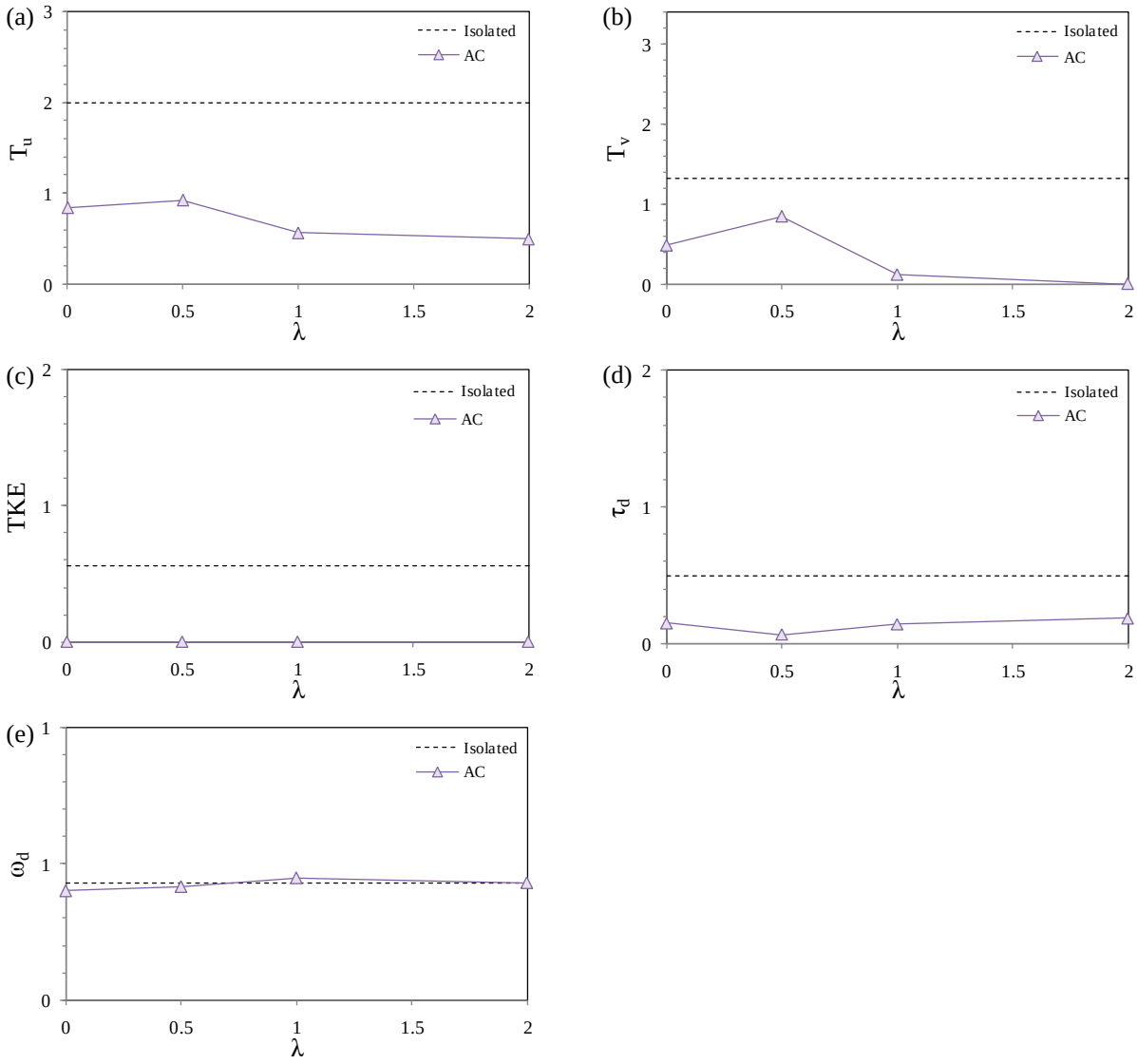

Figure 6.64: Comparison between the area of maximum T_u, T_v, *TKE*, τ_d, and ω_d between the isolated dune and volumetric ratio AC: (a) T_u – area of 0.16-0.2 contour; (b) T_v – area of 0.1 contour (c) *TKE* – area of 0.04 contour; (d) τ_d – area of 0.01 contour; (e) ω_d – area of -5 to -10 contour. The contour area is approximated using the area of an ellipse.

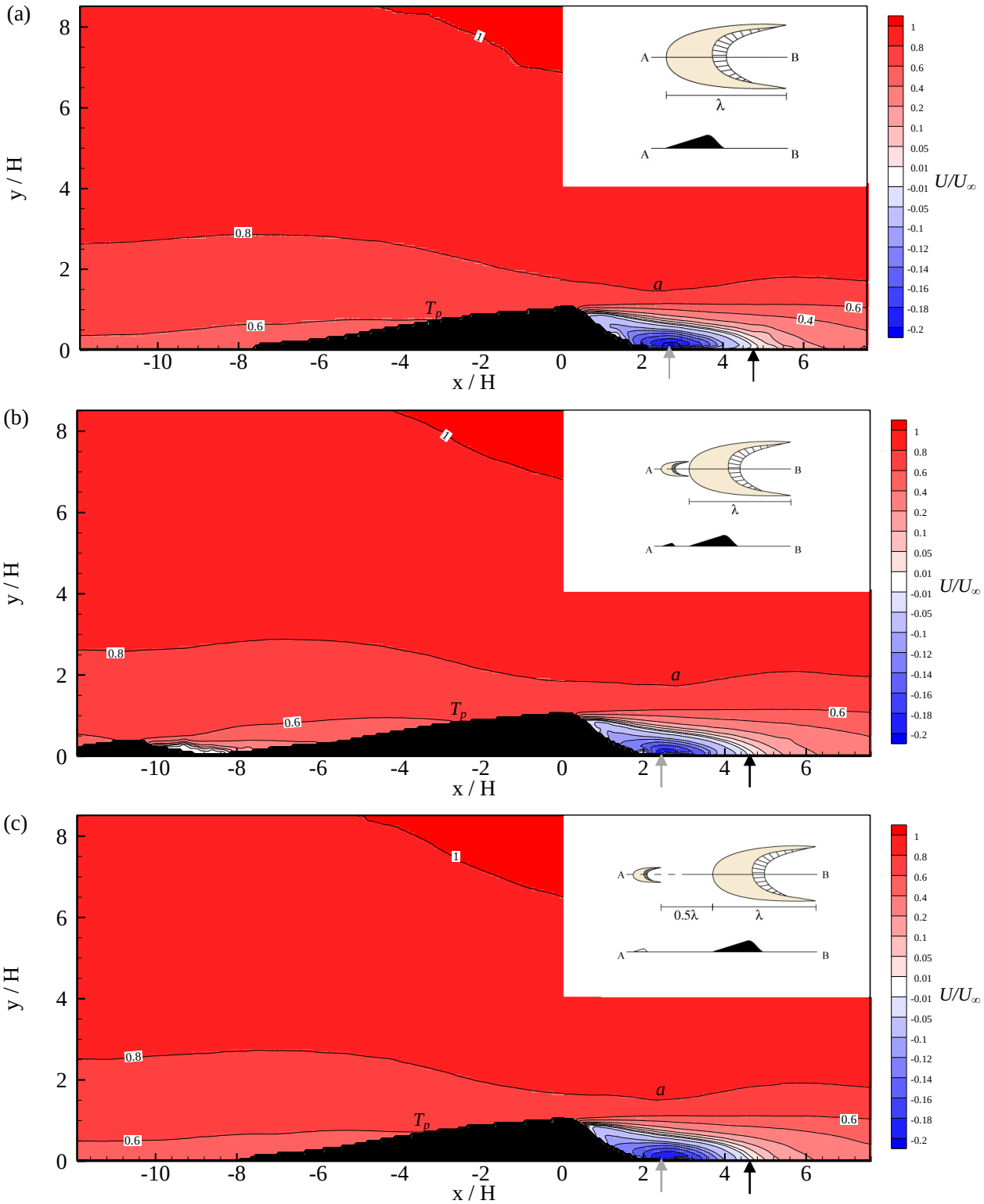

Figure 6.65 (continued on next page)

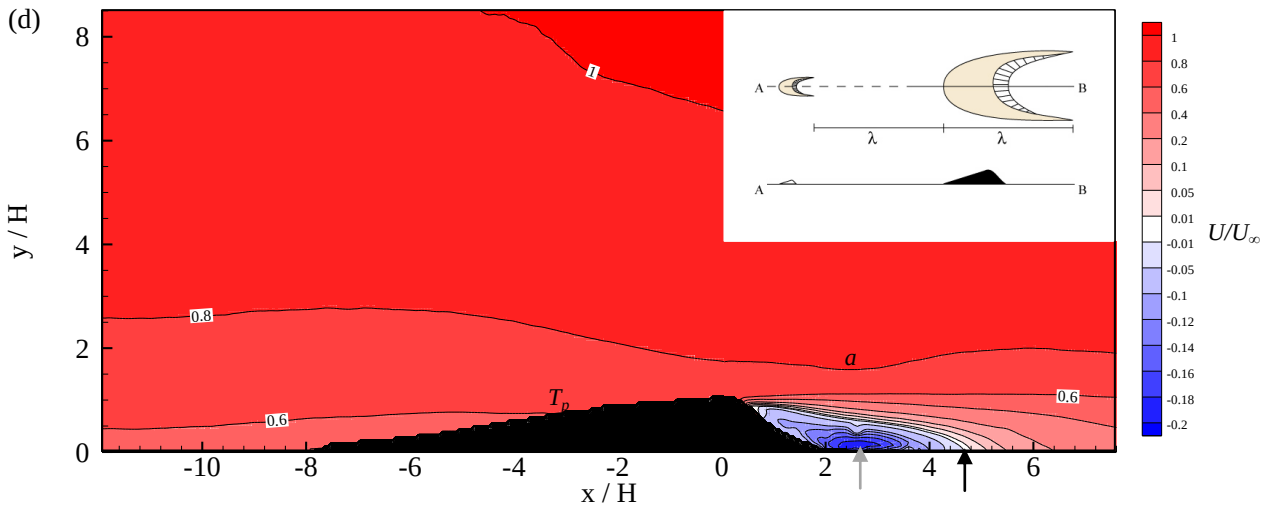

Figure 6.65: The U/U_∞ velocity field for the AD volumetric ratio: (a) Isolated condition (*Re*=59,806); (b) 0λ condition (*Re*=60,924); (c) 0.5λ condition (*Re*=57,942); (d) 1λ condition; (*Re*=58,408). The black triangular object represents the dune profile. The upper right schematic featured in the plot depicts the experimental condition from a plan view and profile view. The contour plot refers to the ensemble average of the streamwise velocity component: red indicates downstream flow direction, blue upstream downward flow motion, and white indicates zero velocity. The gray arrow indicates the maximum upstream velocity in the separation bubble. The black arrow indicates the flow reattachment point. The maximum velocity region is labeled '*a'*. The 0.6 contour line termination point is labeled 'T_p'.

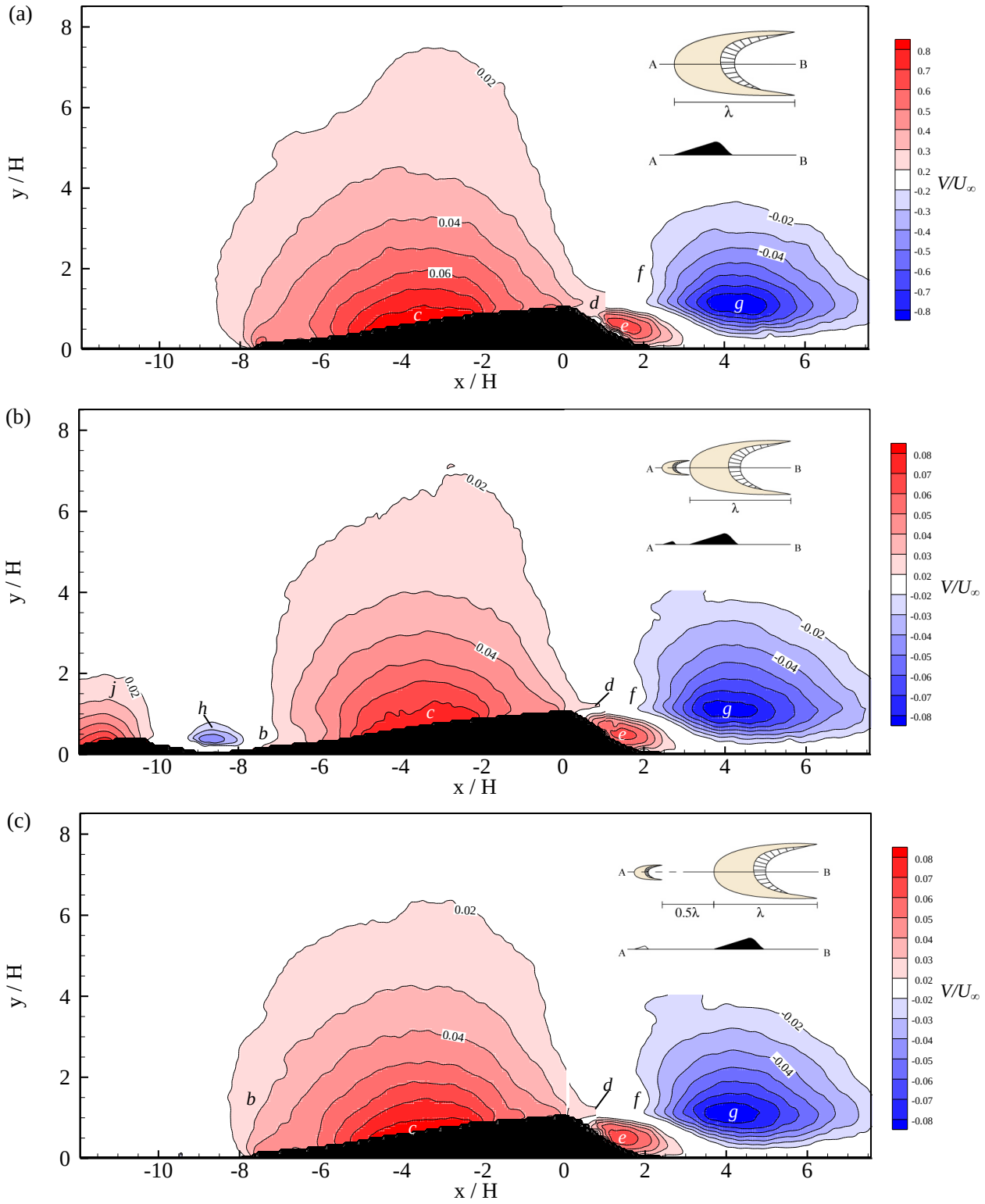

Figure 6.66 (continued on next page)

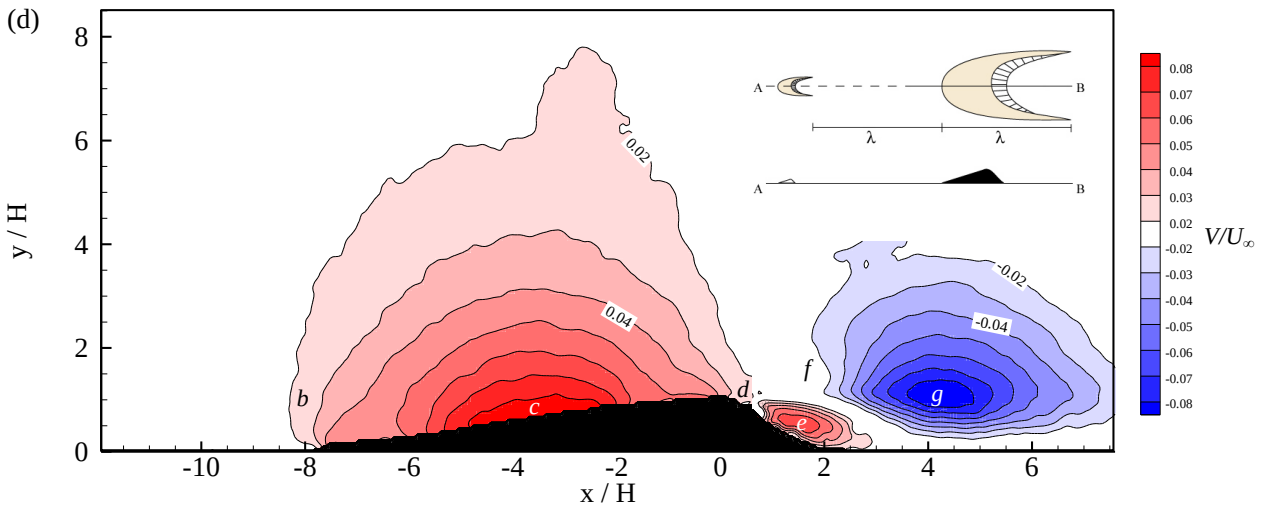

Figure 6.66: The V/U_∞ velocity field for the AD volumetric ratio: (a) Isolated condition (*Re*=59,806); (b) 0λ condition (*Re*=60,924); (c) 0.5λ condition (*Re*=57,942); (d) 1λ condition; (*Re*=58,408). The black triangular object represents the dune profile. The upper right schematic featured in the plot depicts the experimental condition from a plan view and profile view. The contour plot refers to the ensemble average of the wall-normal velocity: red indicates upward flow direction, blue indicates downward flow direction and white indicates zero velocity. The flow features referred to in the text are identified with labels *b-j*: *b* – contour inflection; *c* – maximum velocity zone; *d* – crestal jet; *e* – upwelling zone; *f* – contour inflection; *g* – expansion zone; *h* – UBD expansion zone; *i* – UBD upwelling zone; *j* – UBD topographic forcing zone.

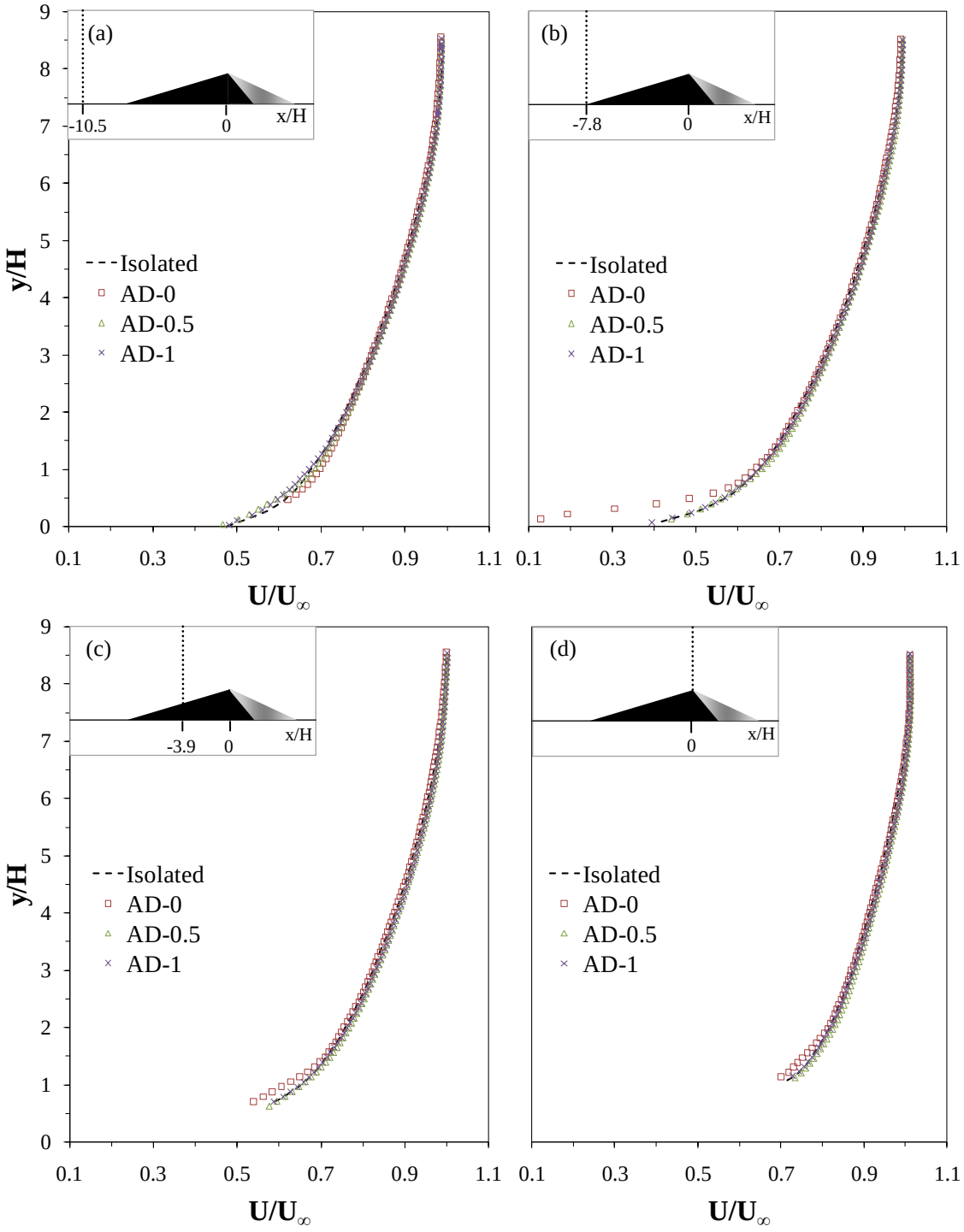

Figure 6.67: Vertical profiles of the streamwise velocity component, U/U_∞, on the stoss-side of the DBD: (a) x/H=-10.5; (b) x/H=-7.8; (c) x/H=-3.9; (d) x/H=0.

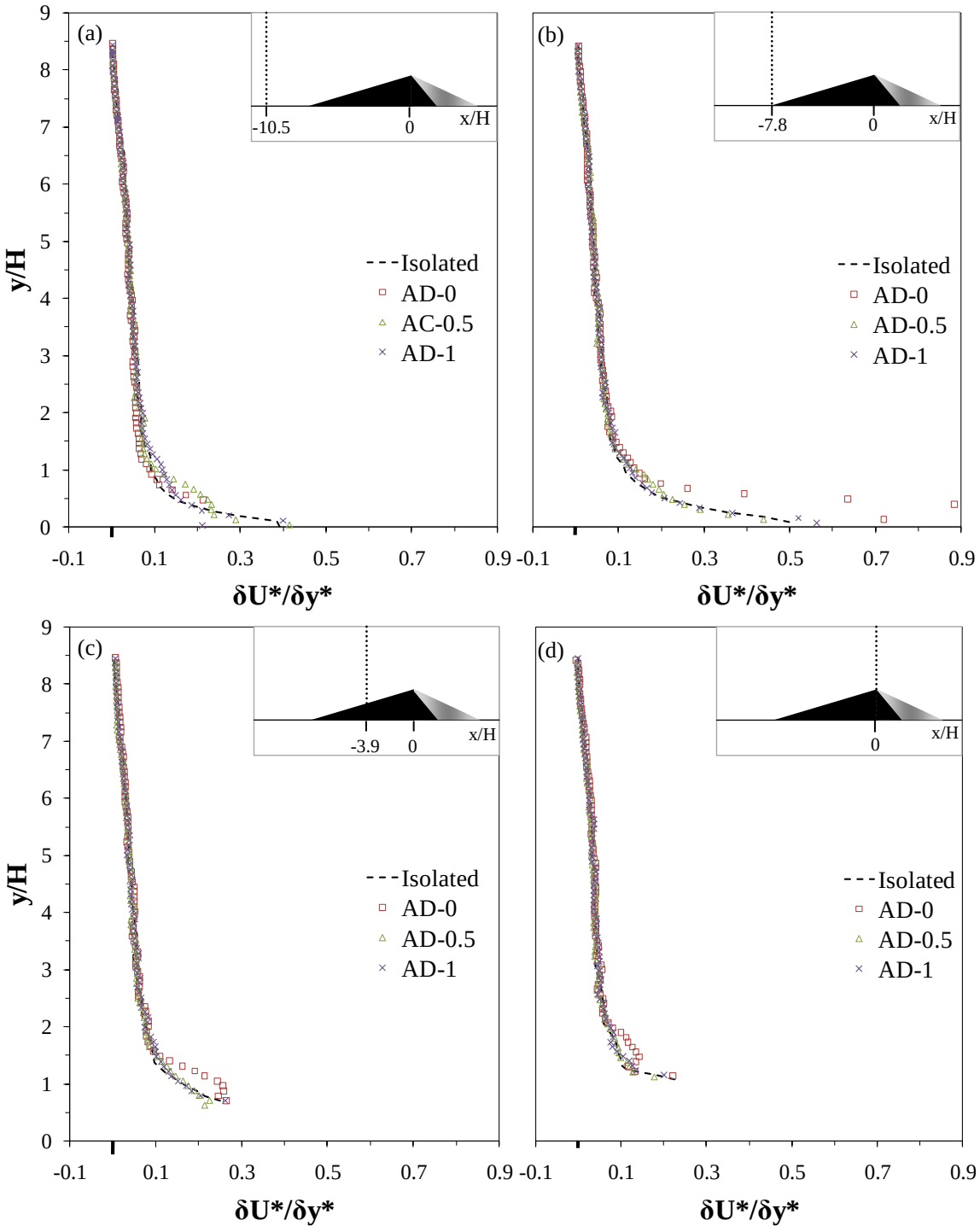

Figure 6.68: Vertical profiles of the streamwise velocity gradient, $\delta U^*/\delta y^*$, on the stoss-side of the DBD: (a) x/H=-10.5; (b) x/H=-7.8; (c) x/H=-3.9; (d) x/H=0.

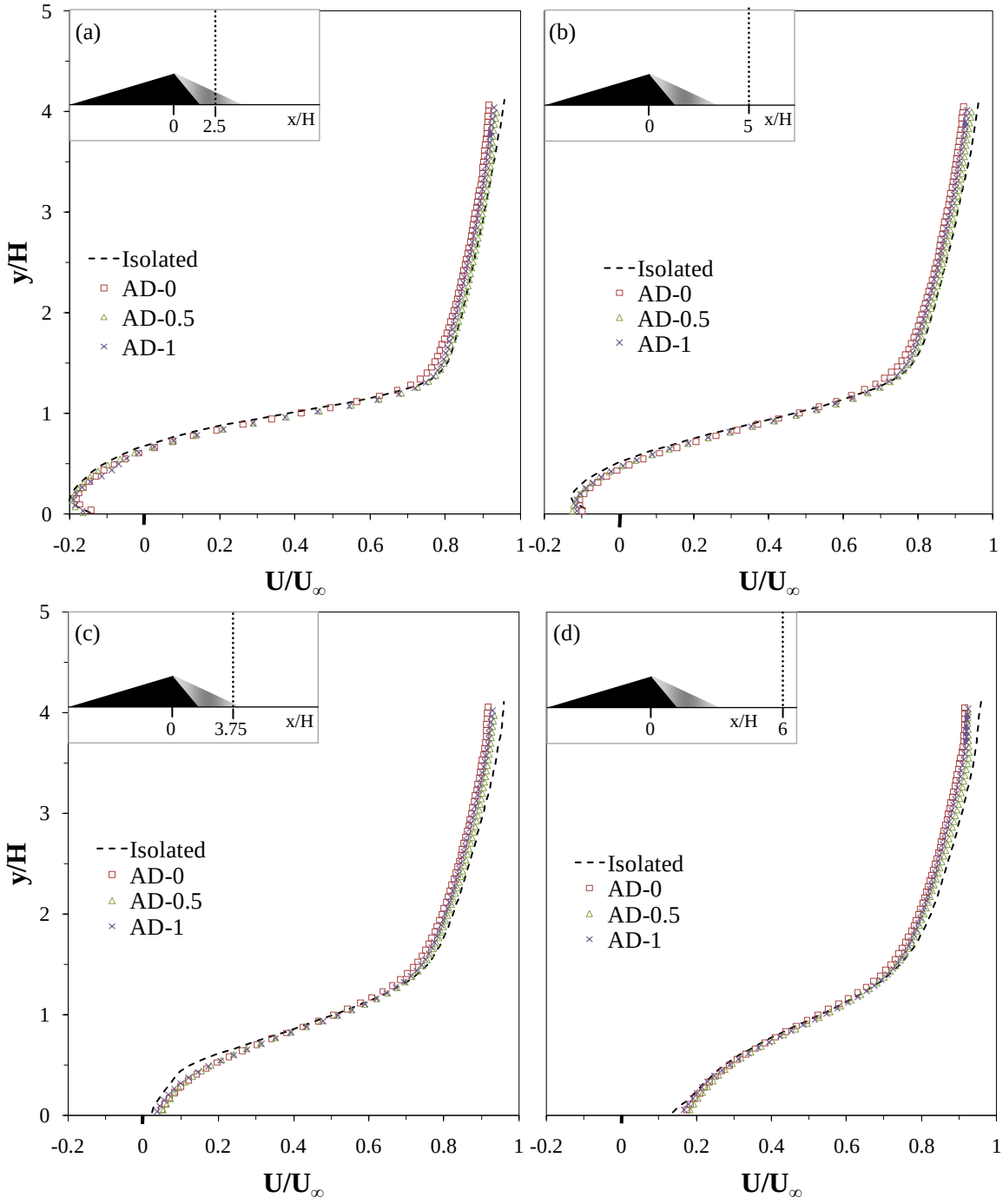

Figure 6.69: Vertical profiles of the streamwise velocity component, U/U_∞, on the lee-side of the DBD: (a) x/H=2.5; (b) x/H=3.75; (c) x/H=5; (d) x/H=6.

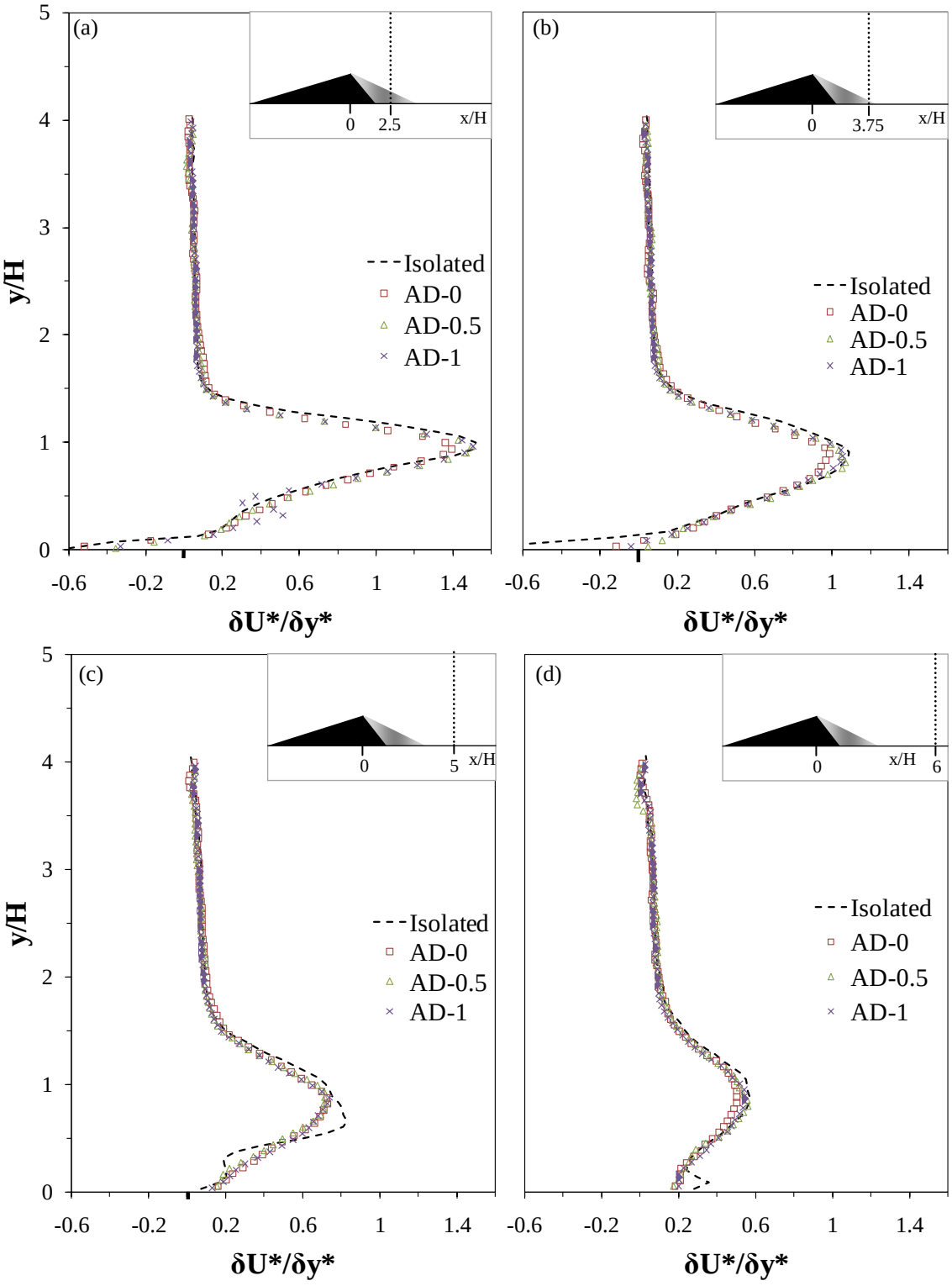

Figure 6.70: Vertical profiles of the streamwise velocity gradient, $\delta U^*/\delta y^*$, on the lee-side of the DBD: (a) x/H=2.5; (b) x/H=3.75; (c) x/H=5; (d) x/H=6.

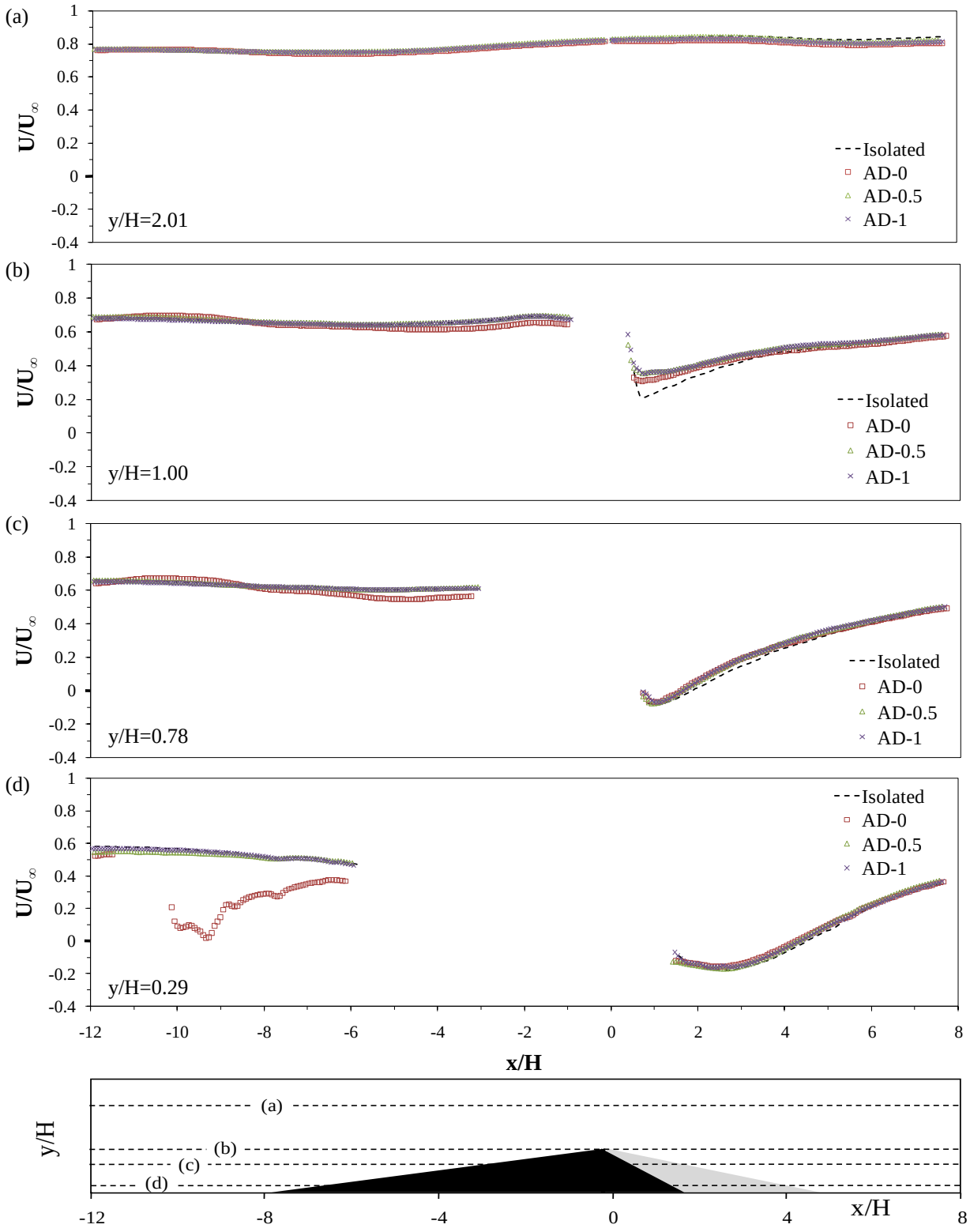

Figure 6.71: Horizontal profile of the streamwise velocity component, U/U_∞: (a) y/H=2.01.; (b) y/H=1.00; (c) y/H=0.78; (d) y/H=0.29.

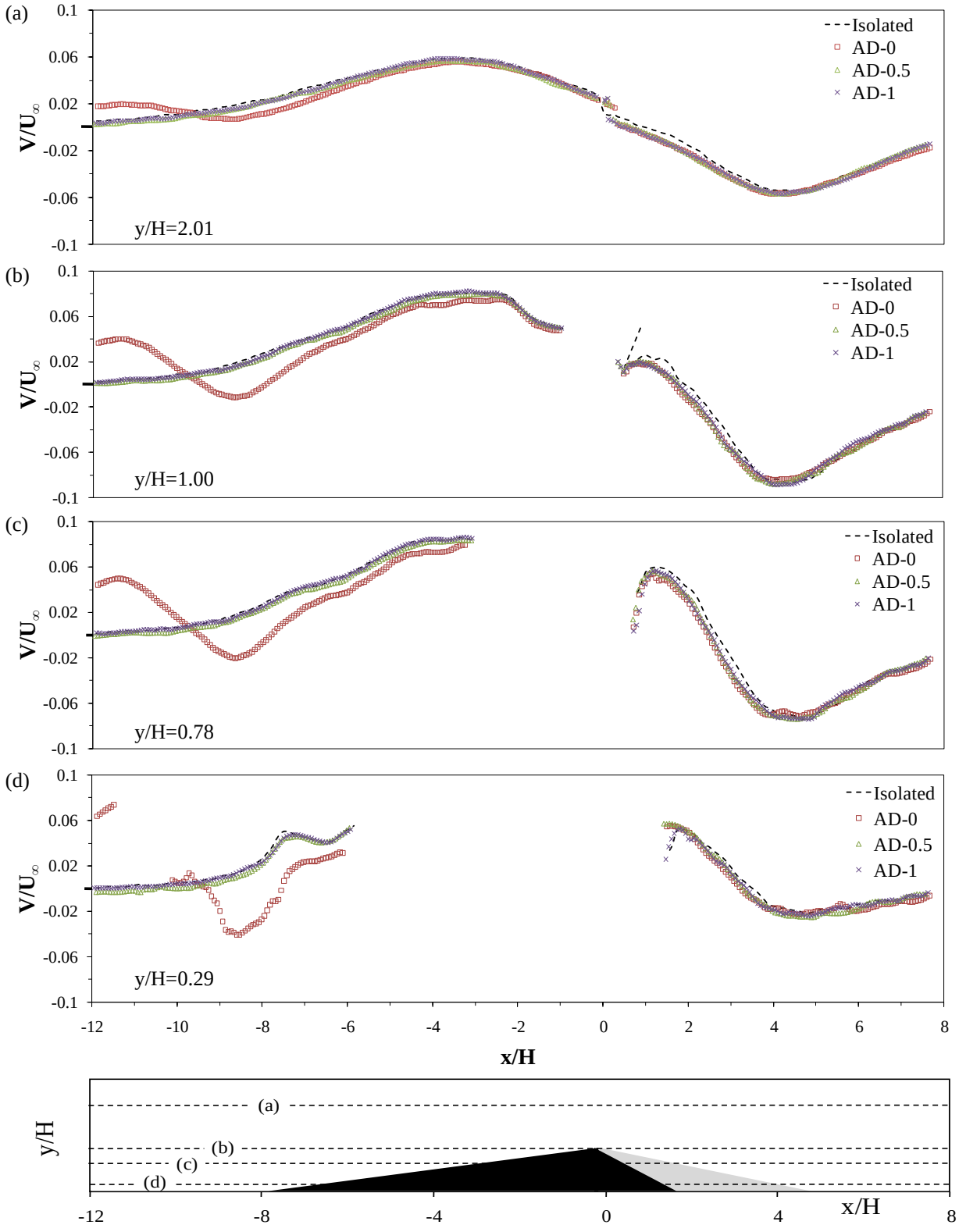

Figure 6.72: Horizontal profile of the wall-normal velocity component, V/U_∞: (a) y/H=2.01.; (b) y/H=1.00; (c) y/H=0.78; (d) y/H=0.29.

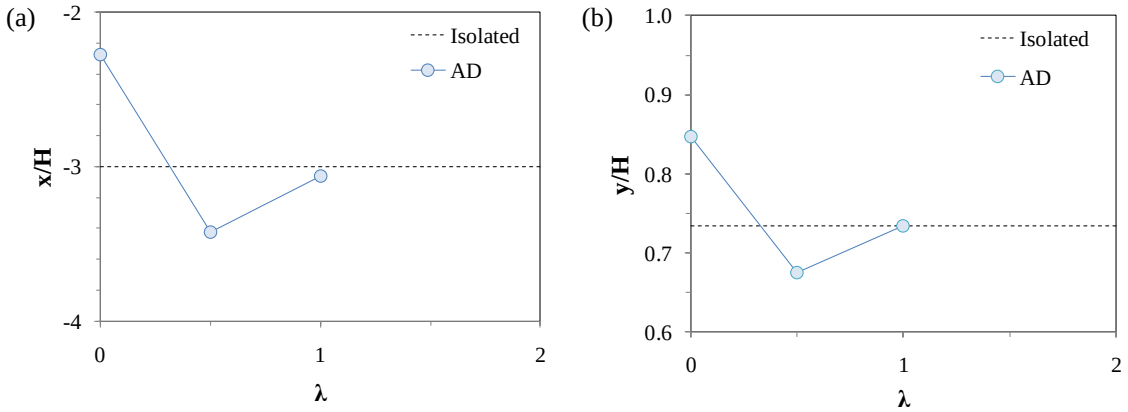

Figure 6.73: The location of the 0.6 U/U contour line termination point along the stoss-slope of the DBD with increasing λ: (a) the horizontal position, *x/H*; (b) the vertical position, y/H. Labeled 'T_p' in Figure 6.54.

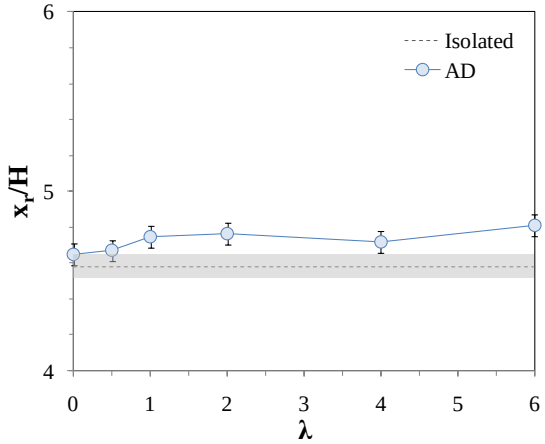

Figure 6.74: The reattachment length x_r of volumetric ratio AD and the isolated dune, with error bars.

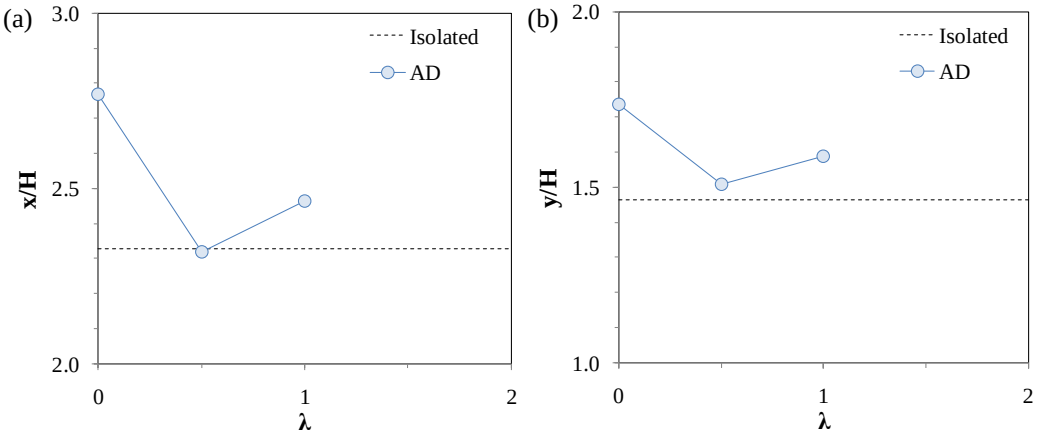

Figure 6.75: The location of the 0.8 contour line minima in the streamwise velocity U/U_∞ component contour map: (a) the horizontal position *x/H*; (b) the vertical position *y/H*.

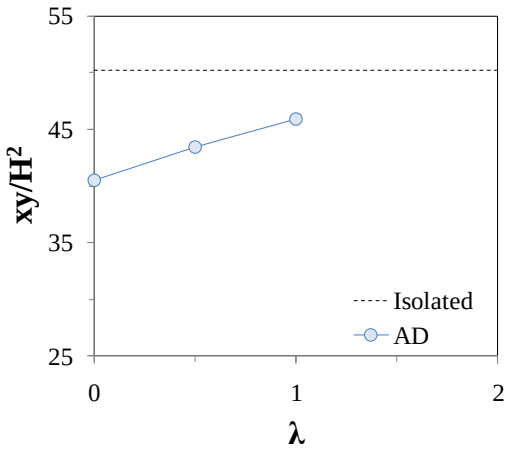

Figure 6.76: The topographic forcing zone area on the stoss-side of the DBD.

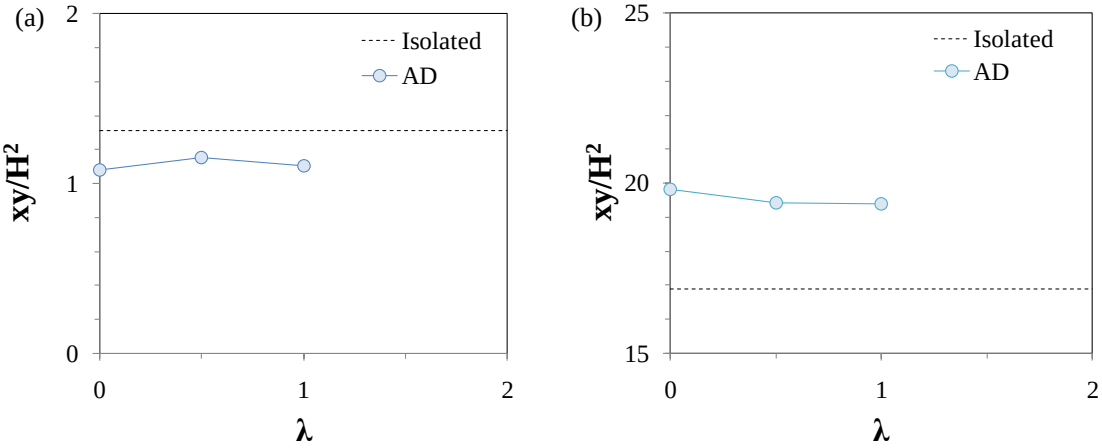

Figure 6.77: The area with increasing λ of (a) the upwelling zone and (b) the expansion zone. The expansion zone extends beyond the field of view, so the complete area is unknown. The area that is provided is the area of the expansion zone that is visible.

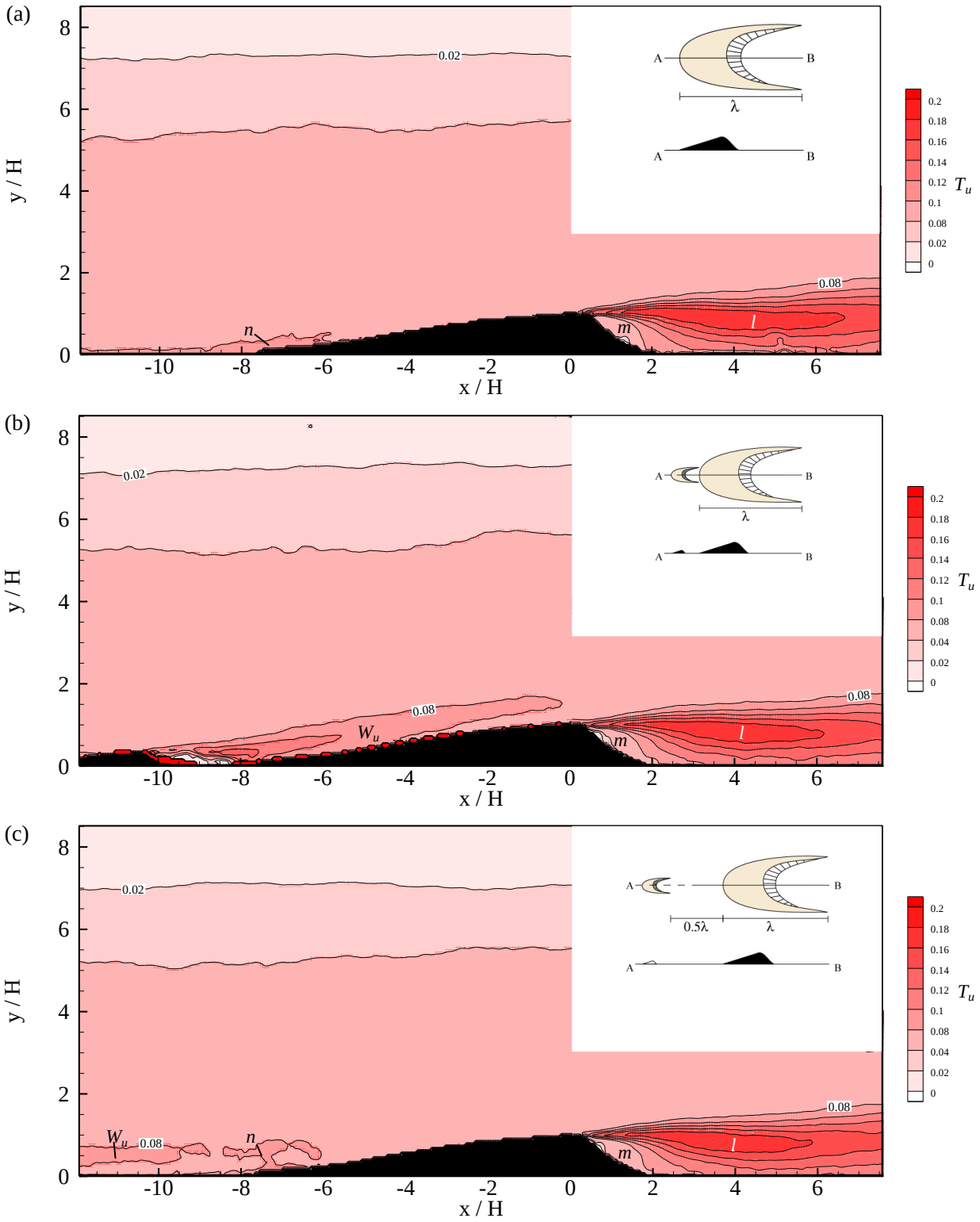

Figure 6.78 (continued on next page)

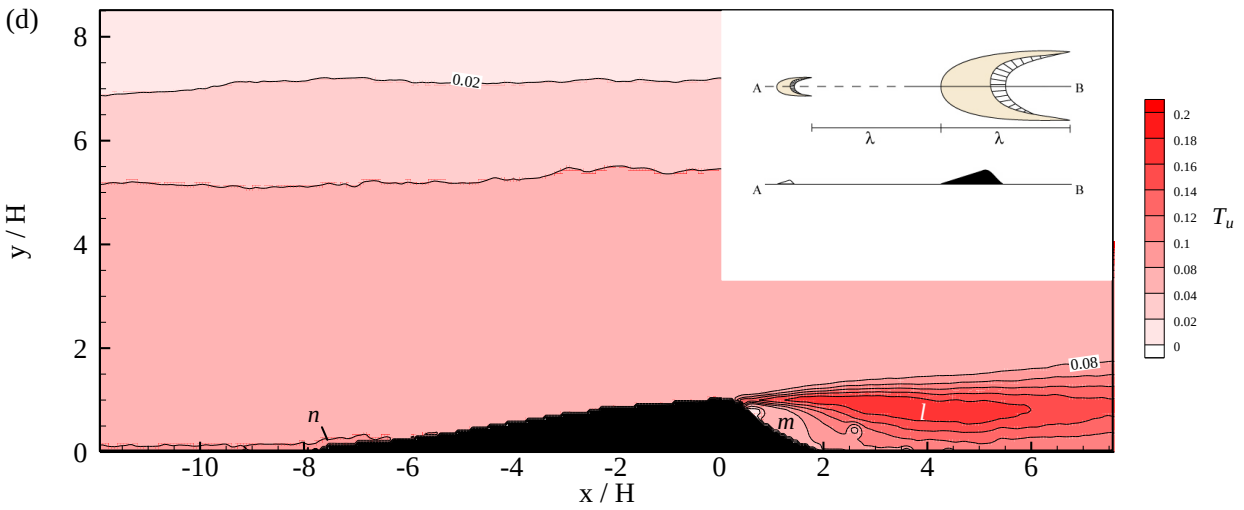

Figure 6.78: Contour maps of the streamwise component of the turbulence intensity ($\sqrt{u'^2}/U_\infty$) for the volumetric ratio AD: (a) isolated dune condition; (b) 0λ spacing; (c) 0.5λ spacing; (d) 1λ spacing. On the stoss-side, the area of high T_u extending from the UBD is labeled 'w_u' while the high T_u at the DBD toe is labeled 'n'. On the leeside, the area of high T_u is labeled 'l' while the area of low T_u is labeled 'm'.

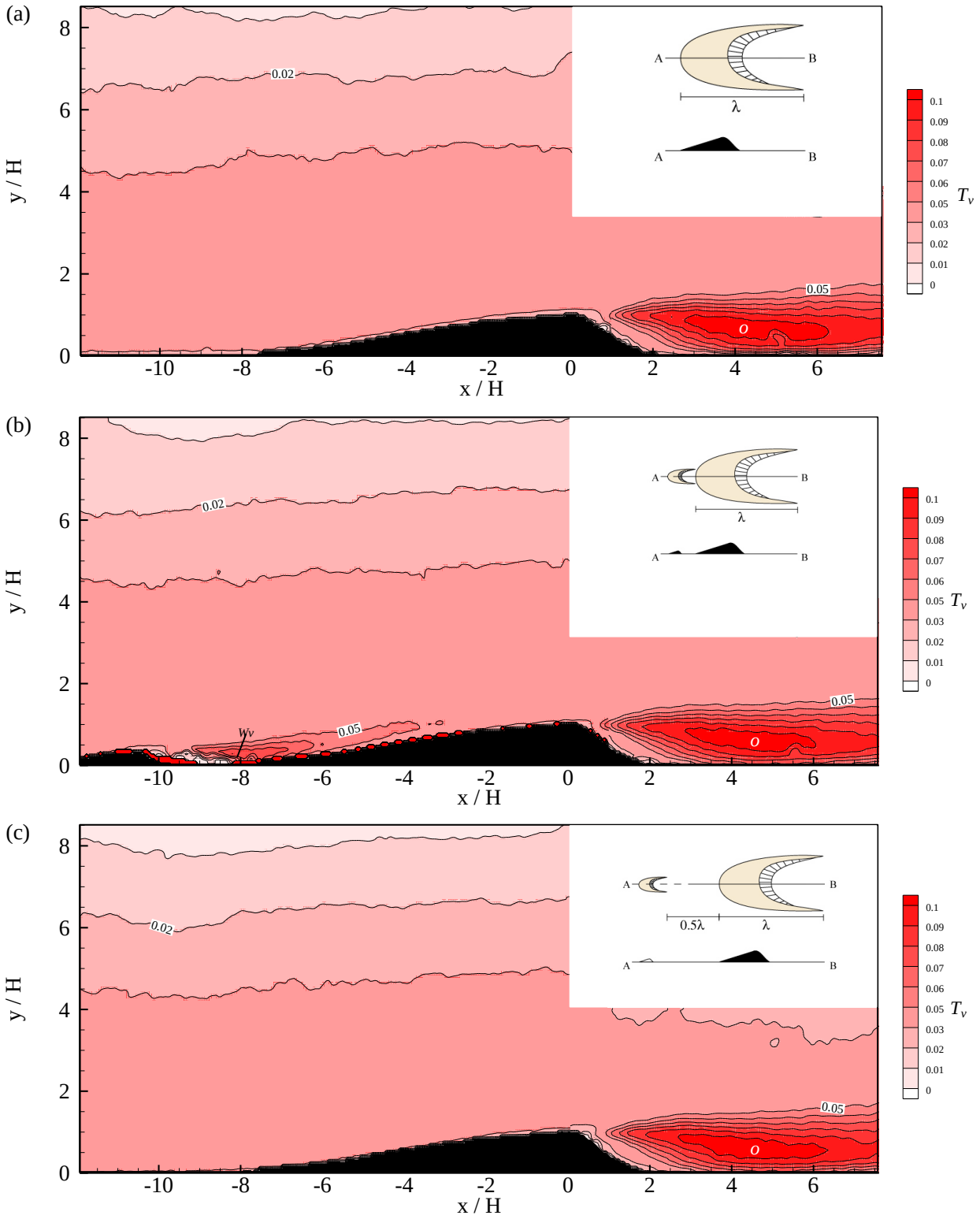

Figure 6.79 (continued on next page)

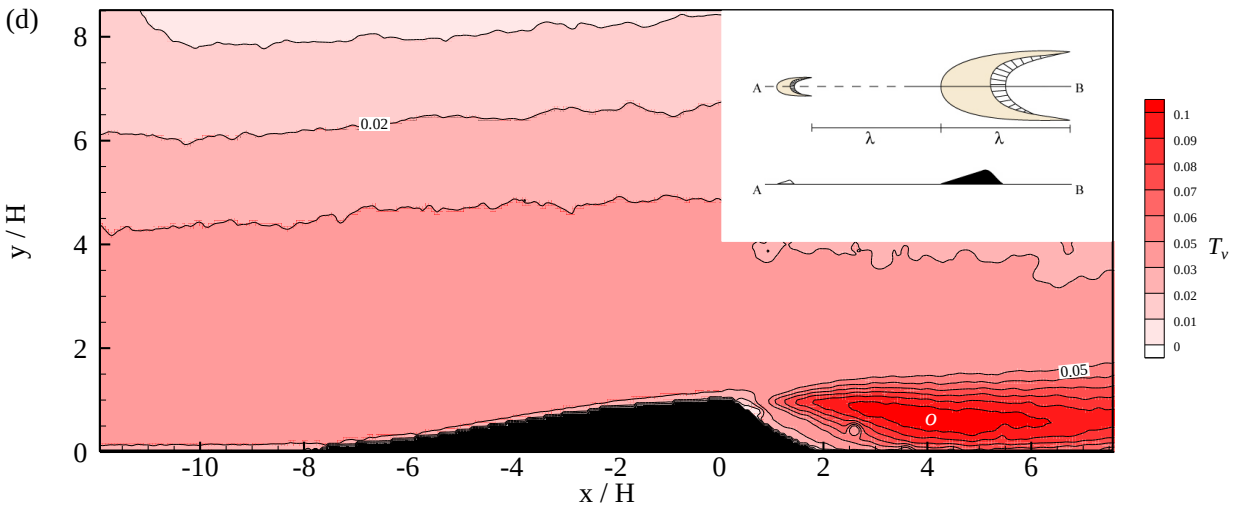

Figure 6.79: Contour maps of the wall-normal component of the turbulence intensity ($\sqrt{v'^2}/U_\infty$) for the volumetric ratio AD: (a) isolated dune condition; (b) 0λ spacing; (c) 0.5λ spacing; (d) 1λ spacing. On the stoss-side, the area of high T_v extending from the UBD is labeled 'w_v'. On the leeside, the area of high T_v is labeled 'o'.

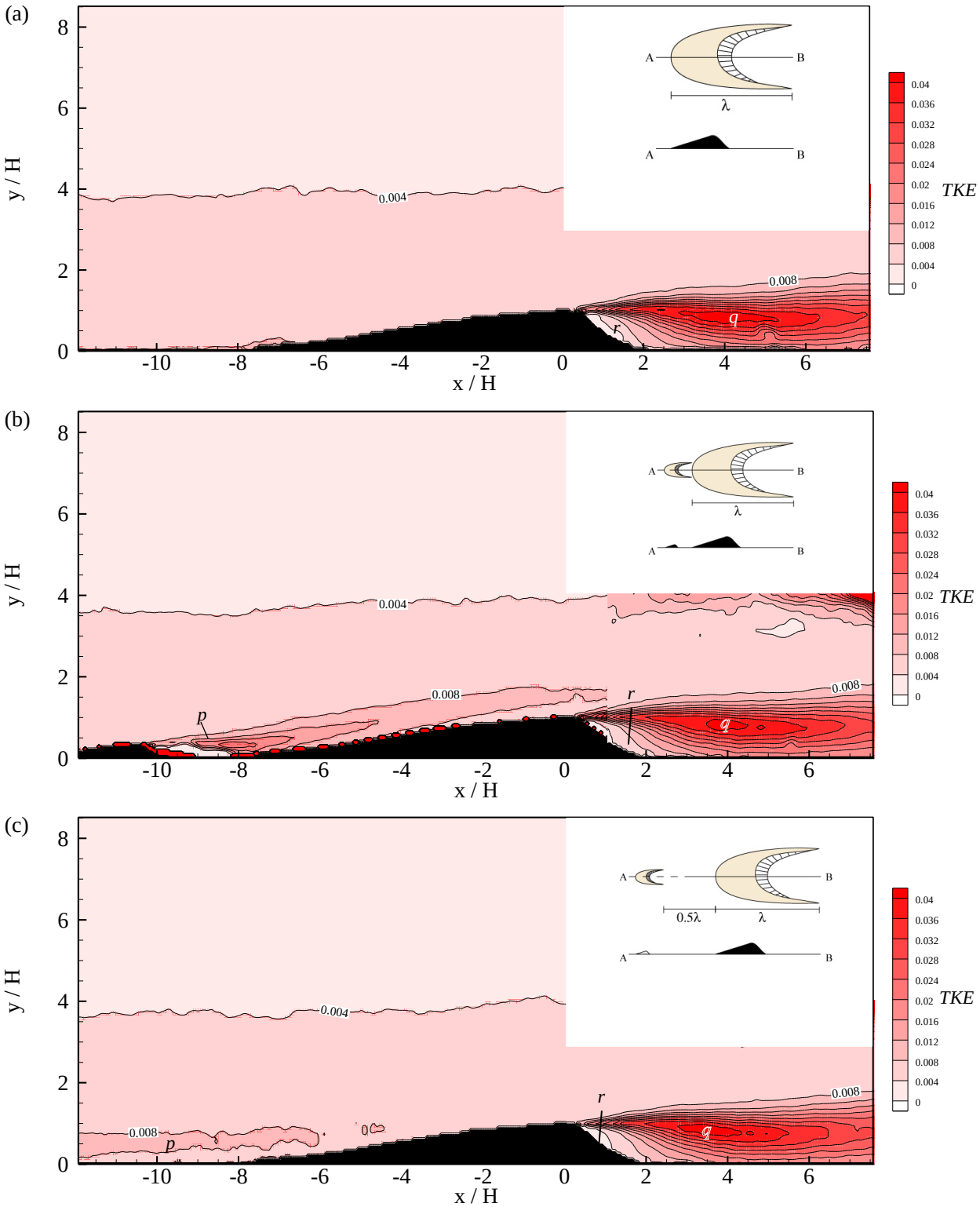

Figure 6.80 (continued on next page)

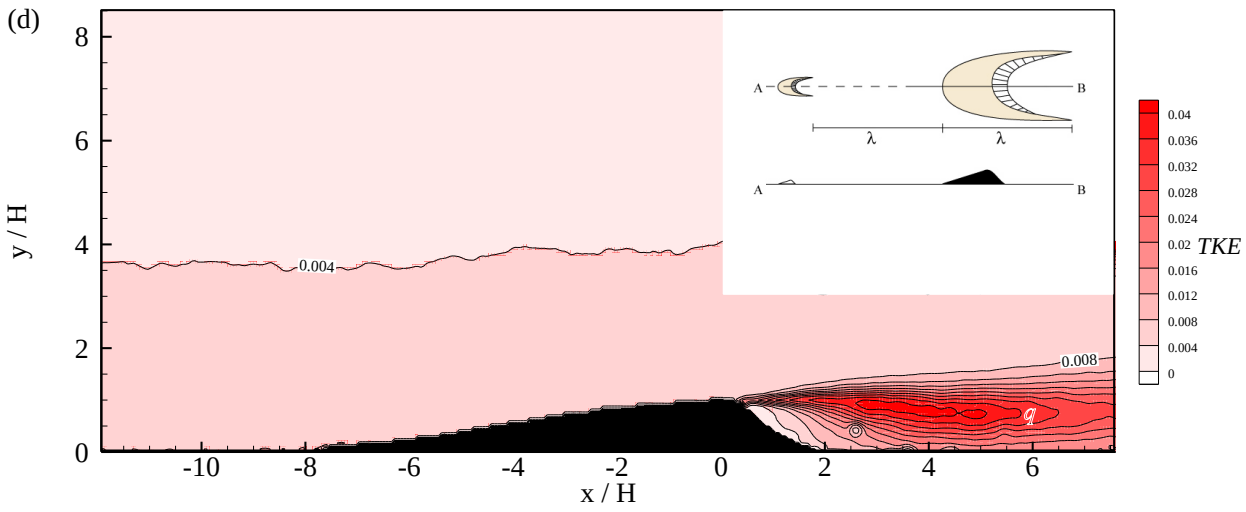

Figure 6.80: Contour maps of the mean turbulent kinetic energy *TKE* ($u'^2 + v'^2/U_\infty^2$) for the volumetric ratio AD: (a) isolated dune condition; (b) 0λ spacing; (c) 0.5λ spacing; (d) 1λ spacing. On the stoss-side, the area of high *TKE* extending from the UBD is labeled 'p'. On the leeside, the area of high *TKE* is labeled 'q' and the area of low T_u is labeled 'r'.

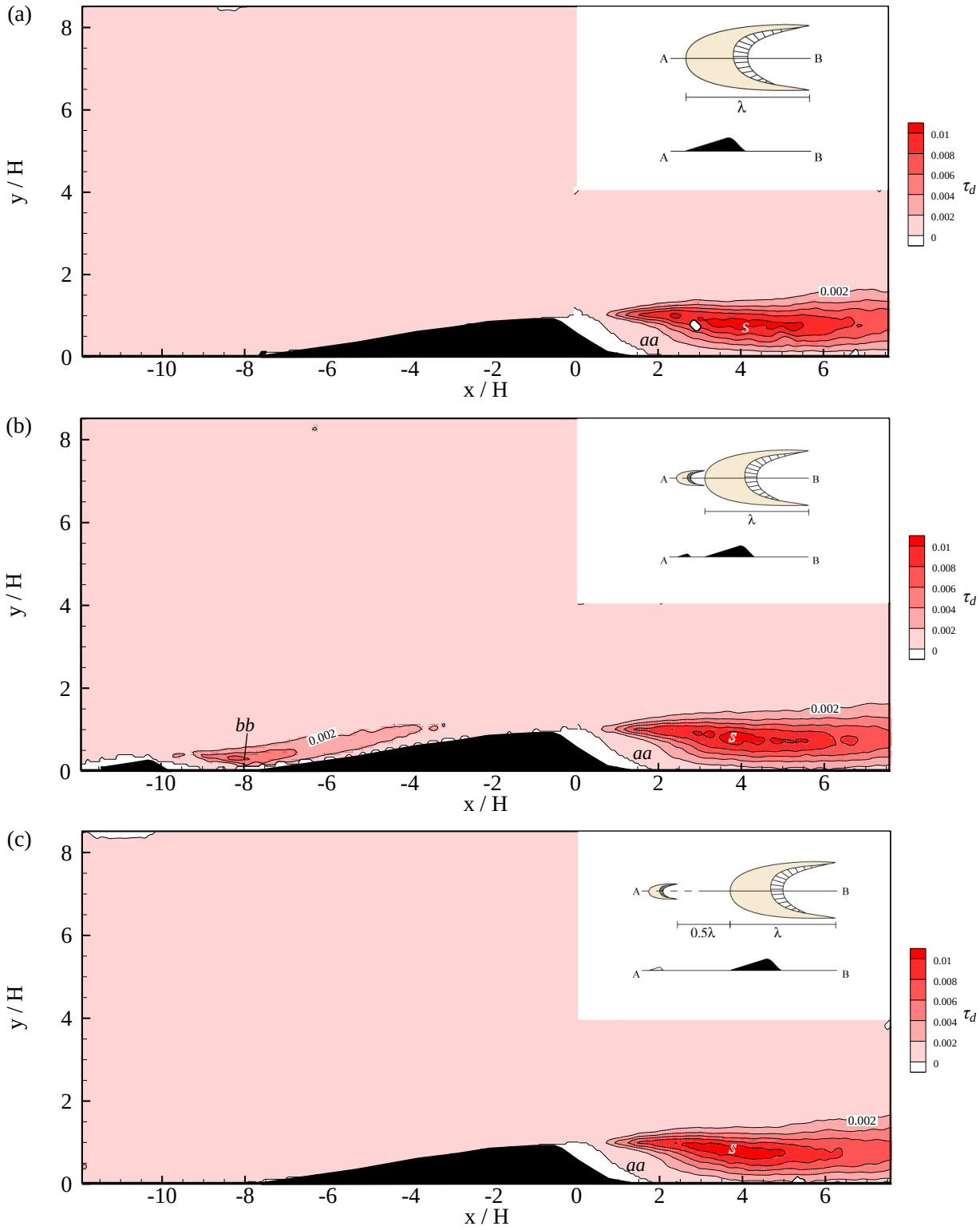

Figure 6.81 (continued on next page)

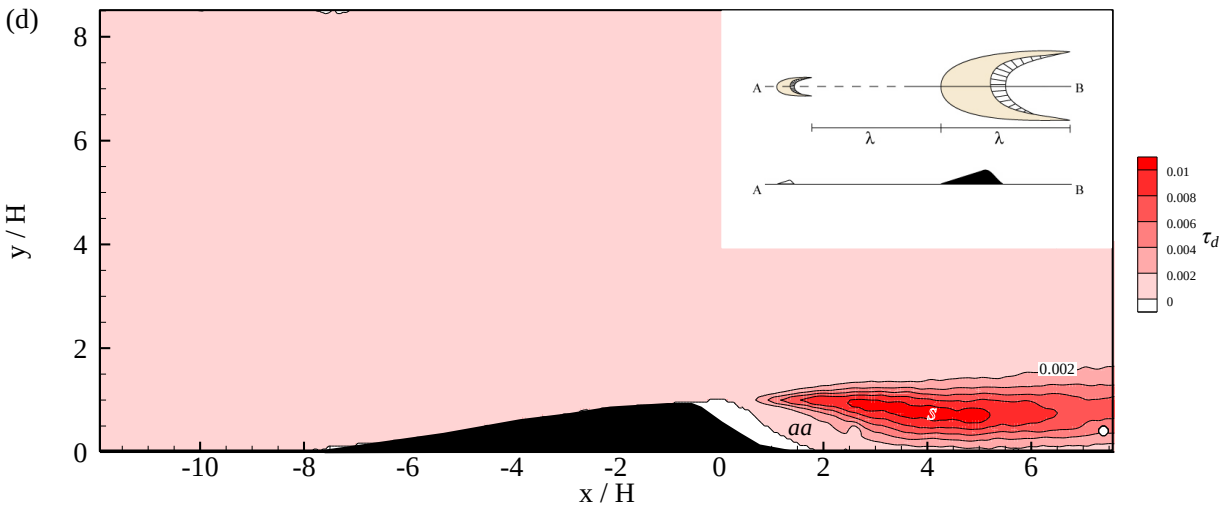

Figure 6.81: Contour maps of the Reynolds stress τ_d ($-\overline{u'v'}/U_\infty^2$) for the volumetric ratio AD: (a) isolated dune condition; (b) 0λ spacing; (c) 0.5λ spacing; (d) 1λ spacing. On the stoss-side, the area of high τ_d extending from the UBD is labeled '*bb'*. On the leeside, the area of high τ_d is labeled '*s'* and the area of low τ_d is labeled '*aa'*.

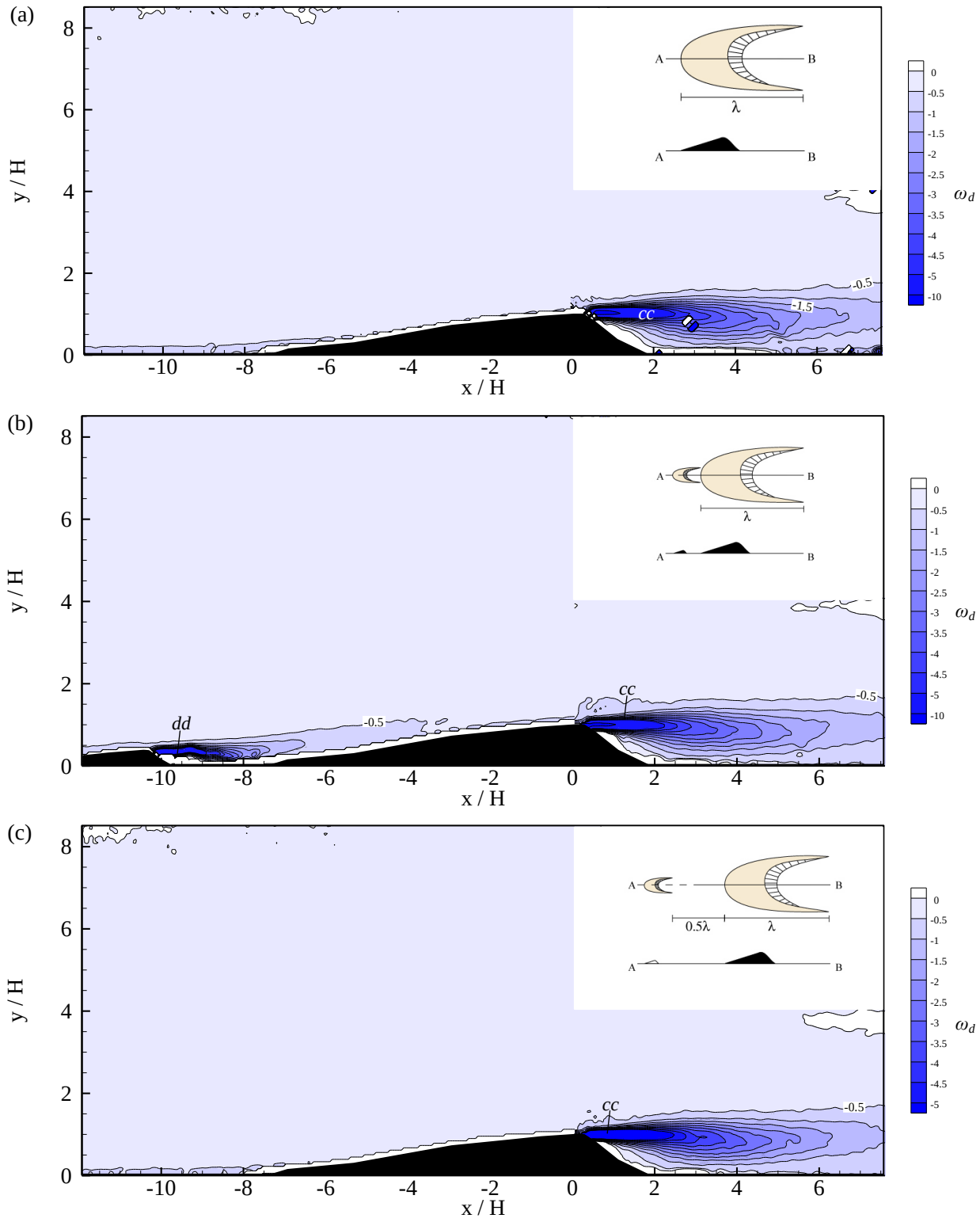

Figure 6.82 (continued on next page)

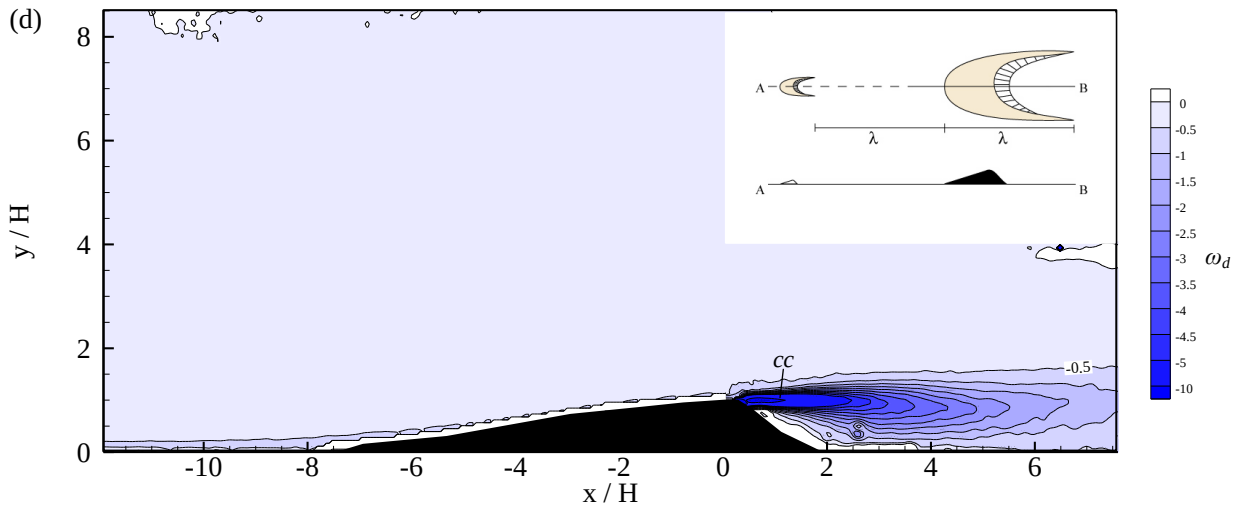

Figure 6.82: Contour maps of the vorticity ω_d for the volumetric ratio AD: (a) isolated dune condition; (b) 0λ spacing; (c) 0.5λ spacing; (d) 1λ spacing. On the stoss-side, the area of high ω_d extending from the UBD is labeled '*dd'*. On the leeside, the area of high ω_d is labeled '*cc'*.

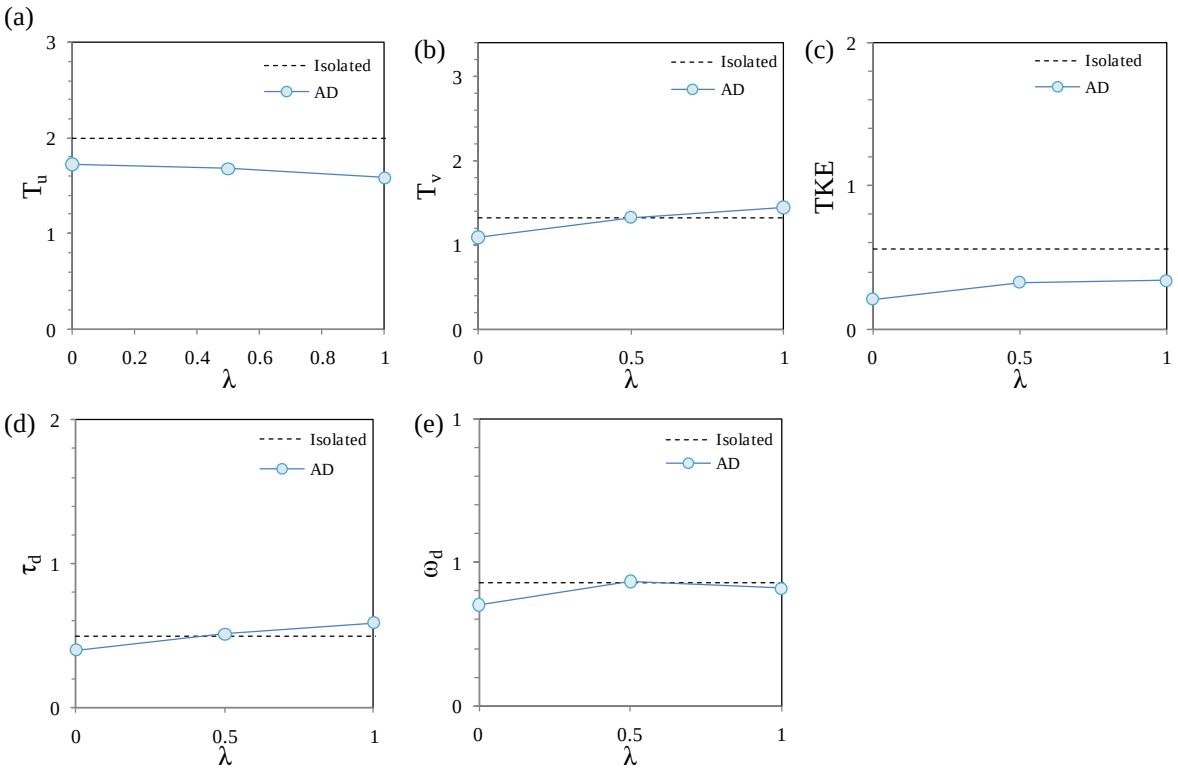

Figure 6.83: Comparison between the area of maximum T_u, T_v, *TKE*, τ_d, and ω_d between the isolated dune and volumetric ratio AC: (a) T_u – area of 0.16-0.2 contour; (b) T_v – area of 0.1 contour (c) *TKE* – area of 0.04 contour; (d) τ_d – area of 0.01 contour; (e) ω_d – area of -5 to -10 contour. The contour area is approximated using the area of an ellipse.

CHAPTER 7

ANALYSIS AND DISCUSSION

In this chapter, an analysis of the data presented in Chapter 6 is provided in order to highlight the effect of λ and emphasize the effect of the volumetric ratio upon the mean and turbulent flow. This chapter will, first, address the reattachment length for different volumetric ratios with respect to λ, followed by quantification of the flow zones identified from the wall-normal velocity component contour maps. A comparative analysis of streamwise and wall-normal velocity in the form of vertical and horizontal profiles is provided, succeeded by horizontal profiles of three turbulence parameters. Finally, the results of this study will be placed within the context of past work, specifically the research of Endo *et al.* (2004).

7.1 Analysis

7.1.1 Reattachment length

The flow reattachment length is influenced more by the relative volumetric ratio than by interdune spacing. The measurement of the reattachment point is defined in section 3.4.2. The reattachment point x_r at each λ is presented in Figure 7.1. The range of reattachment lengths derived from this study agree well with reattachment lengths reported in past literature (e.g. Engel, 1981; Bennett and Best, 1995). The longest reattachment lengths occur for volumetric ratio AB at 0λ-2λ, exceeding the isolated dune reattachment length by 0.6*H*-0.74*H*. The vortices shed from the upstream barchan dune maintain coherence at all interdune spacings when they reach the downstream barchan dune shear layer. The interaction of the upstream and downstream barchan dune shear layers results in a larger separation bubble and a longer reattachment length, as also observed by Fernandez *et al.* (2006) in the case of superimposed bedforms. The shortest reattachment lengths occur in the case of AA at 0λ, being 0.32*H* shorter than the isolated dune x_r, and are caused by 'sheltering' of the downstream barchan dune by the upstream barchan dune. The reattachment lengths for volumetric ratios AC and AD exceed the isolated dune x_r at 1λ-6λ, but fall within the isolated dune x_r estimated error at both 0λ and 0.5λ. The comparable x_r for the isolated dune and AC and AD volumetric ratios is the result of the production of smaller and less intense coherent structures from the upstream dune that have little effect on the larger structures generated in the leeside of the larger downstream dune.

7.1.2 Quantitative analysis of V/U_∞ zones

Chapter 6 describes three zones in the wall-normal contour maps: (a) a zone of topographic forcing; (b) a zone of upwelling; and (c) a zone of expansion. The zones of topographic forcing and upwelling are characterized by upwards flow; the zone of expansion is characterized by downwelling flow. The area of the three zones is presented in Figure 7.2a-c, with respect to λ and volumetric ratio.

The isolated dune exhibited the greatest area of topographic forcing, followed by volumetric ratio AD, AC, AB and AA (Figure 7.2a). One exception to the volumetric ratio order occurs at 1λ and 2λ, where the topographic forcing area belonging to volumetric ratio AB exceeds that of AC. There is a clear trend between the area of the zone of topographic forcing and the volumetric ratio, as shown by comparing the area of topographic forcing. The effect of the UBD size and proximity is involved in the erosion mechanisms occurring on the stoss-side and caused by the UBD wake (Endo *et al.*, 2004). With increasing volumetric ratio, the effect of the UBD wake is more appreciable, thus explaining the trend of decreasing topographic forcing area.

The volumetric ratios AC and AD (Figure 7.2b) follow the same trend for the area of the upwelling zone (defined as the area within the 0.04-0.08 contours), with the greatest area occurring at 0.5λ. Volumetric ratio AA has a smaller area of upwelling than the isolated dune and volumetric ratios AB and AC at 0λ, which is expected since it has the shortest reattachment length. However, volumetric ratio AD has a similar area of upwelling to AA at 0λ despite having a larger reattachment length. Volumetric ratio AB has the greatest area of upwelling at 0λ, 1λ and 2λ; at 0.5λ, the area is smaller than the isolated dune area and the intensity is reduced compared to the other spacings in AB, indicating less upwelling.

Regarding Figure 7.2b, the results show that the presence of the UBD generates a greater area of expansion (along the streamwise-wall-normal plane) relative to the expansion zone of the isolated dune. The expansion zone extends beyond the fields of view, and thus the area is biased. However, no significant differences are apparent among the different dune configurations with the exception of λ=0, where the dimensions of the expansion zone are increased.

7.1.3 Vertical profile analysis and volumetric ratio effect

Within this analysis, the profiles extracted from four locations are examined. These are considered representative for the flow behavior in four zones: stoss-side, DBD crest, recirculation region and leeside. Following the comparative analysis, the profiles obtained for different volumetric ratios are presented and discussed independently for each location (x/H=-10.5, 0. 2.5, and 5). In each figure, the profiles obtained for different λ are considered separately and ordered from λ=2 to λ=0 in order to draw attention to the importance of the parameter λ.

7.1.3.1 DBD stoss-side (x/H=-10.5): Figures 7.3 and 7.4

The velocity on the stoss-side of the DBD is reduced by the presence of the UBD. In comparison to the isolated dune, the near-floor velocity in the vertical range $0<y/H<2$ is decreased relative to the isolated dune, due to the UBD wake, constituting a 'sheltering effect'. This phenomenon is not appreciable for high λ but becomes clearer for 0.5λ and 1λ. The velocity reduction is particularly relevant for AA and AB; this is demonstrated by the fact that for λ=0, the profiles of volumetric ratio AB, the profiles show some reverse flow due to the recirculation region of UBD.

7.1.3.2 DBD crest(x/H=0): Figures 7.5 and 7.6

The velocity at the crest is also affected by the UBD, but is perceivable throughout the range of λ only for AA; for AB, when λ=1 and 0.5, some effect is observable, but only within the elevation range $1.1<y/H<4.0$. The 'sheltering effect' is less pronounced at high λ; moreover, the 'sheltering effect' is diminished at x/H=0 in comparison to the velocity at x/H=-10.5, indicating that the effect is progressively reduced with downstream distance.

7.1.3.3 DBD recirculation region (x/H=2.5): Figures 7.7 and 7.8

Downstream of the crest, two regions can be distinguished: the first refers to the region $y/H>1$; the second refers to the region $y/H<1$ (i.e. separation bubble). The behavior in the first region is similar to the behavior discussed in the previous section (x/H=0). This is due to the fact that the UBD sheltering effect is extended beyond the DBD crest and is most visible at the closest interdune spacing (0λ). Regarding the behavior in the second region, there is no apparent difference between the velocity profiles at different volumetric ratios with respect to the isolated dune. This indicates that the DBD produces its own sheltering effect, which isolates the flow behavior within the DBD separation bubble from the influence of the UBD flow, producing a

spatial discontinuity across the shear layer between the first and second regions. The shear layer acts as a boundary by sheltering the flow within the separation bubble from the outer flow; however, the shear layer is still subjected to the influence of the UBD wake, resulting in variable reattachment lengths (discussed in section 7.1.1).

7.1.3.4 DBD separation bubble edge (x/H=5): Figures 7.9 and 7.10

The UBD influence upon the DBD shear layer, as mentioned above, is demonstrated by the variation in reattachment lengths for different volumetric ratios and by the differences observed within the velocity profiles at the location x/H=5. The flow has already reattached for AA, AC, AD and the isolated dune at this location; contrarily, we observe at AB the flow has yet to reattach for every λ. Some interesting considerations are made focusing upon the 0λ spacing, where three regions characterized by different behavior are distinguishable:

(1) y/H>1.3, for every volumetric ratio, the velocity is smaller than the isolated dune, decreasing in the following order: AD/AC, AB, and AA.
(2) 0.8<y/H<1.3, there is a transitional zone where the velocities for volumetric ratios AC and AB collapse with the isolated dune velocity, while the velocity for AA and AB are similar but slightly smaller relative to the isolated dune velocity.
(3) y/H<0.8, the velocity for AA, AC and AD is greater than the isolated dune while the velocity for AB is still smaller.

From (1) it is evident that in the DBD wake outer region (y/H>1.3) the volumetric ratio plays a clear role, as evidenced by the fact that the degree of deceleration of the velocity increases with increasing volumetric ratio. This suggests that the height of the UBD, and thus the size of the coherent turbulent structures exiting from the UBD crest, plays a strong role in the wake outer region where the UBD sheltering effect is consistent (i.e. with a higher dune, the spanwise vortices are bigger and therefore, there is a stronger UBD sheltering effect). From (2) and (3), it is shown that the only configuration for which the velocity is everywhere smaller than the isolated dune is for volumetric ratio AB, while for the other volumetric ratios there is a vertical transition with respect to the velocity of the isolated dune (from smaller to higher velocities, moving towards the floor).

In the lowest region (y/H<0.8), the volumetric ratios AA, AC and AD share similar velocities, contrary to the upper regions where the velocity for the case of AA is significantly smaller. Also,

the velocity of AB is smaller than that of AA. This suggests that in the lowest region, the sheltering effect mechanism is not exhaustive in explaining the observed behavior. There should be an additional mechanism compensating the difference in UBD size and decelerating the flow in the DBD wake. A possible explanation can be found by considering two additional parameters: the distance between the UBD horns and the DBD and the distance between the UBD horns themselves, which determine the effects of longitudinal vorticity exiting from the UBD horns: this appears to play a significant role in sustaining turbulence intensity within the DBD wake and lengthening the DBD separation bubble. For instance, in the case of AB, the distance between UBD horns and the centerline axis of the dunes is smaller than the case AA. This is presumably favoring the interaction between the UBD longitudinal and the DBD spanwise vorticity, which results in a stronger velocity reduction within the DBD wake.

7.1.4 U/U_∞ horizontal profile analysis and volumetric ratio effect

In the following paragraphs, the horizontal profiles of the streamwise velocity component are presented at two different heights (y/H=1.00 and 0.29). For each location, the results relative to different λ are reported separately, to acknowledge the effect of λ, but the comparison between the volumetric ratios is emphasized. The results from the horizontal profiles are particularly relevant as they clearly show how the velocity of fluid over the DBD stoss-side is influenced by the UBD wake.

7.1.4.1 Crest-height (y/H=1.00): Figure 7.11

The effect of the UBD is discernable on the stoss-side for AA and AB at 1λ-0λ, and for AC and AD at 0λ. On the leeside, which features the wake outer region, the UBD effect is appreciable for AA and AB, manifested by significantly reduced velocities. At λ=0 and 0.5, between $0<x/H<2$, the velocity of AB is greater than the isolated dune, but at $x/H>2$, the profile intersects the isolated dune profile, and the velocity of AB remains smaller than that of the isolated dune. A similar behavior is observed for the case of AA at 0λ. The velocity of volumetric ratios AC and AD is greater than the isolated dune within the horizontal range $0<x/H<3.8$, but with downstream distance, the velocity of AC and AD tends to collapse with the isolated dune velocity.

7.1.4.2 Near-floor region (y/H=0.29): Figure 7.12

The results show that on the stoss-side when λ=1-2, no significant differences are present as the volumetric ratio increases. At λ=0.5, the velocity reduction due to the UBD wake becomes apparent. When λ=0. The horizontal profiles show there is an abrupt decrease in velocity, a result of the UBD wake. The strongest velocity reduction is found for configuration AB. The velocities of configurations AC and AD reflect the presence of the UBD and the UBD separation bubble, which is manifested as a local dip in velocity. In the leeside, the horizontal profiles at y/H-=0.29 intersect the velocity within the separation bubble, and illustrate that there is no appreciable effect on the velocity within the horizontal range $1.5<x/H<3$. It is evident that AB is affected by the UBD downstream of $x/H=4$.

7.1.5 V/U_∞ horizontal profile and volumetric ratio effect

In the following paragraphs, the horizontal profiles of the wall-normal velocity component are presented at two different heights ($y/H=1.00$ and 0.29) and discussed below. At each location, the results are divided according to λ; however, the comparison between the volumetric ratios is emphasized within the text. The results from the horizontal profiles are particularly relevant as they clearly show how the velocity of fluid over the DBD stoss-side and leeside is influenced by the UBD flow features (UBD topographic forcing zone, UBD upwelling zone, and UBD expansion zone).

7.1.5.1 Crest-height ($y/H=1.00$): Figure 7.13

On the stoss-side, the velocity is greatly affected by the presence of the UBD at 0λ. The dominant affect is due to the UBD expansion zones. The expansion zone progressively approaches the DBD with decreasing λ. The differences between volumetric ratios are significant and depend on both the size of the UBD, which controls the size of the expansion zone, and the position of the UBD crest relative to the DBD. In other words, in the case of AA, the expansion zone is larger than the other volumetric ratios, but is also located further upstream; likewise, in the case of AD, the expansion zone is the smallest out of the volumetric ratios, but is furthest downstream, where it is close to the DBD dune. In addition, the expansion zone is characterized by negative V/U_∞ (down welling fluid), which accounts for the great disparity between the velocity of the isolated dune and AA-AD. In the leeside, the velocities are once again dominated by the expansion zone, but experience greater magnitudes of velocity than the velocity found in

the UBD expansion zone. At 0λ, AB experiences slower down welling fluid than AA, AC and AD and the isolated dune.

7.1.5.2 Near-floor region (*y/H*=0.29): Figure 7.14

On the stoss-side, there is a negligible effect of the UBD at λ=2-0.5. At 0λ, there is a pronounced reduction in the velocity found at AA relative to the isolated dune velocity, a result of the UBD wake. Volumetric ratios AB-AD reflect the presence of the UBD and its flow features, such as the UBD topographic forcing zone, UBD upwelling zone and UBD expansion zone; again, these features generate a unique horizontal profile.

7. 1.6 Turbulence parameters

In Figure 7.15, horizontal profiles of three key turbulent parameters, the streamwise and wall-normal components of turbulent intensity and Reynolds stress are examined at one height; the vertical location selected optimizes the maximum turbulence parameter in the stoss-side and leeside. The profiles are only considered at 0λ, given that this is the spacing with the greatest UBD effect, and also to emphasize the critical changes that occur with volumetric ratio. The streamwise turbulence intensity and the Reynolds stress were obtained at *y/H*=0.86 while the wall-normal turbulence intensity was obtained at *y/H*=0.6, due to the vertically lower position of the maximum turbulence intensity.

7.1.6.1 Streamwise component of turbulence intensity T_u

In the stoss-side, the isolated dune remains stable at 7.7% T_u. Among the tandem configurations, the greatest increase in T_u occurs at AA and AB, relative to the isolated dune (Figure 7.15a). There is a common trend for the volumetric ratios AB-AD: T_u increases and then decreases with downstream distance. It appears that volumetric ratio AA also follows this trend, but only the decreasing portion is visible within the field of view. This can be attributed to the zone of maximum turbulence within the UBD leeside which extends along the shear layer; with decreasing volumetric ratio, the zone of maximum turbulence shifts downstream. On the leeside, the UBD effect is minimal; the AB configuration exhibits the greatest T_u. The UBD effect on AA, AC and AD decreases T_u downstream of *x/H*=4.4.

7.1.6.2 Wall-normal component of turbulence intensity T_v

In the stoss-side, the isolated dune averages ~3.7% T_v. The pattern of T_v for AA-AD, is similar to T_u. AA and AB are similar to one another, and also share the greatest intensities in the stoss-side, followed by AC and AD. The T_v of AA and AB decreases with downstream distance. The T_v of AC and AD increases with downstream distance, indicating turbulence production, and then decreases as it approaches the DBD. In the leeside, there is no appreciable change in T_v, except to highlight that AB has the greatest turbulence intensity downstream of x/H=4.1.

7.1.6.3 Reynolds stress τ_d

In the stoss-side, the pattern of Reynolds stress is similar to T_u. Again, the greatest influence of the UBD is at AA and AB; the horizontal profiles show that the streamwise velocity fluctuations dominate. In the leeside, the τ_d occurring at volumetric ratio AB is significantly greater than the τ_d occurring at AA, AC and AD, as well as the isolated dune.

7.2 Figures

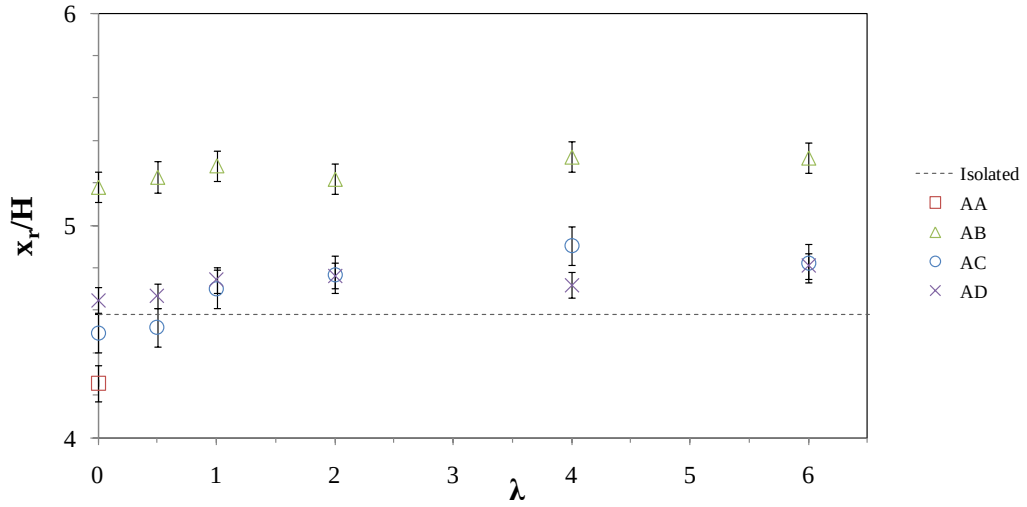

Figure 7.1: The DBD reattachment length x_r with respect to λ for volumetric ratios AA-AD.

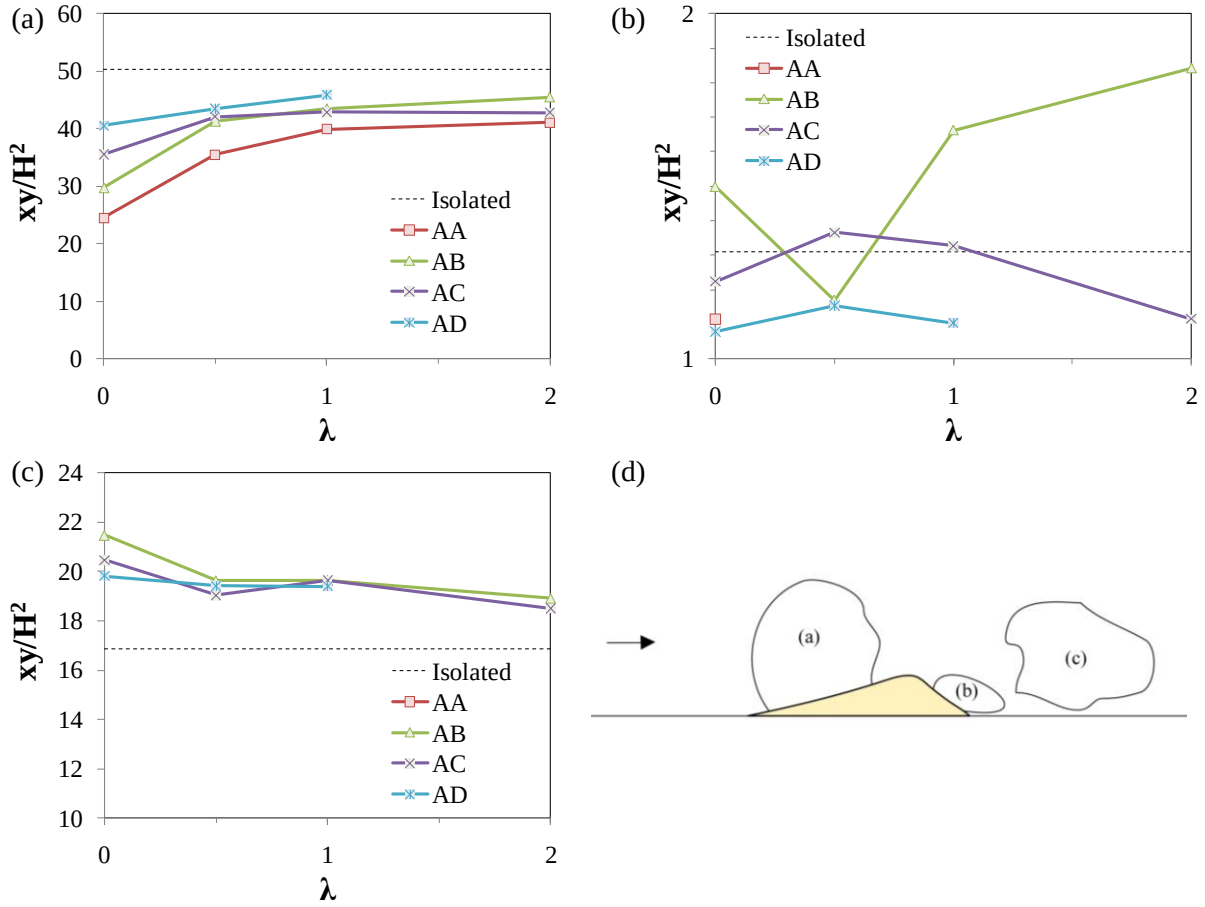

Figure 7.2: The comparison of the area of zones identified in the wall-normal contour maps for volumetric ratios AA-AD: (a) area of the topographic forcing zone; (b) area of the upwelling zone; (c) area of the expansion zone; (d) schematic showing the location of the zones relative to the downstream barchan dune in (a)-(c).

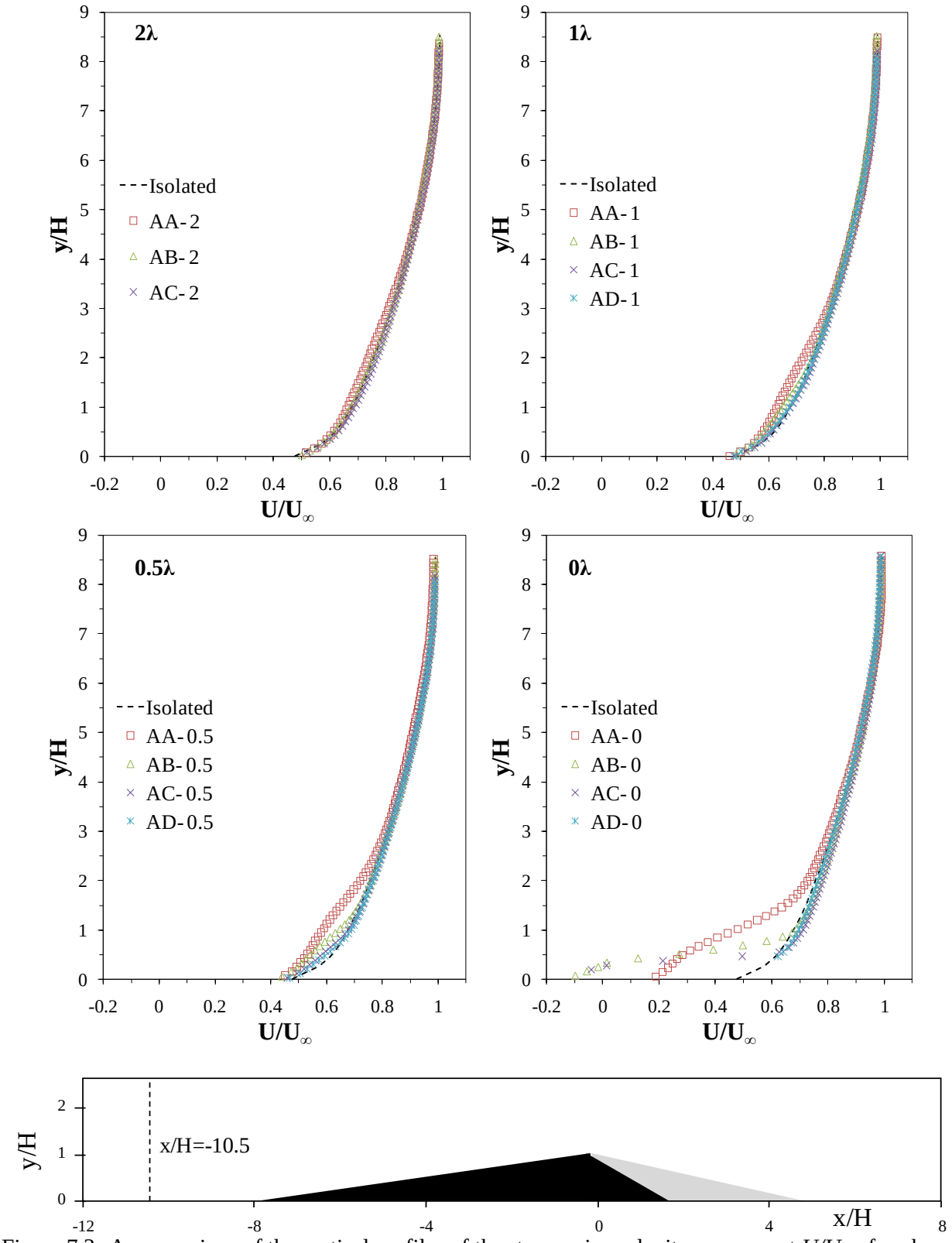

Figure 7.3: A comparison of the vertical profiles of the streamwise velocity component U/U_∞ of each volumetric ratio at -10.5*H*. The vertical profiles are divided by the respective wavelength of the data: 2λ, 1λ, 0.5λ, 0λ.

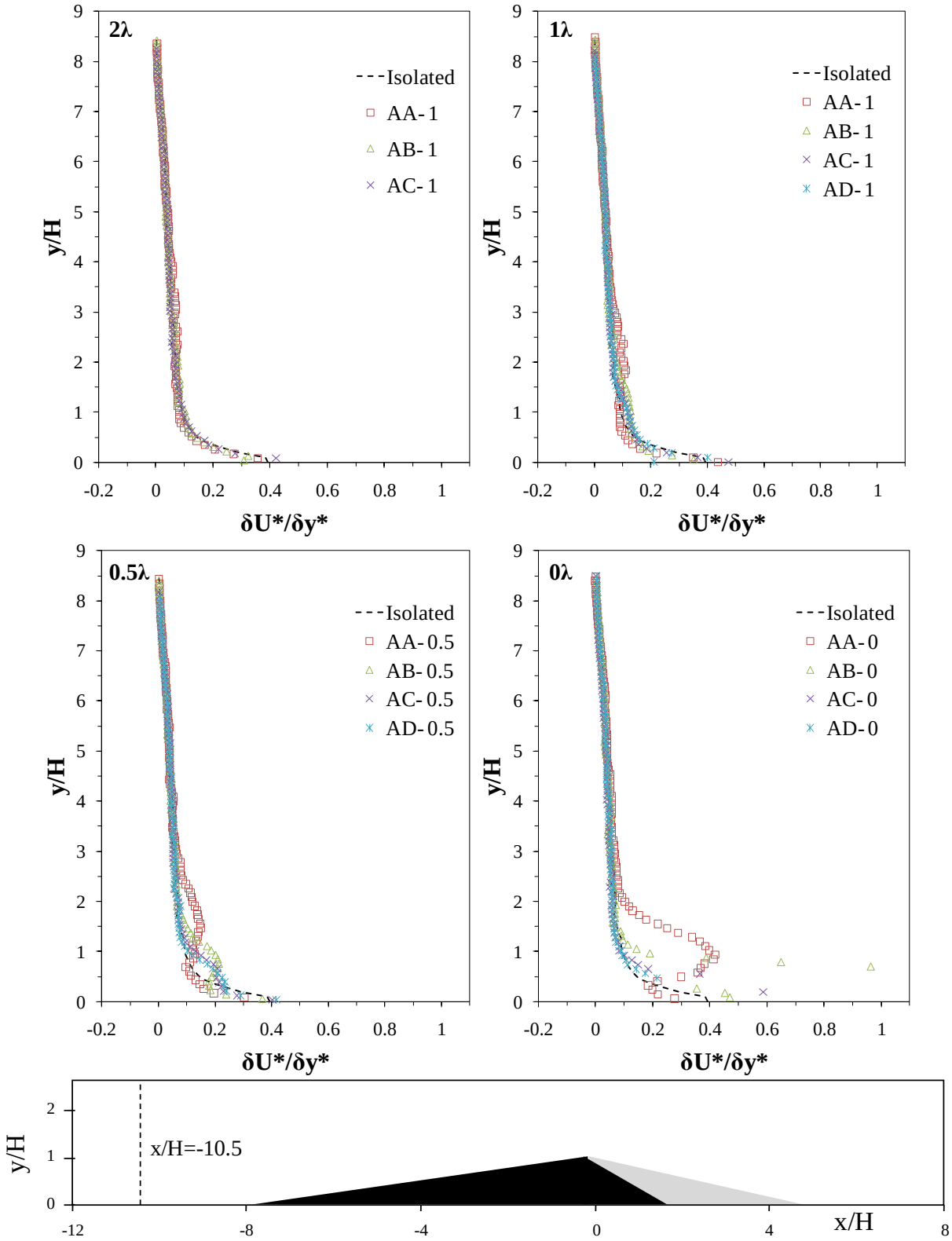

Figure 7.4: A comparison of the vertical profiles of the streamwise velocity gradient $\delta U^*/\delta y^*$ of each volumetric ratio at -10.5*H*. The vertical profiles are divided by the respective wavelength of the data: 2λ, 1λ, 0.5λ, 0λ.

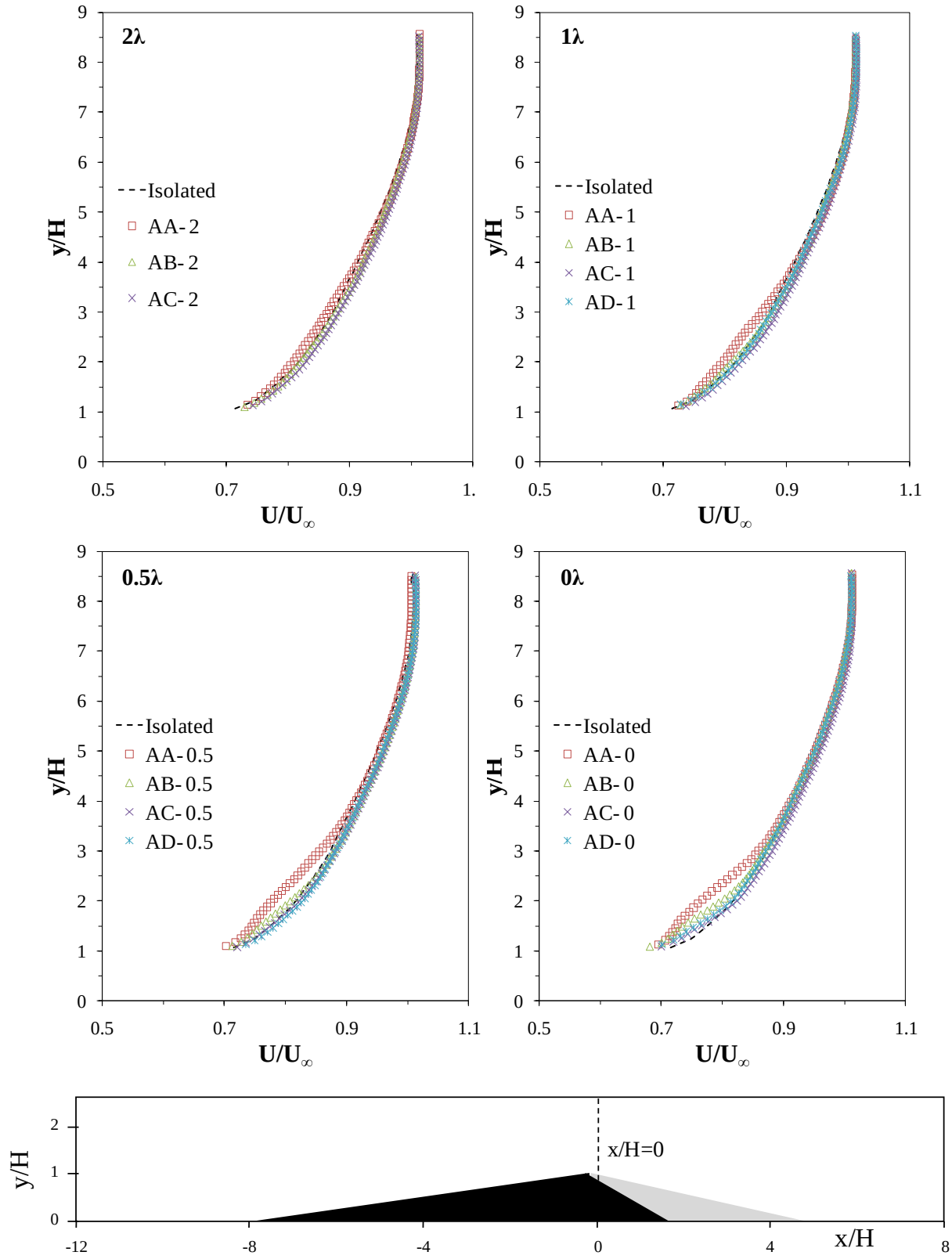

Figure 7.5: A comparison of the vertical profiles of the streamwise velocity component U/U_∞ of each volumetric ratio at 0*H*. The vertical profiles are divided by the respective wavelength of the data: 2λ, 1λ, 0.5λ, 0λ.

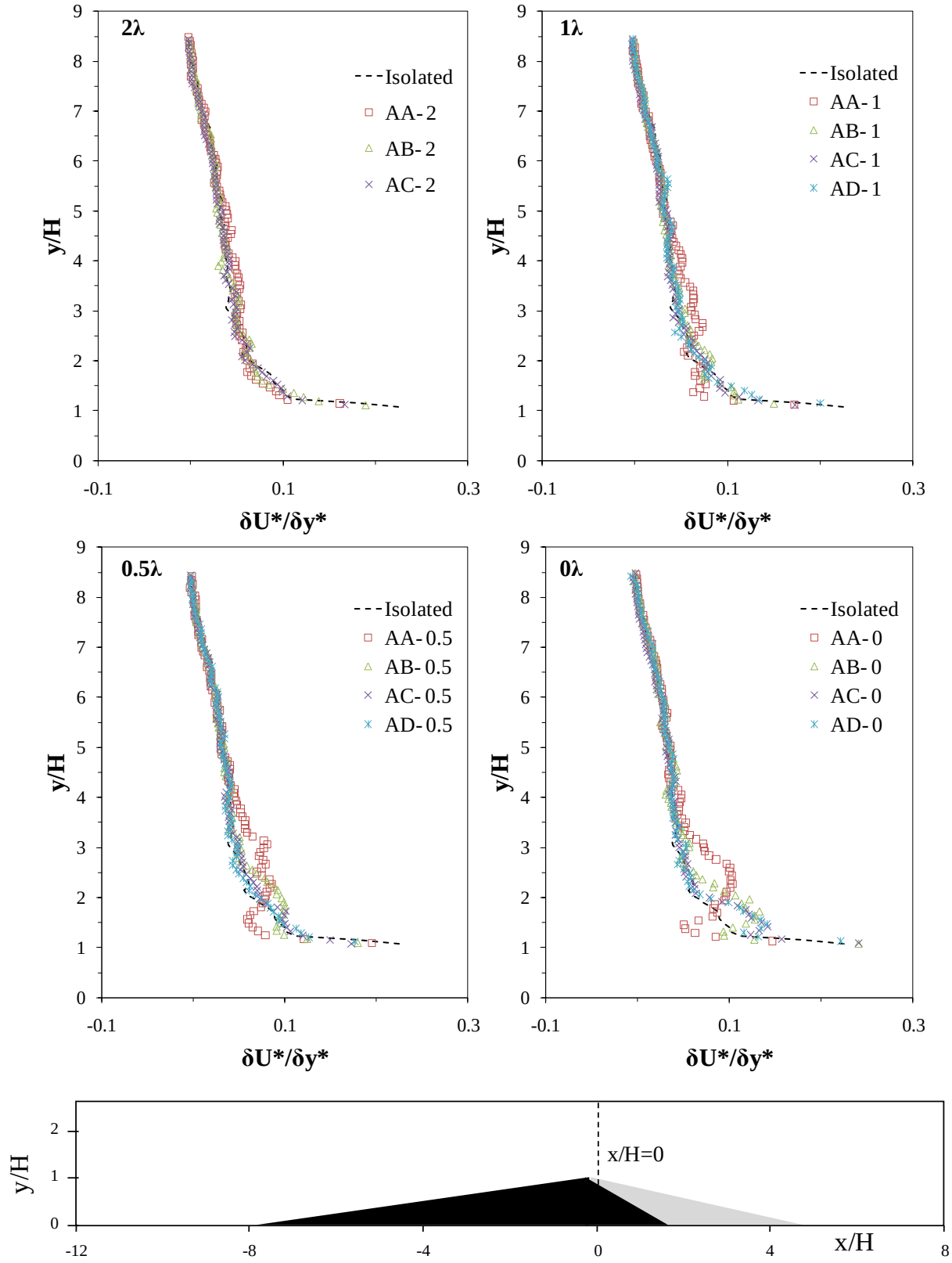

Figure 7.6: A comparison of the vertical profiles of the streamwise velocity gradient $\delta U^*/\delta y^*$ of each volumetric ratio at 0*H*. The vertical profiles are divided by the respective wavelength of the data: 2λ, 1λ, 0.5λ, 0λ.

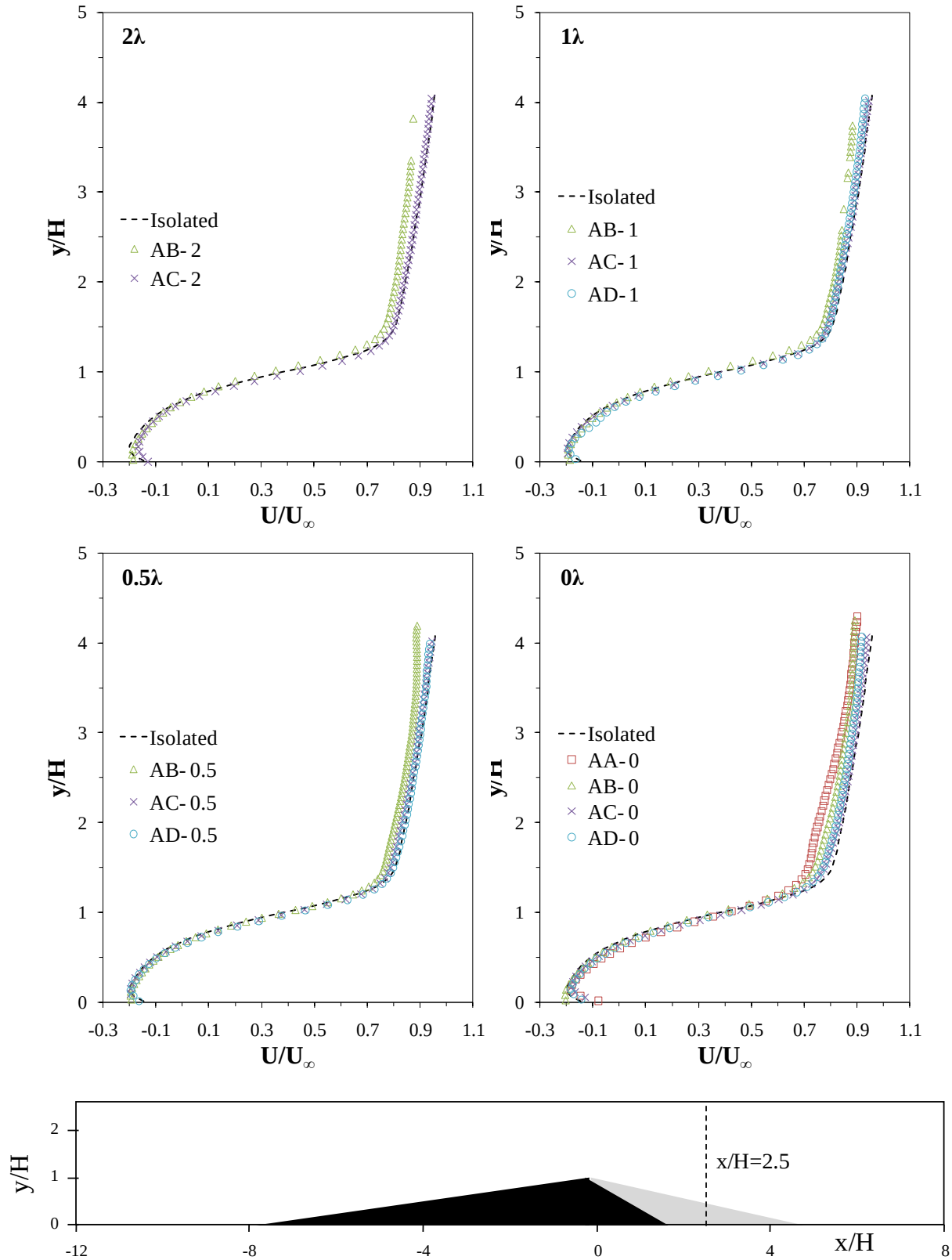

Figure 7.7: A comparison of the vertical profiles of the streamwise velocity component U/U_∞ of each volumetric ratio at 2.5*H*. The vertical profiles are divided by the respective wavelength of the data: 2λ, 1λ, 0.5λ, 0λ.

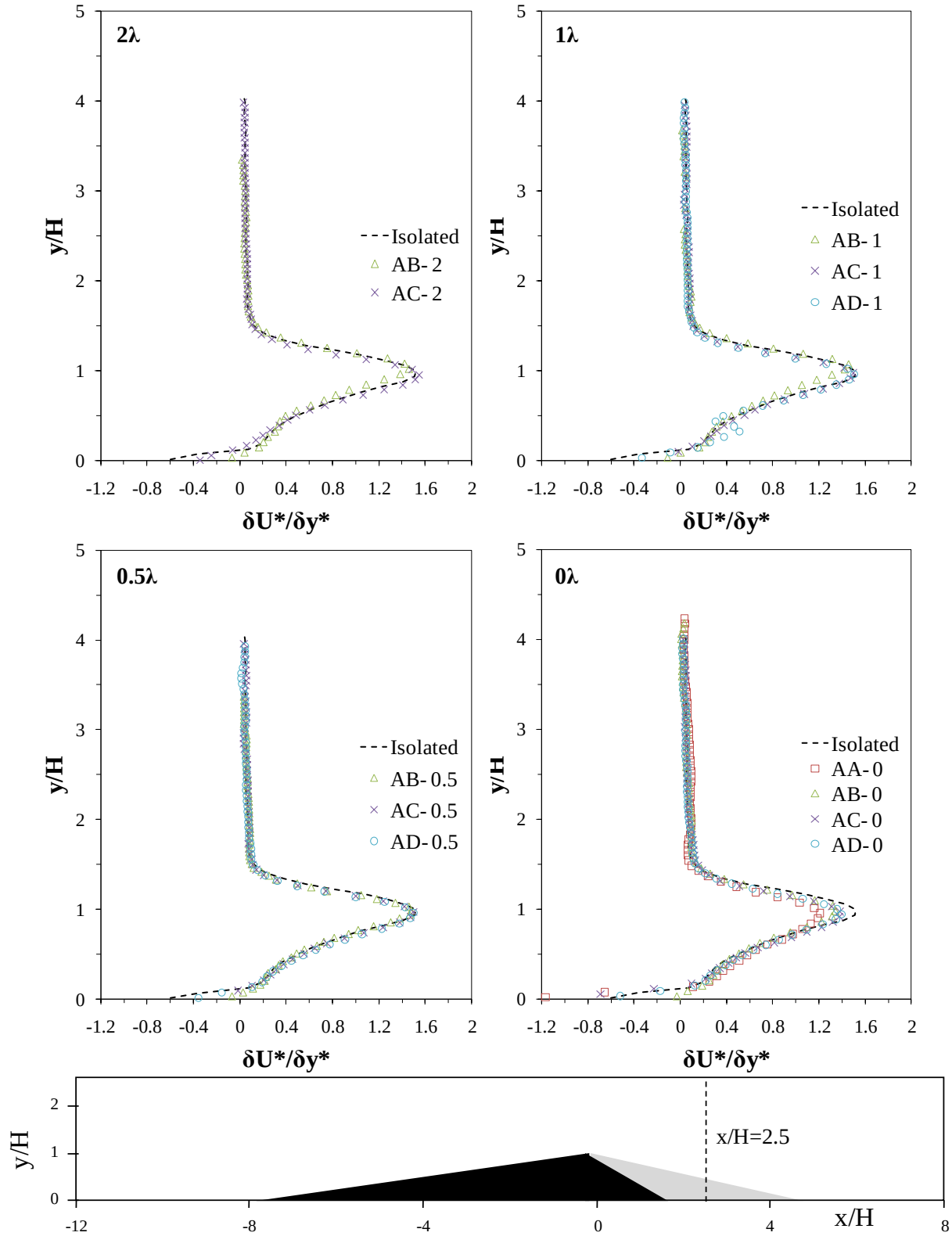

Figure 7.8: A comparison of the vertical profiles of the streamwise velocity gradient $\delta U^*/\delta y^*$ of each volumetric ratio at 2.5*H*. The vertical profiles are divided by the respective wavelength of the data: 2λ, 1λ, 0.5λ, 0λ.

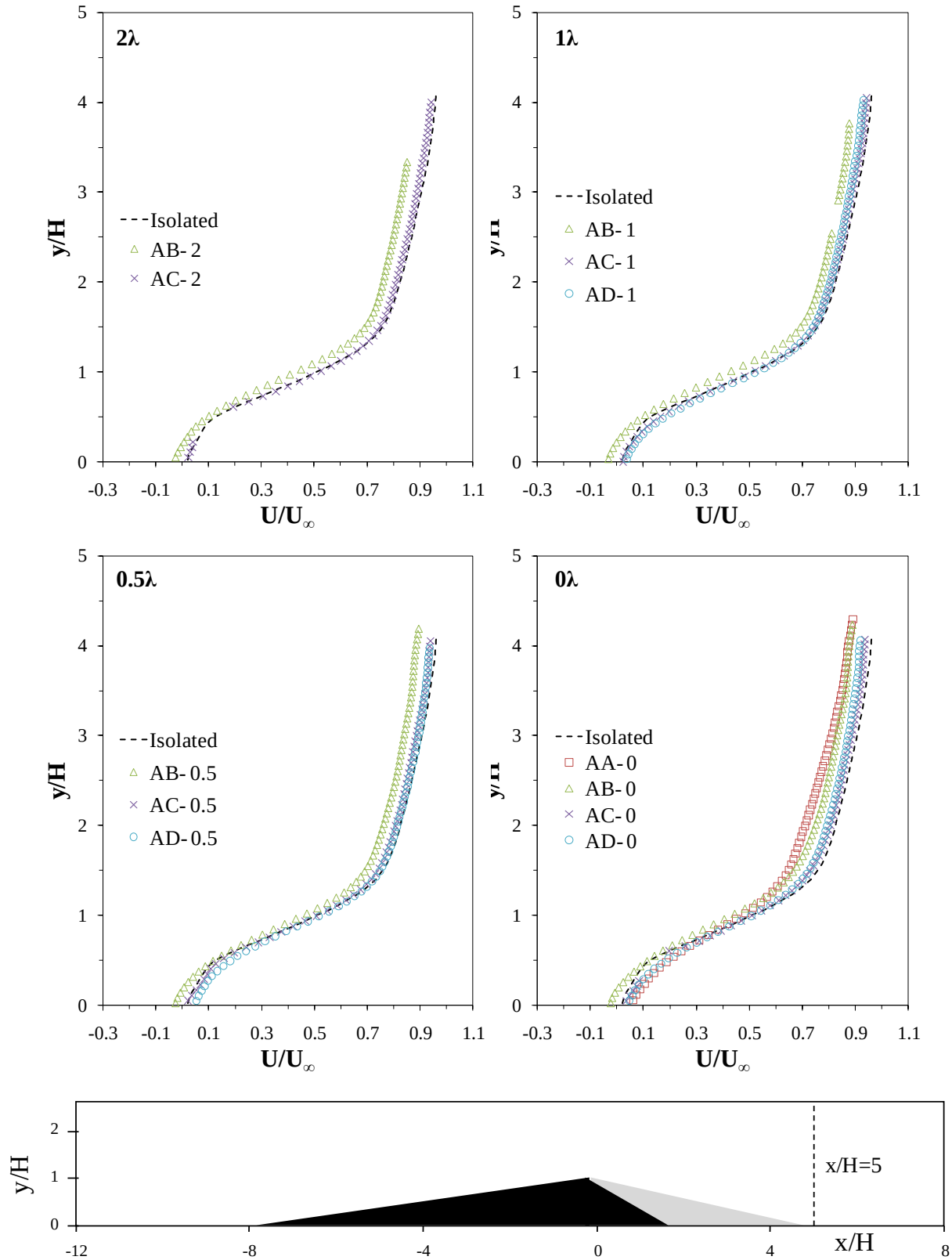

Figure 7.9: A comparison of the vertical profiles of the streamwise velocity component U/U_∞ of each volumetric ratio at 5*H*. The vertical profiles are divided by the respective wavelength of the data: 2λ, 1λ, 0.5λ, 0λ.

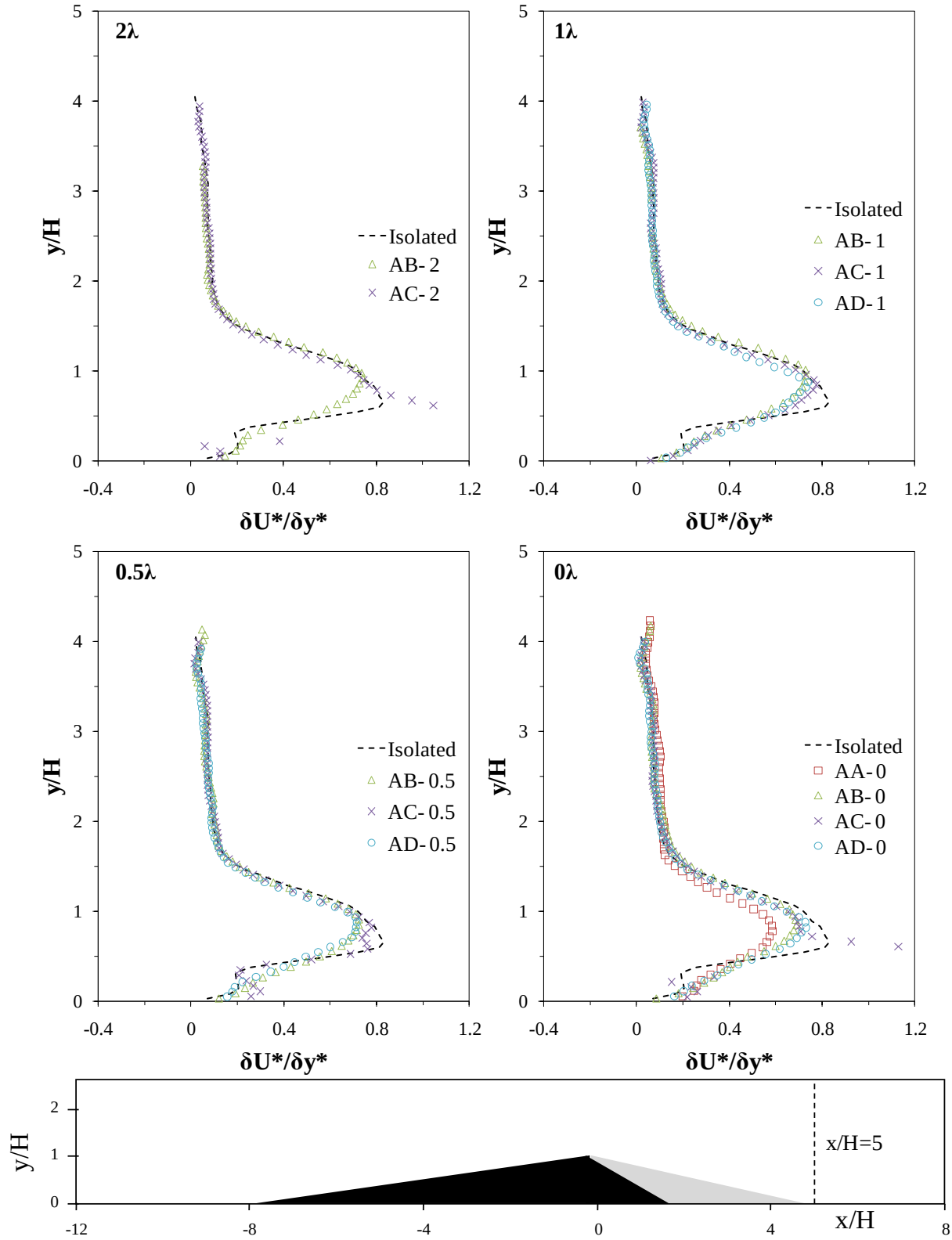

Figure 7.10: A comparison of the vertical profiles of the streamwise velocity gradient $\delta U^*/\delta y^*$ of each volumetric ratio at 5*H*. The vertical profiles are divided by the respective wavelength of the data: 2λ, 1λ, 0.5λ, 0λ.

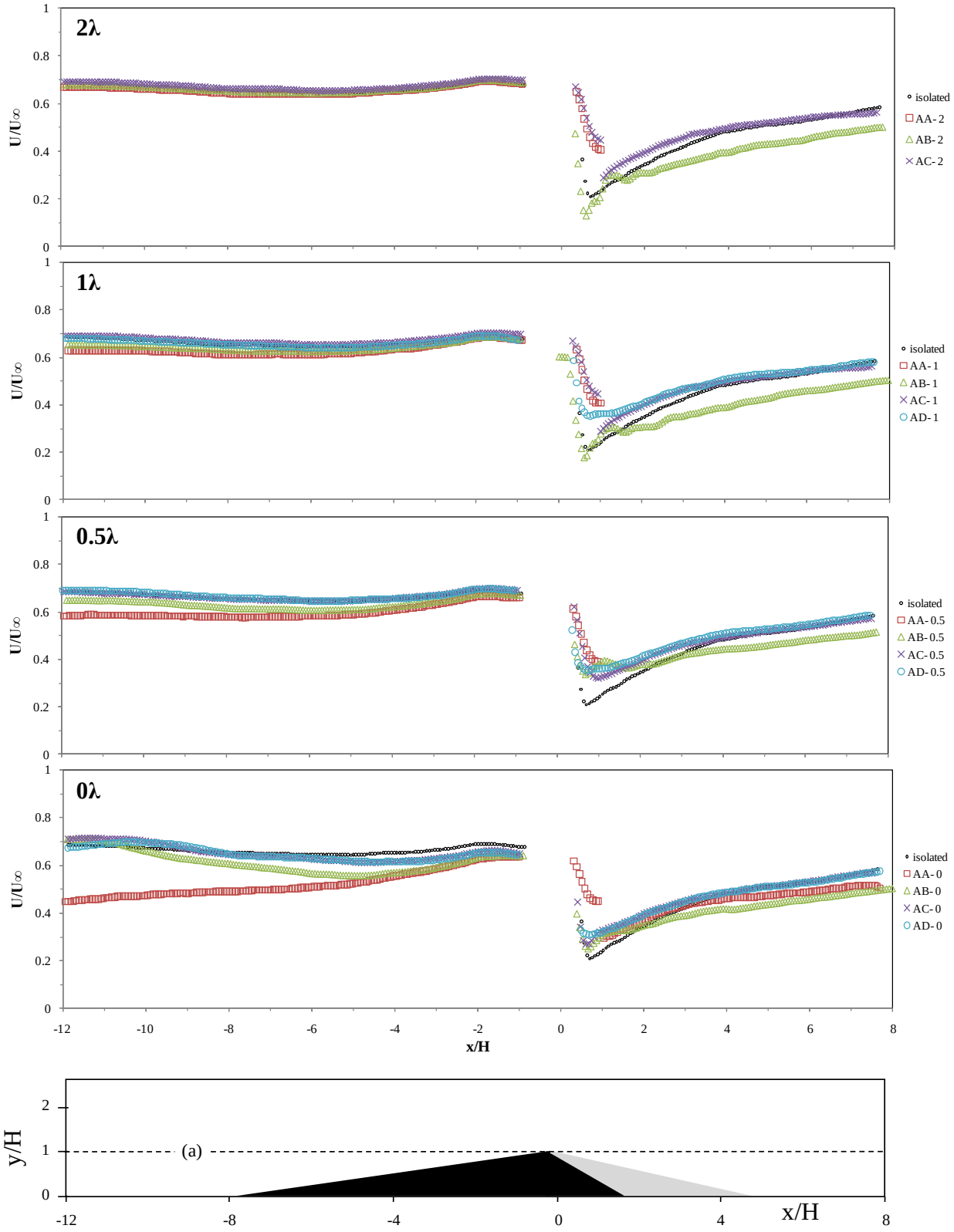

Figure 7.11: Horizontal profiles of the streamwise velocity component U/U_∞ at (a) y/H=1.00. The horizontal profiles are divided by the respective wavelength of the data: 1) 0λ; 2) 0.5λ; 3) 1λ; 4) 2λ.

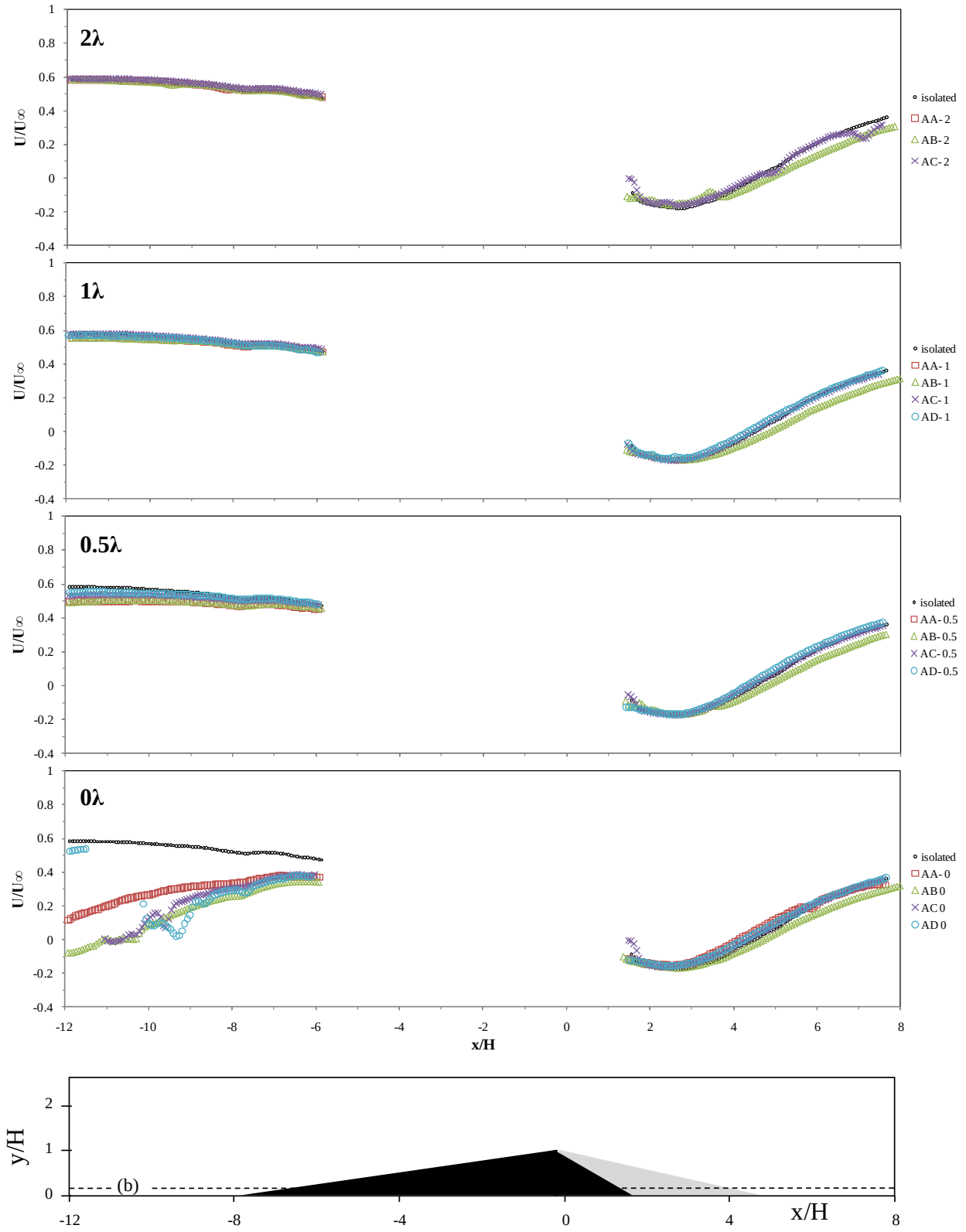

Figure 7.12: Horizontal profiles of the streamwise velocity component U/U_∞ at (b) y/H=0.29. The horizontal profiles are divided by the respective wavelength of the data: 1) 0λ; 2) 0.5λ; 3) 1λ; 4) 2λ.

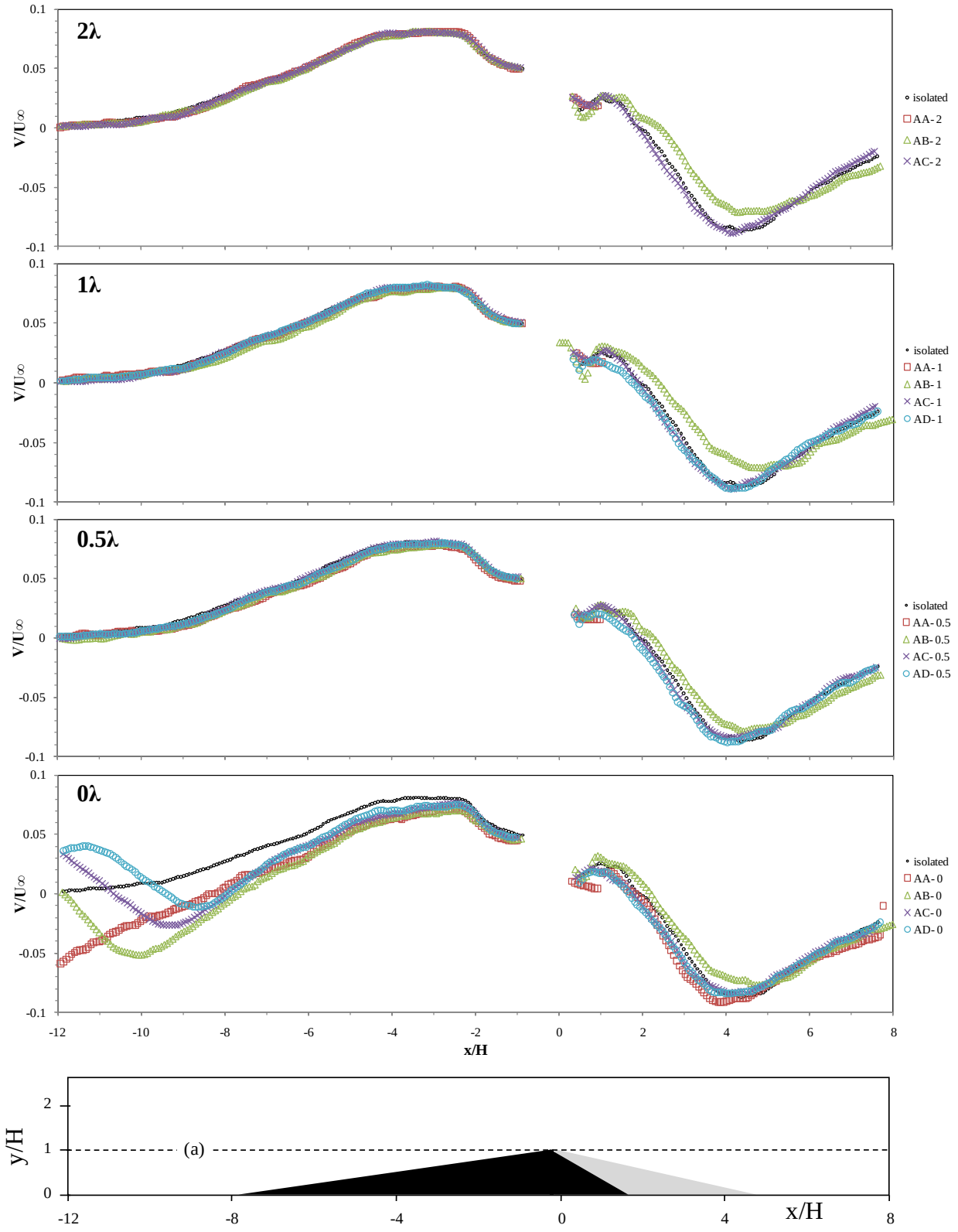

Figure 7.13: Horizontal profiles of the wall-normal velocity component V/U_∞ at (a) y/H=1.00. The horizontal profiles are divided by the respective wavelength of the data: 1) 0λ; 2) 0.5λ; 3) 1λ; 4) 2λ.

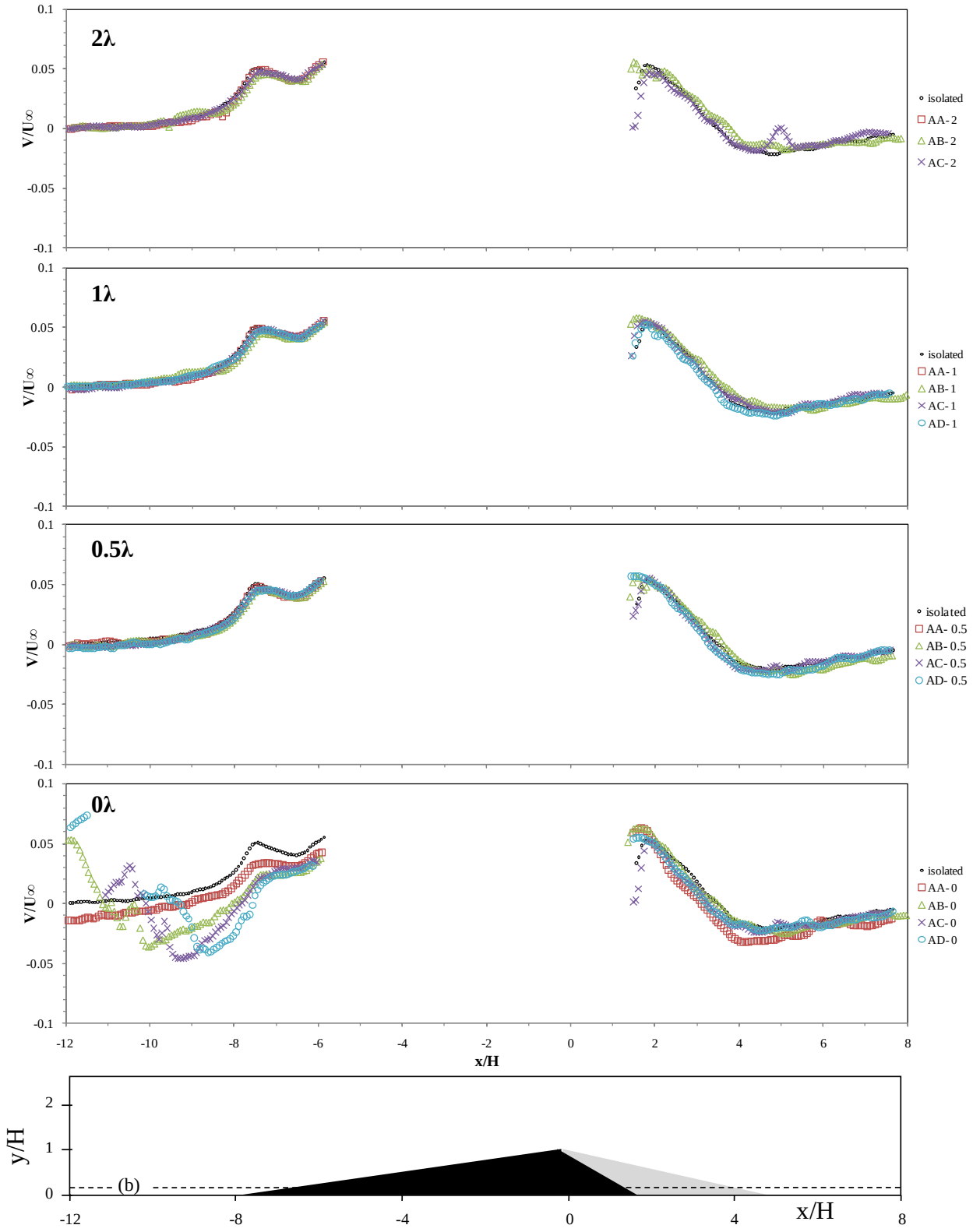

Figure 7.14: Horizontal profiles of the wall-normal velocity component V/U_∞ at (b) y/H=0.29. The horizontal profiles are divided by the respective wavelength of the data: 1) 0λ; 2) 0.5λ; 3) 1λ; 4) 2λ.

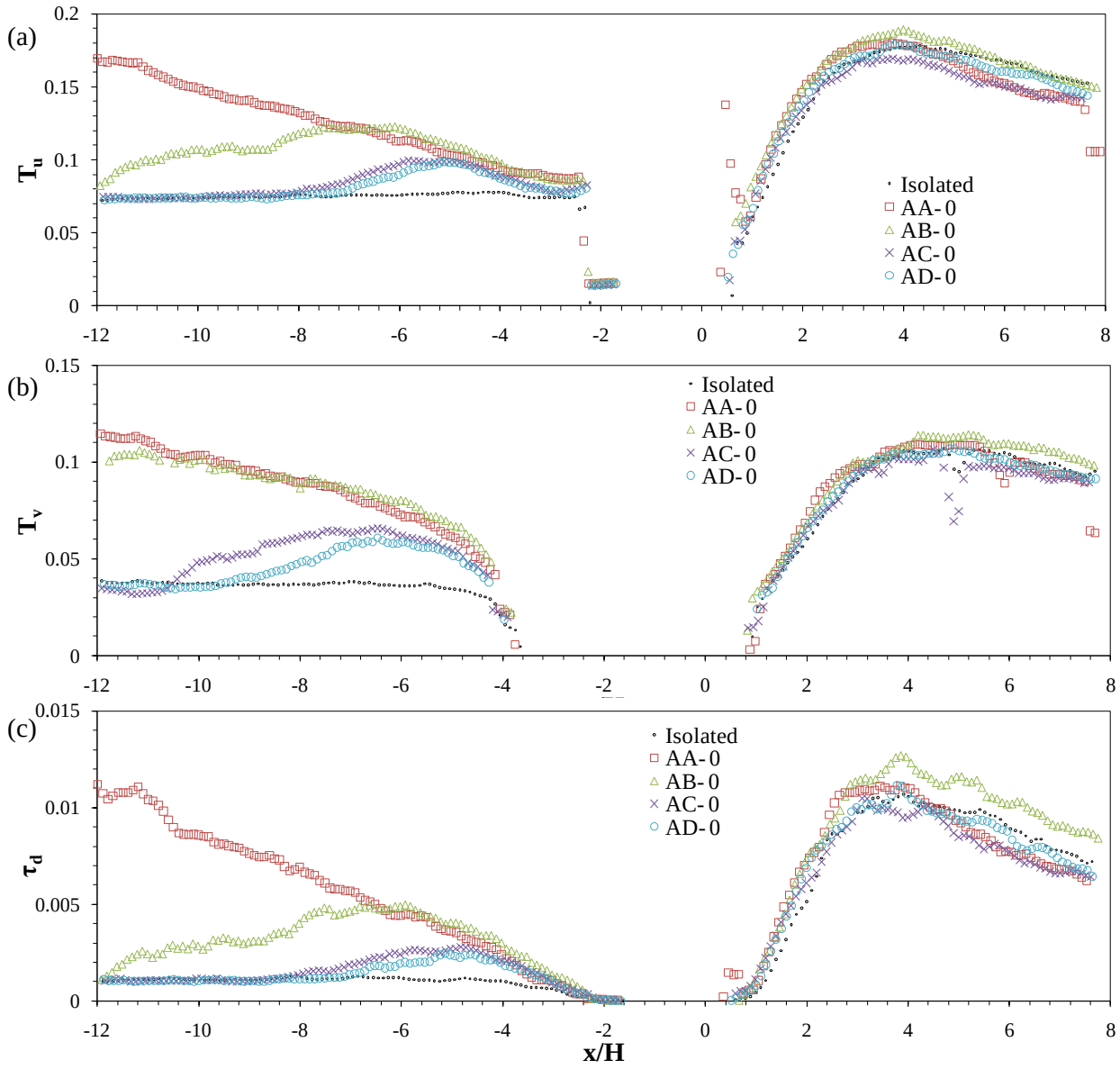

Figure 7.15:(a) and (b) are the streamwise and wall-normal components of the turbulence intensity, T_u and T_v, respectively and (c) the dimensionless Reynolds stress τ_d for the condition of λ=0.

7. 3 Discussion

The experimental setup of the present study reproduced the volumetric ratios employed by Endo *et al.* (2004). The experiments conducted by Endo *et al.* (2004) show three barchan dune binary interactions producing three modes of behavior: (a) 'absorption'; (b) 'ejection'; and (c) 'split' (see section 4.2.1). The results of the present study only apply to the first stage shown in Figure 7.16 as the interaction is defined by the morphodynamics, which are not considered in the present fixed bed research. The results presented in this thesis give insight towards understanding the mechanisms controlling the mass and momentum exchange in the initial phases of a barchan dune interaction. As demonstrated in the previous section, the increase in volumetric ratio significantly alters the flow structure upstream and downstream of the downstream barchan dune. The sheltering effect induced by the upstream barchan dune on the downstream flow is evident at the greatest volumetric ratio (AA), 1:1, as evidenced by the reduction in the area of the zone of topographic forcing on the downstream barchan dune stoss-side, the dampening of turbulence and the reduction of velocity in the downstream barchan dune leeside. Furthermore, the reattachment length at 0λ was significantly shorter than the benchmark isolated dune, in addition to the other volumetric ratios.

The volumetric ratio (AB), associated with the 'split' behavior, exhibits the greatest turbulence production, in addition to a reduction in velocity in the downstream barchan dune leeside. The longest reattachment lengths in the downstream barchan leeside were observed at this ratio. One explanation for the growth of the separation bubble and the increased production in turbulence is through the interaction of the upstream barchan dune shear layer with the shear layer of the downstream barchan dune, which has been documented in Fernandez *et al.* (2006). The upstream barchan dune reattachment point at 0λ is located close to the toe of the DBD, at x/H=-9.7. The leeside shear layer of the upstream dune extends onto the stoss-side of the downstream barchan, and is proposed to be responsible for dune 'splitting'. The turbulence intensity along the shear layer in the upstream barchan leeside is greater at ratio AB than the smaller ratios AC and AD due to the greater height of the upstream barchan dune. This may account for the different erosion of the downstream barchan dune found for the 'splitting' behavior of Endo *et al*. (2004) as compared to the 'absorption' and 'ejection' behaviors.

The volumetric ratio (AC) associated with the 'ejection' behavior, despite having a larger upstream barchan dune than in volumetric ratio AD, possessed a velocity field that more closely

resembled the isolated barchan dune velocity than ratio AD. The upstream barchan dune wake in ratio AC amplified the wake in the leeside, reducing the streamwise velocity component. In the leeside, the turbulence intensity was the lowest at ratio AC of all the volumetric ratios. Volumetric ratio AD associated with the 'absorption' behavior demonstrated a larger effect on the flow field than was initially hypothesized, and the turbulence intensity was greater than volumetric ratio AC. On the stoss-side and crest, the streamwise velocity component was slightly enhanced beyond the benchmark isolated barchans dune.

The downstream barchan dune leeside in ratios AC and AD is characterized by a slightly longer reattachment length than the isolated barchan, except at λ=0 and 0.5 for ratio AC. The downstream barchan dune leeside at ratios AC and AD shows reduced turbulence intensity. The separation zone length of the upstream barchan is smaller than that found at ratio AB, and is also characterized by smaller turbulence intensities; thus, the ability of the upstream barchan dune to erode a larger downstream dune could be expected to be limited in these cases. The upstream barchan separation zone reattaches at the downstream barchan toe at 0λ for ratios AC and AD. In the case of the 'ejection' behavior documented by Endo *et al.* (2004), the second stage (Figure 7.16b) clearly shows the excavation of the DBD stoss-side due to the upstream barchan separation bubble. However, the interdune spacings used in the present study are unable to resolve this issue. The 'absorption' behavior of Endo *et al*. (2004) does not exhibit nearly the same amount of sediment erosion on the downstream barchan stoss-side compared to the larger ratios (Figure 7.16a). The second stage in Figure 7.16a resembles bedform superimposition, where the UBD begins to ascend the stoss-side, which is not modeled in the present study.

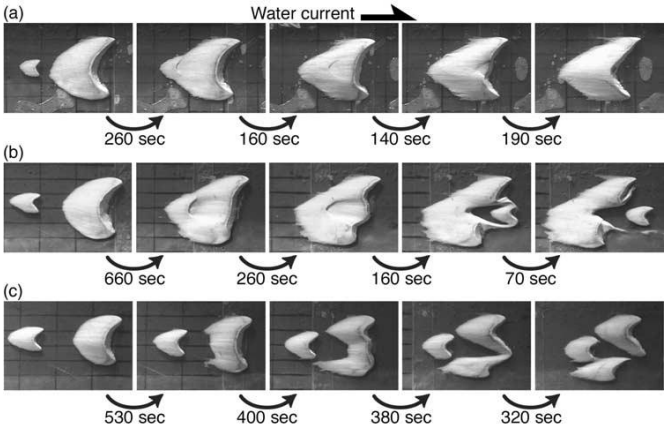

Figure 7.16: A time series of three barchan dune interactions: (a) absorption; (b) ejection; (c) split (After Endo *et al*., 2004).

Chapter 8

Conclusions and future directions

8.1 Conclusions

This aim of this study was to address recurring questions posed in the literature (Endo *et al*., 2004; Best, 2005; Fernandez et al., 2006, etc.) regarding the nature of flow over interacting barchan dunes, and the effect of interdune spacing and volumetric ratio on the separation bubble and turbulence intensity. The present research has presented two-dimensional experimental data detailing the changes to the mean and turbulence flow fields of a downstream barchan dune with the introduction of an upstream barchan dune.

The barchan dune form induces flow separation at the crest, generating a region of high vorticity where vortices are periodically shed. The free stream flow and recirculation region interact, forming a turbulent shear layer, which is the site of fluid and momentum exchange. The mean nature of flow over an isolated barchan dune and interacting barchan dunes may be summarized by identifying zones of maximum velocity and up- and down- welling fluid. The results of the isolated barchan dune clearly define the regions of flow identified in past research - the existence of the flow separation bubble, a bounding shear layer, the expanding flow downwind of the dune, an internal boundary layer, and a region of maximum velocity, which is located ~2.3H downstream from the crest. The flow over an isolated barchan dune is topographically forced on the stoss-side. The flow regions identified for the isolated dune are also present in the tandem configurations, but vary according to the size of the upstream barchan dune and the distance between the dunes. The region of maximum streamwise velocity moves upstream and upwards at the largest volumetric ratios, while at the smallest volumetric ratios, it moves downstream and upwards, relative to the isolated dune. The flow separation zone lengths vary significantly at the larger volumetric ratios, in comparison to the isolated dune reattachment length.

Volumetric ratio is the primary parameter in determining the effect of the upstream barchan dune upon the velocity in the downstream barchan dune wake outer region, followed by the interdune distance. The presence of an upstream barchan dune of equal volume to the downstream barchan dune (V_r=1) induces a ‘sheltering effect’ on the flow, manifested by a significantly shorter separation bubble and reduced velocity. Within the downstream barchan dune leeside, the flow within the separation bubble is isolated from the outer flow and the effects of the upstream

barchan dune. The shear layer acts as a spatial boundary between the outer flow, which is still affected by the upstream barchan dune, and the separation bubble. After the flow reattaches, the velocity field is also subjected to the sheltering effect of the upstream barchan dune.

The volumetric ratio associated with 'splitting' behavior (V_r=0.175) shows distinct behavior, exhibiting the longest reattachment lengths and the greatest turbulence intensities in the downstream barchan leeside. The upstream barchan shear layer appears to play a role in enhancing turbulence intensity within the downstream dune wake and may contribute towards the lengthening of the downstream barchan flow separation zone. In the case of V_r=0.175, the distance between the UBD horns and the centerline axis of the dunes is smaller than in the case of V_r=1. The volumetric ratio 0.175 favors the interaction between the up- and down- stream barchan dune shear layers, which results in a stronger velocity reduction within the downstream barchan dune wake and produces greater turbulence intensity. The upstream dune also creates a shear layer in its leeside that extends onto the stoss-side of the downstream barchan, and is proposed to be responsible for dune 'splitting' over mobile beds. However, the size of the upstream barchan dune is not solely responsible for the observed changes at V_r=0.175. Additionally, it is suggested that the distance between the upstream barchan horns (i.e. the barchan width) may play an important role in that the horns of the upstream barchan dune determine the location where the flow is steered onto the downstream barchan dune.

For the volumetric ratios associated with the 'ejection' and 'absorption' behaviors (Vr=0.056 and 0.025, respectively), the upstream barchan dune does not impact significantly flow in the leeside of the downstream barchan dune. The reattachment length showed a minor increase at these volumetric ratios, but not to the same extent as the reattachment lengths at the greater volumetric ratio. It is speculated that this is most likely due to the generation of small coherent turbulent structures in the leeside of the upstream barchans which, although they may reach the downstream barchan dune shear layer, are too insignificant in intensity and size to interact with the large structures generated in the leeside of downstream barchan dune.

8.2 Future directions

This study has demonstrated how bedform spacing and volumetric ratio significantly influence the flow field for a range of volumetric ratios and has provided an initial attempt to quantify those effects. Additional research is required to fully investigate the dynamics between barchan

dunes, namely to examine the flow field over hybrid stages within a barchan dune interaction, examine the flow over offset barchan dunes, as well as simulating a real barchan dune field by examining the effects of introducing multiple upstream barchan dunes. Moreover, the set of experiments conducted in this study only examined the streamwise-wall-normal plane aligned with the centerline axis of the barchan dune; subsequently, only the head of the coherent turbulent structures has been visualized. Further work in the spanwise-wall-normal-plane is required to address the extent and structure of the coherent turbulent structures present. In addition, it would be worthwhile to investigate the extent and nature of the turbulent structures exiting the barchan dune along the horns by examining longitudinal sections between the centerline axis and the horn edge. Additionally, another simplification within the present study is that it does not consider the effect of mobile bedload and suspended sediment on the flow, an effect which has been documented by Sukhodolov *et al.* (2006). It would thus also be worthwhile obtaining data on the mean and turbulent flow over mobile barchans, as opposed to the fixed-bed method employed within this study; however, introduction a mobile bed does pose many challenges, particularly with respect to using PIV.

REFERENCES

ADAMS, E.W., JOHNSTON, J.P. and EATON, J.K., 1984. Experiments on the structure of turbulent reattaching flow. Tech. Rep. MD-43, Thermosciences Division, Dep. of Mech. Engineering, Stanford University, Stanford, CA 94305.

AL-AWADHI, J.M., AL-DOUSARI, A. and AL-ENEZI, A., 2000. Barchan dunes in northern Kuwait. *Arab Gulf Journal of Scientific Research,* **18**(1), 32-40.

ALLEN, J.R.L., 1968. Current ripples. Amsterdam: North-Holland, pp. 433.

ALLEN, P.A., 1997. Earth Surface Processes. Oxford: Blackwell Science, pp. 404.

ALMEIDA, G.P., DURÃO, D.F.G. and HEITOR, M.V., 1993. Wake flows behind two-dimensional model hills. *Experimental Thermal and Fluid Science,* **7**(1), 87-101.

ANDREOTTI, B., CLAUDIN, P. and DOUADY, S., 2002a. Selection of dune shapes and velocities part 1: Dynamics of sand, wind and barchans. *European Physical Journal B,* **28**(3), 321-339.

ANDREOTTI, B., CLAUDIN, P. and DOUADY, S., 2002b. Selection of dune shapes and velocities part 2: A two-dimensional modelling. *European Physical Journal B,* **28**(3), 341-352.

ARMALY, B.F., DURST, F., PEREIRA, J.C.F. and SCHOENUNG, B., 1983. Experimental and theoretical investigation of backward-facing step flow. *J. Fluid Mech.,* **127**, 473-496.

BABAKAIFF, C.S. and HICKIN, E.J., 1996. Coherent flow structures in Squamish River Estuary, British Columbia, Canada. In: P.J. ASHWORTH, S.J. BENNETT AND S.J. MCLELLAND, eds, *Coherent Flow Structures.* Chichester: Wiley, pp. 312-342.

BADDOCK, M.C., LIVINGSTONE, I. and WIGGS, G.F.S., 2007. The geomorphological significance of airflow patterns in transverse dune interdunes. *Geomorphology,* **87**(4), 322-336.

BAGNOLD, R.A., 1941. The physics of blown sand and desert dunes. London: Methuen, pp. 265.

BALACHANDAR, R., HYUN, B. and PATEL, V.C., 2007. Effect of depth on flow over a fixed dune. *Canadian Journal of Civil Engineering,* **34**(12), 1587-1599.

BALACHANDAR, R. and PATEL, V.C., 2008. Flow over a fixed rough dune. *Canadian Journal of Civil Engineering,* **35**(5), 511-520.

BEAUDOIN, J., CADOT, O., AIDER, J., and WESFREID, J.E., 2004. Three-dimensional stationary flow over a backward-facing step. *European Journal of Mechanics, B/Fluids,* **23**(1), 147-155.

BENNETT, S. and VENDITTI, J.G., 1997. Turbulent flow and suspended sediment transport over fixed dunes, In: S.S.Y. Wang, E.J. Langendoen, and F.D. Shields, Jr., eds, *Proceedings of the Conference on Management of Landscapes Disturbed by Channel Incision: Stabilization, Rehabilitation, and Restoration,* 1997, Center for Computational Hydroscience and Engineering, The University of Mississippi, 949-955.

BENNETT, S.J. and BEST, J.L., 1996. Mean flow and turbulence structure over fixed, two-dimensional dunes: implications for sediment transport and bedform stability. *Sedimentology,* **42**(3), 491-513.

BESLER, H., 2002. Complex barchans in the Libyan Desert: dune traps or overtaking solitions? *Zeitschrift für Geomorphologie N.F.,* **126**, 59-74.

BEST, J.L. and LEEDER, M.R., 1993. Drag reduction in turbulent muddy seawater flows and some sedimentary consequences. *Sedimentology,* **40**(6), 1129-1137.

BEST, J., 2005. The fluid dynamics of river dunes: A review and some future research directions. *Journal of Geophysical Research F: Earth Surface,* **110**(4), F04S02.

BEST, J. and KOSTASCHUK, R., 2002. An experimental study of turbulent flow over a low-angle dune. *Journal of Geophysical Research C: Oceans,* **107**(9), 18-1.

BISHOP, M.A., 2007. Point pattern analysis of north polar crescentic dunes, Mars: A geography of dune self-organization. *Icarus,* **191**(1), 151-157.

BLUMBERG, D.G., 2006. Analysis of large aeolian (wind-blown) bedforms using the Shuttle Radar Topography Mission (SRTM) digital elevation data. *Remote Sensing of Environment,* **100**(2), 179-189.

BOURKE, M.C., EWING, R.C., FINNEGAN, D. and MCGOWAN, H.A., 2009. Sand dune movement in the Victoria Valley, Antarctica. *Geomorphology,* **109**, 148-160.

BOURKE, M.C., EDGETT, K.S. and CANTOR, B.A., 2008. Recent aeolian dune change on Mars. *Geomorphology,* **94**(1-2), 247-255.

BRADLEY, E.F., 1980. An experimental study of the profiles of wind speed, shearing stress and turbulence at the crest of a large hill. *Quarterly Journal Royal Meteorological Society,* **106**(447), 101-123.

BRADSHAW, P. and WONG, F.Y.F., 1972. The reattachment and relaxation of a turbulent shear layer. *J.Fluid Mech.,* **52**(1), 113-135.

BREED, C.S. and BREED, W.J., 1979. Dunes and other windforms of central Australia (and a comparison with linear dunes on the Moenkopi plateau, Arizona). In: *Apollo-Soyuz Test Project.Vol 2: earth observtions and photography, NASA SP-412*, 319-358.

BREUER, M., PELLER, N., RAPP, C. and MANHART, M., 2009. Flow over periodic hills - Numerical and experimental study in a wide range of Reynolds numbers. *Computers and Fluids,* **38**(2), 433-457.

BUCKLES, J., HANRATTY, T.J. and ADRIAN, R.J., 1984. Turbulent flow over large-amplitude wavy surfaces. *Journal of Fluid Mechanics,* **140**, 27-44.

BULLARD, J.E., WIGGS, G.F.S. and NASH, D.J., 2000. Experimental study of wind directional variability in the vicinity of a model valley. *Geomorphology,* **35**(1-2), 127-143.

CARLING, P.A., GÖLZ, E., ORR, H.G. and RADECKI-PAWLIK, A., 2000. The morphodynamics of fluvial sand dunes in the River Rhine, near Mainz, Germany. I. Sedimentology and morphology. *Sedimentology,* **47**(1), 227-252.

CASTRO, I.P. and WIGGS, G.F.S., 1994. Pulsed-wire anemometry on rough surfaces, with application to desert sand dunes. *Journal of Wind Engineering and Industrial Aerodynamics,* **52**(C), 53-71.

CHEPIL, W.S., 1958. The use of evenly spaced hemispheres to evaluate aerodynamic forces on a soil surface. *Trans. Am. Geophys. Unnion,* **39**, 397-403.

CLAUDIN, P. and ANDREOTTI, B., 2006. A scaling law for aeolian dunes on Mars, Venus, Earth, and for subaqueous ripples. *Earth and Planetary Science Letters,* **252**(1-2), 30-44.

CLOS-ARCEDUC, A., 1969. Essai d'Explication des Formes Dunaires Sahariennes, Etud. Photo Interpretation. Paris: Inst. Geogr. Natl., No. 4.

COLEMAN, S.E. and MELVILLE, B.W., 1996. Initiation of bed forms on a flat sand bed. *Journal of Hydraulic Engineering,* **122**(6), 301-309.

COLEMAN, S.E. and MELVILLE, B.W., 1994. Bed-form development. *Journal of Hydraulic Engineering - ASCE,* **120**(5), 544-560.

COLEMAN, S.E., NIKORA, V.I., MCLEAN, S.R., CLUNIE, T.M., SCHLICKE, T. and MELVILLE, B.W., 2006. Equilibrium hydrodynamics concept for developing dunes. *Physics of Fluids,* **18**(10), 105104-105104.

COOKE, R., WARREN, A. and GOUDIE, A., 1993. Desert Geomorphology. London: UCL Press, pp. 526.

DANIELL, J.J. and HUGHES, M., 2007. The morphology of barchan-shaped sand banks from western Torres Strait, northern Australia. *Sedimentary Geology,* **202**, 638-652.

DAUCHOT, O., LECHÉNAULT, F., GASQUET, C. and DAVIAUD, F., 2002. "Barchan" dunes in the lab. *Comptes Rendus - Mecanique,* **330**(3), 185-191.

DERICKSON, D., KOCUREK, G., EWING, R.C. and BRISTOW, C., 2008. Origin of a complex and spatially diverse dune-field pattern, Algodones, southeastern California. *Geomorphology,* **99**(1-4), 186-204.

DONG, Z., QIAN, G., LUO, W. and WANG, H., 2007. A wind tunnel simulation of the effects of stoss slope on the lee airflow pattern over a two-dimensional transverse dune. *Journal of Geophysical Research F: Earth Surface,* **112**(3), F03019.

DONG, Z., QINAN, G., LU, P., LUO, W. and WANG, H., 2009. Turbulence fields in the lee of two-dimensional transverse dunes simulated in a wind tunnel. *Earth Surface Processes and Landforms,* **34**(2), 204-216.

DONG, Z., WANG, X. and CHEN, G., 2000. Monitoring sand dune advance in the Taklimakan Desert. *Geomorphology,* **35**(3-4), 219-231.

DURÁN, O., SCHWÄMMLE, V. and HERRMANN, H., 2005. Breeding and solitary wave behavior of dunes. *Physical Review E - Statistical, Nonlinear, and Soft Matter Physics,* **72**(2), 1-5.

DURÁN, O., SCHWÄMMLE, V., LIND, P.G. and HERRMANN, H.J., 2009. The dune size distribution and scaling relations of barchan dune fields. *Granular Matter,* **11**(1), 7-11.

DURST, F. and TROPEA, C., 1981. Turbulent, backward-facing step flows in two-dimensional ducts and channels. *Proc.Third Intl Symp.on Turbulent Shear Flows, University of California, Davis,* 181-185.

ELBELRHITI, H., ANDREOTTI, B. and CLAUDIN, P., 2008. Barchan dune corridors: Field characterization and investigation of control parameters. *Journal of Geophysical Research F: Earth Surface,* **113**(2), F02S15.

ELBELRHITI, H., CLAUDIN, P. and ANDREOTTI, B., 2005. Field evidence for surface-wave-induced instability of sand dunes. *Nature,* **437**(7059), 720-723.

EMBABI, N.S. and ASHOUR, M.M., 1993. Barchan dunes in Qatar. *Journal of Arid Environments,* **25**(1), 49-69.

ENDO, N., TANIGUCHI, K. and KATSUKI, A., 2004. Observation of the whole proces of interaction between barchans by flume experiments. *Geophysical Research Letters,* **31**(12), L12503.

ENGEL, P., 1981. Length of flow separation over dunes. *Journal of the Hydraulics Division, ASCE,* **107** (HY10, Proc. Paper 16549), 1133-1143.

ERNSTSEN, V.B., NOORMETS, R., WINTER, C., HEBBELN, D., BARTHOLOMÄ, A., FLEMMING, B.W. and BARTHOLDY, J., 2005. Development of subaqueous barchanoid-shaped dunes due to lateral grain size variability in a tidal inlet channel of the Danish Wadden Sea. *J. Geophys. Res. F: Earth Surface,* **110**(4), F04S08.

ETHERIDGE, D.W. and KEMP, P.H., 1978. Measurements of turbulent flow downstream of a rearward-facing step. *Journal of Fluid Mechanics,* **86**(pt 3), 545-566.

EWING, R.C., KOCUREK, G. and LAKE, L.W., 2006. Pattern analysis of dune-field parameters. *Earth Surface Processes and Landforms,* **31**(9), 1176-1191.

FEHLMAN, H.M., 1985. *Resistance components and velocity distributions of open channel flows over bedforms,* Colorado State University, Ft. Collins.

FENTON, L.K. and BANDFIELD, J.L., 2003. Aeolian processes in Proctor Crater on Mars: Sedimentary history as analyzed from multiple data sets. *J. Geophys. Res.,* **108**(E12), 5129.

FERNANDEZ, R., BEST, J. and LÓPEZ, F., 2006. Mean flow, turbulence structure, and bed form superimposition across the ripple-dune transition. *Water Resources Research,* **42**(5), W05406.

FINKEL, H.J., 1959. The barchans of southern Peru. *Journal of Geology,* **67**, 614-647.

GABEL, S.L., 1993. Geometry and kinematics of dunes during steady and unsteady flows in the Calamus River, Nebraska, USA. *Sedimentology,* **40**(2), 237-269.

GAY, P., 1962. Origen, distribución y movimiento de las arenas eólicas en al área de Yauca a Palpa. *Boletín de la Sociedad Geológica del Perú,* **37**, 37-58.

GIRI, S. and SHIMIZU, Y., 2006. Numerical computation of sand dune migration with free surface flow. *Water Resources Research,* **42**(10), W10422.

GREELEY, R. and IVERSON, J.D., 1985. Wind as a geological process: on Earth, Mars, Venus, and Titan. Cambridge; London; New York: Cambridge University Press. pp. 333.

GROH, C., REHBERG, I. and KRUELLE, C.A., 2009. How attractive is a barchan dune? *New Journal of Physics,* **11**. 023014.

HASTENRATH, R.L., 1987. The barchan dunes of southern Peru revisited. *Z. Geomorphol. N.F.,* **31**(2), 167-178.

HASTENRATH, R.L., 1967. The barchans of the Arequipa region, southern Peru. *Z. Geomorphol.,* **11**(3), 300-331.

HERRMANN, H.J., 2006. Pattern formation of dunes. *Nonlinear Dynamics,* **44**(1-4), 315-317.

HERRMANN, H.J., 2002. Evolution and shapes of dunes. *Comptes Rendus Physique,* **3**(2), 197-206.

HERRMANN, H.J. and SAUERMANN, G., 2000. Shape of dunes. *Physica A: Statistical Mechanics and its Applications,* **283**(1), 24-30.

HERRMANN, H.J., SAUERMANN, G. and SCHWÄMMLE, V., 2005. The morphology of dunes. *Physica A: Statistical Mechanics and its Applications,* **358**(1 SPEC. ISS.), 30-38.

HERSEN, P., ANDERSEN, K.H., ELBELRHITI, H., ANDREOTTI, B., CLAUDIN, P. and DOUADY, S., 2004. Corridors of barchan dunes: Stability and size selection. *Physical Review E - Statistical, Nonlinear, and Soft Matter Physics,* **69**(1 1), 113041-1130412.

HERSEN, P. and DOUADY, S., 2005. Collision of barchan dunes as a mechanism of size regulation. *Geophysical Research Letters,* **32**(21), 1-5.

HESP, P.A. and HASTINGS, K., 1998. Width, height and slope relationships and aerodynamic maintenance of barchans. *Geomorphology*, **22**(2), 193-204.

HESSE, R., 2009. Do swarms of migrating barchan dunes record paleoenvironmental changes? - A case study spanning the middle to late Holocene in the Pampa de Jaguay, southern Peru. *Geomorphology*, **104**, 185-190.

HOLMES JR., M.H. and GARCIA, M.H., 2008. Flow over bedforms in a large sand-bed river: A field investigation. *Journal of Hydraulic Research*, **46**(3), 322-333.

HOWARD, A.D., MORTON, J.B., GAD-EL-HAK, M. and PIERCE, D.B., 1978. Sand transport model of barchan dune equilibrium. *Sedimentology*, **25**, 307-338.

HUNT, J.C.R., RICHARDS, K.J. and BRIGHTON, P.W.M., 1988. Stably stratified shear flow over low hills. *Quarterly Journal - Royal Meteorological Society*, **114**(482 A), 859-886.

HYUN, B.S., BALACHANDAR, R., YU, K. and PATEL, V.C., 2003. Assessment of PIV to measure mean velocity and turbulence in open-channel flow. *Experiments in Fluids*, **35**(3), 262-267.

IKATURA, T. and KISHI, T., 1980. Open channel flow with suspended sediment on sand waves, *Int. Ass. of Hydraul. Res.* 1980.

ILLING, L.V., 1954. Bahamian calcareous sands. *Bull. Am. Assoc. Pet. Geol.*, **38**, 1-95.

ISOMOTO, K. and HONAMI, S., 1989. Effect of inlet turbulence intensity on the reattachment process over a backward-facing step. *Journal of Fluids Engineering, Transactions of the ASME*, **111**(1), 87-92.

JACKSON, P.S. and HUNT, J.C.R., 1975. TURBULENT WIND FLOW OVER A LOW HILL. *Quarterly Journal of the Royal Meteorological Society*, **101**(430), 929-955.

JACKSON, R.G., 1976. Sedimentological and fluid-dynamic implications of the turbulent bursting phenomenon in geophysical flows. *Journal of Fluid Mechanics*, **77**, 531-560.

JEROLMACK, D.J. and MOHRIG, D., 2005. A unified model for subaqueous bed form dynamics. *Water Resources Research*, **41**(12), 1-10.

JIMENEZ, J.A., MAIA, L.P., SERRA, J. and MORAIS, J., 1999. Aeolian dune migration along the Ceara^ coast, north-eastern Brazil. *Sedimentology*, **46**(4), 689-701.

JOHNS, B., SOULSBY, R.L. and XING, J., 1993. A comparison of numerical model experiments of free surface flow over topography with flume and field observations. *J.Hydr.Res.*, **31**(2), 215-228.

JULIEN, P.Y., KLAASSEN, G.J., TEN BRINKE, W.B.M. and WILBERS, A.W.E., 2002. Case study: Bed resistance of Rhine River during 1998 flood. *Journal of Hydraulic Engineering*, **128**(12), 1042-1050.

KADOTA, A. and NEZU, I., 1999. Three-dimensional structure of space-time correlation on coherent vortices generated behind dune crest. *Journal of Hydraulic Research*, **37**(1), 59-80.

KATSUKI, A., NISHIMORI, H., ENDO, N. and TANIGUCHI, K., 2005. Collision dynamics of two barchan dunes simulated using a simple model. *Journal of the Physical Society of Japan*, **74**(2), 538-541.

KENYON, N.H. and STRIDE, A.H., 1967. The tide-swept continental shelf sediments between the Shetland Isles and France. *Sediment. Geol.*, **9**, 159–173.

KEYLOCK, C.J., HARDY, R.J., PARSONS, D.R., FERGUSON, R.I., LANE, S.N. and RICHARDS, K.S., 2005. The theoretical foundations and potential for large-eddy simulation (LES) in fluvial geomorphic and sedimentological research. *Earth-Science Reviews*, **71**(3-4), 271-304.

KHALAF, F.I. and AL-AJMI, D., 1993. Aeolian processes and sand encroachment problems in Kuwait. *Geomorphology*, **6**(2), 111-134.

KIM, J., KLINE, S.J. and JOHNSTON, J.P., 1978. Investigation of separation and reattachment of a turbulent shear layer: Flow over a backward-facing step. In: *Rpt. MD-37*, Mech. Eng. Dept., Stanford University, Stanford, CA.

KISS, T., SIPOS, G. and KOVÁCS, F., 2009. Human impact on fixed sand dunes revealed by morphometric analysis. *Earth Surf. Process. Landforms*, **34**, 700-711.

KLEINHANS, M.G., 2004. Sorting in grain flows at the lee side of dunes. *Earth-Science Reviews*, **65**(1-2), 75-102.

KOCUREK, G. and DOTT JR, R.H., 1981. Distinctions and uses of stratification types in the interpretation of eolian sand. *Journal of Sedimentary Petrology*, **51**(2), 579-596.

KOCUREK, G. and EWING, R.C., 2005. Aeolian dune field self-organization - Implications for the formation of simple versus complex dune-field patterns. *Geomorphology*, **72**(1-4), 94-105.

KOSTASCHUK, R., 2000. A field study of turbulence and sediment dynamics over subaqueous dunes with flow separation. *Sedimentology,* **47**(3), 519-531.

KOSTASCHUK, R. and VILLARD, P., 1996. Flow and sediment transport over large subaqueous dunes: Fraser River, Canada. *Sedimentology,* **43**(5), 849-863.

KOSTASCHUK, R.A. and CHURCH, M.A., 1993. Macroturbulence generated by dunes: Fraser River, Canada. *Sedimentary Geology,* **85**(1-4), 25-37.

KROY, K. and GUO, X., 2004. Comment on "relevant length scale of barchan dunes". *Physical Review Letters,* **93**(3), 039401.

KROY, K., SAUERMANN, G. and HERRMANN, H.J., 2002. Minimal model for aeolian sand dunes. *Physical Review E - Statistical, Nonlinear, and Soft Matter Physics,* **66**(3), 031302-031302.

KUEHN, D.M., 1980. Effects of adverse pressure gradient on the incompressible reattaching flow over a rearward-facing step. *AIAA Journal,* **18**(3), 343-346.

LANCASTER, N., 1996. The role of field experiments in studies of dune dynamics and morphology. *Annals of Arid Zone,* **35**(3), 171-186.

LANCASTER, N., 1995. Geomorphology of Desert Dunes. London: Routledge. pp. 312.

LANCASTER, N., 1989. The Namib Sand Sea: dune forms, processes and sediments. A.A. Balkema: Rotterdam. pp. 180.

LANCASTER, N., NICKLING, W.G., MCKENNA NEUMAN, C.K. and WYATT, V.E., 1996. Sediment flux and airflow on the stoss slope of a barchan dune. *Geomorphology,* **17**(1-3 SPEC. ISS.), 55-62.

LANGFORD, R.P., ROSE, J.M. and WHITE, D.E., 2009. Groundwater salinity as a control on development of eolian landscape: An example from the White Sands of New Mexico. *Geomorphology,* **105**(1-2), 39-49.

LAPOINTE, M., 1992. Burst-like sediment suspension events in a sand bed river. *Earth Surface Processes & Landforms,* **17**(3), 253-270.

LE, H., MOIN, P. and KIM, J., 1997. Direct numerical simulation of turbulent flow over a backward-facing step. *Journal of Fluid Mechanics,* **330**, 349-374.

LEEDER, M.R., 1983. On the interactions between turbulent flow, sediment transport and bedform mechanics in channelized flows. In: J.D. Collinson and J. Lewin, eds, *Modern and ancient fluvial systems, Special Publication of the International Association of Sedimentologists,* **6**, 5-18.

LETTAU, K. and LETTAU, H., 1969. Bulk transport of sand by the barchans of the Pampa de La Joya in Southern Peru. *Z.Geomorphol.N.F.,* **13**(2), 182-195.

LIMA, A.R., SAUERMANN, G., HERRMANN, H.J. and KROY, K., 2002. Modelling a dune field. *Physica A: Statistical Mechanics and its Applications,* **310**(3-4), 487-500.

LIVINGSTONE, I., WIGGS, G.F.S. and WEAVER, C.M., 2007. Geomorphology of desert sand dunes: A review of recent progress. *Earth-Science Reviews,* **80**(3-4), 239-257.

LONG, J.T. and SHARP, R.P., 1964. Barchan-dune movement in Imperial Valley, California. *Geological Society of America Bulletin,* **75**(2), 149-156.

LONSDALE, P. and MALFAIT, B., 1974. Abyssal dunes of foraminiferal sand on the Carnegie Ridge. *Geol. Soc. Am. Bull.,* **85**, 1697–1712.

LONSDALE, P. and SPIESS, F.N., 1977. Abyssal bedforms explored with a deeply towed instrument package. *Marine Geology,* **23**(1-2), 57-75.

LOPEZ, F., FERNANDEZ, R. and BEST, J., 2000. Turbulence and coherent flow structure associated with bedform amalgamation: An experimental study of the ripple-dune transition. *Joint conference on Water Resources Engineering and Water Resources Planning and management,* American Society of Civil Engineers, Minneapolis, Minnesota.

LUCKI, T.S. and TEIDERMAN, W.G., 1988. Turbulent structure in low-concentration, drag-reducing flows. *J. Geophys. Res.,* **190**, 241-263.

LYN, D.A., 1993. Turbulence measurements in open-channel flows over artificial bed forms. *J. Hydraul. Div. Am. Soc. Civ. Eng.,* **119**, 306-326.

LYNCH, K., JACKSON, D.W.T. and COOPER, J.A.G., 2008. Aeolian fetch distance and secondary airflow effects: The influence of micro-scale variables on meso-scale foredune development. *Earth Surface Processes and Landforms,* **33**(7), 991-1005.

MADDUX, T.B., 2002. *Turbulent Open Channel Flow Over Fixed Three-Dimensional Dune Shapes*, University of California, Santa Barbara.

MADDUX, T.B., NELSON, J.M. and MCLEAN, S.R., 2003a. Turbulent flow over three-dimensional dunes: 1. Free surface and flow response. *J. Geophys. Res.*, **108**(F1), 6009.

MADDUX, T.B., MCLEAN, S.R. and NELSEN, J.M., 2003b. Turbulent flow over three-dimensional dunes: 2. Fluid and bed stresses. *J. Geophys. Res.*, **108**(F1), 6010.

MASON, P.J., 1986. Flow over the summit of an isolated hill. *Boundary-Layer Meteorology*, **37**(4), 385-405.

MASON, P.J. and KING, J.C., 1984. Atmospheric flow over a succession of nearly two-dimensional ridges and valleys. *Quarterly Journal - Royal Meteorological Society*, **110**(466), 821-845.

MASON, P.J. and SYKES, R.I., 1979. Three-dimensional numerical integrations of the Navier-Stokes equations for flow over surface-mounted obstracles. *J Fluid Mech*, **91**(3), 433-450.

MCCORQUODALE, J.A. and GIRATALLA, M.K., 1973. Flow over natural and artificial ripples. In: *Proc. 15th Congr. Int. Ass. Hydraul. Res.*, **1**, A22-1-A22-6.

MCCULLOCH, D.S. and JANDA, R.J., 1964. Subaqueous river channel barchan dunes. *Journal of Sedimentary Petrology*, **34**, 694.

MCKEE, E.D., ed, 1979. *A Study of Global Sand Seas.* US Geological Survey Professional Paper 1052 edition. University Press of the Pacific.

MCKENNA NEUMAN, C., LANCASTER, N. and NICKLING, W.G., 2000. The effect of unsteady winds on sediment transport on the stoss slope of a transverse dune, Silver Peak, NV, USA. *Sedimentology*, **47**(1), 211-226.

MCLEAN, S.R. and SMITH, J.D., 1979. Turbulence measurements in the boundary layer over a sand wave field. *J. Geophys. Res.*, **84**(C12), 7791-7808.

MCLEAN, S.R., 1990. The stability of ripples and dunes. *Earth Science Reviews*, **29**(1-4), 131-144.

MCLEAN, S.R., NELSON, J.M. and WOLFE, S.R., 1994. Turbulence structure over two-dimensional bed forms: implications for sediment transport. *Journal of Geophysical Research*, **99**(C6), 729-747.

MCLEAN, S.R., NIKORA, V.I. and COLEMAN, S.E., 2008. Double-averaged velocity profiles over fixed dune shapes. *Acta Geophysica*, **56**(3), 669-697.

MCLEAN, S.R. and SMITH, J.D., 1986. A model for flow over two-dimensional bed forms. *Journal of Hydraulic Engineering - ASCE*, **112**(4), 300-317.

MCLEAN, S.R., WOLFE, S.R. and NELSON, J.M., 1999. Predicting boundary shear stress and sediment transport over bed forms. *Journal of Hydraulic Engineering*, **125**(7), 725-736.

MENDOZA, C. and SHEN, H.W., 1990. Investigation of turbulent flow over dunes. *Journal of Hydraulic Engineering*, **116**(4), 459-477.

MIAO, T., MU, Q. and WU, S., 2001. Computer simulation of aeolian bedforms. *Progress in Natural Science*, **11**(5), 391-392.

MIERLO, M.C.L.M. and DE RUITER, J.C., 1988. Turbulence measurements over artificial dunes. Delft Hydraulics Laboratory, Delft, the Netherlands. Report Q789.

MOMIJI, H. and BISHOP, S.R., 2002. Estimating the windward slope profile of a barchan dune. *Sedimentology*, **49**(3), 467-481.

MOMIJI, H., CARRETERO-GONZLEZ, R., BISHOP, S.R. and WARREN, A., 2000. Simulation of the effect of wind speedup in the formation of transverse dune fields. *Earth Surface Processes and Landforms*, **25**(8), 905-918.

MOMIJI, H. and WARREN, A., 2000. Relations of sand trapping efficiency and migration speed of transverse dunes to wind velocity. *Earth Surface Processes and Landforms*, **25**(10), 1069-1084.

MORGAN, P.E., RIZZETTA, D.P. and VISBAL, M.R., 2006. High-order numerical simulation of turbulent flow over a wall-mounted hump. *AIAA Journal*, **44**(2), 239-251.

MUELLER, A. and GYR, A., 1986. On the vortex formation in the mixing layer behind dunes. *Journal of Hydraulic Research*, **24**(5), 359-375.

MULLIGAN, K.R., 1995. Field methods in a study of the process-response system controlling dune morphology, Salton Sea, California. In: V.P. TCHAKERIAN, ed, *Desert Aeolian Processes.* Chapman and Hall, pp. 131-150.

NAKAGAWA, H. and NEZU, I., 1987. Experimental investigation on turbulent structure of barckward-facing step flow in an open channel. *Journal of Hydraulic Research*, **25**(1), 67-88.

NELSEN, J.M., MCLEAN, S.R. and WOLFE, S.R., 1993. Mean flow and turbulence fields over two-dimensional bed forms. *Water Resources Research,* **29**(12), 3935-3953.

NELSON, J.M., SHREVE, R.L., MCLEAN, S.R. and DRAKE, T.G., 1995. Role of near-bed turbulence structure in bed load transport and bed form mechanics. *Water Resources Research,* **31**(8), 2071-2086.

NELSON, J.M. and SMITH, J.D., 1989. Mechanics of flow over ripples and dunes. *J. Geophys. Res.*, **94**(C6), 8146-8162.

NEWELL, N.D. and RIGBY, J.R., Geological studies on the Great Bahama Bank. *Soc. Econ. Palaeontologists Mineralogists, Spec. Publ. 5,* , 15-79.

NEZU, I. and NAKAGAWA, H., 1989. Turbulent structure of backward-facing step flow and coherent vortex shedding from reattachment in open-channel flows. *Turbulent Shear Flows,* **6**, 313-337.

NINO, Y. and BARAHONA, M., 1997. Barchan-ripples: Emergence, evolution and flow-sediment interactions. In: *Proceedings Environmental and Coastal Hydraulics: Protecting the Aquatic Habitat*, **B**(2), 1037- 1042.

NISHIMORI, H., YAMASAKI, M. and ANDERSEN, K.H., 1998. A simple model for the various pattern dynamics of dunes. *International Journal of Modern Physics B,* **12**(3), 257-272.

NORRIS, R.M., 1966. Barchan dunes of Imperial Valley, California. *J. Geol.*, **74**, 292-306.

OGINK, H.J.M., 1989. Hydraulic roughness of single and compound bed forms. *Part XI, Rep. on Model Investigations, A36*, Delft Hydraulics, Emmeloord, The Netherlands.

OJHA, S.P. and MAZUMDER, B.S., 2008. Turbulence characteristics of flow region over a series of 2-D dune shaped structures. *Advances in Water Resources,* **31**(3), 561-576.

ORTIZ, P. and SMOLARKIEWICZ, P.K., 2009. Coupling the dynamics of boundary layers and evolutionary dunes. *Physical Review E - Statistical, Nonlinear, and Soft Matter Physics*, **79**(4), 041307.

ORTIZ, P. and SMOLARKIEWICZ, P.K., 2006. Numerical simulation of sand dune evolution in severe winds. *International Journal for Numerical Methods in Fluids,* **50**(10), 1229-1246.

ÖTÜGEN, M.V., 1991. Expansion ratio effects on the separated shear layer and reattachment downstream of a backward-facing step. *Experiments in Fluids,* **10**(5), 273-280.

PAARLBERG, A.J., DOHMEN-JANSSEN, C.M., HULSCHER, S.J.M.H. and TERMES, P., 2009. Modeling river dune evolution using a parameterization of flow separation. *Journal of Geophysical Research F: Earth Surface,* **114**(1), F01014.

PAARLBERG, A.J., DOHMEN-JANSSEN, C.M., HULSCHER, S.J.M.H. and TERMES, P., 2007. A parameterization of flow separation over subaqueous dunes. *Water Resources Research,* **43**(12), W12417.

PARKER GAY JR., S., 1999. Observations regarding the movement of barchan sand dunes in the Nazca to Tanaca area of southern Peru. *Geomorphology,* **27**(3-4), 279-293.

PARSONS, D.R., BEST, J.L., ORFEO, O., HARDY, R.J., KOSTASCHUK, R. and LANE, S.N., 2005. Morphology and flow fields of three-dimensional dunes, Rio Paraná, Argentina: Results from simultaneous multibeam echo sounding and acoustic Doppler current profiling. *Journal of Geophysical Research F: Earth Surface,* **110**(4), F04S03.

PARSONS, D.R., WIGGS, G.F.S., WALKER, I.J., FERGUSON, R.I. and GARVEY, B.G., 2004. Numerical modelling of airflow over an idealised transverse dune. *Environmental Modelling and Software,* **19**(2), 153-162.

PARTELI, E.J.R., SCHWÄMMLE, V., HERRMANN, H.J., MONTEIRO, L.H.U. and MAIA, L.P., 2006. Profile measurement and simulation of a transverse dune field in the Lençóis Maranhenses. *Geomorphology,* **81**(1-2), 29-42.

PATEL, V.C. and LIN, C.L., 2004. Turbulence modeling in flow over a dune with special reference to free surface and bed roughness effects. In: *Proc., 6th Int.Conf.on Hydroscience and Engineering (ICHE-2004).*

PERIC, M., RUGER, M. and SCHEUERER, G., 1988. Calculation of the two-dimensional turbulent flow over a sand dune model. *Rep.No.SRR-TN-88-O2,* University of Erlangen, Germany.

PRASAD, A.K. and JENSEN, K., 1995. Scheimpflug stereocamera for particle image velocimetry in liquid flows. *Applied Optics,* **34**(30), 7092-7099.

PYE, K. and TSOAR, H., 1990. Aeolian Sand and Sand Dunes. London: Unwin Hyman. pp. 400.

QIAN, G., DONG, Z., LUO, W. and WANG, H., 2009. Variations of horizontal and vertical velocities over two-dimensional transverse dunes: A wind tunnel simulation of the effect of windward slope. *Journal of Arid Environments,* **73**(12), 1109-1116.

RA, S.H. and CHANG, P.K., 1990. Effects of pressure gradient on reattaching flow downstream of a rearward-facing step. *Journal of Aircraft,* **27**(1), 93-95.

RASMUSSEN, K.R., IVERSEN, J.D. and RAUTAHEMIO, P., 1996. Saltation and wind-flow interaction in a variable slope wind tunnel. *Geomorphology*, **17**(1-3 SPEC. ISS.), 19-28.

RAUDKIVI, A.J., 1966. Bed forms in alluvial channels. *J. Fluid Mech.*, **26**, 507-514.

RAUDKIVI, A.J., 1963. Study of sediment ripple formation. *ASCE J. Hydraul. Div.*, **89**(HY6), 15-36.

RIFAI, M.F. and SMITH, K.V.H., 1971. Flow over triangular elements simulating dunes. *J. Hydraul. Div. Am. Soc. Civ. Eng.*, **97**, 963-976.

ROBERT, A.R. and UHLMAN, W., 2001. An experimental study on the ripple-dune transition. *Earth Surf. Process. Landforms*, **26**, 615-629.

SAUERMANN, G., ROGNON, P., POLIAKOV, A. and HERRMANN, H.J., 2000. The shape of the barchan dunes of Southern Morocco. *Geomorphology*, **36**(1-2), 47-62.

SCHATZ, V. and HERRMANN, H.J., 2006. Flow separation in the lee side of transverse dunes: A numerical investigation. *Geomorphology*, **81**(1-2), 207-216.

SCHINDLER, R.J. and ROBERT, A., 2005. Flow and turbulence structure across the ripple-dune transition: An experiment under mobile bed conditions. *Sedimentology*, **52**(3), 627-649.

SCHWÄMMLE, V. and HERRMANN, H.J., 2005. A model of barchan dunes including lateral shear stress. *European Physical Journal E*, **16**(1), 57-65.

SEIFERT, A. and PACK, L.G., 2002. Active flow separation control on wall-mounted hump at high Reynolds numbers. *AIAA Journal*, **40**(7), 1363-1372.

SINHA, S.N., GUPTA, A.K. and OBERAI, M.M., 1981. Laminar separating flow over backsteps and vacities Part 1: backsteps. *AIAA Journal*, **19**(12), 1527-1530.

SLATTERY, M.C., 1990. Barchan migration on the Kuiseb River Delta, Namibia. *South African Geographical Journal*, **72**, 5-10.

SMITH, J.D. and MCLEAN, S.R., 1977. Spatially averaged flow over a wavy surface. *J Geophys Res*, **82**(12), 1735-1746.

SOULSBY, R.L., ATKINS, R., WATERS, C.B. and OLIVER, N., 1991. Field measurements of suspended sediments over sandwaves. In: B. SOULSBY, ed, *Euromech 262 - Sand Transport in Rivers, Estuaries and the Sea.* Rotterdam: Balkema, 155-162.

STOESSER, T., BRAUN, C., GARCÍA-VILLALBA, M. and RODI, W., 2008. Turbulence structures in flow over two-dimensional dunes. *Journal of Hydraulic Engineering*, **134**(1), 42-55.

SUKHODOLOV, A.N., FEDELE, J.J. and RHOADS, B.L., 2006. Structure of flow over alluvial bedforms: An experiment on linking field and laboratory methods. *Earth Surface Processes and Landforms*, **31**(10), 1292-1310.

SWEET, M.L. and KOCUREK, G., 1990. An empirical model of aeolian dune lee-face airflow. *Sedimentology*, **37**(6), 1023-1038.

TAYLOR, P.A., MASON, P.J. and BRADLEY, E.F., 1987. Boundary-layer flow over low hills. *Boundary-Layer Meteorology*, **39**(1-2), 107-132.

TODD, B.J., 2005. Morphology and composition of submarine barchan dunes on the Scotian Shelf, Canadian Atlantic margin. *Geomorphology*, **67**(3-4), 487-500.

TSOAR, H., 1985. Profiles analysis of sand dunes and their steady state significance. *Geografiska Annaler*, **Series A 67 A**(1-2), 47-59.

TSOAR, H., 1984. The formation of seif dunes from barchans—a discussion. *Z. Geomorphol. N.F.*, **28**(1), 99-103.

TSOAR, H., LEVIN, N., PORAT, N., MAIA, L.P., HERRMANN, H.J., TATUMI, S.H. and CLAUDINO-SALES, V., 2009. The effect of climate change on the mobility and stability of coastal sand dunes in Ceará State (NE Brazil). *Quaternary Research*, **71**(2), 217-226.

VAN DIJK, P.M., ARENS, S.M. and VAN BOXEL, J.H., 1999. Aeolian processes across transverse dunes. II: Modelling the sediment transport and profile development. *Earth Surface Processes and Landforms*, **24**(4), 319-333.

VAN MIERLO, M.C.L.M. and DE RUITER, J.C.C.C., 1988. Rivers: Turbulence measurements above artificial dunes. Delft, Netherlands: TOW A55, Q789, Vol. 1 and II, Delft Hydraulics, .

VANONI, V.A. and HWANG, L.S., 1967. Relation between bed form and friction in streams. *J. Hydraul. Div. Am. Soc. Civ. Eng.*, **93**(HY3), 121-144.

VANONI, V.A. and NOMICOS, G.N., 1960. Resistance properties of sediment laden streams. *Trans. Am. Soc. Civ. Eng.*, **125**, 1140-1175.

VENDITTI, J.G., 2007. Turbulent flow and drag over fixed two- and three-dimensional dunes. *Journal of Geophysical Research F: Earth Surface*, **112**(4), F04008-F04008.

VENDITTI, J.G. and BAUER, B.O., 2005. Turbulent flow over a dune: Green River, Colorado. *Earth Surface Processes and Landforms*, **30**(3), 289-304.

VENDITTI, J.G. and BENNETT, S.J., 2000. Spectral analysis of turbulent flow and suspended sediment transport over fixed dunes. *Journal of Geophysical Research C: Oceans*, **105**(C9), 22035-22047.

VENDITTI, J.G., CHURCH, M.A. and BENNETT, S.J., 2005. Bed form initiation from a flat sand bed. *Journal of Geophysical Research F: Earth Surface*, **110**(1), F01009.

VILLARD, P. and KOSTASCHUK, R., 1998. The relation between shear velocity and suspended sediment concentration over dunes: Fraser Estuary, Canada. *Marine Geology*, **148**(1-2), 71-81.

VITTAL, N., RANGA RAJU, K.G. and GARDE, R.J., 1977. Resistance of two dimensional traingular roughness. *J. Hydraul. Res.*, **15**, 19-36.

WALKER, I.J., 2000. Secondary airflow and sediment transport in the lee of transverse dunes. Ph.D. Dissertation, Department of Geography, University of Guelph, Guelph.

WALKER, I.J., 1999. Secondary airflow and sediment transport in the lee of a reversing dune. *Earth Surface Processes and Landforms*, **24**(5), 437-448.

WALKER, I.J., HESP, P.A., DAVIDSON-ARNOTT, R.G.D., BAUER, B.O., NAMIKAS, S.L. and OLLERHEAD, J., 2009. Responses of three-dimensional flow to variations in the angle of incident wind and profile form of dunes: Greenwich Dunes, Prince Edward Island, Canada. *Geomorphology*, **105**(1-2), 127-138.

WALKER, I.J. and NICKLING, W.G., 2003. Simulation and measurement of surface shear stress over isolated and closely spaced transverse dunes in a wind tunnel. *Earth Surface Processes and Landforms*, **28**(10), 1111-1124.

WALKER, I.J. and NICKLING, W.G., 2002. Dynamics of secondary airflow and sediment transport over and in the lee of transverse dunes. *Progress in Physical Geography*, **26**(1), 47-75.

WALMSLEY, J.L. and SALMON, J.R., 1985. A boundary-layer model for wind flow over hills: comparison of model results with Askervein 1983 data. *Paper A14*, p.81-90.

WALMSLEY, J.L., SALMON, J.R. and TAYLOR, P.A., 1982. On the application of a model of boundary-layer flow over low hills to real terrain. *Boundary-Layer Meteorology*, **23**(1), 17-46.

WANG, Z.T., ZHANG, J.W., ZHANG, Q.H., QIANG, M.R., CHEN, F.H. and LING, Y.Q., 2008. Barchans of Minqin: Sediment transport. *Geomorphology*, **96**(1-2), 233-238.

WANG, Z., TAO, S., XIE, Y., and DONG, G., 2007. Barchans of Minqin: Morphometry. *Geomorphology*, **89**(3-4), 405-411.

WASSUN, R.J., 1984. Late Quaternary palaeoenvironments in the desert dunefields of Australia. In: *Late Cainozoic palaeoclimates of the Southern Hemisphere. Proc. SASQUA symposium, Swaziland, 1983*, 419-432.

WERNER, B.T. and KOCUREK, G., 1999. Bedform spacing from defect dynamics. *Geology*, **27**(8), 727-730.

WESTPHAL, R.V., JOHNSTON, J.P. and EATON, J.K., 1984. *Experimental Study of Flow Reattachment in a Single-sided Sudden Expansion*, NASA TR 3765, Report MD-41.

WIGGS, G.F.S., LIVINGSTONE, I. and WARREN, A., 1996. The role of streamline curvature in sand dune dynamics: Evidence from field and wind tunnel measurements. *Geomorphology*, **17**(1-3 SPEC. ISS.), 29-46.

WIJBENGA, J.H.A., 1990. Flow resistance and bedform dimensions for varying flow conditions - A literature review (main text) and (annexes). *Rep.No.A58 on Literature Study*, Delft Hydraulics, Delft, the Netherlands.

WILSON, I.G., 1972. Aeolian bedforms - their development and origins. *Sedimentology*, **19**, 173-210.

WIPPERMANN, F.K. and GROSS, G., 1986. The wind-induced shaping and migration of an isolated dune: A numerical experiment. *Boundary-Layer Meteorology*, **36**(4), 319-334.

WU, Y. and CHRISTENSEN, K.T., 2007. Outer-layer similarity in the presence of highly-irregular surface roughness. *Phys. Fluids* **19** (8), 085108, 6382-6393.

WYNN, R.B., MASSON, D.G. and BETT, B.J., 2002. Hydrodynamic significance of variable ripple morphology across deep-water barchan dunes in the Faroe-Shetland Channel. *Marine Geology*, **192**(1-3), 309-319.

YALIN, M., 1977. Mechanics of Sediment Transport. Oxford: Permagon. pp. 298.

YANG, S. and TAN, S., 2008. Flow resistance over mobile bed in an open-channel flow. *Journal of Hydraulic Engineering*, **134**(7), 937-947.

YOON, J.Y. and PATEL, V.C., 1996. Numerical model of turbulent flow over sand dune. *Journal of Hydraulic Engineering*, **122**(1), 10-17.

YOU, D., WANG, M. and MOIN, P., 2006. Large-eddy simulation of flow over a wall-mounted hump with separation control. *AIAA Journal*, **44**(11), 2571-2577.

YUE, W., LIN, C. and PATEL, V.C., 2006. Large-eddy simulation of turbulent flow over a fixed. Two-dimensional dune. *Journal of Hydraulic Engineering*, **132**(7), 643-651.

YUE, W., LIN, C. and PATEL, V.C., 2005. Coherent structures in open-channel flows over a fixed dune. *Journal of Fluids Engineering, Transactions of the ASME*, **127**(5), 858-864.

YUE, W., LIN, C. and PATEL, V.C., 2005. Large eddy simulation of turbulent open-channel flow with free surface simulated by level set method. *Physics of Fluids*, **17**(2), 1-12.

ZEMAN, O. and JENSEN, N.O., 1987. Modification of turbulence characteristics in flow over hills. *Quarterly Journal - Royal Meteorological Society*, **113**(475), 55-80.

APPENDIX A

BARCHAN DUNE FIELD AND EXPERIMENTAL MORPHOLOGICAL DATA

Author	Dune No.	DIMENSIONS					
		windward length (Lw)	slipface length (Ls)	Averaged Horn Length (Lh)	Total Length (Lt)	Total horn width (W)	Slipface height (H)
Hastenrath (1967)	26	26.3	11.3		37.6	56.5	6
	25	22	5.6		27.6	33.4	3
	23	27.5	9.8		37.3	49	5.2
	21	25	8.3		33.3	46.8	4.4
	5	20	5.3		25.3	35.5	2.8
	3	17	2.7		19.7	20.4	1.4
	2	18	5.3		23.3	29	2.8
	1	18	4.9		22.9	30	2.6
	40	16	3		19	23.5	2.1
	40B	16	3.2		19.2	21.5	1.7
	40A	14	1.9		15.9	15.4	1
	8	24	6		30	37.5	3.2
	7	17.5	4.5		22	28.5	2.4
	6	18	4.6		22.6	27.2	2.4
	18	17	4.7		21.7	29.3	2.5
	28	20	5.4		25.4	31	2.9
	19	22	5.9		27.9	40.8	3.1
	17	35	9.5		44.5	69.7	5
	28B (dune complex)	18	1.5		19.5	10.6	0.7
	32 (dune complex)	29	6.3		35.3	37.6	3.3
	30 (dune complex)	45	4		49	13.5	2.1
	31 (dune complex)	54	4		58	20	2.1
	29 (dune complex)	31	9.7		40.7	37.1	5.1
	12	28	8.5		36.5	49.9	4.5
	11	30	8.6		38.6	38.5	4.6
	10	27	7.7		34.7	44.8	4.1
	9	29	7.5		36.5	41	4
	116	23.6	6.8		30.4	38.4	3.6
	114	30	9		39	41.6	4.8
	112	25	5.5		30.5	32	2.9
	113	29	7.6		36.6	42	4
	115	23	9.8		32.8	37	5.2
	110	28	9.4		37.4	44.1	5
	111	20	5.1		25.1	28.7	2.7
	109	22	7.2		29.2	36.7	3.8
	108	28	7.2		35.2	48.2	3.8
	117	25	7.2		32.2	42.2	3.8
	118	28	8.5		36.5	47.2	4.5
	31	10	3.5		13.5	21.8	1.9
	124	16.5	0.7		17.2	12.3	0.4
	125	28	8.6		36.6	47	4.6
	126	23	5.5		28.5	35	2.9
	127	25	6.3		31.3	39.8	3.3
	128	23	6.6		29.6	37.4	3.5
	129	28	8.1		36.1	48.8	4.3
	130	27	7		34	46.9	3.7
	131	27	7.1		34.1	40	3.8
	132	26	4.1		30.1	33	2.2
	133	27	5.8		32.8	40.7	3.1
	134	32	9.4		41.4	51.5	5
	134A	18	2.3		20.3	18	1.2
	107	24	6.3		30.3	35.4	3.3
	106	24	6.7		30.7	38.4	3.5
	27	23.7	6.6		30.3	33.2	3.3
	30 (Ruth)	14.2	2.2		16.4	20	1.1
	22 (Laura)	26.2	5.2		31.4	30	2.6
	(regina)	13.4	2.6		16	21	1.3
	(rosa)	12.1	1.2		13.3	11	0.6
	20 (marie)	29.4	10		39.4	59	5
	29 (Dedee)	20.2	2.4		22.6	27	1.2

Table A.1: Compilation of barchan dune morphological data acquired in the field.

Norris (1966)	Tule Wash Barchan				65.2272	204.216	9.38784
	Tule Wash Barchan				61.5696	202.692	9.32688
	Tule Wash Barchan				54.5592	210.312	10.48512
	Tule Wash Barchan				59.436	219.456	10.24128
	Tule Wash Barchan				62.1792	220.3704	10.42416
	Tule Wash Barchan				78.6384	188.976	10.45464
	Tule Wash Barchan				73.152	184.404	10.2108
	Tule Wash Barchan				61.8744	170.688	9.7536
	Tule Wash Barchan				60.3504	176.784	10.2108
	Tule Wash Barchan				60.96	163.068	10.0584
	Tule Wash Barchan				60.96	172.212	9.84504
	Tule Wash Barchan				64.6176	163.068	11.21664
	Tule Wash Barchan				57.912	170.688	10.3632
	Tule Wash Barchan				54.864	162.4584	10.9728
	Tule Wash Barchan				62.484	158.496	9.87552
Hastenrath (1987)	1	21.5	6.2	20.5	48.2	37	3.9
	2	14.8	3.3	13.5	31.6	20.5	2.1
	4	17.7	4.2	20	41.9	26.5	2.7
	8	19.6	5	23.5	48.1	29.5	3.1
	25	15.5	3.5	14.5	33.5	23	2.2
	27	25.5	6.1	26.5	58.1	42	3.8
Long & Sharp (1964)	1	79.248			121.92	198.12	7.9248
	4	76.2			144.78	152.4	7.0104
	6	97.536			187.452	129.54	6.7056
	7	33.528			88.392	45.72	2.7432
	10	48.768			82.296	213.36	7.9248
	11	48.768			156.972	115.824	7.62
	12	33.528			65.532	50.292	3.3528
	13	73.152			213.36	198.12	12.192
	14	53.34			109.728	85.344	6.4008
	15	60.96			103.632	56.388	6.096
	16	70.104			91.44	45.72	3.9624
	20	85.344			137.16	114.3	6.4008
	21	67.056			176.784	167.64	7.3152
	22	36.576			67.056	51.816	3.3528
	24	100.584			164.592	152.4	8.2296
	26	33.528			71.628	60.96	4.572
	27	96.012			179.832	109.728	8.2296
	28	51.816			91.44	42.672	4.2672
	29	108.204			185.928	251.46	7.62
	30	36.576			65.532	41.148	3.048
	34	76.2			144.78	83.82	6.096
	45	35.052			62.484	54.864	4.2672
Sauermann et al. (2000)	1	30	7	32.45	69.4	49.4	3.2
	2	32	6.7	24.7	63.4	37.9	3.5
	3	39.2	5.5	23.1	67.8	40.3	3.1
	4	55.5	13.3	65.6	134.4	90	7.3
	5	41.6	11.4	40.2	93.2	78.5	6.4
	6	29	7	21.65	57.7	38.9	3
	7	60.5	17	59.1	136.6	96.3	8.5
	8	34	4.5	9.15	47.6	28.5	2.3
Khalaf & Al-Ajmi (1993)	1	91	16.3	42.3	137	54	7
	2	44	4.6	21.8	70	43.5	2.8
	3	36.5	5.3	23.8	63	40	3.2
	4	75	7	36.3	146	65	3.3
	5	44	9	23	67	44	3.8
	6	25.2	3.6	17.9	39.5	34	2.3
	7	18.2	3.1	7.7	24	15.7	1.8
	8	51	9	34.5	88	52	5
	9	46	2.8	11	52	26	1.9
	10	36	3.4	10.9	41	25	2

Table A.1 (continued from previous page)

Wang et al. (2007)	B1			14.6735		49.044	3.773
	B2	19.477		5.292		19.49	1.961
	B3	30.426		38.417		53.82	2.901
	B4	37.577		36.6055		53.372	2.834
	B5	50.097		12.823		31.776	2.159
	B6	29.742		25.2135		75.019	3.976
	B7	57.254		15.4715		33.004	1.879
	B8	28.366		15.02		27.031	1.868
	B9	72.588		61.208		75.858	6.139
	B10	40.277		54.283		91.065	3.795
	B11	114.057		37.4235		90.24	4.098
	B12	59.238		99.4345		128.592	6.931
	B13	28.366		15.02		27.031	1.868
	B14	40		38.058		48.909	2.462
	B15	58.133		69.764		98.211	5.853
	B16	68.832		103.1335		125.311	6.754
	B17	74.939		18.3415		66.568	1.509
	B18	29.83		21.04		30.408	1.699
	B19	22.268		17.8195		18.153	1.956
	A1	38.474		36.448		48.998	3.562
	A2	68.71		53.312		52.551	4.513
	A3	44.035		44.1765		52.184	4.758
	A4	62.601		66.6175		74.436	6.363
	A5	94.394		85.5785		165.71	9.382
	A6	48.431		16.3595		22.602	2.881
	A7	84.384		30.0695		49.046	4.910
	A8	65.906		46.8225		77.33	5.778
Finkel (1959)	1	18		28.9		33.5	3.12
	2	19		26.1		33.1	2.51
	3	15.5		18		23.4	2.53
	4	9		9.2		11.4	1.37
	5	17		33.3		37.7	3.33
	6	15		23.5		24.9	3.34
	7	20		22.1		26.5	2.31
	8	21		29		39.2	3.12
	9	25		31.8		42.1	3.3
	10	26		30.4		53.3	3.77
	11	30		42.8		50.4	4.67
	12	27		38.8		55.5	4.57
	13	23.5		33		42.8	4.24
	16	36		44.6		66	5.3
	17	40		43.5		59.5	4.69
	18	22		19.2		32.5	1.47
	19	23		30.7		37.4	3.34
	20	29		50.1		51.7	6
	21	25		44.5		45.3	4.1
	22	29		47.6		53.5	5.07
	23	19		24		29.6	2.42
	25	20		28.1		34.8	2.85
	26	30		59.2		61.4	5.44
	27	26		35.7		45.9	3.77
	28	21		23.5		32.6	2.89
	29	14		14.6		21.8	2.55
	30	16		15.8		21.3	1.56
	31	19		32.3		37.8	3.34
	32	20		19.6		25.7	2.05
	33	23		37.2		54	3.66
	40	14		18.6		27.5	2.56
	41	14		16.4		22.8	2.09
	42	13					1.64
	43	25		26.8		40.7	2.92
	44	16		13.2		21.1	1.72
	45	37		39.1		24.2	4.17
	46	22		17		29	1.58
	47	21		30		33.4	3.13
	48	21		21.7		30.3	2.71
	49	27		37.7		44.5	3.82
	50	31		33.2		40.4	3.75
	51	27		27.7		38.4	3.57
	52	18		17.3		22.8	2.23
	53	22		23.2		32.4	2.85
	54	19		24.2		30.1	3.08

Table A.1 (continued from previous page)

APPENDIX B

CONVERTING A 2-D CONTOURED IMAGE INTO A 3-D INTERPOLATED SURFACE

1. Within ArcMap, open a new worksheet and add the contoured image (Figure B.1) by Hersen (2004) as a tiff (abbreviation for 'Tagged Image File Format').

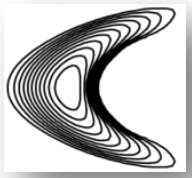

Figure B.1. An image of an idealized barchan dune with contour lines (Hersen, 2004).

2. Browse to ArcCatalog (a software component of ArcGIS) to create a new Feature-Class within a Personal Geodatabase Feature-Class (note that a Feature-Class houses one type of data, such as lines, points, or polygons, and may exist independently or within a Geodatabase) (Figure B.2).

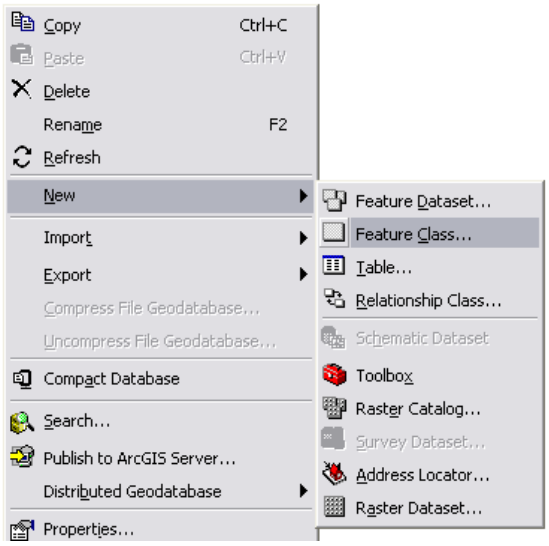

Figure B.2: A screen capture illustrating how to create a new feature class within ArcCatalog. Right-click in the right-hand window to display the menu above.

3. Return to ArcMap and start an ArcEditor session (an editor component within ArcMap) (Figure B.3), selecting the new Feature-Class as the 'target'. Begin digitizing the contours in the image. These polylines will be stored in the Feature-Class (Figure B.4).

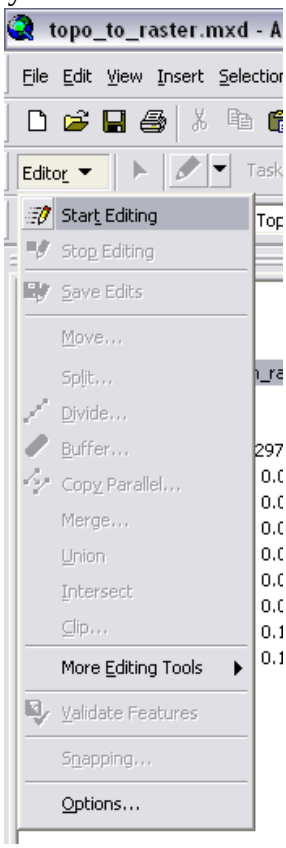

Figure B.3: A screen capture of how to begin a editor session within ArcGIS.

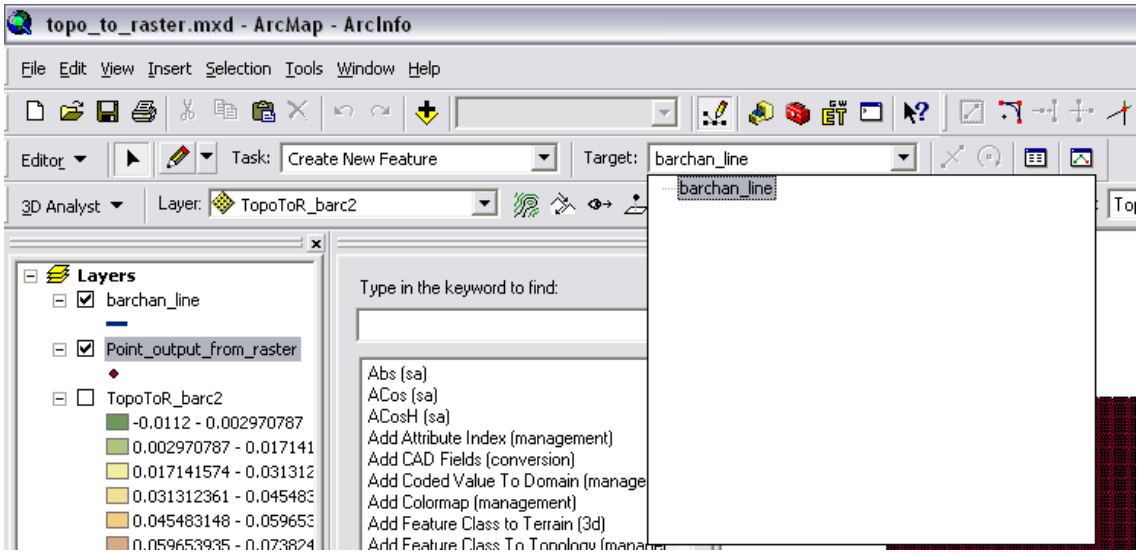

Figure B.4: A screen capture of how to specify the target feature class to house the data the user is creating or editing.

4. The final contour images will appear as in Figure B.5.

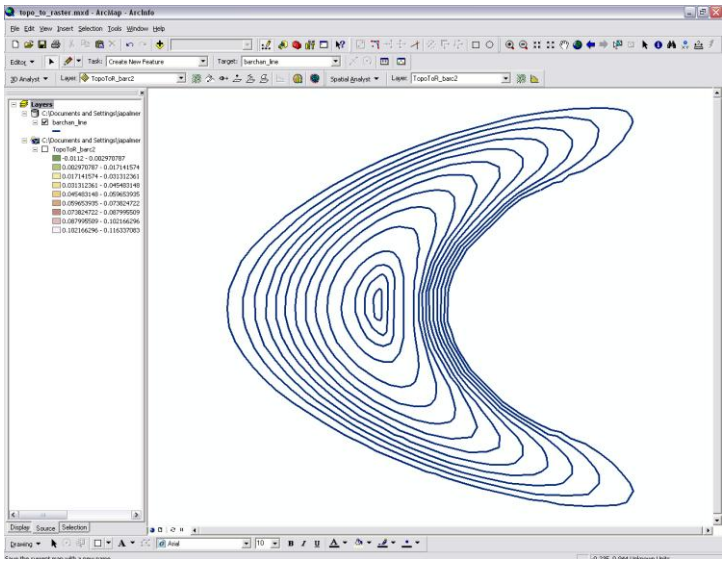

Figure B.5: Screen capture of ArcGIS Session depicting digitized contour lines.

4. Returning to ArcCatalog, create a new field, "vert" (data-type is float), within the polyline Feature-Class to accommodate assigned vertical values of each contour.
    a. To do this, open ArcCatalog and select the Feature-Class. Click on the "Preview" tab. On the bottom is a drop down menu. Select "Table" (Figure B.6).

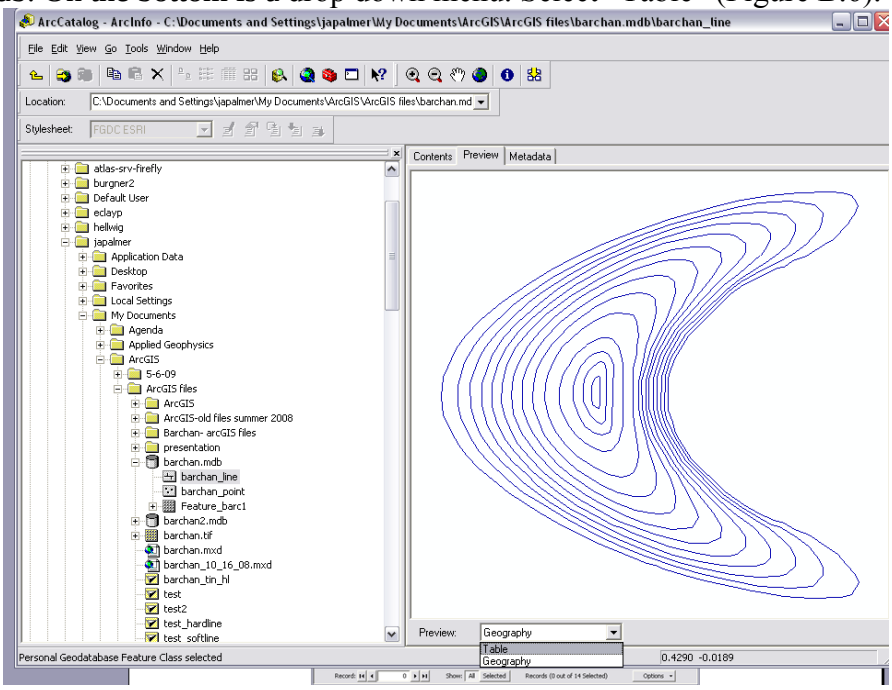

Figure B.6: A screen capture illustrating how to view the data in table format to generate a new field.

b. Once you are looking at the table, maximize ArcCatalog so you can see the options menu. Select “Add Field” (Figure B.7).

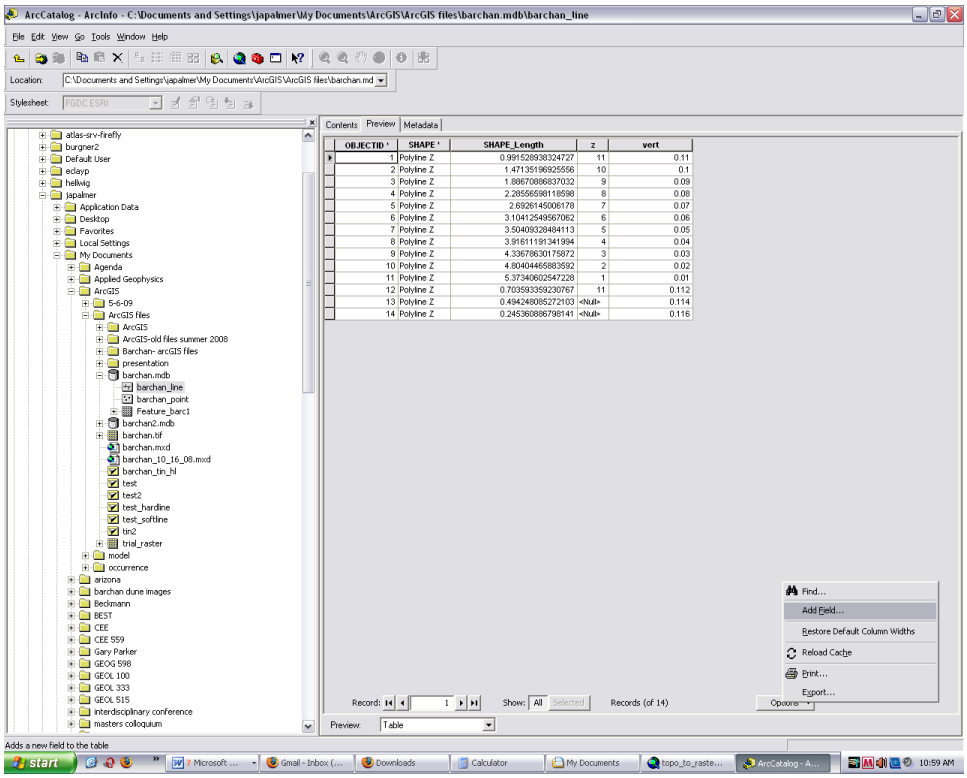

Figure B.7: A screen capture of ArcCatalog showing the Feature-Class in table format. The options tab opens a menu where you can create a new field - "Add field".

5. Back in ArcMap, open the attributes table of the Feature-Class and enter the values for “vert” (Figure B.8).

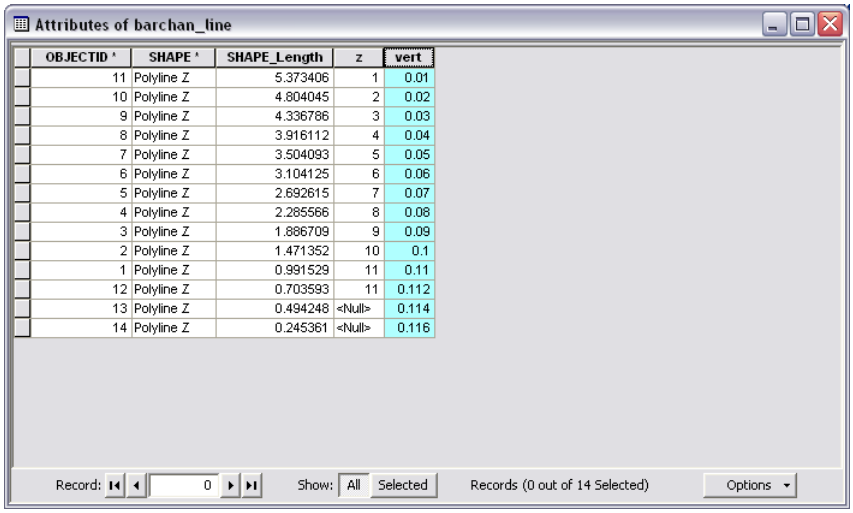

Figure B.8: A screen capture of the newly created field "Vert" with entered values representing the vertical height of each contour line.

6. Open ArcToolbox within ArcMap (Figure B.10). To do this, click on the icon at the top of the window as shown in Figure B.9.

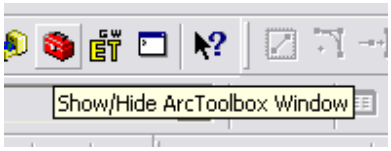

Figure B.9: The red toolbox opens "ArcToolbox".

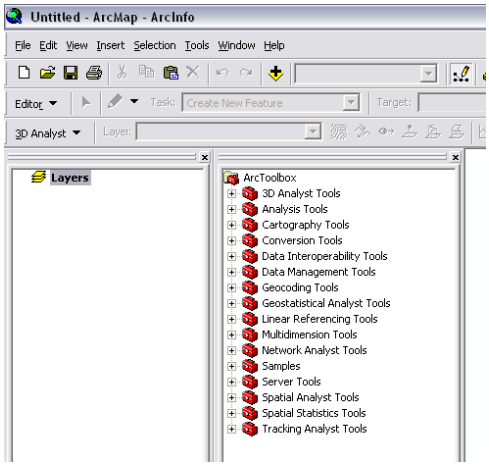

Figure B.10: A screen capture of ArcToolbox embedded in ArcMap.

7. Click on the bottom tab “Index” (Figure B.11).

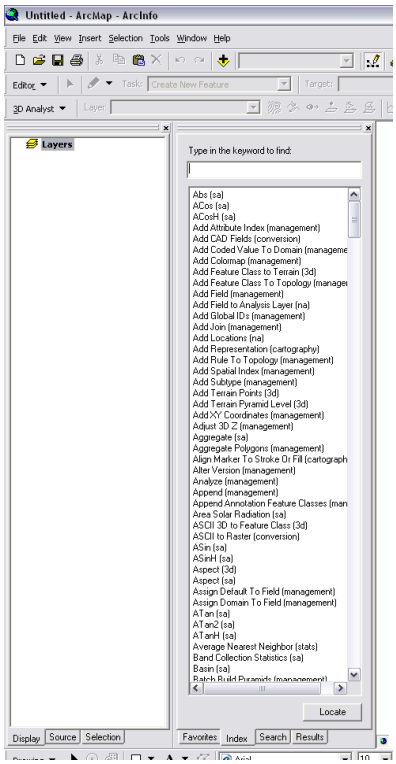

Figure B.11: ArcToolbox Index.

8. Type in “topo to raster” in ArcToolbox to create a 3D surface (Figures B.12 and B.13). Select the polyline Feature-Class for “Input feature data”. Keep default output cell size. You can change the name and location of the output raster file.

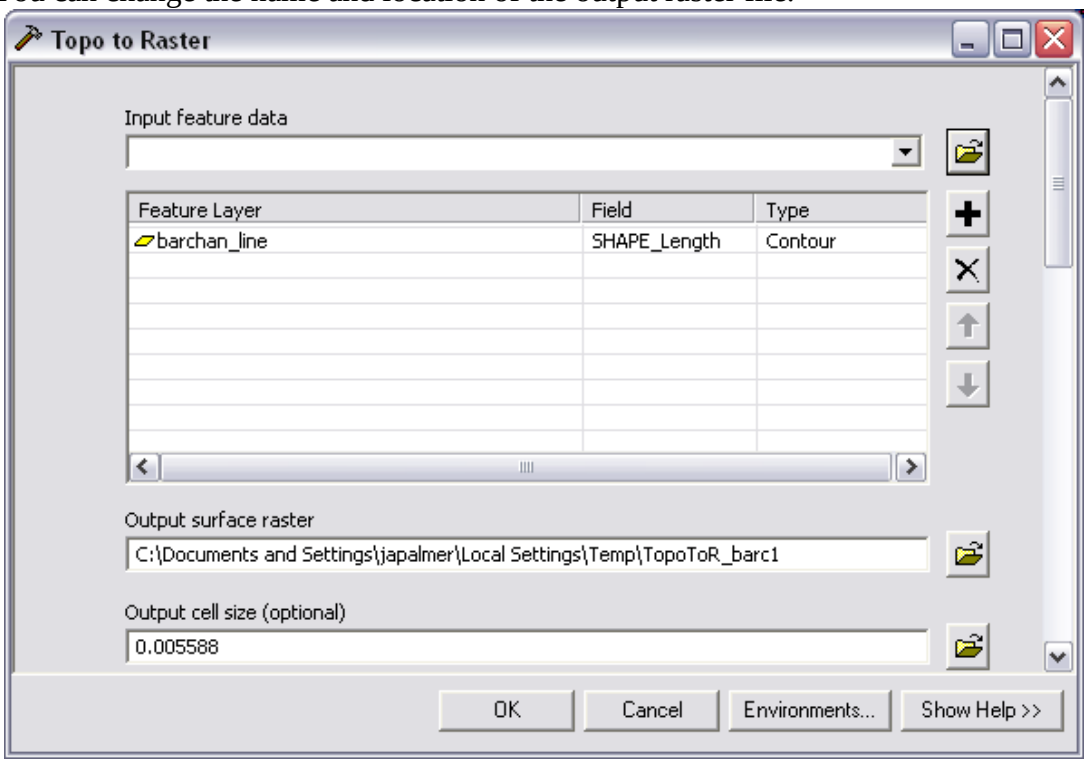

Figure B.12: A screen capture of the ArcToolbox “Topo to Raster” tool.

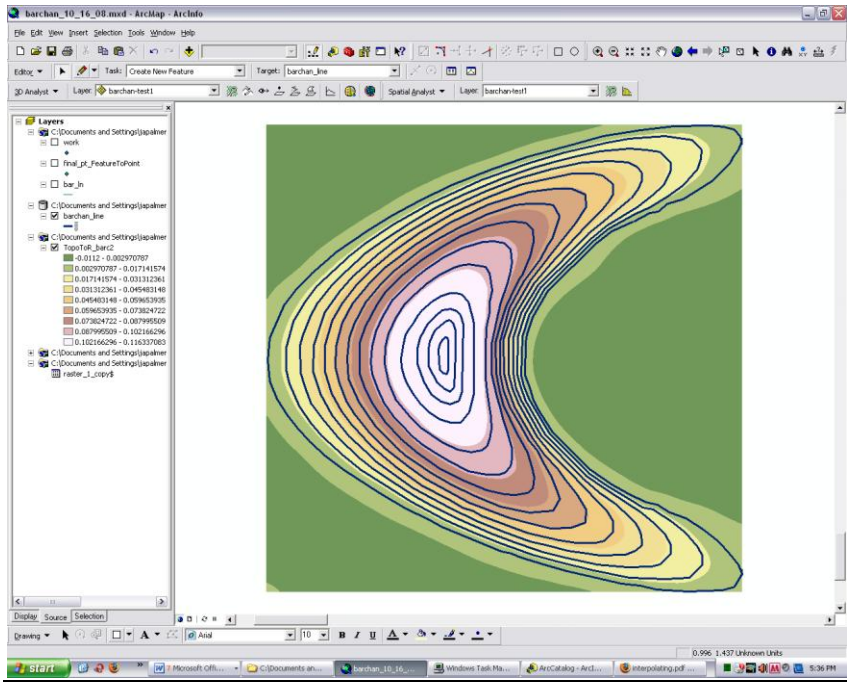

Figure B.13: An example of the contour polyline Feature-Class superimposed on the newly generated Raster (mult-colored rectangle).

9. Use “raster to point” tool in ArcToolbox to generate an x,y,z point file (Figures B.14 and B.15).

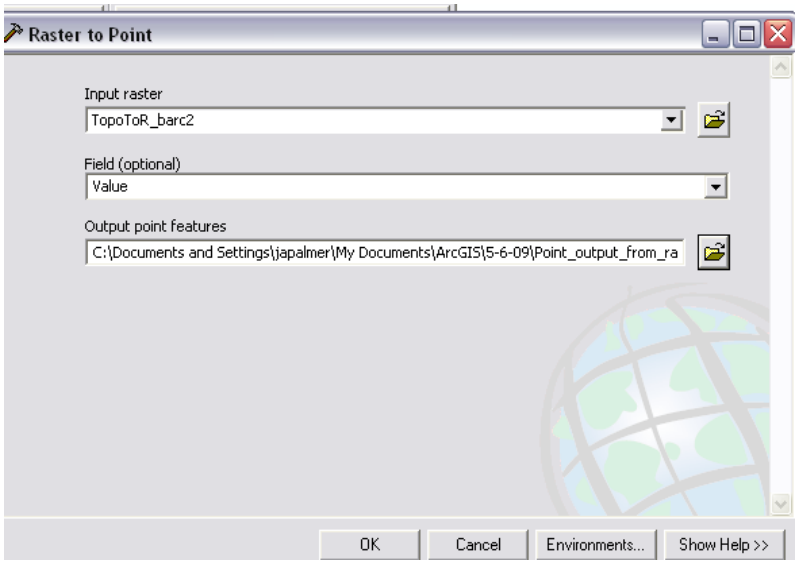

Figure B.14: A screen capture of the ArcToolbox "Raster to Point" tool.

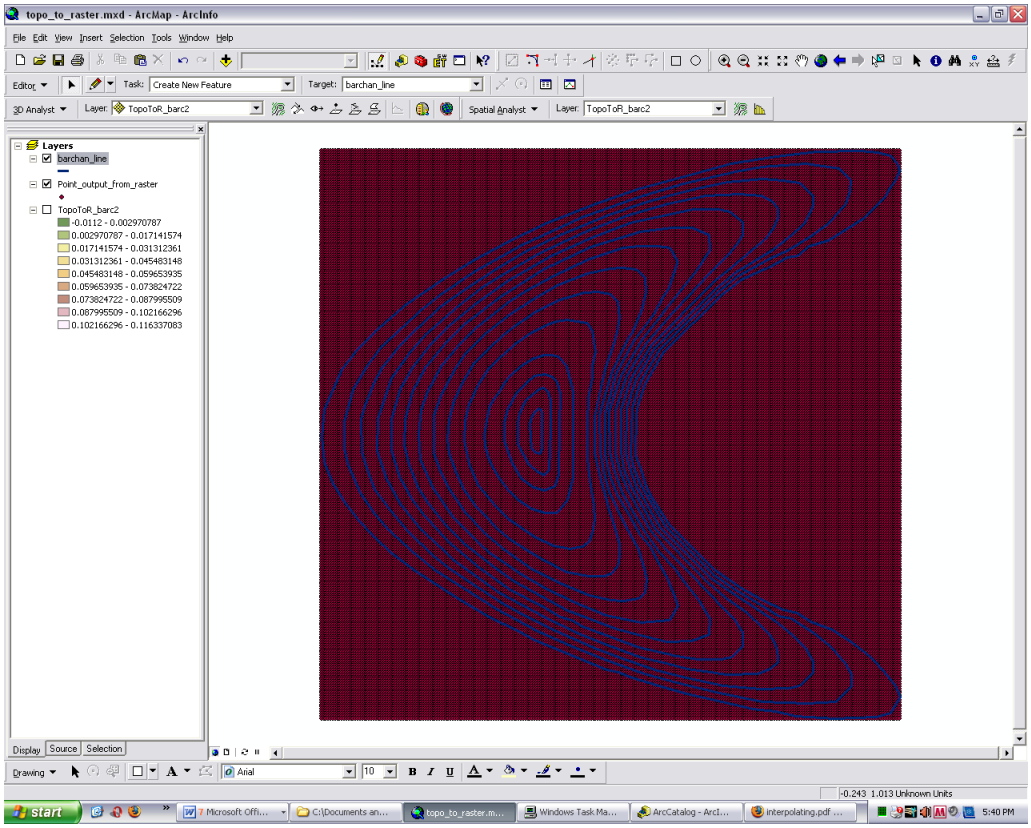

Figure B.15: An example of the raster converted into a grid of points (red dots). The contour polylines (blue) are superimposed above the point grid.

9. To assign x and y coordordinates, go to the ArcToolbox “Favorites Tab” located at the bottom of the screen, next to the index tab. Click on Data management tools. Click on

features. Select “add xy coordinates”. This function will assign each point an x and y position. The point will retain its z position and will have a name such as “Grid Code”.

10. Export the point file as a .dbf or .csv file (Figure B.16).

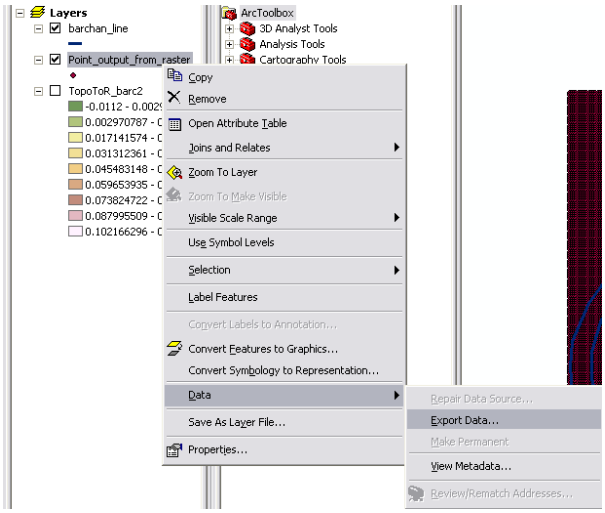

Figure B.16: A screen capture of how to locate “export data”: Right-click on the point file, browse to “Data”, and select “Export Data”.

11. Convert the xyz point file into a matrix grid.

12. Import the matrix grid into the 3D printer format (Z-Print is the program).

APPENDIX C

PRODUCING PHYSICAL BARCHAN DUNE MODELS

Contact: Darren Stevensen
Phone: 217-244-5669
Website: http://www.itg.uiuc.edu/printing/3D/

1. Convert the barchan dune 3-D point file (x,y,z) into a grid/matrix.
2. Import into z-print, the 3-D printer program.
3. Adjust the barchan dune model to the desired dimensions.
4. To produce multiple barchan dune models, copy the model and paste it. Move it above or below the first model within the available volume (i.e. stacking the models).
5. Begin the print job and remove the barchan models the next day.
6. Carefully remove the models from the 3-D printer (Figure C.1). This requires delicacy so as not to damage the fragile unconsolidated plaster. To remove the models there is a combination of vacuuming the plaster around the model (Figure C.2), and using a sturdy piece of cardboard to lift the model out of the printer (Figures C.3 and 4).
7. Place the model in a hood with a vacuum attached to the hood, and use pressurized air to blow off any remaining plaster (Figure C.5).
8. The barchan dune models are now ready to be adhered (Figure C.6)
9. Move the models to another hood (for chemicals) and glue them using a glue-Xylene mixture (Figure C.7).

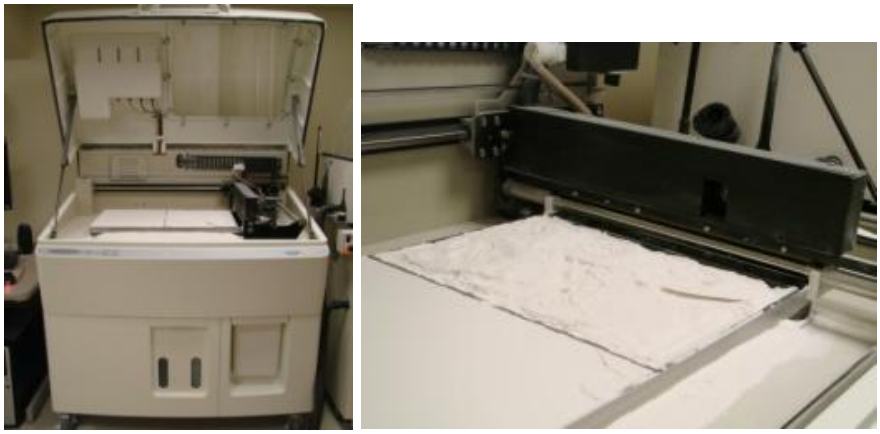

Figure C.1: The 3-D printer featuring barchan dune models on the right-hand side.

Figure C.2: Vacuuming the plaster around the dune model.

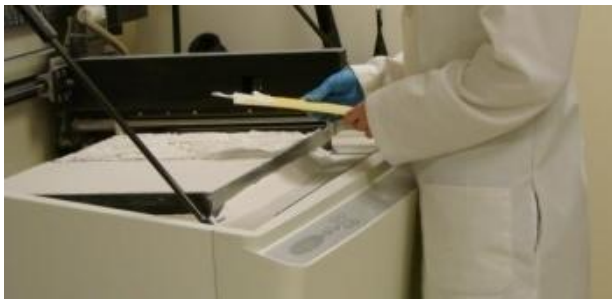

Figure C.3: Removing one barchan dune model with a small and rigid piece of cardboard.

Figure C.4: Demonstrating how to remove the barchan dune with cardboard. Wedge the cardboard piece underneath the strongest section of the barchan dune (i.e. not the horns).

Figure C.5: Remove the excess plaster with (a) a brush and (b) pressurized air.

Figure C.6: The barchan dune plaster models are ready to be glued.

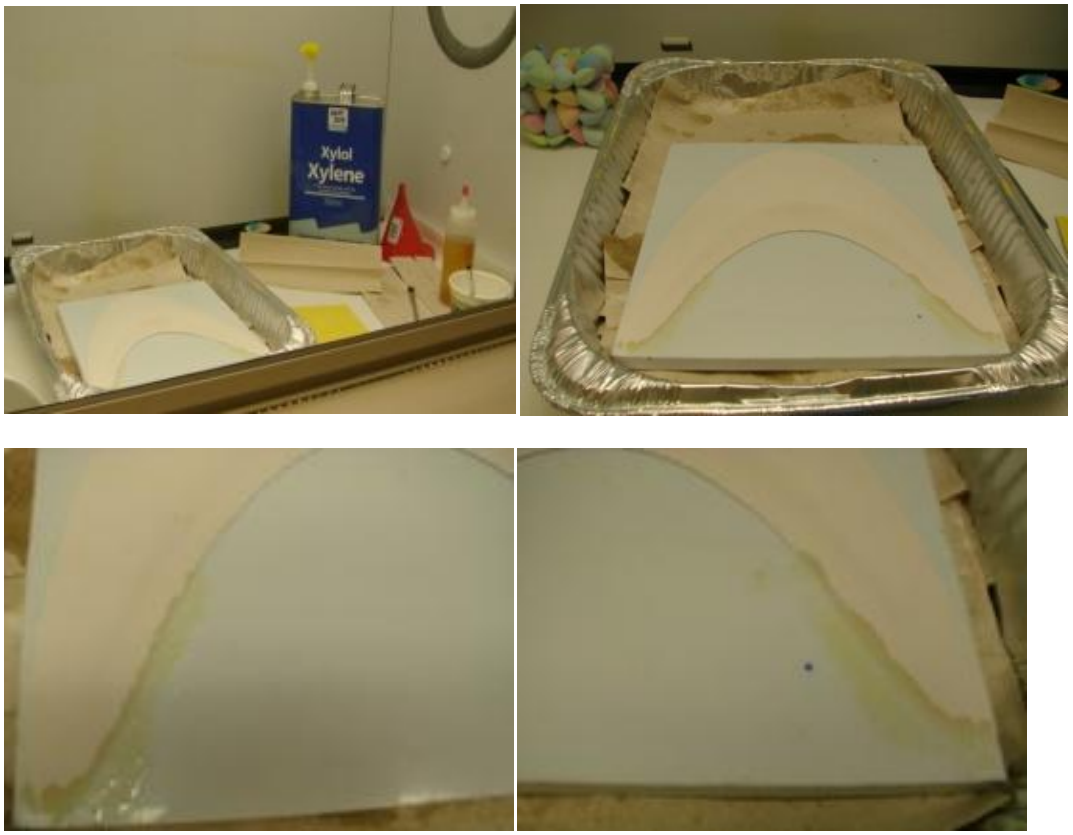

Figure C.7: A mixture of Elmer's glue and Xylene are added to the surface of the barchan dune. The barchan dune is first placed on a polypropylene board and adhered at the horns and the toe to prevent warping. Let the barchan dune models dry for 6 hours and remove from the boards with a razor blade.

APPENDIX D

RHODAMINE-PAINT MIXTURE FORMULA AND DIRECTIONS

Formula

3 grams Rhodamine 6G

10 ml Ethanol

500 ml transparent acrylic paint (water soluble)

Safety

Wear a lab coat, face mask, gloves and goggles. Work under a flume hood. Rhodamine 6G is toxic if ingested. Rhodamine B is a carcinogen.

Directions

1. Solve the Rhodamine 6G in Ethanol, maintaining a ratio of 3 grams to 10 ml.
2. The solution will turn bright pink. The Rhodamine will dissolve quickly and easily into the Ethanol.
3. Add the solution to the acrylic paint (preferably, keep the paint in a paint can). The Rhodamine will clump and be difficult to solve in the paint.
4. Bring the paint can to a hardware store. Have someone at the paint department mix the paint for you in the mixing machine.
5. Apply coats of Rhodamine-paint mixture using a foam brush for best results.

Notes

Efficiency can range from 30% and higher.

Source: La Vision (www.lavision.de)